ASSESSMENT OF THE WEAR AND CORROSION BEHAVIOUR OF TITANIUM CARBIDE-STAINLESS STEEL COMPOSITES

by

Chukwuma C. Onuoha

Submitted in partial fulfilment of the requirements
for the degree of Doctor of Philosophy

at

Dalhousie University
Halifax, Nova Scotia
June 2013

DALHOUSIE UNIVERSITY

DEPARTMENT OF PROCESS ENGINEERING AND APPLIED SCIENCE

The undersigned hereby certify that they have read and recommend to the Faculty of Graduate Studies for acceptance a thesis entitled "ASSESSMENT OF THE WEAR AND CORROSION BEHAVIOUR OF TITANIUM CARBIDE–STAINLESS STEEL COMPOSITES" by Chukwuma C. Onuoha in partial fulfilment of the requirements for the degree of Doctor of Philosophy.

Dated: June 17, 2013

External Examiner: _____

Research Co-Supervisors: _____

_____

Examining Committee: _____

_____

Departmental Representative: _____

DALHOUSIE UNIVERSITY

DATE: June 17, 2013

AUTHOR: Chukwuma C. Onuoha

TITLE: ASSESSMENT OF THE WEAR AND CORROSION BEHAVIOUR OF TITANIUM CARBIDE-STAINLESS STEEL COMPOSITES

DEPARTMENT OR SCHOOL: Department of Process Engineering and Applied Science

DEGREE: PhD CONVOCATION: October YEAR: 2013

.....

Signature of Author

DEDICATION

This thesis is dedicated to my loving wife, Irene, and my son Francis, for their patience, support and endurance throughout this programme.

Also I would dedicate this thesis to my supervisors, Dr. Kevin Plucknett and Dr. Georges Kipouros for their personal support and encouragements.

TABLE OF CONTENTS

LIST OF TABLES xi

LIST OF FIGURES xiv

ABSTRACT xxix

LIST OF ABBREVIATIONS AND SYMBOLS USED xxx

ACKNOWLEDGEMENTS xxxi

1 Introduction 1

2 Literature Review 4

2.1 Cermets 4

2.2 Titanium Carbide (TiC) use in Cermets 5

2.2.1 Titanium Carbide Powder Fabrication 8

2.3 Stainless steels 8

2.3.1 Classification of Stainless Steels 9

2.3.2 Austenitic Stainless Steels 9

2.3.3 Ferritic Stainless Steels 10

2.3.4 Martensitic and Precipitation Hardening Stainless Steels. 10

2.3.5 Duplex Stainless Steels 10

2.4 Processing stages for cermet fabrication 11

2.4.1 Powder Pressing 11

2.4.2 Sintering 15

2.4.3 Liquid Phase Sintering 20

2.4.4 Melt Infiltration 25

2.5 Characterisation and Properties of Ceramic-Metal Composites 27

2.5.1 Wear 27

2.5.2 Adhesive Wear 29

2.5.3 Abrasive Wear 33
2.5.4 Fatigue Wear 37
2.6 Brief Overview of the Wear Behaviour of Cermets 39
2.7 Corrosion 42
2.7.1 Uniform Corrosion 43
2.7.2 Galvanic Corrosion 43
2.7.3 Crevice Corrosion 44
2.7.4 Pitting Corrosion 46
2.7.5 Intergranular Corrosion 49
2.7.6 Selective Leaching 52
2.7.7 Erosion-Corrosion 53
2.7.8 Stress Corrosion Cracking (SCC) 55
2.7.9 Hydrogen Embrittlement 56
2.8 Corrosion Prevention 56
2.9 Brief Overview on the Corrosion Behaviour of Cermets 56
3 Materials and Experimental Methods 60
3.1 Raw Materials 60
3.1.1 Titanium Carbide and Stainless Steel Powders 60
3.2 Experimental Procedure 63
3.2.1 Sample Preparation 63
3.2.1.1 Powder preparation and uniaxial pressing 64
3.2.1.2 Isostatic Pressing 65
3.2.1.3 Melt Infiltration 66
3.2.1.4 Density Measurement 67
3.2.1.5 Sample Surface Preparation 67

3.2.2 Hardness and Indentation Fracture Resistance Evaluation 68
3.2.3 Reciprocating Wear Testing 69
3.2.4 Electrochemical Testing 72
3.2.4.1 Open Circuit Potential 75
3.2.4.2 Potentiodynamic Polarisation 75
3.2.4.3 Tafel Extrapolation 78
3.2.4.4 Cyclic Polarisation 79
3.2.4.5 Potentiostatic Polarisation 82
3.2.5 Post Corrosion Chemical Analysis 83
4 The Reciprocating Wear Behaviour of TiC-304L Stainless Steel Composites Prepared by Melt Infiltration 84
4.1 Abstract 84
4.2 Introduction 85
4.3 Experimental Procedure 86
4.3.1 Sample Preparation 86
4.3.2 Materials Characterisation Procedure 87
4.3.3 Reciprocating Wear Test Procedure and Characterisation 87
4.4 Results and Discussion 89
4.4.1 Densification Behaviour and Microstructure of the Composites 89
4.4.2 Cermet Hardness and Indentation Fracture Resistance 92
4.4.3 Reciprocating Wear Behaviour 94
4.4.4 Microstructural Observations Following Reciprocating Wear 99
4.4.5 Chemical Composition of the Tribolayer 114
4.5 Conclusions 118
4.6 Acknowledgements 119

5 The Effects of Grain Size on the Reciprocating Wear Behaviour of TiC-316L Stainless Steel Cermets 120
5.1 ABSTRACT 120
5.2 Introduction 121
5.3 Experimental Procedure 123
5.3.1 Sample Preparation 123
5.3.2 Materials Characterisation Procedure 123
5.3.3 Reciprocating Wear Test Procedure and Characterisation 125
5.4 Results and Discussion 125
5.4.1 Characterisation of the As-Fabricated Cermets 125
5.4.3 Microstructural Observations Following Reciprocating Wear 137
5.4.4 Chemical Composition of the Tribolayer 144
5.5 Conclusions 148
5.6 Acknowledgements 150
6 Corrosion Behaviour of TiC-304L Stainless Steel Cermets in a Synthetic Saline Solution 151
6.1 ABSTRACT 151
6.2 Introduction 152
6.3 Experimental procedure 154
6.3.1 Sample Preparation and Characterisation 154
6.3.2 Electrochemical Testing 154
6.4 Results and Discussion 156
6.4.1 Sample Analysis Following Melt Infiltration 156
6.4.2 Electrochemical Measurements 158
6.4.3 Post Corrosion Chemical Analysis 168
6.4.4 Post-Corrosion Microstructural Characterisation 171

6.5 Conclusions 177
6.6 Acknowledgements 178
7 The Effects of Grain Size on the Corrosion Behaviour of TiC-316L Stainless Steel Cermets in a Synthetic Seawater Solution 179
7.1 ABSTRACT 179
7.2 Introduction 180
7.3 Experimental Procedure 182
7.3.1 Raw Materials and Cermet Processing 182
7.3.2 Cermet Characterization 182
7.3.3 Electrochemical Testing 183
7.4. Results and Discussion 184
7.4.1 Microstructural Analysis 184
7.4.2 Electrochemical Measurements 188
7.4.3 Post Corrosion Chemical Analysis 201
7.4.4 Post-Corrosion Microstructural Characterisation 205
7.5 Conclusions 211
7.6 Acknowledgements 212
8 The Corrosion Behaviour of TiC-Stainless Steel Cermets in a Synthetic Seawater Solution 213
8.1 ABSTRACT 213
8.2 Introduction 214
8.3 Experimental procedure 216
8.3.1 Sample Preparation and Characterisation 216
8.3.2 Electrochemical Testing 218
8.4 Results and Discussion 220
8.4.1 Cermet Characterisation 220

8.4.2 Electrochemical Measurements 223
8.4.3 Post Corrosion Chemical Analysis 240
8.4.4 Corroded Sample Characterisation 246
8.5 Conclusions 255
8.6 Acknowledgements 255
9 Conclusions and Recommendations for Future Work 257
9.1 Performance Ranking of Cermets 260
9.2 Contributions to Original Thought 260
9.3 Recommendations for Future Work 263
REFERENCES 264
Appendix A: Materials Characterisation 281
Appendix B: Electrochemical Data 288
Appendix C: Reciprocating Wear Data 294

LIST OF TABLES

Table 2.1: Typical reactions involved in the consolidation of TiC via powder metallurgy routes [23,28]. 8

Table 2.2: Table showing galvanic series in seawater [46]. 44

Table 3.1: Composition of the TiC starting powder (obtained from Pacific Particulate Materials Ltd). 60

Table 3.2: Compositions of the raw stainless steel powders [97]. 61

Table 4.1: The mean grain size for the TiC-304L cermets as a function of steel content; values were determined for a minimum of 300 grains, using the lineal intercept method [125]. 91

Table 4.2: An example of the tribolayer composition determined using EDS, for TiC-30 vol. % 304L, after dry sliding for 120 minutes under an 80 N load. 116

Table 5.1: The mean grain size for fine and coarse grained TiC-316L cermets as a function of steel content; values were determined for a minimum of 300 grains, using the lineal intercept method [125]. 127

Table 5.2: Typical tribolayer composition (in wt %) determined using EDS analysis (from images of Figure 5.14), for fine and coarse grained TiC-20 vol. % 316L cermets, after sliding for 2 hours under 20 and 80N load. 148

Table 6.1: Typical 304L stainless steel alloy composition. 155

Table 6.2: Open circuit potentials for the TiC-304L cermets and pure 304L stainless steel. 159

Table 6.4: Extrapolation of the pitting potential from cyclic polarisation curves. 166

Table 7.1: Open circuit potential values determined for the fine- and coarse-grained TiC-316L cermets; values are an average of 4 repeat tests (standard deviation values are given in parenthesis). 189

Table 7.2: CorrWare derived results for the Tafel extrapolation procedure, following electrochemical measurements. 191

Table 7.3: A comparison of Tafel derived corrosion rates determined for various high-density, thermal spray cermet materials [198-199], TiC cermets prepared with a 304L binder [196], and the materials developed in the present study*. 194
Table 7.4: Electrochemical results following potentiodynamic polarisation showing critical current density and minimum current density in the pseudopassive region of fine and coarse-grained TiC based cermets. 197
Table 7.5: EDS analysis of the TiC-316L cermets showing a high amount of TiC and oxygen following potentiostatic polarisation testing. 200
Table 8.1: Nominal compositions for the stainless steel grades used in the present work [97]. 217
Table 8.2: OCP values determined for the cermets as a function of the steel binder content. Each value is the mean of 10 repetitions (standard deviation shown in parentheses). 226
Table 8.3: OCP values determined for the 'pure' steels. Each individual value is the mean of 10 repetitions (standard deviation values are shown in parentheses). 226
Table 8.4: The Tafel-derived values of i_{corr} and E_{corr} determined for the cermets and 'pure'steels. The presented values are the mean for 4 repetitions (standard deviation values are shown in parentheses). 227
Table 8.5: The measured corrosion rates for the 'pure' steels used in the present work, based on Tafel extrapolation of potentiodynamic polarization data. 229
Table 8.6: Electrochemical results following potentiodynamic polarisation, showing the critical current density, i_{crit}, and the minimum current density in the pseudopassive region, i_{pass}, for the cermets. 233
Table 8.7: Extrapolation of the pitting and protection potentials from the cyclic polarisation curves. 237
Table 8.8: The applied voltages used for potentiostatic polarisation testing of the TiC-stainless steel cermets and the 'pure' stainless steel. 240

Table 9.1: Performance ranking of all the studied cermets.....262

Table 10.1: Mean grain size and sintering conditions of all the studied cermets. 286

Table 10.2: EDS chemical composition analysis (wt %) of infiltrated TiC-316L cermet with 30 vol. % steel binder content and the 316L starting powder.....287

Table 10.3: EDS chemical composition analysis (wt %) of TiC-304L cermets (cermets with 10 and 30 vol. % 304L steel binder) following potentiostatic (analysis taken from images of Figure 10.7). Evidence of higher amount of oxygen at lower binder (TiC- 10 vol. % 304L cermet) content is apparent leading to lowest passivation current density as shown in Figure 10.5.....293

Table 10.4: An example of the wear debris generation determined using EDS (analysis of Figure 10.18), for TiC- 30 vol. % 316L, after dry sliding for 120 minutes under 80N load. The wear debris contains cermets elements as well as WC from counter face sphere. 305

LIST OF FIGURES

Figure 2.1: The NaCl-type structure of TiC [22] **6**

Figure 2.2: The Ti-C phase diagram [7]. **7**

Figure 2.3: Pressure variations in uniaxial pressing due to die-wall friction and particle-particle friction, which lead to non-uniform density of the pressed compact [41] **13**

Figure 2.4: Two modes of isostatic pressing: (a) wet-bag pressing and (b) dry-bag pressing [37] **14**

Figure 2.5: Illustrative images showing the stages of microstructural change during sintering (a)Powder particles after compaction. (b) Particle coalescence and pore formation as sintering begins. (c) As sintering proceeds, the pores change size and shape [40] **16**

Figure 2.6: Schematic images of the two sphere sintering model [42] **17**

Figure 2.7: An illustrative diagram showing the various mass transport paths that provide neck growth and pore shrinkage. Surface diffusion (provides no densification) and bulk transport (gives densification) are the two transport mechanisms [43] **18**

Figure 2.8: An illustrative diagram of transport mechanisms in solid state sintering showing volume diffusion existing as bulk and surface transport mechanisms [45] **19**

Figure 2.9: A schematic diagram showing the stages of LPS processing using a mixture of two powders. The base powder remains solid during sintering and the additive powder is responsible for liquid formation [42]. **20**

Figure 2.10: Illustrative diagram showing the process of solution-reprecipitation [42] **21**

Figure 2.11: An illustrative diagram showing good (left and poor (right) wetting conditions. A low-contact angel promotes wetting, while a high contact angle resists wetting [46] **22**

Figure 2.12: An illustrative scanning electron microscopy image showing the surface of a sample where the non-wetting liquid exuded to the compact surface to form small spheres [46] **23**

Figure 2.13: An illustrative diagram showing the dihedral angle for a solid-liquid system, and the surface energy equilibrium between two intersecting solid grains with a partially penetrating liquid phase [46] **24**

Figure 2.14: An illustrative diagram showing the relationship between dihedral angle and solid-solid to solid-liquid energy ratio [47] **25**

Figure 2.15: Schematic illustration of the infiltration sequence where capillary forces pull a molten metal into the open pores of a sintered compact [42] **26**

Figure 2.16: SEM images showing complete melt-infiltration for a TiC-20 vol. % stainless steel cermet. **27**

Figure 2.17: Schematic representation of a tribosystem [51] **29**

Figure 2.18: An illustrative diagram showing contact, adhesion, material transfer due to electron transfer, and adhesive bond formation. Typically the softer or weaker material is transferred to the stronger material [51], [52] **30**

Figure 2.19: An illustrative diagram showing alternative models for the production of wear debris and deformation by adhesive contact of asperities [53]. **31**

Figure 2.20: Schematic illustration of possible mechanism of wear debris formation due to adhesive transfer [53] **32**

Figure 2.21: Schematic diagram showing formation and removal of a transfer particle [53] **32**

Figure 2.22: Schematic illustration showing two- and three-body modes of abrasive wear [53] **34**

Figure 2.23: Schematic diagram showing mechanisms of abrasive wear: microcutting, fracture, fatigue and grain pull-out [53]. **35**

Figure 2.24: Schematic diagram of abrasive wear processes as a result of plastic deformation following a cutting deformation mode [50] **36**

Figure 2.25: Schematic diagram showing the abrasive wear process as a result of plastic deformation by a ploughing mode [50] **37**

Figure 2.26: Schematic diagram showing the process of the surface crack initiation and propagation [53] **38**

Figure 2.27: Schematic diagram showing the mechanisms of wear particle formation due to growth of surface initiated cracks [53] **39**

Figure 2.28: Schematic plot showing the relationship between mechanical properties and select microstructural parameters: (a) Hardness as a function of the carbide volume fraction and grain size, and (b) fracture toughness as a function of the carbide volume fraction and grain size [62] **41**

Figure 2.29: Schematic diagram showing the various forms of Corrosion [65] **42**

Figure 2.30: An illustrative diagram showing the mechanism of crevice corrosion [67] **45**

Figure 2.31: An illustrative diagram showing an autocatalytic pitting process in a corrosion pit. The metal, M is being heavily pitted by an aerated and aggressive NaCl solution. There is rapid dissolution in the pit, while oxygen reduction takes place on the adjacent metal surfaces [93]. **47**

Figure 2.32: Illustrative diagram showing the effects of alloying elements on the resistance to pitting corrosion [34] **49**

Figure 2.33: A schematic diagram showing the crystallographic mismatch between the grain boundary area and the orderly structures within the adjacent grains [70] **50**

Figure 2.34: Schematic illustration of chromium carbide particles that have precipitated along grain boundaries in stainless steel, and the attendant zones of chromium depletion [40] **51**

Figure 2.35: Illustrative diagram showing weld decay in a stainless steel. Regions along which the grooves have formed were sensitised as the weld cooled [36] **51**

Figure 2.36: An illustrative diagram showing the disruption of a passive protective film by an erosion-corrosion process [71] **53**

Figure 2.37: Illustrative photograph showing impingement failure of an elbow that was part of a steam condensate line [33]. **54**

Figure 2.38: A photograph showing cavitation-erosion damage of a cylinder liner of a diesel engine [71]. **54**

Figure 2.39: A schematic illustration of three conditions that promote the occurrence of SCC [71]. **55**

Figure 2.40: An illustrative diagram showing relationship between the critical current density of the binder phase area versus the Co binder content for WC-Co [74]. **57**

Figure 2.41: The effect of binder content on the corrosion resistance of WC-Co cermets in 0.00294 M tannic acid solution (UFW3, UFW10, FW15 represent 3, 10 and 15 wt. % of Co content) [75]. **58**

Figure 3.1: A representative SEM image of the as-received TiC ceramic powder. **61**

Figure 3.2: Representative SEM images of the as-received steel powders**:** (a) 316L, (b) 304L and (c) 410L. **63**

Figure 3.3: Flowchart illustrating sequence involved in the preparation of cermets sample for further evaluation. **64**

Figure 3.4: Picture of the cold isostatic pressing machine used in the present study **65**

Figure 3.5: Photograph of TiC-304L cermets with aluminium holder following polishing operation, the vol. % of steel binder is indicated in each box. **68**

Figure 3.6: (a) Photograph of the UMT reciprocating wear testing system. **70**

Figure 3.7: Photograph of a Nanovea PS50 System optical profilometry used in the present study **72**

Figure 3.8: The electrochemical flat cell used in the present work, in which all the corrosion experiments are performed. **74**

Figure 3.9: The electrochemical testing potentiostat (EG & G PARC Model 273A, Princeton Applied Research, USA) used in the present work. **74**

Figure 3.10: A schematic illustration of a standard three-electrode flat cell configuration, showing the main functions of the potentiostat [8]. **75**

Figure 3.11: A representative diagram of potentiodynamic polarisation plot showing the active and passive regions [8]. **76**

Figure 3.12: An illustrative diagram showing standard potentiodynamic anodic polarisation plot of 430 stainless steel [9]. **77**

Figure 3.13: Illustrative diagram showing the Tafel extrapolation technique for determination of corrosion current density and corrosion potential for corrosion rate measurement [10]. **79**

Figure 3.14: A typical cyclic polarisation plot showing pitting hysteresis loop [8]....8**1**

Figure 3.15: Schematic representation of a cyclic polarisation curve [15] **81**

Figure 4.1: The effects of steel binder content upon the sintered density of the TiC-304L cermets processed at 1500°C for 1 hour. **89**

Figure 4.2: DIC optical micrograph of TiC prepared with 20 vol. % 304L stainless steel binder, highlighting the degree of microstructural uniformity that is achieved using melt-infiltration **90**

Figure 4.3: SEM images of the TiC-304L cermets prepared with (a) 20 and (b) 30 vol. % stainless steel binder **91**

Figure 4.4: The hardness of TiC-304L cermets as a function of steel binder content (measured with a 1 kg load) **92**

Figure 4.5: The indentation fracture resistance of the TiC-304L cermets as a function of steel binder content (measured with a 50 kg load), determined for both median and Palmqvist cracking **93**

Figure 4.6: (a) The evolution of the COF for the TiC-stainless steel cermets as a function of time and binder content (for a 40 N applied load). (b) The effect of applied load on the COF after 120 minutes of dry sliding, as a function of steel binder content..... **95**

Figure 4.7: (a) The volumetric wear loss as a function of applied load and dry sliding time, for TiC prepared with 20 vol. % 304L binder. (b) The specific wear rate of TiC-304L stainless steel cermets as a function of applied load **97**

Figure 4.8: DIC optical images of the edges of wear tracks obtained for TiC with 20 vol. % 304L stainless steel after 15 minutes total sliding time (~181 m sliding distance), under loads of (a) 40 N and (b) 80 N **100**

Figure 4.9: SEM images of the edge of wear tracks formed in TiC-20 vol. % 304L cermets under conditions of: (a) 40 N applied load for 15 minutes, and (b) 80 N load for 60 minutes..... **101**

Figure 4.10: DIC optical images of the ends of wear tracks obtained for TiC with 20 vol. % 304L stainless steel, under the following sliding conditions: (a) 40 N load maintained for 15 minutes (~181 m total sliding distance) and (b) 80 N load maintained for 60 minutes (~724 m total sliding distance). The sliding direction is horizontal for both images **103**

Figure 4.11: (a) SEM image of the end of a wear track in TiC-20 vol % 304L stainless steel (40 N load maintained for 30 minutes (total sliding distance ~362 m); note that the darker regions present within the tribolayer, on the left hand side of this image, arise from a charging artefact. (b) Inset region from (a), highlighting the gradual build-up of the tribolayer at the end of the wear track, together with retained TiC grains that are still largely intact (arrowed). The sliding direction is horizontal for both images.....**104**

Figure 4.12: (a) SEM image of the end of a wear track in a TiC-10 vol. % 304L stainless steel cermet after testing at 80 N applied load for 15 minutes; sliding direction is horizontal for all images (b) Inset region 1 shows the edge of the tribolayer/unworn material, highlighting a section of spalled tribolayer on the left hand side, and several small cracks between TiC grains (arrowed). (c) Inset region 2 demonstrates the removal of large areas of the tribolayer and the exposure of the underlying damaged material, including isolated TiC grains that are believed to have been at the original polished surface prior to testing (arrowed) **106**

Figure 4.13: Typical SEM images of the wear track formed on the TiC-20 vol. % 304L samples after testing using a 20 N load for 2 hours duration. (a) The initial formation of a tribolayer is apparent in terms of material present between the TiC grains (dark regions), along with evidence of TiC grain fragmentation; a thin 'ring' of the steel binder is also often seen around the edges of the TiC grains. (b) Significant TiC grain fragmentation is observed in this region, in the form of fine particulate matter mixed with a secondary phase of equivalent contrast to the steel binder, which highlights the early stages of tribolayer development **108**

Figure 4.14: SEM images of the wear track of the TiC-10 vol. % 304L cermet after wear testing at 20 N load for 2 hours (total sliding distance ~1.45 km); sliding direction is horizontal for all images. (a) Circled areas appear to show the early stage of tribolayer formation, with a series of parallel laminae that are oriented nominally perpendicular to the sliding direction. (b) The general build-up of damaged areas within the microstructure is apparent on the left hand side of this image, which also shows some small regions of tribolayer formation (arrowed). (c) Inset region from (b) demonstrating regions of initial TiC grain fragmentation (circled) **110**

Figure 4.15: SEM images of the evolution of the wear track with increasing load and time for TiC cermets with 10 vol. % 304L stainless steel binder (in each example the sliding direction is horizontal): (a) 40 N applied load, maintained for 15 minutes, (b) 40 N applied load maintained for 60 minutes **111**

Figure 4.16: A comparison of (a) secondary electron and (b) back-scattered electron SEM images of the wear track formed in TiC-20 vol. % 304L stainless steel (80 N load for 60 minutes) **112**

Figure 4.17: SEM images of TiC-30% 304L cermets showing wear debris generated at (a) 40N and (b) 80N load **114**

Figure 4.18: EDS mapping of the TiC-30% 304L cermet following wear testing (80N applied load for 120 minutes), showing the build-up of oxide containing tribolayer at the edge of the wear track, and the absence of any significant O beyond the periphery of the track **115**

Figure 4.19: EDS mapping of a WC-Co counter face sphere following wear testing, showing the transfer of tribolayer onto WC-Co surface. Spalling of the tribolayer is also apparent, revealing the underlying WC-Co **117**

Figure 5.1: Representative SEM images of fine (a,c,e) and coarse (b,d,f) grained TiC-316L cermets prepared with: (a,b) 10 vol. % 316L, (c,d) 20 vol. % 316L, and (e,f) 30 vol. % 316L binder **127**

Figure 5.2: (a) The effects of binder content upon the contiguity of fine- and coarse-grained TiC-316L cermets. (b) The effects of binder content upon the mean free path of fine- and coarse-grained TiC- 316L cermets [46] **129**

Figure 5.3: The hardness of fine and coarse grained TiC-316L cermets as a function of steel binder content (measured with a 1 kg load) **130**

Figure 5.4: The indentation fracture resistance of fine and coarse grained TiC-316L cermets as a function of steel binder content (measured with a 50 kg load), determined for both median and Palmqvist cracking. (a) IFR using Anstis technique (b) IFR using Niihara technique **131**

Figure 5.5: The evolution of the COF for the fine and coarse grained TiC-stainless steel cermets as a function of applied load and steel binder content after 120 minutes of dry sliding **133**

Figure 5.6: The specific wear rate of fine and coarse grained TiC-316L stainless steel cermets as a function of applied load and binder content **135**

Figure 5.7: Wear tracks of fine and coarse grained TiC-based cermets with 20 vol. % 316L stainless steel binder. (a) Fine grained cermet with wear tracks in order of 20 to 80N load, from left to right, with a total length of 5.03mm.(b) Coarse grained cermet with wear tracks in order of 80 to 20N load, from left to right, with a total length of 5.03mm. The pushing of the material at the end of the track is apparent **137**

Figure 5.8: SEM images of the wear track formed on the fine and coarse grained TiC- 30 vol. % 316L after testing using 20N and 80 load for 2 hours duration. (total sliding distance ~1.45Km); sliding direction is vertical for all images. (a, b) 30 vol. % 316L of fine and coarse grained cermet at 20N load showing initial formation of tribolayer and build of material at the end of the wear track, (c, d) 30 vol. % 316L of fine and coarse grained cermet at 80N load depicting increase in build-up of tribolayer with increase in load.....**139**

Figure 5.9: SEM images of the wear track formed on the fine and coarse grained TiC- 30 vol. % 316L after testing using 20N for 2 hours duration. (total sliding distance ~1.45Km); sliding direction is vertical for all images. (a, b) 30 vol. % 316L of fine grained and coarse grained cermets showing evidence of ploughing and an initial binder deformation and extrusion which is more pronounced for coarse grained cermets (i.e. Figure 5.9 b) than fine grained cermets.....**140**

Figure 5.10: SEM images of the wear track formed on the fine and coarse grained TiC- 20 vol. % 316L after testing using 40N for 2 hours duration. (total sliding distance ~1.45Km); sliding direction is vertical for all images. (a, c) 20 vol. % 316L of fine grained cermet showing evidence of tribolayer spallation and binder deformation. (b, d) 20 vol. % 316L of coarse grained cermet showing evidence of more pronounced binder deformation **141**

Figure 5.11: SEM images of the wear track formed on the coarse grained cermets after testing for 2 hours duration. (total sliding distance ~1.45Km) (a, and b) 10 vol. % 316L of coarse grained cermets at 20N and 80N load showing evidence of light and intense spallation of tribolayer at higher load. (c, and d) 20% vol. % of coarse grained cermets at 20N and 40N load showing evidence of TiC fragmentation **142**

Figure 5.12: SEM Micrographs of fine and coarse grained TiC-20 vol. % 316L showing wear debris generated at 20N (a, c) and 40N load (c, d) . The coarser morphology of the wear debris generated by coarse grained cermets (b and d) is apparent **144**

Figure 5.13: EDS mapping of the fine and coarse grained TiC- 30 vol. % 316L cermets following wear testing (80N applied load for 2 hours), showing the build-up of oxide containing tribolayer at the edge of the wear track, and the absence of any significant O beyond the edge of the wear tack. (a) Fine grained cermets, (b) Coarse grained cermets.....**146**

Figure 5.14: EDS image of the fine and coarse grained TiC- 20 vol. % 316L cermets following wear testing (20N and 80N applied load for 2 hours), showing an increase in the build-up of oxide containing tribolayer generated at 20N (a, b) and 80N load (c, d) . (a) Fine grained cermets at 20N (a) and 80N (c). (b) Coarse grained cermets at 20N (b) and 80N (d). It is apparent that tribolayer generation increases with load as confirmed by the chemical composition of the tribolayer shown in Table 5.2 .....**147**

Figure 6.1: Optical (a,c,e) and SEM images (b,d,f) show a uniform distribution of TiC in the 304L steel binder, and good wetting/infiltration of the melt during processing: (a,b), 10 vol. % 304L, (c,d) 20 vol. % 304L, and (e,f) 30 vol. % 304L **158**

Figure 6.2: Open circuit potential vs. time of cermets and 304L stainless steel **159**

Figure 6.3: Tafel plot of TiC-304L steel cermets and 304L stainless steel **160**

Figure 6.4: Corrosion rate vs. binder volume content (%) after Tafel extrapolation **161**

Figure 6.5: Corrosion rate by weight loss analysis after potentiodynamic polarization.....**162**

Figure 6.6: Combined potentiodynamic polarization plots for each TiC 10-30 vol. % 304L cermets.....**164**

Figure 6.7: Cyclic polarization of TiC-304L cermets and 304L stainless steel: (a) TiC with 10 vol. 304L, (b) TiC with 20 vol. % 304L, (c) TiC with 30 vol. % 304L, and (d) 304L stainless steel.....**165**

Figure 6.8: Potentiostatic polarization of the cermets and 304L stainless steel above the pitting potential. (a) 304L stainless steel, (b) TiC-304L cermets **167**

Figure 6.9: ICP results of the filtered particulate material removed from the solution remaining in flat cell upon completion of corrosion testing **168**

Figure 6.10: ICP analysis of the filtered solution remaining in flat cell upon completion of corrosion testing, showing the metal ions present in the solution (i.e. after removal of any fine particulate material) **169**

Figure 6.11: EDS elemental analysis of the sample surfaces following corrosion testing: (a) TiC with 10 vol. % 304L, (b)TiC with 20 vol. % 304L, and (c) TiC with 30 vol. % 304L... **171**

Figure 6.12: SEM images showing corroded surface of TiC-304L cermets and 304L stainless steel showing heavy pitting on the 304L steel and less substantial effects on the cermets after the Tafel experiments: (a) TiC with 10 vol. 304L, (b) TiC with 20 vol. % 304L, (c) TiC with 30 vol. % 304L, and (d) 304L stainless steel **172**

Figure 6.13: SEM images showing the corroded surfaces of TiC-304L cermets after potentiodynamic polarization: (a,b) 10 vol. % 304L, (c,d) 20 vol. % 304L, and (e,f) 30 vol. % 304L..... **174**

Figure 6.14: SEM images showing corroded surface of TiC-304L cermets and 304L stainless steel after cyclic polarization: (a) TiC with 10 vol. 304L, (b) TiC with 20 vol. % 304L, (c) TiC with 30 vol. % 304L, and (d) 304L stainless steel..... **176**

Figure 6.15: SEM images showing corroded surface of the TiC-304L cermets and 304L stainless steel after potentiostatic polarization above their pitting potentials: (a) TiC with 10 vol. % 304L, (b) TiC with 20 vol. % 304L, (c) TiC with 30 vol. % 304L, and (d) 304L stainless steel **177**

Figure 7.1: Representative SEM images of TiC-316L cermets prepared with: (a,b) 10 vol. % 316L, (c,d) 20 vol. % 316L, and (e,f) 30 vol. % 316L binder..... **185**

Figure 7.2: The mean grain size as a function of binder content for both fine- and coarse-grained TiC-316L cermets..... **186**

Figure 7.3: (a) The effects of binder content upon the contiguity of fine- and coarse-grained TiC-316L cermets. (b) The effects of binder content upon the mean free path of fine- and coarse-grained TiC-316L cermets..... **187**

Figure 7.4: The open circuit potential as a function of time for: (a) fine-grained TiC-316L cermets and (b) coarse-grained TiC-316L cermets..... **189**

Figure 7.5: Representative examples of the Tafel plots for: (a) the fine-grained TiC-316L cermets and (b) the coarse-grained TiC-316L cermets..... **190**

Figure 7.6: The Tafel-derived corrosion rates for both the fine- and coarse-grained TiC-316L cermets **192**

Figure 7.7: The corrosion rates, determined by weight loss measurements, for both the fine- and coarse-grained TiC-316L cermets **193**

Figure 7.8: Representative potentiodynamic polarisation curves obtained for: (a) fine-grained TiC-316L cermets and (b) coarse-grained TiC-316L cermets **196**

Figure 7.9: Representative potentiostatic polarisation curves for: (a) the fine-grained TiC-316L cermets and (b) the coarse grained TiC-316L cermets **199**

Figure 7.10: ICP-OES analyses of the filtered material removed from the post-test potentiodynamic polarisation solutions for: (a) fine-grained and (b) coarse-grained TiC-316L cermets **202**

Figure 7.11: ICP-OES analyses of the retained solution (following filtration) following potentiodynamic polarisation testing, for (a) fine-grained and (b) coarse-grained TiC-316L cermets **203**

Figure 7.12: EDS analysis of the TiC-316L cermets both before and after corrosion tests: (a) fine-grained and (b) coarse-grained. Note that the compositional balance is comprised of O **205**

Figure 7.13: SEM images of the fine-grained TiC-316L cermets following potentiodynamic polarisation testing: (a,b) 10 vol. % 316L, (c,d) 20 vol. % 316L, and e,f) 30 vol. % 316L binder **206**

Figure 7.14: SEM images of the coarse-grained TiC-316L cermets following potentiodynamic polarisation testing: (a,b) 10 vol. % 316L, (c,d) 20 vol. % 316L, and (e,f) 30 vol. % 316L binder **207**

Figure 7.15: SEM images of the fine-grained TiC-316L cermets following potentiostatic polarisation testing: (a,b) 10 vol. % 316L, (c,d) 20 vol. % 316L, and (e,f) 30 vol. % 316L binder **209**

Figure 7.16: SEM images of the coarse-grained TiC-316L cermets following potentiostatic polarisation testing: (a,b) 10 vol. % 316L, (c,d) 20 vol. % 316L, and (e,f) 30 vol. % 316L binder **210**

Figure 8.1: Representative SEM images of TiC-stainless steel cermets prepared with: (a) TiC-10 vol. % 304L, (b) TiC-20 vol. % 304L, (c) TiC-30 vol. % 304L, (d) TiC-10

vol. % 316L, (e) TiC-20 vol. % 316L, (f) TiC-30 vol. % 316L, (g) TiC-10 vol. % 410L, (h) TiC-20 vol. % 410L, and (i) TiC-30 vol. % 410L **221**

Figure 8.2: The effects of binder composition and content on the various microstructural parameters assessed for the TiC-stainless steel cermets developed in the present work: (a) grain size, (b) contiguity, and (c) the binder mean free path **223**

Figure 8.3: Representative OCP curves, demonstrating the effects of binder content for each of the TiC-stainless steel cermets, together with comparison of the 'pure' stainless steels: (a) TiC-304L, (b) TiC-316L, (c) TiC-410L, and (d) the 'pure' grades of stainless steel . **225**

Figure 8.4: The effects of binder composition and content upon the Tafel derived corrosion rates for the TiC-stainless steel cermets **228**

Figure 8.5: The effects of binder composition and content upon the corrosion rates derived from weight loss measurements for the TiC-stainless steel cermets **230**

Figure 8.6: Representative potentiodynamic polarisation curves, demonstrating the effects of binder content for each of the TiC-stainless steel cermets, together with comparison of the 'pure' stainless steels: (a) TiC-304L, (b) TiC-316L, (c) TiC-410L, and (d) the 'pure' grades of stainless steel **232**

Figure 8.7: Representative cyclic polarisation curves, demonstrating the effects of binder content for each of the TiC-stainless steel cermets, together with comparison of the 'pure' stainless steels: (a) TiC-304L, (b) TiC-316L, (c) TiC-410L, and (d) the 'pure' grades of stainless steel **236**

Figure 8.8: Representative potentiostatic polarisation curves, demonstrating the effects of binder content for each of the TiC-stainless steel cermets, together with comparison of the 'pure' stainless steels: (a) TiC-304L, (b) TiC-316L, (c) TiC-410L, and (d) the 'pure' grades of stainless steel **239**

Figure 8.9: ICP-OES chemical analyses of the filtered material removed from the post-test solutions after corrosion testing of the TiC-stainless steel cermets: (a) TiC-304L, (b) TiC-316L, and (c) TiC-410L **242**

Figure 8.10: ICP-OES chemical analyses of the remaining post-test solution, following filteration to remove particupalte material, after corrosion testing of the TiC-stainless steel cermets: (a) TiC-304L, (b) TiC-316L, and (c) TiC-410L **244**

Figure 8.11: Comparative EDS elemental analyses of the surface of TiC-stainless steel samples prepared with 30 vol. % steel binder, both before and after corrosion testing: (a) TiC-304L, (b) TiC-316L, and (c) TiC-410L **246**

Figure 8.12: Representative SEM images of the corroded surfaces of the TiC-stainless steel cermets following potentiodynamic polarisation testing, for cermets with, respectively: (a-c) 10, 20 and 30 vol. % 304L, (d-f) 10, 20 and 30 vol. % 316L, and (g-i) 10, 20 and 30 vol. % 410L..... **247**

Figure 8.13: Representative SEM images of the corroded surfaces of the TiC-304L cermets and 'pure' 304L steel following cyclic polarisation testing: (a) 10 vol. % 304L, (b) 20 vol. % 304L, (c) 30 vol. % 304L, and (d) 'pure' 304L stainless steel **248**

Figure 8.14: Representative SEM images of the corroded surfaces of the TiC-316L cermets and 'pure' 316L steel following cyclic polarisation testing: (a) 10 vol. % 316L, (b) 20 vol. % 316L, (c) 30 vol. % 316L, and (d) 'pure' 316L stainless steel **249**

Figure 8.15: Representative SEM images of the corroded surfaces of the TiC-410L cermets and 'pure' 410L steel following cyclic polarisation testing: (a) 10 vol. % 410L, (b) 20 vol. % 410L, (c) 30 vol. % 410L, and (d) 'pure' 410L stainless steel **250**

Figure 8.16: Representative SEM images of the corroded surfaces of the TiC-304L cermets and 'pure' 304L steel following potentiostatic polarisation testing: (a) 10 vol. % 304L, (b) 20 vol. % 304L, (c) 30 vol. % 304L, and (d) 'pure' 304L stainless steel..... **252**

Figure 8.17: Representative SEM images of the corroded surfaces of the TiC-316L cermets and 'pure' 316L steel following potentiostatic polarisation testing: (a) 10 vol. % 316L, (b) 20 vol. % 316L, (c) 30 vol. % 316L, and (d) 'pure' 316L stainless steel **253**

Figure 8.18: Representative SEM images of the corroded surfaces of the TiC-410L cermets and 'pure' 410L steel following potentiostatic polarisation testing: (a) 10 vol. % 410L, (b) 20 vol. % 410L, (c) 30 vol. % 410L, and (d) 'pure' 410L stainless steel **254**

Figure 10.1: XRD trace and PDF Peaks **282**

Figure 10.2: Infiltrated density of cermets (% TD) (a) Regular TiC-steel cermets, (b) Fine and coarse grained TiC-316L cermets. All the cermets had sintered densities in excess of 97% of theoretical confirming that melt infiltration allows for the formation of high density cermets, even when low steel contents are used (i.e. 5 vol. %) **283**

Figure 10.3: XRD of as-sintered TiC-304L cermets. All the major peaks are TiC and the observation is consistent with other cermets.....**284**

Figure 10.4: A representative histogram of fine grained TiC –10 vol. % 316L cermets used for the determination mean grain sizes of all the studied cermets.....**285**

Figure 10.5: Representative potentiodynamic polarisation curves for TiC-304L cermets at 1.5V..... **289**

Figure 10.6: SEM of TiC-304L cermets following potentiostatic polarization at 1.5V(a) TiC-10 vol. % 304L (b) TiC-30 vol. % 304L cermets. The less corrosion attack on TiC-10 vol. % 304L cermets is evident and also confirming the lowest current in the passivation region as shown in Figure 9.5 .....**290**

Figure 10.7: EDX image of TiC-304L cermets following potentiostatic polarization at 1.5V. (a) TiC- 10 vol. % 304L cermets, (b) TiC-30 vol. % 304L cermets.....**291**

Figure 10.8: EDX spectral analysis of TiC-304L cermets (analysis taken from images of Figure 10.7). (a) TiC-10 vol. % 304L (b) TiC-30 vol. % 304L cermets **292**

Figure 10.9: The hardness (measured with a 1 kg load) and indentation fracture resistance (measured with a 50 kg load) as a function of steel binder content. (a) TiC-316L cermets, (b) TiC-410L cermets. It is apparent that for the two cermets, hardness is dependent on TiC content while indentation fracture resistance is dependent on the steel binder content **295**

Figure 10.10: The effect of applied load on the COF after 120 minutes of dry sliding, as a function of steel binder content. (a) TiC-316L cermets, (b) TiC-410L cermets. It is apparent that COF increases with binder content **296**

Figure 10.11: The volumetric wear loss as a function of applied load and dry sliding time. (a) TiC prepared with 20 vol. % 316L binder, (b) TiC prepared with 20 vol. % 410L binder. It can be seen that volumetric wear loss increases with time **297**

Figure 10.12: The specific wear rate as a function of applied load. (a) TiC-316L cermets, (b) TiC-410L cermets. The specific wear rate increases with load and binder content.....**298**

Figure 10.13: An optical profilometry images showing wear tracks of TiC- 20 vol. % 316L cermets at different loads. (From left to right, 20 to 80N load).

(a) Optical profilometer images (b) Wear track profile of (a). It is evident that wear resistance increases with decrease in load judging from the depth of the wear track. This observation is consistent with all the studied cermets **299**

Figure 10.14: SEM images of the wear track formed on TiC- 10 vol. % 316L after testing using 20N and 80 load for 2 hours duration.(total sliding distance ~1.45Km); sliding direction is vertical for all images. (a, b) 10 vol. % 316L of at 20N load showing initial formation of tribolayer and build of material at the end and edge of the wear track, (c, d) 10 vol. % 316L at 80N load depicting increase in build-up of tribolayer and spallation with increase in load **300**

Figure 10.15: SEM images of the wear track formed on TiC- 10 vol. % 410L after testing using 20N and 80 load for 2 hours duration.(total sliding distance ~1.45Km); sliding direction is vertical for all images. (a, b) 10 vol. % 410L of at 20N load showing initial formation of tribolayer and build of material at the end and edge of the wear track, (c, d) 10 vol. % 410L at 80N load depicting increase in build-up of tribolayer and spallation with increase in load.....**301**

Figure 10.16: SEM images showing a typical tribolayer that is generated at higher load after testing using 80N load for 2 hours duration.(total sliding distance ~1.45Km); sliding direction is vertical for all images. (a) 20 vol. % 316L (b) 20 vol. % 410L **302**

Figure 10.17: SEM Micrographs showing wear debris generated at 60N load, (a) TiC-30 vol. % 316L (b) TiC-30 vol. % 410L cermets. The morphology of the wear debris suggests a combination of 3-body and adhesive wear mechanism **303**

Figure 10.18: A representative EDS image of wear debris generation of TiC-30 vol. % 316L, after dry sliding for 120 minutes under 80N load (analysis shown in Table 10.3). It is apparent that the morphology of the wear debris changed (compared with Figure 10.17a at 60N load) at higher load from spherical to coarser, plate-like and irregular structure inferring the change of wear mechanisms at different loads **304**

Figure 10.19: EDS analysis on wear scar of WC-6Co counter face sphere used on TiC-30 vol. % 410L, after dry sliding for 120 minutes under 80N load. (a) EDS image of the WC-6Co counter face sphere (b) Spectral analysis of the counter face sphere(shown in a). It is apparent that there is mutual transfer of material from cermet material to the WC-6Co counter face sphere (and vice-versa). **306**

ABSTRACT

Ceramic metal composites, or cermets, currently have widespread applications in the chemical, automotive and oil and gas sectors, due to their combination of high wear resistance, and aqueous corrosion resistance. In the present study, a family of novel titanium carbide (TiC)-stainless steel cermets has been produced as potential materials for use as erosion and corrosion resistant materials. The development of the TiC-stainless steel cermets is based on a simple melt infiltration technique, with the stainless steel "binder" contents varied from 5 to 30 vol.%, using the austenitic grades 304L and 316L, and the martensitic grade 410L. These materials have subsequently been evaluated for their wear and corrosion response, as well as characterisation of their basic mechanical properties and microstructure.

Reciprocating wear tests involved a ball-on-flat geometry (using a WC-Co counter face sphere), with loads varied from 20 to 80 N, for up to 120 minutes. The wear tracks were assessed using a high-resolution optical profilometer, in order to determine the wear volume. The specific wear rate of the cermets was found to increase with both the applied load and the steel binder content. To investigate the morphology of worn surfaces, scanning electron microscopy (SEM), and associated energy dispersive x-ray spectroscopy (EDS) were used, in order to fully understand the operative wear mechanisms. A transition from two- to three-body abrasive wear was observed, together with the formation of a oxygen-rich tribolayer, indicating that adhesive wear was also occurring on the cermets.

In order to assess the electrochemical behaviour of the cermets in a simulated seawater environment, the samples were evaluated using potentiodynamic, cyclic and potentiostatic polarisation tests, with basic corrosion parameters and rates subsequently determined through Tafel extrapolation and weight loss measurement. Each stage of electrochemical assessment was then evaluated by characterising the corroded surfaces and solution using SEM, EDS and inductively coupled plasma optical emission spectrometry. Microstructural observations using SEM images revealed significant degradation of the samples, with steel binder preferentially dissolved while TiC remained relatively unaffected. The corrosion rate of the cermets increases with steel binder content, which is attributed to the preferential dissolution of the binder.

LIST OF ABBREVIATIONS AND SYMBOLS USED

XRD	X-ray diffraction
SEM	Scanning electron microscope
EDS	Energy-dispersive x-ray spectroscopy
ICP-OES	Inductively coupled plasma optical emission spectrometry
HIP	Hot isostatic pressing
HV	Vickers hardness
IFR	Indentation fracture resistance
LPS	Liquid phase sintering
θ	Contact angle
φ	Dihedral angle
γ_{sv}	Solid-vapour surface energy
γ_{sl}	Solid-liquid surface energy
γ_{lv}	Liquid –vapour surface energy.
CIP	Cold isostatic press
MIS	Melt infiltration/sintering
COF	Coefficient of friction
UMT	Universal Micro Tribometer
OCP	Open circuit potential
SCE	Saturated calomel electrode
E_{corr}	Corrosion potential
E_{prot}	Protection potential
E_{pit}	Pitting potential
I_{corr}	Corrosion current density
I_{crit}	Critical current density
Epp	Pseudo-passive current density
EW	Equivalent weight

ACKNOWLEDGEMENTS

The financial support of Petroleum Research Atlantic Canada (PRAC) and the Natural Sciences and Engineering Research Council of Canada (NSERC), the Canada Foundation for Innovation, the Atlantic Innovation Fund, and other partners who helped fund the Facilities for Materials Characterisation, managed by the Dalhousie University Institute for Materials Research, as well as the support of Minerals Engineering Centre, are gratefully acknowledged.

I would like to acknowledge the constant support and close supervision of my supervisors, Dr Kevin Plucknett and also Dr Georges Kipouros, for their encouragements and guidance throughout this programme. Without their assistance, the body of my thesis would not have been possible. Also I would like to thank my co-supervisor, Dr Zoheir Farhat, for his advice and assistance in the wear portion of my research and Dr Steve Corbin for his assistance in this research. My external examiner, Dr Jingli Luo is also acknowledged for making the extra efforts to participate in my PhD defence despite having very hectic schedules at University of Alberta.

I would also thank Dr Aboulwahab Ibrahim, Dean Grijm and Patricia Scallion, for technical assistance in this research. I would also like to thank all the people who helped me by any means throughout this thesis, with assistance with experiments, analysis, and suggestions especially Md Aminul Islam, Rabin, Momotaj, Tyler, Chelsea, Chenxin, Steve, Allison Chua, Zhila, Ikenna and Hung-Wei Liu. The encouragement and support of my parents, brothers and sisters and my in-laws are also acknowledged.

Finally, I would like to thank my Wife Irene, and my son Francis, for their love and support throughout this programme. Above all, I would thank the almighty God for divine favour and protection throughout this programme.

1 Introduction

The use of ceramic metallic composites (or cermets) has gained increasing acceptance in a wide variety of industrial applications, due to their outstanding potential for use in mechanically demanding, highly corrosive, and extreme tribological environments. Among the various ceramic components used in cermets, titanium carbide (TiC) is considered as a highly promising reinforcing material due to its high hardness, melting point, chemical and thermal stability, and wear resistance. TiC also has good wettability by many potential metallic binder materials when they are molten. As a consequence, TiC-based cermets are finding widespread applications in the manufacturing (i.e. machining), chemical processing, transportation, and defence industries.

TiC-based cermets are becoming more prominent due to their improved capabilities when compared to the more traditional 'hardmetals', based on tungsten carbide-cobalt (WC-Co) [1]. This is an obvious comparison, between TiC and WC-Co cermets, as WC-Co is already used widely throughout the industrial sectors previously outlined, having been developed for approaching 100 years. However, in spite of that extensive developmental period, TiC-based cermets have several properties that are superior to those of WC, such as increased hardness and toughness, as well as a lower mass (the density of WC is ~3 times that of TiC [2]). These properties, in addition to TiC having lower raw materials and hence fabrication costs, could lead to TiC-based cermets replacing WC for many applications.

TiC-based cermets are prepared with a metallic binder, which can significantly increase the materials toughness, forming a ceramic-metal composite, and imparting the beneficial properties of both phases without incorporating the more detrimental characteristics. A variety of binders have been used in TiC-based cermets, including Ni, Fe and Co [3-5]. More recently, ductile intermetallic alloys such as Fe- and Ni-based aluminides have been employed, which offer increased potential for use at elevated temperatures [6, 7]. Fe based alloys are widely used metallic materials because of their low cost and good mechanical properties. Fe alloys, particularly austenitic stainless steels, can exhibit higher strength, stiffness, and ductility when compared to the lightweight alloys such as those based on Al. The use of stainless steels as a binder for TiC is proposed when a combination of good corrosion and wear resistance, as well as high toughness of the composite, are the ultimate requirements. Despite the previously outlined

potential benefits that may be derived by using steel metal binders in the development of TiC-based cermets, little attention has been given to this class of material to date. The present work has focused on the development of a family of novel TiC-based cermets using stainless steel binders, including the austenitic (304L and 316L) and martensitic (410L) grades. A particularly important aspect of this work has been assessment of the resulting wear and corrosion behaviour.

A simple melt infiltration technique (i.e. a method by which the molten metallic phase of a cermet is introduced to the ceramic phase through capillary action from outside the initial ceramic preform) was employed to densify the cermets, utilising porous TiC preforms prepared using a combination of uniaxial and cold isostatic pressing. Following the melt infiltration process, the infiltrated samples are ground and polished, prior to wear and electrochemical testing. The reciprocating wear tests involved a ball-on-flat geometry (using a WC-Co counter face sphere), with loads varied from 20 to 80 N, for periods of up to 120 minutes. The resultant wear tracks were assessed using a high-resolution optical profilometer and scanning electron microscopy (SEM). In order to assess the electrochemical behaviour of the cermets in a simulated seawater environment (3.5 wt. % NaCl), the samples were evaluated using potentiodynamic, cyclic and potentiostatic polarisation tests, with basic corrosion parameters and rates subsequently determined through Tafel extrapolation. Each stage of electrochemical assessment was then evaluated by characterising the corroded surfaces using SEM, with associated energy dispersive X-ray spectroscopy (EDS), and X-ray diffraction (XRD). In addition, the remaining solutions following testing were characterised using inductively coupled plasma optical emission spectrometry (ICP-OES).

The present thesis is divided into nine chapters, which follow the progression of the work throughout the project. Chapter 2 presents a background literature review and the associated theory necessary for a general understanding of the principles covered in the present research, together with an overview of the current status of cermet research. Chapter 3 provides additional information relating to the raw and processed materials, together with details of the experimental procedure not fully accounted for in the submitted journal papers (i.e. the material presented in Chapters 4 to 8). In terms of the subsequent chapters, Chapters 4 and 5 focus on the wear response of TiC-304L cermets and the effects of grain size on the wear behaviour of TiC-316L cermets respectively. Chapters 6 to 8 detail various aspects of the corrosion behaviour of TiC-

steel based cermets. These focus on the corrosion behaviour of TiC-304L cermets (Chapter 6), the effects of grain size on the corrosion behaviour of TiC-316L cermets (Chapter 7), and an overall comparison of the corrosion response of TiC-based cermets with a variety of steel binders (i.e. 304L, 316L and 410L), including comparison with the corrosion performance of the baseline stainless steels (Chapter 8). Any additional results that is not presented and discussed in Chapters 4 to 8, is provided in the Appendices. Finally, Chapter 9 provides a summary of the overall conclusions gathered throughout this research study, an outline of the contributions to original thought, and recommendations for future work.

2 Literature Review

This chapter presents the theory necessary for a general understanding of the principles covered in the present research. It contains a general review of the types of material developed and characterised in the present study, which includes an overview of cermets, titanium carbide (TiC) and TiC powder fabrication methods, stainless steels, and the processing stages for cermet fabrication. A detailed study of the characterisation approaches for the cermets (i.e. wear and corrosion) has also been covered, with a brief overview on the wear and corrosion behaviour of cermets in general.

2.1 Cermets

Ceramic-metal composites, or cermets, are a class of structural material that has the combination of a hard ceramic phase and a tough, ductile metallic phase. The ceramic phases, which constitute approximately 50-95% by volume, are embedded in a continuous matrix of elemental metal or an alloyed binder. The combination of metal and non-metal in cermets occurs on a microscale. Cermets incorporate the desirable qualities and suppress the undesirable properties of both of the individual ceramic and metal constituents. The excellent wear resistance of cermets, owing to the combination of a tough metal binder with hard carbide, has resulted in their application as cutting tool materials [8]. Cermet cutting tools are light in weight when compared to conventional "hard-metals" (i.e. tungsten carbide-cobalt (WC-Co)), which have densities ranging from 12 to 15 gcm^{-3}, while cermets more typically have densities of only around 6-7.5 gcm^{-3}, which is even lighter than steel. Cermets invariably posses high mechanical strength, toughness and thermal conductivity [9]. A high thermal conductivity leads to a low temperature gradient during metal turning operations, resulting in less thermal stresses and cracks, and is thus greatly preferred for high speed cutting tool materials [9].

Control of the properties of the cermets is generally performed through the addition of a metallic 'binder' phase, which may be customised in terms of composition. These binders can be chosen from a wide variety of alloys, usually with Fe, Al, Ni and /or Co as the primary addition(s). The metal binder will bring specific qualities to the cermets, such as corrosion resistance, ductility, oxidation resistance, hardness, thermal conductivity, and/or thermal shock resistance. By adding

various amounts or compositions of the binder alloys, cermets can be tailored to specific purposes. It should be noted that the mechanical properties or corrosion resistance of the metals are not solely responsible for determining their effect on the cermets, and that their sintering behaviour will greatly impact the final product. In other words, the wetting response of the molten metal on the ceramic is a critical factor that determines the final properties of the cermets. If the metallic binders fail to wet the ceramic particles during sintering, the mechanical properties will be adversely affected, possibly resulting in the material being unsuitable for the desired application. Cermets are used in the manufacturing, chemical processing, aerospace, automotive, and oil and gas sectors, because of their unique combination of high wear resistance and hardness, excellent strength characteristics, and good aqueous corrosion resistance. The continuing development, characterisation and advancement of these high performance wear and corrosion resistant composites has improved upon current performance standards, and they are considered to be particularly promising materials in petroleum sector applications, for example as coatings for erosion/corrosion protection, pump seals, etc [8-13].

2.2 Titanium Carbide (TiC) use in Cermets

The outstanding properties of transition metal carbides, which include high hardness, melting point, thermal conductivity, strength (even at high temperatures), wear and corrosion resistance, and a high degree of chemical stability, have led to their extensive applications in many fields such as, wear-resistant parts and high-temperature structural materials [14-16]. It is generally known that titanium carbide (TiC) is one of the most important compounds among the transition metal carbides, because of its excellent combination of physical and chemical properties, such as a high melting temperature (3067°C), boiling temperature (4820°C), Vickers hardness (28-35 GPa), Young's modulus (410-450 GPa), resistance to corrosion and oxidation, abrasion resistance, and high thermal shock resistance, as well as a low density (4.93 g/cm^3), reasonable flexure strength (240-400 MPa), and good thermal conductivity (21 $W/m^2 \times K$) [14,17-20]. Due to these favourable properties, TiC-based cermets are widely used as abrasive, anti-wear and aerospace materials [13, 21-22]. At the same time, TiC can also be used as a substitute for WC in cermets because they have similar properties of high hardness and wear resistance. In addition, Ni is often successfully used as a metallic binder for TiC, which is significantly cheaper and less toxic than Co, which is invariably used as a binder for WC [23-24]. Currently, approximately 10 % of the world's consumption of Co is for use as a binder material for WC components [25]. Ni

has more stable supply sources than Co, and at the time of writing costs only half as much [25-26].

As with most of the refractory carbides, TiC possesses a face-centred cubic (FCC) unit cell, with the carbon atoms occupying the interstitial positions [27]. TiC has the NaCl-type crystal structure, as shown in Figure 2.1 [28]. In this case, the large light spheres represent the Ti atoms and the small dark spheres represent the C atoms in the interstitial sites.

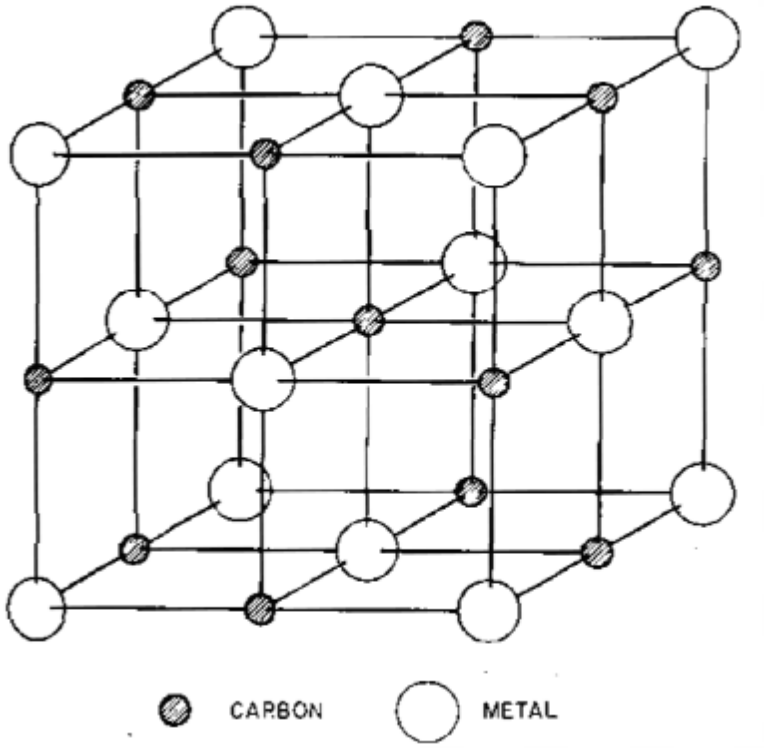

Figure 2.1: The NaCl-type structure of TiC [29].

Since TiC is an interstitial compound, it does not have an exact stoichiometry. It has been shown that it can exist as TiC_x, with $0.47<x<1.0$ [27]. The melting point of TiC varies from approximately 1918 to 3067°C, which is dependent on the Ti:C ratio. The lattice parameter of the stoichiometric TiC compound is 0.43305 nm [27]. It is established that some of the properties of TiC are dependent on the stoichiometry, and these can therefore change considerably with composition. Below the minimum Ti:C compositional ratio there is a mixture of TiC and Ti in solid solution, while above the maximum ratio there will be a mixture of TiC and C. The Ti-C phase diagram is shown in Figure 2.2 [14].

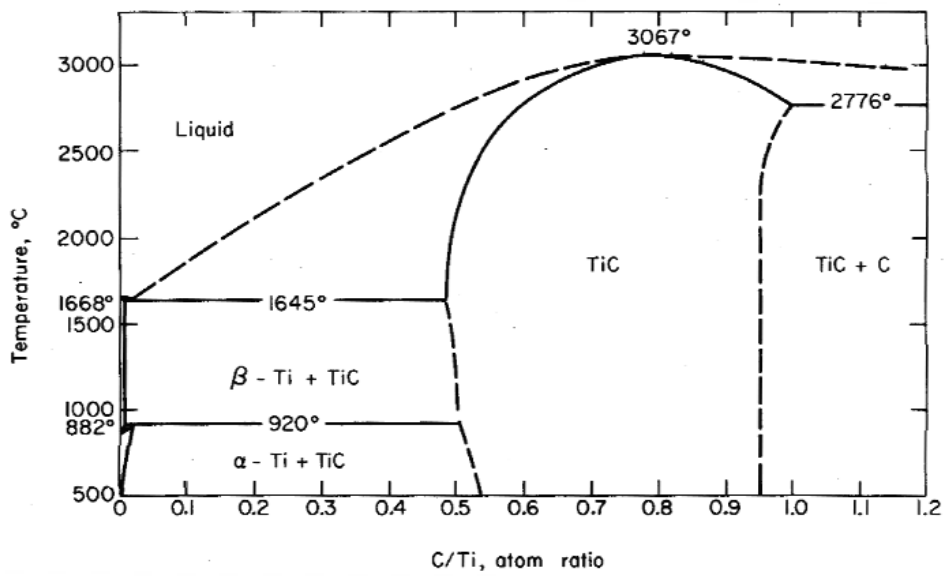

Figure 2.2: The Ti-C phase diagram [14].

The high melting point of TiC makes it a potential material for high temperature applications [14, 24]. Monolithic TiC, however, is brittle at ambient temperatures, and metals such as Ni, Co, and Fe have been incorporated as a ductile second phase to improve its fracture toughness. TiC-based composites with Ni alloys and Fe alloys are currently used in high performance applications where wear and corrosion are the main sources of material failure [14]. A wide range of metallic binders can be chosen for TiC-based cermets, depending upon the respective applications. The potential use of stainless steels is advantageous relative to 'pure' Fe, due to their superior corrosion resistance and tensile properties [30]. Fe-based alloys are widely used metallic materials because of their low cost and good mechanical properties. In particular, austenitic stainless steels exhibit good strength and stiffness. However, austenitic stainless steels also have relatively poor wear resistance, due to their low hardness [31]. As stated previously, a ductile second phase is used to improve the toughness of the cermets, and will also typically result in improved wear resistance. In this way, a composite structure is created in which the wear and corrosion resistance properties of the matrix carbide are combined with the enhanced toughness of the metallic phase [32]. However, this form of ductile phase toughening typically results in a decrease in the hardness values of the composites, due to the lower elastic modulus and hardness of the ductile phase [33-34].

2.2.1 Titanium Carbide Powder Fabrication

TiC powders are typically synthesised by one of three processes: (1) the direct carbonisation of Ti metal or titanium hydride (TiH_2), or combustion synthesis of TiC, (2) gaseous pyrolysis of titanium halide, such as $TiCl_4$, in a carbon-containing atmosphere, (3) the carbothermal reduction of TiO_2, with carbon, in a controlled atmosphere at high temperature [35]. Of these approaches, the most widely used process for TiC production is carbothermal reduction of TiO_2 in the presence of C. Carbothermal reduction produces large amounts of powder, makes use of inexpensive precursor materials, and thus remains relatively inexpensive and cost effective. Carbothermal reduction of TiO_2 takes place in the temperature range 1700-2100^oC following [23]:

$$TiO_{2(s)} + 3C_{(s)} = TiC_{(s)} + 2CO_{(g)} \qquad \text{Equation 2.1}$$

Other industrial-scale methods of production of TiC powder as well as their associated reaction equations are outlined in Table 2.1.

Table 2.1: Typical reactions involved in the consolidation of TiC via powder metallurgy routes [23,28].

Method	**Reaction**
Direct reaction between metallic elements or metallic hybrids and graphite, under vacuum or inert gas	$Ti_{(s)} + C_{(s)} \rightarrow TiC_{(s)}$ $TiH_{2(s)} + C_{(s)} \rightarrow TiC_{(s)} + H_{2(g)}$
Reaction of the Ti with carburizing gas	$Ti_{(s)} + C_nH_{1-n(s)} \rightarrow TiC_{(s)} + H_{2(g)}$
Chemical reaction between $TiCl_4$, H_2 and C	$TiCl_{4(g)} + 2H_{2(g)} + C_{(s)} = TiC_{(s)} + 4HCl_{(l)}$

2.3 Stainless steels

Stainless steel is a generally accepted terminology applied to Fe-based alloys that have at least 10.5 % Cr. They are ferrous alloys containing enough Cr (usually ~12 %) to passivate in some environment, such as air and/or water, and are expected to form a passive film, which is mainly

chromium oxide (Cr_2O_3). During the production of stainless steel, chromium is usually added during the melting stage, and forms a homogenous mixture with the Fe and other elements such as Ni and Mo, which enhance the alloy's corrosion resistance. There are several basic stainless steel grades, such as 304 and 316. Grade 304, the basic '18-8' alloy (18 % Cr, 8 % Ni), is the most commonly used of the 300 series steels, and has excellent corrosion resistance in most applications. Grade 316 has superior corrosion resistance than 304, because of an addition of at least 2 % Mo, which significantly increases the metal's resistance to salt corrosion [36, 37]. Generally, 'plain-carbon' steel has at least 95 % Fe, with up to 2% C; the strength of steel is determined by the carbon content. For stainless steel the C is low, usually less than 0.08 %. Their strength is primarily obtained from metallurgical structure, rather than the carbon content; heat treatment can be used to differentiate carbon steel and stainless steel to a certain extent. While carbon steels can be strengthened by heat treatment, the 300 series stainless steels cannot. In comparison, stainless steels can be strengthened by work hardening the structure. As stated previously, the 300 series stainless steel grades (304 and 316) contain Ni (from 8 to 14 %), in addition to the Cr that must be present to have adequate corrosion resistance. The addition of 2 to 3 % of Mo to Grade 316 stainless steels also makes it more resistant to pitting corrosion [36-38].

2.3.1 Classification of Stainless Steels

Three digit codes are currently used by the American Iron and Steel Institute (AISI) to identify wrought stainless steels by their structure. The first digit defines the following classes:

AISI 300 Series: This class is the austenitic steels with Ni as the primary austenite stabiliser.

AISI 200 Series: This group is the austenitic steels that contain Mn and N as Ni substitutes.

AISI 400 Series: These are the ferritic and martensitic steels, with little or no Ni.

Another identifier for steels is the addition of "L", which denotes a low C content, and is important where intergranular corrosion is an issue. Generally, stainless steels are classified as austenitic, ferritic, martensitic, duplex, and precipitation hardening [38-42].

2.3.2 Austenitic Stainless Steels

Austenitic stainless steels are the most corrosion resistant and widely used grades. In addition to their Cr content, the presence of Ni strengthens the passive film and increases the resistance to strong acids, while also stabilising the FCC crystal structure. They have excellent corrosion

resistance and low-temperature toughness, as well as very good formability. The common grades of austenitic stainless steels work harden extremely well. They are nonmagnetic, unlike the other groups of stainless steels, although cold working can produce enough ferrite to make them very slightly magnetic [38]. They are heavily used in the pulp and paper industry. Types 304, 316L, and 317 are used in the process vessels and piping, and for heat-exchanger tubing in evaporators. When chlorides are present, higher Cr- and Mo-containing grades are required [37], because of their superior corrosion resistance. Types 316 and 317 have a greater resistance to pitting in marine and chemical industry environments than type 304. Other variations of type 316 include a low C grade (316L), and a N-containing grade for increased strength (316N).

2.3.3 Ferritic Stainless Steels

Ferritic stainless steels have the body-centered cubic (BCC) structure, and as such cannot be hardened by heat treatment, and will harden only moderately with cold work. They are generally straight Cr types, with 11-27 % Cr and a low C content. They have good corrosion resistance, with an almost total immunity to stress corrosion cracking (SCC). Despite having poor tensile strength (in the 400-650 MPa range), they can also be successfully used at elevated temperature, when high strength is not required. They also possess good ductility and formability, together with excellent weldability. The type 430 ferritic stainless steel grade is the basic alloy that is subsequently modified with further alloying additions for specific applications [38].

2.3.4 Martensitic and Precipitation Hardening Stainless Steels.

Martensitic and precitipitation hardenable classes of stainless steels are chosen for mechanical strength. The corrosion resistance of these steels is lower than the other grades of stainless steel, and applications are generally limited to mildly corrosive environments. Because of the high strength levels, both types are susceptible to hydrogen induced cracking [37]. The basic martensitic alloy is Type 410, with modifications made to it for special purposes.

2.3.5 Duplex Stainless Steels

Duplex stainless steels are Cr-Mo alloys of Fe with sufficient austenite stabilisers (i.e. Ni and N), to achieve a balance of ferrite plus austenite. This results in a favorable combination of two

phases. The austenite confers ductility, and the ferrite, resistance to SCC. Mo strengthens the passive film and improves pitting resistance. Carbides tend to precipitate at the austenite-ferrite interface, preventing sensitisation to intergranular corrosion by grain boundary precipitation. These steels are used in more severe conditions of temperature and chloride content, where the usual austenitic grades are susceptible to pitting, crevice corrosion, and SCC [37].

2.4 Processing stages for cermet fabrication

2.4.1 Powder Pressing

Powder pressing is one of the most common forming processes used in the development of ceramic-based materials. The two main pressing approaches are (i) uniaxial and (ii) isostactic pressing. Uniaxial pressing in a die and isostactic pressing are both used for the compaction of dry powders, which typically contain < 2 wt. % water, and semi-dry powders, which contain approximately 5 to 20 wt. % water [43, 44]. In the ceramic industry, die compaction is one of the most widely used operations, allowing the fabrication of simple shapes rapidly and with accurate dimensions. In essence, powder (usually containing a small amount of water or other compaction binder to reduce die wall friction) is compacted into the desired shape by pressure. By using coarse and fine particles mixed in appropriate proportions during compaction, the degree of compaction is maximised and fraction of void space is minimised. There is usually no plastic deformation of the particles during compaction, converse to the case with ductile metal powders. One function of the binder is to lubricate the powder particles as they move past one another in the compaction process, thereby minimising the die wall and inter-particle friction, the former of which can cause damage to the pressing equipment.

For uniaxial pressing operations (i.e. where the pressure is applied in one direction), the powder is compacted in a hardened die. The formed piece takes on the configuration of the die and platens through which the pressure is applied. This method is employed to shapes that are relatively simple. However, the production rates are high, and the process is relatively inexpensive [43-46]. Despite having the above-mentioned benefits, uniaxial die compaction has its own drawbacks. These problems include improper component density or size, die wear, sample cracking and density variations. The green body formed during die compaction should ideally be free of macroscopic flaws and with minimal density gradients, the latter of which can

lead to the development of crack-like voids in the sintered body, and potentially cracking and warping during sintering. Density gradients can also enhance the formation of flaws in the compact on ejection from the die. One way to minimise density gradient in powder compaction is by uniform die filling which reduces the amount of internal movement of the powder during compaction. In addition, as noted earlier, lubricants can aid in reducing the friction between the particles as well as die-wall friction. Stress gradients (and hence density gradients) due to die-wall friction are reduced as the ratio of the length to diameter (L/D) of the compact is decreased, as illustrated in Figure 2.3 [47]. For a single-action mode press, the ratio should be less than 1. In order to reduce the degree of flaw formation during uniaxial compaction, the following measures are recommended. The use of binder to increase the compact strength, reduction of the applied pressure to minimise the extent of elastic springback, slow release of the pressure to reduce the rate of springback, and the use of a lubricant to reduce die-wall friction [43-46].

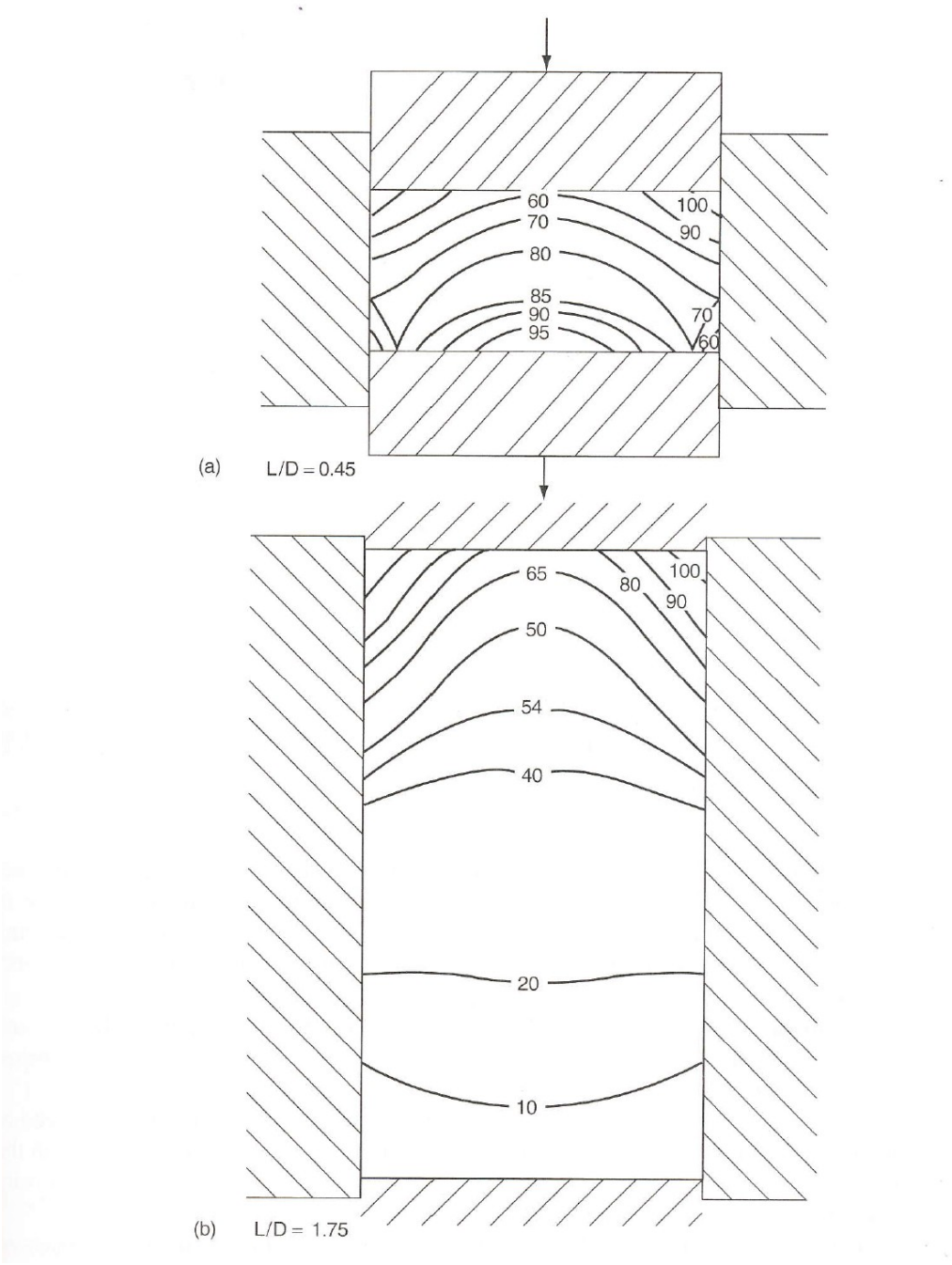

Figure 2.3: Pressure variations in uniaxial pressing due to die-wall friction and particle-particle friction, which lead to non-uniform density of the pressed compact [47].

In comparison, isostatic pressing (shown in Figure 2.4 [43]) involves the application of a uniform hydrostatic pressure to the powder contained in a flexible rubber container. There are two modes

of isostatic pressing: (i) wet-bag pressing and (ii) dry-bag pressing. In wet-bag pressing, a flexible rubber mould is filled with powder, submerged in a pressure vessel filled with oil, and compacted through the application of high pressure (where the fluid is the pressure-transmitting medium).

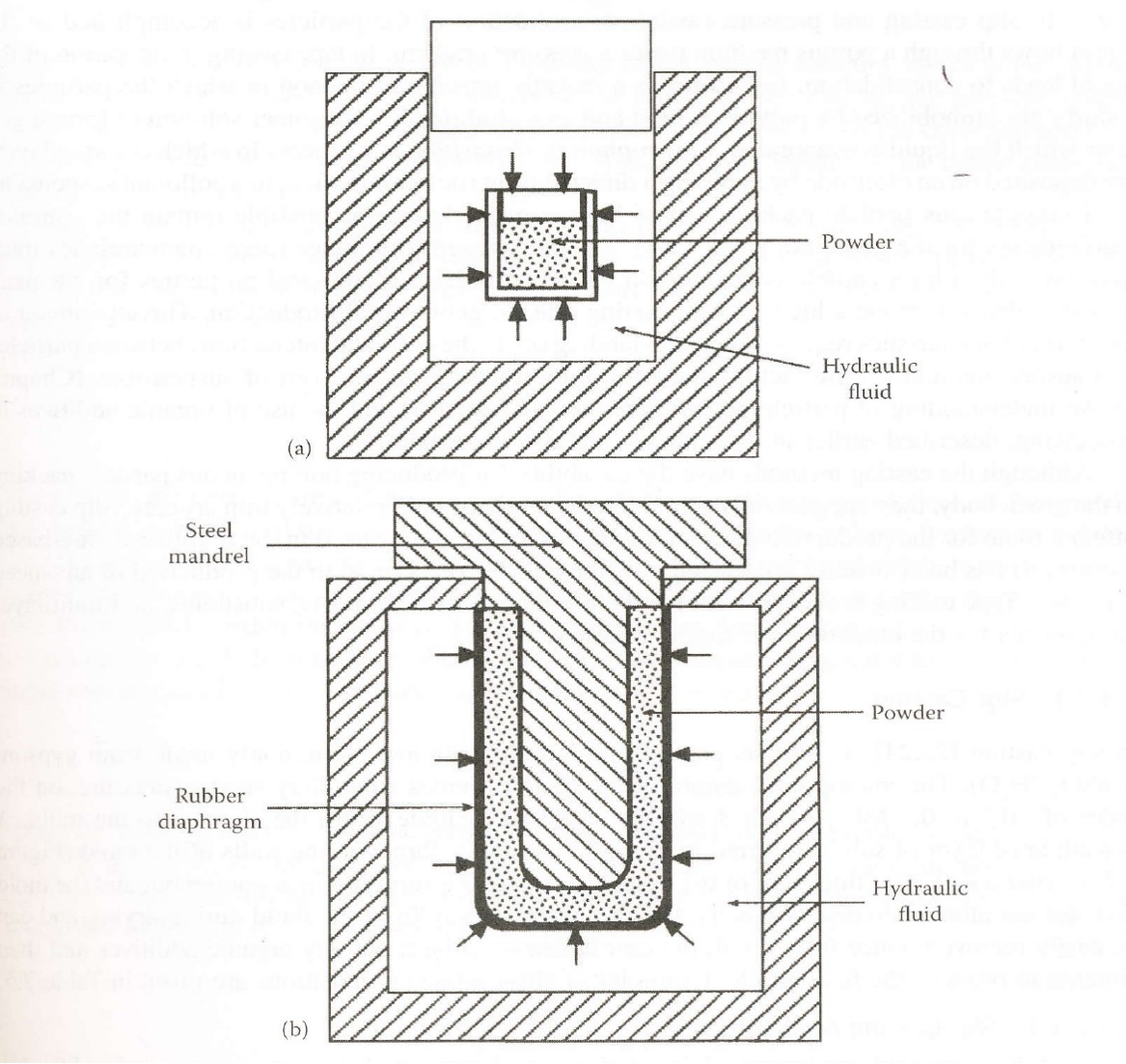

Figure 2.4: Two modes of isostatic pressing: (a) wet-bag pressing and (b) dry-bag pressing [43].

Following the pressing operation, the mould is removed from the pressure vessel and the green body is retrieved. Wet-bag pressing is used for the formation of complex shapes and for large component sizes. For dry-bag pressing, the mould is fixed in the pressure vessel and need not be removed. The pressure is applied to the powder situated within a fairly thick rubber mould. This pressing technique is easier to automate than wet-bag pressing. It is used in the formation of

spark plug insulators, by compressing a porcelain powder around a metal core, as well as for plates and hollow tubes. Compared to die compaction, the formation of flaws in isostatically pressed compacts is much less severe, but delamination and fracture (caused by elastic springback) can still occur if the applied pressure is released too rapidly. In the production of cermets, uniaxial and isostatic compaction are followed by a firing operation (i.e. sintering), in order to fully densify the component. During firing the formed piece shrinks, and experiences a reduction of porosity and an improvement in mechanical integrity. These changes occur by coalescence of the powder particles into a more dense mass [46].

2.4.2 Sintering

Sintering is a technique used for the powder processing of ceramics or ceramic-metallic composites (i.e. cermets), where powder compacts are consolidated via thermal energy. This consolidation causes the powder preforms to shrink, with a concurrent reduction in porosity, and an increase in mechanical integrity. This is brought about by the coalescence of the powder particles into a more dense mass, due to diffusion occurring at and across the grain boundaries. The basic mechanism of sintering is illustrated in Figure 2.5 [46]. After pressing, many of the powder particles touch one another (Figure 2.5(a)). During the initial sintering stage, necks form along the contact regions between adjacent particles, in addition, a grain boundary forms within each neck, and every interstice between the particles eventually becomes an isolated pore (Figure 2.5(b)). As sintering progresses, the pores become smaller and more spherical in shape (Figure 2.5(c)).

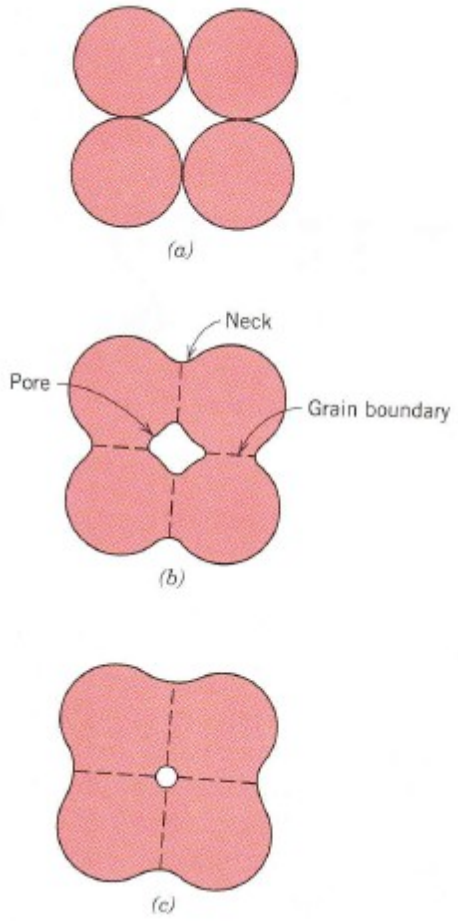

Figure 2.5: Illustrative images showing the stages of microstructural change during sintering (a) Powder particles after compaction. (b) Particle coalescence and pore formation as sintering begins. (c) As sintering proceeds, the pores change size and shape [46].

The driving force for sintering is the reduction in total particle surface area, as surface energies are larger in magnitude than grain boundaries energies. Sintering is carried out below the melting temperature of the material; so that a liquid phase is normally not present (liquid phase sintering is discussed in the following section). The mass transport necessary to effect the changes shown in Figure 2.5 is accomplished by atomic diffusion, from the bulk region of the particles to the neck [46].

The simple two-sphere sintering model can be used to explain the sintering theory. Consider two spherical particles in contact, as shown in Figure 2.6 [48]. In powder compacts there are many such contacts on each particle. The bonds between contacting particles enlarge and merge as

sintering progresses. The two sphere sintering model demonstrates the development of the interparticle bond during sintering, starting with a point contact. Neck growth creates a new grain boundary at the particle contact and, if time is sufficient, the two particles will eventually coalesce into a single larger particle [48].

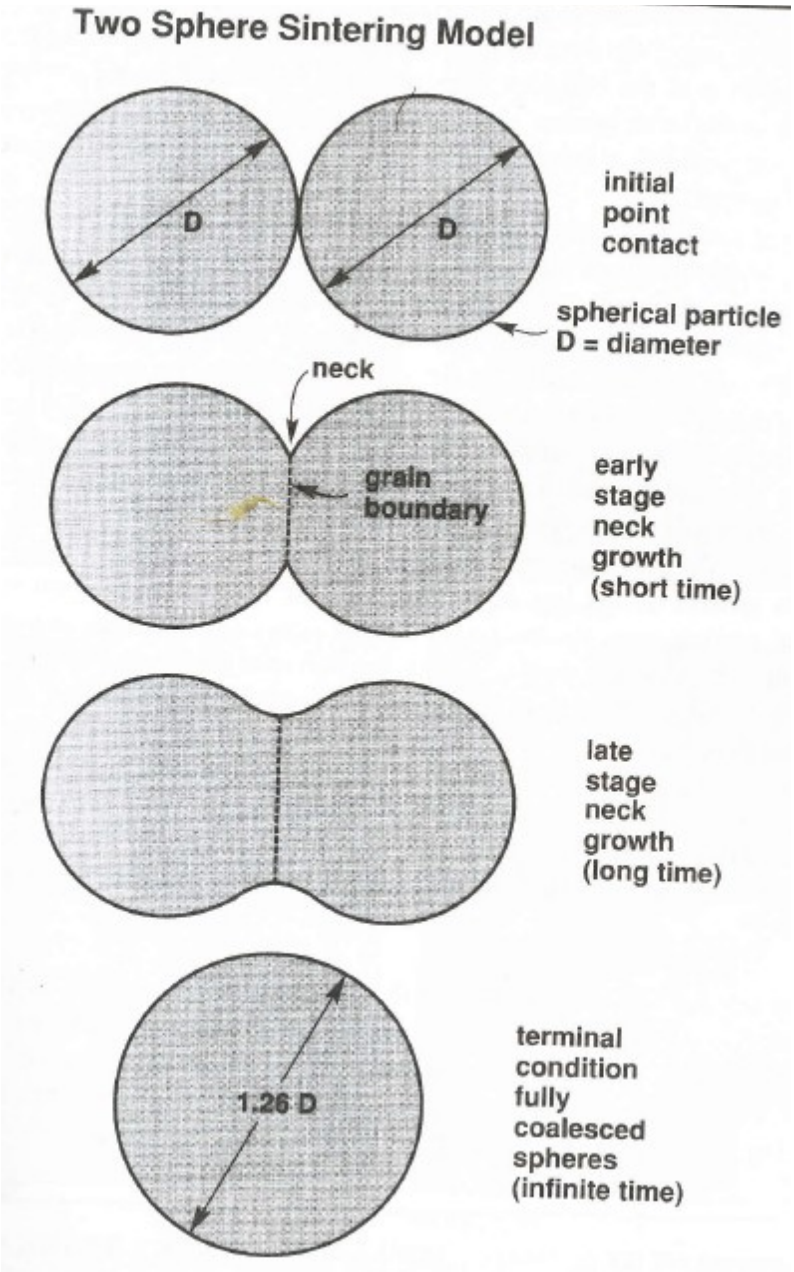

Figure 2.6: Schematic images of the two sphere sintering model [48].

At each contact, a grain boundary grows to replace the solid-vapour interface. As shown in Figure 2.6, prolonged sintering causes the two particles to coalesce into a single sphere, with a final diameter approximately 1.26 times the original diameter [48]. The primary characteristic of initial stage of sintering is the rapid growth of the interparticle neck. During the intermediate stage, the pore structure becomes less rough, and has an interconnected, cylindrical character. Grain growth can occasionally occur in the later portion of the intermediate stage of sintering, giving a larger average grain size with fewer grains. By the final stage of sintering, the residual pores are largely spherical and closed, and grain growth may become evident [48].

As outlined previously, solid state sintering occurs as a result of the formation of interparticle bonds between two touching particles. In other words, for powder particles to effectively sinter properly mass must be moved in between them. Mass transport encourages the formation of a neck between the two touching particles and, as sintering advances, the neck grows and the particles coalesce. Different thermally activated mass transport mechanisms arise during solid state sintering, which help to explain the densification through the movement of atoms or vacancies to/from the boundary between the two powder particles that form the neck. These mechanisms are surface transport and bulk transport mechanisms [48]. An illustrative diagram showing the various types of surface and bulk transport mechanism is presented in Figure 2.7 [49].

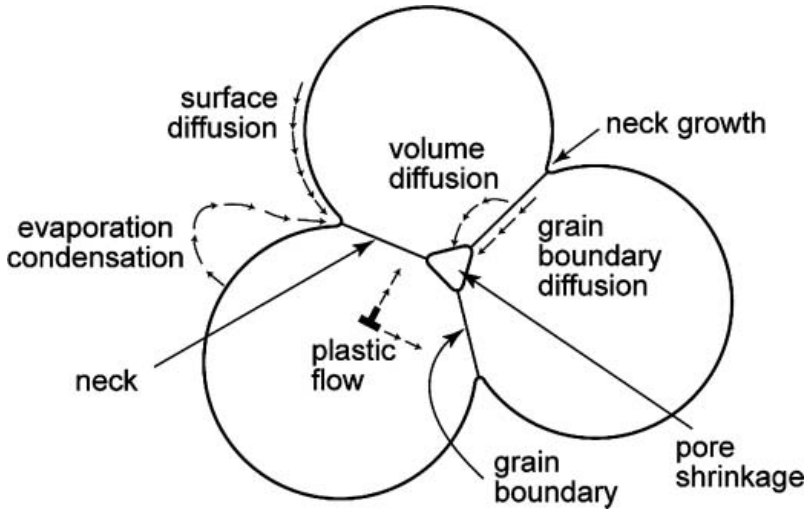

Figure 2.7: An illustrative diagram showing the various mass transport paths that provide neck growth and pore shrinkage. Surface diffusion (provides no densification) and bulk transport (gives densification) are the two transport mechanisms [49].

In surface transport mechanisms, there is transport of atoms from one surface to another leading to neck growth without shrinkage or densification. Furthermore, surface transport is the coarsening mechanism that involves the movement of material from particle surface to the neck thereby reducing the surface energy; as such there would be a resultant increase in neck growth (with concurrent reduction in overall surface area) but no densification, as there is no mass transfer between the particles. It occurs mostly at lower temperature. There are three types of surface transport mechanisms: evaporation-condensation, surface diffusion and volume diffusion [48, 50].

However, the bulk transport mechanism is more prevalent at higher temperatures and includes volume diffusion and grain boundary diffusion. This is a transport mechanism where atoms are transported from the bulk of the particle (grain boundary and/or particle interior) to an external surface (usually at the pore surface near the neck). It is the densification mechanisms (i.e. leads to shrinkage) in which the contacting plane between adjacent particles serves as the source for diffusional transport and the neck is also the sink. In other words, diffusional transport takes place along the grain boundary or through the lattice, as illustrated in Figure 2.7 [48-50].

It should be noted that volume diffusion exists as both surface and bulk transport mechanisms, but these are not depicted in Figure 2.7 [49]. Figure 2.8 [51] illustrates volume diffusion existing as both surface and bulk transport mechanisms.

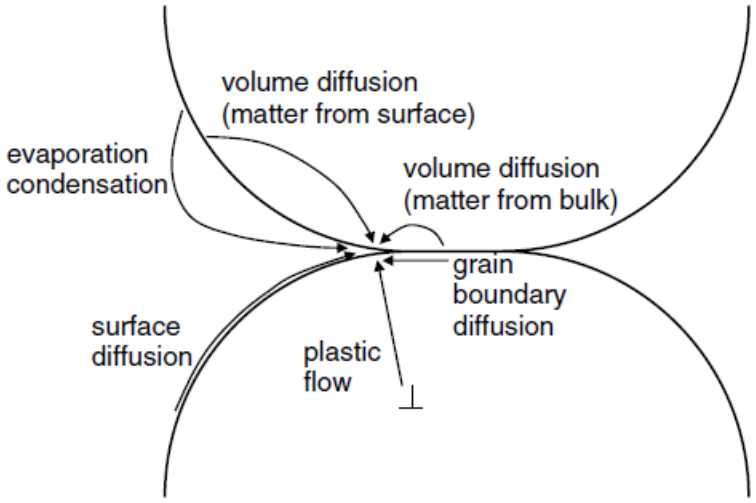

Figure 2.8: An illustrative diagram of transport mechanisms in solid state sintering showing volume diffusion existing as bulk and surface transport mechanisms [51].

2.4.3 Liquid Phase Sintering

Liquid phase sintering (LPS) is a process for forming high performance, multiple-phase components from powders. It involves sintering under conditions where solid grains coexist with a liquid phase that wets the solid material [52]. An illustrative diagram showing the various stages in liquid phase sintering is shown in Figure 2.9 [48].

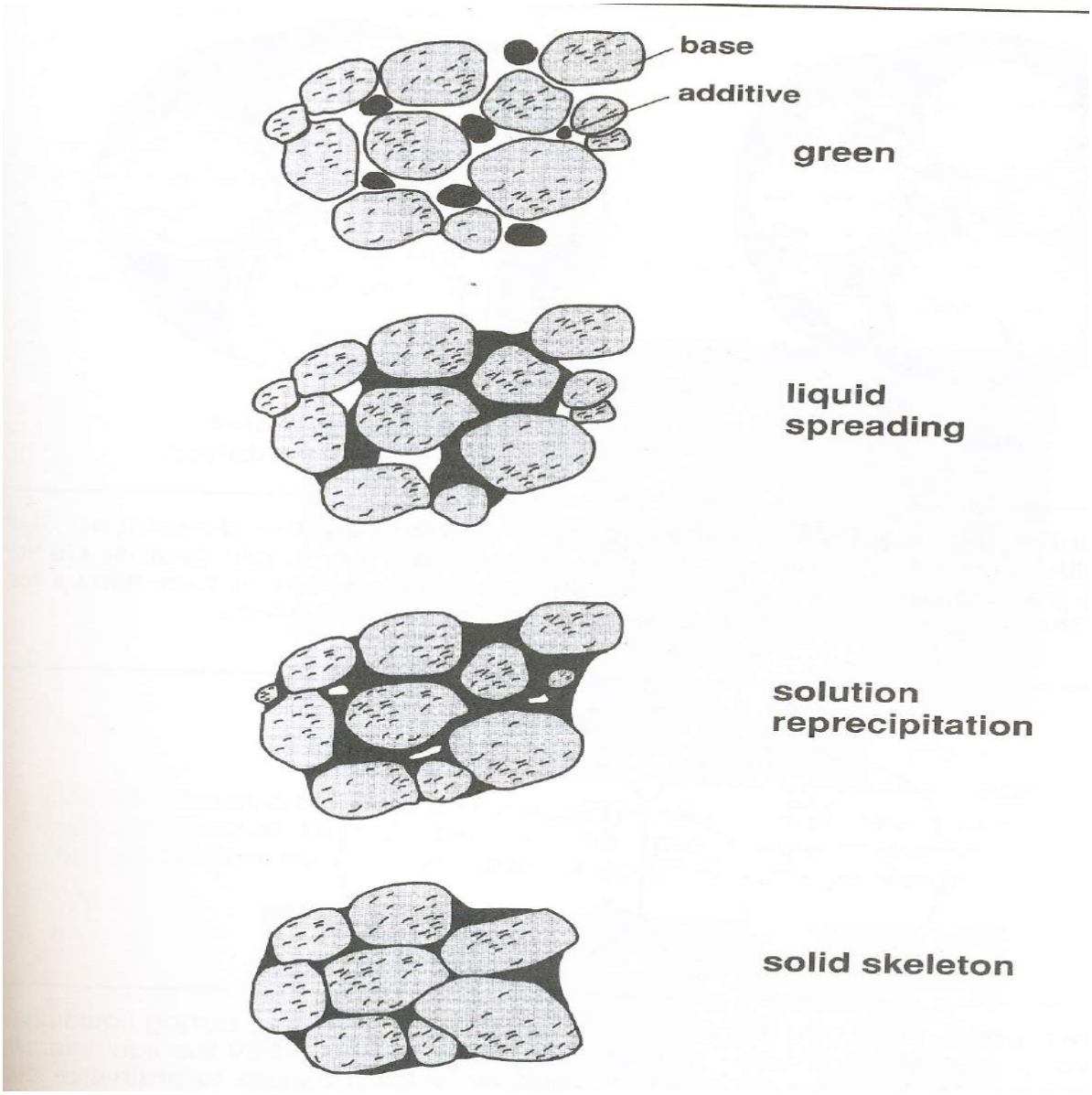

Figure 2.9: A schematic diagram showing the stages of LPS processing using a mixture of two powders. The base powder remains solid during sintering and the additive powder is responsible for liquid formation [48].

Many variants of LPS are applied to a wide range of engineering materials. An example application of LPS is in the production of high-speed metal cutting inserts. LPS is applied to alloys and composites that melt over a range of temperatures. It is important that the solid grains are at least partially soluble in the liquid. This solubility causes the liquid to wet the solid. A capillary force is generated that pulls the grains together. The solid material also softens at high temperature, which further assists densification. Liquids are associated with high-diffusion rates, providing a rapid sintering response or the potential to lower sintering temperatures. Since the final product is a composite with customised properties, LPS is the dominant commercial sintering process [52].

The coarsening process in LPS is shown in Figure 2.10 [48]. In LPS, once the liquid is formed it will flow to wet the particles. Initially, particle rearrangement contributes to densification. With continued heating, the solid phase dissolves into the liquid and the amount of liquid grows until it is saturated with solid component. The liquid phase then becomes a carrier for the solid phase atoms in a process termed solution-reprecipitation (or Ostwald ripening), wherein the small grains dissolve and the material is reprecipitated on to the surface of the larger grains. Solution reprecipitation allows for grain growth by the dissolution of the smaller grains with subsequent solid phase precipitation on the larger grains.

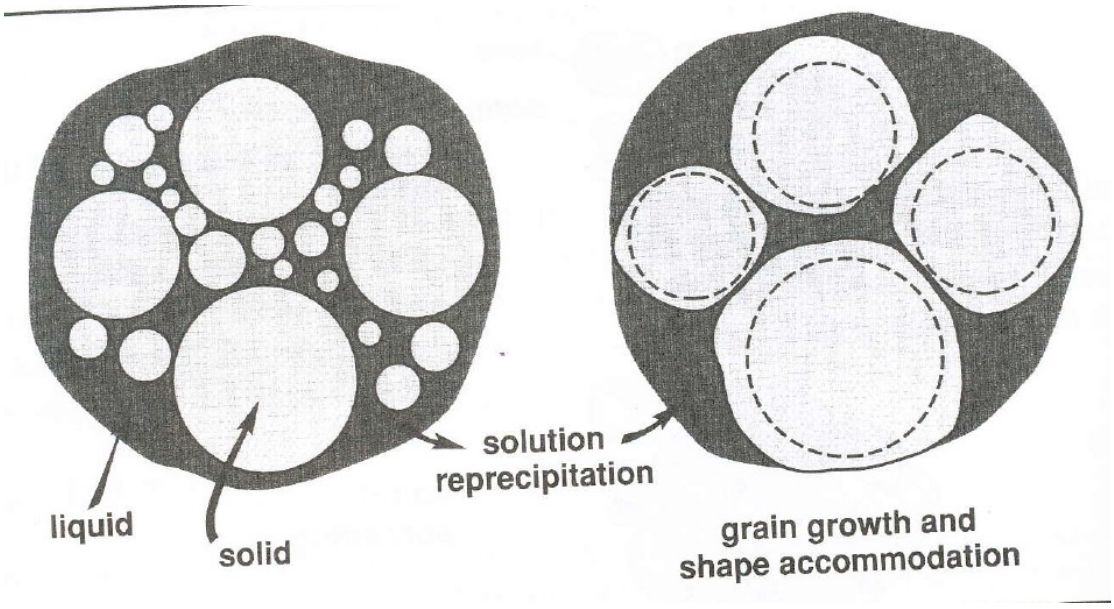

Figure 2.10: Illustrative diagram showing the process of solution-reprecipitation [48].

Besides grain growth, the process provides grain shape accommodation, which in turn allows for a better packing of the solid and release of liquid to fill any remaining pores. The solubility of solid grains is inversely proportional to the grain size; hence small grains preferentially dissolve in the liquid phase and, over time, the grain count decreases while the grain size increases [48].

Generally, the densification during liquid phase sintering is dependent on the melt contact angle (and consequently dihedral angle) and excellent liquid phase sintering is obtained when both angles are small [53]. The liquid should have a low contact angle [48]. The contact angle is simply the transition point between the wetting and non-wetting of the liquid as illustrated in Figure 2.11 [50, 52]. Unlike in solid state sintering, the densification rates are faster in liquid phase sintering because of the presence of the liquid phase, which results in more rapid material transport through enhancing the diffusion rate. The liquid must wet and spread over the solid grains for effective liquid phase sintering to occur.

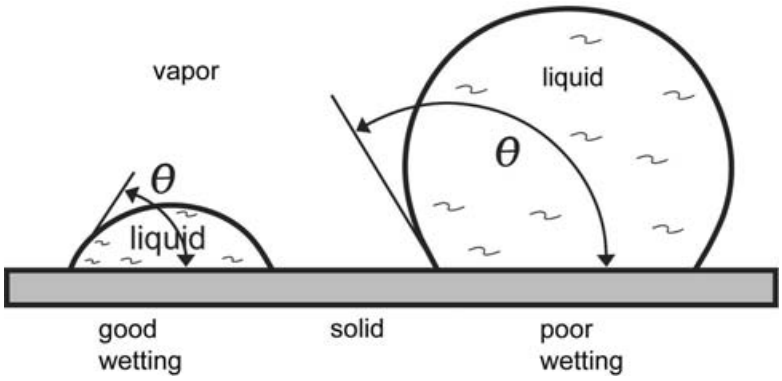

Figure 2.11: An illustrative diagram showing good (left) and poor (right) wetting conditions. A low-contact angel promotes wetting, while a high contact angle resists wetting [52].

The wetting liquid should have small contact angle θ, which is defined by the equilibrium of surface energies (wetting occurs when the total free energy is reduced) by the formula [53].

$$Cos\theta = \frac{\gamma_{sv} - \gamma_{sl}}{\gamma_{lv}} \qquad \text{Equation 2.2}$$

where γ_{sv}, γ_{sl} and γ_{lv} represent the solid-vapour surface energy, solid-liquid surface energy, liquid-vapour surface energy, respectively. As presented in Figure 2.11 [52], the low-contact

angle promotes liquid spreading over the solid grains, thereby providing a strong capillary attraction that helps in the densification of the system. Factors that influence the surface chemistry or solubility have an effect on the contact angle. For instance it is reported that the addition of Mo to TiC-Ni cermets decreases the contact angle from 30º to 0º, hence improving densification [52]. Generally, good wetting occurs because of the solubility of the solid grains in the liquid and the presence of the liquid aids faster diffusion of the atomic species in the liquid, hence leading to better densification, as noted previously. There are many known systems that exhibit these favourable features, including cermets like TiC-steel (present system) [54-55], TiC-Ni and WC-Co cermets [48].

However, Figure 2.11 [52] also shows a scenario with a high contact angle, inferring poor wetting characteristics (i.e. the liquid retreats from the solid grains), which leads to swelling of the compact; in other words, a low contact angle encourages densification whereas a high contact angle can lead to swelling [52]. An illustrative example, showing a system with non-wetting characteristics (i.e. high contact angle), is presented in Figure 2.12 [52].

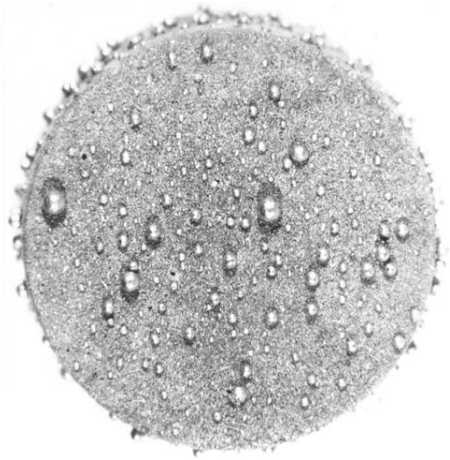

Figure 2.12: An illustrative scanning electron microscopy image showing the surface of a sample where the non-wetting liquid exuded to the compact surface to form small spheres [52].

Another parameter that influences the densification during LPS is the dihedral angle. Figure 2.13 [52] shows the dihedral angle and surface energy equilibrium between two intersecting solid grains with a partially penetrating liquid phase (smaller value of dihedral angle favours liquid phase sintering) [53].

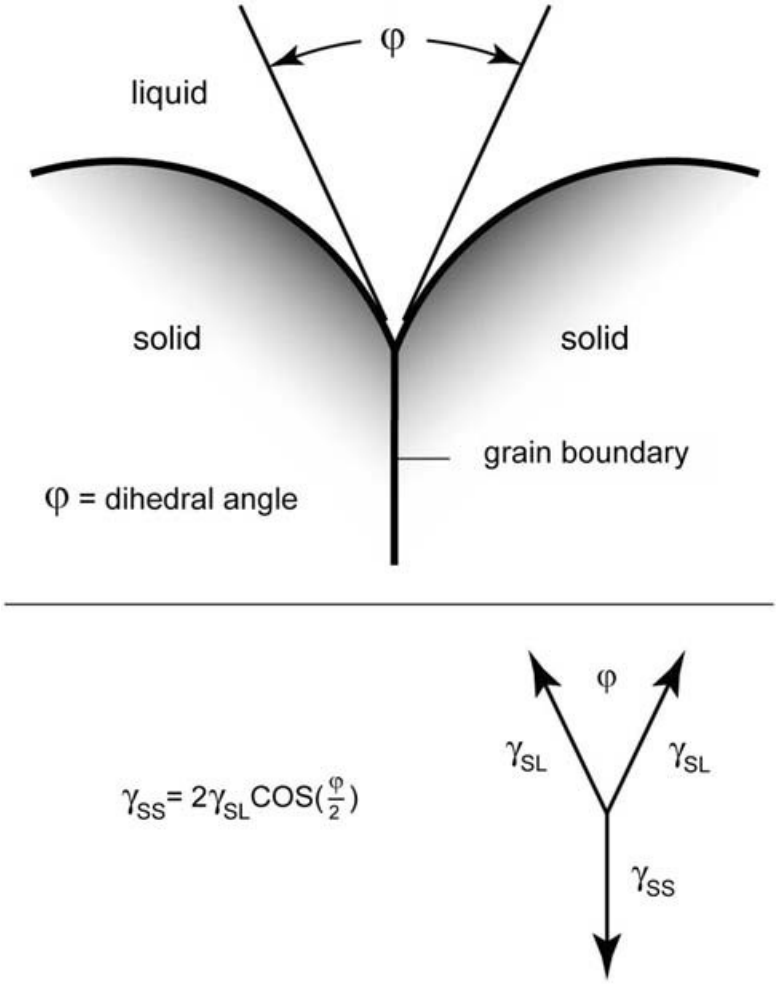

Figure 2.13: An illustrative diagram showing the dihedral angle for a solid-liquid system, and the surface energy equilibrium between two intersecting solid grains with a partially penetrating liquid phase [52].

As can be seen in Figure 2.13 [52] the dihedral angle φ is formed at the intersection of the solid – solid grain and the liquid. Dihedral angle is determined by the ratio of the grain boundary energy to the solid-liquid surfaces by the given formula [53]:

$$2\gamma_{sl}Cos\left[\frac{\varphi}{2}\right]=\gamma_{ss} \qquad \text{Equation 2.3}$$

where γ_{ss} and γ_{sl} are interfacial surface energies for the solid and liquid, respectively.

Generally, if the energy ratio (i.e. solid-solid to solid-liquid energy ratio) is greater than 2, then the dihedral angle is 0º, which means that there would be penetration of liquid between the grain

boundaries of the two solid phase particles. For instance, in Figure 2.14 [53], it can be seen that as the energy ratio is close to 2, the dihedral angle approaches 0º, inferring a better penetration of the liquid between the grain boundaries of the solid phase.

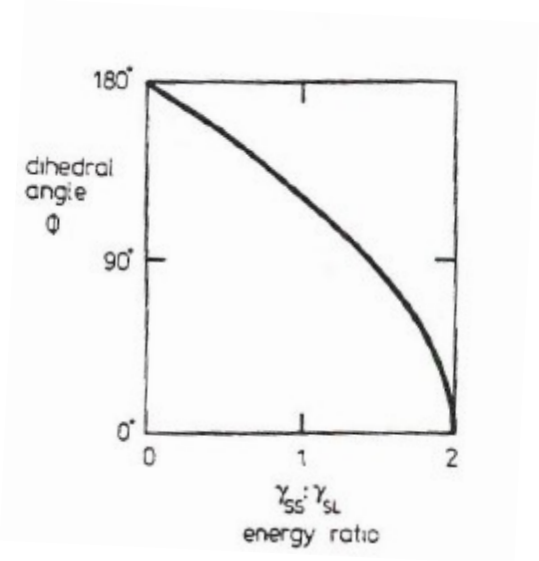

Figure 2.14: An illustrative diagram showing the relationship between dihedral angle and solid-solid to solid-liquid energy ratio [53].

2.4.4 Melt Infiltration

Melt-infiltration is another technique that can be used to densify a ceramic, by filling or partially filling the porosity of a particular compact or a porous ceramic with a liquid that subsequently is solidified (Figure 2.15 [48]). This process is essentially a variation of the LPS method. However, it is generally not a production technique that is performed to obtain the hard phase in cermets, but is a method of applying the binder phase into the cermet structure once a green body has been formed from the hard phase. In this approach, LPS must occur to sinter the piece (to gain further densification when the infiltrated liquid volume is significantly less than the porosity prior to infiltration), as the liquid binding phase must be free to move in order to infiltrate the green body.

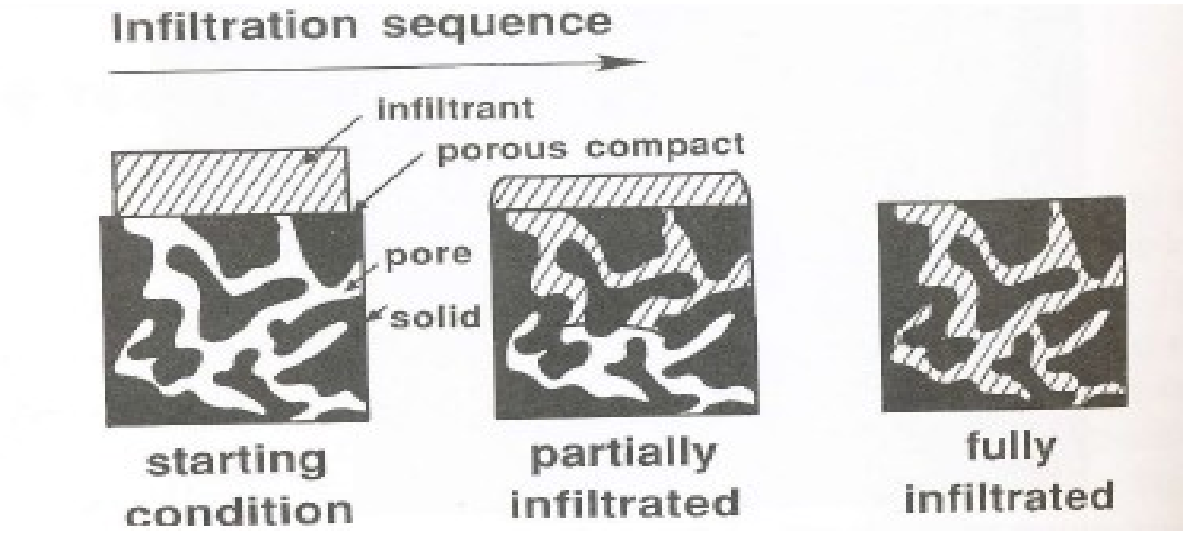

Figure 2.15: Schematic illustration of the infiltration sequence where capillary forces pull a molten metal into the open pores of a sintered compact [48].

Melt infiltration is used for improving the density of cermets, which is achieved by infiltrating the ceramic pore structure with a metallic binder (for instance using a molten steel binder for TiC ceramics, as in the present work). In the production of cermets, for instance TiC-steel based cermets, the TiC is the ceramic phase and offers hardness and wear resistance but lacks ductility. The toughness is improved through the melt infiltration process by infiltrating the steel metal binder into the porous compact of TiC, thereby leading to a highly dense TiC-steel composite with improved properties.

Capillary wicking of the liquid occurs, due to small pore sizes and a low contact angle of the liquid on the solid. As shown schematically in Figure 2.15 [48], the capillary pressure causes liquid to flow into the porous compact. In some instances the infiltrant will completely fill the pore space, exhibit good flow and wetting of the pore structure, and will not leave a residue. Despite the beneficial effect of infiltration outlined previously, there are some problems encountered with melt-infiltration. Generally, the infiltrant is formed on one surface of the sintered material and capillary action draws the liquid into the pores. Because of the directional flow of the liquid, it may erode the surface from which the infiltrant is fed (until the amount of dissolved solid phase reaches the solubility limit). Swelling of the compact can occur as metallurgical reactions take place. For that reason, infiltration cycle times are often short, to keep

dimensional changes to less than 2 %. density is the most improved property obtained by infiltration [48].

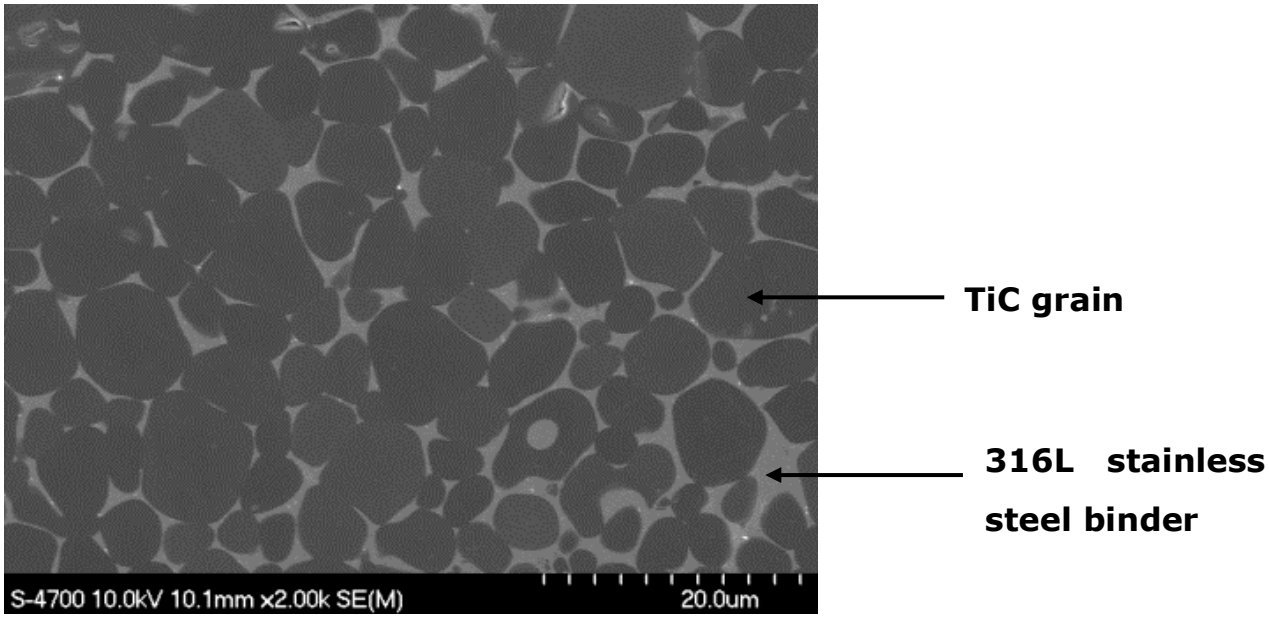

Figure 2.16: SEM images showing complete melt-infiltration for a TiC-20 vol. % stainless steel cermet.

2.5 Characterisation and Properties of Ceramic-Metal Composites

Following review of the development of the TiC-steel based cermets using the melt infiltration techniques, the literature review in the next section is focused on the wear and corrosion behaviour of cermets (i.e. characterisation and properties of developed cermets).

2.5.1 Wear

Wear is simply surface damage that is encountered when one or both of two solid surfaces are in rolling, sliding or impact motion relative to one another and is mostly observed through surface interactions at asperities. During the process of wear, material on the contacting surfaces could be displaced so that properties of the solids, at least near the surface, are altered, although little or no material may actually be lost. As the wear process advances, some material may be removed from a surface and could result in the transfer to the mating surface (adhesion) or break loose as a wear particle (three-body wear). Wear is generally observed when material is lost and also

involves damage due to material displacement on a given body with no net change in weight or volume [56].

The study of tribology is comprised of three important components; wear, friction and lubrication. The dissipation of surface materials leads to wear, dissipation of load between two surfaces moving relative to each other leads to lubrication, while dissipation of energy leads to friction [49-50]. The wear processes can also be explained in terms of an "tribosystem", which includes a solid body, a counter-body, an interfacial element and the environment. The overall interaction between the different parameters in the tribosystems will lead to different wear types, which could be sliding, rolling and impact wear [57-58]. A schematic illustration of a tribosystem is shown in Figure 2.17 [57].

There are many operative wear mechanisms but the most studied ones are abrasive, adhesive, fatigue, impact (by erosion and percussion), chemical (sometimes known as corrosive wear) and electric-arc-induced wear. Summarily, the adhesive wear process involves the interaction of asperities on two opposed surfaces in motion, leading to fusion of the metals and subsequently fracture of the asperities. Abrasive wear on the other hand, is the removal of material from one surface by the harder asperities of another surface. Fatigue wear is observed due to a cyclic stress state on the metal surface leading to a mechanical damage to surface and sub-surface regions. The damage that is accumulated would eventually lead to failure via fracture. Lastly, corrosive wear is the synergistic interaction between chemical reactions and wear processes occurring simultaneously [56-58].

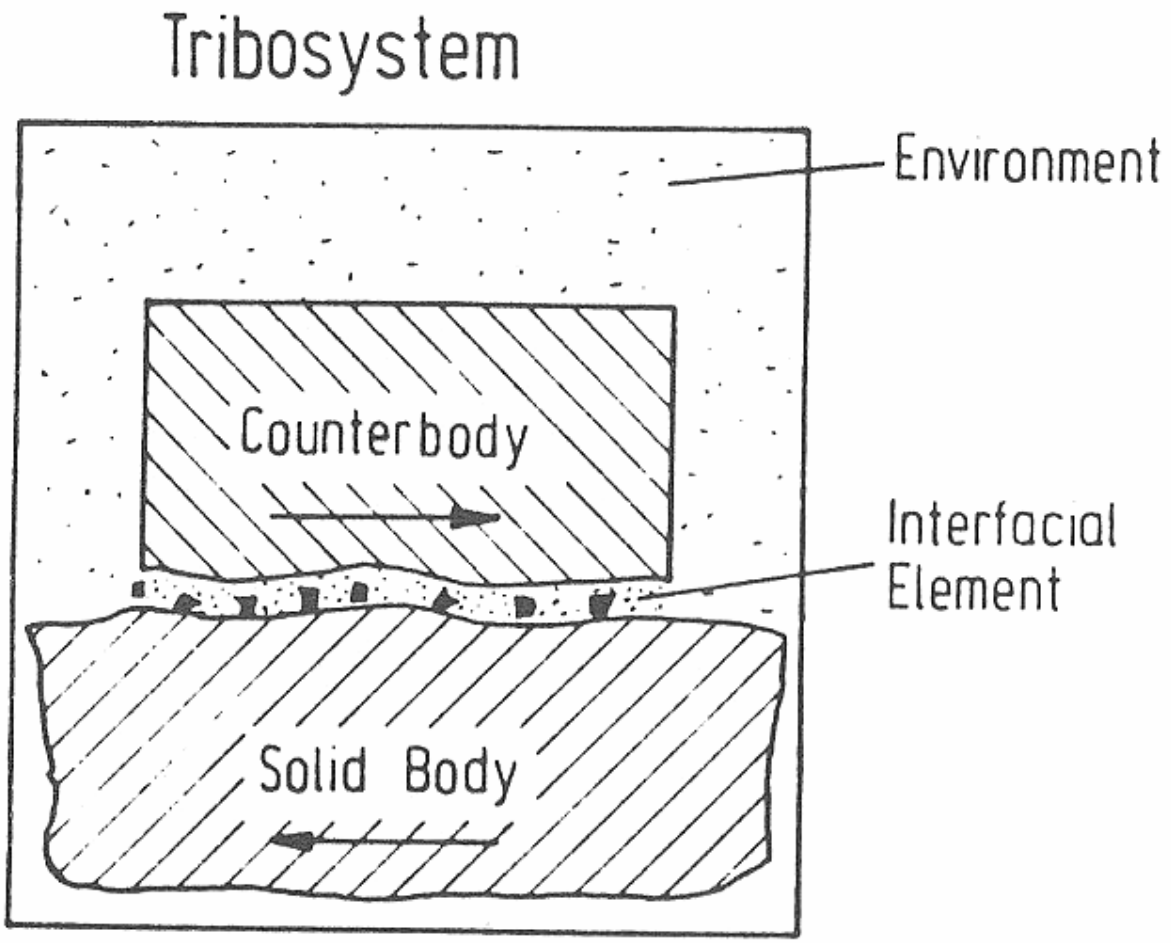

Figure 2.17: Schematic representation of a tribosystem [57].

Abrasive and adhesive wear are the major themes for this present research and as such would be discussed in further detail in the following sections.

2.5.2 Adhesive Wear

Adhesive wear is simply the interaction of asperities on two opposed surfaces in motion. For instance, when two flat solid bodies are in sliding contact, adhesion occurs at the asperity contacts at the interface, leading to sharing of these contacts. This sharing could result in detachment of a fragment from one surface and attachment to the other surface. As the sliding process progresses, the transferred fragments may eventually come off the surface on which they are transferred and be transferred back to the original surface, or they could potentially form loose wear particles. In addition, some of these transferred fragments could be fractured by

fatigue as a result of repeated loading and unloading action resulting in formation of loose particles or wear debris [56].

There are situations where adhesive forces could be minimised. For instance, the presence of adsorbed gases, lubrication, oxidation, or an oxide layer (passive films) can all slightly reduce the adhesive forces of the two surfaces during sliding motion by potentially acting as a barrier that reduces the amount of real contact area [59]. Electron transfer also promotes the formation of adhesive bonds. For instance, if two different metals are adhered together, it is stated that the metal with higher electron density will donate its electrons to the other in the process known as the "Jellium model" [60]. The principle of adhesion and transfer due to material contact is illustrated with a schematic diagram shown in Figure 2.18 [59, 60]. The adhesive wear mechanism is believed to take place by the following steps. In the first instance, sliding commences and friction is relatively low as a result of surface contamination. The frictional force increases with the rate at which the surface contamination is removed from the sliding interface. When the surface contamination is completely removed, then adhesion of contacting asperities will occur, leading to an increase in friction force provided that tribochemical oxidation does not occur.

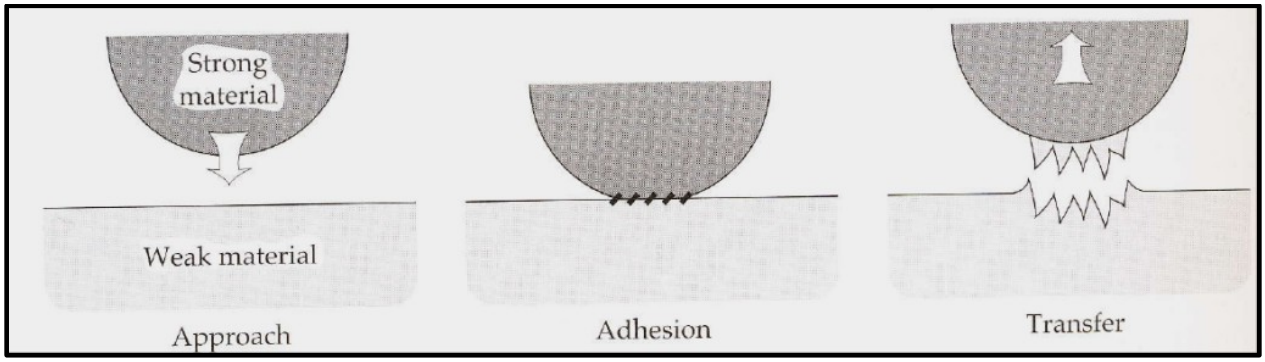

Figure 2.18: An illustrative diagram showing contact, adhesion, material transfer due to electron transfer, and adhesive bond formation. Typically the softer or weaker material is transferred to the stronger material [59-60].

Subsequently the weaker material will fracture and transfer to the stronger material could occur, as illustrated in Figure 2.18 [59-60]. This could potentially lead to the formation of a transfer

layer or film. Fracture and transfer film formation are not the only possible adhesive wear mechanisms following adhesion of sliding asperities, other mechanisms could be the asperity fracture following adhesion by brittle fracture of the weaker asperity, as illustrated in Figure 2.19 [59-60].

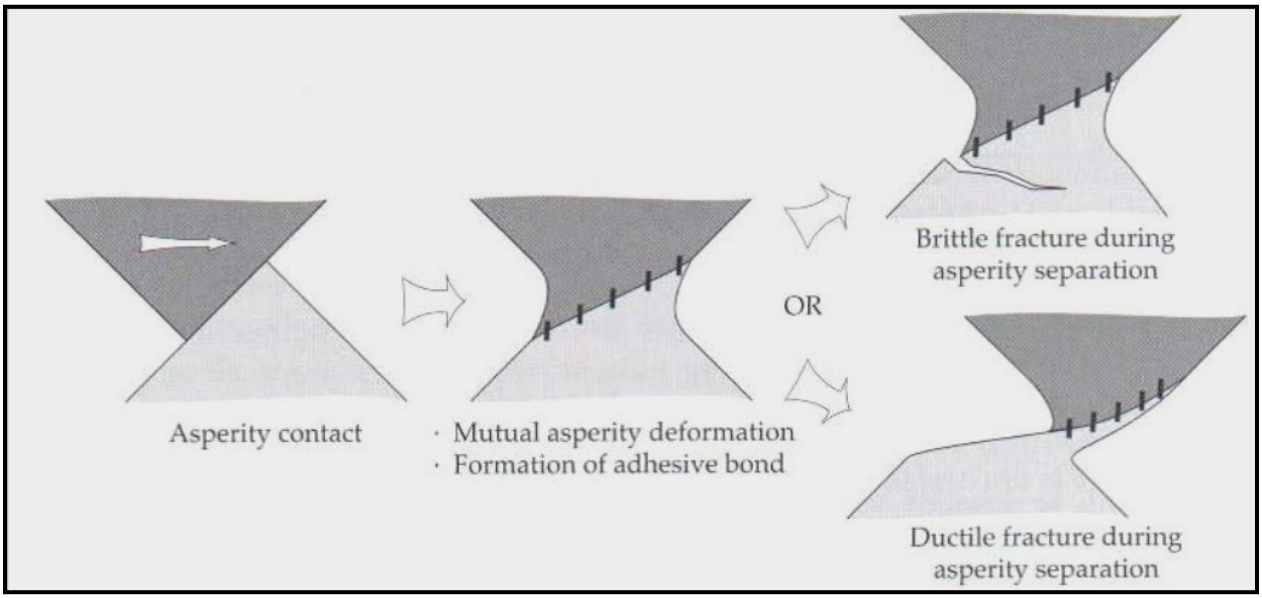

Figure 2.19: An illustrative diagram showing alternative models for the production of wear debris and deformation by adhesive contact of asperities [60].

Generation of plate-like wear debris could possibly be produced as a result of adhesive wear, as demonstrated in Figure 2.20 [60]. During the adhesive wear process, continuous adhesion and transfer of materials may result in a relatively round debris particle that is composed of material from both sliding surfaces. As the particles continue to grow during the adhesive wear process, they could possibly become flattened by plastic deformation, as it is sandwiched between the sliding surfaces. The adhesive wear process will continue to grow the transferred particle until a critical thickness is reached and it detaches [59-60]. A schematic illustration showing the formation and removal of transfer particle is shown in Figure 2.21 [60].

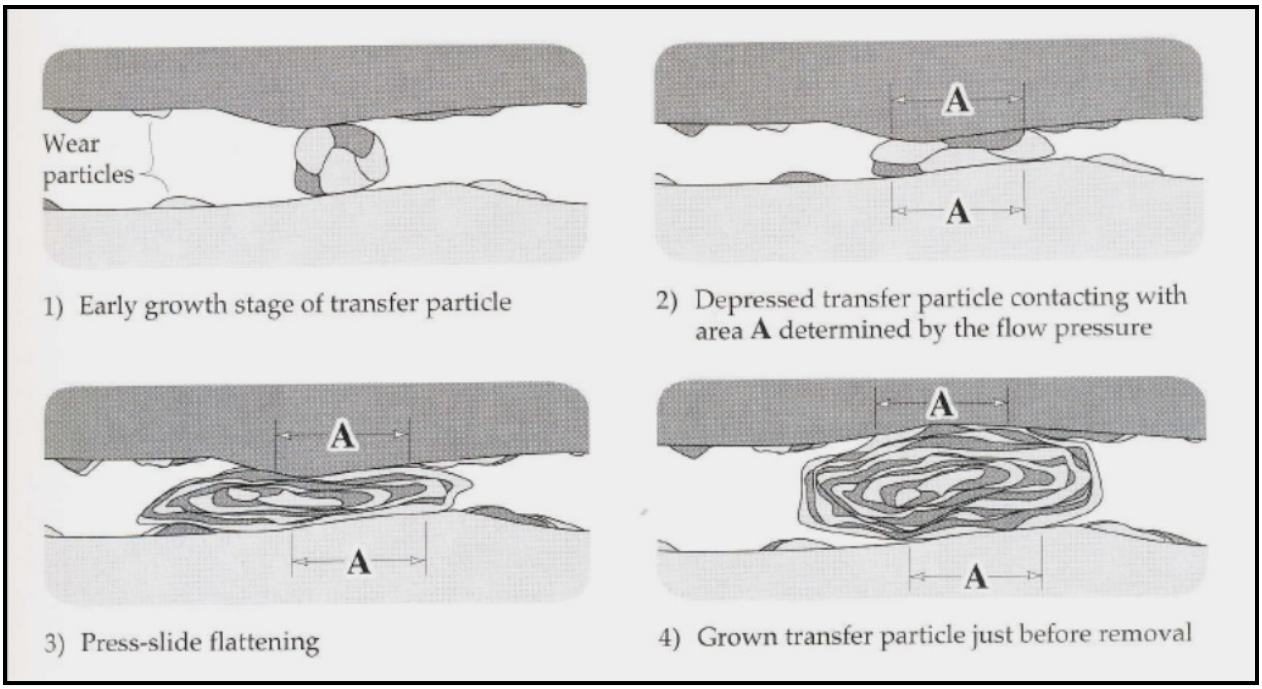

Figure 2.20: Schematic illustration of possible mechanism of wear debris formation due to adhesive transfer [60].

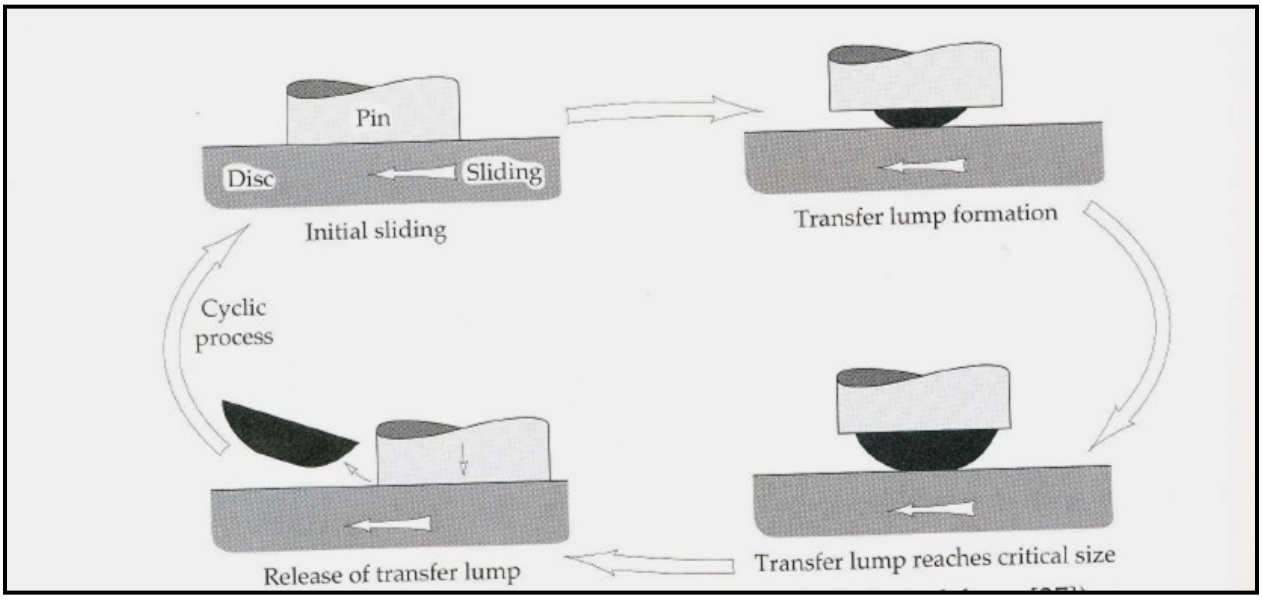

Figure 2.21: Schematic diagram showing formation and removal of a transfer particle [60].

2.5.3 Abrasive Wear

Abrasive wear has been reported to account for at least 50% of wear problems that are encountered in industry today. It is mostly experienced when hard particles such as rocks or metal fragments slide or roll under pressure across a surface, potentially leading to cutting of grooves in a similar manner to a cutting tool, displacing elongated chips or slivers of metal [61]. Abrasive wear processes simply occur when asperities of a rough, hard surface or hard particles slide on a softer surface, leading to damage at the interface by plastic deformation and/or fracture. For materials that have high ductility or possess high fracture toughness (metals and alloys), hard asperities or hard particles would result in the plastic flow of the softer material. Evidence of plastic flow is seen in metallic, ceramic, and even in some brittle materials like ceramics. Ideally, the contacting asperities of the metal deform plastically even when low loads are applied. However, for materials that possesses low fracture toughness (such as very brittle ceramics and glasses), wear processes can occur potentially by brittle fracture, in which the worn zone exhibits significant cracking [56].

Abrasive wear modes could be two-body or three-body, depending on the way the asperities pass over the worn surfaces. In a two-body abrasive wear scenario, the hard asperities or rigidly held grits pass over the surface in a manner similar to cutting tool, like the action of sandpaper on a surface. On the other hand, a three-body abrasive wear mode is observed when the grits roll or slide over the surface, since they are not rigidly held in place in either contacting surface. In a three-body abrasive wear process, small particles of abrasive material are normally trapped between the two other surfaces, and they possess sufficiently greater hardness that they abrade one or both of the mating surfaces in a three-body wear action [61-64].

In terms of comparison between two-body and three-body abrasive wear modes, two-body wear is faster, whereas three-body wear is almost ten times slower than two-body abrasive wear, since it has to compete with the other mechanisms that are taking place, for instance adhesive wear [61-64]. Secondly, two-body abrasive wear occurs in a similar fashion to mechanical operations such as machining, grinding and cutting, while in three-body abrasive wear, slower mechanisms of material removal is involved [61-64]. At the start of the abrasive wear process, the wear mechanism that is believed to be predominant at the initial phase is abrasive and/or adhesive wear, which generates wear particles (wear debris) that become trapped at the interface, leading

to three-body abrasive wear [56, 64]. An illustrative diagram of two-body and three-body abrasive wear modes is shown in Figure 2.22 [60].

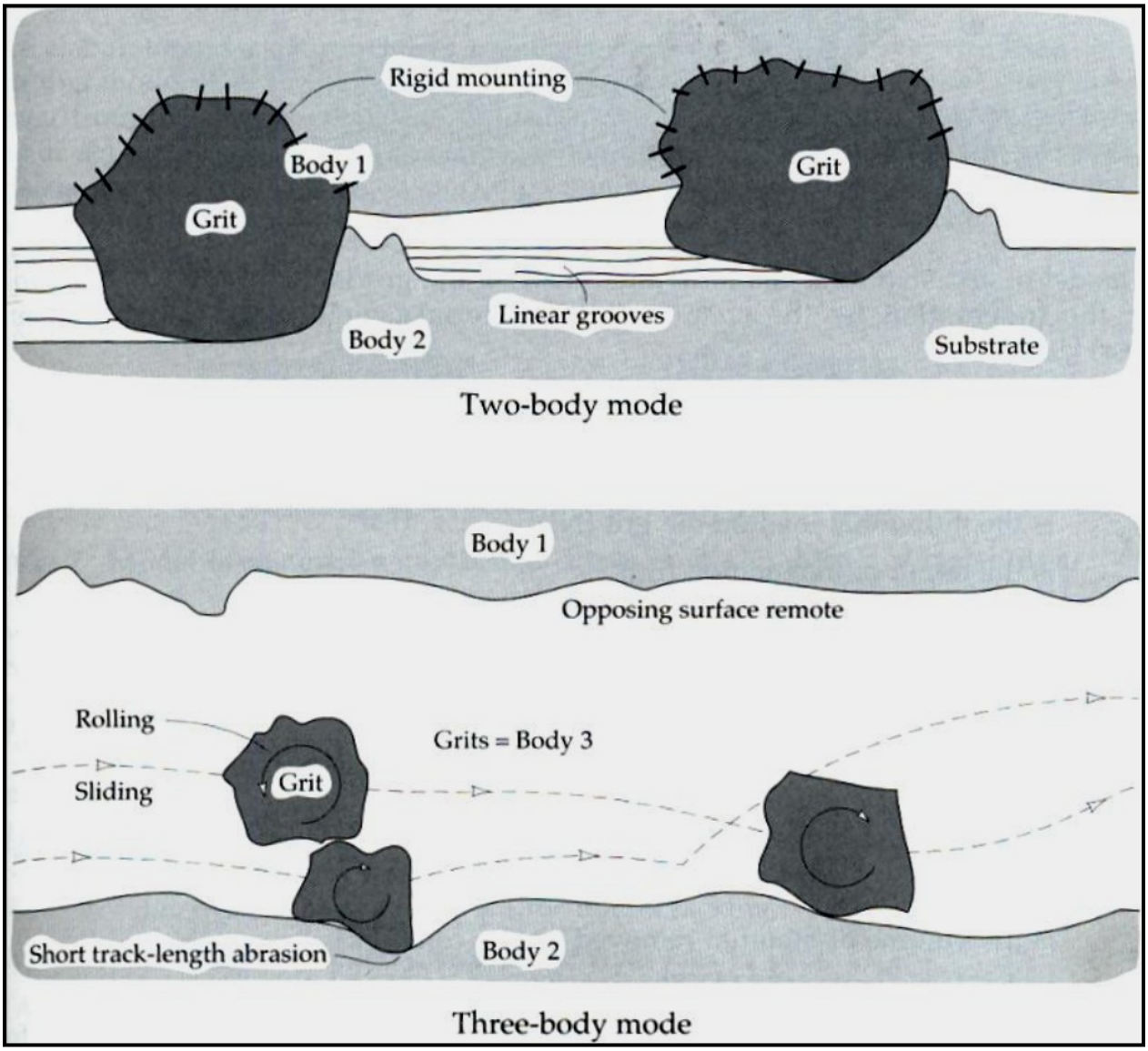

Figure 2.22: Schematic illustration showing two- and three-body modes of abrasive wear [60].

As stated previously, abrasive wear mechanisms occur as a result of sliding or rolling of hard particles on the surface of a softer material, leading to deformation and wear by different mechanisms. The illustrative diagram shown in Figure 2.23 [60] is used to explain the different abrasive wear mechanisms, which include cutting, ploughing, grain-pull, fatigue and brittle fracture [56, 59-64].

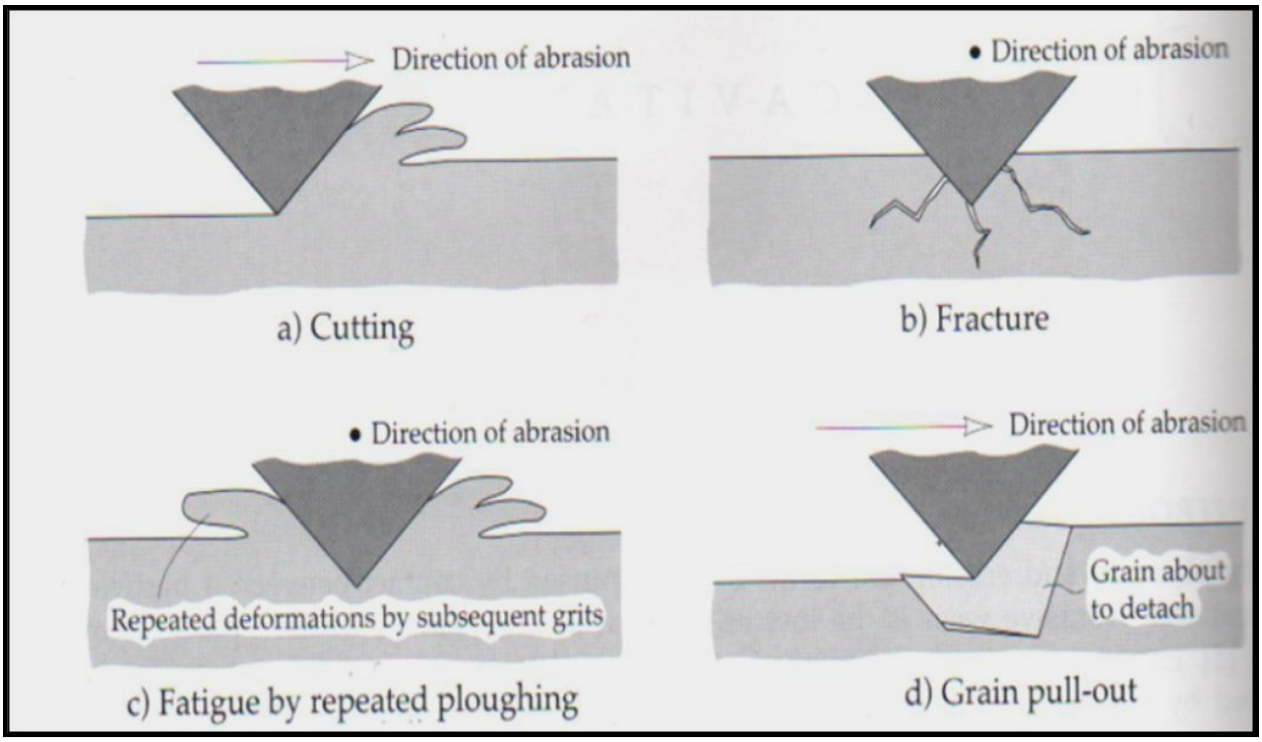

Figure 2.23: Schematic diagram showing mechanisms of abrasive wear: microcutting, fracture, fatigue and grain pull-out [60].

During cutting operations, the hard particle is embedded in the softer material and dragged, potentially leading to intense plastic deformation and material displacement around the edge of the hard particles. A more illustrative diagram showing cutting abrasive wear mode is presented in Figure 2.24 [56].

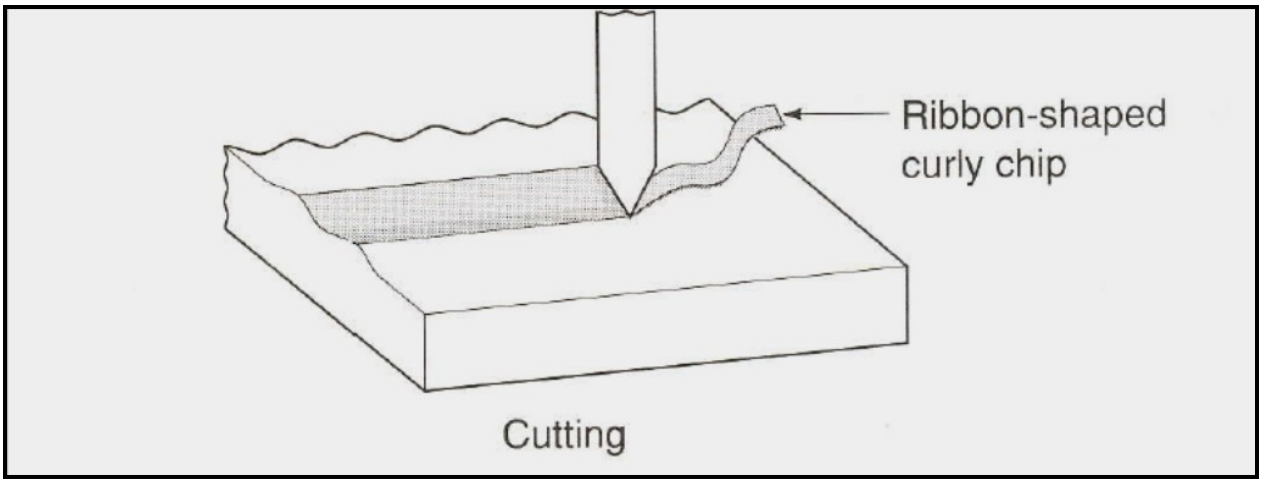

Figure 2.24: Schematic diagram of abrasive wear processes as a result of plastic deformation following a cutting deformation mode [56].

If the abraded material is brittle, for instance, ceramic materials, fracture of the worn surface could occur, as presented in Figure 2.23(b) [60]. In this particular instance, the wear debris that is generated is the result of crack convergence. However, if a ductile material is abraded by a blunt grit, in this instance, cutting is unlikely and the worn surface is repeatedly deformed, as presented in Figure 2.23(c) [60]. In this instance hence wear debris formation is the result of metal fatigue [56, 59-64].

In addition to the above outlined mechanisms, fatigue by repeated ploughing can occur, leading to the formation of ridges along the sides of the ploughed grooves. The continuous ploughing would lead to a point where the ridges become completely flattened and eventually fracture after a series of repeated loading and unloading cycles, as shown in Figure 2.23(c) [60] and elaborated in more detail in Figure 2.25 [56, 65].

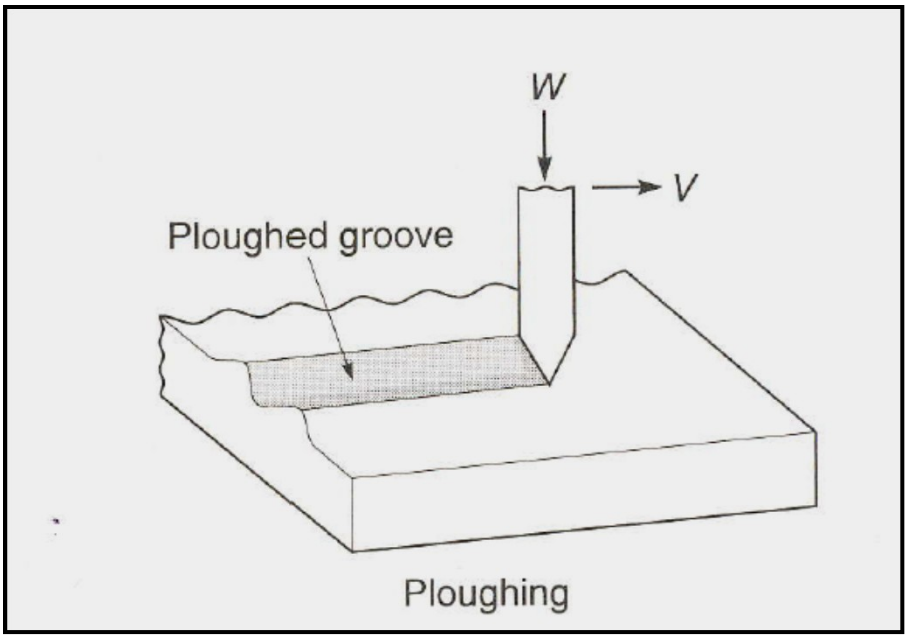

Figure 2.25: Schematic diagram showing the abrasive wear process as a result of plastic deformation by a ploughing mode [56].

The last abrasive wear mechanism is grain detachment or grain pull-out (Figure 2.23(d) [60]), which can be a relatively rare form of abrasive wear mostly found in ceramic materials. It can become extremely rapid, especially when inter-grain bonding is weak and the grain size is large (i.e. a coarse carbide grain size). On most occasions, the entire grain is lost as wear debris debris ([56, 59-66])

2.5.4 Fatigue Wear

Fatigue wear processes occur as a result of repeated rolling and sliding. It is simply the wear process that is caused by high cyclic contact stresses, leading to generation of sub-surface cracks. In this process, wear is determined by the mechanics of crack initiation, crack growth and fracture [60]. An illustrative diagram showing the process of surface crack initiation and propagation is shown in Figure 2.26 [60].

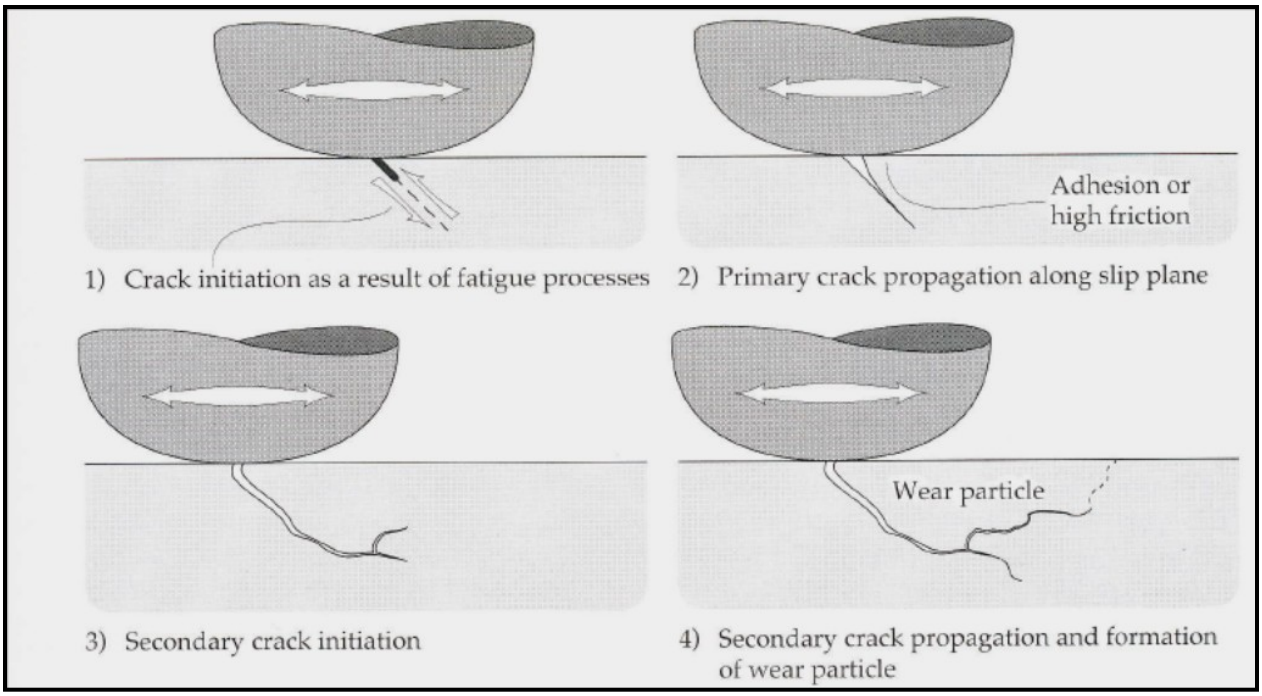

Figure 2.26: Schematic diagram showing the process of the surface crack initiation and propagation [60].

Delamination wear, which was proposed and thoroughly investigated by Suh [65] is perhaps the most recognised theory that explains fatigue wear processes during metal sliding. This model proposed that the spallation of flake-like wear debris generated from the surface of sliding contacts is caused by sub-surface crack initiation, propagation and crack linkage [59, 65]. An illustrative diagram showing mechanisms of the removal of flake-like wear debris is shown in Figure 2.27 [60].

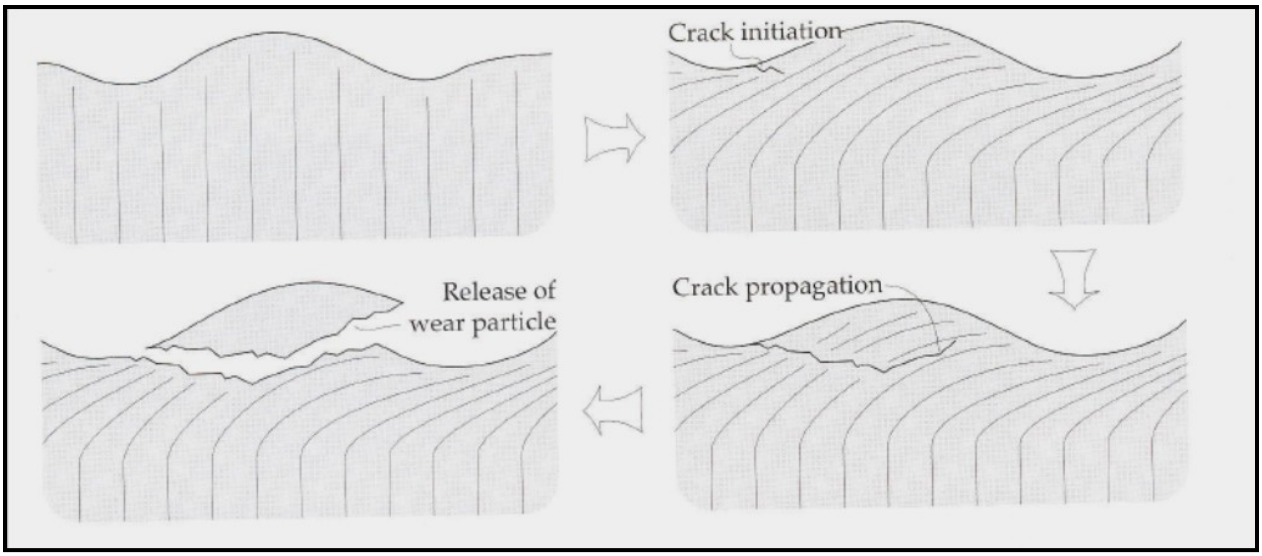

Figure 2.27: Schematic diagram showing the mechanisms of wear particle formation due to growth of surface initiated cracks [60].

This previous section (Section 2.51) has presented general information on the principles of wear but a brief overview on wear behaviour of cermets similar to material in this research is presented in the following section (a more detailed review is presented in Chapters 4 and 5).

2.6 Brief Overview of the Wear Behaviour of Cermets

TiC-based cermets have been reported to show high abrasive wear resistance [67]. They possess high wear resistance and good 'specific' mechanical properties, such as specific strength (i.e. strength divided by density), because of their relatively low density. This combination of properties makes them a candidate substitute material for the more commonly used WC-Co based "hard-metals [68]. These properties are derived from the incorporation of the ductile and strong phase of the metallic binder, and the wear and corrosion properties of the matrix carbide, thereby developing a wear and corrosion resistant TiC-based composite. However, it has been reported that increasing ductile phase toughness results in a drop in the hardness values of the composites [33].

It is generally assumed that the wear behaviour of the cermet is a direct function of both the hardness and toughness [69], and optimum wear behaviour is obtained when both of these properties are fully maximised [54]. In the view of this, the processing technique used in the

production of TiC based cermets should be carefully selected. This is because the processing technique influences the tribological properties of heterogeneous materials like cermets [70]. Therefore, any technique that would result in negligible porosity in the composite, and ensure an effective homogenous distribution of the carbide phase in the metallic binder phase, with no interfacial debonding, should be employed. For the present work, the above mentioned benefits are derived using melt infiltration in the production of TiC-steel based composites which ensures the production of highly dense materials of above 98% of theoretical density, even with a very small amount of metallic binder (as low as 5 vol. %). The grain boundary microstructure and composition play an important role in the wear behaviour of these types of heterogeneous materials. With some alloys, the interfaces are the weak link, causing brittle fracture or grain boundary sliding whereas in other materials, they may be responsible for strengthening by impeding dislocation movement. The stresses generated by grain boundary crystallization can also determine the tribological behaviour of composites [54].

It is generally known that microstructural features like volume fraction of the metal binder phase, the carbide grain size, binder mean free path and contiguity of the carbide influence the mechanical and tribological behaviour of cermets [71]. By either lowering the metal binder content or decreasing the carbide grain size, the hardness of the composite increases and an increase of hardness is invariably accompanied by a loss of bulk fracture toughness in conventional materials [72-77]. The relationship between carbide grain size with hardness and fracture toughness is presented in Figure 2.28 [78].

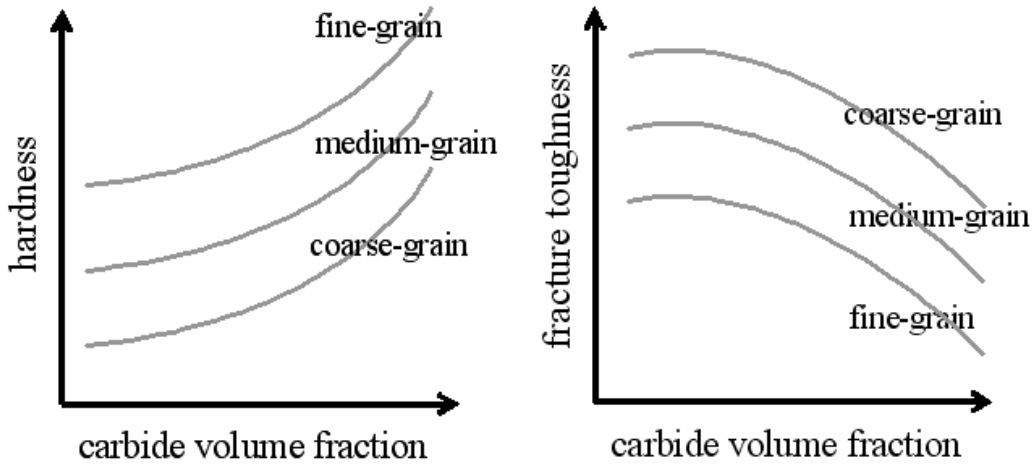

Figure 2.28: Schematic plot showing the relationship between mechanical properties and select microstructural parameters: (a) Hardness as a function of the carbide volume fraction and grain size, and (b) fracture toughness as a function of the carbide volume fraction and grain size [78].

A few researchers have shown that the abrasive wear of cermets involves gross plastic deformation due to yielding and extrusion of the binder metal, spalling due to crack propagation, and carbide fragmentation [72, 73, 75-77]. As a consequence, improved wear resistance in cermets is obtained at higher carbide content [30]. Altering the ceramic grain size also influences the wear behaviour of the cermets. For instance, Gurland and colleagues [79] reported an improvement in the hardness and wear resistance of WC-Co cermets by decreasing the carbide grain size. When the carbide grain size is reduced, for the same constant volume of binder content, there would be an accompanied decrease in binder mean free path leading to an increase in the level of plastic constraint (due to the greater interfacial area between the carbide grains), this in turns makes dislocation motion and shear difficult, resulting in the observed increase in hardness and wear resistance of the cermets [72, 76, 80]. In contrast, Cutler and colleagues [81] reported an improvement in fracture toughness as the grain size or binder mean free path of the cermets increases. The reason for the improved fracture toughness with an increase in carbide grain size is as a result of decrease in constraint for the plastic deformation of the metallic binder ahead of the propagating crack. Since at constant metal binder content, the binder mean free path decreases with a decrease in carbide grain size, hence a decrease in grain size is expected to reduce the toughening contribution [71]. This section (Section 2.6.4) has contained a brief review

on the wear behaviour of cermets. The following section is focused on background knowledge relating to the corrosion of materials and a brief overview on the corrosion behaviour of cermets.

2.7 Corrosion

Corrosion is simply the unintentional and destructive attack of a material as a result of reaction with the environment. There are different types of corrosion and the initiation and subsequent degree of attack is influenced by both material and environmental factors. Metallic corrosion can be classified into uniform, galvanic, crevice, pitting, intergranular, selective leaching, erosion-corrosion, and stress corrosion cracking [37, 38, 46]. An illustrative diagram showing the general forms of corrosion is shown in Figure 2.29 [82].

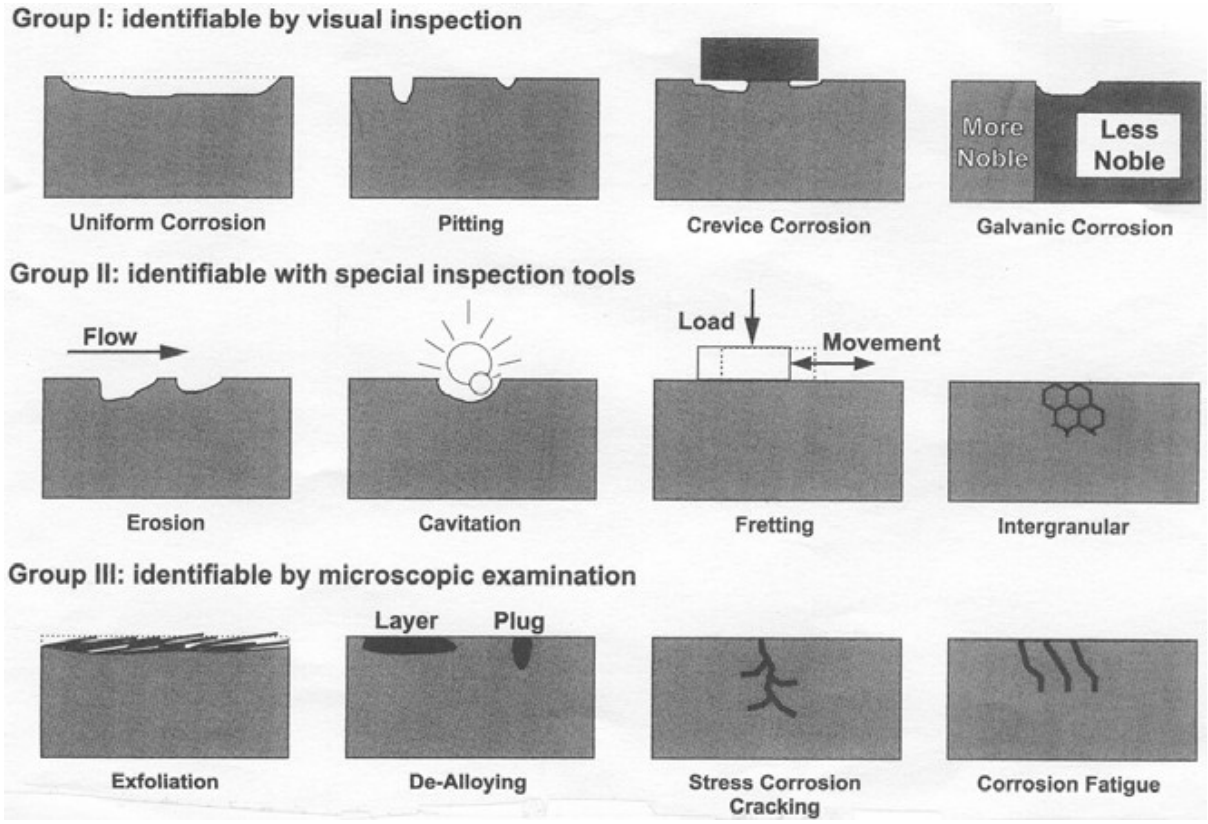

Figure 2.29: Schematic diagram showing the various forms of Corrosion [82].

2.7.1 Uniform Corrosion

Uniform corrosion is the most common form of corrosion, because of the simplicity in the design, prediction and control. It can be seen as a form of electrochemical corrosion where the whole exposed surface of the metal is attacked in equal intensity and often leaves behind a scale or deposit. A typical example is the general rusting of iron [46].

2.7.2 Galvanic Corrosion

Galvanic corrosion is an electrochemical form of corrosion that occurs when metals or alloys with different compositions are electrically coupled together in a conducting electrolyte. The principle of galvanic corrosion is simply based on the scenario that when two conducting metals or alloys are coupled in a conducting electrolyte, greater corrosive attack would be experienced for the more active metal than for the less active (more noble) one; this response is obviously dependent on their relative positions in the galvanic series. The galvanic series is a ranking of metals and alloys based on their order of reduction potentials in a given environment (like sea water), and this potential is generally measured with respect to a standard calomel electrode (SCE) [46, 83]. A table showing a typical galvanic series is presented in Table 2.2.

Galvanic corrosion is mostly experienced as a result of poor design, and can be controlled by proper materials selection and design. By coupling dissimilar metals that are closer together in the galvanic series in a conducting electrolyte, the galvanic corrosion effect is minimized [46, 83]. However, changes in electrolyte composition and temperature could alter the potential positioning in the galvanic series [37]. Secondly, the degree of galvanic attack is also assessed based on the relative anode-to-cathode surfaces that are exposed to the conducting electrolyte. Thus, for a given cathodic area, the galvanic corrosion effect is minimised by using a larger anode over a smaller anode, since the corrosion rate is dependent on current density (current density is current per unit area of the corroding surface) [37, 46, 83].

Table 2.2: Table showing galvanic series in seawater [46].

	Platinum
	Gold
	Graphite
	Titanium
	Silver
	316 Stainless steel (passive)
	304 Stainless steel (passive)
	Inconel (80Ni–13Cr–7Fe) (passive)
	Nickel (passive)
↑	Monel (70Ni–30Cu)
Increasingly inert (cathodic)	Copper–nickel alloys
	Bronzes (Cu–Sn alloys)
	Copper
	Brasses (Cu–Zn alloys)
	Inconel (active)
	Nickel (active)
	Tin
	Lead
Increasingly active (anodic)	316 Stainless steel (active)
	304 Stainless steel (active)
↓	Cast iron
	Iron and steel
	Aluminum alloys
	Cadmium
	Commercially pure aluminum
	Zinc
	Magnesium and magnesium alloys

2.7.3 Crevice Corrosion

Crevice corrosion is a localised form of electrochemical corrosion that is caused by differences in concentration of ions or dissolved gases in the electrolytic solution between two regions of the same metal piece. The major ingredient of crevice corrosion is the formation of a 'differential aeration cell'. A typical example of crevice corrosion is observed in crevices and recesses, or under deposits of dirt or corrosion products on metal surfaces where the electrolytic solution is stagnant and the localised depletion of dissolved oxygen at these positions leads to preferential corrosion [46, 84]. An illustrative diagram showing the mechanisms of crevice corrosion is presented in Figure 2.30 [84]. In the first stage, the anodic metal dissolution ($m = m^{+} + e^{-}$) and cathodic reduction ($O_2 + 2H_2O + 4e^{-} = 4OH^{-}$) processes would occur uniformly throughout the entire metal surface, in addition to the crevice exterior.

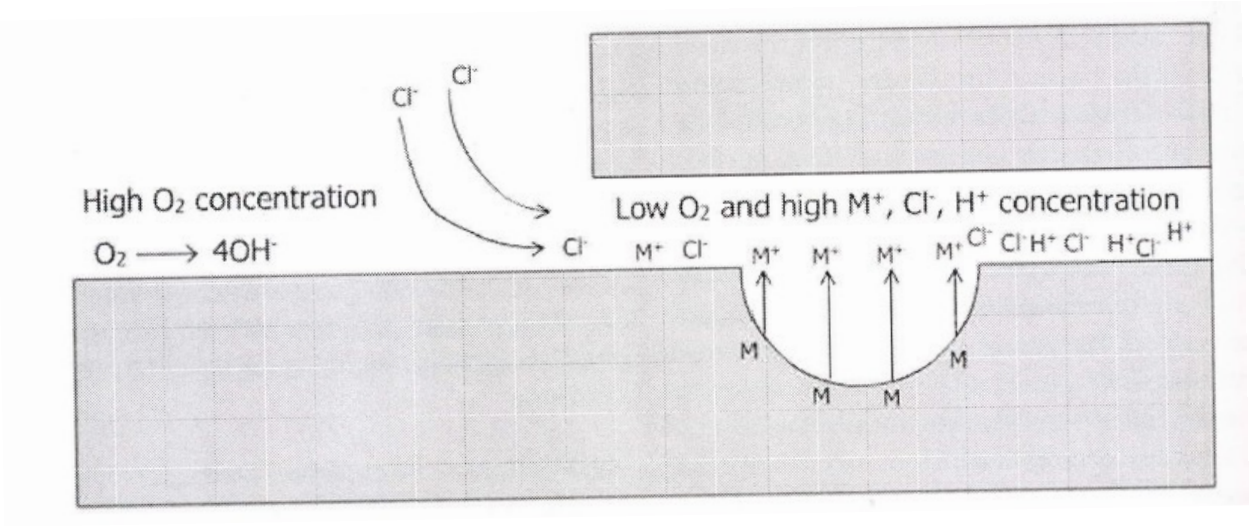

Figure 2.30: An illustrative diagram showing the mechanism of crevice corrosion [84].

Subsequently, the oxygen in the crevice interior (i.e low oxygen concentration) is consumed after reaching some incubation period, but the decrease in the cathodic reaction rate at the crevice exterior (i.e. high oxygen concentration) is negligible, which is as a result of the small anode to large cathodic area that is involved. This would lead to corrosion of the metal inside the crevice because of a lower pH and acidity in the crevice region [46].

The detailed stages involved in the crevice corrosion mechanism are explained based on the findings of Oldfield and colleagues [84, 85]. The first stage of the crevice corrosion process involves the depletion of oxygen in the crevice, which is due to the consumption in the cathodic reaction. The depletion of oxygen in the crevice would lead to the oxidation of the metal at the anode (i.e. metal dissolution), as shown in Figure 2.30 [84], which increases the concentration of metal ions. The second stage involves a localised increase in the acidity in the pit due to hydrolysis. As the metal ion concentration within the crevice is increased due to metal dissolution, the chloride ions would migrate from the bulk solution (cathodic region) to the crevice (anodic region) to maintain charge neutrality. Also, at this stage, hydrolysis of metal chloride would occur which causes an increase in acidity within the crevice. Due to this increased acidity, the pH is reduced and also the metal cations (which could be Fe^{2+}, Ni^{2+}, Cr^{3+} in the case of a common stainless steel) move out of the crevice while the aggressive chloride anions (Cl^-) move inside the crevice, leading to an increase in the aggressiveness of the solution inside the crevice mouth. During the third stage of crevice corrosion, accelerated corrosion

occurs which is as a result of breakdown of the passive protective film (due to the aggressiveness of the solution formed in stage 2). The passive film breaks down at a "critical crevice solution" (i.e. the concentration of the solution where passive film breaks down). In the final stage of the crevice corrosion process, it continues to propagate and would generally terminate when metal perforation occurs. The process is autocatalytic in nature and will continue until termination (rapid metal dissolution inside the crevice is continuous until termination) [46, 84, 85]. Passive scale forming alloys, like aluminium and stainless steels, are susceptible to crevice corrosion because the protective oxide layers are often destroyed by H^+ and Cl^- ions [46].

2.7.4 Pitting Corrosion

Pitting corrosion is another form of localised corrosion where a small area of the metal surface corrode preferentially, which leads to the formation of pits or holes, while the remaining part of the surface remains relatively free from attack. When corrosion pits occur in a metal surface, they often penetrate from a horizontal surface in a nearly perpendicular direction. Pitting corrosion can be very difficult to detect and sometimes leads to catastrophic failure, even with relatively low material loss. Pits can also act as initiation sites for SCC and can be seen as an insidious type of corrosion [84].

Crevice and pitting corrosion mechanisms are quite similar in that metal oxidation occurs within the pit, whereas the oxygen reduction occurs at the surface. However, pitting and crevice corrosion can be distinguished from their respective initiation phases. Pitting corrosion is initiated by metallurgical factors alone, whereas crevice corrosion is initiated by differential concentration of oxygen or an ion in the electrolytic solution [41, 46].

A schematic diagram showing the mechanism of pitting corrosion is shown in Figure 2.31 [86]. Pitting corrosion is explained by the following sequence of processes [84]. The first stage involves the formation of anodic sites, through disruption of the protective passive oxide layer on the metal surface. The dissolution of the metal occurs at the anode and the anode dissolution reaction is shown by:

$$M \rightarrow M^{n+} + ne^- \qquad \text{Equation 2.4}$$

The anodic reaction (Equation 2.4) is balanced by the complimentary cathodic reaction of oxygen on the adjacent metal surface:

$$O_2 + 2H_2O + 4e^- \rightarrow 4OH^-$$ Equation 2.5

The first stage in pitting corrosion process is the initiation stage of pitting.

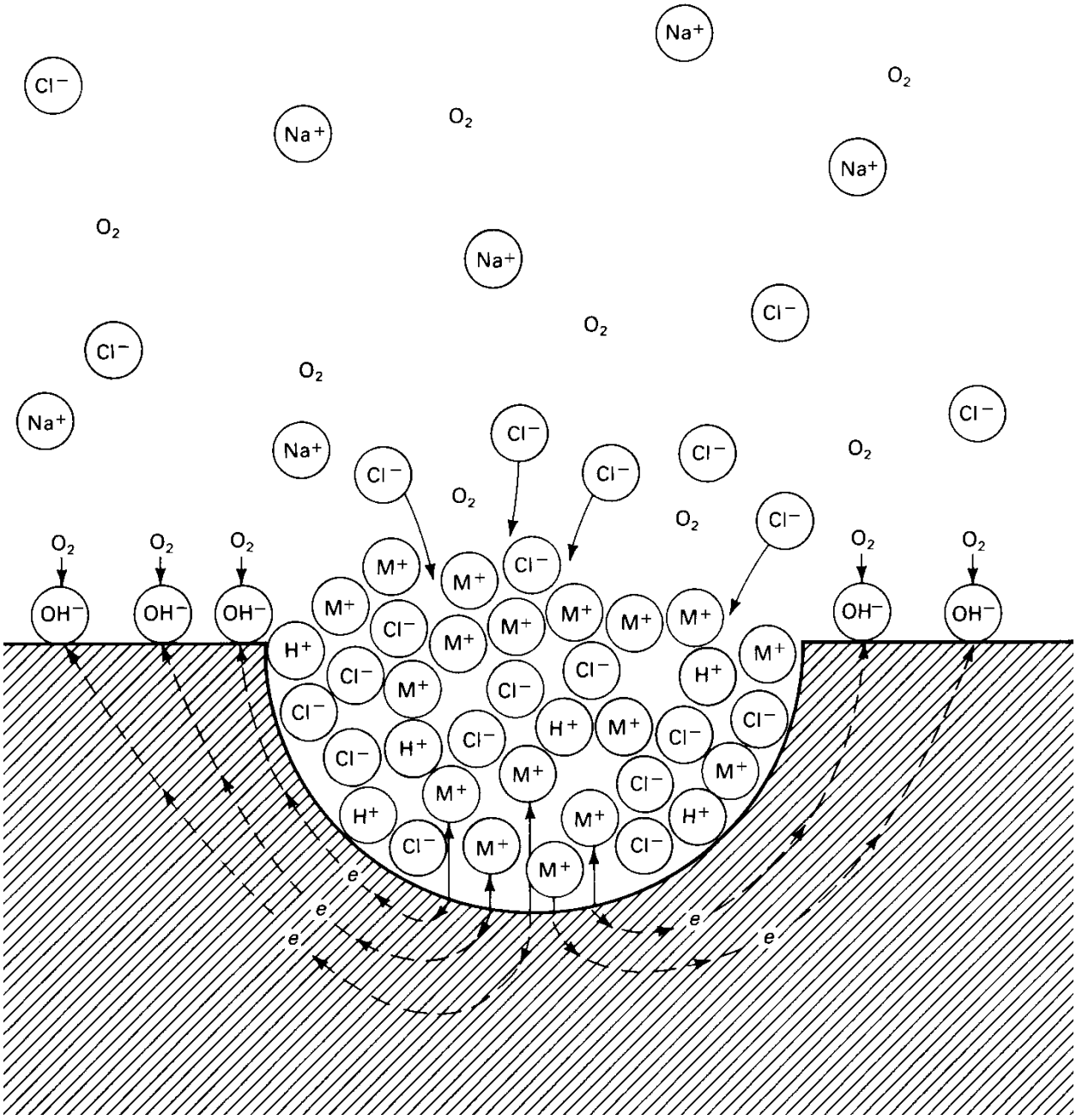

Figure 2.31: An illustrative diagram showing an autocatalytic pitting process in a corrosion pit. The metal, M is being heavily pitted by an aerated and aggressive NaCl solution. There is rapid dissolution in the pit, while oxygen reduction takes place on the adjacent metal surfaces [86].

During the second stage of the pitting process, continuous metal dissolution in the anodic region produces an excess of positive ions (M^+), which are attracted by aggressive chloride negative anions from the electrolyte (Cl^-) in order to balance the charge:

$$M^+Cl^- + H_2O \rightarrow MOH + H^+Cl^- \qquad \text{Equation 2.6}$$

The OH^- ions also migrate to balance the positive charge leading to the hydrolysis reaction, as shown in Equation 2.6. In the third stage, the presence of aggressive chloride anions (Cl^-) and H^+ cations would hinder the repassivation process, due to the acidity of the pit and the reduced pH at the bottom of the pit. pH values of 1.5 and 1.0 have been reported in the bottom of the pit [84]. The fourth stage of pitting corrosion is a continuation of third stage, which involves a progressive increase in the rate of metal dissolution at the anodic pit surface, due to continual migration of the aggressive chloride ions, leading to the formation of increasing amounts of M^+Cl^- and H^+Cl^- through a hydrolysis reaction, as shown in Equation 2.6. In the fifth stage, the metal dissolution progresses until metal perforation occurs, and as a time dependent process (autocatalytic in nature), the intensity of metal dissolution increases with time. The second through to the fifth stages represent the propagation stages of the pitting mechanism. For the last stage, the metal is finally perforated and the reaction is completed at this point, which is known as pitting termination [84].

Although stainless steels are known to be susceptible to pitting corrosion, alloying with 2% molybdenum enhances their resistance, which explains why 316L grade stainless steel has a better pitting resistance than 304 grade stainless steel [41, 46]. Figure 2.32 [40] is used to illustrate the effects of alloying elements on pitting corrosion. The pitting potential increases as the chromium content is raised above the critical 12% value needed to make stainless steel**.** In a manner similar to the case of chromium, increasing the concentration of nickel (an austenitic stabiliser) also enhances the pitting resistance of iron-chromium alloys [87]. As stated previously, small addition of molybdenum in the presence of chromium improves the resistance of stainless steel to pitting corrosion. The addition of small amount of other elements, such as tungsten and nitrogen, also has positive effects on the pitting resistance of stainless steels [40, 87-89].

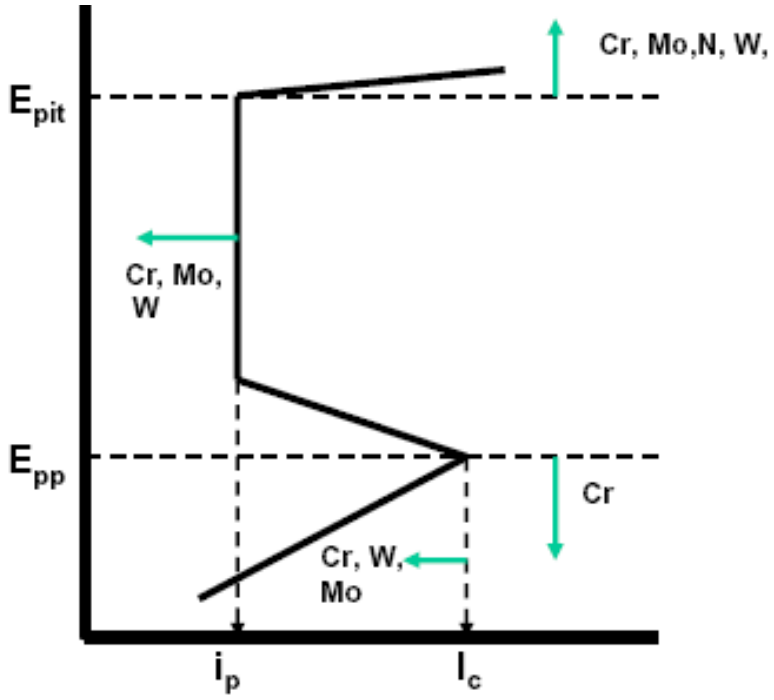

Figure 2.32: Illustrative diagram showing the effects of alloying elements on the resistance to pitting corrosion [40].

2.7.5 Intergranular Corrosion

Intergranular corrosion can be defined as the specialised type of attack that takes place preferentially at the grain boundaries of a metal, with little or no attack on the main body of the grains. The grain boundary has a small effective area and acts as an anode, whereas the larger area of the grain core is the cathode. Consequently, the small anode to large cathode ratio leads to rapid attack, penetrating deeply into the metal (corrosion rate is dependent on current density, which increases as the anode area is extremely small). The grain boundary area can be seen as an area of crystallographic mismatch that exist between the orderly structures within the adjacent grains [38].

A schematic diagram showing the crystallographic mismatch between the grain boundary area and the orderly structures within the adjacent grains, is shown in Figure 2.33 [38]. The mismatch that exists between the grain boundary area and the orderly structures makes the grain boundary slightly more chemically active (i.e. anodic) than the adjacent grain area (i.e. cathodic), and when exposed to a corrosive environment, attack is initiated preferentially along the grain boundaries, leading to intergranular corrosion [36]. Depletion of the corrosion-resistant elements

(for instance chromium in stainless steel) at the grain boundary promotes the susceptibility of such materials to intergranular corrosion. Sensitisation of stainless steel is the most common form of intergranular corrosion. This occurs when an austenitic stainless steel is heated or cooled through the specific temperature range of about 427 to 899ºC, leading to the formation of chromium carbide ($Cr_{23}C_6$) as a result of combination of chromium and carbon segregated along the grain boundaries. The negative effect of sensitisation to corrosion resistance is that it leads to the depletion of chromium, and thus lowers the corrosion performance in the areas adjacent to the grain boundary [36].

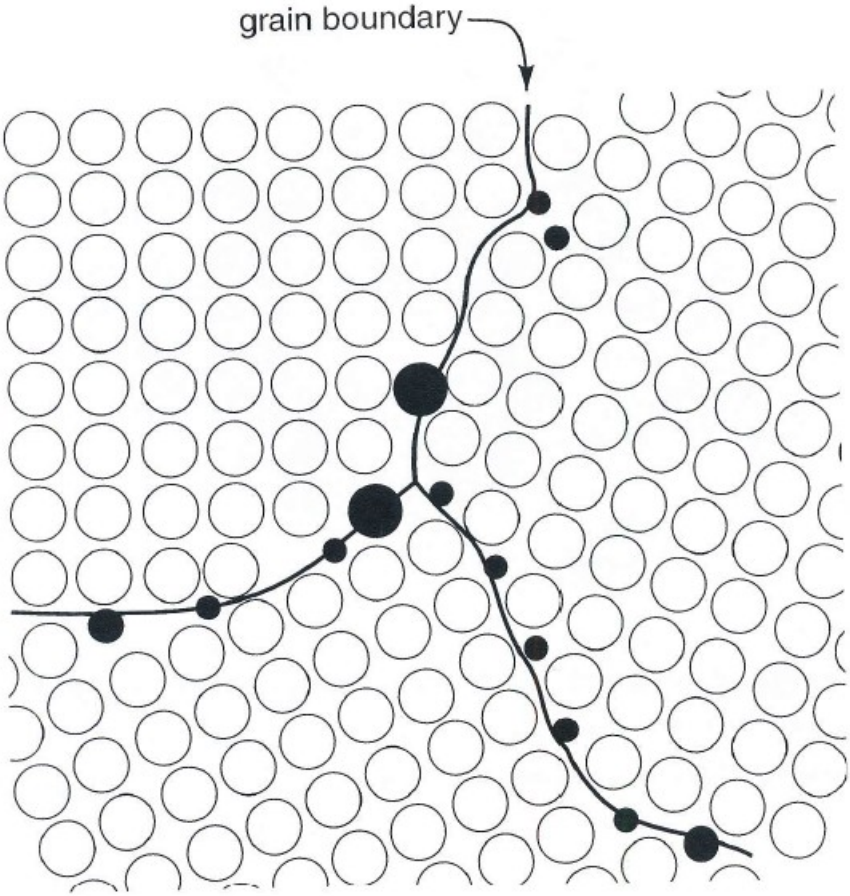

Figure 2.33: A schematic diagram showing the crystallographic mismatch between the grain boundary area and the orderly structures within the adjacent grains [38].

An illustrative diagram showing the precipitation of chromium carbide along the grain boundary is presented in Figure 2.34 [46]. Intergranular corrosion poses a considerable problem in the welding of stainless steels, as a result of carbide precipitation in a process known as “weld

decay" [46]. An illustrative diagram showing the weld decay behaviour of stainless steel is shown in Figure 2.35 [42].

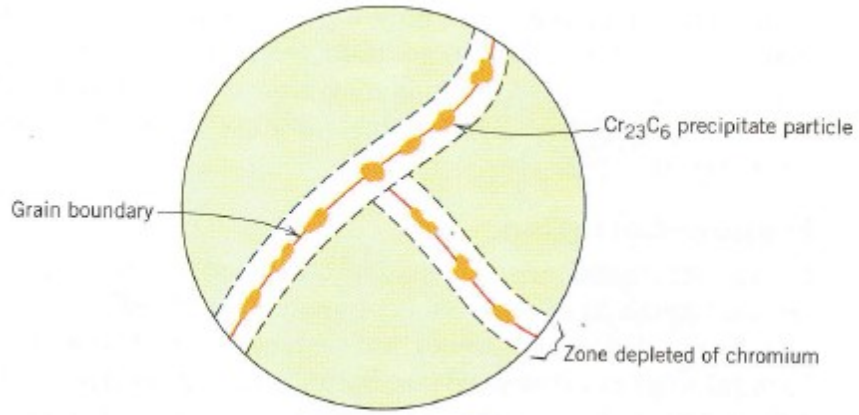

Figure 2.34: Schematic illustration of chromium carbide particles that have precipitated along grain boundaries in stainless steel, and the attendant zones of chromium depletion [46].

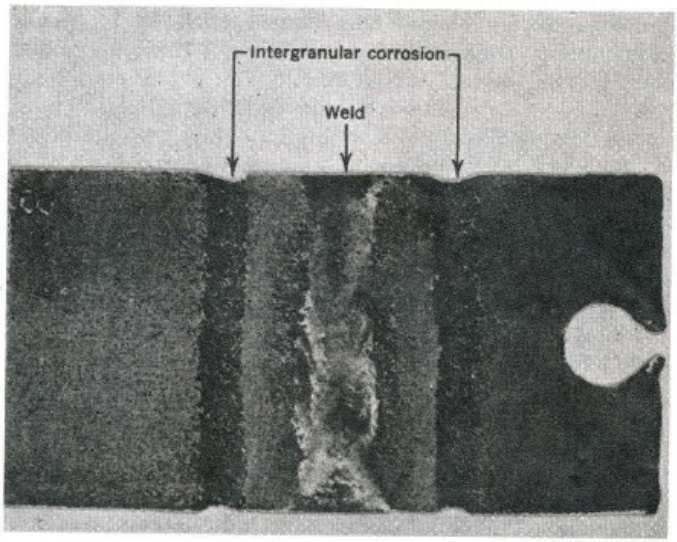

Figure 2.35: Illustrative diagram showing weld decay in a stainless steel. Regions along which the grooves have formed were sensitised as the weld cooled [42].

Other activities, such slow cooling from the annealing temperature and stress relieving in the sensitisation range, could promote carbide precipitation, leading to intergranular corrosion [36].

Intergranular corrosion of stainless steels can be minimised by alloying the steel with another metal (i.e. a carbon stabiliser), such as niobium or titanium. These metals are chosen because of their greater affinity to form carbides than chromium, thereby leaving chromium in solid solution. For instance, the use of Ti-stabilised (Type 321) or Nb-stabilised (Type 347) stainless steels reduces the susceptibility to intergranular corrosion. A second way to reduce the susceptibility of intergranular corrosion is by subjecting the sensitised material to a high-temperature heat treatment (above the sensitisation temperature), thereby allowing all the chromium carbide particles to re-dissolve. Lowering the carbon content, typically to below 0.03 wt. % (to reduce carbide formation), is another way to reduce the susceptibility to intergranular corrosion. For instance, grade 316L is preferred over 316 stainless steel because it is less vulnerable to intergranular corrosion due to the low carbon content [36, 46].

2.7.6 Selective Leaching

Selective leaching simply means the preferential removal of one of the important components of an alloy by corrosion. The most common example of selective leaching is dezincification of zinc from brass. In this process, the noble (more active) component of an alloy is preferentially removed, like zinc in brass. Another typical example of selective leaching is the removal of iron from gray cast iron, in the process known as graphitization [36].

There are two types of dezincification of brass, the first one is known as “plug-type” which occurs in localised areas of the metal and is mostly seen in low zinc alloys, whereas the second is the “layer-type”, which occurs uniformly over the surface and is more predominant in high zinc alloys. To a greater extent, the nature of the environment has an influence on the type of attack. For instance, the layer-type of dezincification occurs in slightly acidic water with a low salt content, and also at room temperature, whereas the plug-type takes place in high salt content, neutral or alkaline water, and above room temperature [36].

Dezincification can be prevented by the following measures. The plug-type of dezincification process is promoted by crevice conditions under a deposit of scale or salt; hence by removing scales and deposits from inside the surface of pipelines, the attack is minimised. Other preventive measures include applying a cathodic protection or removing stagnant acidic corrosives [36].

2.7.7 Erosion-Corrosion

Erosion-corrosion is simply the corrosion attack that occurs after the disruption of the protective passive film by mechanical action, leading to exposure of the bare metal to the aggressive corrosion environment. It is the corrosion attack that is mostly experienced when rapidly flowing solutions (particularly those containing abrasive particulate matter) disrupt the protective oxide layer, or deposits that could have offered protection to the metal, leading to thinning or removal of surface films [37, 46, 90]. A schematic diagram showing the disruption, or erosion-corrosion, of a surface film is shown in Figure 2.36 [90].

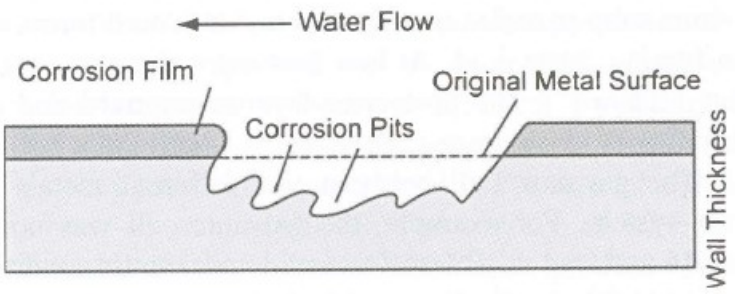

Figure 2.36: An illustrative diagram showing the disruption of a passive protective film by an erosion-corrosion process [90].

Erosion corrosion damage is particularly likely for pipe elbows, turbines, pumps, tube constrictions and other structural features that could change flow direction or velocity, and promote turbulence. It is more prevalent if the corrodent is in the liquid phase and in most cases, the suspended solids aggravate the erosion of the protective surface films, leading to degradation of the exposed material to the corrosive environment. It is more vulnerable in two-phase flow, in which steam and water vapour condensate droplets are combined [37]. A photograph showing the effect of erosion-corrosion at a pipe elbow is shown in Figure 2.37 [39].

Generally, metals that form protective oxide layers, such as stainless steels and titanium, are relatively immune to erosion-corrosion in many oxidising environments [37, 90]. Cavitation corrosion is another type of erosion-corrosion mechanism that occurs when the velocity of the flow is so high that pressure reduction is sufficient enough to nucleate water vapour bubbles, leading to implosion on the surface. This implosion produces very high pressure bursts that disrupt the protective oxide layer, and even dislodge metal particles in the process [37, 90]. The

appearance of the attack usually takes the form of roughened pits, which would eventually lead to heavy penetration [37]. An image showing the appearance of a material following cavitation-erosion damage is shown in Figure 2.38 [90].

Figure 2.37: Illustrative photograph showing impingement failure of an elbow that was part of a steam condensate line [39].

Figure 2.38: A photograph showing cavitation-erosion damage of a cylinder liner of a diesel engine [90].

2.7.8 Stress Corrosion Cracking (SCC)

SCC is caused by the combined action of stress and a corrosive environment. It is a type of corrosion attack that is associated with triple actions resulting from a static tensile stress, the local environment and the metallurgical state of the material, leading to materials failure. It is a very dangerous failure mode and sometimes unpredictable; sudden catastrophic failures often occur without any warning signs. There must be a susceptible metal, a specific corrosive environment and the presence of tensile or residual stress, for stress-corrosion cracking to occur [38]. An illustration showing the requirements of SCC is presented in Figure 2.39 [90].

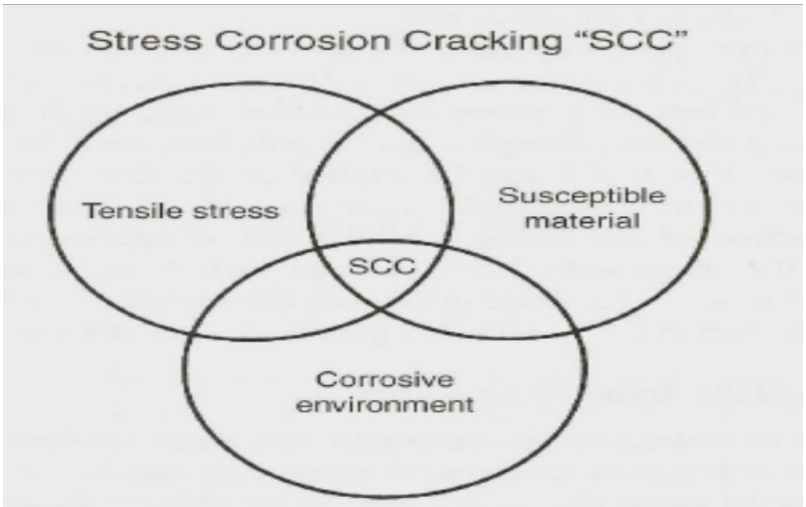

Figure 2.39: An illustration of three conditions that promote the occurrence of SCC [90].

There are various forms of SCC. The first one is sulphide SCC, which is prevalent in the oil and gas industry, and occurs in hydrogen sulphide containing environments. The second type is chloride SCC, which is frequently seen in austenitic stainless steels under the action of an applied tensile stress, in addition to the presence of oxygen, chloride ions and elevated temperature. Chloride stress corrosion cracking is more vulnerable to steels at higher temperature above 60°C due to the weakness of the protective oxide layer, although they can still crack at room temperature in a highly contaminated environments where the pH is very low [38]. The last type is caustic SCC, which is prevalent in caustic environment where the concentration of hydrogen is high. The caustic cracking of steels and Inconel tubes have been reported in alkaline solutions [84]. Through the elimination of stress and proper heat treatment, to anneal out any residual stress, SCC can potentially be mitigated [46].

2.7.9 Hydrogen Embrittlement

Hydrogen embrittlement can be defined as a failure mode that occurs when metals or alloys lose their ductility and tensile strength, as a result of the penetration of atomic hydrogen to the metal. Hydrogen-induced cracking and hydrogen-stress cracking are examples of hydrogen embrittlement. It is difficult to predict and can lead to catastrophic brittle failures, due to rapid crack growth and propagation in the presence of an applied or residual stress. The mechanism of hydrogen embrittlement involves the diffusion of atomic hydrogen into the crystal lattice of a metal, and even a low concentration of atomic hydrogen can lead to cracking [46]. High strength steels are more susceptible to hydrogen embrittlement, and activities like welding, heat treatment in hydrogen-containing furnace atmospheres, acid pickling, or electroplating operations encourage the permeation of hydrogen into the lattice of a metal [36, 46].

There are both similarities and differences between hydrogen embrittlement and SCC. In both failure modes, a conventionally ductile metal will experience sudden brittle fracture when exposed to both tensile stress and an aggressive corrosive atmosphere. However, while application of cathodic protection mitigates SCC, it may lead to the initiation or enhancement of hydrogen embrittlement [46].

2.8 Corrosion Prevention

Through the careful application of materials selection design, environmental alterations, use of corrosion inhibitors, design changes, coatings and cathodic protection, corrosion mitigation can be enhanced [36].

This section has presented background knowledge governing the corrosion of materials; the following section presents a brief overview on the corrosion behaviour of cermets (further detailed review is provided in Chapters 6, 7 and 8).

2.9 Brief Overview on the Corrosion Behaviour of Cermets

It is generally expected that microstructural parameters such as the metal binder content or carbide grain size may affect the overall corrosion behaviour of ceramic-metallic composites.

Understanding how these microstructural parameters affect the corrosion behaviour of cermets is very important, as this class of material offers potential for use in highly erosive and corrosive environments. Ceramic-based materials are generally known to possess excellent corrosion resistance, but the presence of a metal binder invariably degrades their corrosion properties [91]. In view of this, several studies on the corrosion behaviour of cermets (mostly WC-Co) have reported preferential binder dissolution (e.g. Co), while the ceramic phase remained relatively unaffected by corrosion [58, 92-94]. The suggested reason for the preferential binder attack is related to the difference in the reduction potentials between the ceramic and metallic phase, thereby opening up the possibility of galvanic corrosion at the ceramic-metal interface [58, 93, 95]. Consequently, superior corrosion performance of cermets can be derived through reduced metal binder content [58, 91]. The relationship between the critical corrosion current density and the metal binder content is illustrated in Figure 2.40 for WC-Co [92].

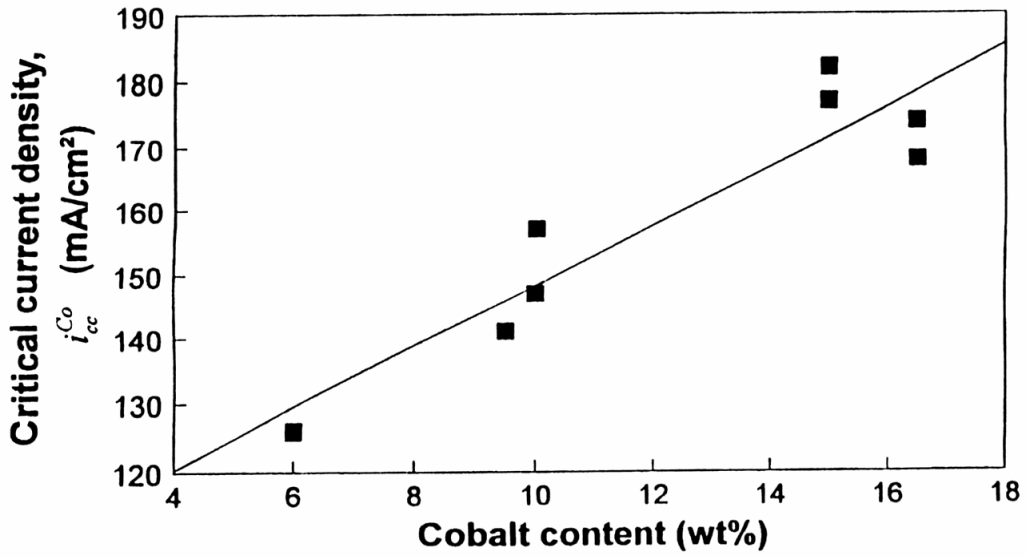

Figure 2.40: An illustrative diagram showing relationship between the critical current density of the binder phase area versus the Co binder content for WC-Co [92].

It is apparent that a lower critical current density is obtained at lower binder contents, inferring better corrosion resistance [92]. Sacks and colleagues [58] also reported an improvement in the corrosion resistance of cermets with lower binder contents, as shown in Figure 2.41 [58]. The improvement in corrosion resistance of cermets with a lower binder content was attributed to

greater binder oxidation at higher Co content, hence as the Co content is increased, the greater the oxidation of the Co and the higher the corrosion rates [58].

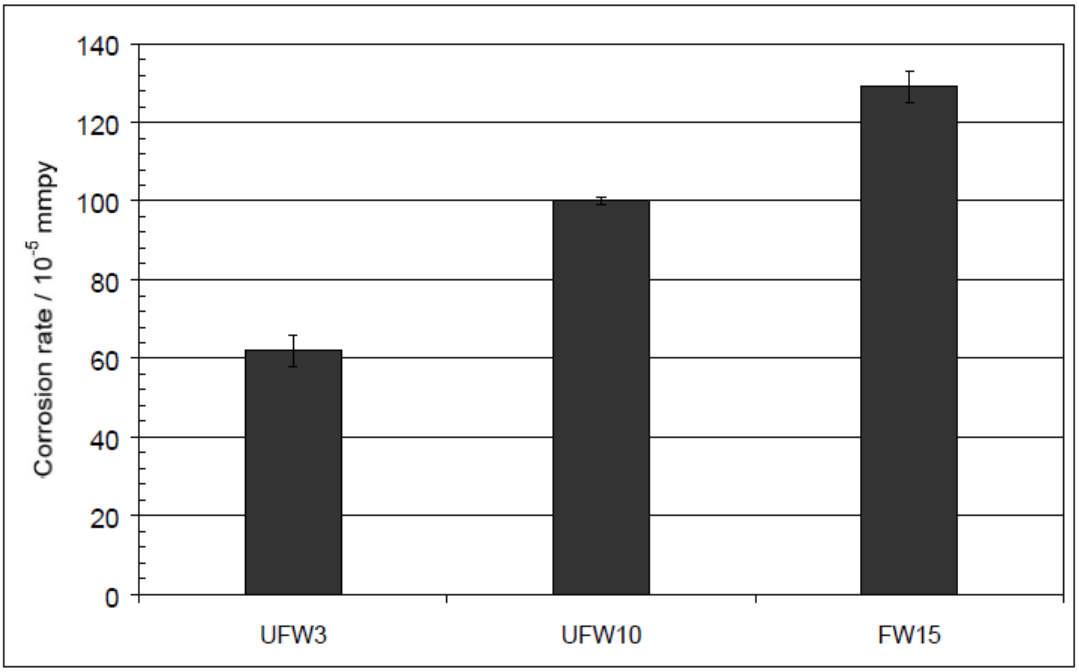

Figure 2.41: The effect of binder content on the corrosion resistance of WC-Co cermets in 0.00294 M tannic acid solution (UFW3, UFW10, FW15 represent 3, 10 and 15 wt. % of Co content) [58].

As outlined previously, other microstructural parameters, such as carbide grain size could influence the corrosion behaviour of cermets. For instance, it is proposed that when the carbide grain size is reduced (compared with a coarse grain size), the metallic binder would be under greater constraint because of the surrounding carbide grains, leading to deterioration in the corrosion performance of the fine-grained cermets [58, 92]. Generally, fine-grained cermets are expected to exhibit poor corrosion resistance over their coarse-grained counterparts, because of higher diffusion rates and contact stresses with an accompanying increase in dislocation density; all of these factors are unfavourable to corrosion performance [51, 92].

In summary, cermets comprise of ceramic phase (TiC in the present case) and a metallic phase (stainless steel) and find applications where wear and corrosion are of ultimate importance. TiC-steel based cermets are mostly produced through liquid phase sintering and the overall properties

are dependent on the success of the sintering stage. The wear mechanism of cermets is complex but consists of a combination of abrasive, adhesive, fatigue and tribo-chemical wear. Improved corrosion resistance of cermets is obtained at higher ceramic content (i.e TiC content), hence the corrosion performance drops at increased metal binder content.

3 Materials and Experimental Methods

The following chapter will outline the materials and methods used to prepare the samples and conduct both the reciprocating wear tests and the electrochemical assessment for all of the TiC-steel cermets. This will include the powder preparation, compaction and sintering stages (vacuum melt infiltration), as well as the sample grinding and polishing steps. It may be noted that some repetition is present relative to the submitted journal papers presented in the later chapters of the thesis. This is unavoidable, as some information needs to be presented within the papers, but not to the level of detail described in the present chapter.

3.1 Raw Materials

3.1.1 Titanium Carbide and Stainless Steel Powders

All samples were prepared using TiC powder (Lot #PL20125339) supplied by Pacific Particulate Materials Ltd (Vancouver, BC, Canada), with a density of 4.93 g/cm^3 and a manufacturer quoted particle size of ~1.3 μm, which was confirmed through subsequent particle size analysis [96]. The particle morphology was assessed using scanning electron microscopy (SEM; Model S-4700, Hitachi High Technologies, Tokyo, Japan), while the crystalline phase composition was determined using X-ray diffraction (XRD; Model D-8 Advance, Bruker AXS, Inc., Madison, WI, USA). Table 3.1 shows the as-received chemical composition, as supplied by the manufacturer, and Figure 3.1 shows a representative SEM image of the TiC powder.

Table 3.1: Composition of the TiC starting powder (obtained from Pacific Particulate Materials Ltd).

	Compositions (wt. %)								
Powder	Free C	Total C	Al	Ca	Fe	N	O	S	Ti
TiC	0.12	19.51	-	-	0.06	0.05	0.39	-	79.87

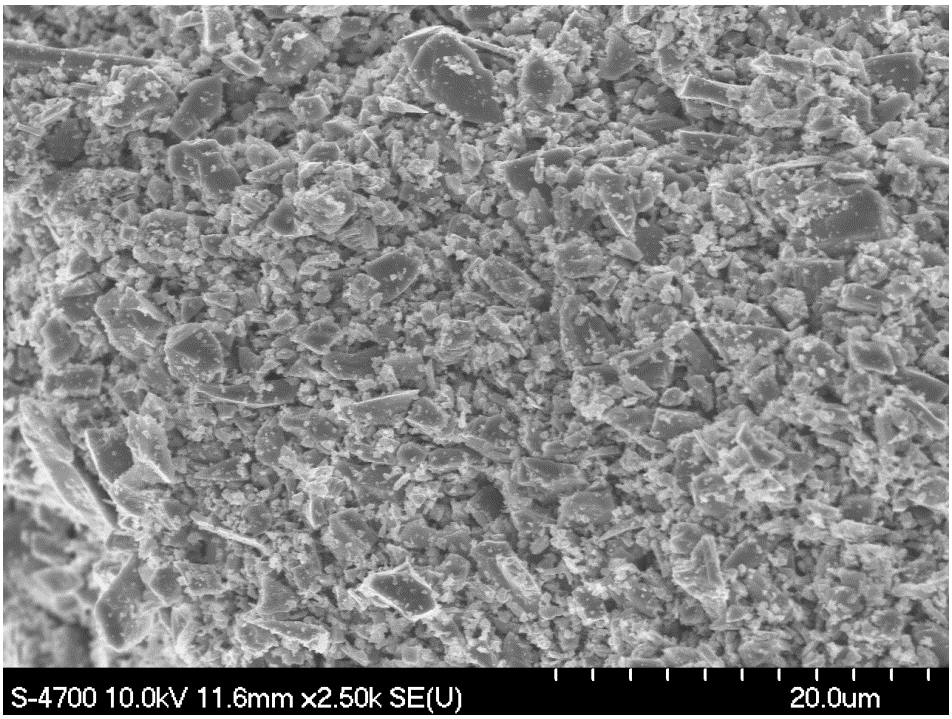

Figure 3.1: A representative SEM image of the as-received TiC ceramic powder.

The steel powders used included austenitic grades 304L (Lot #K19M09) and 316L (Lot #A04S008), and the martensitic grade 410L (Lot # 123M43), and these were sourced from Alfa Aesar (Ward Hill, MA, USA); the designation L for each powder refers to low carbon content. Each of the steel powders had a nominal particle size of -100 mesh. Representative SEM images of as-received steel powders are shown in Figure 3.2, and the typical compositions of the raw steel powder used in this study is presented in Table 3.2 [97].

Table 3.2: Compositions of the raw stainless steel powders [97].

Type	**Nominal composition (max. wt. %)**									**Density**
	Cr	**Ni**	**C**	**Mn**	**Si**	**P**	**S**	**N**	**Mo**	**(g/cm^3)**
304-L	18-20	8-12	0.03	2	1	0.045	0.03	0.1	-	8.03
316-L	16-18	10-14	0.03	2	1	0.045	0.03	0.1	2-3	8.03
410-L	11.5-13.0	0.50	0.03	1	1	0.04	0.03	-	0.5	7.75

(a) 316L

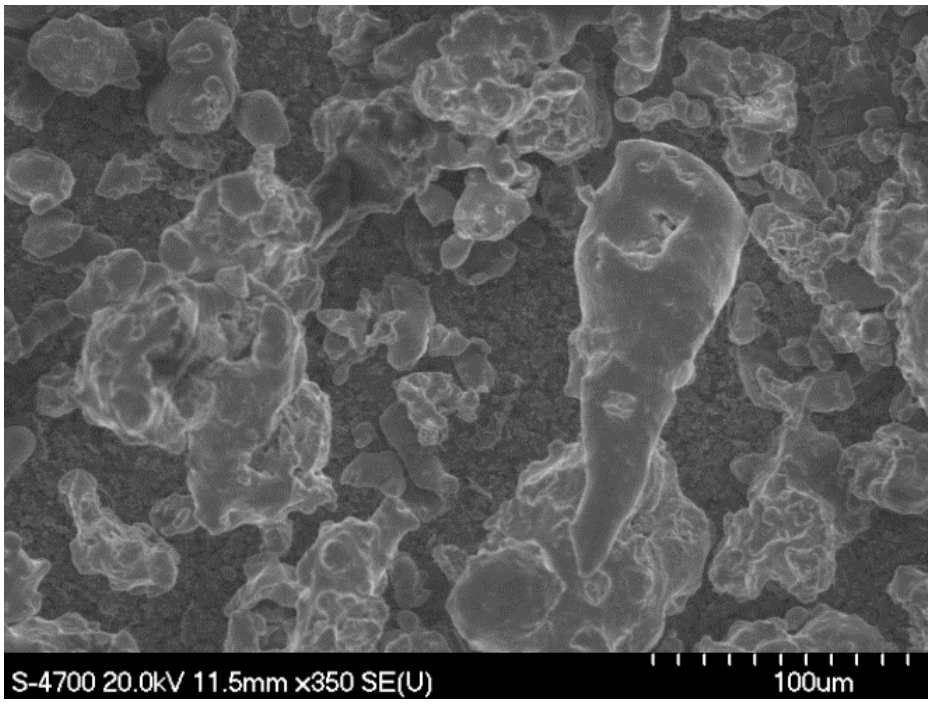
S-4700 20.0kV 11.5mm x350 SE(U)
100um

(b) 304L

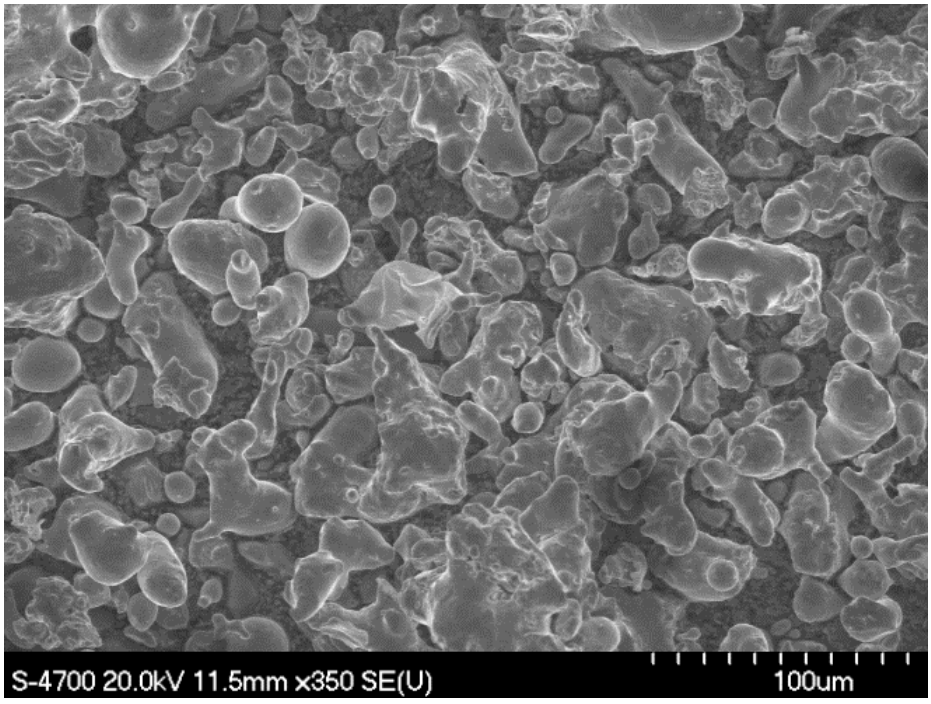
S-4700 20.0kV 11.5mm x350 SE(U)
100um

(c) 410L

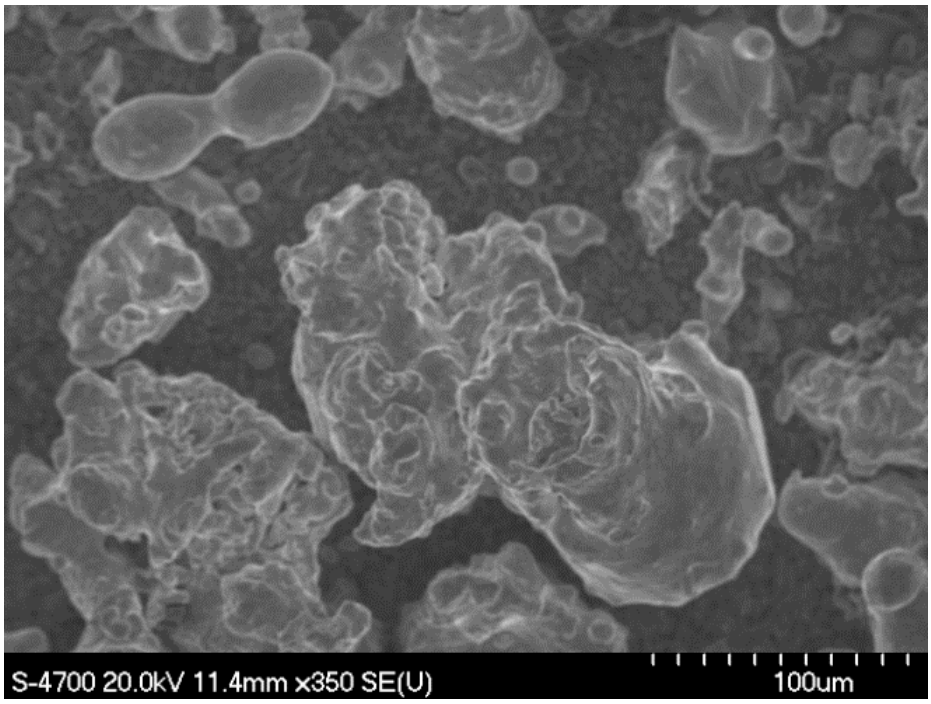

Figure 3.2: Representative SEM images of the as-received steel powders**:** (a) 316L, (b) 304L and (c) 410L.

3.2 Experimental Procedure

The following sections detail the methods used to produce the TiC-stainless steel cermet samples, and also to prepare them for further testing (i.e. surface grinding and polishing). The procedures used to analyse the wear and corrosion behaviour of the cermets are also described.

3.2.1 Sample Preparation

The preparation of samples for mechanical, tribological and electrochemical testing is a multistep process. Figure 3.3 outlines a breakdown of the process used in the processing of cermets samples ready for subsequent evaluation.

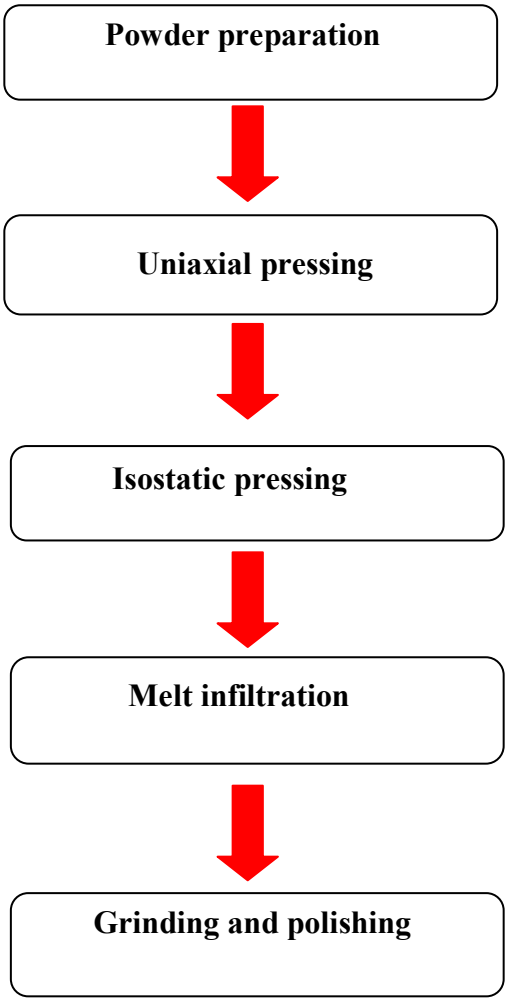

Figure 3.3: Flowchart illustrating sequence involved in the preparation of cermet samples for further evaluation.

3.2.1.1 Powder preparation and uniaxial pressing

Each powder sample was uniaxially pressed using a standard tabletop press (Model S/N 41000-102, Carver Inc., Wabash, USA). The cylindrical, hardened steel dye was first coated with stearic acid, which acts as a lubricant to ensure easy removal of the samples and no loss of form or integrity. The TiC samples were prepared using ~7.5g of TiC powder, which is loaded into the steel die, as well as ~12 drops of hexane to improve lubrication and ease of compaction. After placing and levelling the powder in the steel die, the powder is uniaxially compacted at 67MPa and held at that pressure for two minutes. A ball valve (with a rotary knob) was used to ensure a very slow release of pressure upon completion of the pressing step, and the pressed sample is

carefully removed from the die, providing disc-shaped pellets ~31.75 mm in diameter x ~4 mm thick. A vacuum sealer was then used to cover each sample in a double layer of plastic sheet ready for cold isostatic pressing (CIP).

3.2.1.2 Isostatic Pressing

Following uniaxial pressing and vacuum bagging of the TiC pressed pellets, the next step is cold isostatic pressing (CIP). The aim of cold isostatic pressing is to apply a uniform compaction pressure to the powder via a high-pressure fluid, which ensures a highly uniform green density ready for subsequent processing. In the present case, the TiC pressed samples were further compressed by CIP (Figure 3.4) at 220 MPa, which was held for 3 minutes (ModelS/N-101462-1, Avure Technologies, Inc., Franklin TN USA).

Figure 3.4: Picture of the cold isostatic pressing machine used in the present study

Measurements were then taken for each TiC green body prior to continuing with sample preparation. In doing so, digital calipers were used to measure the diameter and height of each sample. A digital balance was used to measure the sample weight to an accuracy of 10^{-4} g. Following CIP processing, each sample was ready for melt infiltration and sintering. Depending on the volume percent of steel required (i.e. the volume fraction of metallic binder determined from the known volume of TiC in the pressed samples), appropriate portions of the steel powder were weighed out (between 5 and 30 vol. % of steel binder was used in the present case). The steel powder was then poured directly on top of each TiC perform, which was placed on a layer of bubble alumina, within a closed alumina crucible ready for the subsequent melt infiltration step.

3.2.1.3 Melt Infiltration

Melt infiltration relies upon forming a liquid (from the low melting steel phase) during the sintering process and ensuring some limited solubility of the TiC grains (hard phase) in the steel liquid phase. There are basic parameters that must be met for successful melt infiltration processing of the cermets. The first is that there should be good solubility of the TiC grains in the steel phase. Secondly, there should be low solubility of the steel in the TiC grains. Lastly, the steel binder should wet the TiC grains (i.e. it must have a low contact angle). The particles that form the liquid phase are sited on top of the TiC ceramic and the high solubility of the TiC grains in the steel melt, encourages the wetting of the TiC by the steel binder, leading to a strong capillary force that pulls the grains together (i.e. particle rearrangement), hence improving the density of the cermets. In addition, the presence of the liquid phase encourages faster diffusion rates than in solid state sintering [52].

In the present case, the appropriate weighed amount of the steel binder (sited on top of the TiC preform on bubble alumina, in a closed crucible was placed within the vacuum furnace, which was evacuated using a mechanical roughing pump. The vacuum was held at ~20 milliTorr throughout the sintering process. The temperature was increased at a rate of 10ºC/minute to the hold temperature. For the current work, a range of temperatures were used, between 1475°C to 1550°C, depending on the steel binder used and whether or not some variation in TiC grain size was required for a specific composition. The sintering temperature was held for various times

between 15 and 240 minutes. Following the hold period the samples were cooled at a nominal rate of 25°C/minute; below ~900°C a natural furnace cool occurred, with a continuously decreasing cooling rate.

3.2.1.4 Density Measurement

Following sintering, the sintered densities of all successfully melt-infiltrated samples were measured using the Archimedes principle, through immersion in water at room temperature. In order to have a reasonable average in each case, six density measurements were carried out prior to polishing of the infiltrated samples.

3.2.1.5 Sample Surface Preparation

The fully infiltrated samples are attached to cylindrical aluminum sample holders using a cyanoacrylate adhesive and then ground flat on one face using a diamond surface grinder (with a 149 μm diamond grit size) to prepare them for final grinding and polishing. The diamond grinding pads used thereafter were decreased in steps from grit sizes of 125 μm down to 15 μm. The grinding stage was then followed by polishing with diamond paste, from 9 μm down to 1/4 μm diamond paste for the final polish stage. Prior to the wear, corrosion, hardness and indentation fracture resistance experiments, each sample was placed in acetone, sited in an ultrasonic bath to remove any residual debris or contaminants, and then dried. The typical appearance of a polished TiC- steel based cermets following the rigorous and thorough polishing operation (takes ~8 hours to have a successful polishing of the cermets) is shown in Figure 3.5. For the pure steel samples used as reference materials for corrosion experiments (i.e. grades 304L, 316L, and 410L sourced from Outokumpu Stainless Bar Inc., Richburg, SC, USA), the samples were ground on silicon carbide paper using successively finer grades, from 240 to 600 grit, and finished with 0.3 down to 0.05 μm alumina polishing suspensions. Following polishing, the samples were rinsed in acetone, within an ultrasonic bath and then dried.

Figure 3.5: Photograph of TiC-304L cermets with aluminium holder following polishing operation, the vol. % of steel binder is indicated in each box.

3.2.2 Hardness and Indentation Fracture Resistance Evaluation

In order to access the mechanical response of the developed composites, measurements of the hardness and indentation fracture resistance (IFR) testing were performed. The hardness and IFR values were obtained using a Vickers diamond pyramid indenter (Model V-100A, Leco, N0 20896, Japan) with 1kg and 50kg applied loads, respectively. The lower load (1kg) was used in this case to avoid sample cracking during loading whereas the higher load (50kg) was used to assess the indentation fracture resistance since the crack length is an indication of the resistance of the cermets to fracture. The load was held for 15 seconds. The IFR was determined by using the approaches proposed by Anstis *et al*.[98] and Niihara [99]. The two approaches were used to

fully assess the crack behaviour of the cermets in order to know the transition from brittle median cracking (i.e. c:a >2.5) expected at lower steel binder content to more ductile Palmqvist cracking (i.e. c:a< 2.5) expected at higher steel binder contents. (c is the indentation crack length and a is the indent diagonal) [100]. In each case a minimum of six indentations were made, taking the average to determine the hardness and IFR, as well as the standard deviation error. The hardness testing was carried out following the procedure outlined in the associated ASTM standard [101].

3.2.3 Reciprocating Wear Testing

Assessment of the wear behaviour of the composites was performed under dry sliding conditions, using a reciprocating wear testing machine (Model Universal Micro Tribometer (UMT); Bruker Corporation, Campbell, CA, USA), as shown in Figure 3.6. This testing system uses an upper WC-Co specimen (Grade 25 with 6wt. % Co, McMaster-Carr, Aurora, OH, USA),(6.35 mm diameter) that contacts a moving flat specimen, which itself slides in a linear back and forth (or reciprocating) motion. A stroke length of 5.03 mm is applied, with an oscillation frequency of 20 Hz, for selected times and load, these conditions represent a total sliding distance of 1.45 km for a 2 hour test. All of the wear testing was conducted at room temperature (22-25°C), and at a relative humidity of 40-55 %. The load is applied downward through the WC-Co ball counter face against the flat sample (i.e. the TiC-steel composite), which itself is mounted on a reciprocating drive. The UMT wear tester simultaneously monitors the dynamic normal load and frictional force during the test. The WC-Co ball is mounted inside a ball holder, which is itself attached to a load sensor that controls and records the normal force during the test. For the present study, applied loads of 20N, 40N, 60N, and 80N were used, for a period of between 15 minutes and 2 hours. The coefficient of friction (COF) value for each tested sample is automatically stored in the UMT software. TiC-stainless steel samples with 10, 20 and 30 vol. % of steel binder were assessed during this portion of the research.

(a)

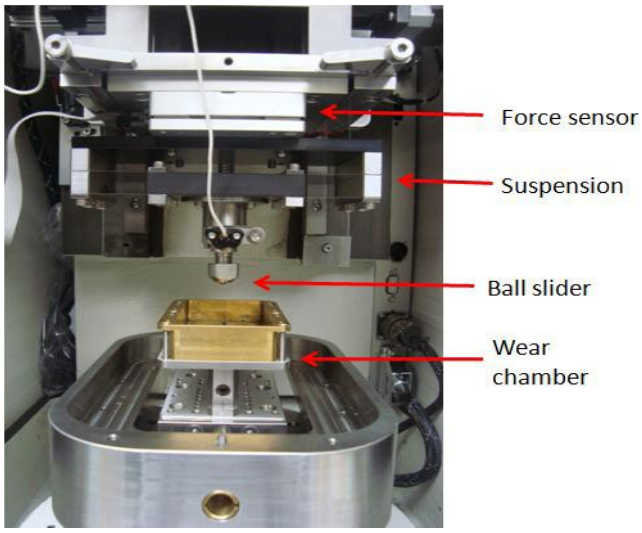

(b)

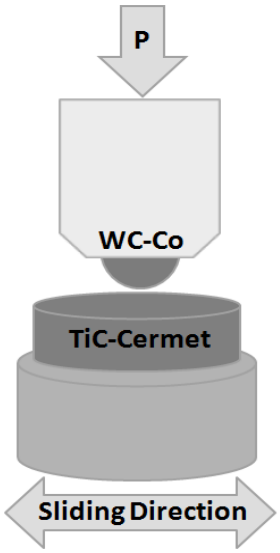

Figure 3.6: (a) Photograph of the UMT reciprocating wear testing system. (b) Schematic representation of the contact and motion of the ball slider and the cermet test sample.

Following the wear testing, the wear debris generated from the tested cermet samples was collected in a clean and dry beaker. Then a few drops of acetone were mixed with the wear debris in the beaker and the contents were transferred to a flat, mirror-polished aluminium stub, ready for further microstructural analysis using the SEM and EDS (the acetone evaporates

rapidly, leaving the debris on the polished aluminium stubs ready for further microstructural analysis).

Following the reciprocating wear tests and collection of the wear debris, the next experimental step involved the determination of the volumetric wear loss and examination of the general three-dimensional features of the wear track using a high-resolution optical profilometer (Model PS50 Optical Profilometer, Nanovea, Irvine, CA). The volumetric wear loss obtained from the optical profilometer was used to calculate the "specific wear rate" using the Lancaster approach [102]. Figure 3.7 shows the optical profilometer (Nanovea PS50 System) used in the determination of reciprocating wear behaviour in the present research. The optical profilometer is a powerful tool for examining both the general features of the wear tracks and determining the volume of the individual wear tracks, using a 130 μm 'optical' pen, similar to the one shown in Figure 3.7. The optical profilometer is capable of examining the whole wear track at once. The wear tracks may also be examined as pseudo three dimensional images, allowing for a comparison of track depths. Using the 130 μm pen, only a maximum depth of 130 μm may be imaged although larger optical pen size can also be used. As such, the samples must be extremely flat, to ensure the whole set of wear tracks (between 11 to 16 mm wide) may be imaged. High and low definition settings are used in analysing samples with optical profilometry. The variation in the measured volume between scan types (low and high resolution) is ± 5.1% [103]. In low definition scans, an average of three scans with 5 μm steps in both X- and Y-directions were conducted. A shorter duration is required to complete these series of scans (~12 hours), in comparison to the high resolution scans, allowing this level of scanning to be routinely completed for all wear test samples, while maintaining constant test conditions for comparison. In comparison, for the high definition scans, a single scan with 2 μm steps (for both the X- and Y-directions) is used to analyse the wear tracks and surrounding surface, which takes a significantly longer time (19-23 hours).

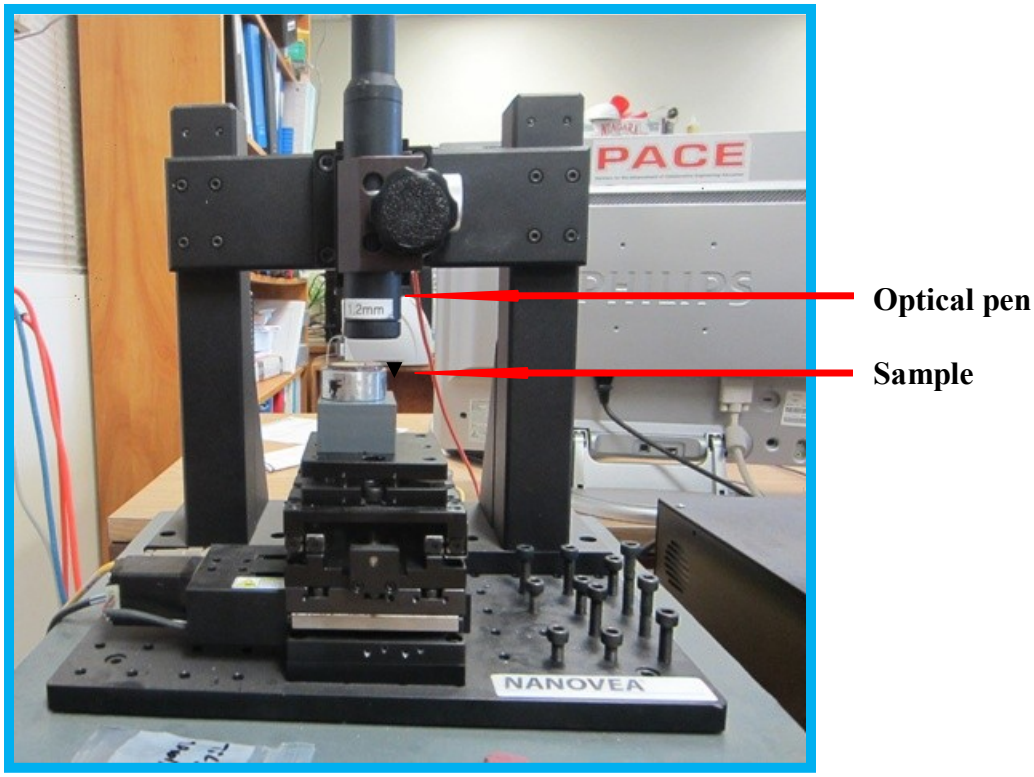

Figure 3.7: Photograph of a Nanovea PS50 System Optical Profilometry used in the present study

Following the volume loss analysis with the optical profilometer, the microstructural features of the wear tracks and resultant wear debris were examined using SEM and EDS, in order to visually assess the wear track and conduct chemical analysis of any tribolayer formed. EDS was also used to confirm whether there was material transfer from the WC-Co counter face sphere to the TiC-steel composite wear surface and vice versa.

3.2.4 Electrochemical Testing

The corrosion behaviour was assessed on the three grades of the TiC-steel composites (i.e. with 304L, 316L and 410L steel, and for binder content varied from 10 to 30 vol. %). The focus for the corrosion studies was on the application of a variety of advanced electrochemical characterisation techniques, including Tafel extrapolation, potentiodynamic polarisation, cyclic polarisation, and potentiostatic polarisation, as well as weight loss measurements. In order to generate baseline data, 'pure' wrought 316L, 304L and 410L steels were also assessed for their corrosion behaviour, which was then compared to that of the cermets. For all of the corrosion

studies, a 'simulated seawater' environment, with 3.5 wt. % NaCl, was used at room temperature (23°C). A standard three-electrode flat cell configuration was employed, with the cermet (or steel) sample acting as the working electrode (an exposed test area of 1cm^2 was used), a platinum mesh as the counter electrode, and a saturated calomel electrode (SCE; 0.241 V versus a standard hydrogen electrode) as a reference. All the potential measurements throughout the corrosion studies will therefore be referred to the reference electrode. A schematic illustration of a standard three-electrode flat cell configuration comprising of the reference, working and counter electrode is shown in Figure 3.8.

The saturated calomel electrode (Ag|AgCl|KCl) was sourced from Accumet (SN01094027 P7). The configured flat cell is connected to a potentiostat (EG & G PARC Model 273A, Princeton Applied Research, USA) and interfaced with an associated computer running Corrware (a corrosion evaluation software for Tafel extrapolation, supplied by Scribner Associates, Inc, USA). The potentiostat (Figure 3.9) controls the potential difference between the reference electrode and the working electrode (i.e. it imposes an applied potential) and also measures the current flow between the working electrode (cermets) and the counter electrode (platinum mesh). An illustrative representation of the functions of the potentiostat in a typical standard three-electrode cell configuration is shown in Figure 3.10 [104].

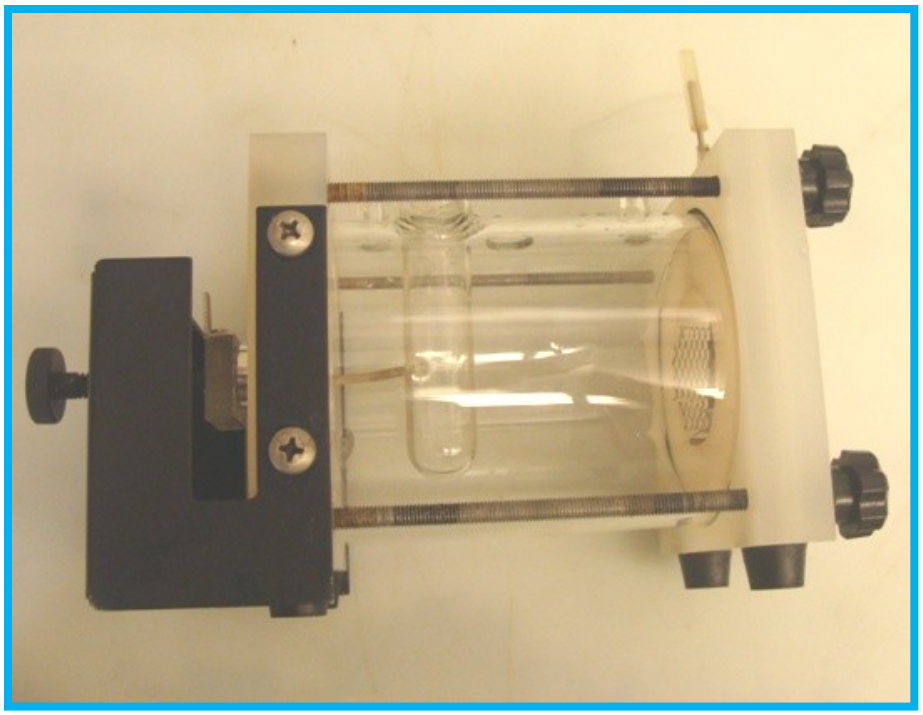

Figure 3.8: The electrochemical flat cell used in the present work, in which all the corrosion experiments are performed.

Figure 3.9: The electrochemical testing potentiostat (EG & G PARC Model 273A, Princeton Applied Research, USA) used in the present work.

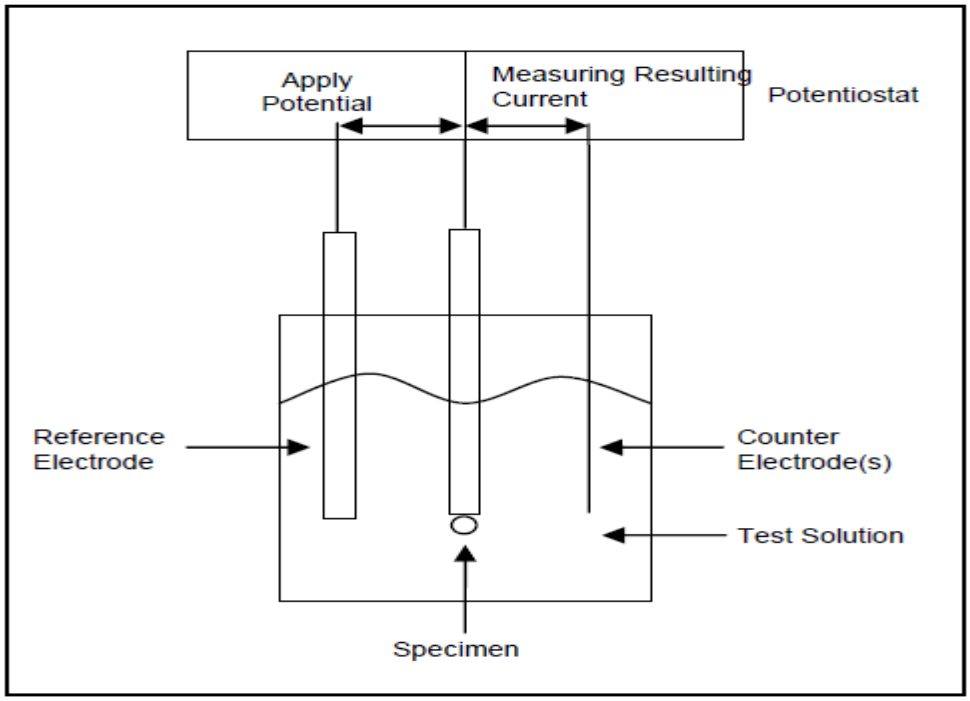

Figure 3.10: A schematic illustration of a standard three-electrode flat cell configuration, showing the main functions of the potentiostat [104].

The following electrochemical techniques were employed in order to study the corrosion behaviour of TiC-steel cermets in a simulated sea water environment.

3.2.4.1 Open Circuit Potential

Open circuit potential means the potential of the system without the application of external current. By applying no current to the sample in the electrolyte and monitoring the change in voltage with time, the OCP measurements are determined. For the present study before any electrochemical measurement is carried out, 4 hours of immersion was allowed to ensure steady-state conditions.

3.2.4.2 Potentiodynamic Polarisation

In the current study, the potentiodynamic polarisation measurements began once steady state conditions were established, following the 4 hours of the OCP measurements. The potentiodynamic polarisation scanning ranged from -750mV (cathodic region) to 3500mV

(anodic region) using a scan rate of 0.1667 mV/s. By changing the applied potential of the working electrode, and monitoring the resultant current as a function of time or potential, the potentiodynamic polarisation response can be measured. This is an electrochemical measurement technique that gives general information about the overall corrosion mechanism (with respect to the active-passive behaviour) in a given metal-solution system. This simply involves varying the potential of the electrode at a selected rate (the scan rate) by application of current through an electrolyte. Potentiodynamic plots invariably have the applied potential as the Y-axis and the logarithm of the measured current in the X axis, with the shape of the resultant plot giving an indication of the corrosion mechanism of the sample in the electrolyte. A representative diagram of a typical active-passive characteristic material (i.e. potentiodynamic polarisation plot) is presented in Figure 3.11 [104].

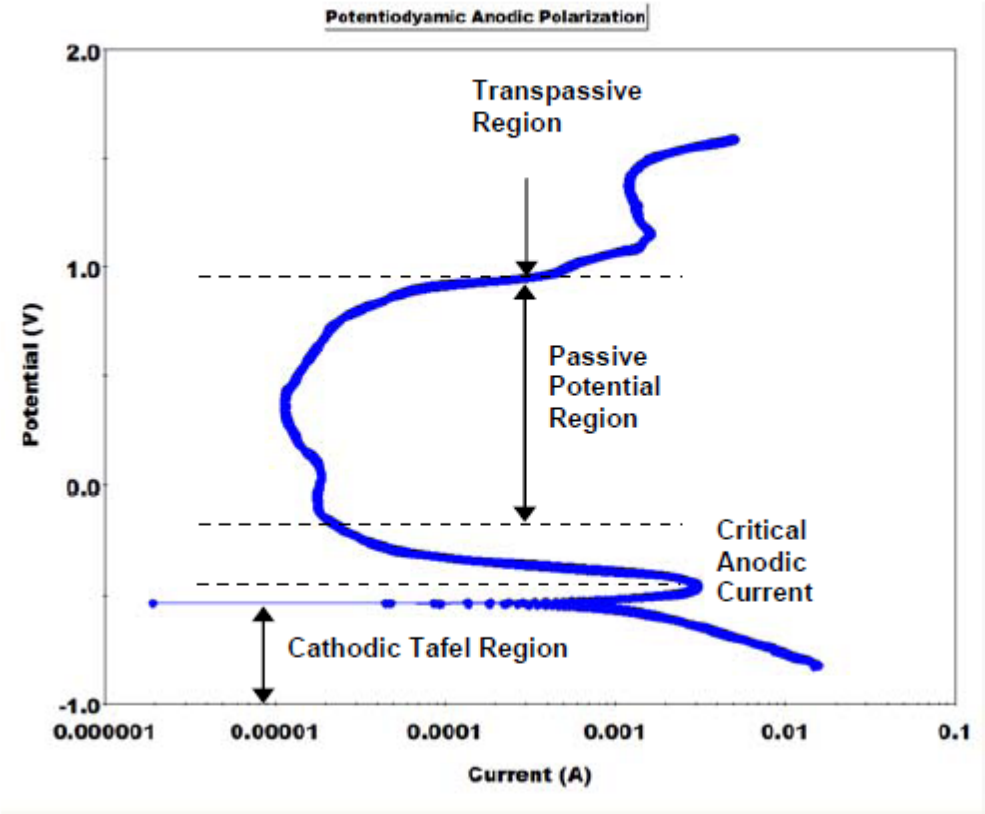

Figure 3.11: A representative diagram of potentiodynamic polarisation plot showing the active and passive regions [104].

Figure 3.12 [105] presents more descriptive features of the typical potentiodynamic curve shown in Figure 3.11 [104]. The region labelled 'A' represents the active region, where corrosion of the metal is taking place, as the applied potential is made more positive. At point 'B', further increase in the rate of corrosion stops, which is believed to be as a result of the formation of a protective oxide layer (hence the onset of passivation). Another feature that can be observed from the potentiodynamic curve is the passivation tendency of a material, for instance from Figure 3.11 [104] and Figure 3.12 [105] (point B) the lower or higher the anodic critical current density provides information about how fast or how slow the material can passivate. Hence, the low current at the peak infers that the specimen passivates quickly. In addition to the passivation tendency, the degree of passivation and the stability of the passive film can de deduced by observation of the current in the passive region and the position of the potential at the transpassive region; a lower current in the passive region infers a higher degree of passivation, whereas higher transpassive potential depicts better stability of the passive film [104].

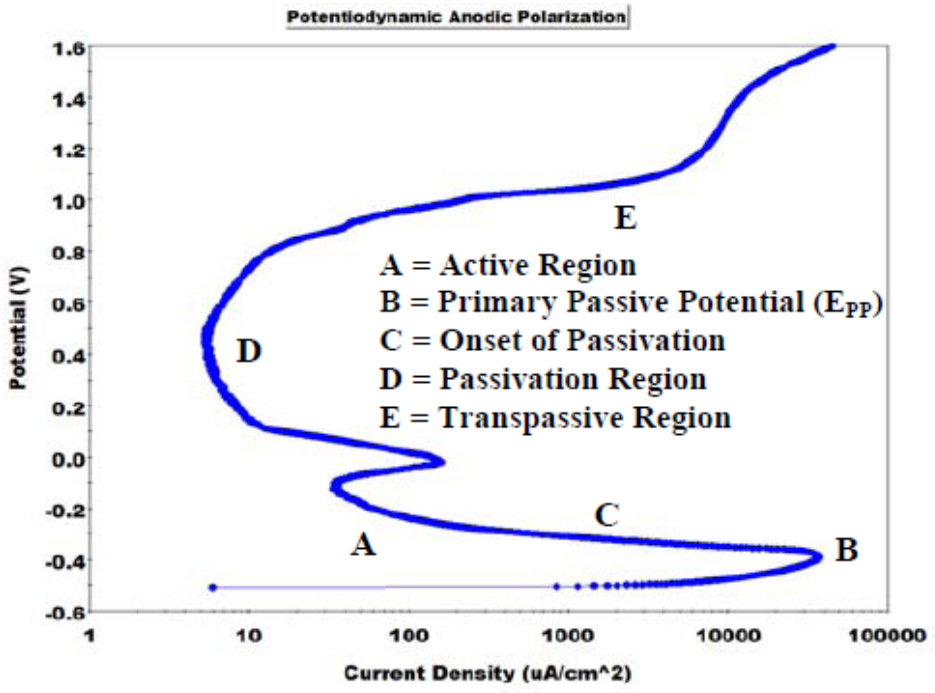

Figure 3.12: An illustrative diagram showing standard potentiodynamic anodic polarization plot of 430 stainless steel [105].

The formation of a protective oxide layer leads to a decrease in the current in region 'C', the current spike at point 'D' indicates a change in current as the potential is increased. The breakdown of the protective oxide layer (passive film) is experienced in region 'E', accompanied by a significant increase in the current. In summary, the potentiodynamic polarisation technique is a powerful tool for studying the corrosion behaviour of materials, or ranking their corrosion susceptibility, gives information about the ability of a material to spontaneously passivate in a particular medium, and the passivation regions of different materials in addition to the corrosion rate in the passive region [104, 106].

3.2.4.3 Tafel Extrapolation

Tafel extrapolation is a technique used in the present study to calculate the corrosion rate of the tested samples, alongside weight loss measurement. The technique involves the extrapolation of corrosion current density, i_{corr}, and corrosion potential, E_{corr}, from the Tafel curve (as illustrated in Figure 3.13[106]), and the use of use of Equation 3.1 [107] to calculate the corrosion rate. The i_{corr} and E_{corr} are extrapolated at the intersection between tangential slopes of the anodic and cathodic curves, as illustrated in Figure 3.13. For the present study, the corrosion potentials and the corrosion current densities were estimated by using instantaneous Tafel-type fit CorrWare corrosion analysis software, outlined earlier.

The Tafel measurement was determined by scanning from -500 mV in the cathodic region to 750 mV in the anodic region. By extrapolating the i_{corr} and E_{corr} from the Tafel extrapolation, the corrosion rate was calculated following [107]:

$$\text{Corrosion rate (mm/year)} = \frac{\left(3.27 \times 10^{-3}\right) \times I_{corr} \times W}{D} \qquad \text{Equation. 3.1}$$

where k is 3.27 x 10^{-3} mm g/μA cm yr, i_{corr} is in μA/cm^2, D is the density in g/cm^3, and W is the equivalent weight, which is considered dimensionless. A comparable corrosion rate, obtained from direct weight loss measurement, was determined by weighing the corroded samples before and after potentiodynamic polarisation, the corrosion rate is then calculated following [37]:

$$\text{Corrosion rate (mm/year)} = \frac{87.6 \times M}{T \times A \times D} \qquad \text{Equation. 3.2}$$

where M is the weight loss in g, D is the density in g/cm^3, A is the area of the sample in cm^2, T is the time of exposure of the metal samples in hours.

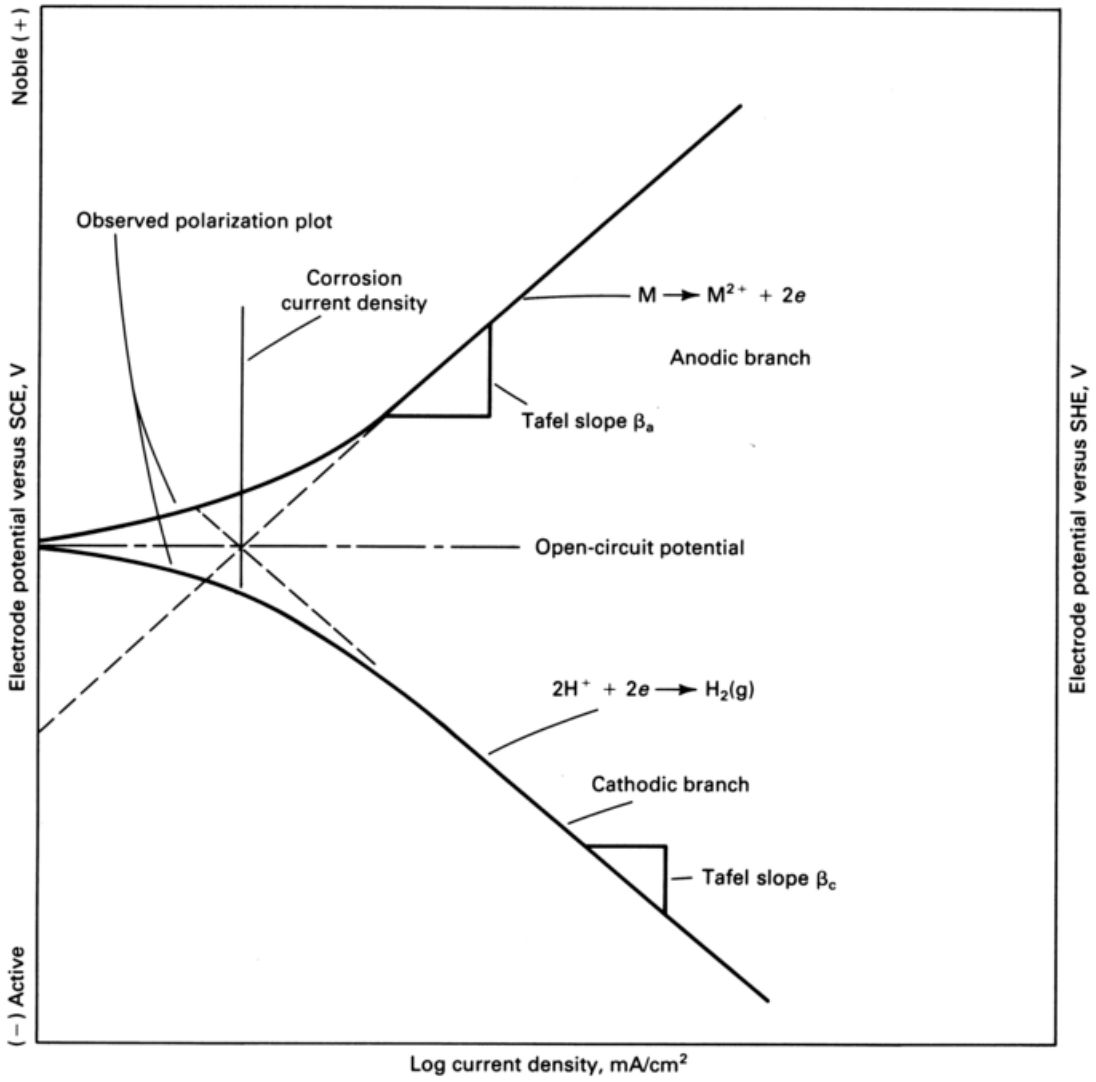

Figure 3.13: Illustrative diagram showing the Tafel extrapolation technique for determination of corrosion current density and corrosion potential for corrosion rate measurement [106].

3.2.4.4 Cyclic Polarisation

Cyclic polarisation is a powerful electrochemical measurement technique used to study the susceptibility of materials to localised corrosion. It is another type of potentiodynamic polarisation method, and is described in ASTM standard practice G61[108], which gives a

reasonable, rapid method of qualitatively predicting the propensity of an alloy to suffer localised corrosion (especially pitting and crevice corrosion). It is mostly used in assessing the susceptibility of stainless steels and nickel alloys to localised corrosion.

During cyclic polarisation, a potential is scanned from the corrosion potential and continued in the anodic direction until a sharp increase in the current is experienced, and is then reversed when the scan reaches the pre-programmed current density value, back to the cathodic region. A threshold current density of 1 mA/cm^2 is usually applied and the final scan potential should be negative with respect to the protection potential [104]. The pitting potential, E_{pit}, is one parameter that can be obtained from a cyclic polarisation curve, and is a non-conservative parameter for assessing the susceptibility of a metal to pitting corrosion, while the protection potential, E_{prot}, is a much more conservative parameter and as such is used as a design criterion in assessing the susceptibility of alloys to pitting corrosion [86, 109]. Illustrative diagrams used to explain the features of cyclic polarisation are presented in Figures 3.14 [104] and 3.15 [110]. During the forward scan, the potential at which a sharp increase in current is experienced is defined as the pitting potential, as shown in Figure 3.14 [104]. The protection (or repassivation) potential is where the reverse segment of the loop closes or intersects with the forward scan, as shown in Figures 3.14 [104] and 3.15 [110]. There are some scenarios where the reverse scan does not cross the forward scan. In that case E_{prot} can be estimated by extrapolating the reverse scan to zero current [104]. The assessment of a material's susceptibility to pitting corrosion can also be determined based on the position of the pitting and protection potentials during cyclic potentiodynamic experiments. For instance, if the pitting potential and the protection potential are the same, there will be little tendency to pit. When a material has a protection potential that is more positive than the pitting potential, that material is immune to pitting, and there will be no tendency to pit.

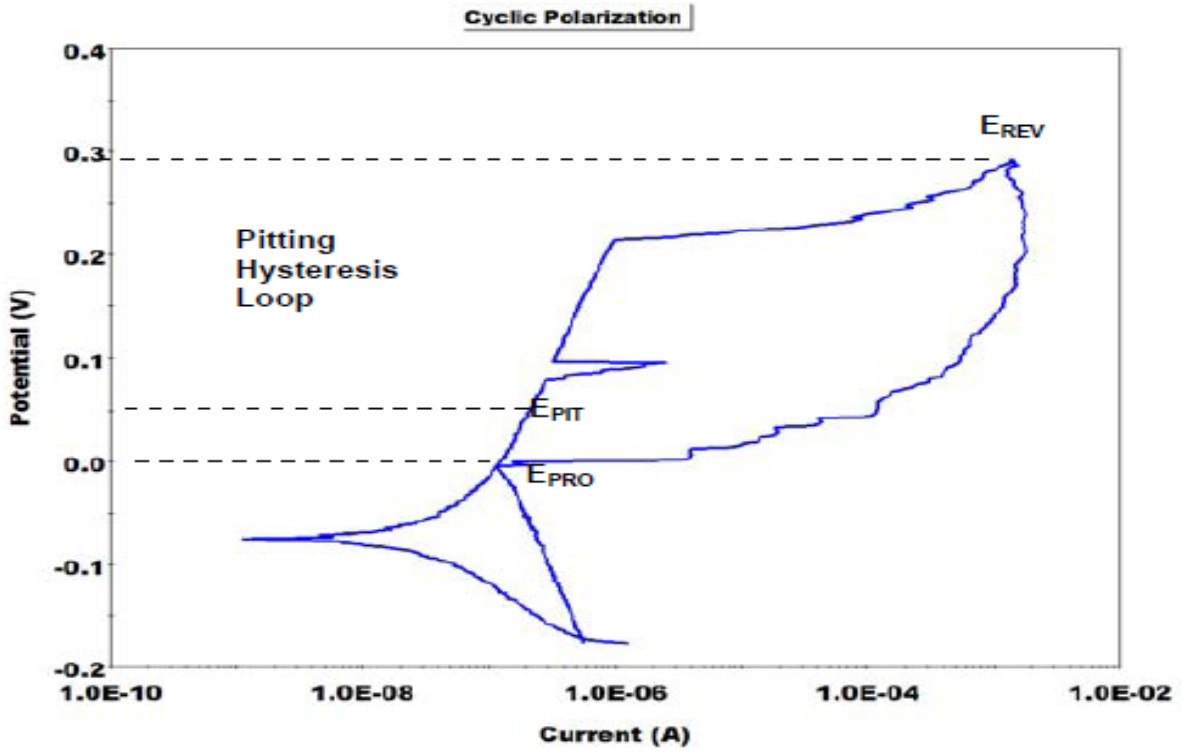

Figure 3.14: A typical cyclic polarisation plot showing pitting hysteresis loop [104].

On the other hand, materials that have a tendency to pit, or are susceptible to pitting corrosion, have a protection potential that is more active (i.e. more negative) than the pitting potential. Another way of assessing the susceptibility of materials to pitting corrosion is based on the size of the loop after the reverse scan. Generally, the reverse scan is at higher current level than the forward scan. The size of the loop is a rough indication of the pitting tendency; the larger the loop, the greater the tendency towards pitting corrosion [104]. As stated previously, pitting experiments are used to rank or predict a material's susceptibility to crevice or pitting corrosion. At the protection potential, neither pitting nor crevice corrosion would occur, while above the pitting potential both pitting and crevice corrosion will occur and, in between the pitting and protection potentials, pitting or crevice corrosion will propagate but new pits will not appear [104]. For the present study, the protection potential, E_{prot}, the pitting potential, E_{pit} and the difference between them ($\Delta E = E_{pit} - E_{prot}$) are used to characterise the material's susceptibility to localised corrosion after the cyclic polarisation experiments.

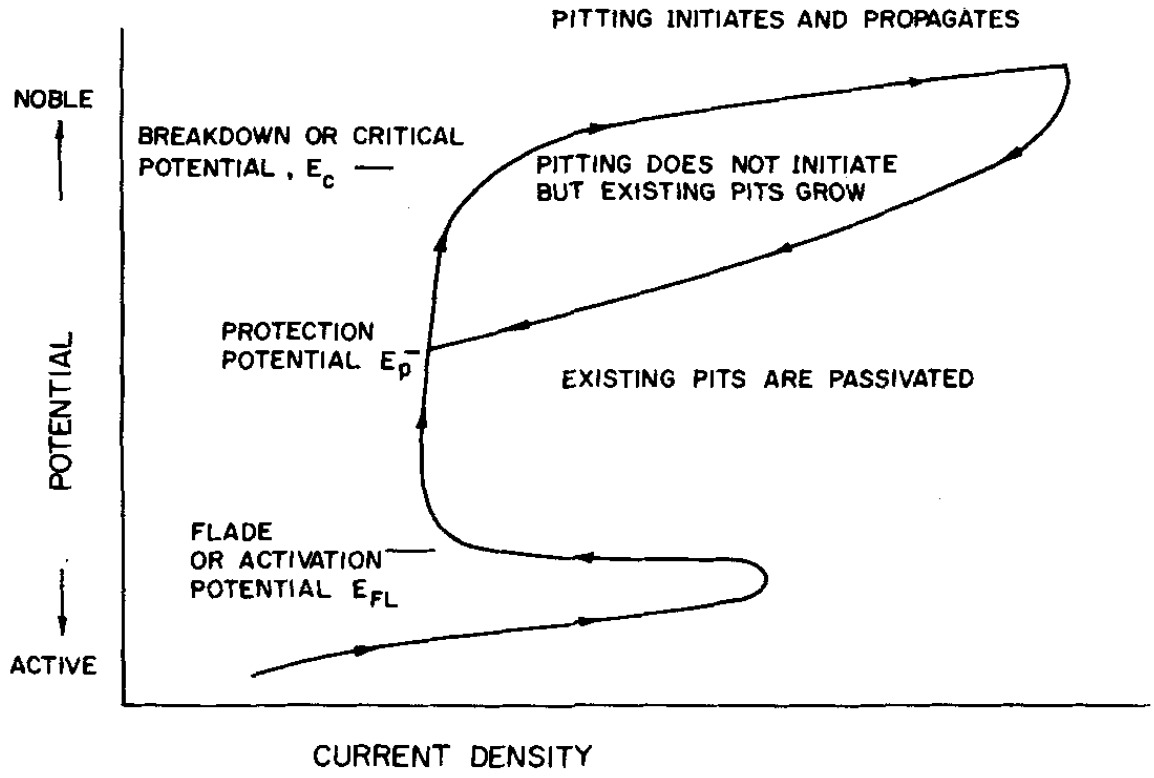

Figure 3.15: Schematic representation of a cyclic polarisation curve [110].

3.2.4.5 Potentiostatic Polarisation

Potentiostatic polarisation simply means applying a constant potential and monitoring the current response with respect to time. This approach is used to measure responses at the pitting or protection potentials, after determining these potentials following the cyclic polarisation experiments. For the present research, potentiostatic polarisation was employed to confirm the pitting potential previously deduced from cyclic polarisation experiments, by selecting a potential slightly above the pitting potential and scanning at that fixed potential while monitoring the current response. It was also used to measure the current response in the pseudo-passive region (explained in Chapter 7), following potentiodynamic polarisation.

3.2.5 Post Corrosion Chemical Analysis

Following corrosion tests, the remaining solutions contained within the electrochemical cell were assessed using inductively coupled plasma optical emission spectroscopy (ICP-OES; Varian Vista Pro (Radial View), Varian, Inc., Mulgrave, Australia), in order to determine the quantities of various metals that were present in the solutions after the corrosion tests. This was conducted on both fine particulate material, filtered from the solution, and the resultant filtered solution itself. The solutions were filtered using a Millipore vacuum system, with a 1.0 μm pore size filter. The particulate-free filtered solutions were analysed directly using the ICP-OES. Conversely, the filtered particulate residue was collected and dried at 105°C. The solid material was scraped off the filter and weighed. Three different types of acids (HF, HNO_3, $HClO_4$) were sequentially added to the samples (i.e. 10 mL conc. HNO_3, 5 mL 70% $HC1O_4$, and 10 to 20 mL 49% HF depending on the amount of silicates the sample contains). Then the samples were boiled to dryness on a hotplate at 150°C overnight. The samples were removed from the hotplate, which was followed by the addition of 10 mL conc. HCl, and then heating the samples again on the hot plate for 10 minutes. After 10 minutes, the samples were removed from the hot plate and 25 mL of double distilled water was added, and then boiled for an additional 10 minutes. The samples were then removed from hotplate and allowed to cool, after which they were filtered through plastic funnels and the residue was then brought back into solution with HCl, made up to 100 ml in volumetric flasks, and analysed using ICP-OES.

In summary, the development of cermets for wear and corrosion characterisation involves a muilti-step process. It involves the weighing and pressing of TiC powder using uni-axial and cold isostatic pressing followed by addition of pre-determined volume % of steel binder (ranging from 5-30 vol. % depending on the properties to be evaluated) on top of the TiC preform. Melt infiltration was carried out at different temperatures and times depending on the cermet and properties to be assessed which is followed by sequential polishing to prepare the infiltrated cermets for to subsequent characterisation involving hardness and indentation fracture resistance, wear and electrochemical measurements.

4 The Reciprocating Wear Behaviour of TiC-304L Stainless Steel Composites Prepared by Melt Infiltration

Chukwuma C. Onuoha, Georges J. Kipouros, Zoheir N. Farhat and Kevin P. Plucknett*

Materials Engineering Programme, Department of Process Engineering and Applied Science, Dalhousie University, 1360 Barrington Street, B3H 4R2, Nova Scotia, Canada.

Status: Published: Wear 303 (2013) 321-333

4.1 Abstract

TiC-based ceramic-metal composites, or cermets, are widely used in applications requiring wear and corrosion resistance. In the present work, a family of novel TiC–stainless steel (grade 304L) cermets has been developed using vacuum melt infiltration (1500°C/1 hour), with steel binder contents varied from 5 to 30 vol. %. Microstructural analysis showed a homogenous distribution of TiC within the steel binder, with mean TiC grain sizes of ~6 μm. Increasing the steel content resulted in an increase in the indentation fracture resistance and a decrease in the hardness. The reciprocating wear resistance of the cermets was assessed using a ball-on-flat geometry, using a WC-Co sphere dry sliding on the polished cermet surface. It was shown that there is an increase in the specific wear rate with both increasing load and binder content. Similarly, a higher coefficient of friction was observed with higher steel binder contents. The morphology of the worn surface was investigated using scanning electron microscopy, and associated energy dispersive x-ray spectroscopy, to more fully understand the operative wear mechanisms. Evidence of a transition from two- to three-body abrasive wear was observed, together with the formation of a tribolayer, indicating that adhesive wear was also occurring.

Keywords: Cermets; Abrasive wear; Adhesive wear; Tribolayer; Dry sliding

*email: kevin.plucknett@dal.ca

4.2 Introduction

The use of ceramic-metal composites, or cermets, has gained acceptance in a wide range of industries due to their considerable potential for use in corrosive and tribological applications. Cermets utilise both the high hardness of the ceramic phase and the ductility of the metallic binder, producing a combination of properties that cannot be achieved by either component when used alone. Among the ceramics that are widely used in these applications, TiC is considered to be a strong candidate for the development of cermets due to its high hardness, melting point, chemical and thermal stability, and wear resistance [9]. TiC also exhibits good melt wettability by many metallic binders, which facilitates cermet processing. Examples of metals that have been used with TiC for cermet formation include Ni, Co, Al, Cu and Fe [111-115].

Fe-based alloys are widely applied metallic materials in their own right, because of their low cost and good mechanical properties [116]. In particular, austenitic stainless steels exhibit higher strength, stiffness, and ductility when compared to aluminium, while also offering the potential to be used at elevated temperatures (up to ~800°C). In addition, select stainless steels can exhibit excellent resistance to aqueous corrosion. Despite these general benefits, austenitic stainless still have a major drawback for use in certain tribological environments, as they have generally poor wear resistance due to their relatively low hardness [117]. Pagounis *et al.* reported that the wear resistance of stainless steel can be improved dramatically by the incorporation of ceramic particles, such as carbides and oxides [70]. Tjong and Lau also demonstrated a significant improvement in the micro-hardness, sliding wear and abrasion wear resistance of 304L stainless steel through the addition of 20 vol. % of TiB_2 [118]. In related work, Degan *et al.*[119] pointed out that the load bearing capacity of the TiC, and its ability to reduce metal-metal contact during sliding, is responsible for its improvement in wear performance of TiC containing metal matrix composites (MMC).

While these previous examples highlight the benefit of adding small volume fractions of ceramic to a metal matrix (i.e. fabricating a MMC), further improvements in wear resistance may be envisaged for the case where the ceramic phase is predominant. Akhtar and Guo reported that 50%-70% TiC additions to a stainless steel binder led to an improvement in wear resistance [120]. TiC-carbon steel cermets have also been assessed as impact resistant materials [121-122]. In that instance it was shown that quenching and subsequent tempering treatments could result in

significant surface hardening. More recently, it has been demonstrated that TiC-based cermets can be prepared to high density by melt infiltration using a moderately wide range of steel contents (from 5 to 30 vol. %) [123].

As a consequence, the use of stainless steels as a low volume fraction binder for TiC cermets may be envisaged when corrosion resistance and toughness of the composite are the ultimate requirement. In this present study, TiC-stainless steel cermets have been developed for potential application in the oil and gas industry (i.e. as hard, corrosion-resistant facings), using 304L grade steel, with binder contents varied from 5 to 30 vol. %. The dry reciprocating wear behaviour of these cermets has been assessed, using a WC-Co contacting counter face sphere, with comparison made to pure 304L steel and other cermets systems.

4.3 Experimental Procedure

4.3.1 Sample Preparation

The TiC powder used in the present study was sourced from Pacific Particulate Materials Ltd. (Vancouver, BC, Canada), with a manufacturer quoted particle size of ~1.3 μm, which was confirmed through subsequent particle size analysis [96]. For the metallic binder, 304-L stainless steel powder was obtained from Alfa Aeser (Ward Hill, MA, USA), with a nominal particle size of -100 mesh. A simple melt infiltration process was used to fabricate the samples, based on the prior development of TiC-Ni_3Al cermets [124]. TiC pellets were prepared by uniaxial pressing ~7.5 g of powder as 31.75 mm diameter discs, at a pressure ~67 MPa. The samples were then vacuum bagged and further compacted by cold isostatic pressing at 220 MPa. After compaction, the TiC pellets were weighed and an appropriate amount of 304-L stainless steel was placed on top of the TiC preform to give binder volume fractions between 5 and 30 vol. %. For sintering, the TiC preforms were placed on a layer of bubble alumina, within a closed alumina crucible. Melt infiltration of the 304-L steel binder into the TiC preforms was conducted at 1500ºC, with this temperature held for 60 minutes. Infiltration was conducted under a dynamic vacuum (~20 mTorr or better), inside a graphite resistance furnace (Materials Research Furnaces, Inc., Suncook, NH, USA), with nominal heating and cooling rates of 10°C/min and 25°C/min, respectively.

4.3.2 Materials Characterisation Procedure

The densities of the infiltrated composites were determined using the Archimedes immersion method in water. The samples were then ground flat using a diamond peripheral wheel, and subsequently polished to a mirror-like finish (starting from a 125 μm diamond pad and finishing with 0.25 μm diamond paste). Microstructural characterisation was conducted on the polished samples, using both optical microscopy (Model BX-51, Olympus Canada, Richmond Hill, Ontario, Canada) and scanning electron microscopy (SEM; Model S-4700, Hitachi High Technologies, Tokyo, Japan). Grain size measurements were made using the linear intercept method [125], from SEM images, where the mean intercept value was multiplied by a factor of 1.56, and ~300 grains were measured for each sample. The hardness and indentation fracture resistance (IFR) of the densified cermets were determined using a Vickers diamond pyramid indenter, with 1 kg and 50 kg applied loads respectively, held for 15 seconds (V-100A, Leco). The lower load was used for hardness testing, specifically to avoid sample cracking during loading. The indentation fracture resistance was determined for both median and Palmqvist-type cracking, using the approaches proposed by Antis *et al* [98], and Niihara [99], respectively. It has previously been demonstrated that Palmqvist-type cracking can be observed in WC-based cermets with moderate Co-binder contents, through the use of sequential polishing [126]. However, such a study was not undertaken in the present work, and the median/Palmqvist transition is simply predicted based on the measured c:a ratio following indentation (where c is the indentation crack length and a is the indent diagonal)[100]. In order to ensure reasonable statistical validity of the measurements, 6 indentations were made for both hardness and indentation fracture resistance.

4.3.3 Reciprocating Wear Test Procedure and Characterisation

In terms of the reciprocating wear tests, TiC samples with 10, 20 and 30 vol. % 304L steel were analysed. The actual wear tests were performed using a universal micro tribometer (UMT; Model UMT-1, Bruker Corp., Campbell, CA, USA). For the wear testing in the present work, a sphere slides against a flat lower sample in a linear back and forth motion (i.e. reciprocating), with a stroke length of 5.03 mm and an oscillation frequency of 20 Hz, for selected times and applied loads. The load is applied through the counter face sphere, perpendicular to the flat sample,

which is mounted on a reciprocating drive. All wear tests were conducted at room temperature (21 ± 2ºC) with a relative humidity of 40-55%. The UMT system is designed to monitor the dynamic normal load, frictional force, and the depth of the wear track during the test. In the present instance, the counterface spheres were 6.35 mm diameter WC-Co balls (Grade 25 with 6 wt. % Co, McMaster-Carr, Aurora, OH, USA), subsequently designated as WC-6Co, sliding against the TiC-stainless steel cermets. This grade of WC-Co was selected due to its having a comparable, or higher, hardness than the present materials. WC-Co has also been used in such sliding wear environments for TiC-Ni_3Al and Ti(C,N)-Ni_3Al cermets [127-128], as well as for a counterface against 'pure' 304L stainless steel [129-130]. The ball was mounted inside a ball holder, which is attached to a load sensor that controls and records forces during the test. For the initial testing conditions, applied loads of 20 to 80 N were used, for up to two hours. This corresponds to approximate Hertzian contact stresses between 1.825 and 3.050 GPa, depending upon the cermet composition and applied load. Further details regarding the approach taken using the UMT system can be found in recent publications on TiC and Ti(C,N) based cermets, prepared with a Ni_3Al alloy binder [127-128].

Following the reciprocating tests, the resultant wear tracks were examined using an optical profilometer (Model PS50 Optical Profilometer, Nanovea, Irvine, CA), to assess both the general features of the wear track and to determine the volume of material removed during testing. The volumetric wear loss measurements obtained from the high optical profilometry were then used to calculate the specific wear rate, k, of the cermet, which is defined as [102].

k = wear volume (mm^3)/(load (N) x total sliding distance (m))

The microstructural features of the wear tracks, the associated wear debris, and the WC-6Co counter face sphere were subsequently examined using SEM, including energy dispersive X-ray spectroscopy (EDS). This includes chemical analysis of any tribolayer that was formed, and also to determine if there was material transfer from the WC-6Co ball to the wear track surface during testing (and vice-versa).

4.4 Results and Discussion

4.4.1 Densification Behaviour and Microstructure of the Composites

The TiC-304L cermets all had sintered densities of 99 % of theoretical, or greater, based on a simple rule of mixtures for the two base constituents (Figure 4.1).

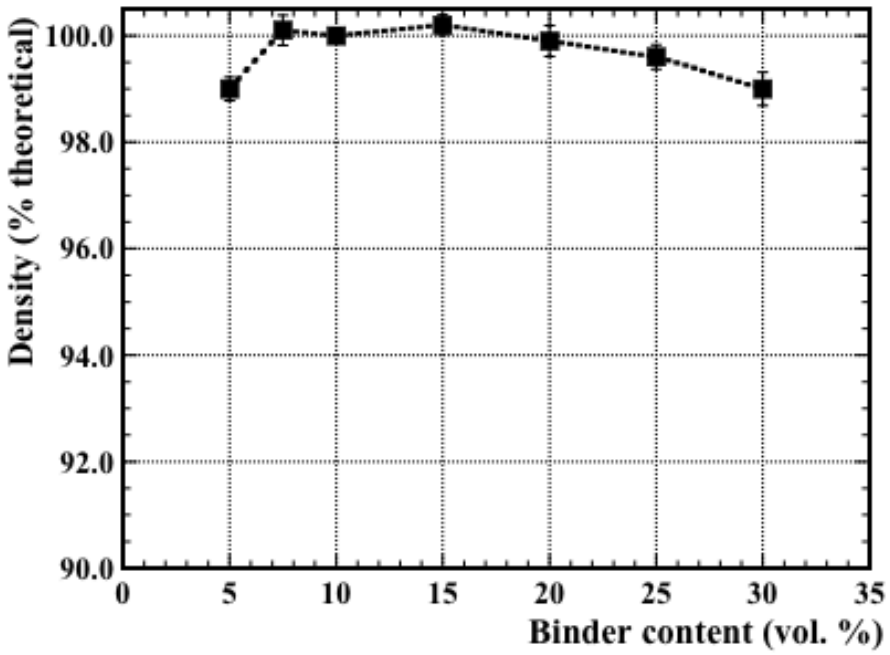

Figure 4.1: The effects of steel binder content upon the sintered density of the TiC-304L cermets processed at 1500°C for 1 hour.

It is apparent that melt infiltration allows for the formation of high-density cermets, even when relatively low steel contents are used (i.e. 5 vol. %). The reason for the small discrepancy in the apparent percentage of theoretical density, in terms of samples with greater than 100 % of theoretical density, is attributed to potential compositional changes during processing, especially for the steel, which can readily incorporate some Ti and C.

Figure 4.2 demonstrates a typical microstructure observed for the TiC-304L cermets, prepared with 20 vol. % steel, using DIC optical imaging. This image reveals a homogenous distribution of TiC grains in the 304L stainless steel binder, and demonstrates the thorough infiltration that arises. Figure 4.3 shows higher magnification SEM images of the cermets prepared with 20 and 30 vol. % 304L steel binder.

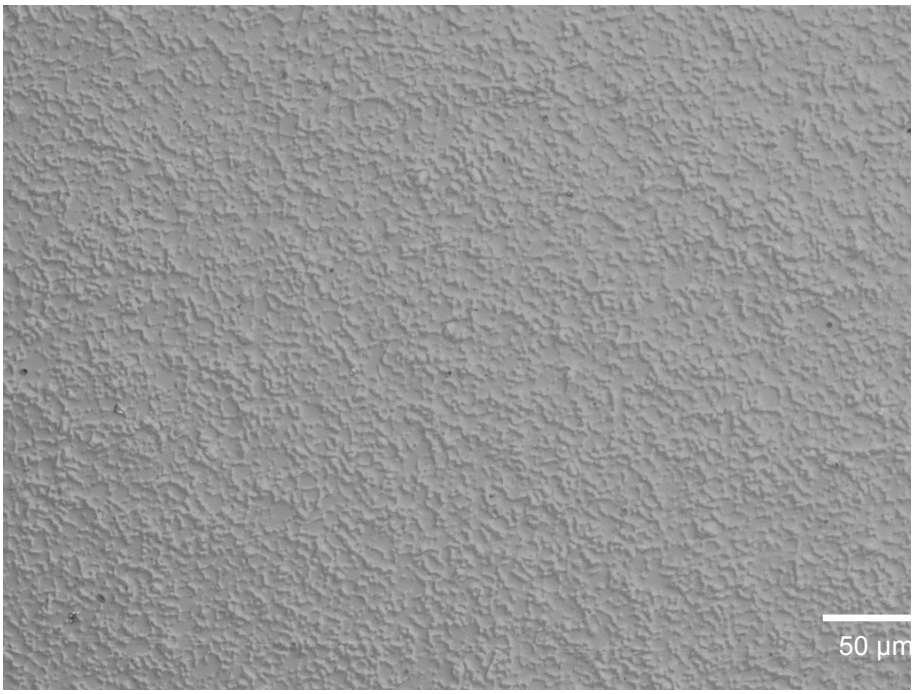

Figure 4.2: DIC optical micrograph of TiC prepared with 20 vol. % 304L stainless steel binder, highlighting the degree of microstructural uniformity that is achieved using melt-infiltration.

(a)

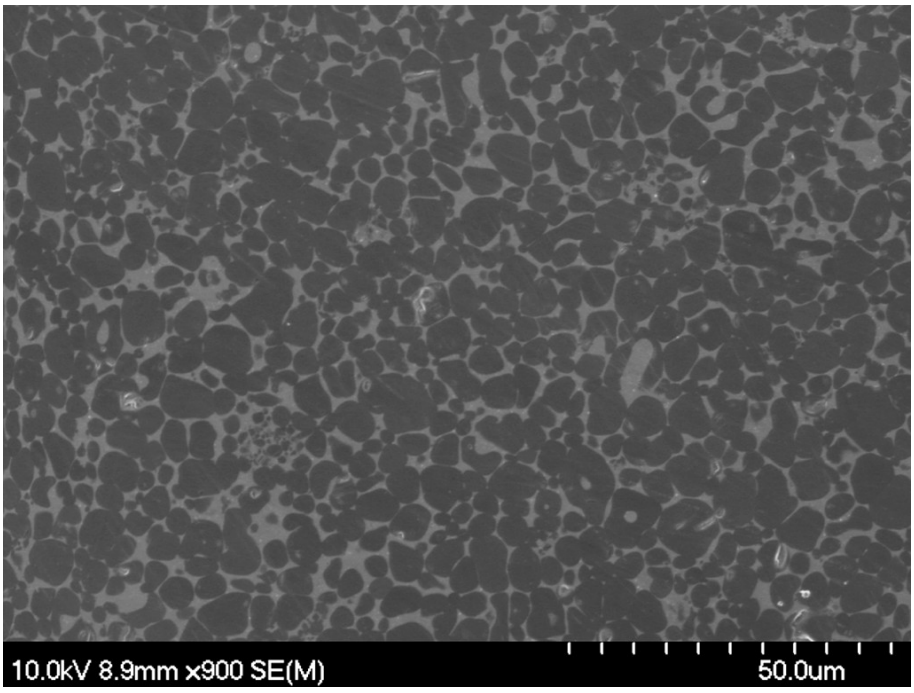

(b)

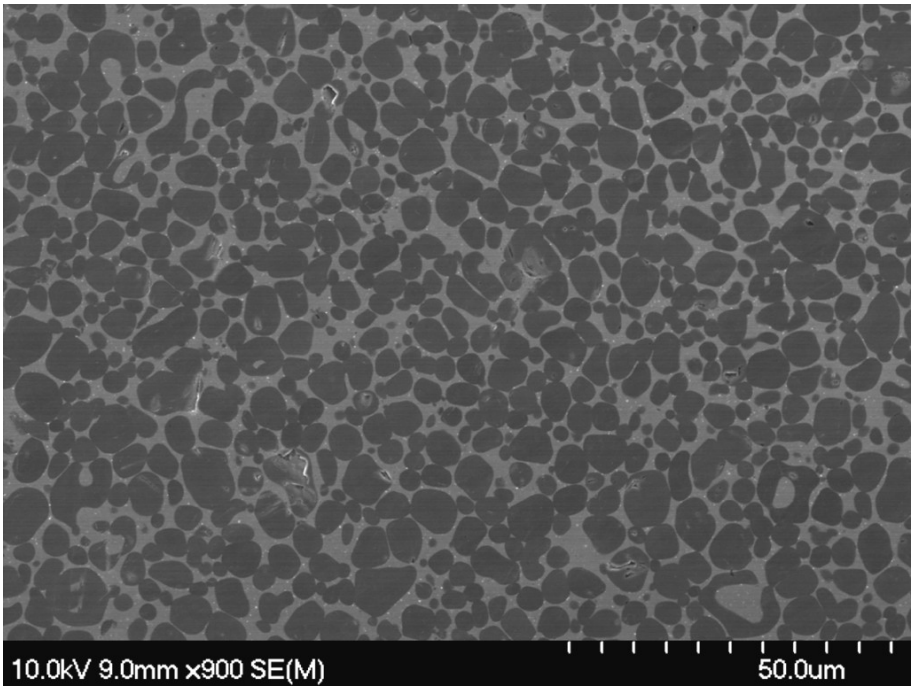

Figure 4.3: SEM images of the TiC-304L cermets prepared with (a) 20 and (b) 30 vol. % stainless steel binder.

Efficient melt infiltration in the absence of applied pressure requires a low contact angle for the molten metal on the substrate [131], and ideally relatively low solubility of the ceramic component in the molten metal. If the solubility is sufficiently low, grain growth can be minimised. In terms of the present materials, Table 4.1 highlights the mean grain size for the TiC cermets, prepared with 10, 20 and 30 vol. % steel, which were determined using the linear intercept method outlined by Mendelson [125].

Table 4.1: The mean grain size for the TiC-304L cermets as a function of steel content; values were determined for a minimum of 300 grains, using the lineal intercept method [125].

Composition	**Mean grain size (µm)**
TiC-10 vol. % 304L	6.80
TiC-20 vol. % 304L	6.25
TiC-30 vol. % 304L	6.45

The SEM images indicate that there is no major reaction between the TiC particles and the steel binder phase, with two distinct phases present, and no evidence of any major interfacial reactions. Similarly, there is no evidence of interfacial debonding in the sintered cermets, confirming the good wettability of the TiC particles by the 304L stainless steel. The homogenous distribution of TiC in the steel binder, high sintered densities and absence of interface debonding can be expected to offer a beneficial effect on both the tribological and mechanical properties of the composites, as there will be minimal potential sites for crack initiation.

4.4.2 Cermet Hardness and Indentation Fracture Resistance

The Vickers hardness response of the TiC-304L cermets is presented in Figure 4.4. It can be seen that the hardness of the composite decreases with increase in binder content, which is predominantly due to relative elastic moduli of the phases (with TiC ~439 GPa and 304L stainless steel ~193 GPa).

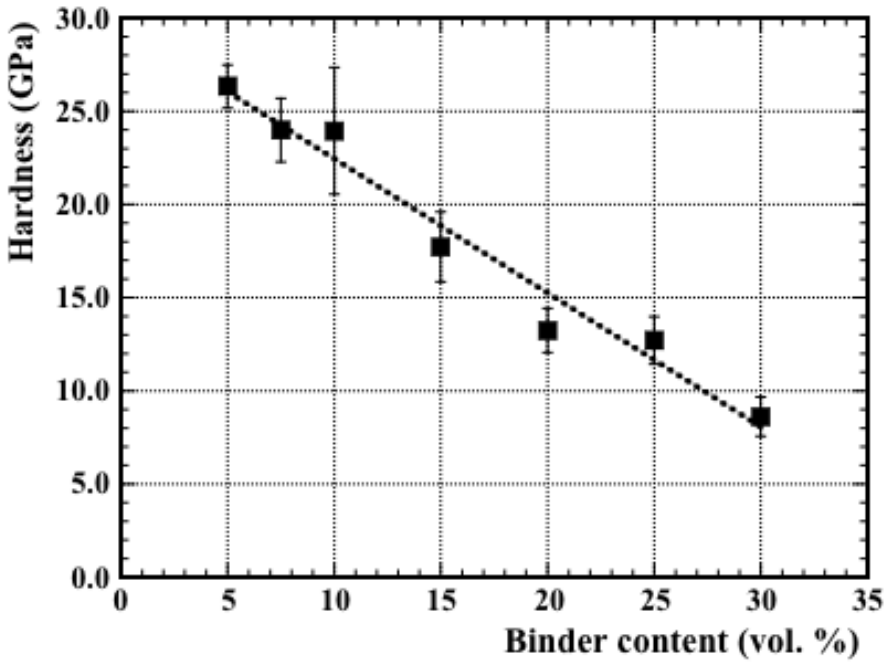

Figure 4.4: The hardness of TiC-304L cermets as a function of steel binder content (measured with a 1 kg load).

The indentation fracture resistance response presented in Figure 4.5, determined using both median (i.e. Anstis *et al*[98]) and Palmqvist (i.e. Niihara[99],) cracking equations, exhibits the

opposite trend; by increasing the steel binder content, the indentation fracture resistance of the cermets is increased. Here the addition of the metal binder is increasing the toughness through the addition of a ductile phase, as 304L can exhibit a room temperature tensile elongation to failure of up to 55 %.

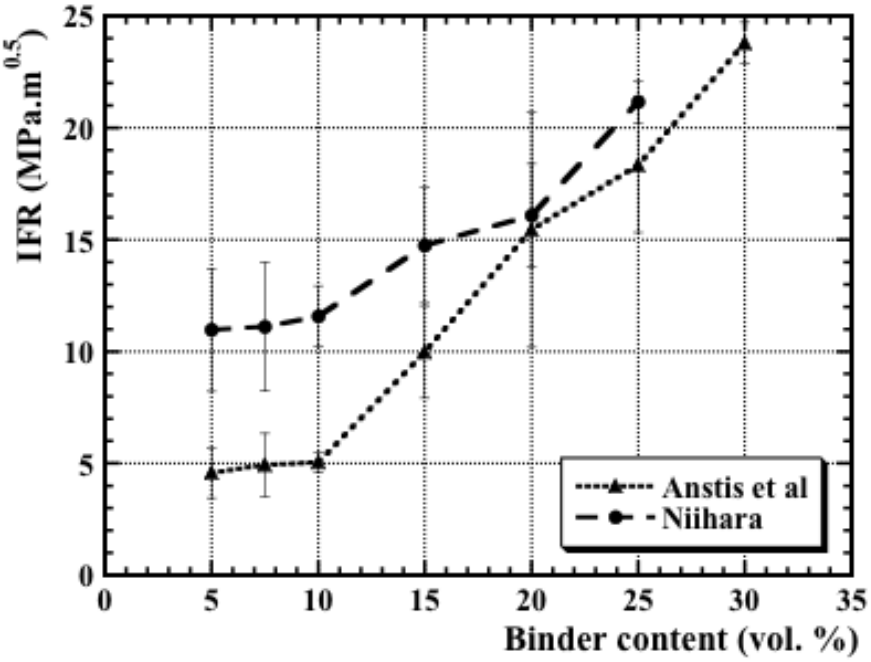

Figure 4.5: The indentation fracture resistance of the TiC-304L cermets as a function of steel binder content (measured with a 50 kg load), determined for both median and Palmqvist cracking.

The ductile phase ligaments between TiC grains can then bridge across cracks, effectively maintaining the matrix integrity. As a consequence, incorporating the steel binder can effectively inhibit crack growth, such that even a 50 kg Vickers indentation load produces minimal cracking, and actually no cracking whatsoever for the highest steel content samples (i.e. 30 vol. %). The data presented in Figure 4.5 effectively highlights a transition in terms of the crack behaviour, showing a more traditional brittle median cracking response for lower 304L binder contents (i.e. c:a > 2.5) and Palmqvist cracking at the higher binder contents (i.e. (c:a < 2.5)[100]. It should be stressed that the actual sub-surface cracking response has not been verified in the present work, for example through the use of sequential polishing, as applied by Shetty for WC-based cermets

[126]. For the present case this transition occurs between 10 and 15 vol. % steel binder, with Palmqvist-type cracking expected at the higher binder contents (i.e. 15 to 30 vol. %).

It can be seen that the addition of the steel binder to TiC makes these cermets relevant in applications requiring both high hardness and toughness, significantly improving the brittle nature of the TiC with the ductile phase of the steel, and enhancing the hardness of the steel with the high modulus TiC phase.

4.4.3 Reciprocating Wear Behaviour

Reciprocating wear tests were used to study the tribological behaviour of the TiC-304L stainless steel composites, with the cermets dry sliding against a hard counter face sphere, which in this instance is comprised of WC-6Co (equivalent to ~10.2 vol. % Co). For the wear testing a reduced sub-set of samples was analysed, in this instance TiC prepared with 10, 20 and 30 vol. % 304L binder. Figure 4.6(a) shows the variation of the 'instantaneous' COF with test duration, as a function of binder content, using a 40N applied load. It can be seen that the COF generally increases with time, as well as with binder content. This general transition of increasing COF with time indicates that the wear mechanism may be gradually changing. It is also apparent that the COF increases with higher binder content, indicating that the steel content plays an important role in controlling the COF.

(a)

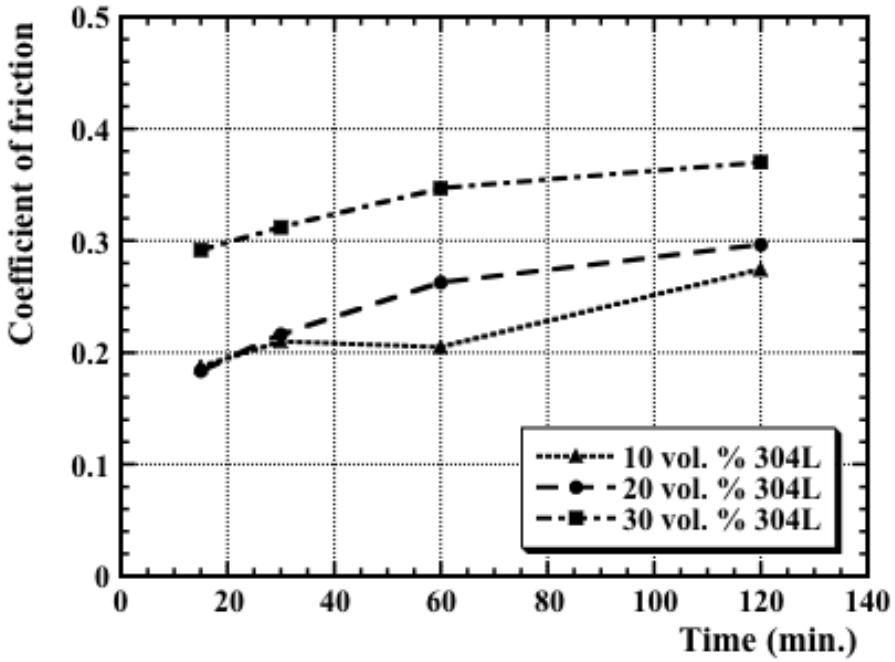

(b)

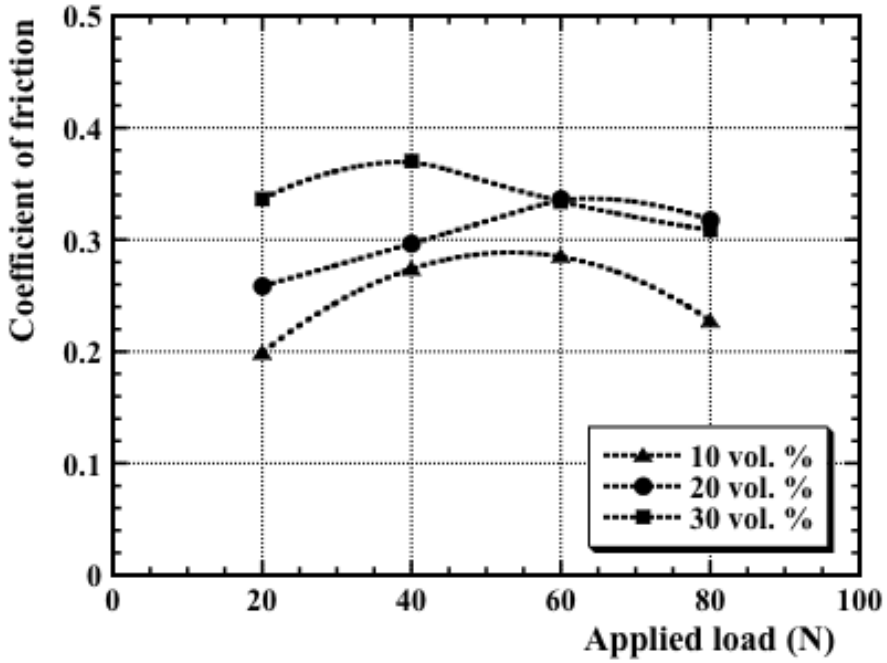

Figure 4.6: (a) The evolution of the COF for the TiC-stainless steel cermets as a function of time and binder content (for a 40 N applied load). (b) The effect of applied load on the COF after 120 minutes of dry sliding, as a function of steel binder content.

Yerokhin and colleagues [129], in characterising a range of coating methods for 304 stainless steel, reported a COF of 0.58-0.63 for uncoated 304 dry sliding against a comparable WC-6Co sphere (6 mm diameter) as used in the present study. In that instance the applied load was relatively conservative, at 2.5 N, although severe adhesive/abrasive wear was reported, with a specific wear rate of 1.07 x 10^{-4} mm^3/Nm [129]. More recently, generally similar COF values were reported by Foerster *et al.*[130], for a 6 mm diameter WC-Co (with an unspecified Co content) sphere sliding against 304 stainless steel, with a steady state COF of ~0.65 achieved after ~0.5 m of dry sliding under a 5 N load.

Figure 6(b) shows the variation of COF with the applied load (determined after 120 minutes of dry sliding). It can be seen that the COF for all the composites evaluated ranges from 0.2-0.36 once a nominally steady state response is recorded. There is generally a small increase in COF with applied load up to 60 N, above which a slight decrease in COF is observed. The slight drop at the highest at the highest load (80 N) could be attributed to the formation and subsequent partial spalling of any tribolayer formed. With the increase in the friction between the TiC cermet and WC-Co counter face sphere, the frictional heating can be expected to increase, resulting in a small temperature rise. While the temperature during testing was not directly evaluated in this work, we have recently studied a family of broadly similar TiC-cermets using a thermal imaging camera (with an identical WC-6Co counter face sphere to the present work), which indicated maximum temperatures of ~60°C at 20 N load, rising to ~100°C under a 60 N load. This temperature rise corresponds closely with those measured by Pirso and colleagues for a variety of cermets at a slightly lower (i.e. 40 N) load [132]. A similar level of temperature increase can be expected in the present work, and it should be stressed that there was no evidence of microstructural change (i.e. oxidation) in the areas immediately adjacent to the wear tracks, which confirms the temperature rise was not significant.

The range of COF values observed for the TiC-304L cermets is broadly consistent with other TiC-based cermet systems. For example, Pirso and colleagues recorded steady state COF values for TiC-NiMo of between 0.25 and 0.3[133]; interestingly, this occurred when sliding against a 0.45 wt. % C steel counter face. Recently, Buchholz *et al.* determined a mean COF of ~3.2 for TiC cermets, prepared with between 20 and 40 vol. % Ni_3Al (alloy IC-50) binder [127], sliding against an identical WC-6Co sphere to the present work. In comparison to the present study, the COF was essentially *independent* of applied load (varied between 20 and 80 N) and cermet

binder content for the TiC-Ni_3Al system, and was relatively stable throughout the test duration. In this respect it is notable that the yield strength of the Ni_3Al alloy IC-50 (~440 MPa[134]) is more than double that of 304L stainless steel (~180 MPa[135]).

Figure 4.7(a) shows the relationship of volumetric wear loss with time for selected samples. It is clear that the volumetric loss increases with time in a nominally linear manner. This observation broadly complies with the Lancaster model, which states that the volumetric wear loss exhibits a linear dependency with both load and time (or distance covered) [103]. Figure 7(b) demonstrates the specific wear rate of the TiC-304L stainless steel composites as a function of applied load. It is clearly apparent that the wear rate increases with both the applied load and the stainless steel binder content. Increasing the binder content results in an associated volume reduction of the high hardness/elastic modulus TiC phase. At the highest TiC content examined (i.e. 10 vol. % 304L), the composite behaviour is dominated by the ceramic phase, and the associated hardness of the composite is high (as shown in Figure 4.4).

(a)

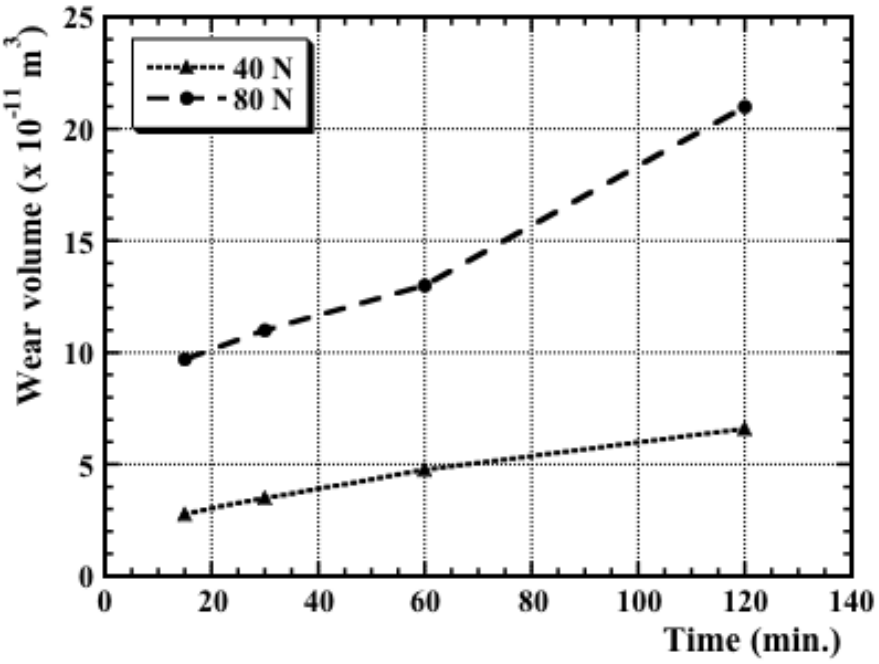

(b)

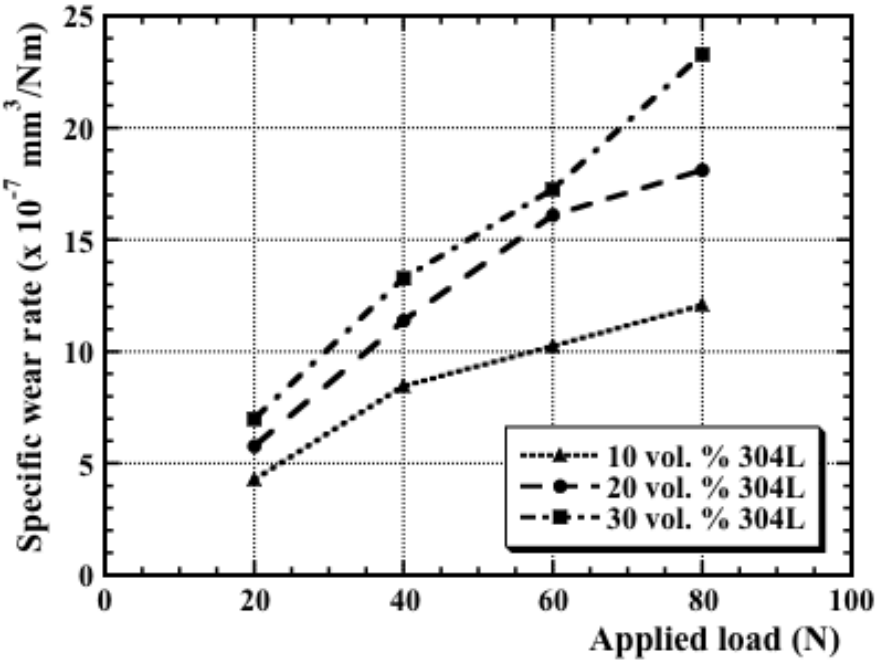

Figure 4.7: (a) The volumetric wear loss as a function of applied load and dry sliding time, for TiC prepared with 20 vol. % 304L binder. (b) The specific wear rate of TiC-304L stainless steel cermets as a function of applied load.

The TiC particles can resist plastic deformation, and offer additional resistance to the effective Hertzian load applied through the WC-Co contacting sphere; this beneficial effect declines through the addition of the comparatively softer steel binder. It should also be noted that there is a *decrease* in the contiguity of the TiC particles (a measure of the carbide-carbide contact) with increasing binder content, and an increase in the binder mean free path (the characteristic ligament length), which can both be anticipated to increase the toughness. Effectively, this makes the composite more ductile in its deformation behaviour, although still relatively elastic in response in comparison to the steel alone (as noted earlier, grade 304L exhibits up to 55 % elongation to failure when tested in tension). The extent of material removal from the binder, in the form of grain pull-out, decreases with increase in TiC content and is related to higher hardness of the TiC. At low loads and higher TiC content, the steel deformation and material removal is effectively minimised by the contiguity of the TiC grains, which form a contacting network that resists compression and extrusion of the softer metallic binder. It is notable, in

comparing the data presented in Figure 4.7(b) with the previously reported specific wear rate of 304 stainless steel in dry sliding against a WC-6Co sphere (i.e. 1.07 x 10^{-4} mm^3/Nm[130]) that the TiC additions result in a two to three orders of magnitude *decrease* in the specific wear rate, highlighting the benefits resulting from the development of these composite cermet structures.

Comparison can be made between the specific wear rates determined in the present work with those for prior studies on a range of cermet systems. Buchholz *et al*., using an identical geometry and test conditions to the present work, demonstrated specific wear rates between ~1.5 and 10 x 10^{-7} mm^3/Nm for fine-grained TiC and Ti(C,N) cermets, prepared with 20 to 40 vol. % Ni_3Al binder [128-129]. Pirso and colleagues examined the dry abrasive wear of WC-Co, Cr_3C_2-Ni and TiC-NiMo, using a block-on-disc geometry, with the cermets sliding against an abrasive Al_2O_3 wheel [68]. In that study WC-Co exhibited the best wear resistance, with specific wear rates ranging from ~5 x 10^{-7} mm^3/Nm for 10 vol. % Co up to ~80 x 10^{-7} mm^3/Nm for 31.6 vol. % Co. WC-Co performed significantly better that Cr_3C_2-Ni, which varied between ~8 x 10^{-7} and 95 x 10^{-7} mm^3/Nm (for a Ni content increasing from 7.7 to 24.3 vol. %). The wear rates observed in the present study compare in a generally favourable manner to those prior studies, even when taking into account the somewhat different test geometry applied by Pirso *et al*. [68]. The slightly lower wear rates observed for the Ni_3Al-based binders can be attributed to a combination of the finer TiC and Ti(C,N) grain size and the higher yield stress of the intermetallic alloy in comparison to the 304L stainless steel, as noted previously.

4.4.4 Microstructural Observations Following Reciprocating Wear

It is important to fully assess the wear response through microstructural and chemical analyses of the wear tracks, as well as assessing the wear debris that is formed. Figure 4.8 shows DIC optical microscope images of the edges of the wear tracks for TiC with 20 vol. % 304L binder, tested for 15 minutes at both 40 and 80 N. SEM images of comparable wear track edges are also shown in Figure 4.9, for the same composition. Several features are apparent from these images. Firstly, when examining the edges of the wear tracks it is clear that there is essentially no plastic deformation outside of the wear track itself, which if present might be viewed as either material 'up-lift' or damage (i.e. TiC grain cracking). This general observation points to an abrasive wear mechanism, either two- or three-body in nature. Initially, it can be expected that the wear

mechanism will be two-body, with the TiC-304L cermet sliding directly against the WC-6Co counter face sphere.

(a)

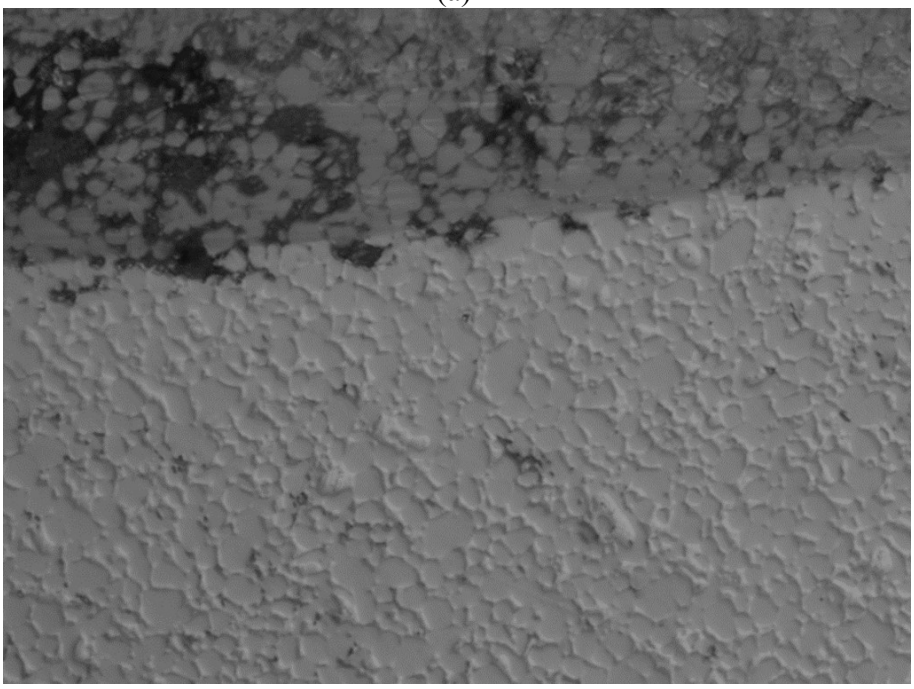

(b)

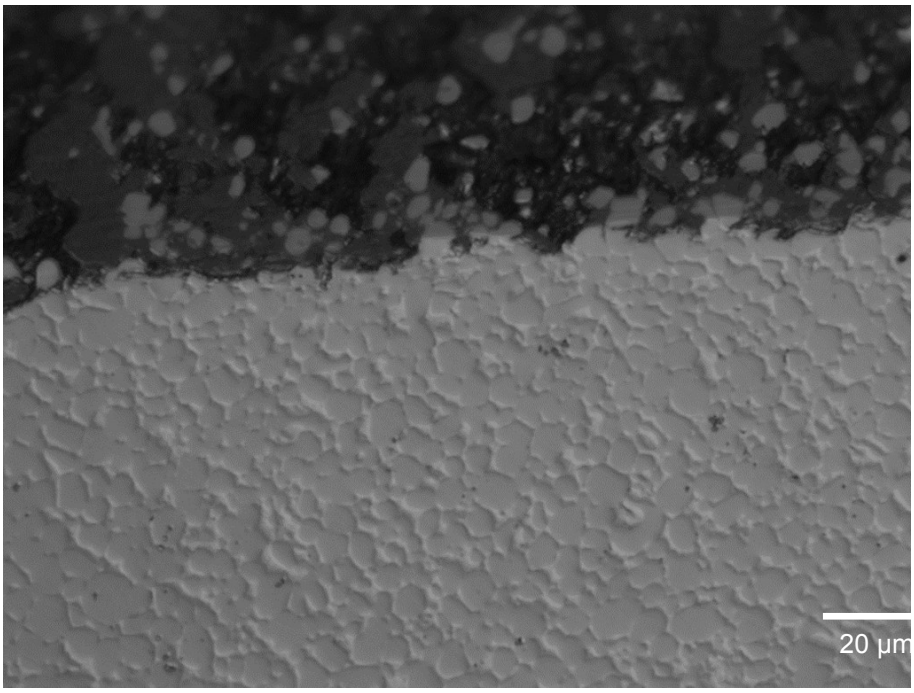

Figure 4.8: DIC optical images of the edges of wear tracks obtained for TiC with 20 vol. % 304L stainless steel after 15 minutes total sliding time (~181 m sliding distance), under loads of (a) 40 N and (b) 80 N.

(a)

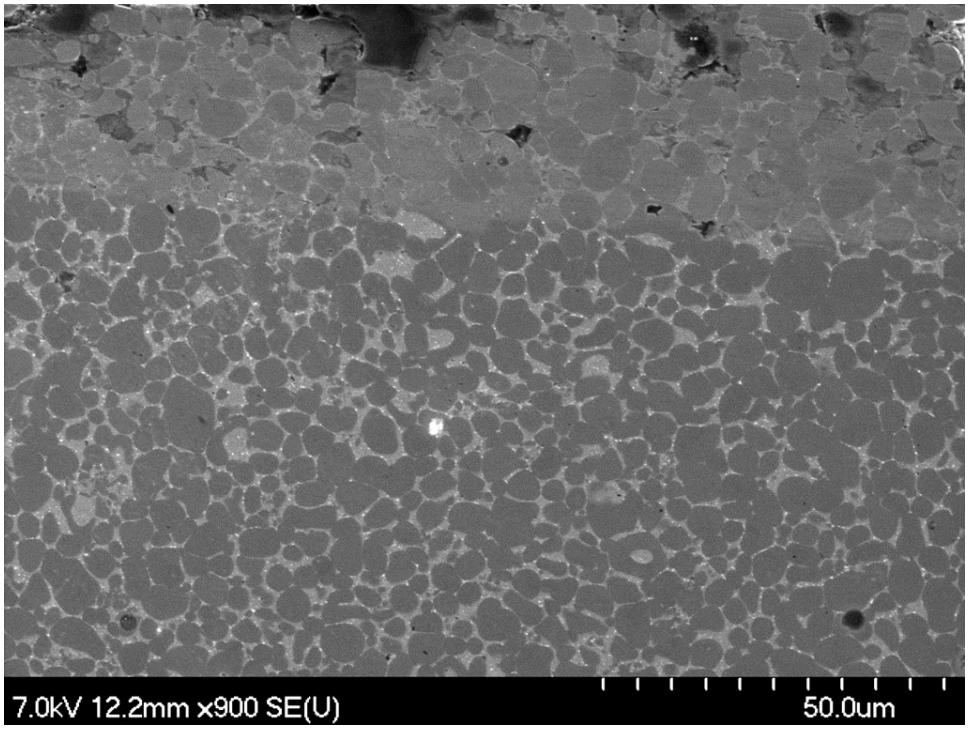

(b)

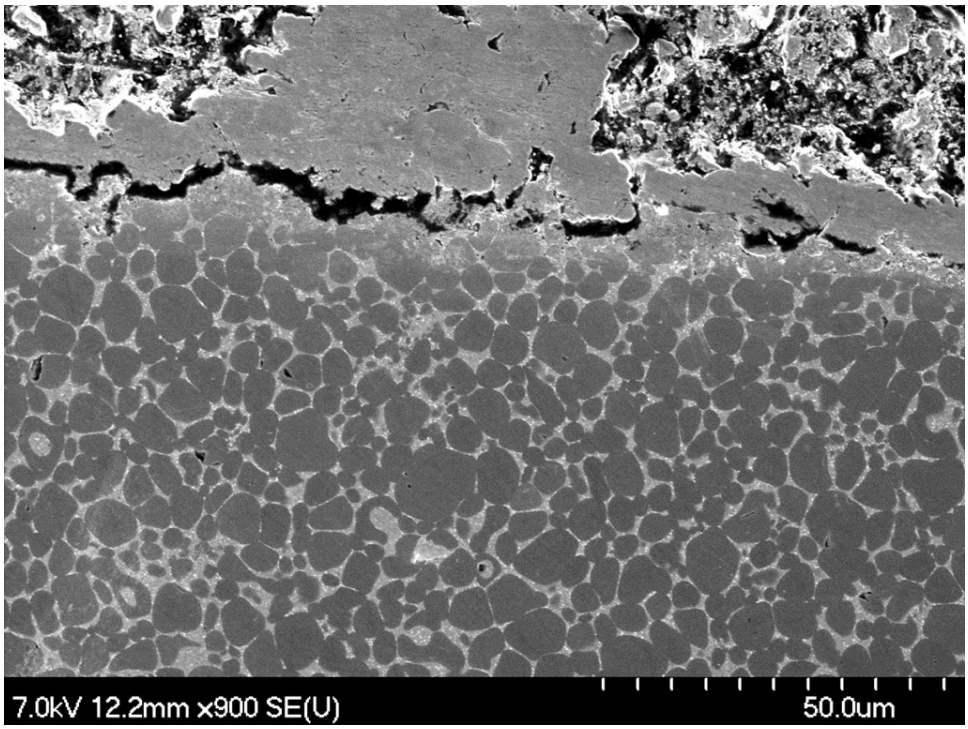

Figure 4.9: SEM images of the edge of wear tracks formed in TiC-20 vol. % 304L cermets under conditions of: (a) 40 N applied load for 15 minutes, and (b) 80 N load for 60 minutes.

However, this will eventually result in the formation of debris between the two counter faces, as TiC grains crack and fragment under the Hertzian contact load, and the steel binder is extruded out from between the TiC grains. As a consequence, there will be a transition from two- to three-body wear, with the debris acting as the third body (characterisation of the wear debris is discussed in a subsequent paragraph). This transition may be observed remotely as a change in the COF, as noted in Section 4.4.3. In the present case there is a general increase in the COF until a steady state is reached. This three-body wear response can ultimately lead to the formation of a tribolayer and a further potential transition to an adhesive wear mechanism. The tribolayer is formed through the repeated, cyclic loading, with the third body material rolled back and forward between the two primary counter faces. This ultimately results in severe attrition, and a massive refinement in the size of the third body particles (such that they eventually form a continuous film). The formation of a tribolayer, or film, is clearly apparent at the edge of the wear track at higher loads and longer test durations, as shown in Figure 4.9(b). It is also notable from this image that regions of the tribolayer are being removed during the wear test.

Figure 4.10 and 4.11 demonstrate typical DIC optical and SEM images, respectively, of the ends of the wear tracks of selected TiC-304L stainless composites.

(a)

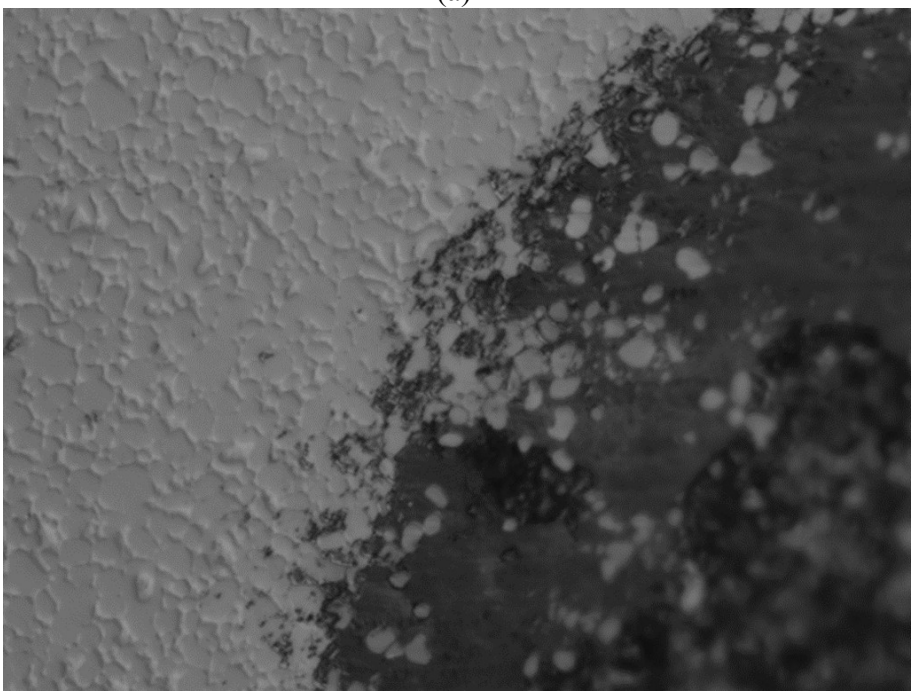

(b)

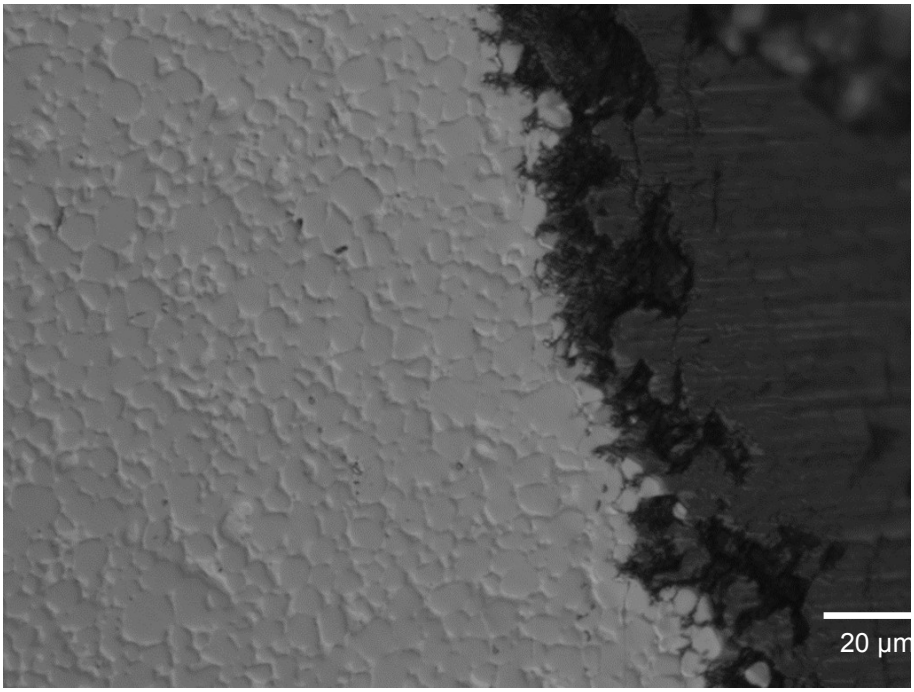

Figure 4.10: DIC optical images of the ends of wear tracks obtained for TiC with 20 vol. % 304L stainless steel, under the following sliding conditions: (a) 40 N load maintained for 15 minutes (~181 m total sliding distance) and (b) 80 N load maintained for 60 minutes (~724 m total sliding distance). The sliding direction is horizontal for both images.

(a)

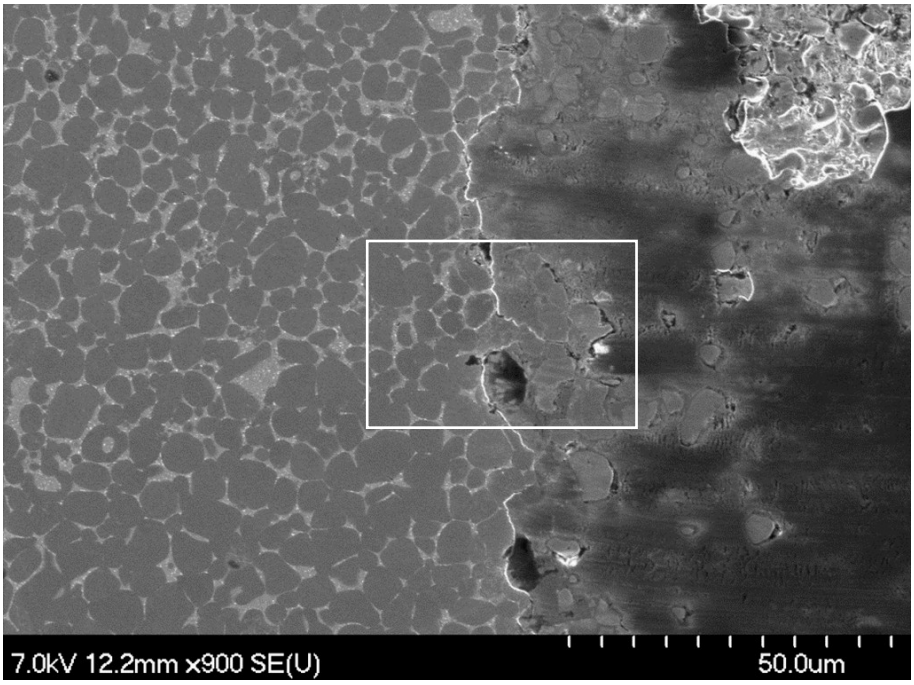

(b)

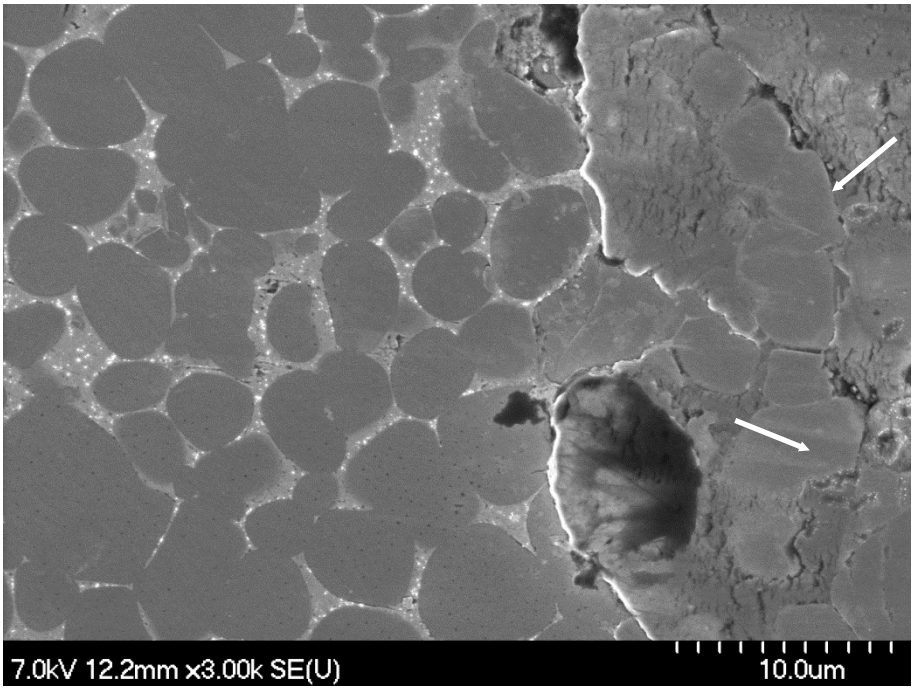

Figure 4.11: (a) SEM image of the end of a wear track in TiC-20 vol % 304L stainless steel (40 N load maintained for 30 minutes (total sliding distance ~362 m); note that the darker regions present within the tribolayer, on the left hand side of this image, arise from a charging artefact. (b) Inset region from (a), highlighting the gradual build-up of the tribolayer at the end of the wear track, together with retained TiC grains that are still largely intact (arrowed). The sliding direction is horizontal for both images.

There is also some evidence of fine laminae formation (nominally perpendicular to the sliding direction) within the tribolayer, while the end of the layer itself has been pushed slightly out of the wear track (highlighted by the higher electron yield at the very edge of the tribolayer). Significant spalling of the tribolayer is regularly evident when it is more fully developed under a higher applied load (Figure 4.12(a)), although at the very ends of the wear tracks there is invariably a relatively undamaged segment of the evolved layer (Figure 4.12(b)); the spalling in this instance appears to be associated with thicker regions of tribolayer. The brittle nature of the tribolayer is therefore clearly demonstrated.

(a)

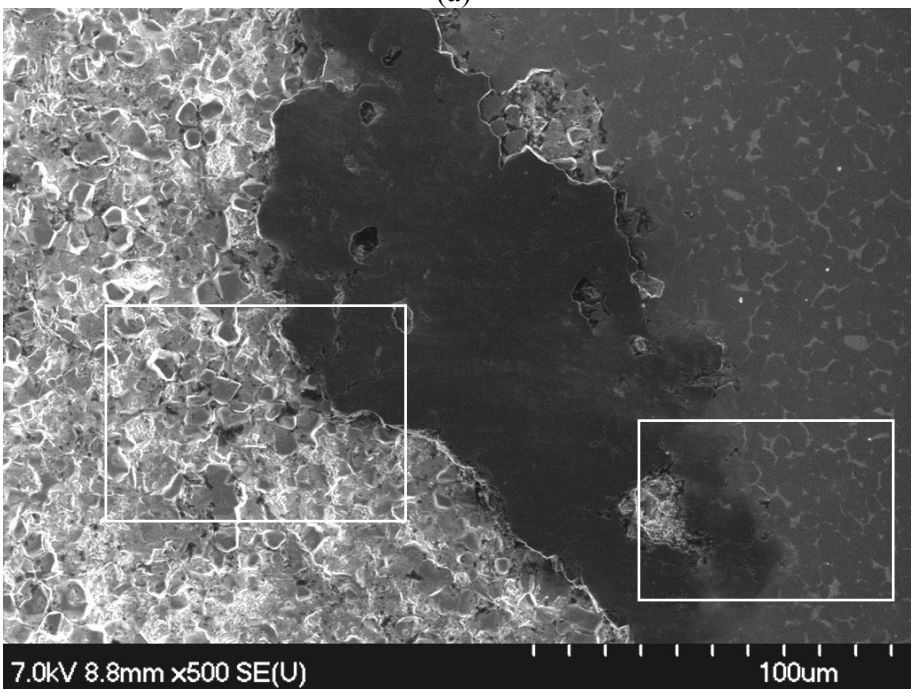

(b)

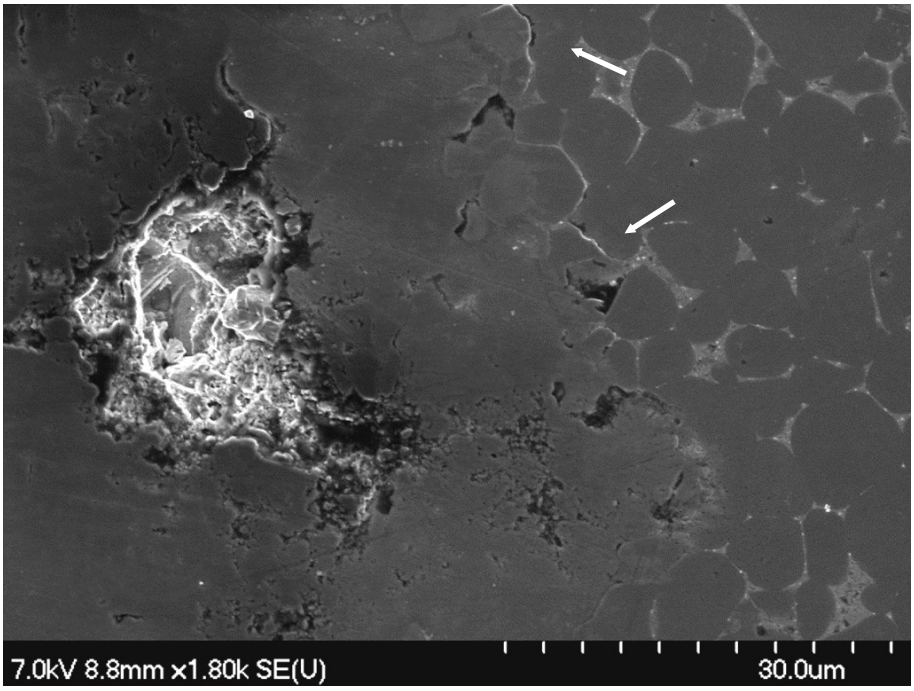

(c)

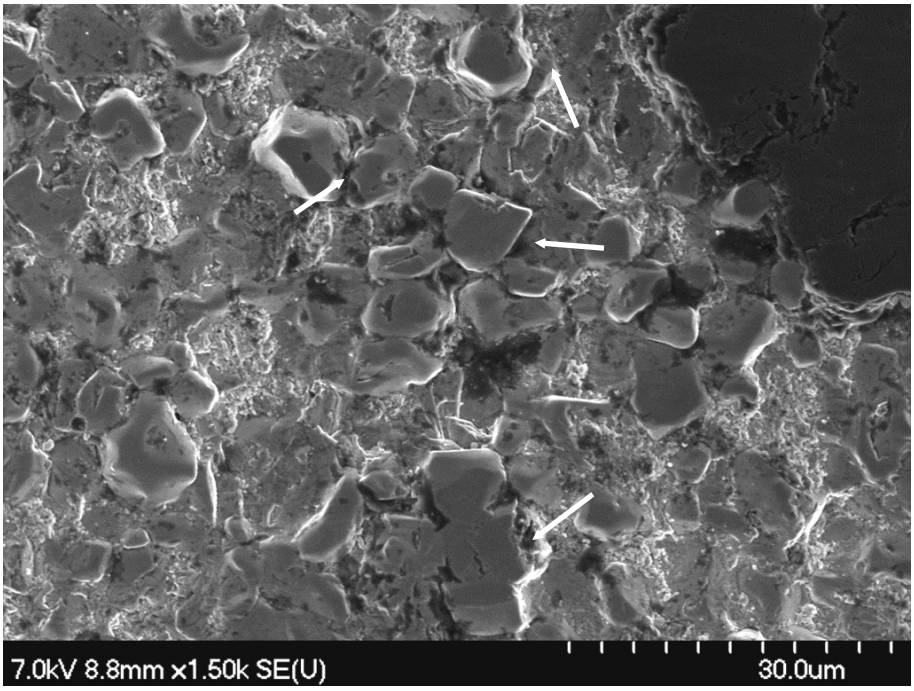

Figure 4.12: (a) SEM image of the end of a wear track in a TiC-10 vol. % 304L stainless steel cermet after testing at 80 N applied load for 15 minutes; sliding direction is horizontal for all images. (b) Inset region 1 shows the edge of the tribolayer/unworn material, highlighting a section of spalled tribolayer on the left hand side, and several small cracks between TiC grains (arrowed). (c) Inset region 2 demonstrates the removal of large areas of the tribolayer and the exposure of the underlying damaged material, including isolated TiC grains that are believed to have been at the original polished surface prior to testing (arrowed).

While there is a clear grey-level contrast between the TiC particles and the surrounding steel matrix (i.e. Figure 4.3), arising predominantly from the differing average atomic mass of the two phases, this contrast is largely lost within the tribolayer indicating an essentially uniform composition; this is discussed in more detail in the following paragraphs relating to compositional changes. There is no evidence for damage to the TiC grains just outside of the wear track at the lower loads. Conversely, at the higher load (80 N), there are regions of minor surface damage in terms of fractured TiC grains, TiC/steel debonding and even slight material 'up-lift' (Figure 4.12(b)). It is apparent from higher magnification images that the spalled regions still appear to contain evidence of the original polished TiC grains (Figure 4.12(c)), which are presumably still retained within the steel binder below the spalled region of tribolayer.

Examining the wear tracks more closely demonstrates a number of features of the damage process. Figure 4.13 highlights the gradual accumulation of finely divided material between intact TiC grains.

(a)

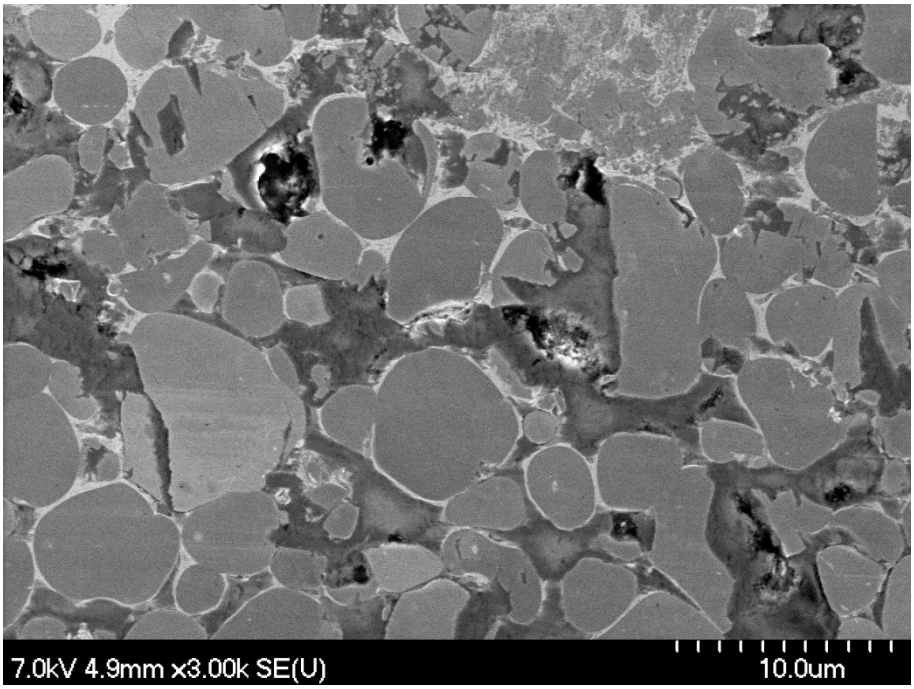

(b)

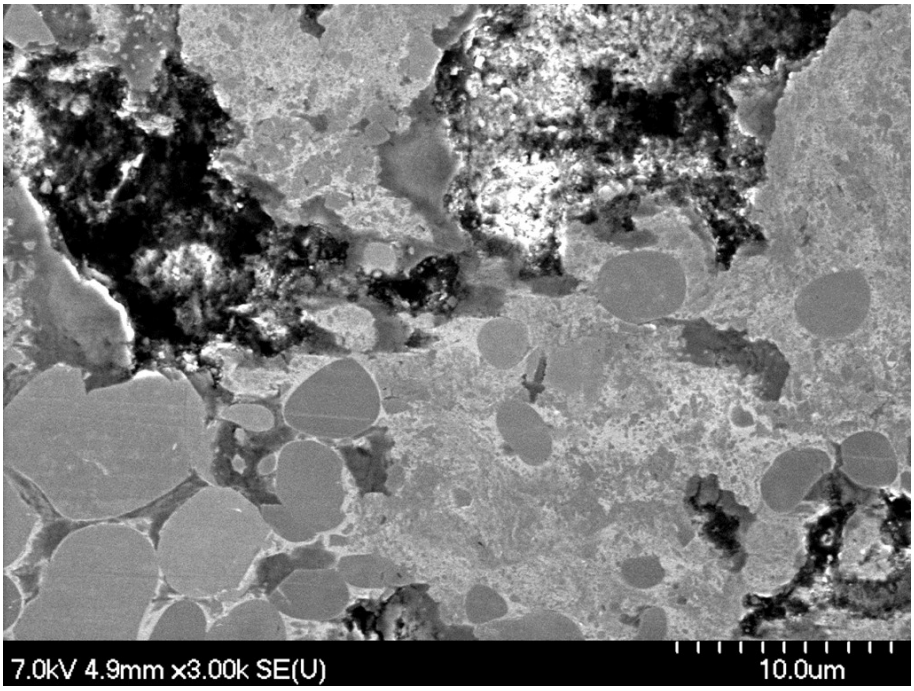

Figure 4.13: Typical SEM images of the wear track formed on the TiC-20 vol. % 304L samples after testing using a 20 N load for 2 hours duration. (a) The initial formation of a tribolayer is apparent in terms of material present between the TiC grains (dark regions), along with evidence of TiC grain fragmentation; a thin 'ring' of the steel binder is also often seen around the edges of the TiC grains. (b) Significant TiC grain fragmentation is observed in this region, in the form of fine particulate matter mixed with a secondary phase of equivalent contrast to the steel binder, which highlights the early stages of tribolayer development.

Based on the contrast levels, this appears to be fine fragments of TiC within a nominally steel matrix, and highlights the early stages of TiC grain failure. There is also evidence of more fully developed regions of tribolayer; these regions have a uniform 'dark-grey' contrast, which is potentially a charging artefact. In Figure 4.14(a) the continued build-up of the tribolayer 'structure' is apparent after testing at the lowest load (i.e. 20 N), with the formation of laminae of material forced in between adjacent TiC grains. There is also evidence of TiC grain fragmentation (Figure 4.14(b,c)), and the deposition of uniform contrast tribolayer material between the TiC grains.

(a)

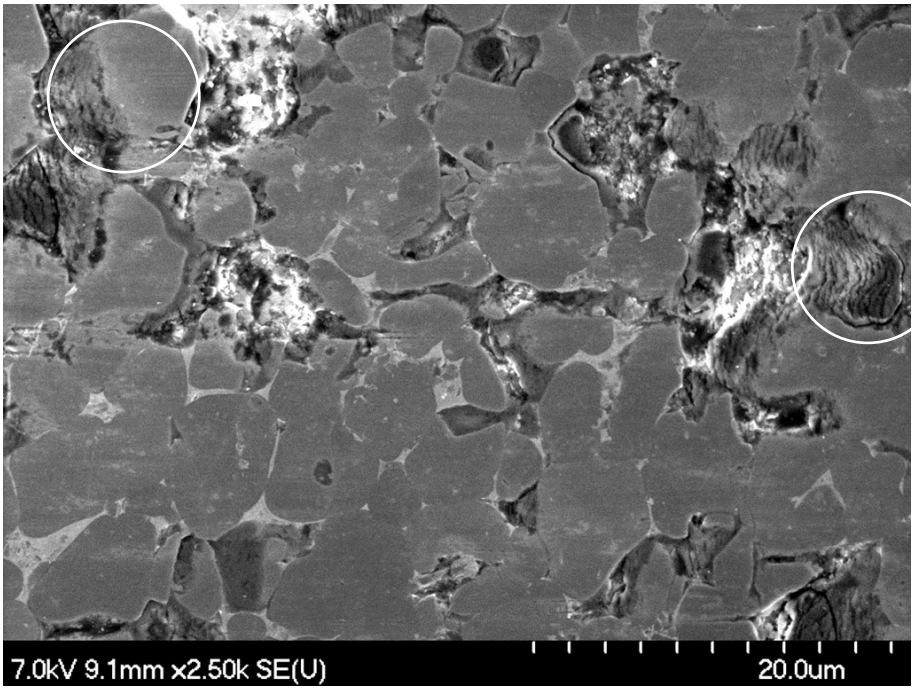

(b)

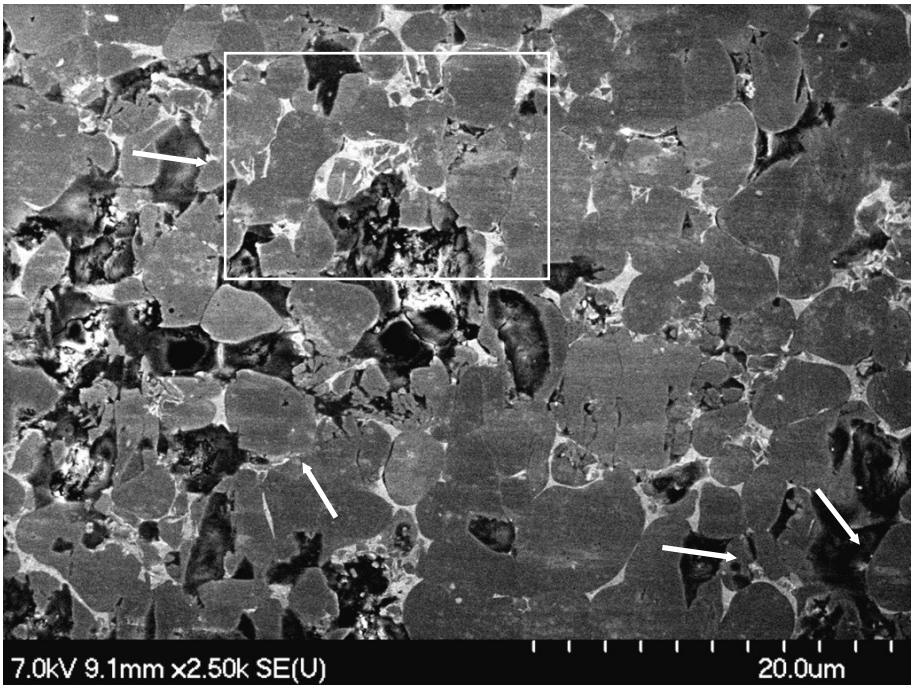

(c)

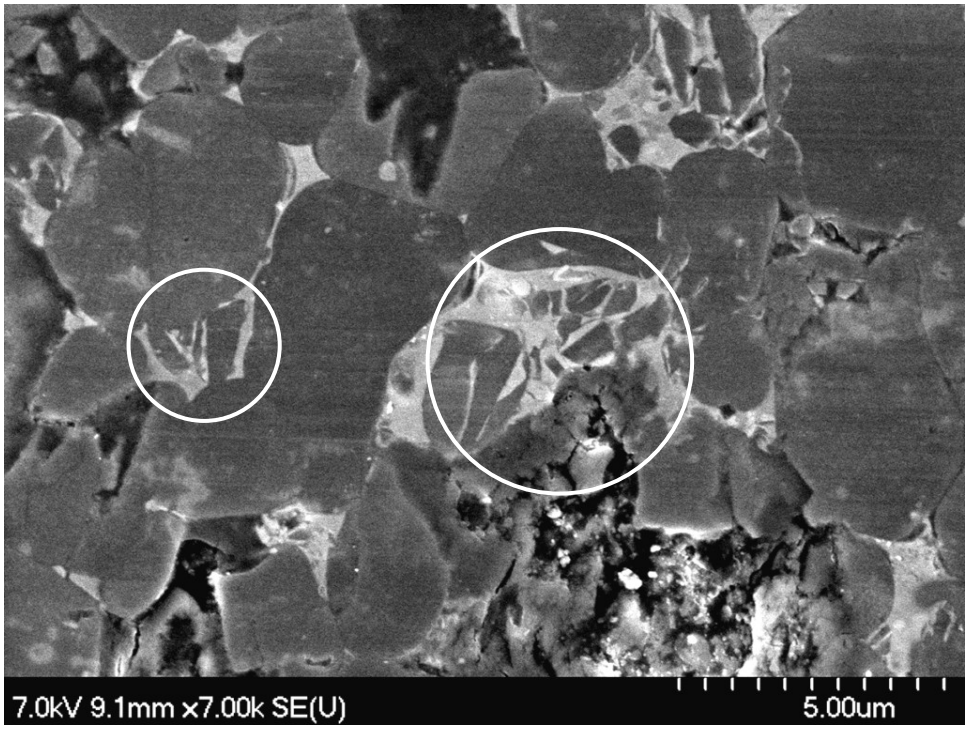

Figure 4.14: SEM images of the wear track of the TiC-10 vol. % 304L cermet after wear testing at 20 N load for 2 hours (total sliding distance ~1.45 km); sliding direction is horizontal for all images. (a) Circled areas appear to show the early stage of tribolayer formation, with a series of parallel laminae that are oriented nominally perpendicular to the sliding direction. (b) The general build-up of damaged areas within the microstructure is apparent on the left hand side of this image, which also shows some small regions of tribolayer formation (arrowed). (c) Inset region from (b) demonstrating regions of initial TiC grain fragmentation (circled).

At higher loads the tribolayer formation is more evolved, with relatively few, isolated TiC grains observed (Figure 4.15). Moderately large areas of predominantly tribolayer are now apparent, with multiple regions exhibiting spallation (Figure 4.15(a,b)). Furthermore, back-scattered electron (BSE) imaging in the SEM, which is highly sensitive to differences in average atomic mass, indicates that the surface (at a moderately low accelerating voltage of 7 kV) is nominally of a constant composition, even though the outlines of individual TiC grains are still visible (Figure 4.16). This infers that a very thin film of the tribolayer is effectively smeared across the

whole surface, and not simply built up between the TiC grains, which clearly occurs during the initial wear stages (i.e. Figure 4.13).

(a)

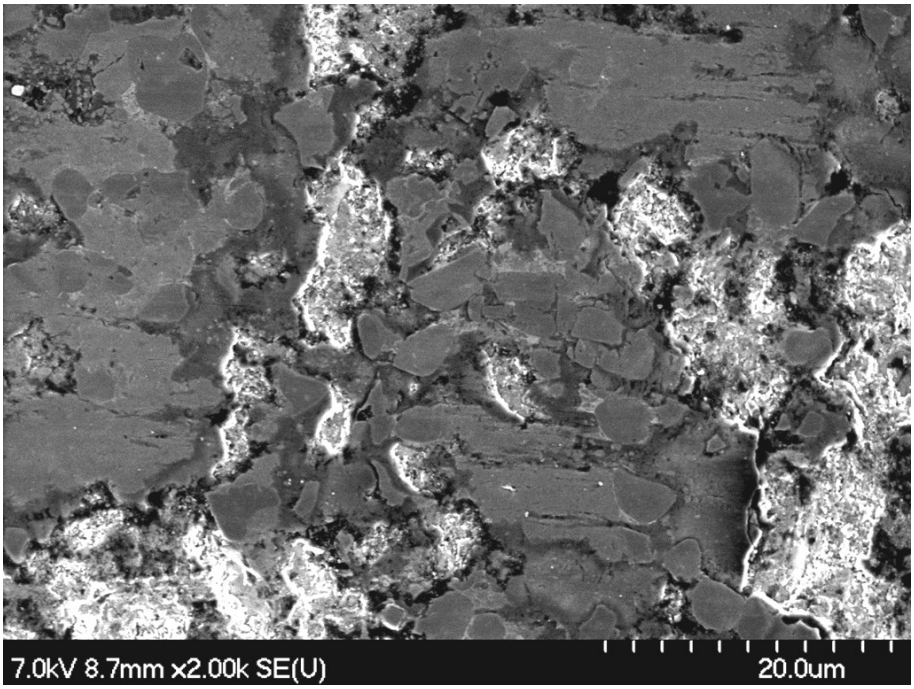

(b)

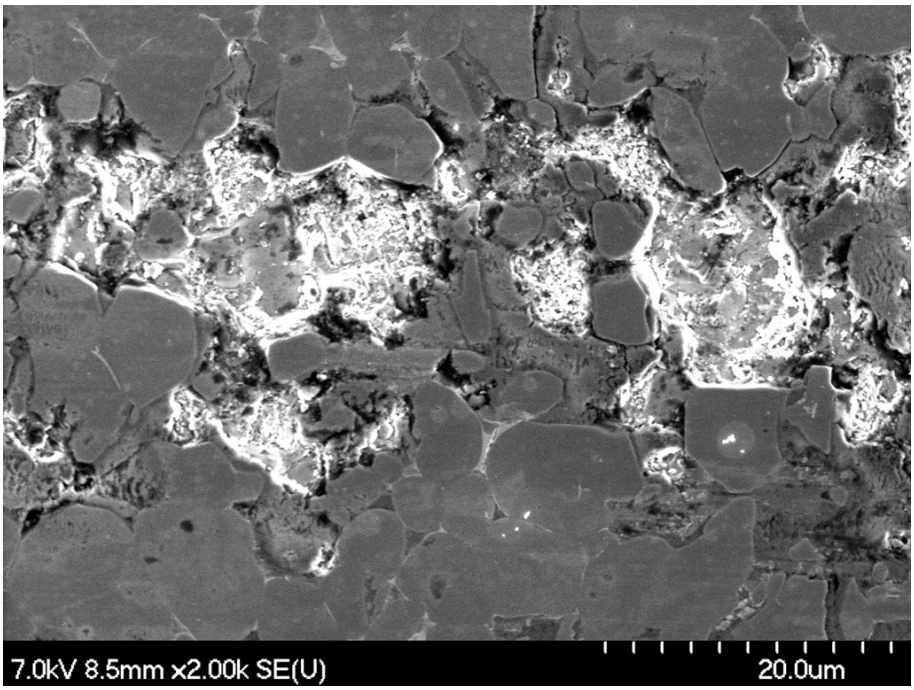

Figure 4.15: SEM images of the evolution of the wear track with increasing load and time for TiC cermets with 10 vol. % 304L stainless steel binder (in each example the sliding direction is

horizontal): (a) 40 N applied load, maintained for 15 minutes, (b) 40 N applied load maintained for 60 minutes.

(a)

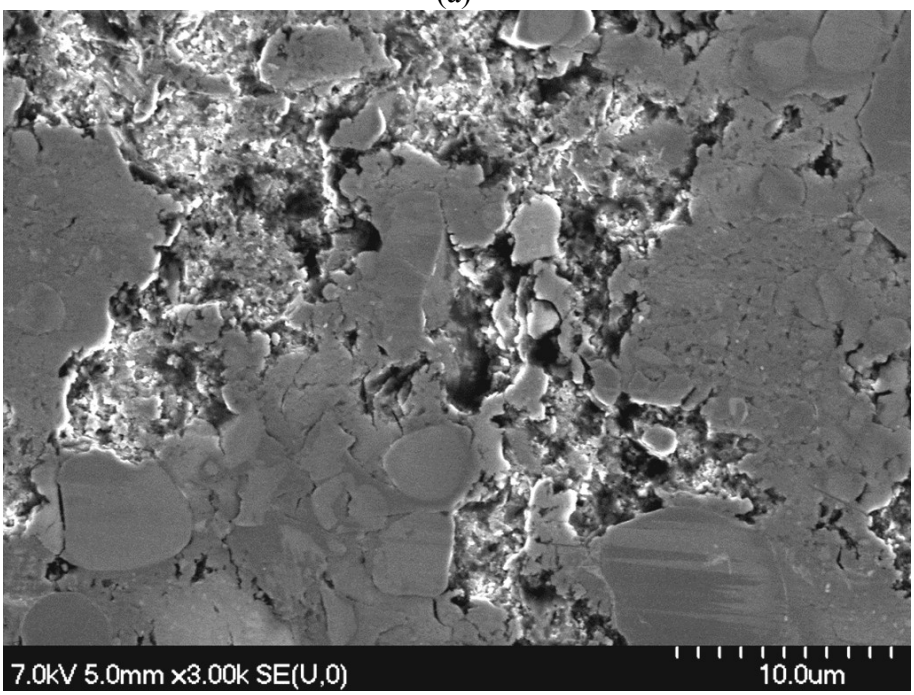

(b)

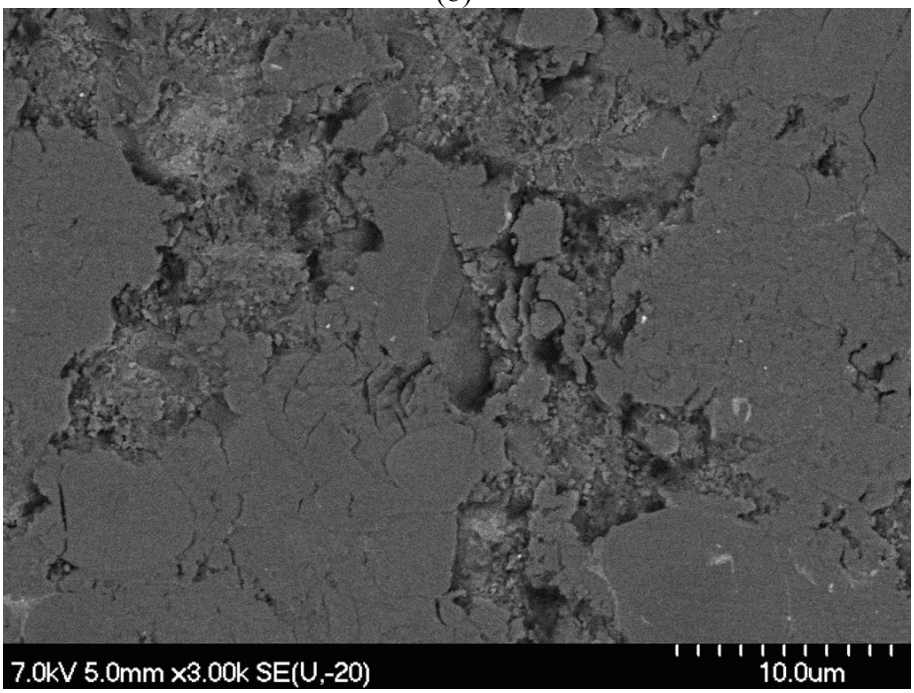

Figure 4.16: A comparison of (a) secondary electron and (b) back-scattered electron SEM images of the wear track formed in TiC-20 vol. % 304L stainless steel (80 N load for 60 minutes).

Figure 4.17: shows SEM micrographs of typical examples of the third body wear debris generated for TiC-30 vol.% 304L steel cermets, at 40 N and 80 N loads, which is ejected from the wear track and recovered for analysis. The morphology of the wear debris shows an aggregate of finer particles at the lower load, which is believed to be fragmented TiC grains, mixed with some of the steel binder; this is debris that can be expected to be formed during the three-body wear period of testing.

Qualitatively, at the higher load the debris appears to be coarser, in terms of particle size, and somewhat 'plate-like' in appearance. This transition likely marks that which occurs when adhesive wear starts to increase, with the debris particles now comprising of segments of the spalled tribolayer that are ejected during reciprocating sliding.

(a)

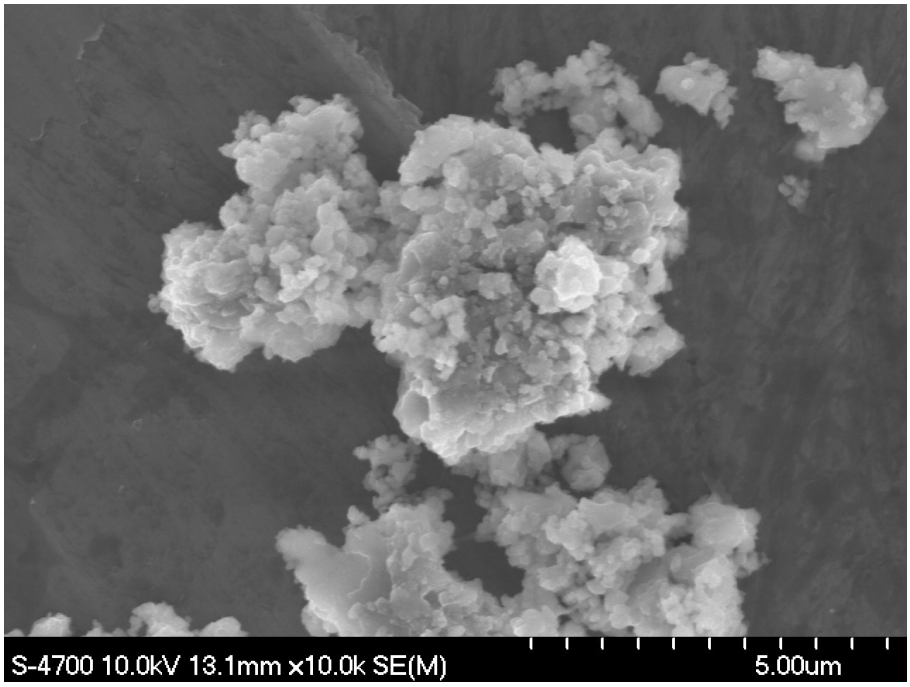

(b)

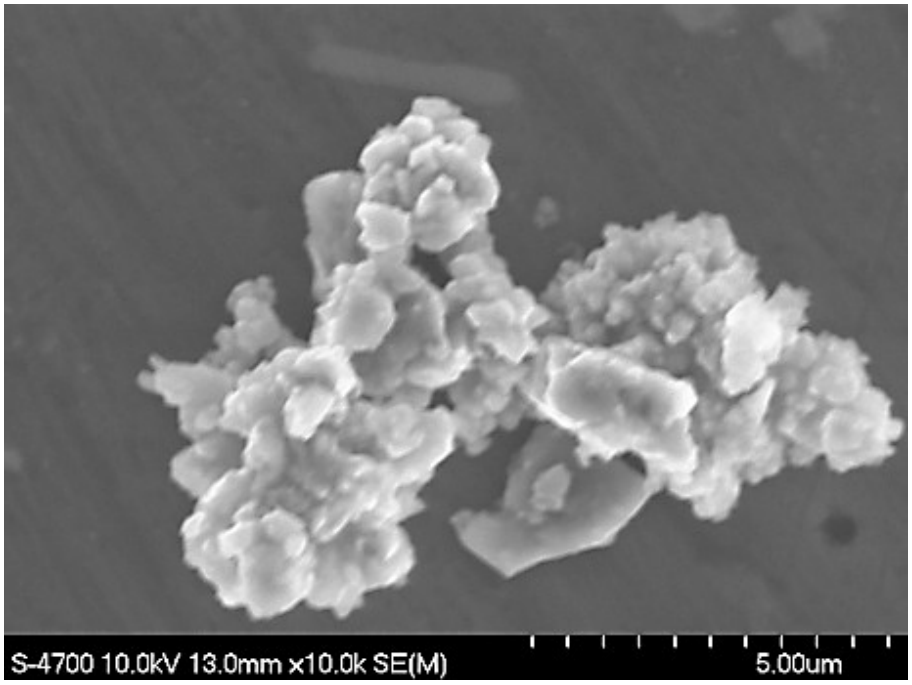

Figure 4.17: SEM images of TiC-30% 304L cermets showing wear debris generated at (a) 40N and (b) 80N load.

4.4.5 Chemical Composition of the Tribolayer

In order to investigate the wear mechanisms in more detail, compositional analysis of the samples was also performed in the SEM using EDS. Figure 4.18 shows the EDS image and selected elemental maps taken from within the wear track of the TiC-20 vol. % 304L cermets, tested at an applied load of 60N. Within the examined region a sizeable portion of the wear track is covered with a tribolayer. The chemical composition, as presented in Table 4.2, confirms that a major component within the tribolayer is O (up to 50 at. % in this region). This can be expected to be mostly in the form of oxides associated with components from the steel binder (i.e. Fe, Cr, Ni and Mo), together with Ti from the TiC, and trace amounts of W from the WC-6Co counter face sphere. It is not clear why the C content is as high as shown, as it can be expected that increasing O incorporation would reduce the C content.

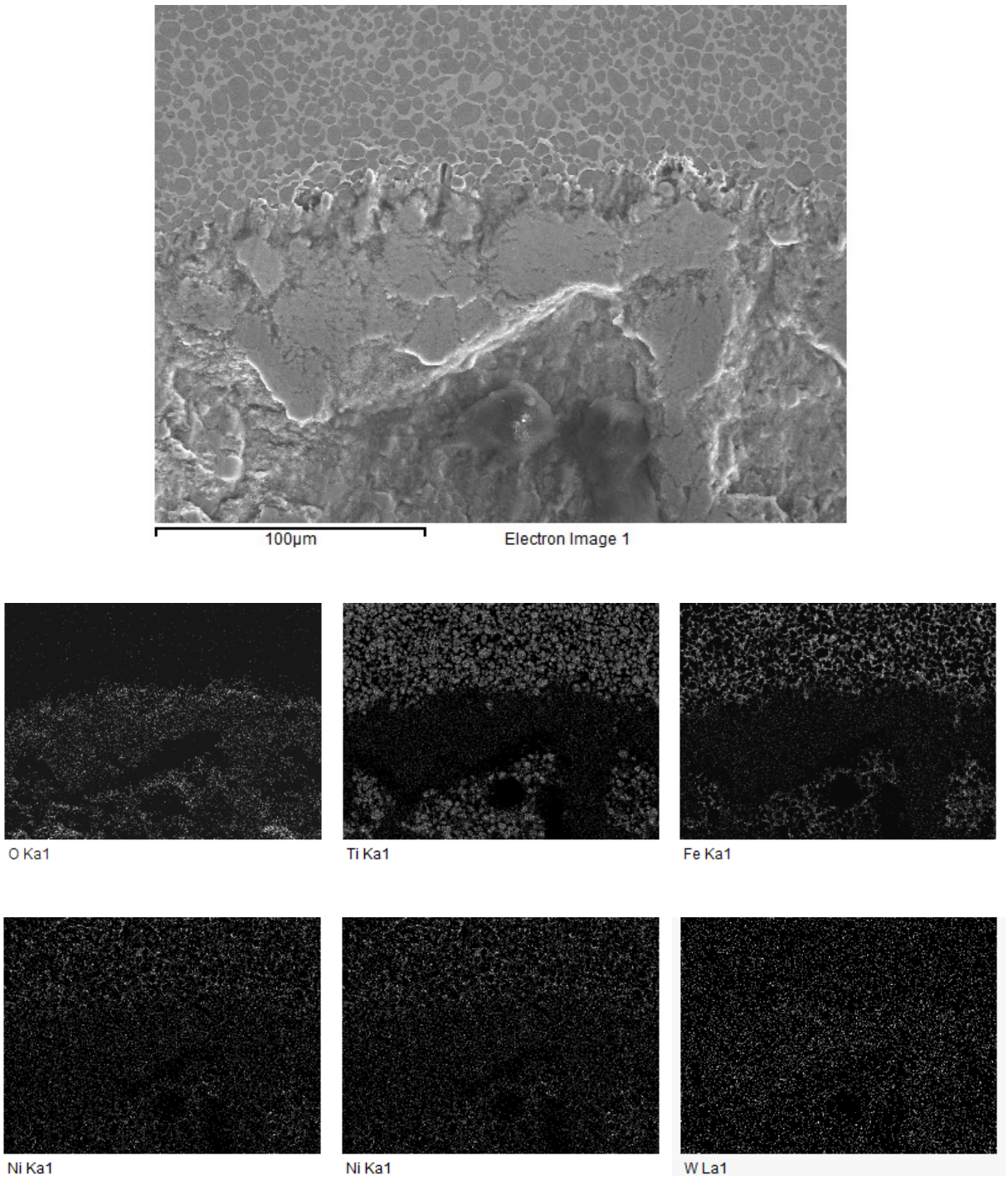

Figure 4.18: EDS mapping of the TiC-30% 304L cermet following wear testing (80N applied load for 120 minutes), showing the build-up of oxide containing tribolayer at the edge of the wear track, and the absence of any significant O beyond the periphery of the track.

Table 4.2: An example of the tribolayer composition determined using EDS, for TiC-30 vol. % 304L, after dry sliding for 120 minutes under an 80 N load.

Element (KLM line)	Weight %	Atomic %
C (K)	8.61	19.08
O (K)	30.23	50.30
Ti (K)	41.02	22.80
Cr (K)	2.65	1.36
Fe (L)	10.56	5.04
Ni (L)	1.36	0.62
Mo (L)	0.09	0.03
W (M)	5.48	0.79

As a consequence, it is believed that the apparently high C content may be a minor contamination artefact from analysis within the SEM, in combination with the presence of the underlying TiC-based cermet (based on the apparent low thickness of the tribolayer). As noted previously, the tribolayer forms through mechanical attrition of the third body material, which is continuously fractured into smaller fragments during dry sliding, and therefore the constant creation of fresh surfaces results in increasing (passive) O incorporation onto the new surface material that is created. Thermal oxidation is not believed to play a major role in this response, based on the temperatures measured during testing of comparable TiC-based materials, where the maximum reached was ~100°C during testing at a 60 N applied load, which is generally typical of that observed during sliding wear of a number of cermet systems [133].

The formation of a tribolayer is also apparent on the WC-6Co counter face sphere from SEM observation, as shown in Figure 4.19. In this instance, a semi-continuous tribolayer is present, which has slightly spalled away from the underlying WC-6Co substrate material. EDS analysis again confirms a high O content, as well as Ti, Fe and C, with Ti and Fe clearly transferred from the TiC-304L cermet.

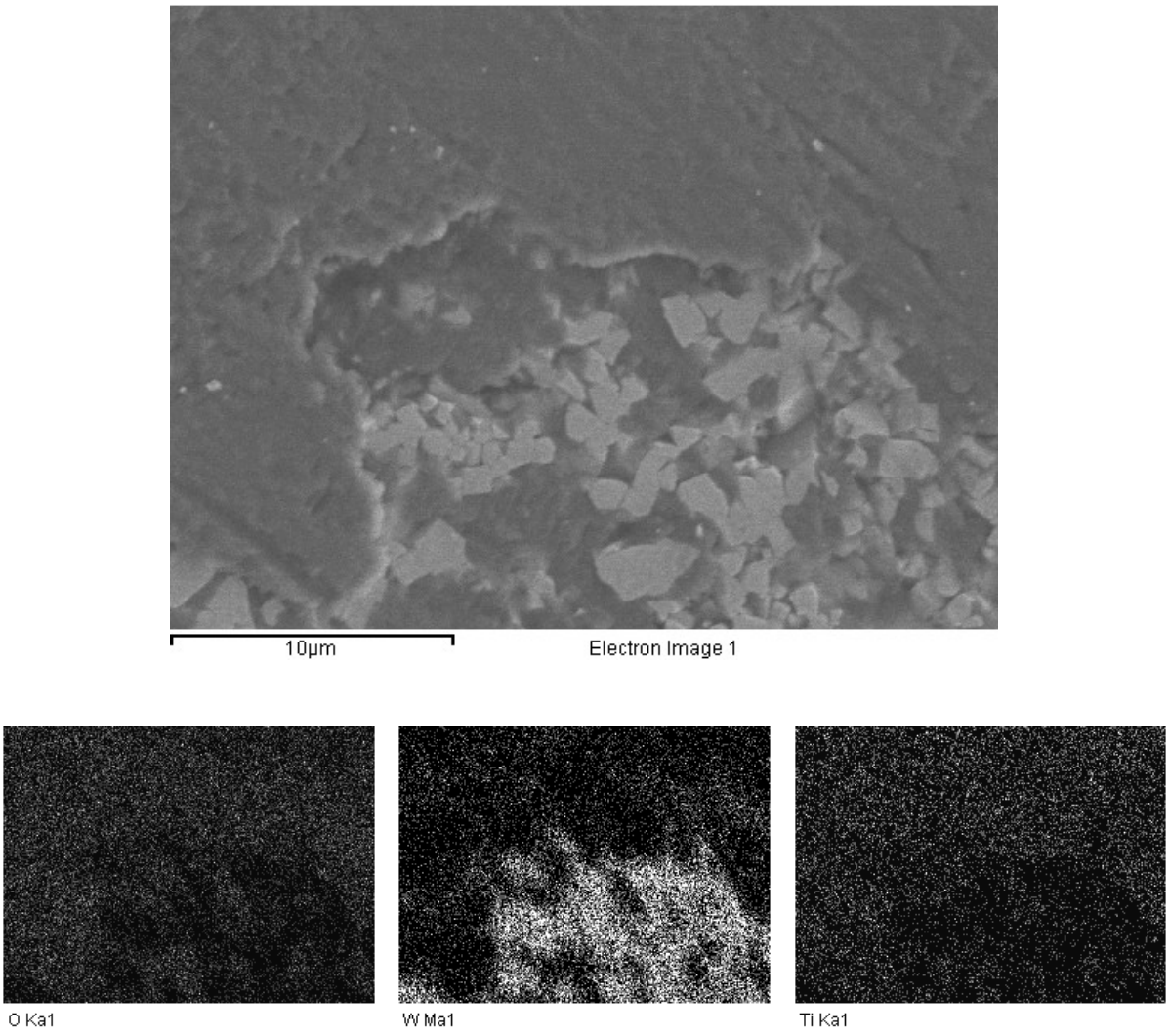

Figure 4.19: EDS mapping of a WC-Co counter face sphere following wear testing, showing the transfer of tribolayer onto WC-Co surface. Spalling of the tribolayer is also apparent, revealing the underlying WC-Co.

The observations gained from both the wear measurements and microscopy characterisation points towards a relatively complex wear response in the present materials. Initially, it is proposed that a two-body abrasive wear scenario arises, with the WC-6Co sphere ploughing the surface of the TiC cermet. However, it is also clear that this quickly transitions to a predominantly three-body abrasive wear mechanism, through binder removal (i.e. extrusion) and TiC grain fragmentation. Eventually there is an associated adhesive component, as evidenced through the formation of a tribolayer. The wear resistance also decreases with an increase in the

steel content, where these mechanisms can be exacerbated. These general observations are in line with prior studies of TiC-based cermets [68, 127, 128], as well as related WC-Co materials [136].

4.5 Conclusions

In the present study, a family of novel TiC-304L stainless steel composites have been developed. These cermets have been evaluated for their hardness and indentation fracture resistance, and for their dry sliding behaviour under reciprocating motion. The following conclusions can be drawn from the experimental study:

(1) Melt infiltration allows for the formation of TiC-304L cermets with high density (>99 % of theoretical), and relatively fine grain size (~6 μm), even when low steel contents are used (i.e. 5 vol. %).

(2) The cermets exhibit high hardness, which increases with TiC content, exhibiting a maximum value in excess of ~2,500 (HV1) with just 5 vol. % steel binder content. In comparison, the indentation fracture resistance of the composites increases with the steel content. Measurement of the c:a ratio from the indents indicates that a transition from a median cracking response to a Palmqvist cracking response occurs between 10 and 15 vol. % steel content.

(3) It was observed that the COF increases slightly during the initial segment of the reciprocating wear tests, when testing at 40 N and above, and typically achieves a steady state value after approximately 60 minutes. At the lowest load (20 N), the COF was generally consistent throughout the test duration. The coefficient of friction increases with binder content, which is attributed to an increasing contact area of the soft 304L steel phase at the tribo-pair interface.

(3) The wear resistance of the cermets increases with increase in the harder TiC phase. In this instance, increasing the TiC content from 70 to 90 vol. % decreases the specific wear rate by approximately a factor of two. The volumetric wear of the cermets varied approximately linearly with time, as predicted by the Lancaster wear equation.

(5) The specific wear rates were typically in the range of 10^{-7} to 10^{-6} mm^3/Nm, depending on both the cermet composition (i.e. 304L content) and applied load. These values were generally

comparable with data presented for other TiC- and WC-based cermets found in the open literature.

(6) Based on the microstructural observations, the overall wear mechanisms observed in essentially all examined conditions is initially two-body abrasive wear, which transitions to a combination of three-body abrasive wear and adhesive/tribo-chemical wear, with the latter evidenced through the formation of tribolayers on both the cermet and the WC-6Co counter face.

(7) The formation of the tribolayer appears to increase with applied load, and to a lesser extent increasing binder content, and generally exhibited a high O content. This was due to high levels of mechanical attrition of the third body particles during reciprocating wear, such that new surfaces are continuously being created as the particle size is refined.

4.6 Acknowledgements

This study was financially supported by Petroleum Research Atlantic Canada (PRAC) and the Natural Sciences and Engineering Research Council of Canada (NSERC). The Canada Foundation for Innovation, the Atlantic Innovation Fund, and other partners who helped fund the Facilities for Materials Characterisation, managed by the Dalhousie University Institute for Materials Research, are also gratefully acknowledged. The authors would also like to thank Dean Grijm and Patricia Scallion for technical assistance.

5 The Effects of Grain Size on the Reciprocating Wear Behaviour of TiC-316L Stainless Steel Cermets

Chukwuma C. Onuoha, Georges J. Kipouros, Zoheir N. Farhat and Kevin P. Plucknett*

Dalhousie University, 1360 Barrington Street, Materials Engineering Program, Department of Process Engineering and Applied Science, B3H 4R2, Nova Scotia, Canada

Status: To be submitted to Wear

5.1 ABSTRACT

TiC-based cermets are used in a variety of applications that require a combination of good wear and corrosion resistance. In the current work, TiC-stainless steel (grade 316L) cermets have been developed, with the TiC grain size varied through heat-treatment for steel binder contents between 10 and 30 vol. %. Microstructural analysis showed mean TiC grain sizes of approximately 4 and 11 μm, respectively, for fine- and coarse-grained cermets, with the grain size nominally consistent as a function of binder content. The wear resistance was assessed in a reciprocating motion, using a WC-Co sphere dry sliding on the polished cermet surface. It is demonstrated that the fine-grained cermets exhibit better wear resistance and hardness, while the coarse-grained equivalents have superior indentation fracture resistance. An increase in the specific wear rate was observed with increasing load and/or binder content for both fine- and coarse-grained cermets. A transition from two- to three-body abrasive wear was apparent, together with the formation of a surface tribolayer, which highlights a transition to an adhesive wear mechanism. The tribolayer showed incorporation of a high concentration of O, which increased with the applied load, together with a predominance of the binder constituents.

Keywords: Cermets; abrasive wear; adhesive wear; tribolayer; dry sliding; scanning electron microscopy

*Contact author email: Kevin.plucknett@dal.ca

5.2 Introduction

Ceramic-metal composites, or cermets, are used in a broad variety of industries, including chemical processing, aerospace, automotive, pulp and paper, oil and gas, etc. Cermets can posses a unique combination of high wear resistance, high hardness, and good strength characteristics, as well as excellent aqueous corrosion resistance. In particular, titanium carbide (TiC) based cermets show considerable potential for substitution into applications where tungsten carbide-cobalt (WC-Co) based materials are more commonly used [54, 67, 68]. TiC-based cermets benefit significantly from reduced mass and better high temperature properties, in comparison to WC-Co. The excellent combination of high hardness, strength and fracture toughness, together with good wear and corrosion resistance, is achieved through the incorporation of a ductile metallic phase with hard ceramic phase (i.e. TiC). Although the ductile phase toughness results in a drop in the hardness values of the composites [33], the improvement in toughness and wear resistance significantly outweighs the decrease. It is generally assumed that the wear behaviour of cermets is a direct function of both the hardness and toughness of the composite, and that optimum wear behaviour is obtained when both of these properties are fully maximised [33, 54].

In terms of specific TiC-based cermet systems, a wide variety of metallic binders have been employed. However, only limited attention has been paid to steel variants, particularly stainless steels. For example, 316 stainless steel has excellent corrosion resistance with good mechanical (i.e. tensile) properties. However, the wear resistance is relatively poor as the steel has a low hardness [137], and 316 is therefore susceptible to many common forms of wear and contact damage, which limits use in tribological applications [59, 137-138]. In order to enhance the wear resistance of stainless steels, several authors have reported an improvement of wear resistance through the incorporation of carbide particles [30, 139-141], such as TiC, to form a metal matrix composite (MMC).

Although the incorporation of carbides into stainless steel improves the wear resistance, altering the microstructural properties of the TiC or steel binder is an additional technique to further improve the wear resistance in the case of TiC-based cermets. The cermet microstructure plays a crucial role in their overall mechanical properties, and the microstructural features that influence the mechanical and tribological properties include the metal binder content, the average carbide grain size, the binder mean free path (i.e. the thickness of the binder ligaments) and the

contiguity of the carbide grains [71]. Decreasing either the binder content or the carbide grain size typically increases the hardness of the cermet; an increase in hardness is invariably accompanied by a decrease in the bulk fracture toughness in conventional materials [142-147]. For instance, it has been shown that carbide size influences the abrasive and erosive wear rate and, when comparing an equivalent carbide volume fraction of fine- and coarse-grained particles, cermets prepared with fine-grained carbide particles provide superior wear resistance, as the binder mean free path is decreased [30, 54,141, 148, 149].

To date, studies of the effects of grain size on the wear behaviour of cermets have largely been limited to WC-Co [11, 71-77, 80, 81, 150, 151]. Some of these investigations have reported an improvement in hardness and wear resistance with a decrease of the carbide grain size and Co binder content, while the fracture toughness invariably shows the opposite trend [71, 72, 76, 77]. If the carbide size is decreased for a fixed binder content, the binder mean free path is also reduced, resulting in greater constraint against deformation, increased hardness and a reduced tendency for binder phase extrusion. These features invariably result in an improvement in the wear resistance. Conversely, an improvement in fracture toughness with an increase in carbide grain size or binder mean free path is attributed to a decrease in the constraint that limits plastic deformation of the metallic binder ahead of the propagating crack [71, 80, 150].

In order to devise an alternative route to further improve the wear performance of novel TiC-316L steel based cermets, which could potentially be used as an erosion and corrosion resistant facing (especially in the mining and/or oil and gas industry), the present study is aimed at investigating the effects of grain size on the dry reciprocating wear behaviour of both fine- and coarse-grained cermets. Melt infiltration has been employed to fabricate these materials, with processing conditions varied to control the grain size, and the stainless steel binder content varied from 10 to 30 vol. %.

5.3 Experimental Procedure

5.3.1 Sample Preparation

The TiC powder was sourced from Pacific Particulate Materials Ltd. (Vancouver, BC, Canada), with a mean particle size of ~1.25 μm [96]. For the metallic binder, 316L stainless steel powder was obtained from Alfa Aeser (Ward Hill, MA, USA), with a nominal particle size of -100 mesh. The cermets were fabricated using a simple melt infiltration process. Disk-shaped TiC pellets (approximately 31.75 mm diameter by 4 mm thick) were prepared by uniaxial pressing, and were then vacuum bagged and further compacted by cold isostatic pressing at 220 MPa. Following compaction, the TiC pellets were weighed and a pre-determined amount of 316L stainless steel was placed on top of the TiC perform; this approach allows control the steel binder volume fraction .For sintering, the TiC preforms and steel powder were placed on a layer of bubble alumina, itself within a closed alumina crucible.

Two different vacuum heat-treatment cycles were developed in order to produce the cermets with what are subsequently referred to as either a fine- or coarse-grained microstructure; for fine-grained cermets melt infiltration was performed at 1475°C for 15 minutes, while for the coarse-grained materials it was performed at 1550°C for 240 minutes. In both cases the 316L steel content was varied between 10 and 30 vol. %. The melt-infiltration cycle was performed under a dynamic vacuum (better than 20 milliTorr), inside a graphite resistance furnace (Materials Research Furnaces, Suncook, NH, USA). The nominal heating and cooling rates were 10°C/min and 25°C/min, respectively.

5.3.2 Materials Characterisation Procedure

Following melt-infiltration, the densities of the TiC-316L cermet were determined using the Archimedes immersion method in water. Samples were then ground flat, using a 149 μm grit diamond peripheral wheel, and subsequently ground and polished for further testing (starting with a 125 μm diamond pad and finishing with 0.25 μm diamond paste). Microstructural characterisation was performed using optical microscopy (Model BX-51, Olympus Canada, Richmond Hill, Ontario, Canada) and scanning electron microscopy (SEM; Model S-4700, Hitachi High Technologies, Tokyo, Japan). Chemical analysis in the SEM was conducted using

energy dispersive X-ray spectroscopy (EDS; Model X-Max/Inca, Oxford Instruments, Concord, MA, USA). The TiC grain size, d_c, was determined using the linear intercept method [125], from digital SEM images, with ~300 grains measured for each compositional/grain size variant. In addition, the contiguity and the binder mean free path length (or binder intercept distance) were measured for each material. The contiguity, C, is a measure of the ratio of carbide-carbide to carbide-binder interfaces, and was determined following [152]:

$$C = \frac{2N_{c/c}}{2N_{c/c} + N_{c/b}} \qquad \text{Equation 5.1}$$

where $N_{c/c}$ and $N_{c/b}$ are the number of carbide/carbide (TiC/TiC) and carbide/binder (TiC/316L) interfaces that are intercepted per unit length, respectively. Based on the contiguity information, the binder ligament size or mean free path (d_b) can be determined, following the relation [153]

$$d_b = \frac{1}{1-C}\left(\frac{V_b}{V_c}\right)d_c \qquad \text{Equation 5.2}$$

where V_b and V_c are the respective volume fractions of 316L binder and TiC.

The hardness and indentation fracture resistance (IFR) of the densified cermets were determined using Vickers indentation (Model V-100A, Leco Corporation, St. Joseph, MI, USA). A 1 kg load was used for hardness measurements, in order to avoid sample cracking at the corners of the indentation during loading. Conversely, a 50 kg was applied for IFR measurements, specifically to induce crack formation. The IFR was determined for both median and Palmqvist-type crack models, using the approaches proposed by Antis and colleagues [98] and Niihara [99], respectively. For the present study the median/Palmqvist transition is simply predicted based on the measured c:a ratio following indentation (with c the indentation crack length and a the indent diagonal length) [100]. In order to ensure reasonable statistical validity, a minimum of 6 indentations were made for both hardness and indentation fracture resistance.

5.3.3 Reciprocating Wear Test Procedure and Characterisation

The reciprocating wear response of both the fine- and coarse-grained cermets was analysed for 316L steel binder contents of 10, 20 and 30 vol. %. Wear tests were performed using a universal micro tribometer (UMT; Model UMT-1, Bruker Corp., Campbell, CA, USA), with a 6.35 mm diameter WC-Co sphere (Grade 25 with 6 wt. % Co (subsequently referred to as WC-6Co); McMaster-Carr, Aurora, OH, USA) sliding against a flat test sample in a reciprocating motion. A stroke length of 5.03 mm was used, at an oscillation frequency of 20 Hz, for 2 hours and applied loads. Further details regarding the wear testing procedure are outlined in previous publications [55] [127-128]. Wear testing was performed at room temperature (21 ± 2ºC), with a relative humidity of 40-55%. Applied loads of 20 to 80 N were used for the reciprocating tests, held for a period of two hours. The resultant wear tracks were examined using an optical profilometer (Model PS50 Optical Profilometer, Nanovea, Irvine, CA), to assess both general features of the wear track and also to quantify the volume of material removed. Based on the volumetric wear loss, the specific wear rate, k, of the cermet was then determined following the basic Lancaster relationship [102].

$$k = \frac{V}{PD}$$

where V is the volume of material removed (in mm^3), P is the applied load (in N), and D is the total sliding distance (in m). The microstructural features of the wear tracks and the associated wear debris, together with the WC-6Co counter face sphere, were subsequently examined using SEM and EDS.

5.4 Results and Discussion

5.4.1 Characterisation of the As-Fabricated Cermets

Typical microstructural SEM images of the fine and coarse-grained TiC-316L cermets are shown in Figure 5.1. The microstructure for both the fine- and coarse-grained variants is characteristically uniform, with no evidence for abnormal growth of the TiC grains. The homogenous distribution of the TiC particles within the steel binder ensures isotropic mechanical properties and uniform distribution of stresses in the sintered cermets [54].

The mean grain sizes of both the fine- and coarse-grained cermets are presented in Table 5.1. It can be seen that the mean grain size is largely independent of binder content, with a slight decrease consistently noted at higher binder content.

(a)

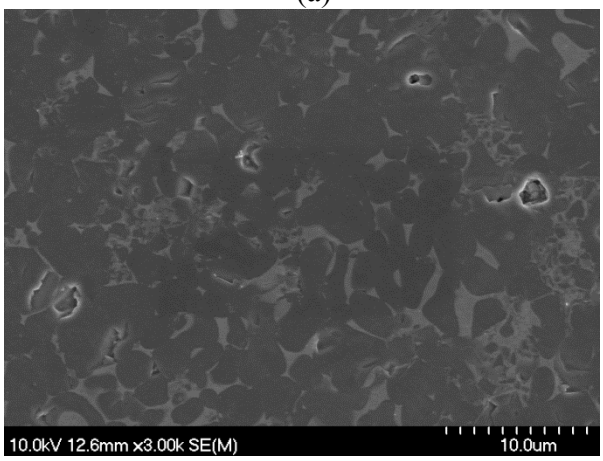

(b)

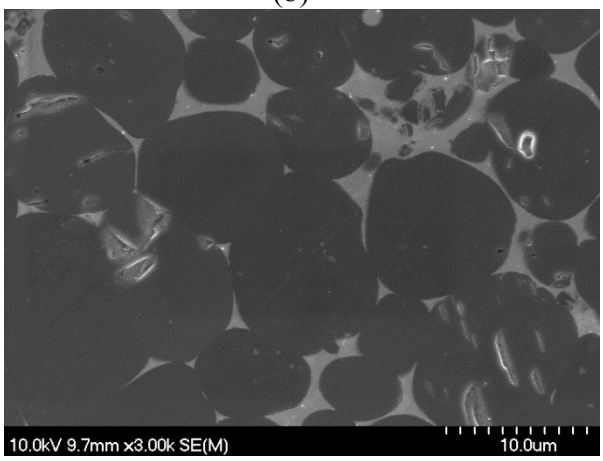

(c)

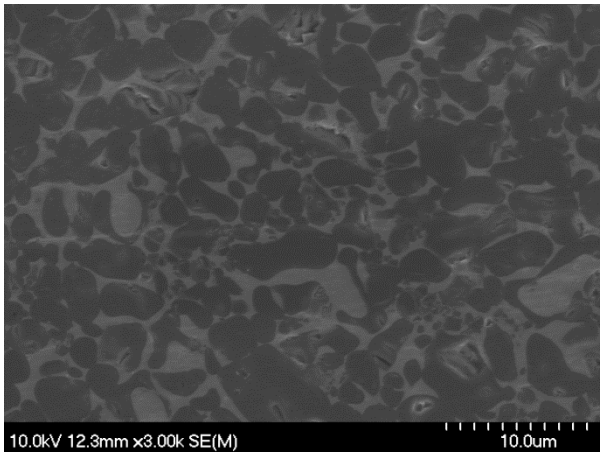

(d)

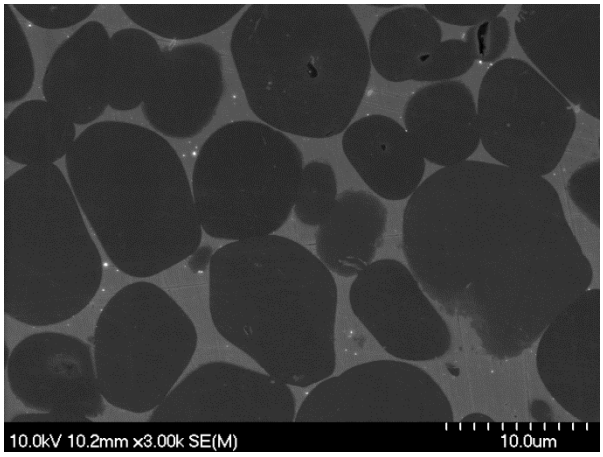

(e) (f)

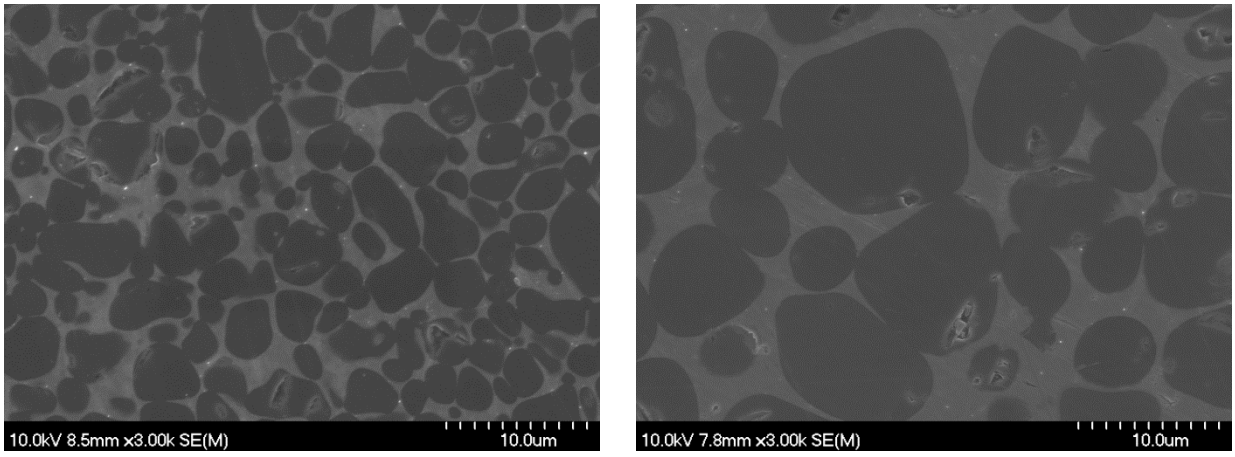

Figure 5.1: Representative SEM images of fine (a,c,e) and coarse (b,d,f) grained TiC-316L cermets prepared with: (a,b) 10 vol. % 316L, (c,d) 20 vol. % 316L, and (e,f) 30 vol. % 316L binder.

Table 5.1: The mean grain size for fine and coarse grained TiC-316L cermets as a function of steel content; values were determined for a minimum of 300 grains, using the lineal intercept method [125].

Steel binder content (vol%)	Mean grain size (µm)	
	Fine-grained	Coarse-grained
30	3.63	10.40
20	3.57	10.47
10	4.03	10.87

This behaviour is broadly similar to observations noted in prior studies on other TiC-based cermet systems, and could infer an interface-limited grain growth response [124], where the rate-limiting step is transport of Ti and C across the interface between the metallic binder and the TiC, rather than diffusion through the steel melt.

The contiguity and binder mean free path data for both the fine- and coarse-grained TiC-316L cermets are presented in Figure 5.2. As can be seen, the contiguity decreases with increasing binder content (Figure 5.2(a)), which is similar to the results of other investigators [124, 153, 154]. In terms of the mean free path dimensions for the binder (Figure 5.2(b), it is apparent for

the coarse-grained cermets that the mean free path length increases with binder content, which is in agreement with studies on TiC and other WC-based cermets [30, 71, 77, 124, 154]. However, it is noted that for the fine-grained cermets the behaviour is more complex, actually showing a slight reduction in mean free path for the 20 vol. % 316L samples in comparison to 10 and 30 vol. %. The reason for this response is unclear at the present time, but could be related to a relatively complex, non-equilibrium grain morphology (i.e. a clear evidence of deviation from moderately spherical grains is shown in Figure 5.1) leading to anomalous mean free path measurement as presented in Figure 5.2(b).

(a)

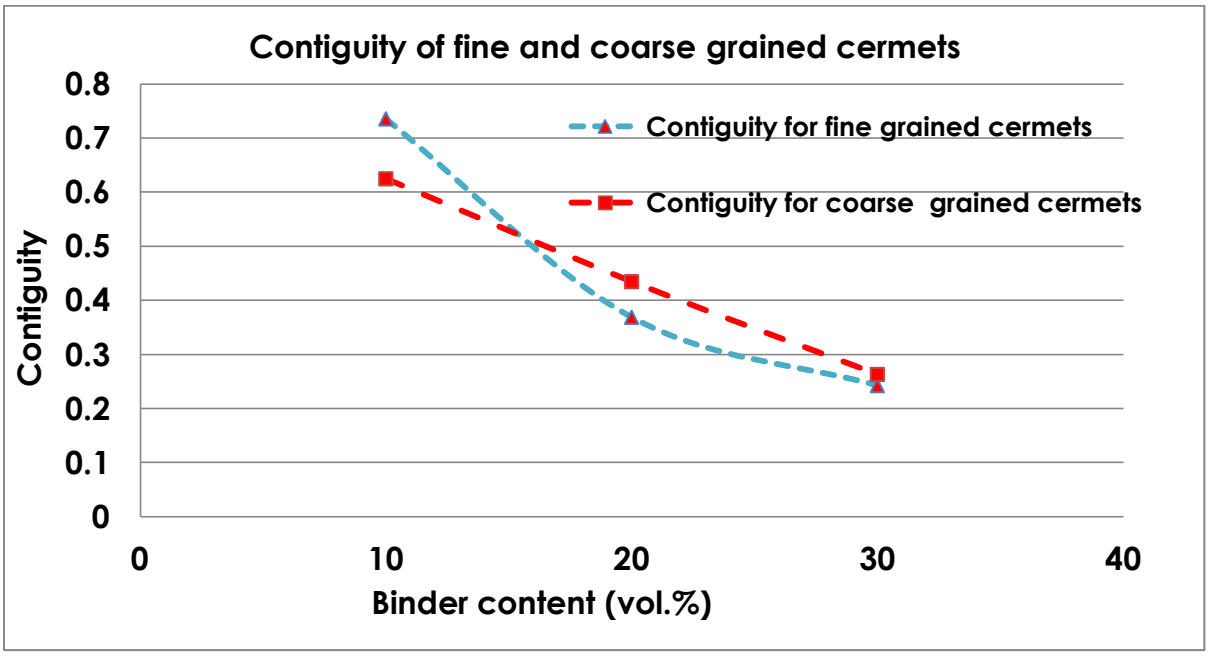

(b)

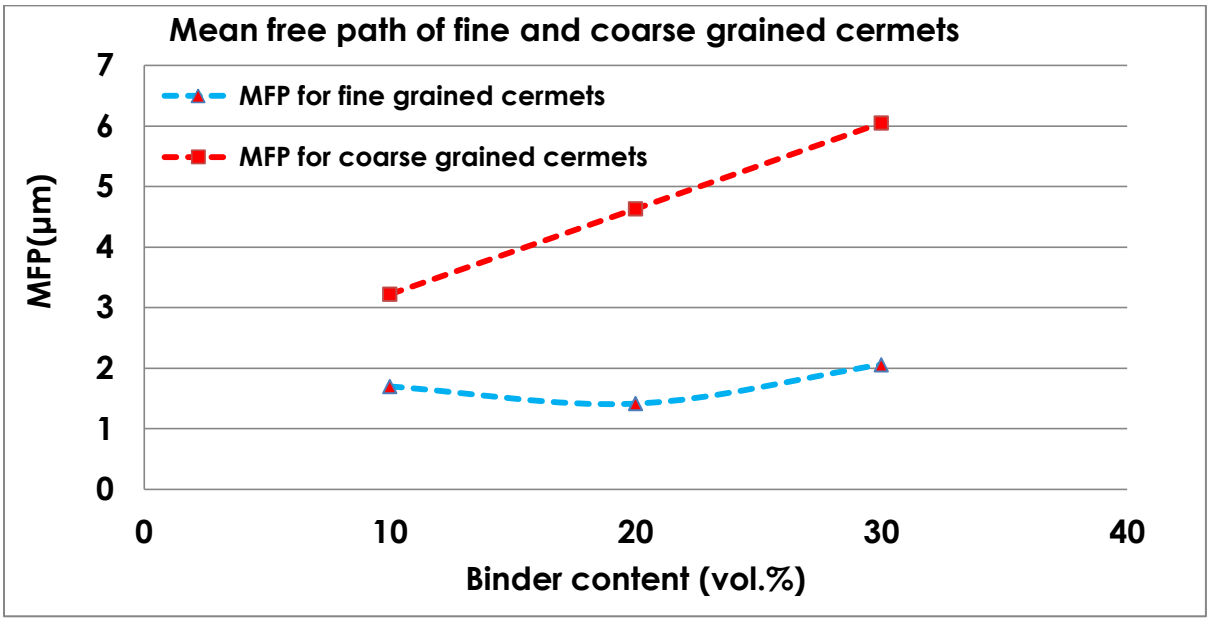

Figure 5.2: (a) The effects of binder content upon the contiguity of fine- and coarse-grained TiC-316L cermets. (b) The effects of binder content upon the mean free path of fine- and coarse-grained TiC- 316L cermets [155].

The Vickers hardness response of the fine and coarse grained TiC-316L cermets is presented in Figure 5.3, and demonstrate the superior hardness of the fine grained cermets. It can be seen that the hardness of the composite decreases with increase in binder content for the fine- and coarse-grained cermets, which is in agreement with our prior studies of a similar material [55]. This is related to the relative elastic moduli of the phases (with TiC ~439 GPa and 316L stainless steel ~193 GPa). The reason for the improved hardness as the grain size is reduced is attributed to the decrease in mean free path and hhence smaller smaller thickness of the binder phase ligament. As the grain size of TiC cermets is reduced, there would also be greater amount of Ti and C that would get dissolved in the steel binder phase which stiffens and strengthens the binder increasingly thereby leading to an improvement in hardness and wear resistance [71, 76].

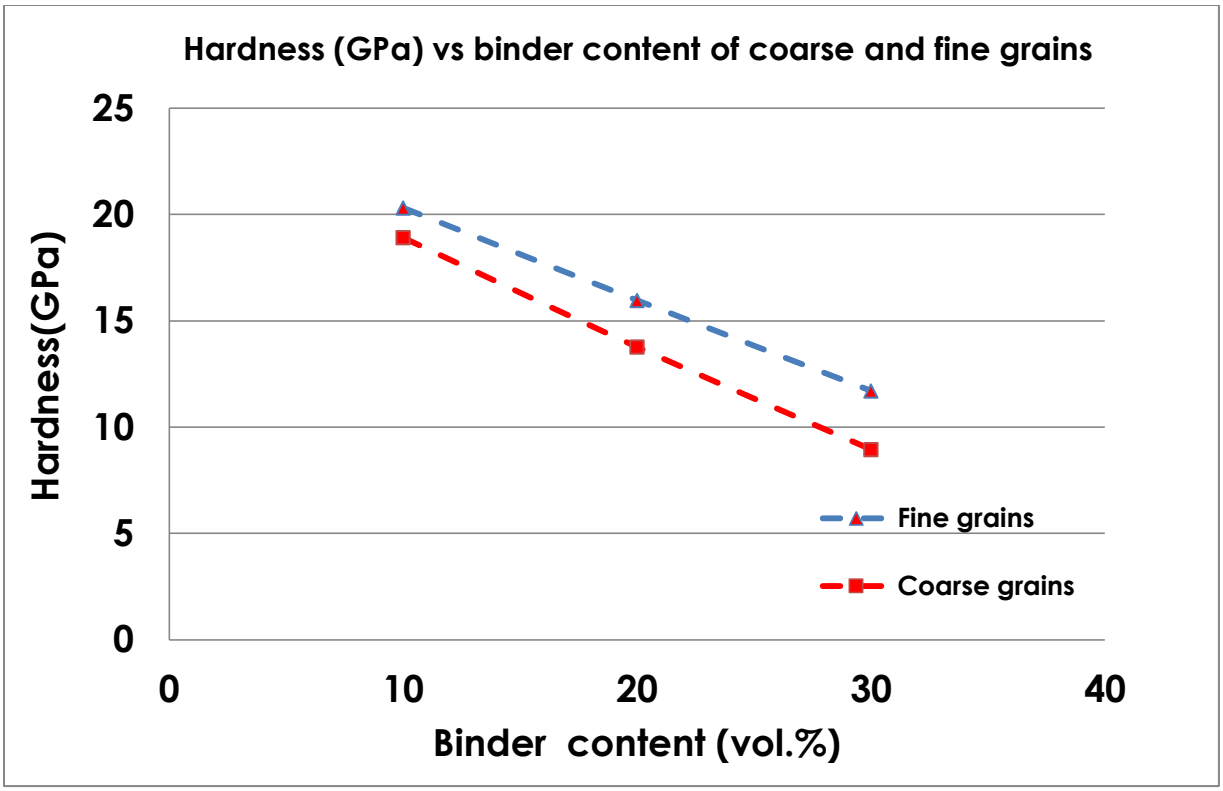

Figure 5.3: The hardness of fine and coarse grained TiC-316L cermets as a function of steel binder content (measured with a 1 kg load).

Secondly, as the carbide size is decreased for given cobalt content, the binder mean free path of the matrix is reduced (Figure 5.2b) resulting in greater constraint against deformation leading to an improved hardness of the cermet. The indentation fracture resistance response of the fine and coarse grained cermets is presented in Figure 5.4, and demonstrates superior indentation fracture resistance (IFR) of the coarse grained cermets over the finer grained counterparts. The IFR determined using both median (i.e. Anstis et al [98]) and Palmqvist (i.e. Niihara [99]) cracking equations, exhibits the opposite trend; by increasing the steel binder content, the IFR of the cermet increases, which is in agreement with our previous studies [55]. The improvement of the IFR of both fine and coarse grained cermets with increase in steel binder content is as a result of beneficial effect of ductile phase addition on the toughness of the TiC-steel based composites.

(a)

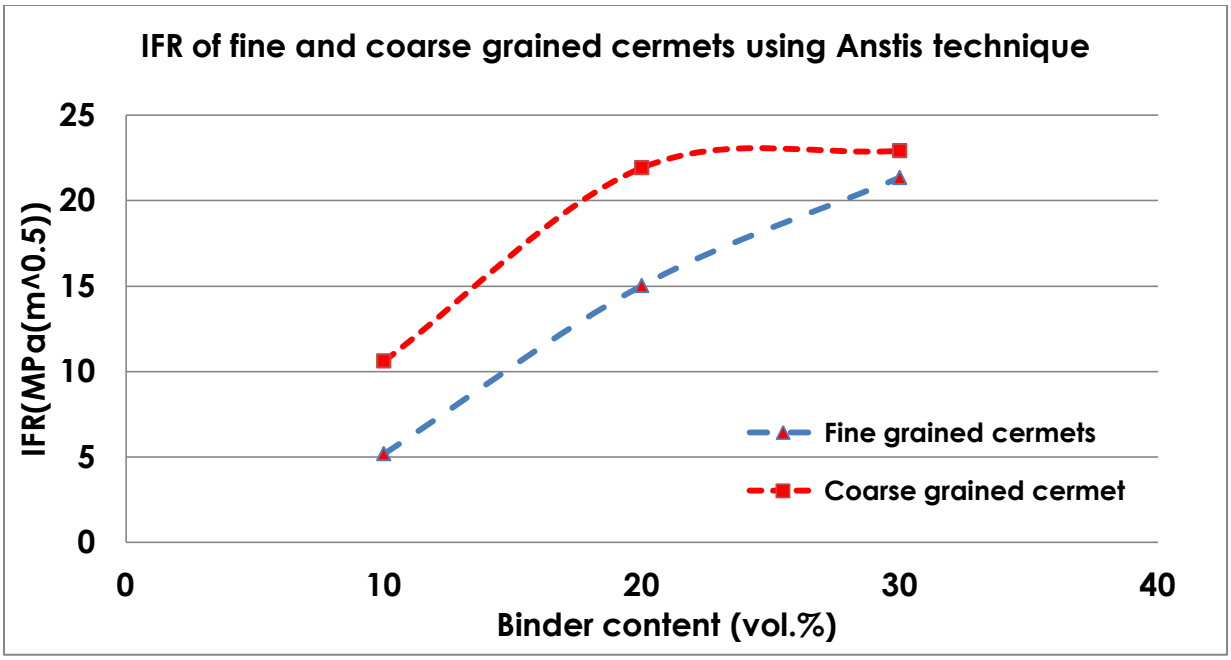

(b)

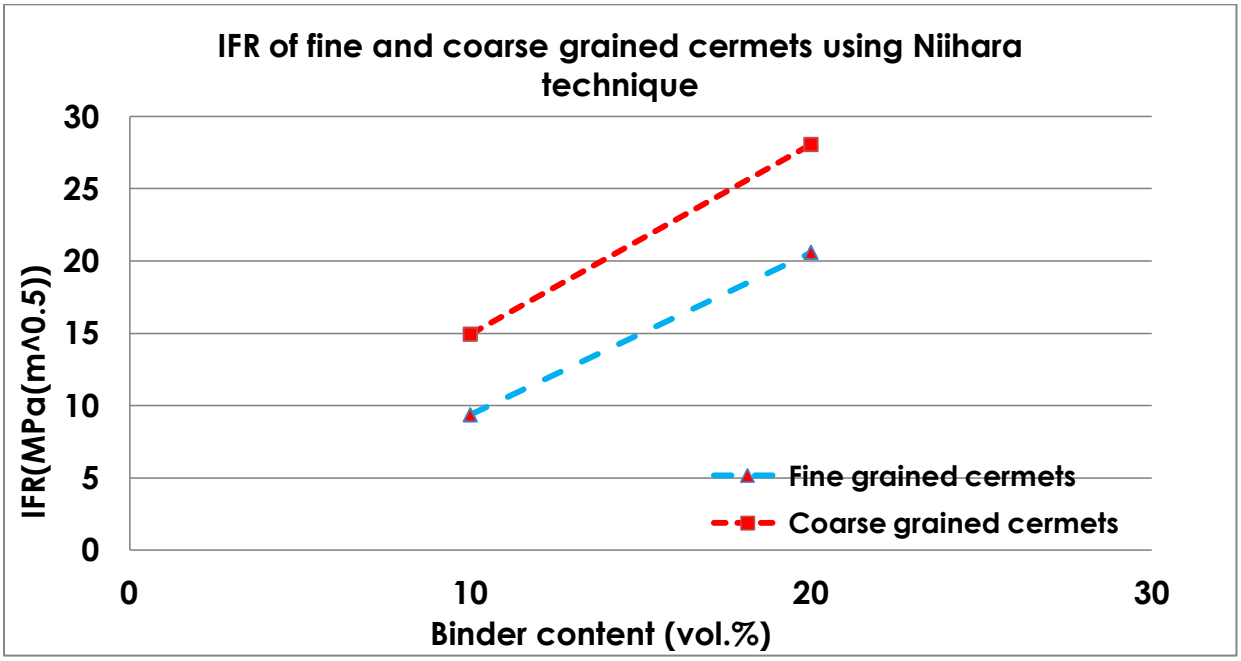

Figure 5.4: The indentation fracture resistance of fine and coarse grained TiC-316L cermets as a function of steel binder content (measured with a 50 kg load), determined for both median and Palmqvist cracking. (a) IFR using Anstis technique (b) IFR using Niihara technique.

Coarse -grained cermets showed superior IFR over fine-grained cermets which is related to their greater binder mean free path (or carbide grain size). This is due to a decrease in constraint for

the plastic deformation of the metallic binder ahead of the propagating crack [30, 80-81, 150, 154]. The presence of the ductile phase ligaments between TiC grains, at increased steel binder, content can effectively improve the fracture resistance of the cermets and as a consequence, incorporating the steel binder can effectively inhibit crack growth, such that even a 50 kg Vickers indentation load produces minimal cracking, and actually no cracking whatsoever for the highest steel content samples (i.e. 30 vol. %) for both fine and coarse grained cermets. The IFR response presented in Figure 5.4 effectively highlights a transition in terms of the crack behaviour, showing a more traditional brittle median cracking response for lower 316L binder contents (i.e. c:a > 2.5) and Palmqvist cracking at the higher binder contents (i.e. (c:a < 2.5) [100]. It should be noted that in the present study, the actual sub-surface cracking response has not been verified, for instance through the use of sequential polishing, as reported by Shetty for WC-based cermets [126]. For the present case this transition (based on the c:a ratio) occurs at 10 vol. % steel binder for fine grained cermets, with Palmqvist-type cracking expected at the higher binder contents (i.e. from 20 vol. % for fine grained cermets and 10 vol. % for coarse grained cermets).

TiC ceramic is brittle and has a low fracture toughness (2-3 MPa [54]), but by incorporating 316L steel binder to TiC-316L cermets, the fracture resistance is drastically improved, hence making it a competitive material in applications where hardness and fracture toughness are required. However, it should be stressed that the decision to coarsen the carbide structure (improvement in fracture toughness) or reduce the carbide structure (improvement in hardness and wear resistance) must be weighed against the typical application of the cermets, hence the finer the carbide grain size, the harder the cermets, and the coarser the carbide grain size, the better the fracture toughness (Figure 5.4), in addition to corrosion resistance [155].

5.4.2 Reciprocating Wear Behaviour

The reciprocating wear tests were used to study the tribological behaviour of the fine- and coarse-grained TiC-316L stainless steel composites, with the cermets dry sliding against a hard counter face sphere, which in this instance is comprised of WC-6Co (equivalent to ~10.2 vol. % Co). Figure 5.5 presents the variation of COF of fine- and coarse-grained cermets with the applied load (determined after 120 minutes of dry sliding). It can be seen that the COF for all the

fine- and coarse- grained cermets evaluated ranges from 0.25 - 0.42 which is broadly similar to the COF values recorded for TiC-304L cermets in our previous studies [55].

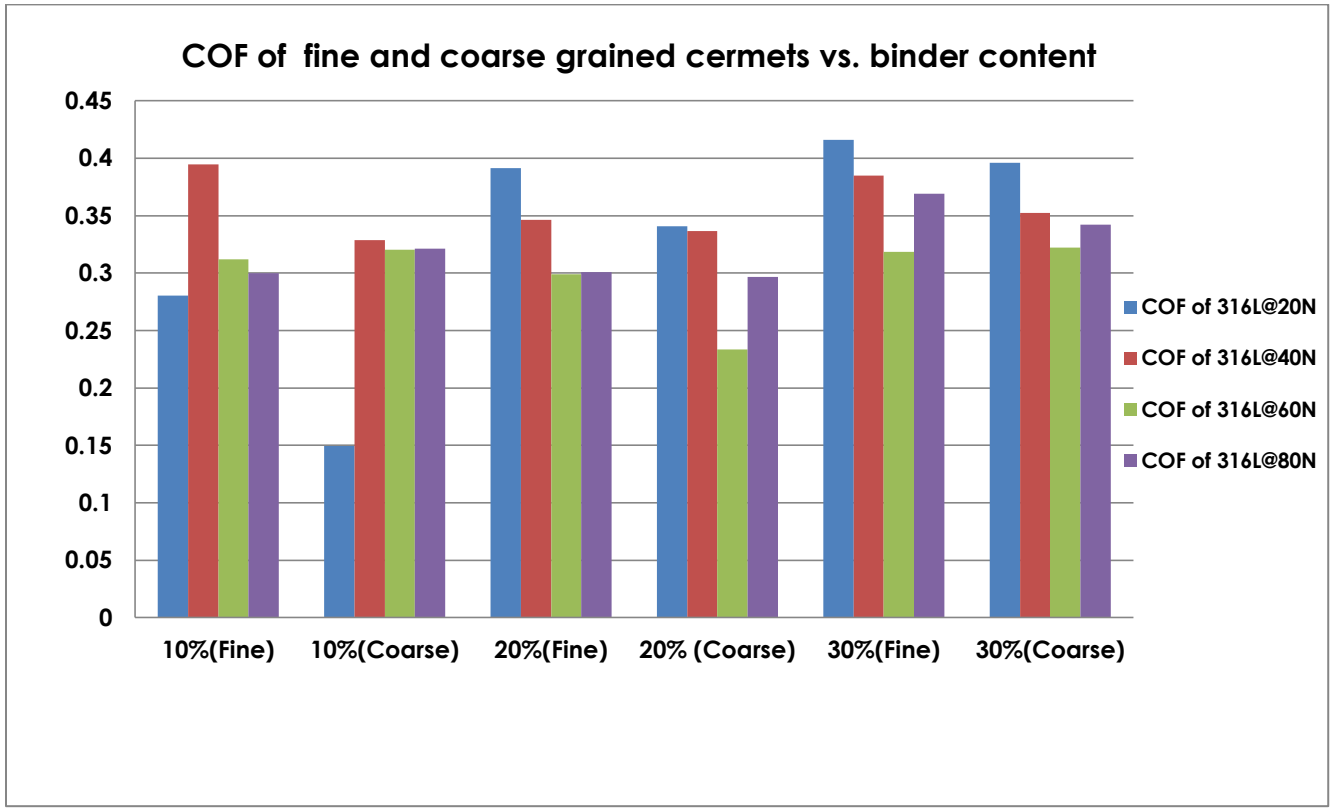

Figure 5.5: The evolution of the COF for the fine and coarse grained TiC-stainless steel cermets as a function of applied load and steel binder content after 120 minutes of dry sliding.

Looking critically at Figure 5.5, it can be seen that COF is independent of load. However, for both fine- and coarse- grained cermets, those with 20 and 30 vol. % steel binder content showed an initial increase in COF at 20N, slight drop at 40 and 60N load and an increase at 80N Load. The slight variation of COF with load in this case could indicate that the wear mechanisms may be gradually changing from an initially 2-body to 3-body abrasive wear scenario, a slight drop to 60N load and slight increase at 80N load could indicate to the formation and subsequent partial spalling of any tribolayer formed. With the increase in friction between the TiC cermet and WC-Co counter face sphere, the frictional heating can be expected to increase, resulting in a small temperature rise.

Comparing the COF of fine- and coarse- grained cermets, it is expected that fine- grained cermets should have higher COF over the coarse grained counterpart due to greater mechanical

attrition or interaction between the WC-Co counter-face sphere with the cermet as a result of greater surface area of the fine grained cermets. However, there seem to be no dependence of COF with carbide grain size. This observation is in an agreement other cermet based systems where there is no dependence of COF with carbide grain size [77, 156]. There is a slight increase in COF of both the fine and coarse grained cermets with binder content, inferring that the steel content plays an important role in controlling the COF. O'Donnell and colleagues [59], in comparing the wear performance of carburized and un-carburized 316L stainless steel, reported a COF of 0.58–0.61 for an untreated 316L stainless steel dry sliding against a WC ball (of unspecified size). In that case the applied load was 5N, although severe adhesive/abrasive wear was reported with a wear rate of 4.25×10^{-4} mm^3/Nm [59]. Similarly, Degan et al, reported a mean COF of 0.679 for 316L stainless steel with much conservative load of 1N, dry sliding against a Al_2O_3 counter sphere [157]. The range of COF values observed for the present fine and coarse grained TiC-316L cermets is broadly consistent with other TiC-based cermet systems. For instance, in our previous publications, we reported a COF of 0.2 - 0.36 for TiC-304L cermets sliding an identical WC-6Co sphere to the present work [55]. Also Buchholz et al. reported a mean COF of a mean COF of ~0.32-0.35 for TiC cermets, prepared with between 20 and 40 vol. % Ni_3Al (alloy IC-50) binder [127], sliding against an identical WC-6Co sphere.

Figure 5.6 presents the variation of specific wear rate at different loads and steel binder contents for fine- and coarse- grained TiC-316L cermets. As can be seen, the wear rate increases with both an increase in steel binder content and load, with fine- grained cermets having the superior wear resistance. However, it can also be seen that the grain size effect is less obvious for 10 vol. % of binder content, especially at lower load, such as 20N, 40N and 60N. At 20N, the size has little effect for all the binder contents. This infers that the wear rate is dependent on the amount of TiC, and has a nominally linear relationship with hardness (Figure 5.3), as reported in our previous studies [55]. When the TiC-cermet and the WC-Co counter-face sphere are brought into sliding contact at the beginning, the soft ductile steel metal binder between TiC particles would undergo severe deformation. The deformed steel metal binder is extruded by compressive stress from the protruding asperities of the WC-Co. Then micro-cracking, fragmentation, and /or pull-out of the TiC particles occur which is expected to be greater with increase in applied load. These effects are less severe as the size of the TiC grains and the steel binder content are reduced. At low loads and higher TiC content, the steel deformation and material removal is

effectively minimised by the contiguity of the TiC grains, which forms a contacting network that resists compression and extrusion of the softer metallic binder.

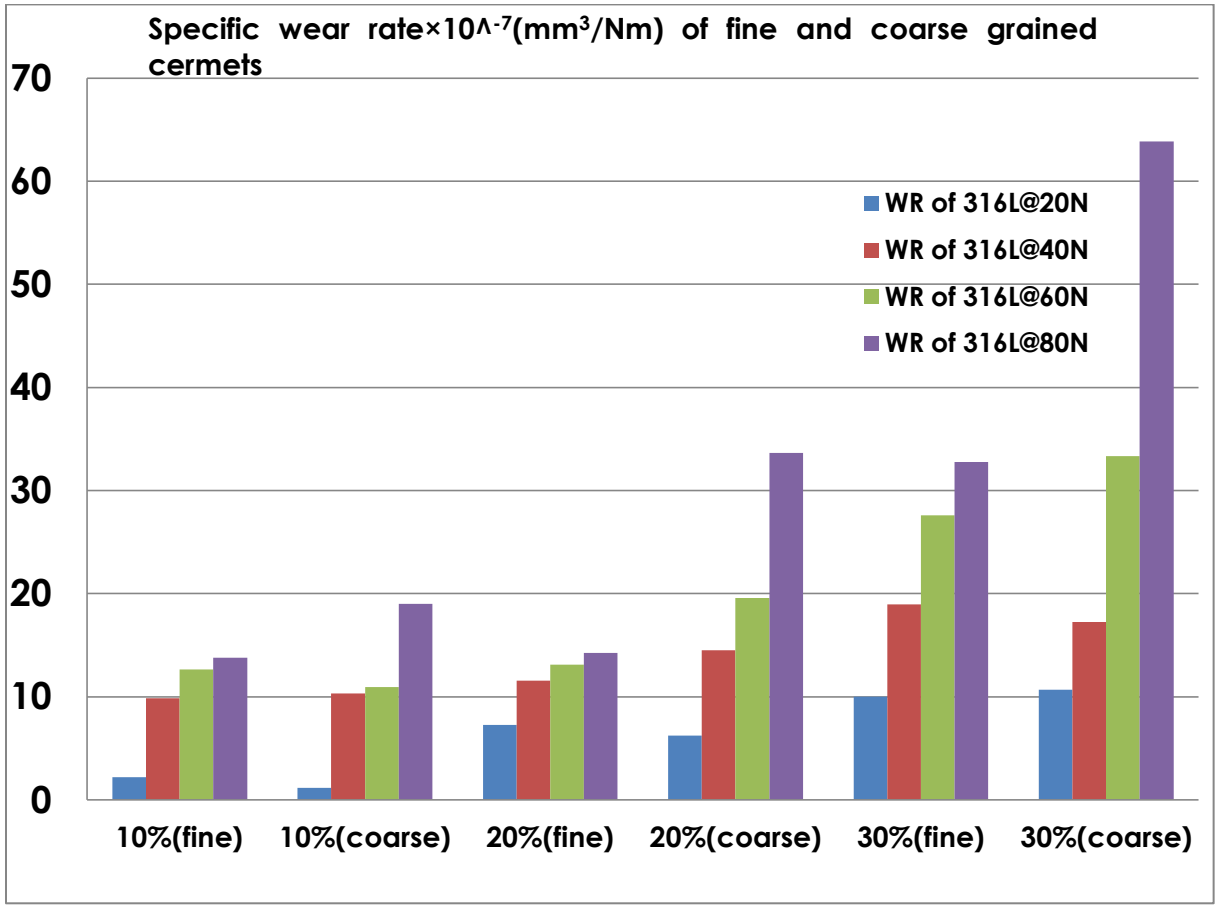

Figure 5.6: The specific wear rate of fine and coarse grained TiC-316L stainless steel cermets as a function of applied load and binder content.

Relating the specific wear rate (Figure 5.6) with contiguity and binder mean free path (Figure 5.2) of the fine- and coarse-grained cermets, it can be seen that wear resistance of the cermets increases with contiguity but decreases with binder mean free path. Hence, the improvement of the wear resistance and hardness of the fine-grained cermets over the coarse-grained cermets is attributed to the decrease in the mean free path as the grain size of the TiC is reduced, leading to greater constraint against deformation due to the greater interfacial area between the grains and a reduced tendency for steel binder phase extrusion, making dislocation motion and shear more difficult, such that the wear resistance improves considerably [76].

Although geometry and test conditions are slightly different with the present cermets, by comparing the data presented in Figure 5.6 with the reported specific wear rate of 316L in dry sliding against a WC sphere (i.e. 4.25×10^{-4} mm^3/Nm [59]) and (8.20×10^{-4} mm^3/Nm [137]), it can be seen that the TiC results in a two to three orders of magnitude decrease in the specific wear rate.

By comparing the specific wear rates determined in the present work to other cermets, it can be seen that the wear rates compare favourably with or better than, other cermets. For instance, Juhani et al examined the dry abrasive wear of fine grained Cr_3C_2-Ni cermets using a block-on-disc geometry, with the cermets sliding against an abrasive Al_2O_3 wheel [158] at 20N load. In their studies, they reported a specific wear rate of 2.6×10^{-4} mm^3/Nm, $6.1\times10^{-4}mm^3/Nm$ and 7.4×10^{-4} mm^3/Nm for Ni binder varied from 10 to 30 wt.% whereas for the fine grained cermets in the present study, at the same load, the specific wear rates are $\sim21\times10^{-8}mm^3/Nm$, $\sim77\times10^{-8}mm^3/Nm$, and $\sim10\times10^{-7}mm^3/Nm$ for 10 to 30 vol. % of 316L steel binder. Similarly, Letunovits and colleagues determined the dry abrasive wear of Cr_3C_2-Ni, TiC-NiMo and WC-Co cermets using an identical test geometry and condition similar to Juhani et al [158], and reported specific wear rates ranging from $\sim5\times10^{-7}$ mm^3/Nm for 10 vol. % Co up to $\sim80\times10^{-7}$ mm^3/Nm for 31.5 vol. % Co for WC-Co cermets, and specific wear rates ranging from $\sim8\times10^{-7}$ to $95\times10^{-7}mm^3/Nm$ for the Cr_3C_2-Ni cermets (Ni content varied from 7.6 to 24.5 vol.%)[68]. In both cases, despite having slightly different test geometry, it is apparent that both the fine- and coarse-grained cermets of the present study compare favourably to the wear resistance of the other studied cermets. By making direct comparison with similar TiC-based cermets having similar test condition and geometry, such as the fine-grained cermets of the present study at the highest carbide content, where wear resistance is expected to be high (i.e. TiC-steel based cermets with 10 vol. % steel binder and at 20N load), it is also apparent that favourable comparison can be drawn. For instance, a specific wear rate of $\sim21\times10^{-8}$ mm^3/Nm, $\sim42\times10^{-8}$ mm^3/Nm, $\sim48\times10^{-8}$ mm^3/Nm, $\sim22\times10^{-8}$ mm^3/Nm for fine grained TiC-316L (present study), TiC-304L cermets (mean grain size of 6.80µm, [55]), TiC-316L cermets (mean grain size of 6.48µm, [159]), TiC-410L cermets (mean grain size of 6.25µm, [159]) respectively. In overall, TiC based cermets have shown excellent wear resistance, hence making them ideal candidate material for hard-facing wear and corrosion resistant coatings.

5.4.3 Microstructural Observations Following Reciprocating Wear

The wear response of the fine and coarse grained cermets have been thoroughly investigated using microstructural and chemical analysis of the wear tracks, as well as assessing the wear debris that is formed. It should be noted that the present study is an extension of prior studies on the wear behaviour of TiC-based cermets with all having similar wear mechanisms, in order to avoid repetition of events, reference should be made to those prior studies for more detailed and more comprehensive wear analysis and mechanisms [55, 127, 128].

In section 5.4.2 of the present study and prior studies [55, 127, 128] we reported an improvement in wear resistance with decrease in load, hence wear rate increases with load. In order to further confirm this, the individual wear tracks have been imaged with the optical profilometer. Optical profilometry is capable of contrasting the macroscopic details of the wear track and the changes in depth than imaging with the SEM. Detailed analysis of optical profilomer on studies of TiC-based cermets is presented in prior studies [55, 127, 128]. Figures 5.8 demonstrate typical images that were captured using the profilometer, as pseudo three dimensional images.

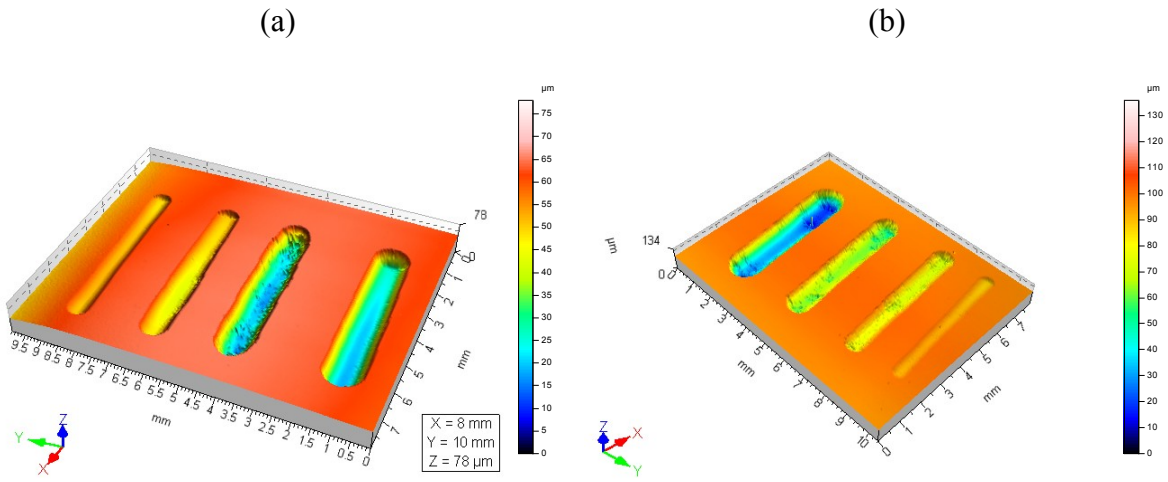

Figure 5.7: Wear tracks of fine and coarse grained TiC-based cermets with 20 vol. % 316L stainless steel binder. (a) Fine grained cermet with wear tracks in order of 20 to 80N load, from left to right, with a total length of 5.03mm.(b) Coarse grained cermet with wear tracks in order of 80 to 20N load, from left to right, with a total length of 5.03mm. The pushing of the material at the end of the track is apparent.

A clear comparison can be obtained of the evolution of the wear tracks with applied load, confirming the wear rate increase with load, judging from the depth of the wear tracks, as a function of load as shown in Figure 5.7. Evidence of ploughing and pushing of the material at the end of the wear track is also apparent at higher loads. The SEM images of the wear track ends for the fine and coarse grained cermets are shown in Figure 5.8. As can be seen, there is an increase of the build-up of ploughed material and the presence of a tribolayer. The ploughed material at the end of the wear track could indicate a combination of 2-and 3-body abrasive wear. 2-body wear is associated with the cutting and ploughing of material, as well as the uplift and deposition of material at both the sides and the ends of wear tracks [127, 160]. This uplift and deposition manifests normally as pronounced lips or ridges surrounding the wear track. The presence of material deposited at the end of the wear track would indicate 2-body wear, but the lack of a significant raised lip would indicate 3-body wear. The combinations of both wear methods indicate abrasive wear, although the presence of the tribolayer indicates a mechanism of adhesive wear. At the beginning of the wear test, it can be expected that the wear process will be 2-body, with the fine- and coarse-grained cermet sliding against the WC-6Co counter face sphere, leading to the formation of debris between the two counter faces, as TiC grains crack and fragment under the Hertzian contact load, and the steel binder is extruded out from between the TiC grains. As a consequence, there will be a transition from 2- to 3-body wear, with the debris acting as the third body.

The change in the COF is used as an indicator of a transition from one wear mechanism to another, although in the present case, there is no clear established trend. However, looking at the COF (Figure 5.5) of fine- and coarse-grained cermets, it is clear that cermets with 20 and 30 vol. % steel binder contents showed an initial increase in COF then slight drop with load and an abrupt increase at 80N load. This could explain the reason for the transition from an initial 2-body to later 3-body abrasive wear mechanism, as stated previously. This 3-body wear response can ultimately lead to the formation of a tribolayer and a further potential transition to an adhesive wear mechanism. The tribolayer is formed through repeated, cyclic loading, with the third body material rolled back and forward between the two primary counter faces. This ultimately results in severe attrition and a massive refinement in the size of the third body particles (such that they eventually form a continuous film).

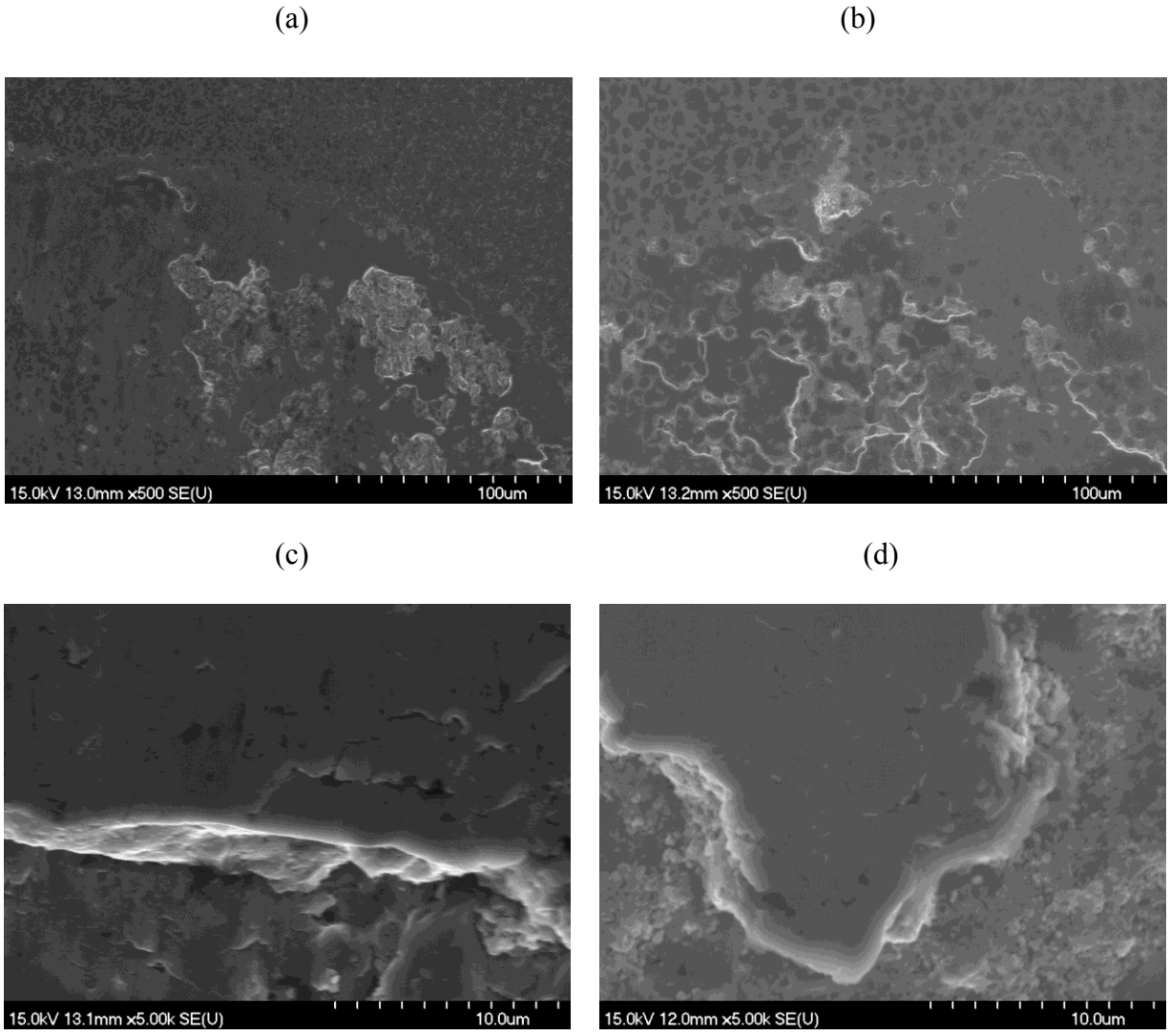

Figure 5.8: SEM images of the wear track formed on the fine- and coarse-grained TiC- 30 vol. % 316L after testing using 20N and 80 load for 2 hours duration.(total sliding distance ~1.45Km); sliding direction is vertical for all images. (a, b) 30 vol. % 316L of fine and coarse grained cermet at 20N load showing initial formation of tribolayer and build of material at the end of the wear track, (c, d) 30 vol. % 316L of fine and coarse grained cermet at 80N load depicting increase in build-up of tribolayer with increase in load.

As the wear process continues, the fragments of TiC (and WC) particles are then able to become embedded in the extruded binder and become part of the tribolayer; detailed composition of the tribolayer is discussed in section 5.4.4. Figure 5.8 (i.e. Figure 5.8(c, and d)) demonstrates the build up and slight increase in the formation of tribolayer at higher loads.

As previously stated in section 5.4.2, the fine-grained cermets are expected to show improved performance over their coarse-grained counterparts due to their enhanced resistance to deformation of the binder phase and also their increased hardness as shown in Figure 5.3. The enhanced resistance of fine-grained cermets to binder deformation is demonstrated in Figure 5.9, where there is little or no evidence of binder extrusion, whereas the coarse-grained cermets showed evidence of binder extrusion during the intial period of wear testing. As previously stated, the presence of material deposited at the end of wear tracks would indicate 2-body wear (as shown in Figures 5.7 and 5.8), but the lack of a significant raised lip at the edges/ends of the wear track would indicate 3-body wear, (Figure 5.9).

(a) (b)

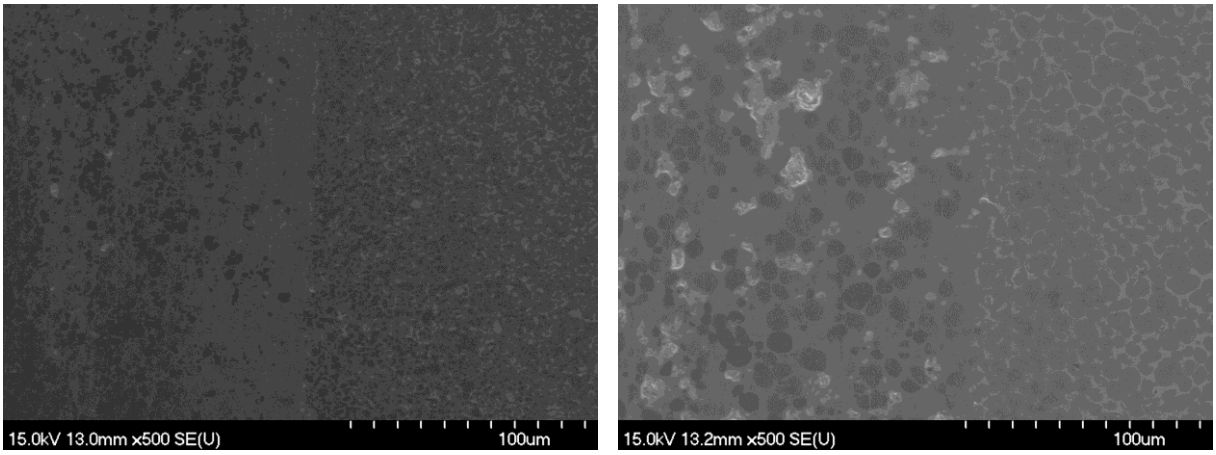

Figure 5.9: SEM images of the wear track formed on the fine and coarse grained TiC- 30 vol. % 316L after testing using 20N for 2 hours duration. (total sliding distance ~1.45Km); sliding direction is vertical for all images. (a, b) 30 vol. % 316L of fine grained and coarse grained cermets showing evidence of ploughing and initial binder deformation and extrusion, which is more pronounced for coarse grained cermets (i.e. Figure 5.9 b) than fine grained cermets.

Although the wear behaviour of cermets is rather complex, prior studies have indicated that the wear process of cermets is initiated by the removal and extrusion of the ductile binder phase, followed by plastic deformation and micro-abrasion [71, 80, 128, 161]. At a higher load, greater binder deformation, TiC grain pull-out, and / or fragmentation and cracking are expected. By comparing the SEM images of fine- and coarse-grained cermets presented in Figure 5.10, evidence of tribolayer spallation and binder extrusion is clearly shown.

(a) (b)

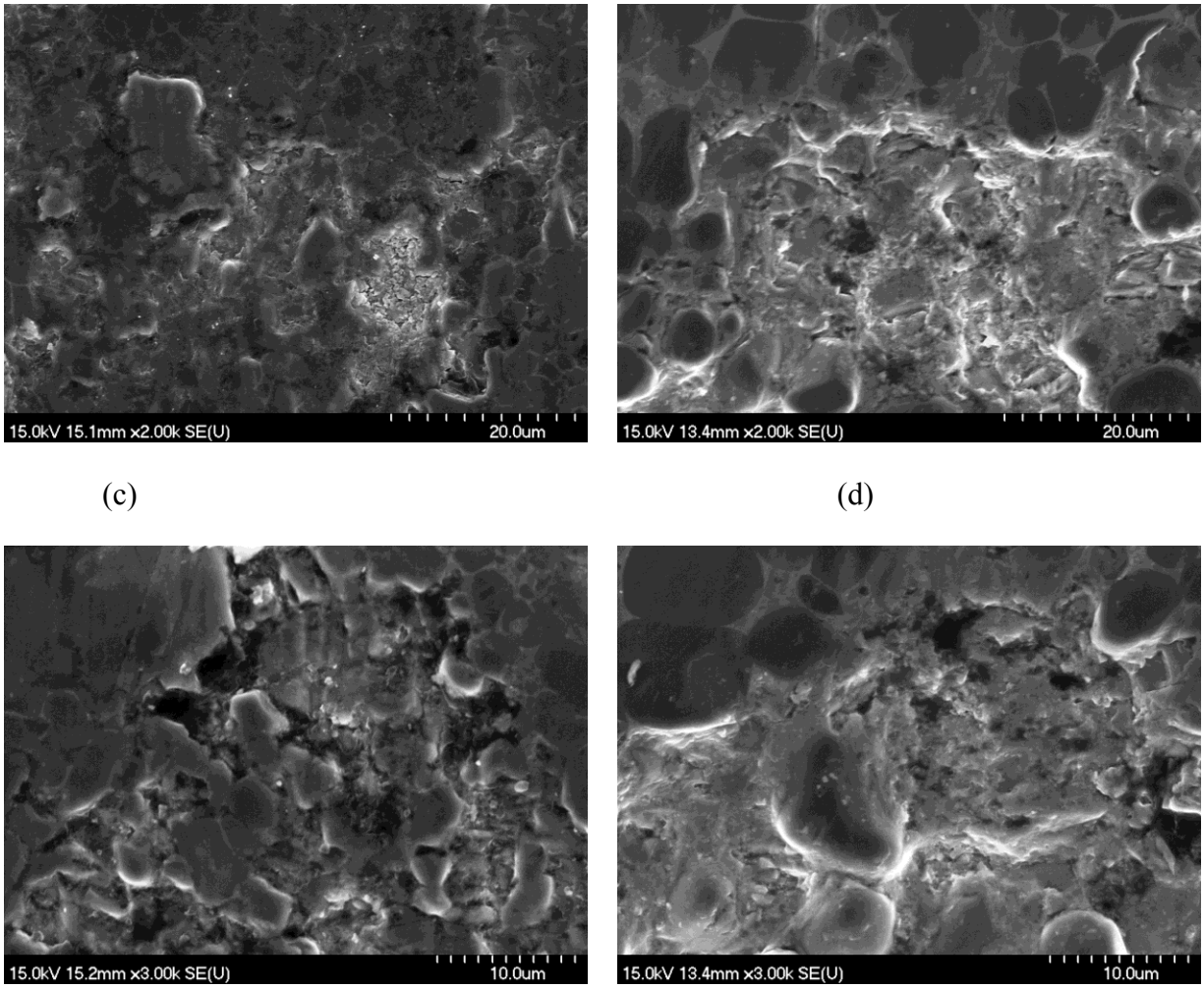

(c) (d)

Figure 5.10: SEM images of the wear track formed on the fine- and coarse- grained TiC- 20 vol. % 316L, after testing using 40N for 2 hours (total sliding distance ~1.45Km); sliding direction is vertical for all images. (a, c) 20 vol. % 316L of fine grained cermet showing evidence of tribolayer spallation and binder extrusion. (b, d) 20 vol. % 316L of coarse grained cermet showing evidence of more pronounced binder extrusion.

Both cermets showed evidence of tribolayer spallation and binder extrusion, however by looking critically at Figure 5.10, it can be seen that there are cavities present on the coarse -grained cermets (i.e. Figure 5.10d) which is believed to be as a result of removal of individual TiC grains, following greater binder extrusion (as a result of higher binder mean free path or ligament size of coarse grained structure) of the soft steel binder phase. Figures 5.11 presents typical evidence of TiC grain fragmentation, as observed on coarse grained cermets.

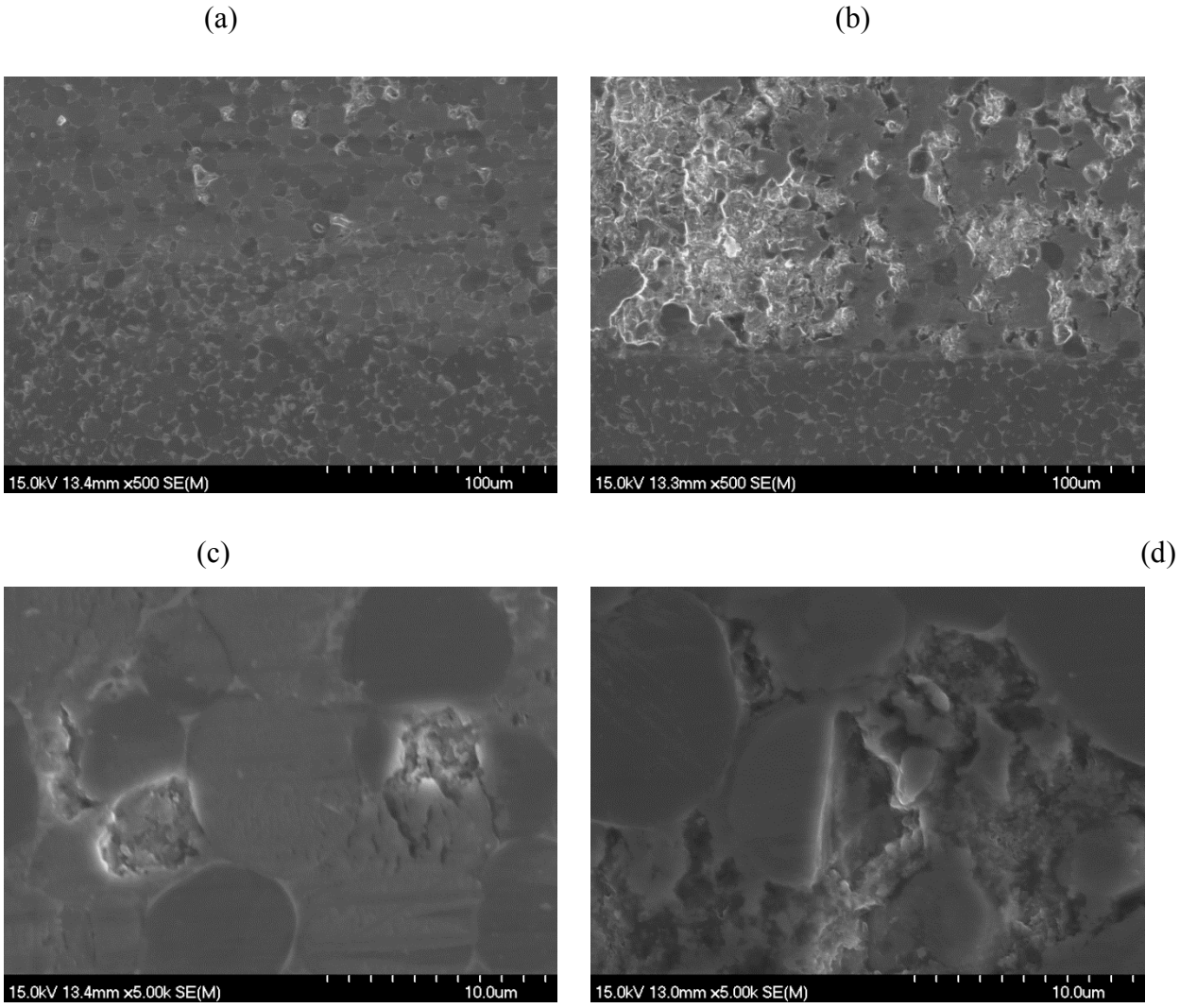

Figure 5.11: SEM images of the wear track formed on the coarse grained cermets after testing for 2 hours duration. (total sliding distance ~1.45Km) (a, and b) 10 vol. % 316L of coarse grained cermets at 20N and 80N load showing evidence of light and intense spallation of tribolayer at higher load. (c, and d) 20% vol. % of coarse grained cermets at 20N and 40N load showing evidence of TiC fragmentation.

The SEM micrographs of typical examples of the third body wear debris generated for the fine- and coarse-grained TiC-30% 316L cermets, at 20N and 40N loads, are presented in Figure 5.12. As the wear process proceeds, there would be more extrusion of the metallic binder phase, micro-cracking, fragmentation of the TiC particles, and the generation of increased tribolayer material. This layer is then removed from the surface periodically by spallation, taking the sub-surface cermet material with it and creating cavities on the surface (Figure 5.10). In other words,

the entrapped debris particles produce further damage on both surfaces, in a third body scenario, and the debris itself undergoes fragmentation during sliding, resulting in the formation of very fine particles at lower loads. At the higher load, the debris appears to be more coarse (evident in Figure 5.12d for coarse grained cermets), in terms of the particle size, and has somewhat 'plate-like appearance' for coarse-grained cermets and 'sandwiched and finer structure' for the fine-grained cermets. The appearance of 'plate-like' or 'sandwiched structure' of the wear debris at higher load could be result of successive adhesion and transfer of relatively round debris composed of material from both sliding surfaces (observed at lower load).

As the wear process continues, the debris particles grows until it becomes flattened by plastic deformation leading to a somewhat 'plate-like or sandwiched structure' indicating an adhesive wear mechanism [59]. By critically comparing the wear debris generated by fine- and coarse - grained cermets both at low and high loads (i.e. Figure 5.12), it can be seen that the debris generated by fine-grained cermets is finer than for the coarse-grained cermets. However, since finer particles are expected to produce less damage on both surfaces (during a three-body wear scenario), finer carbide grained size cermets would show a lower wear rate. This could also explain while the tribolayer formed on the finer grained cermets, as shown in Figure 5.12 is finer than the coarse counterparts, and another supportive reason while the finer grained cermets have better wear resistance than the coarser grained counterpart materials [77].

(a) (b)

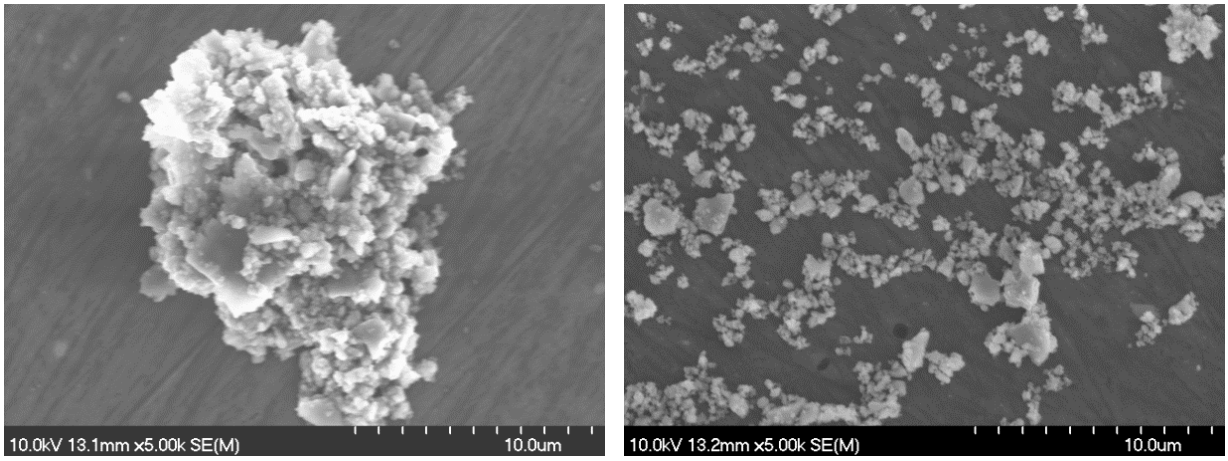

(c) (d)

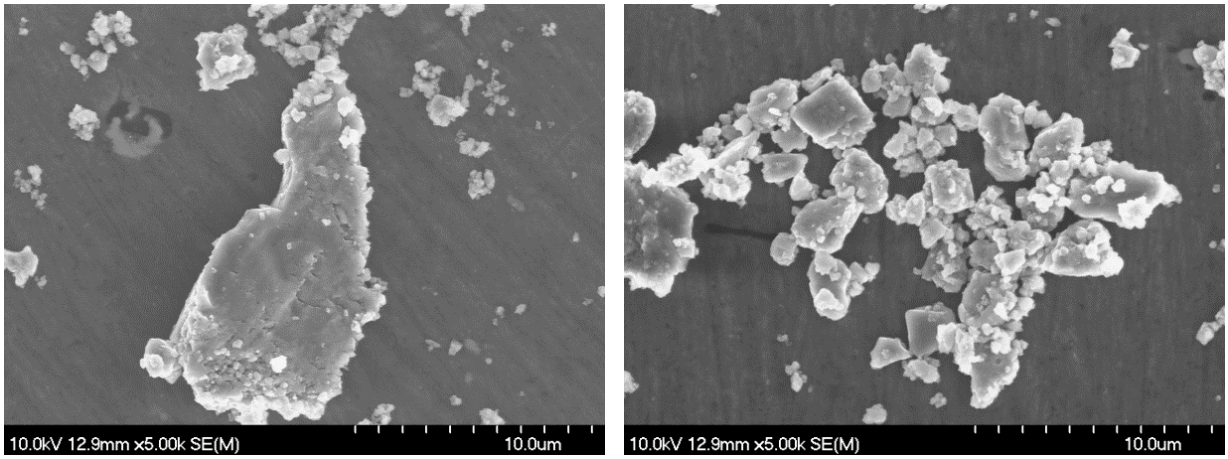

Figure 5.12: SEM Micrographs of fine and coarse grained TiC-20 vol. % 316L showing wear debris generated at 20N (a, c) and 40N load (c, d) . The coarser morphology of the wear debris generated by coarse grained cermets (b and d) is apparent.

5.4.4 Chemical Composition of the Tribolayer

In order to go one further step in understanding the wear mechanisms of the fine- and coarse - grained TiC-316L cermets, compositional analysis of the samples was also performed in the SEM using EDS. Figure 5.13 shows EDS images and selected elemental maps taken from within the wear track of fine- and coarse- grained TiC-30 vol. % 316L cermets, tested at an applied load of 80N. Within the examined region a sizeable portion of the wear track is covered with a tribolayer. The chemical composition, as presented in Table 5.2, confirms that a major component within the tribolayer is O. This can be expected to be mostly in the form of oxides associated with components from the steel binder (i.e. Fe, Cr, Ni and Mo), together with Ti from the TiC, and trace amounts of W from the WC-6Co counter face sphere. As noted previously, tribolayer formation increases with load, and the tribolayer forms through mechanical attrition of the third body material, which is continuously fractured into smaller fragments during dry sliding, and therefore the constant creation of fresh surfaces results in an increasing O incorporation onto the new surface material that is created (formed through passive oxidation). The EDS image shown in Figure 5.14, and the associated EDS chemical analysis of the

tribolayer presented in Table 5.2, confirm that the formation of tribolayer increases with load (an increase in oxygen content is evident).

By thoroughly assessing the wear behaviour of fine and coarse grained TiC-316L cermets using both the wear measurements and microscopy characterization, the wear mechanisms point to an initial two-body abrasive wear, with the WC-6Co sphere ploughing the surface of the TiC cermet. However, it is evident that that there is transition from two-body abrasive wear to a predominantly three-body abrasive wear mechanism, through binder removal (i.e. extrusion) and TiC grain fragmentation. Eventually there is an associated adhesive component, as evidenced through the formation of a tribolayer. The degree of binder extrusion is more severe on coarse grained cermets than fine grained cermets.

(a)

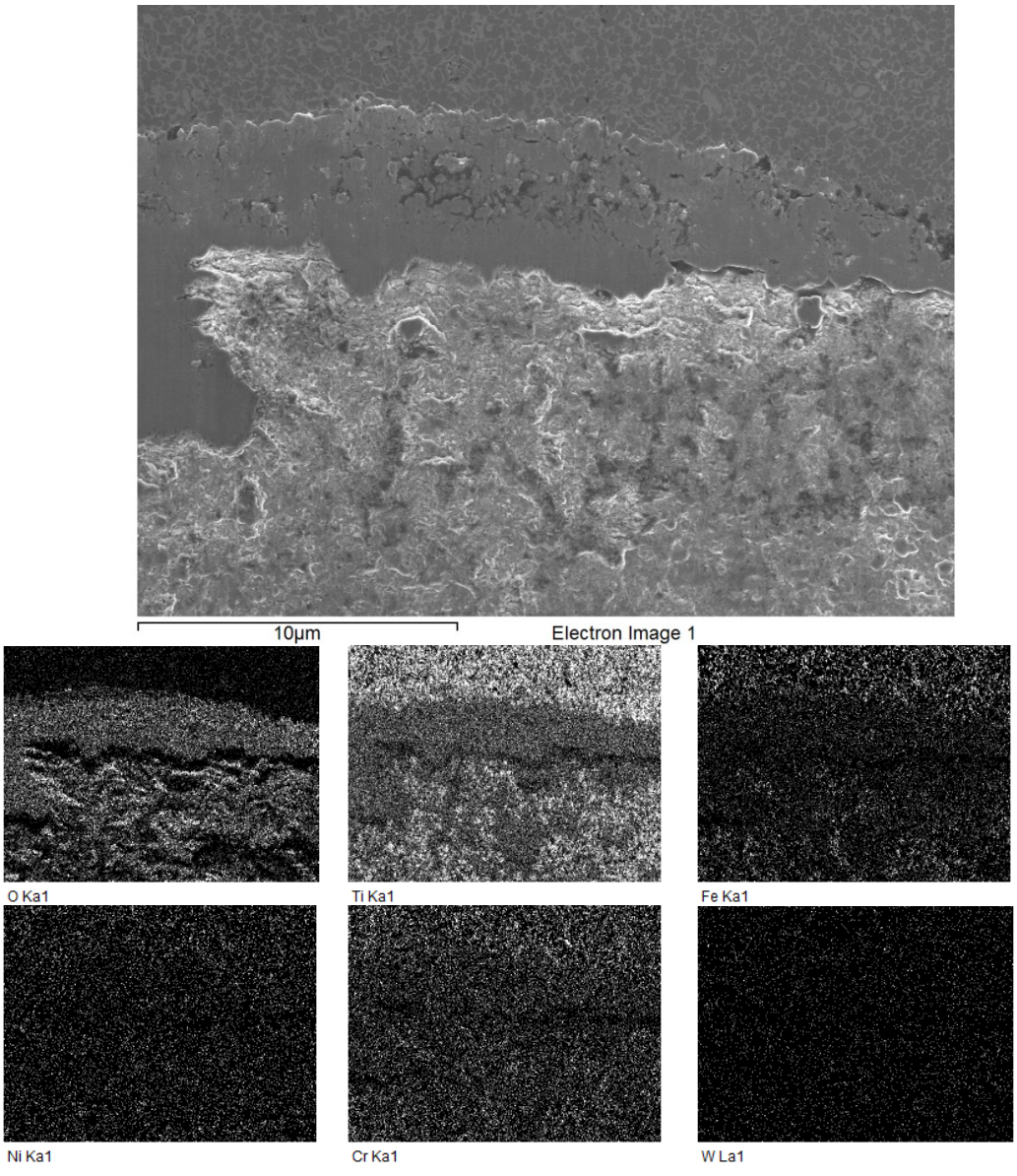

(b)

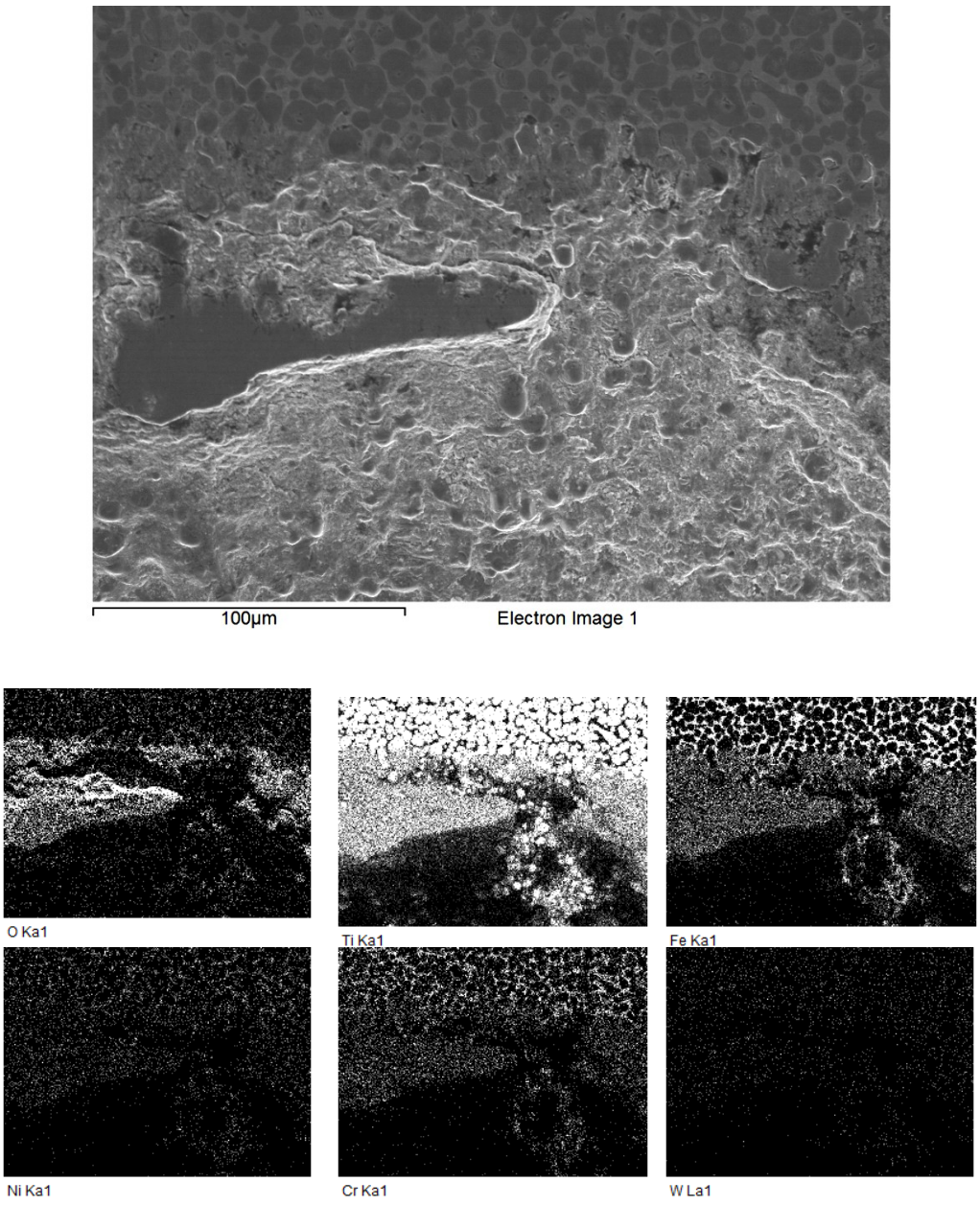

Figure 5.13: EDS mapping of the fine- and coarse-grained TiC- 30 vol. % 316L cermets following wear testing (80N applied load for 2 hours), showing the build-up of an oxide containing tribolayer at the edge of the wear track, and the absence of any significant O beyond the edge of the wear tack; (a) fine grained cermets, (b) coarse grained cermets.

(a) (b)

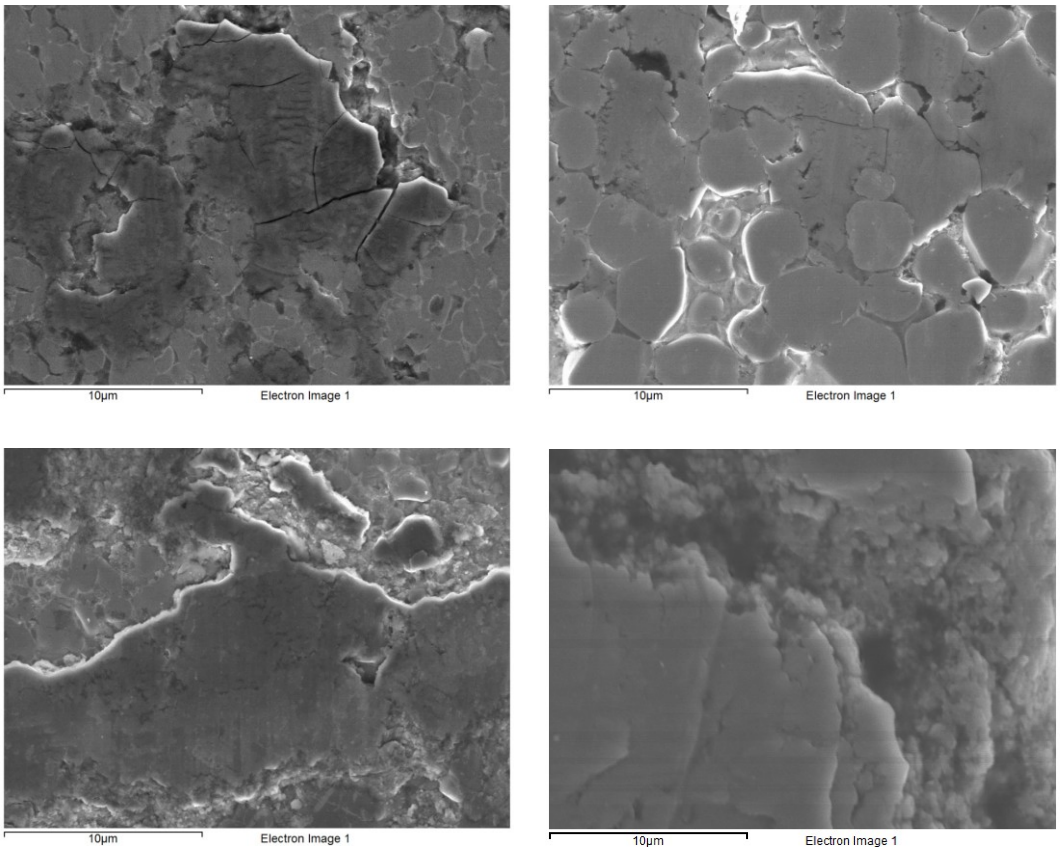

(c) (d)

Figure 5.14: EDS image of the fine- and coarse -grained TiC- 20 vol. % 316L cermets following wear testing (20N and 80N applied loads for 2 hours), showing an increase in the build-up of an oxide containing tribolayer generated at 20N (a, b) and 80N load (c, d) . (a) Fine-grained cermets at 20N (a) and 80N (c). (b) Coarse-grained cermets at 20N (b) and 80N (d). It is apparent that tribolayer generation increases with load, as confirmed by the chemical composition of the tribolayer shown in Table 5.2.

Table 5.2: Typical tribolayer composition (in wt %) determined using EDS analysis (from images of Figure 5.14), for fine and coarse grained TiC-20 vol. % 316L cermets, after sliding for 2 hours under 20 and 80N load.

	Fine-grained cermets		Coarse-grained cermets	
Element (line)	Applied load	Applied load	Applied load	Applied load
	20N	80N	20N	80N
C(K)	11.46	7.02	11.63	10.63
O(K)	22.44	31.92	21.23	33.12
Ti(K)	43.99	35.32	51.52	33.3
Cr(K)	3.11	3.84	1.71	2.13
Fe(L)	14.83	15.93	9.42	15.69
Ni(L)	1.58	2.06	1.31	1.98
Mo(L)	0.15	0.5	0.16	0.27
W(M)	2.23	3.18	2.79	2.64

Both fine- and coarse-grained cermets showed an improvement in wear resistance with an increase in TiC content which is in agreement with prior wear studies on TiC based cermets [30, 55, 68, 127-128, 160]. Fine-grained cermets also showed superior wear resistance than coarse grained cermets, which mirrors observations of other related studies on WC-Co materials [72, 76-77].

5.5 Conclusions

Melt-infiltration techniques have been employed to develop high density fine- and coarse-grained TiC-316L cermets, and their hardness, indentation fracture resistance, and dry reciprocating wear behaviour have been assessed. The following conclusions can be drawn from the experimental study:

(1) Both fine-and coarse-grained cermets showed an improvement in hardness with an increase in TiC content, with the fine-grained cermets having superior hardness.

(2) Both fine- and coarse-grained cermets showed an improvement in IFR with an increase in steel binder content, with the coarse grained cermets showing superior IFR.

(3) Fine-grained cermets showed superior wear resistance to coarse-grained cermet and, the wear resistance for both fine and coarse grained cermets increases with a decrease in the load and binder content.

(4) The is no clear dependence of COF with grain size, but there but there is slight increase with binder content for both fine and coarse grained cermets.

(5) The formation of thick oxide films (tribolayer) increases with load, and to a lesser extent with binder content, which is attributed to high levels of mechanical attrition of the third-body particles during reciprocating wear, such that new surfaces are continuously being created as the particle size is refined.

(6) The specific wear rates of fine-and coarse-grained cermets were typically in the range of 10^{-7} to 10^{-6} mm^3/Nm, depending on both the cermet composition (i.e. 316L content) and applied load. These values compared favorably with data presented for other TiC- and WC-based cermets found in the open literature.

(7) The dominant wear mechanisms in both the fine- and coarse-grained TiC-316L cermets are 2-body and 3-body abrasive wear, combined with an adhesive wear and tribo-chemical mechanism (formation of tribolayer).

(8) Based on the microstructural observations, it can be stated that although both fine- and coarse- grained cermets showed evidence of binder extrusion, the difference in wear mechanisms observed between the two cermets is based on the degree of binder deformation, which is more pronounced for coarse- grained rather than fine-grained cermets.

5.6 Acknowledgements

The authors would like to thank Petroleum Research Atlantic Canada (PRAC) and the Natural Sciences and Engineering Research Council of Canada (NSERC) for financial support of this study. The Canada Foundation for Innovation, the Atlantic Innovation Fund, and other partners who helped fund the Facilities for Materials Characterisation, managed by the Dalhousie University Institute for Materials Research, are also gratefully acknowledged. The authors would also like to thank Dean Grijm and Patricia Scallion for technical assistance.

6 Corrosion Behaviour of TiC-304L Stainless Steel Cermets in a Synthetic Saline Solution

Chukwuma C. Onuoha, Georges J. Kipouros, Zoheir N. Farhat and Kevin P. Plucknett*

Dalhousie University, 1360 Barrington Street, Materials Engineering Program, Department of Process Engineering and Applied Science, B3H 4R2, Nova Scotia, Canada

Status: Submitted to Journal of Corrosion Science 2013

6.1 ABSTRACT

In the present study, novel TiC-304L stainless steel cermets have been evaluated as potential materials for use in aqueous corrosion environments. A range of electrochemical techniques has been applied in order to study the corrosion response in a NaCl aqueous solution. Corroded samples were characterised using SEM and XRD. Post-corrosion solutions were also analysed by ICP-OES to determine the dissolved solute ions in the solution. It is shown that by increasing the steel binder content the corrosion resistance of the cermets decreases, which is related to the preferential dissolution of the metal binder, while the TiC ceramic remains largely unaffected.

Keywords: Ceramic composites, Electrochemical characterisation, Polarisation testing, Potentiostatic testing, SEM, ICP-OES

*Contact author email: kevin.plucknett@dal.ca

6.2 Introduction

Ceramic-metal composites, or cermets, are important materials for applications that require good wear and corrosion resistance, and are consequently viewed as promising candidates in a variety of petroleum sector applications, for example as coatings for erosion/corrosion protection, cutting bits, pump seals, etc [10, 11, 34, 54, 68, 162]. In particular, cermets based on titanium carbide (TiC) matrices have received considerable attention due to their excellent combination of properties [23, 163-165]. However, while the mechanical and tribological properties of TiC-based cermets have been relatively widely studied, limited research has been conducted to evaluate the ability of these materials to withstand aqueous corrosion. It has been shown that TiC behaves similarly to pure titanium, in that there is formation of a passive titanium dioxide (TiO_2) protective oxide layer, which aids in slowing the progression of corrosion [166].

Cermet development requires the use of an appropriate metallic binder, and stainless steels have been shown to offer some potential for use in TiC-based cermets [30, 55, 123, 167]. In spite of the intrinsic corrosion resistance of stainless steels in seawater, due to ability to form a passive layer, some researchers have reported a decrease in corrosion resistance by increasing the amount of metal binder in ceramic metallic composites [91, 168]. Many single-phase ceramics are known to be highly resistant to corrosion [12, 23, 93, 163, 164], but because of the presence of the metallic binder phase, cermets are often less resistant in comparison [91]. This can be attributed to the preferential dissolution of the metal binder, and potentially a galvanic effect between the component materials, since the binder and ceramic base material typically exhibit differing galvanic potentials.

Several researchers have studied the aqueous electrochemical response of a range of cermet systems, and it is generally indicated that the binder metallic phase affects the corrosion response due to its selective dissolution [8, 58, 94, 169-174], while the ceramic phase remains relatively unaffected. For example, in tungsten carbide-cobalt (WC-Co) 'hardmetals' a residual WC skeleton is formed, which eventually becomes unstable, leading to loss of the WC grains after dissolution of the surrounding Co binder [169, 170]. Cermets are heterogeneous materials, which can therefore suffer galvanic corrosion. Aggressive media preferably attack the metallic binder while the ceramic phase, such as WC, remains largely immune. This is because of a higher reduction potential of WC when compared to the binder. After dissolution of the binder, the micron or sub-micron sized WC grains are no longer strongly adhered within the composite, which leads to formation of a skeleton of WC that has almost no tensile strength or wear resistance [93]. In acidic media, WC has an electrochemical character that is more

noble than Co, and consequently corrosion generally progresses by oxidation of the binder phase, which is expected to be followed by loss of the WC grains [58].

As noted earlier, to date limited research has been conducted to assess the corrosion behaviour of TiC based cermets. Previous studies of TiC-steel composites have mainly focused on the variation of the wear properties [55]. However, in order to design a material that would have superior wear *and* corrosion resistance in a seawater environment, the corrosion behaviour of TiC based cermets needs to be assessed. Wu and colleagues investigated the corrosion behaviour of 304-grade stainless steel, reinforced with TiC particles, in a 5 wt. % HCl aqueous solution [95]. They demonstrated that the addition of TiC to the steel did not result in rapid pit propagation, but a high corrosion rate was maintained throughout the whole immersion period. Addition of 6 wt. % TiC into the steel increased the corrosion rate slightly, compared with a 2 wt. % TiC addition, due to an increase in both the TiC particle and Cr-rich carbide concentration, which consequently increased galvanic corrosion. In addition, high concentrations of corrosion pits were observed in the pure 304 stainless steel, while the pits were essentially absent following the addition of TiC. The steel matrix/TiC particle interfacial regions were observed to be preferred sites for pitting and/or dissolution.

Kubarsepp *et al.* studied the corrosion behaviour of TiC-(Fe,Cr,Ni) cermets in both sulphuric and phosphoric acid [175], and reported that there was selective dissolution of the metallic components in the two corrosive solutions, leaving an exposed carbide skeletal network on the sample surface after corrosion. In this instance the layer of corrosion product formed was firmly bound, and contains mainly carbide grains; the corrosion resistance was reported to increase with carbide phase content (i.e. reduced binder volume fraction). Similarly, Ren and colleagues reported an improved corrosion resistance for TiC-304 stainless steel coatings, when compared to 304 stainless steel alone, when tested in a 1M H_2SO_4 solution [176]. Qian and Xiong showed that the corrosion resistance of Ti(C,N)-based cermets is governed by binder corrosion when tested in a solution of 5% HNO_3 and 50% NaOH [177]. This is because the corrosion resistance of the cermets increased with decrease of Ni binder phase.

The aim of the present work is to study the corrosion behaviour of a family of novel TiC-304L stainless steel cermets, within a simulated sea water environment, using a combination of electrochemical measurements, weight loss investigation, and chemical and microstructural analysis. The corrosion response of the cermets has also been compared to the performance of a standard 304L stainless steel.

6.3 Experimental procedure

6.3.1 Sample Preparation and Characterisation

All TiC-based samples were prepared using 'as-received' TiC powder (Grade TiC-2012, Pacific Particulate Materials, Vancouver, BC), with a mean particle size of ~1.3 μm [96]. Samples were prepared using a simple melt-infiltration process. TiC preforms were prepared with a starting powder of ~7.5g of TiC, uniaxially pressed to a pressure of ~67 MPa in a steel die, giving disc-shaped pellets ~31.75 mm in diameter x ~4 mm thick. The samples were then bagged and further compacted by cold isostatic pressing at ~220 MPa. Following compaction, the TiC pellets were weighed and a known amount of -100 mesh steel powder (Lot #K19M09, Alfa Aesar, Ward Hill, MA, USA) was placed on top of the TiC preform to give nominal final binder contents from 10 to 30 vol. %. For melt-infiltration, the combined TiC/steel samples were sited on a layer of bubble alumina within an alumina crucible. Infiltration was conducted at 1500°C in a graphite resistance furnace (Materials Research Furnaces, Suncook, NH, USA), with heating and cooling rates of 10°C/min and 25°C/min respectively, under a dynamic vacuum of approximately 20 milliTorr. The sintering temperature was held for 60 minutes. The infiltrated cermets densities were then determined using the Archimedes immersion method in water.

In order to prepare samples for microstructural analysis and corrosion testing, they were initially ground flat using a coarse grit peripheral diamond grinding wheel, followed by further grinding and polishing using successively finer grades of diamond, starting with a 125 μm diamond pad and finishing with 0.25 μm diamond paste. Microstructural characterisation was conducted on the polished samples using both optical microscopy (Model BX-51, Olympus Corporation, Tokyo, Japan) and scanning electron microscopy (SEM; Model S-4700, Hitachi High Technologies, Tokyo Japan). Grain size measurements were obtained using the linear intercept method [178], from digital SEM images, where the mean intercept value is multiplied by a factor of 1.56.

6.3.2 Electrochemical Testing

The corrosion behaviour of the TiC-304L steel cermets was assessed in a simulated seawater environment, with a 3.5 wt% NaCl aqueous solution used as the electrolyte at room temperature, 23°C. A standard three-electrode flat cell configuration was employed, with the cermet sample acting as the working electrode (an exposed test area of $1cm^2$ was used), a platinum mesh as the counter electrode, and a saturated calomel electrode (SCE; 0.241 V versus a standard hydrogen electrode) as a reference

electrode. All the potential measurements throughout the corrosion studies will therefore be referred to the reference electrode. In order to compare the corrosion rates of the composites, a commercially sourced 304L stainless steel (Outokumpu Stainless Bar Inc., Richburg, SC, USA) was used as a baseline material. The nominal composition of 304L stainless steel is shown in Table 6.1.

Table 6.1: Typical 304L stainless steel alloy composition.

Alloy	**Cr**	**Ni**	**C**	**N**	**Mo**	**Mn**	**S**	**Ti**	**Fe**
304L	18.330	8.090	0.025	0.080	0.390	1.400	0.025	0.003	Bal.

Prior to potentiodynamic polarisation measurements, 4 hours of immersion was allowed to ensure steady-state conditions. For potentiodynamic polarisation experiments (EG&G Princeton Applied Research Potentiostat/Galvanostat Model 273, Princeton Applied Research, Oak Ridge, TN, USA), the potential was scanned from -0.75 to +3.5 V_{SCE} at a scan rate of 0.167 mVs^{-1}. The corrosion potentials (E_{corr}) and the corrosion current densities (I_{corr}) were estimated by using an instantaneous Tafel-type fit corrosion analysis software (CorrWare, Scribner Associates, Inc., Southern Pines, SC, USA). In the cyclic potentiodynamic polarisation test, a scan was initiated 4 hours after the specimen was immersed in the solution. The scan was initiated from the open circuit potential (OCP) to the point where a significant current increase was observed in the anodic direction. As the scan reached a user-programmed threshold current value and/or offset potential, it was reversed and the sample was then scanned in the cathodic (negative direction). When the reverse and forward scans intersect, the scan was discontinued. The Tafel-derived corrosion rate (mm/year) is then calculated by the formula [107]:

$$\text{Corrosion rate (mm/year)} = \frac{\left(3.27\times10^{-3}\right)\times I_{corr}\times W}{D} \qquad \text{Equation 3.1}$$

where W is the equivalent weight of alloy, D is the density of alloy (in g/cm^3), and I_{corr} (in μAcm^{-2}) is the corrosion current density of the specimen extrapolated from the Tafel polarisation plot.

For comparative purposes, a direct measure of corrosion loss was also conducted. In this instance the cermet samples were weighed before and after corrosion, and the measured weight loss was then used to calculate the corrosion rate using the formula [37]:

$$\text{Corrosion rate (mm/year)} = \frac{87.6\times M}{T\times A\times D} \qquad \text{Equation 3.2}$$

where M is the weight loss (in g) after exposure time, T (in hours), and A (in cm^2) is the area of the exposed specimen.

After the potentiodynamic tests, microstructural evaluation of the corroded surfaces was carried out using optical microscopy, SEM, with associated energy dispersive x-ray spectroscopy (EDS). Following corrosion tests, the remaining solution contained within the electrochemical cell was assessed using inductively coupled plasma optical emission spectroscopy (ICP-OES; Varian Vista Pro (Radial View), Varian, Inc., Mulgrave, Australia) in order to determine the quantities of various metals that were present in solution after corrosion tests. This was conducted on both fine particulate material filtered from the solution and the resultant filtered solution. The samples were filtered using a Millipore vacuum system, with a 1.0 μm filter. The filtrate was analysed directly using ICP-OES. The filtered particulate residue was collected and dried at 105°C. The solid material was scraped off the filter, weighed, and dissolved in acids (HF, HNO_3, $HClO_4$) to dryness in Teflon beakers. The residue was then brought back into solution with HCl, made up to 100 ml in volumetric flasks, and analysed using ICP-OES.

6.4 Results and Discussion

6.4.1 Sample Analysis Following Melt Infiltration

As discussed in previous publications [55,123], the TiC-304L cermets were consistently prepared to in excess of 99 % of theoretical density, thus confirming that there was essentially no surface connected porosity that could affect the corrosion testing. Figure 6.1 demonstrates the typical microstructures for the TiC cermets prepared with 10-30 vol. % 304L stainless steel binder, observed using both optical microscopy and SEM. It is apparent that the high sintered densities of these cermets are confirmed by SEM, and there is good homogeneity of the microstructure, with little evidence of anomalous grain growth. The mean grain size, calculated using the linear intercept method, was broadly consistent for each composition at ~6 μm [55].

(a)

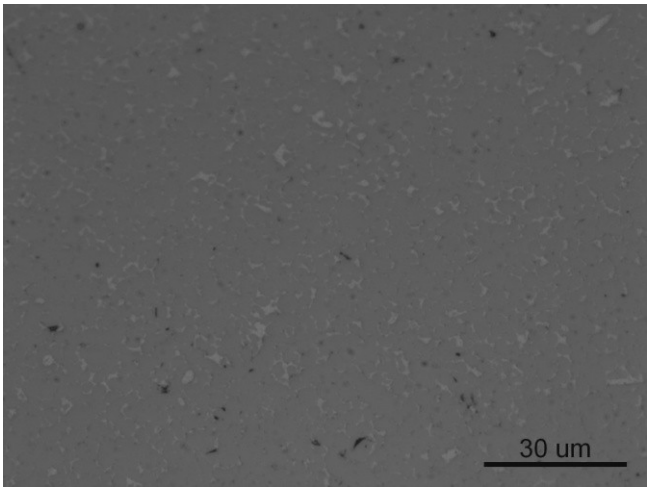
30 um

(b)

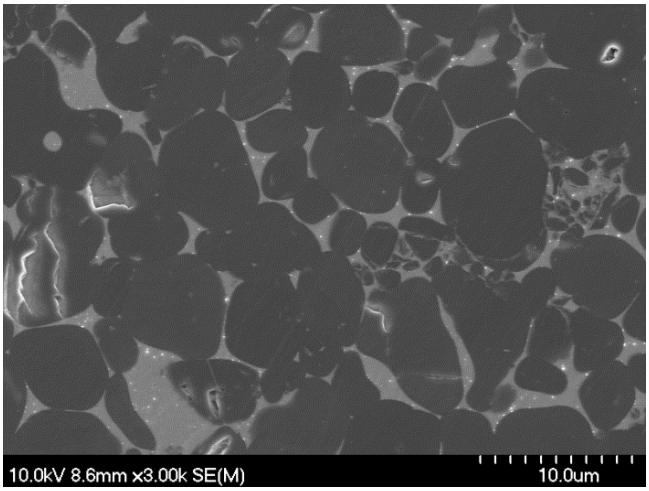
10.0kV 8.6mm x3.00k SE(M)
10.0um

(c)

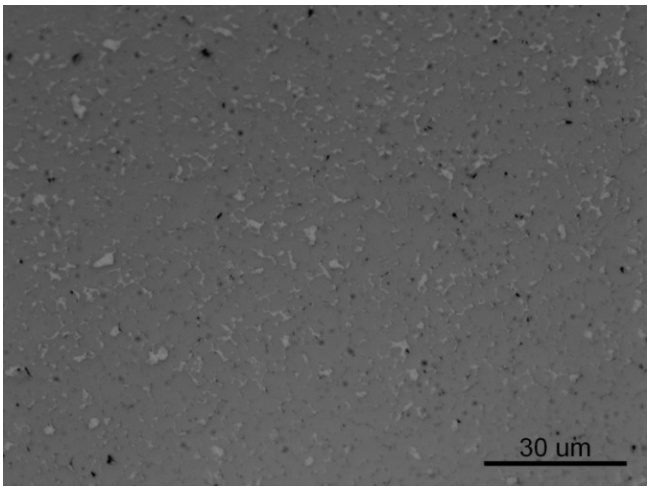
30 um

(d)

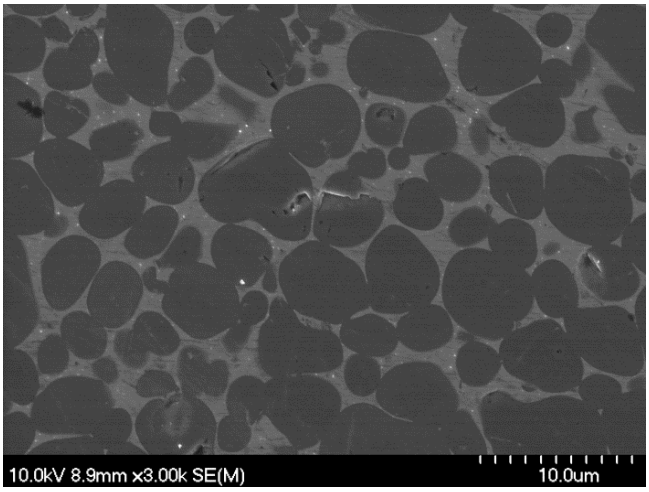
10.0kV 8.9mm x3.00k SE(M)
10.0um

(e) (f)

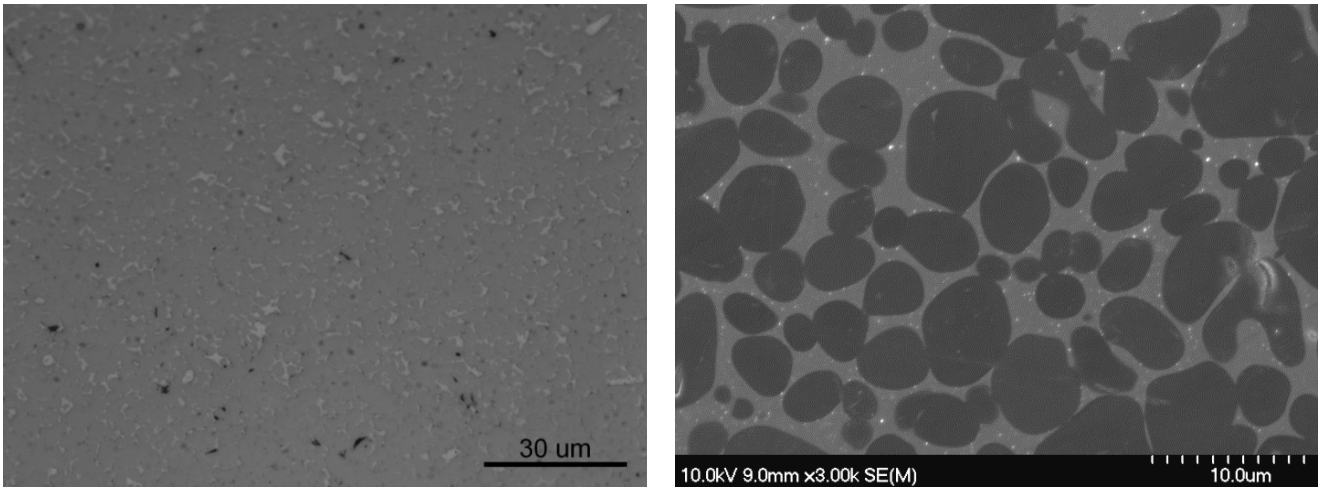

Figure 6.1: Optical (a,c,e) and SEM images (b,d,f) show a uniform distribution of TiC in the 304L steel binder, and good wetting/infiltration of the melt during processing: (a,b), 10 vol. % 304L, (c,d) 20 vol. % 304L, and (e,f) 30 vol. % 304L.

6.4.2 Electrochemical Measurements

From the plot of OCP against time, as shown in Figure 6.2, it can be seen that by increasing the 304L steel binder content, the OCP becomes more negative. The relative parameters determined from the OCP analysis for each of the cermet compositions, and the 304L steel alone, is presented in Table 6.2.

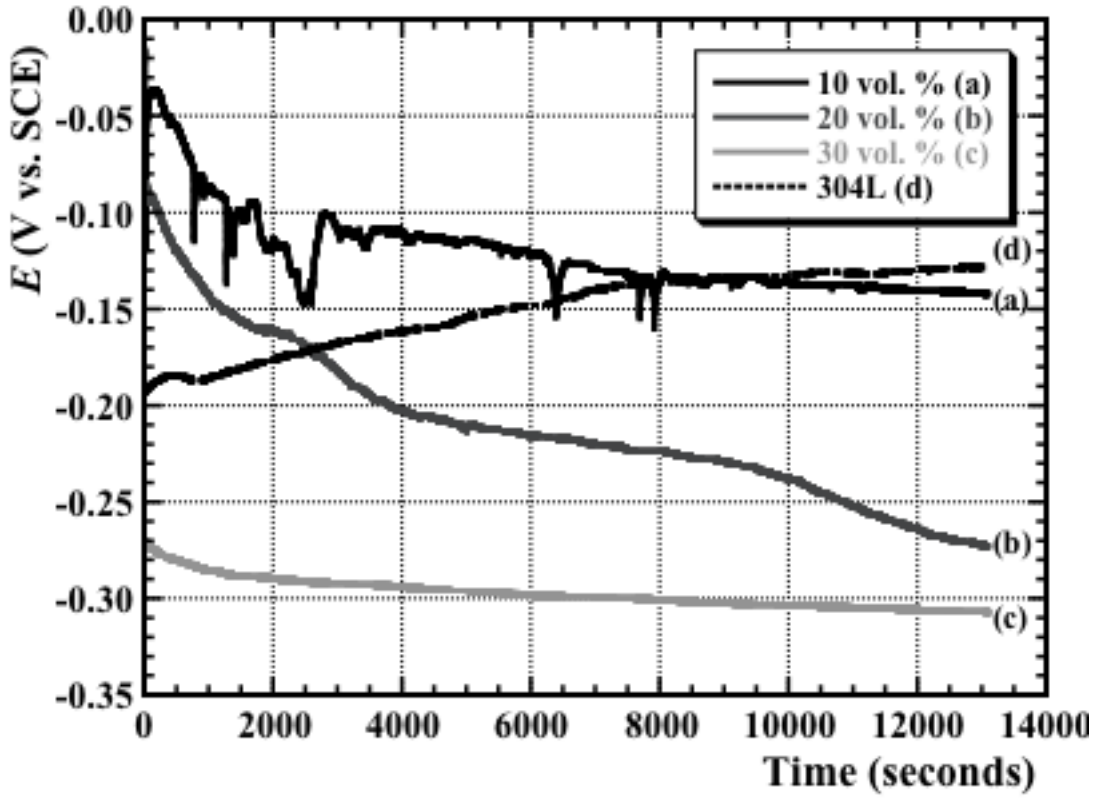

Figure 6.2: Open circuit potential vs. time of cermets and 304L stainless steel.

Table 6.2: Open circuit potentials for the TiC-304L cermets and pure 304L stainless steel.

Sample	**OCP (V vs. SCE)**[1]
TiC-10 vol. % 304L	-0.224 (0.039)
TiC-20 vol. % 304L	-0.260 (0.027)
TiC-30 vol. % 304L	-0.278 (0.031)
304L stainless steel	-0.105 (0.021)

[1]Values are mean (standard deviation); N = 10

The OCP is also called the natural potential, and can be used to determine the effect of alloying elements on corrosion resistance. In this sense, as the value of OCP increases, or becomes more noble, the passivity of the alloy also increases. As a consequence, through measurement of the OCP, the ability of an alloy's passive layer to protect itself (at least temporarily) from corrosion can be assessed.

Hence the more noble the OCP is, the better the passivation that the material exhibits [179]. Conversely, if the OCP is more 'active' in character, it may indicate the likely de-passivation characteristics of the material [179]. It can be seen from Figure 6.2 that the OCP of 304L stainless steel alone is more noble than for the cermets, indicating a better corrosion resistance of the pure steel in direct comparison.

Figure 6.3 shows a comparison of the Tafel curves obtained for the TiC-304L cermets with the pure 304L stainless steel, with accompanying extrapolation analysis from these curves shown in Table 6.3.

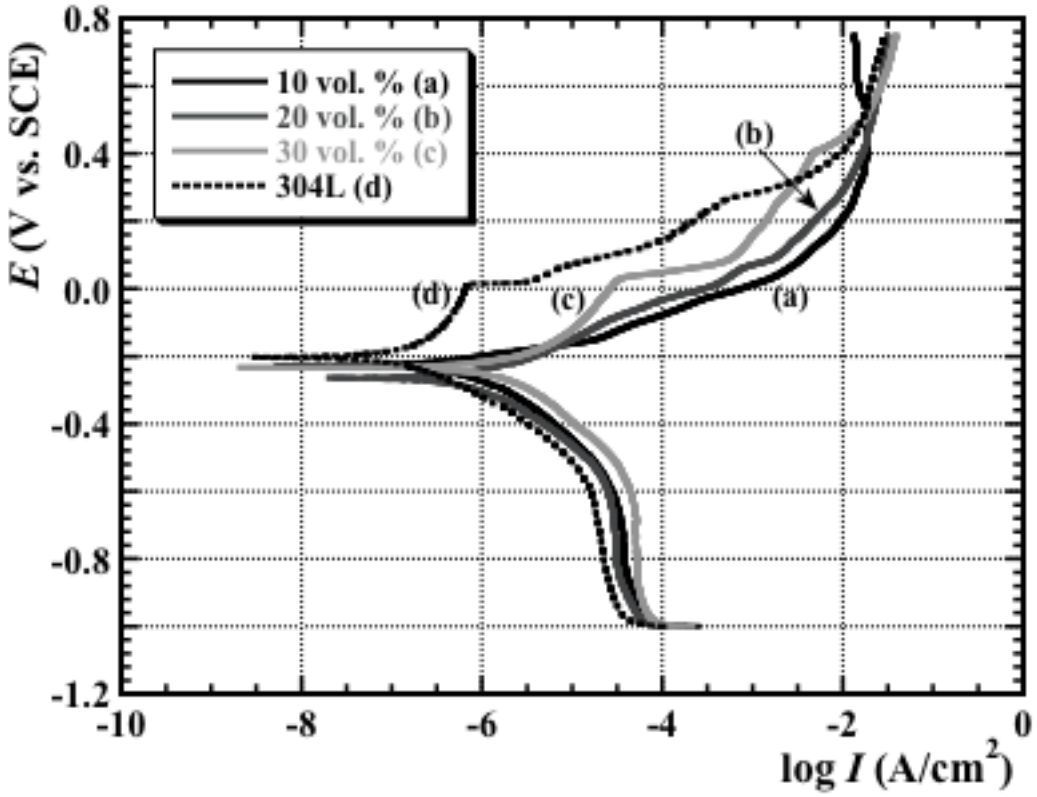

Figure 6.3: Tafel plot of TiC-304L steel cermets and 304L stainless steel.

As it can be seen, the corrosion current density (I_{corr}) increases with an increase in the steel binder content. This is related to selective dissolution of the binder. The effects of binder content upon the calculated corrosion rate (in mm/year), determined using Equation 6.1, following the Tafel experiments are shown in Figure 6.4.

Table 6.3: Extrapolated E_{corr} and I_{corr} after corrosion experiment.

Sample	E_{corr} (V vs. SCE)[1]	I_{corr} (μA/cm^2)[1]
TiC-10 vol. % 304L	-0.210 (0.047)	0.576 (0.206)
TiC-20 vol. % 304L	-0.288 (0.023)	0.922 (0.033)
TiC-30 vol. % 304L	-0.264 (0.029)	1.440 (0.235)
304L stainless steel	-0.204 (0.023)	0.221 (0.013)

[1]Values are mean (standard deviation); N = 4

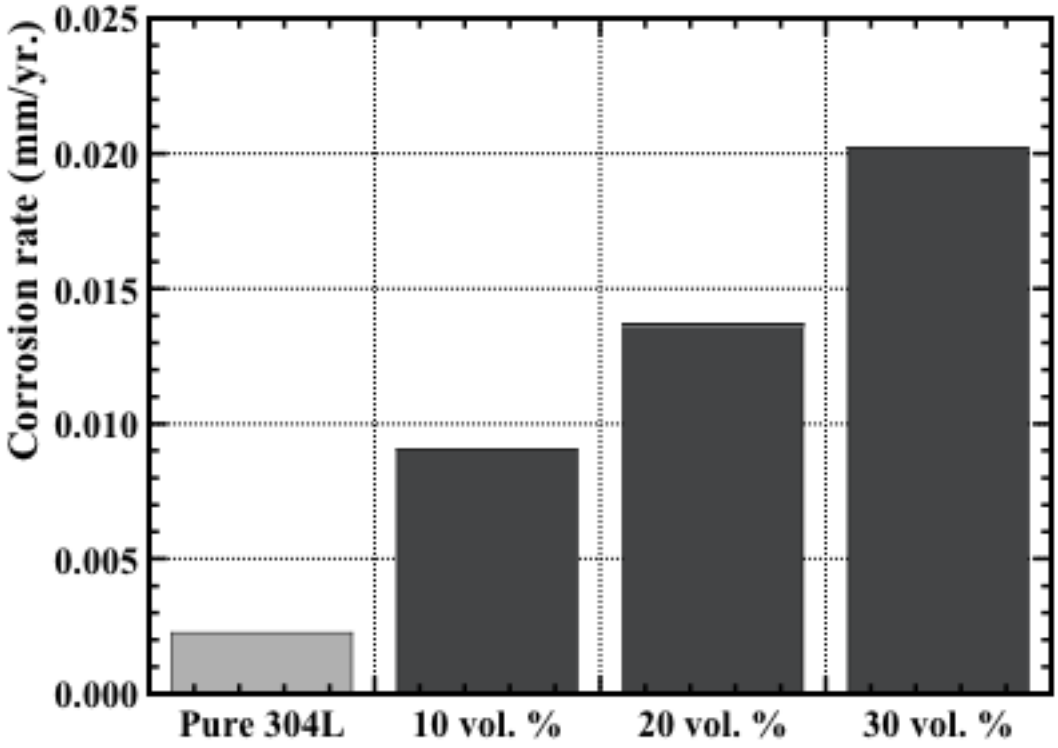

Figure 6.4: Corrosion rate vs. binder volume content (%) after Tafel extrapolation.

As it can be seen, the corrosion rate increases with the steel binder content, while the 304L stainless steel alone has a better corrosion resistance than the cermets. This general observation can be related to the preferential dissolution of the metal binder, which is discussed in more detail in *Sections 6.4.3* and *6.4.4*. The loss of corrosion resistance with increase in steel binder content can be attributed to a galvanic effect, due to the incorporation of two dissimilar materials in the cermet microstructure (i.e. the TiC ceramic and 304L stainless steel) within a conducting electrolyte. The corrosion potential of

pure TiC in 3 wt. % NaCl is 0.28 V [180], which is more noble than the corrosion potential of 304L stainless steel in the present study with a similar electrolyte. It is believed that the difference in corrosion potentials between the ceramic phase, TiC, and the metallic phase, 304L stainless steel, in a conducting electrolyte will lead to galvanic activity at the interfaces, which makes cermets with greater steel binder content prone to more extensive dissolution, leading to an increase in corrosion rate.

For comparative purposes, a separate weight loss study was conducted on the cermets before and after corrosion, in order to determine the weight of material that was removed after the corrosion experiments. The corrosion rate calculated from weight loss following the potentiodynamic experiments is shown in Figure 6.5.

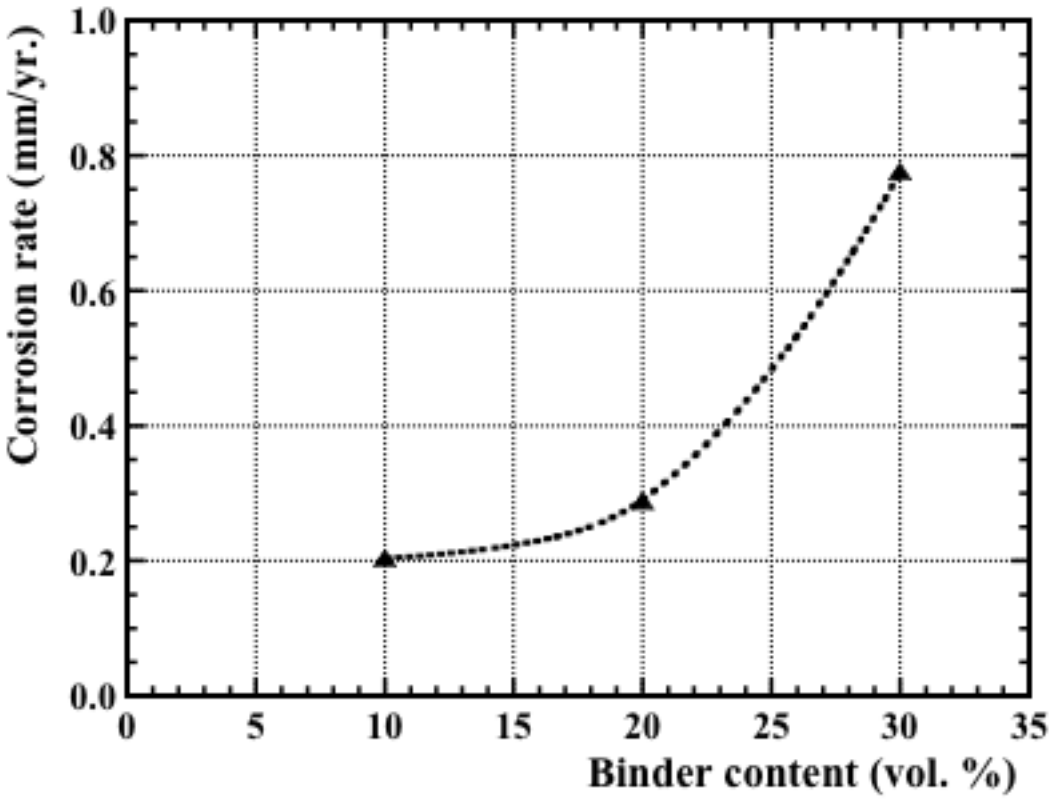

Figure 6.5: Corrosion rate by weight loss analysis after potentiodynamic polarization.

As it can be seen, the corrosion rate by weight loss increases with increase in steel binder content, in a manner similar to the Tafel derived data. The corrosion rate results obtained from both Tafel experiment and weight loss determination are in good agreement with the findings of Sacks [58], who studied the corrosion behaviour of WC-Co composites in tannic acid-sand electrolytes, and reported an increase in corrosion rate with increase in cobalt binder content. That work showed that there was a

preferential dissolution of the cobalt binder, while the WC grains retain their sharp facets and are effectively not attacked during the corrosion tests. Their interpretation was that the increase in corrosion rates with increase in cobalt content is related to binder oxidation in the corrosion medium. Effectively, this infers that the corrosion of cermets is governed primarily by metal binder oxidation (i.e. Co oxidation in the case of WC/Co). As a consequence, the more cobalt that is present, the more susceptible the metal is to attack, hence leading to higher corrosion rates, as indicated by Stern's rule [58, 92]. To further confirm this, other authors have also reported improved corrosion resistance with lowered binder content in their respective cermet systems [58, 94, 175]. The potentiodynamic curves of TiC-304L cermets are shown in Figure 6.6, and it can be seen that the critical current density and breakdown potentials increase with the steel binder content. This behaviour is similar to the observations of Sacks [58] for WC/Co, who reported an increase in critical current density with Co binder content.

It has been proposed that the corrosion behaviour of cermets is dependent of the electrochemical potential of the system [12]. At open-circuit conditions or under small applied potentials, the binder phase undergoes selective dissolution; while in the higher potential range the dissolution of the hard phase takes place [8, 94, 170, 172, 174, 181-182]. The phenomenon of pseudo-passivity has been reported to exhibit itself at high electrochemical potentials, where the passive current density is approximately an order of magnitude higher than true passively behaving materials [8, 94, 172] . The pseudo-passive state is reported to occur when the presence of non-adherent, but diffusion-inhibiting, corrosion products lead to a limitation of the current density. In contrast to real passive conditions, these current densities consequently remain comparatively high [8, 12, 94, 172]. Similar features, relating to pseudo-passive behaviour, are believed to be exhibited in the present TiC-steel cermets. From Figure 6.6, it can be seen that the potentiodynamic curve has active, passive and transpassive regions, but the passive current densities are relatively high. The TiC cermets have pseudo-passive passive current densities of approximately 0.015, 0.028 and 0.057 A cm^{-2}, for stainless steel contents of 10, 20 and 30 vol. %, respectively. In comparison, the passive current density for a truly passive behaving material is reported to be around 10 $\mu A\ cm^{-2}$ [8, 172, 183], and any material exhibiting a passive current that is several orders of magnitude higher than this is regarded as exhibiting pseudo-passive behaviour [8, 94, 172]. The passive current densities of the present cermets are all approximately four orders of magnitude greater than for a truly passive material, indicating that pseudo-passivity is likely to be occurring for the TiC-stainless steel cermets.

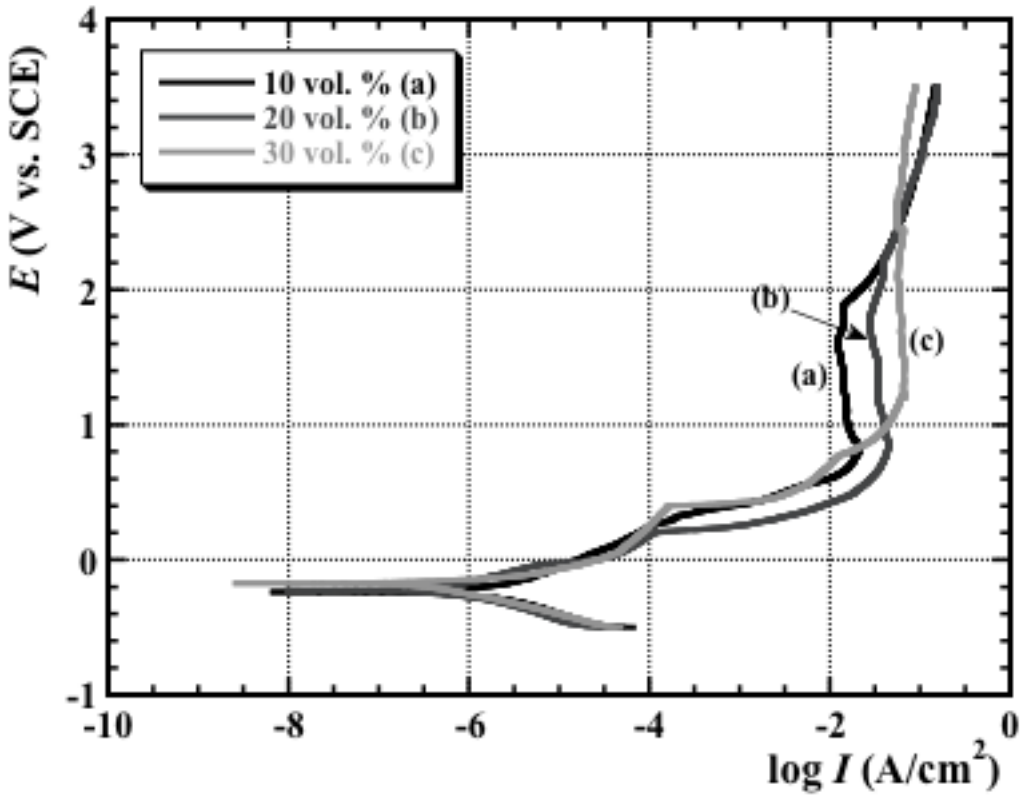

Figure 6.6: Combined potentiodynamic polarization plots for each TiC 10-30 vol. % 304L cermets.

The reason for a very high current in the pseudo-passive region is attributed to the formation of a weak and poorly-adherent surface oxide, which will also exhibit cracks and/or porosity, thereby allowing the penetration of the aggressive electrolyte [8]. It should be stated that the definition of pseudo-passivity can lead to some confusion on the phenomena description, and this is further investigated in our recent study [155]. The cyclic polarisation curves obtained for both the TiC-304L cermets and the pure 304L steel are presented in Figure 6.7. It is apparent for both the cermets and the 304L stainless steel that they have a protection potential, E_{prot}, that is more negative than the pitting potential, E_{pit}, indicating that the likelihood of localised corrosion is relatively high. The pitting potential and repassivation (or protection potential) are the most important electrochemical parameters in the cyclic potentiodynamic polarisation curves, as shown in Figure 6.7. The values of E_{pit} and E_{prot} value can then be used to determine the pitting corrosion susceptibility, following:

$$\Delta E = E_{pit} - E_{prot} \qquad \text{Equation 6.3}$$

As can be seen from Equation 6.3, an increase of E_{pit} improves the resistance of the materials to pitting corrosion. It has also been demonstrated that a decrease of ΔE provides a higher level of ability towards self-healing of the passive films [95].

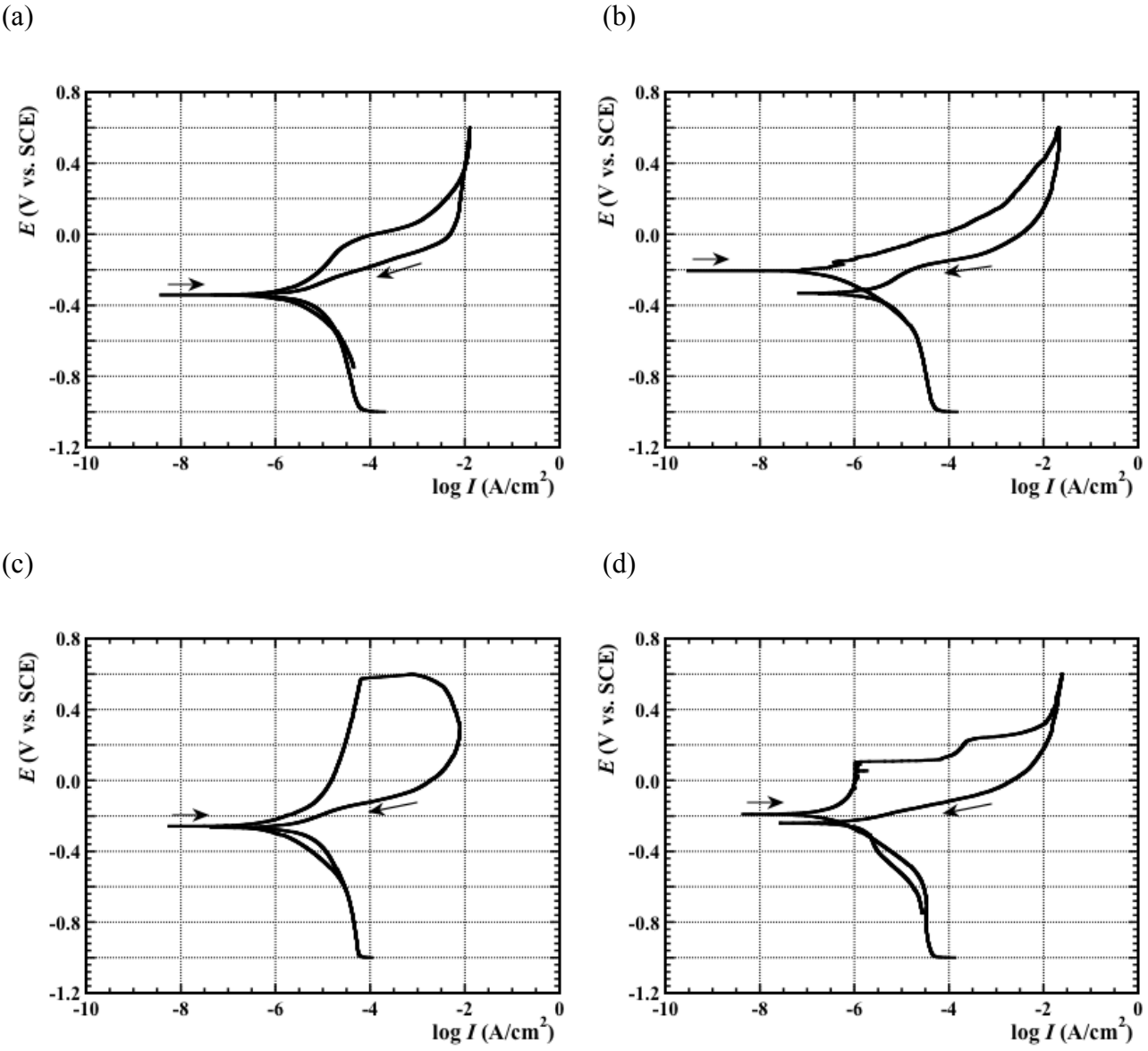

Figure 6.7: Cyclic polarization of TiC-304L cermets and 304L stainless steel: (a) TiC with 10 vol. 304L, (b) TiC with 20 vol. % 304L, (c) TiC with 30 vol. % 304L, and (d) 304L stainless steel.

From Table 6.4, and Figure 6.7, it can be seen that none of the cermets or the 304L steel exhibited a more noble protection potential when compared to the pitting potential. Since all of the protection potentials are lower than the pitting potential, localised corrosion is possible. However, since only the TiC-10% 304L cermet has a measurable value for ΔE, this indicates that it has the best self-healing

capability of the passive film. Based on these observations, it can be stated that the TiC-10% 304L cermet has the lowest susceptibility to pitting corrosion and the highest level of self-healing ability for all of the examined cermets.

Table 6.4: Extrapolation of the pitting potential from cyclic polarisation curves.

Sample	E_{pit} (V_{SCE})	E_{prot} (V_{SCE})	E_{pit} - E_{prot} (V_{SCE})
TiC-10 vol. % 304L	-0.068	-0.339	0.271
TiC-20 vol. % 304L	0.150	No protection	NA
TiC-30 vol. % 304L	0.567	No protection	NA
304L stainless steel	0.101	No protection	NA

As shown in Table 6.4, for the cermets, the pitting potential increases with steel binder content. It appears that no other cyclic polarisation studies on TiC-steel based cermets have been reported to compare the results of the present study.

In order to further confirm the probability of localised corrosion and the observations from cyclic polarisation, potentiostatic polarisation was also conducted at an applied voltage above the pitting potential for all the studied materials, as shown in Figure 6.8. The applied voltage is 0.10725V, 0.02075V, 0.2475V, and 0.575V for 304L, 10, 20 and 30 vol. % steel binder. Generally, the likelihood of localised corrosion is confirmed, depending on the nature of the current response after potentiostatic polarisation tests above the pitting potential. If the current decreases with time, it means that the pits would have been repassivated, leading to a drop in current. Conversely, an increase in current with time confirms the tendency of localised corrosion, as is clearly seen in Figure 6.8 for both the cermets and the 304L stainless steel. It can also be seen that although the TiC-10% 304L cermets showed an increase in current with time, the effect is relatively small, highlighting the superior capacity of this composition towards self healing of the passive film when compared to the other cermets studied. The large oscillations observed for the pure 304L stainless steel present evidence of localised corrosion and an aggressive attack by chloride ions on the passive film formed [184].

(a)

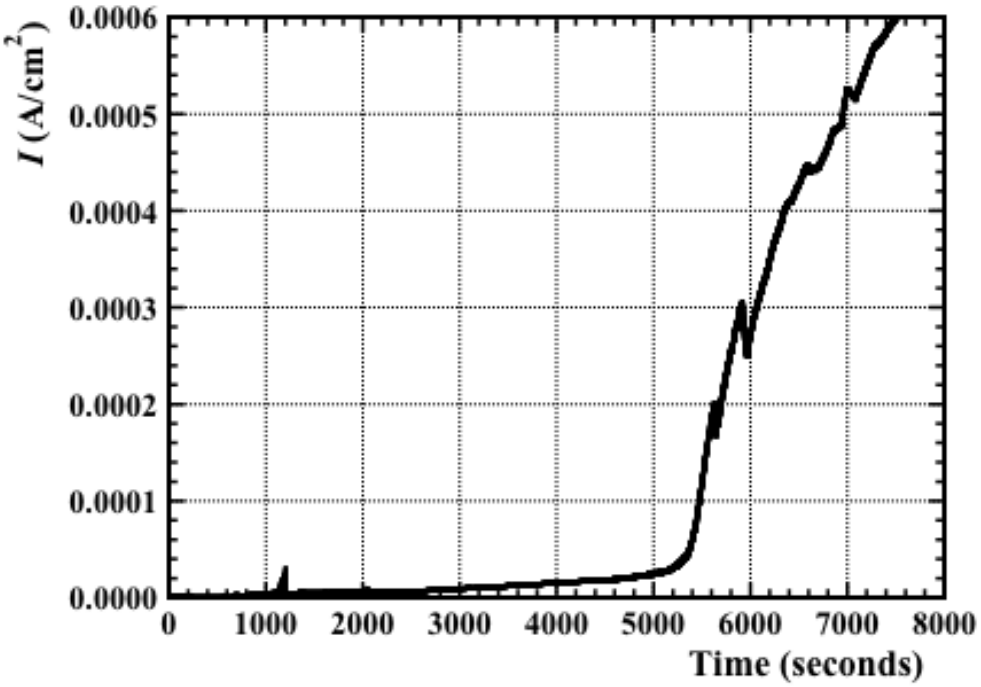

(b)

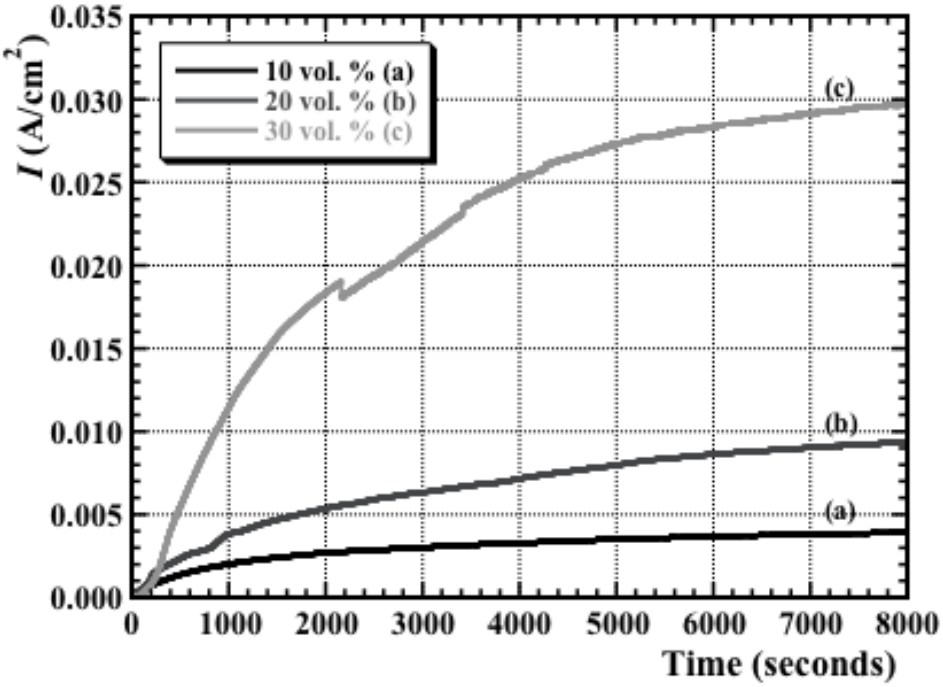

Figure 6.8: Potentiostatic polarization of the cermets and 304L stainless steel above the pitting potential. (a) 304L stainless steel, (b) TiC-304L cermets.

6.4.3 Post Corrosion Chemical Analysis

After the corrosion experiments, the remaining solution from the electrochemical cell was analysed using ICP-OES, in order to determine both the solids (in terms of fine particulate matter) and ions present in the solution, as demonstrated in Figure 6.9 and Figure 6.10, respectively.

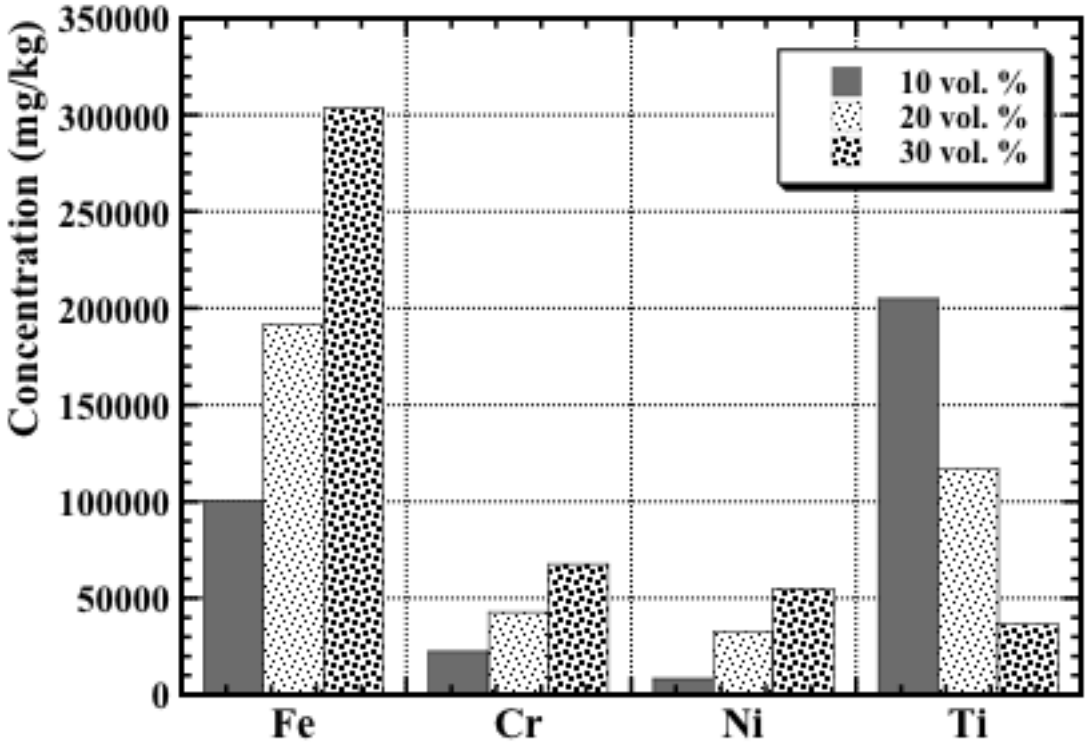

Figure 6.9: ICP results of the filtered particulate material removed from the solution remaining in the flat cell upon completion of corrosion testing.

The solid constituents were first removed by filtration from the retained solution, prior to ICP-OES testing. As shown in Figure 6.9, with an increasing binder content there are increasing quantities of the steel binder apparent following corrosion testing (i.e. Fe, Ni, and Cr), with a concurrently decreasing amount of Ti. An increase in the steel binder constituents suggests that the preferential attack of the 304L stainless steel binder progressed nominally linearly with increasing binder content.

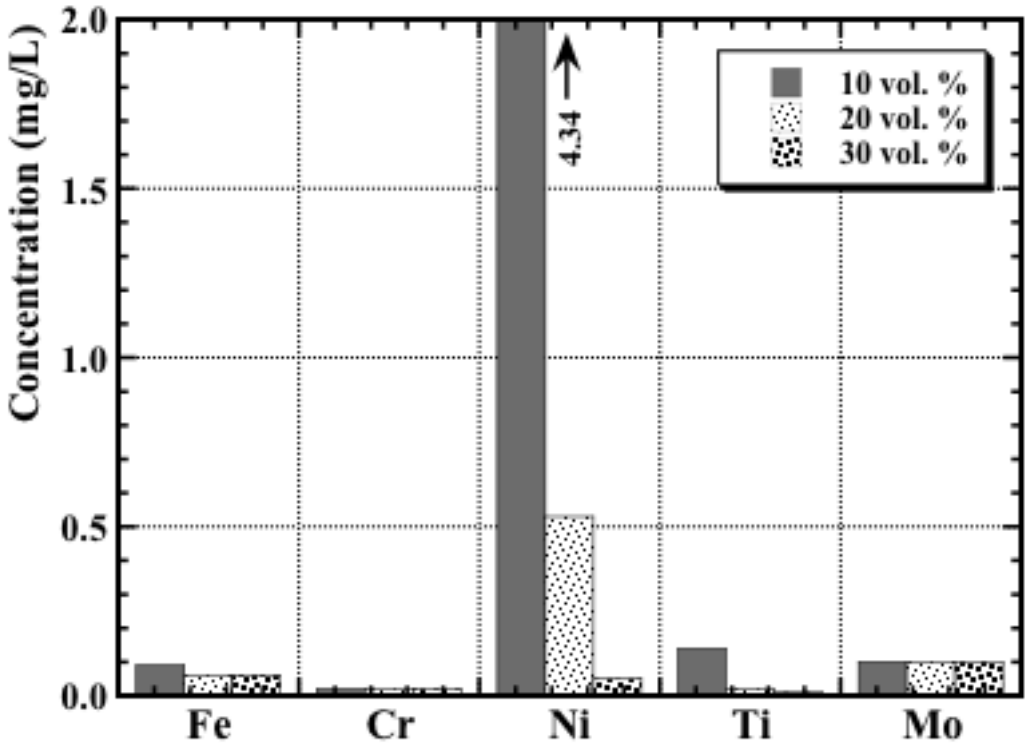

Figure 6.10: ICP analysis of the filtered solution remaining in flat cell upon completion of corrosion testing, showing the metal ions present in the solution (i.e. after removal of any fine particulate material).

In terms of the ion content within the filtered solution, as shown in Figure 6.10, it is apparent that it is predominantly Ni, with relatively minor amounts of the other cermet elements. The loss of Ni ions in the solutions could explain the reason while the corrosion resistance of the cermets is lower when compared to the pure 304L stainless steel. The absence of Fe ions from the solution could potentially indicate precipitation of Fe in some form. This would then lead to a higher content in the solids component, relative to Ni, as the pH of the NaCl solution is around 5.3-5.8, which is fairly close to the highly acidic corrosive pH range (0-4) and justifies the Fe precipitation [216].

In addition to the analysis of the corrosion medium after electrochemical testing, the influence of the tests on the cermet composition was also analysed. Figure 6.11 presents EDS data from both before and after corrosion. As it can be seen, the amount of TiC present increases after corrosion, which is actually an indication of removal of the steel metal binder from between the carbide grains. At the lowest binder content, the dissolution rate is relatively limited, and it increases with binder volume fraction, giving rise to the appearance of an increasing amount of TiC being present.

(a)

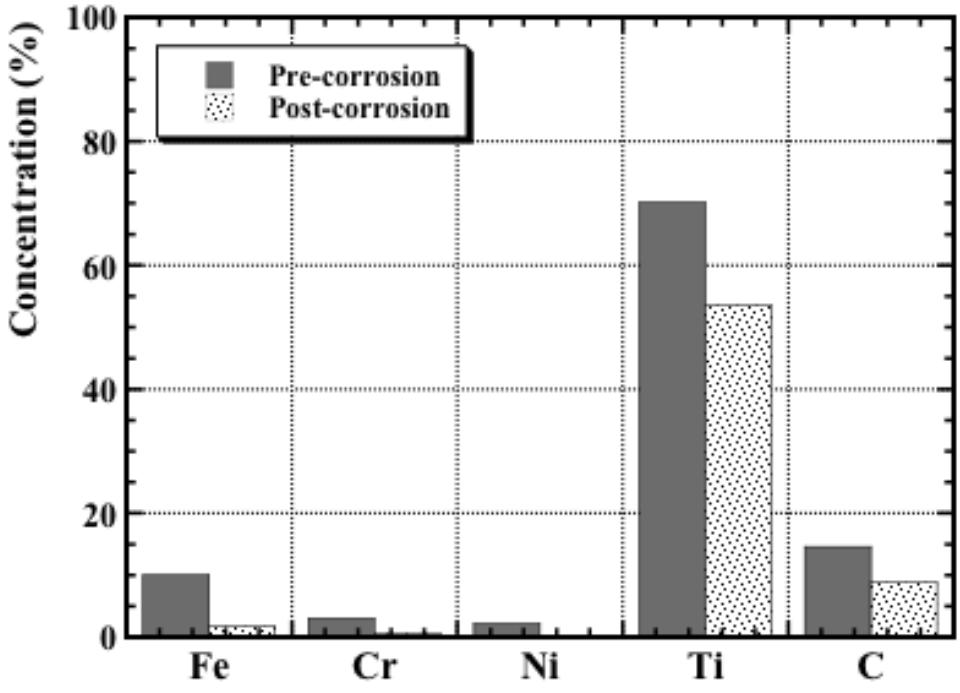
Concentration (%)
100
80
60
40
20
0
Pre-corrosion
Post-corrosion
Fe
Cr
Ni
Ti
C

(b)

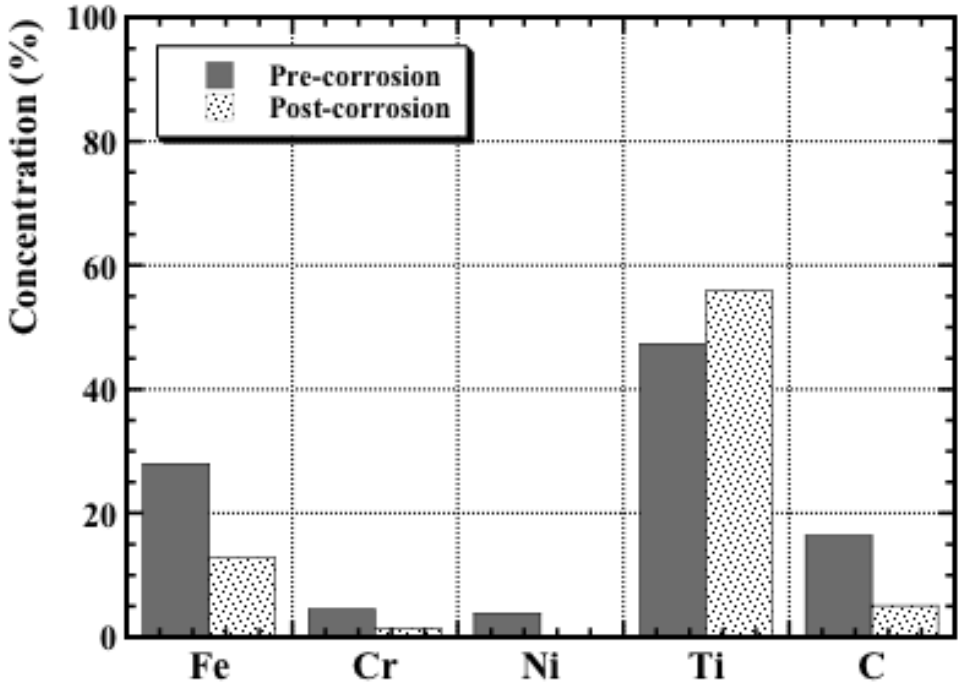
Concentration (%)
100
80
60
40
20
0
Pre-corrosion
Post-corrosion
Fe
Cr
Ni
Ti
C

(c)

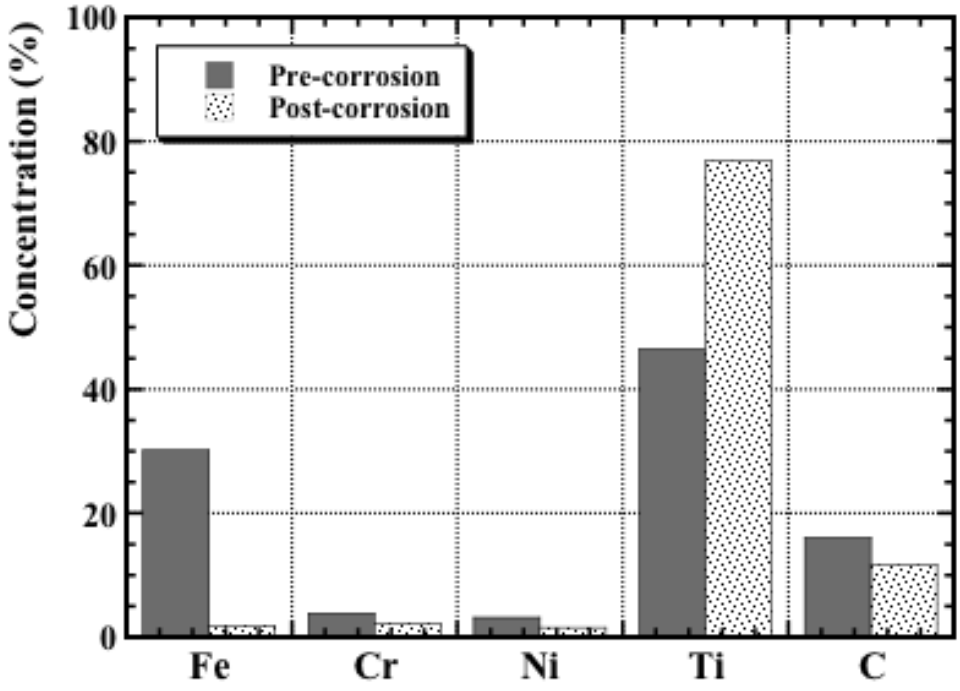

Figure 6.11: EDS elemental analysis of the sample surfaces following corrosion testing: (a) TiC with 10 vol. % 304L, (b)TiC with 20 vol. % 304L, and (c) TiC with 30 vol. % 304L.

At the highest steel binder content, the post corrosion analysis infers that essentially all of the metal binder has been removed, and only TiC (and the surrounding void space) remains. These results are therefore in agreement with ICP data, in that with increasing steel binder content comes an accelerated corrosion behaviour, and hence more Fe, Cr and Ni are liberated from the cermet and remain in solution while the TiC matrix is largely intact. It should be stressed that in terms of the overall concentration, there is also an increasing O component following corrosion testing (not shown in Figure 6.11).

6.4.4 Post-Corrosion Microstructural Characterisation

From Figure 6.12, it can be seen that there is clear evidence of pitting on the pure 304L stainless steel samples after the Tafel polarisation experiments. However, there is less of an effect on the cermets, although the TiC-30 vol. % 304L samples showed evidence of preferential binder dissolution. It can also be seen that the cermets with lower binder contents (i.e. 10 and 20 vol. % 304L) have a less pronounced corrosion attack after the polarisation experiments. The lower extent of corrosion for these

reduced binder content cermets, when compared to the 304L stainless steel, could suggest that the presence of adherent TiO_2 contributed to the stability of the passive film for the cermets as observed in our recent study [155].

(a) (b)

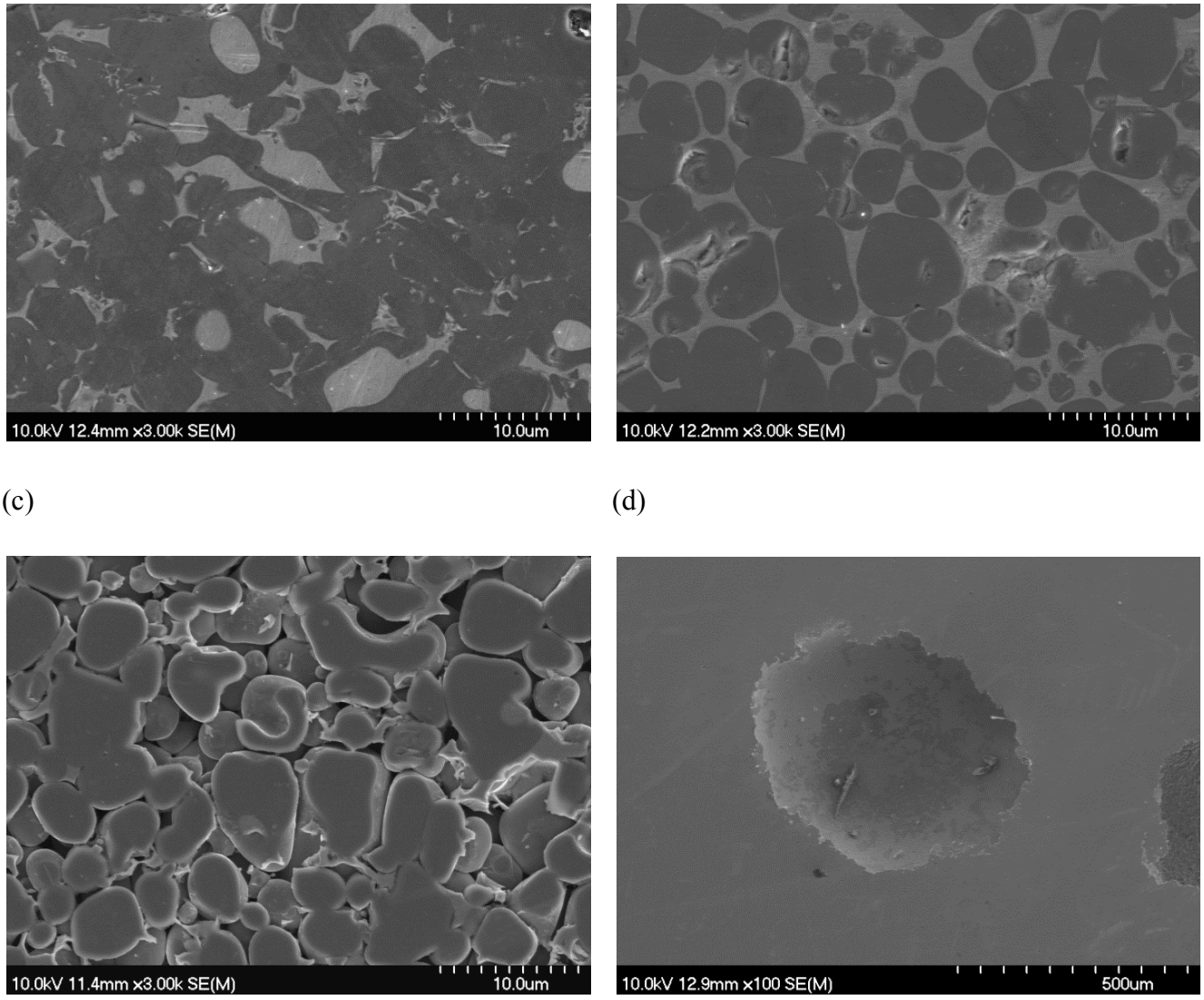

(c) (d)

Figure 6.12: SEM images showing corroded surface of TiC-304L cermets and 304L stainless steel showing heavy pitting on the 304L steel and less substantial effects on the cermets after the Tafel experiments (scanned from -1.0 to 0.7V): (a) TiC with 10 vol. 304L, (b) TiC with 20 vol. % 304L, (c) TiC with 30 vol. % 304L, and (d) 304L stainless steel.

Example SEM images of the TiC-304L cermets following potentiodynamic corrosion are shown in Figure 6.13. The appearance of preferential dissolution of the metal binder is clear, the extent of which

increases with binder content, while the TiC grains appear largely unaffected. This observation confirms the prior results that the corrosion resistance of the cermets decreases with an increase in the steel binder content. A further potential factor is that Ti is known to be highly resistant to pitting and crevice corrosion in seawater, with an even higher crevice corrosion resistance in seawater than either 316 or 304 stainless steel [39, 41].

(a)

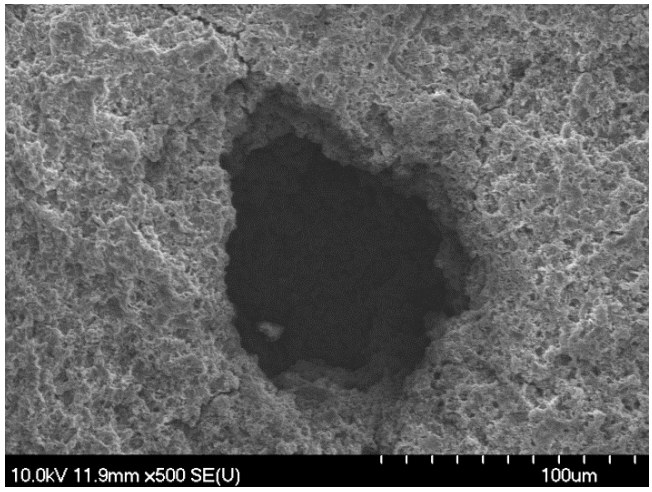

(b)

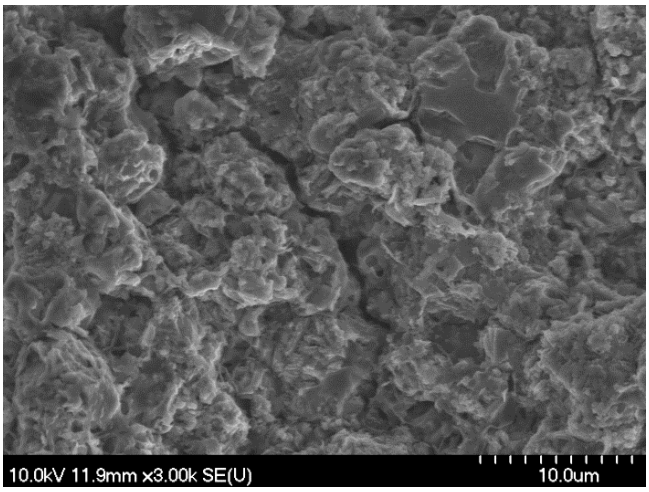

(c)

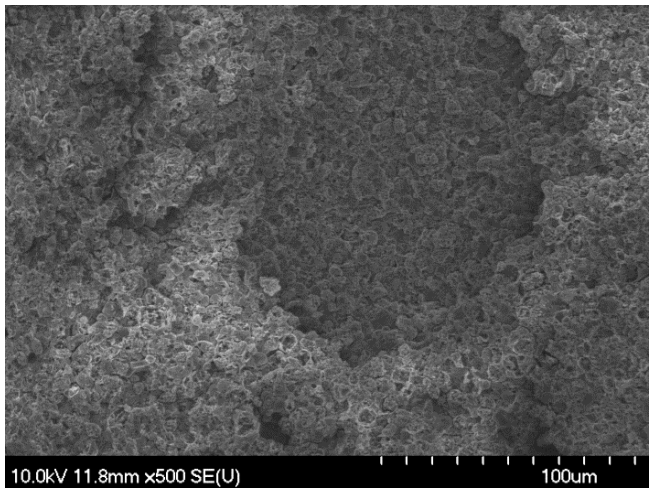

(d)

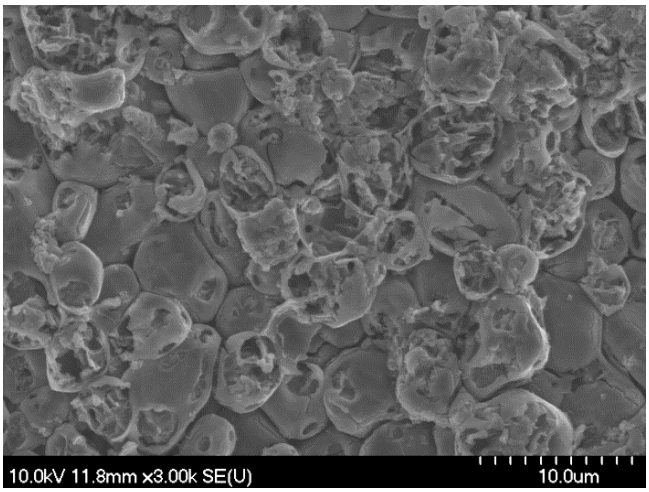

(e) (f)

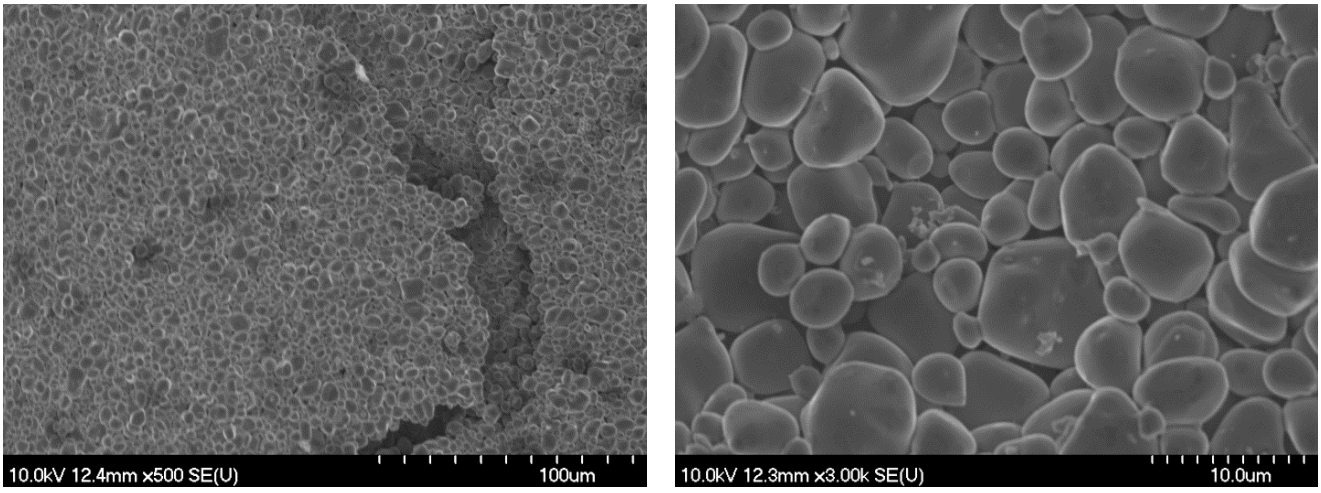

Figure 6.13: SEM images showing the corroded surfaces of TiC-304L cermets after potentiodynamic polarisation: (a,b) 10 vol. % 304L, (c,d) 20 vol. % 304L, and (e,f) 30 vol. % 304L.

This behaviour is due to the ability of Ti to form a strong and adherent protective oxide that can withstand corrosion attack; TiC can be anticipated to form a similar Ti_xO_y scale (i.e. TiO_2) [166, 185, 186]. It can be seen that the TiC-10 vol. % 304L cermets are the least prone of the current composites in terms of preferential attack, which arises from the response dominated by TiC and its naturally forming protective oxide layer to withstand further corrosion. Clearly, for a higher TiC content there can be expected to be a concurrently higher presence of the TiO_2 surface oxide, which is believed to contribute to the higher corrosion resistance of cermets with lower binder, as shown in Figures 6.12 and 6.13.

Similar results were reported for the corrosion behaviour of TiC-containing, 304 stainless steel metal matrix composites in an aqueous HCl solution [95]. Wu and colleagues reported a massive dissolution of the steel matrix, while the TiC particles were unaffected, due to a significant galvanic effect between the two materials [95]. It was also noted that the presence of large numbers of Cr-rich carbides, in addition to the TiC (which is more noble than the 304 stainless steel), in the steel led to extensive pitting of the matrix in general. Lastly, they stated that since the size of the TiC particle reinforcement phase was significantly greater than that of the Cr-rich carbides, the residual stress state in the matrix adjoining the TiC reinforcement (due to the difference in the coefficient of thermal expansion) made them more susceptible to dissolution and pitting [95]. As a consequence, the large difference in the coefficient of thermal expansion (CTE) between TiC and the steel matrix (CTE of TiC ~7.4 x 10^{-6} K^{-1} [187] and 304/304L stainless steel ~18-19 x 10^{-6} K^{-1} [188, 189] results in a high dislocation density at

the interface, in particular in the vicinity of the larger TiC particles, which accelerates the corrosion [58, 190, 191]. TiC is reasonably electrical conductive (~$2\times10^{6}\ \Omega^{-1}m^{-1}$[192]) and, as noted, more noble than 304 stainless steel in terms of its electrochemical characteristics, which creates galvanic activity at the interface between the two materials, leading to serious dissolution of the steel [95, 190, 191]. Several other authors have also reported improved corrosion resistance with lowered binder contents in specific cermet systems [58, 94, 175].

Typical SEM images of both the cermets and the 304L stainless steel, following cyclic polarisation testing, are shown in Figure 6.14. The presence of large pits is apparent on the 304L surface (Figure 6.14(d)), while for the cermets, evidence of localised corrosion can be observed at the interfaces between the TiC grains and the 304L binder. Clearly, this is likely to be related to a galvanic effect existing between the two dissimilar materials in the conducting, simulated seawater environment.

(a) (b)

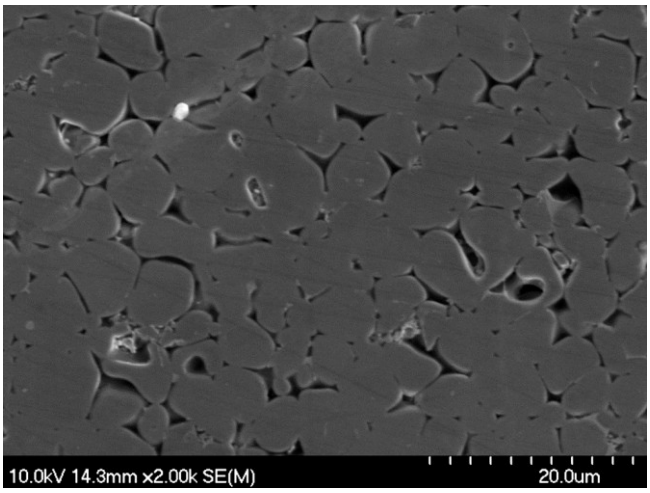

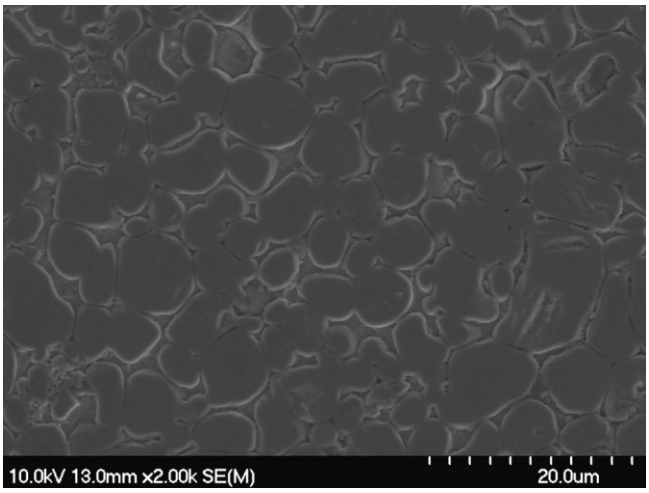

(c) (d)

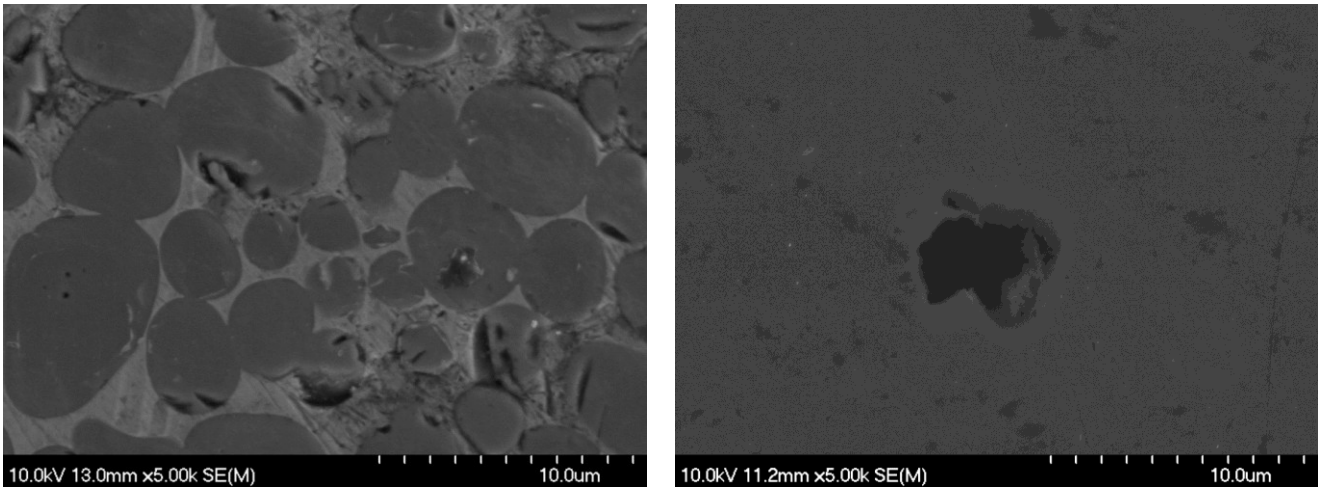

Figure 6.14: SEM images showing corroded surface of TiC-304L cermets and 304L stainless steel after cyclic polarization: (a) TiC with 10 vol. 304L, (b) TiC with 20 vol. % 304L, (c) TiC with 30 vol. % 304L, and (d) 304L stainless steel.

Figure 6.15 displays selected SEM images of the samples after potentiostatic polarisation tests, conducted at a voltage above the pitting potential. There is evidence of heavy pitting on the surface of the baseline 304L stainless steel. Conversely, on the cermets, the corrosion attack occurs preferentially at the binder/TiC interface, and the extent of dissolution increases with binder content. It is also apparent for the cermets that the TiC grains appear essentially unaffected.

(a) (b)

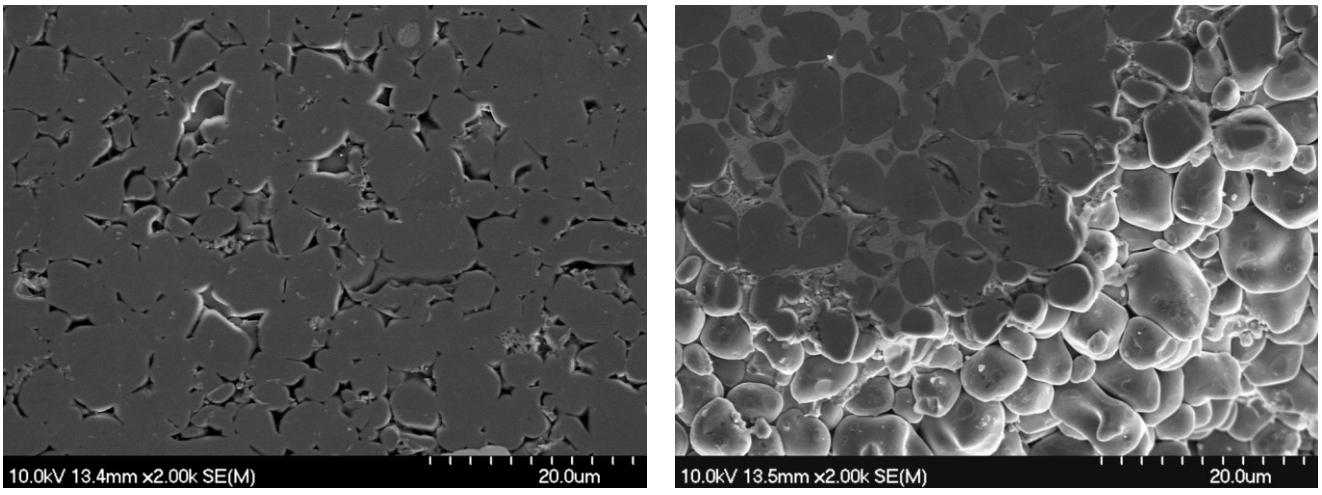

(c) (d)

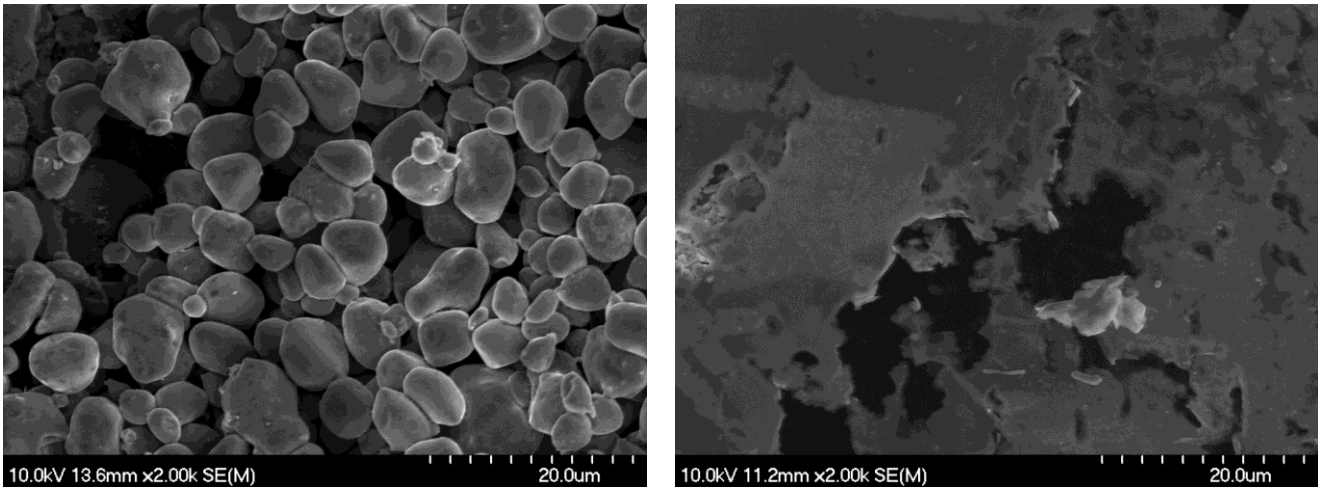

Figure 6.15: SEM images showing corroded surface of the TiC-304L cermets and 304L stainless steel after potentiostatic polarization above their pitting potentials: (a) TiC with 10 vol. % 304L, (b) TiC with 20 vol. % 304L, (c) TiC with 30 vol. % 304L, and (d) 304L stainless steel.

The presence of large pits forming on the 304L stainless steel is in agreement with the results obtained from potentiostatic polarisation testing, shown previously in Figure 6.8. In that instance there was an increase in the current, with clear evidence of oscillatory perturbations, which infers surface attack on the passive films by the aggressive chloride ions in solution.

6.5 Conclusions

A series of novel TiC-304L stainless steel cermets have been developed, with steel binder contents varied from 10 to 30 vol. %. The corrosion performance of the cermets was examined using a variety of electrochemical test methods, and their response has been compared to baseline 304L stainless steel. It was demonstrated that the overall corrosion resistance of the baseline steel is better than the cermets with the higher binder levels (i.e. 20 and 30 vol. %). However, the corrosion response is generally comparable to the cermets prepared with the lowest binder content, which also offers the advantage of significantly better wear resistance than 304L stainless steel.

It was shown that the critical current density and breakdown potential increase with steel binder content in the cermets. Microstructural studies revealed that there is dissolution of the steel metal binder during electrochemical tests, while the TiC grains remain largely unaffected. The corrosion rate of the cermets increases with steel binder content, which is attributed to the preferential dissolution of the binder.

Chemical analyses, using both ICP-OES and EDS, confirmed this increase in dissolution of the steel at higher binder contents.

In terms of the present cermets, from the electrochemical characterisation approaches that were followed it can be concluded that those with the lowest binder content (i.e. TiC-10 vol. % 304L) have the potential to offer an excellent combination of wear and corrosion resistance, as dissolution of the binder is significantly reduced and pitting corrosion is avoided, while the high TiC content considerably enhances the composite wear resistance.

6.6 Acknowledgements

This study was financially supported by Petroleum Research Atlantic Canada (PRAC) and the Natural Sciences and Engineering Research Council of Canada (NSERC). The Canada Foundation for Innovation, the Atlantic Innovation Fund, and other partners who helped fund the Facilities for Materials Characterisation, managed by the Dalhousie University Institute for Materials Research, are also gratefully acknowledged. The authors would also like to thank Dean Grijm and Patricia Scallion for technical assistance.

7 The Effects of Grain Size on the Corrosion Behaviour of TiC-316L Stainless Steel Cermets in a Synthetic Seawater Solution

Chukwuma C. Onuoha, Georges J. Kipouros, Zoheir N. Farhat and Kevin P. Plucknett*

Dalhousie University, 1360 Barrington Street, Materials Engineering Program, Department of Process Engineering and Applied Science, B3H 4R2, Nova Scotia, Canada

Status: Submitted to Journal of Corrosion Science 2013

7.1 ABSTRACT

The aqueous corrosion behaviour of fine- and coarse-grained TiC-316L cermets has been investigated using a range of electrochemical techniques, to assess their response in a NaCl solution. The corrosion assessment methods included Tafel extrapolation, in combination with potentiodynamic and potentiostatic polarisation. Corroded samples were subsequently characterised using SEM and EDX, while the post-corrosion solutions were analysed using ICP-OES. The highest corrosion resistance was achieved at the lowest binder contents, while those with a more coarse grain structure showed superior resistance due to a reduced TiC-316L interfacial area.

Keywords: Ceramic composites; Electrochemical characterisation; Polarisation testing; Potentiostatic testing; SEM; ICP-OES

*Contact author email: Kevin.plucknett@dal.ca

7.2 Introduction

Ceramic metal composites, or cermets, are widely used in applications such as coatings for erosion/corrosion protection, wood and rock cutting tools, pump seals, and abrasive slurry nozzles, because of their combination of good wear and corrosion resistance [11, 34, 58, 68, 162, 169]. Cermets based on titanium carbide (TiC) are of particular interest, due to their reduced mass and improved elevated temperature properties. In particular, they show significant potential as substitutes for the more widely used tungsten carbide-cobalt (WC-Co) based hard metals [68].

Several studies of the corrosion behaviour of cermets, and in particular WC-Co, have demonstrated that corrosion is invariably governed by selective dissolution of the metallic binder, while the ceramic phase remains relatively unaffected [8, 93-94, 170, 172, 174, 193, 194]. Similar observations have also been made for non-WC containing cermet systems, such as those based on TiC and titanium carbonitride (Ti(C,N)) [91, 195, 196]. In addition, a large number of studies have been performed on related coating materials, often on steel substrates, invariably with similar outcomes in terms of the proposed degradation mechanisms [176, 197-199]. As a consequence, the corrosion resistance of cermets is typically reduced when the metal binder content is increased. However, it has also been proposed that the corrosion behaviour of cermets is governed by the corrosion medium [175, 200]. Kubarsepp and colleagues [200] studied the corrosion resistance of sintered TiC-steel alloys in various acids, and stated that there was selective dissolution of the metal binder and an increase in corrosion resistance with TiC content when evaluated in both 20 vol.% NaOH and 3 vol.% H_2SO_4 solutions. Conversely, there was a decrease in corrosion resistance with TiC content when the cermets were tested in HNO_3 solutions (10-60 vol. %); it was postulated that the difference in corrosion mechanisms is due to the fact that TiC has insufficient corrosion resistance in HNO_3 solutions. Selective dissolution of the TiC accelerates the rate of dissolution of the steel binder in that instance [175, 200]. Consequently, corrosion in HNO_3 is accompanied by degradation of the steel binder, while 'pure' stainless steels of similar composition tend to exhibit passivation in solutions of HNO_3, and have a higher corrosion resistance than the cermets [175, 200].

Corrosion studies on cermets have shown that by increasing the amount of binder phase, the rate of corrosion invariably increases [58, 195, 196]. However, in comparison relatively little attention has been given to the effect of the ceramic grain size on the corrosion behaviour of cermets. It is generally noted that reducing grain size enhances the wear behaviour of cermet systems [201, 202]. There are a number of microstructural effects that can be anticipated in terms of reducing grain size. For instance, the binder mean free path can also be expected to decrease, which results in increasing levels of plastic

constraint, due to the greater interfacial area between the grains and the binder which has the effect of strengthening the binder phase, making dislocation motion and shear more difficult [76]. This in turn increases the resistance of the binder to deformation and removal, hence increasing the wear resistance of the cermet. However, in terms of the corrosion resistance, an increase in interfacial area, accompanied by a reduction in carbide grain size, may be anticipated to be detrimental, as there is a greater area for galvanic attack. In addition, a potentially higher dislocation density may be expected to lead to a reduced corrosion resistance. However, with that in mind, Human and Exner found essentially no influence of grain size on the corrosion behaviour of WC-Co cermets in acidic solutions [8, 172]. Conversely, Tomlinson *et al.* [174] reported an increase of the passive current densities by increasing grain size in acidic solution. The effects of grain size on the corrosion behaviour of WC-Co based hardmetals in alkaline solutions have also been assessed, and an increase in corrosion resistance with a decrease in WC grain size was reported [203]. It was noted that the corrosion behaviour is strongly influenced by the dissolved W and C content in the Co binder, and that the W and C content in the binder increases with a decrease in the WC grain size, which improves the corrosion resistance [203]. However, in principle it is generally expected that by reducing the carbide grain size, there will be an increase in the interfacial surface area, which could enhance the formation of galvanic couples on the material surface, thereby leading to the loss in corrosion performance. A second consideration is that for finer grained cermets, it can be expected that there will be a higher overall dislocation density, as the interfaces will be regions of atomic disorder, which then will reduce the corrosion resistance. A high dislocation density would therefore favour corrosion, by promoting increased diffusion rates [203]. It may then be postulated that where the binder ligaments are the thinnest (which is promoted by decreasing grain size), the binder is under greater constraint due to the surrounding carbide grains, and hence attack may begin in these areas [58, 92, 181].

In a recent investigation, for TiC-304L steel cermets, we reported an improvement in corrosion resistance with a decrease in the metal binder content, with localised corrosion occurring at the interface between the TiC grains and the 304L steel binder [196]. The present study is an extension of that work, and involves an assessment of the effects of grain size on the corrosion behaviour of TiC-316L stainless steel composites, in a simulated seawater environment. A range of electrochemical characterisation techniques was applied, including Tafel extrapolation, potentiodynamic polarisation and potentiostatic polarisation, in combination with microstructural and chemical analysis.

7.3 Experimental Procedure

7.3.1 Raw Materials and Cermet Processing

The TiC powder used in the present study was obtained from Pacific Particulate Materials Ltd (Vancouver, BC, Canada), and has a mean particle size of ~1.25 μm [96, 123]. The steel powder used was austenitic grade 316L, with a nominal particle size of -100 mesh, which was sourced from Alfa Aesar (Ward Hill, MA, USA); the designation L refers to low carbon content. TiC pellets (~31.75 mm diameter x 4 mm thick) were uniaxially pressed to a pressure of ~67 MPa. The samples were further compacted by cold isostatic pressing at a pressure of ~220 MPa. Following compaction, the TiC pellets were weighed and the steel binder powder, varied from 10 to 30 vol. %, was placed on top of the TiC preform. For melt-infiltration processing, the TiC preform and steel powder combinations were sited on a layer of bubble alumina, within an alumina crucible. Two heat-treatment cycles were applied to produce cermets with what are subsequently referred to as either a fine- or coarse-grained microstructure. In order to achieve this, melt infiltration was performed at 1475°C for 15 minutes, to produce the fine-grained cermets, and at 1550°C for 240 minutes, in order to generate the coarse-grained cermets. Melt-infiltration was conducted under a dynamic vacuum (better than 20 milliTorr) inside a graphite resistance furnace (Materials Research Furnaces, Suncook, NH, USA), with nominal heating and cooling rates of 10°C/min and 25°C/min, respectively; the cooling rate effectively decreases below ~900°C due to the furnace thermal mass.

7.3.2 Cermet Characterization

After melt-infiltration, the composite densities were determined using the Archimedes immersion method in water. Surface preparation for both microstructural analysis and corrosion testing was then achieved by grinding and polishing of the samples, using successively finer grades of diamond, starting with a coarse 125 μm diamond pad and finishing with 0.25 μm diamond paste. Microstructural characterisation was conducted using optical microscopy (Model BX-51, Olympus Corp., Tokyo, Japan) and scanning electron microscopy (SEM; Model S-4700 Hitachi High Technologies, Tokyo Japan), on the polished surfaces. Grain size measurements were made using the linear intercept method, from digital SEM images of the fine- and coarse -grained TiC-steel cermets [125]; a minimum of 300 TiC grains were measured for each sample. In addition to grain size measurements, two further microstructural parameters were determined for the cermets, namely the contiguity and the binder mean free path length (or binder intercept distance). The contiguity, C, a measure of the ratio of carbide-

carbide to carbide-binder interfaces that are intercepted per unit line length, was determined following [152]:

$$C = \frac{2N_{c/c}}{2N_{c/c} + 2N_{c/b}} \qquad \text{Equation 5.1}$$

where $N_{c/c}$ and $N_{c/b}$ are the number of carbide-carbide (i.e. TiC-TiC) and carbide-binder (i.e. TiC-steel) interfaces, respectively. The mean free path of the steel binder, d_b, can then be determined following [152]:

$$d_b = \frac{1}{1-C}\left(\frac{V_b}{V_c}\right)d_c \qquad \text{Equation 5.2}$$

where V_b and V_c are the volume fractions of binder and carbide (it is assumed that $V_b + V_c = 1$ for the present materials), respectively, and d_c is the mean carbide intercept distance determined from the grain size measurements.

7.3.3 Electrochemical Testing

The corrosion behaviour of the TiC-316L cermets was assessed in a simulated seawater environment, with a 3.5 wt. % NaCl aqueous solution used as the electrolyte. Experiments were performed using a standard three-electrode flat cell, with the cermet samples as the working electrode (with an exposed sample area of 1 cm^2), a platinum mesh as the counter electrode, and a saturated calomel electrode (SCE; 0.241 V versus a standard hydrogen electrode) as the reference. Prior to potentiodynamic polarisation measurements, 4 hours of immersion in the synthetic seawater was maintained to ensure steady-state conditions. For the actual polarisation experiments, the potential was scanned from -0.75 to +3.5 $V_{SCE,}$ at a scan rate of 0.1667 mV/s. Potentiostatic polarisation was conducted at 1.5 V, for a period of 8 hours, which is the potential chosen from the pseudo-passive region. The potentiostatic tests were conducted in order to gain further insight on the phenomenon of pseudo-passivity of the cermets.

The corrosion potentials (E_{corr}) and the corrosion current densities (i_{corr}) were estimated by determining an instantaneous, Tafel-type fit (EG & G Princeton Applied Research Potentiostat/ Galvanostat Model 273, Princeton Applied Research, USA) using CorrWare corrosion analysis software (Scribner Associates, Inc., USA). The corrosion rate (in mm/year) was then calculated using the relationship [107]:

$$\text{Corrosion rate (Tafel)} = \frac{3.27 \times 10^{-3} \times i_{corr} \times W}{D} \qquad \text{Equation 3.1}$$

where W is the equivalent weight of alloy, D is the density of alloy (in g/cm^3), and i_{corr} (in μA/cm^2) is the corrosion current density of each of the specimens, extrapolated from the Tafel polarisation plots.

The material lost by corrosion can also be assessed through weight loss measurements, for comparative purposes. In this instance the cermet samples were weighed before and after corrosion, and their mass loss values were then used to calculate a corrosion rate (in mm/year) using the relationship [37]:

$$\text{Corrosion rate (weight loss)} = \frac{87.6 \times M}{T \times A \times D} \qquad \text{Equation 3.2}$$

where M is the weight loss (in g) after exposure time, T (in hours), D is the density of alloy (in g/cm^3), and A (in cm^2) is the area of the exposed specimen.

Microstructural evaluation of the corroded surfaces was conducted using optical microscopy, SEM, energy dispersive X-ray spectroscopy (EDS). In addition, the remaining solution contained within the three-electrode cell after electrochemical tests was examined using inductively coupled plasma optical emission spectroscopy (ICP-OES; Varian Vista Pro (radial view), Varian Inc., Mulgrave, Australia), in order to determine the quantities of the sample constituents now present in the solution. The solutions were filtered (1.0 μm pore size) using a Millipore vacuum system, to allow removal of any fine particulate material released from the corroding surfaces. The remaining filtered solution was then analysed directly using ICP-OES. In order to chemically assess the removed particulate material, the residue that had collected on the filter was dried at 105ºC, weighed, dissolved in acids (HF, HNO_3, $HClO_4$) in Teflon beakers, and then dried again. The residue was then brought back into solution with HCl, made up to 100 ml in volumetric flasks, and analysed by ICP-OES.

7.4. Results and Discussion

7.4.1 Microstructural Analysis

Representative SEM images of the fine and coarse-grained TiC-316L cermets are shown in Figure 7.1. As can be seen for both the fine and coarse-grained cermets, the microstructure is characteristically uniform, with no evidence for abnormal grain growth. Complete infiltration of the cermets has occurred for each processing variant, and all materials were fabricated to in excess of 99 % of the respective theoretical density (determined based on a simple rule of mixtures for a TiC and 316L combination).

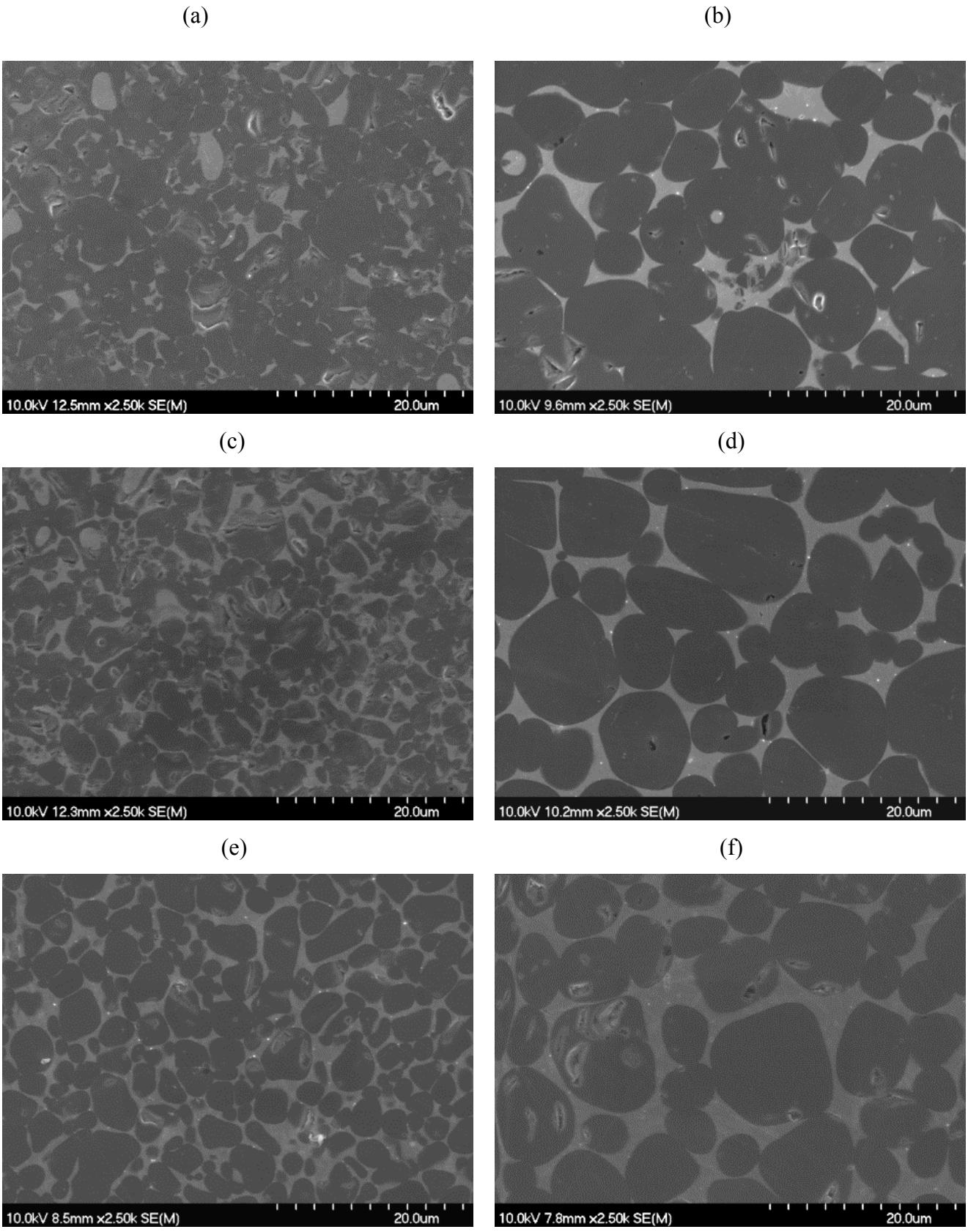

Figure 7.1: Representative SEM images of TiC-316L cermets prepared with: (a,b) 10 vol. % 316L, (c,d) 20 vol. % 316L, and (e,f) 30 vol. % 316L binder.

The mean grain size of fine- and coarse-grained cermets is presented in Figure 7.2. It is apparent that the mean grain size is largely independent of binder content, with a slight decrease consistently noted with increasing binder content. This response is broadly similar to observations with other TiC-based cermet systems, and highlights the likelihood of an interface-limited grain growth response [124], where the rate-limiting step is transport of Ti and C across the interface between the metallic binder and the TiC, rather than diffusion through the steel melt.

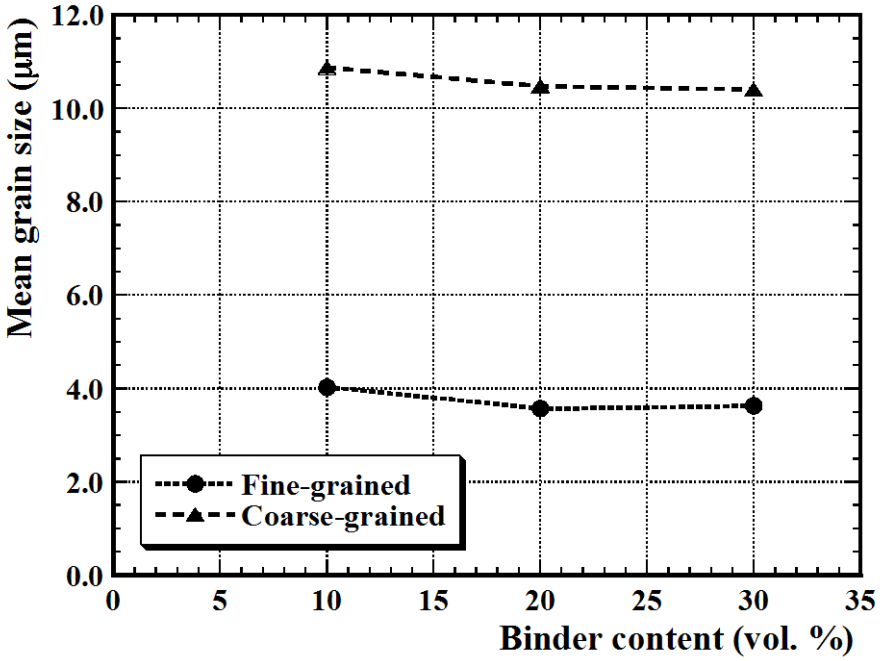

Figure 7.2: The mean grain size as a function of binder content for both fine- and coarse-grained TiC-316L cermets.

Figure 7.3 presents the contiguity and binder mean free path data for both the fine- and coarse-grained TiC-316L cermets. As is typically observed in similar materials [124], the contiguity decreases with increasing binder content (Figure 7.3(a)). In terms of the mean free path dimensions for the binder (Figure 7.3(b), it is apparent for the coarse-grained cermets that the path length increases with binder content, which is in agreement with prior studies on TiC-Ni_3Al cermets [124]. However, for the fine-grained cermets the behaviour is more complex, actually showing a slight reduction in mean free path for the 20 vol. % 316L samples in comparison to 10 and 30 vol. %.

(a)

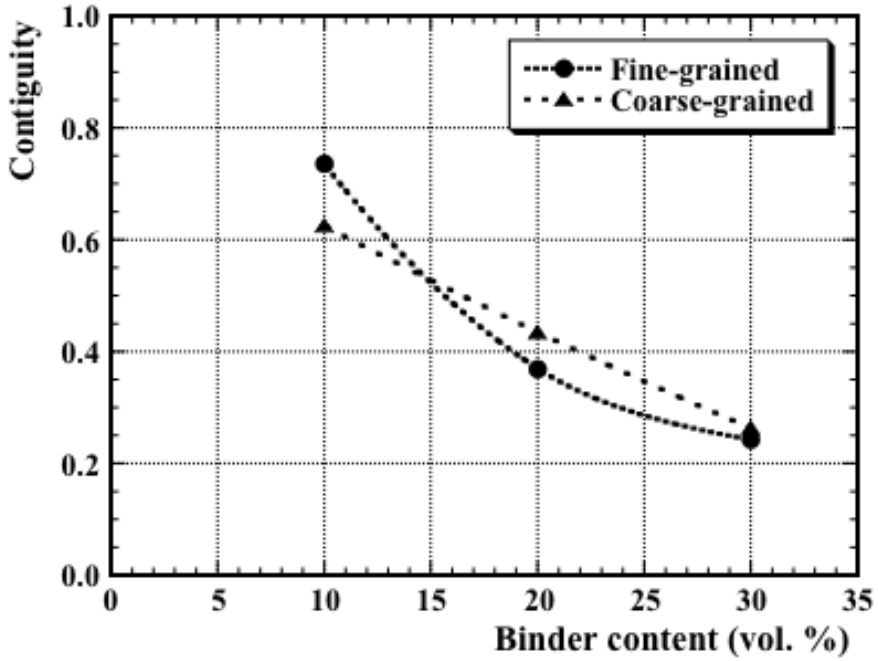

(b)

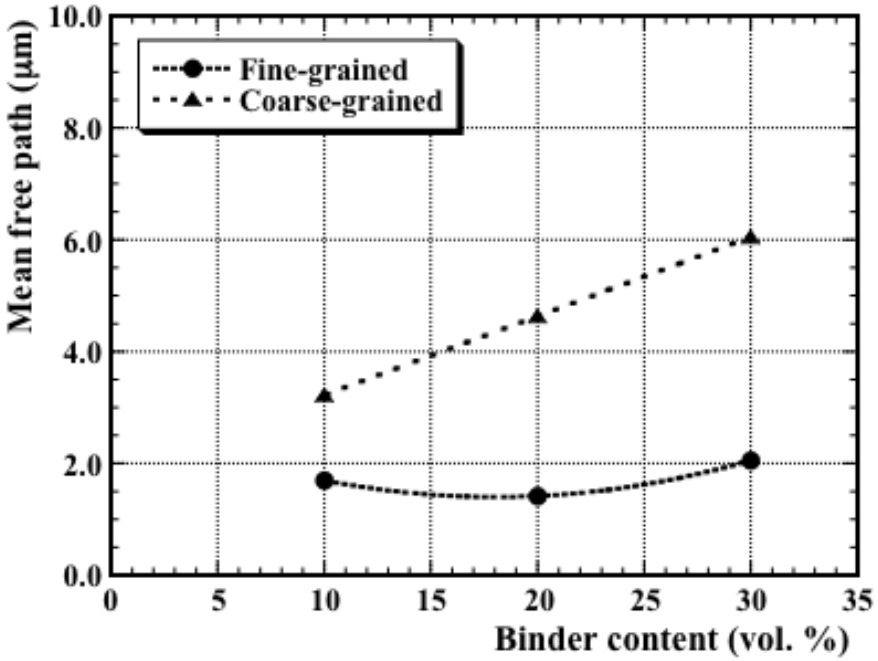

Figure 7.3: (a) The effects of binder content upon the contiguity of fine- and coarse-grained TiC-316L cermets. (b) The effects of binder content upon the mean free path of fine- and coarse-grained TiC-316L cermets.

This response is not fully understood, however it is clear from Figure 7.1 that sintering at 1475°C for 15 minutes results in a relatively complex, non-equilibrium grain morphology (i.e. a clear deviation from moderately spheroid grains), with irregular grain shapes and even hollow 'O' and 'C'-shaped grains. As a consequence, this deviation from nominally spherical will result in a higher interfacial area between the carbide and binder phases when processing under such conditions. This morphological variation may therefore lead to the anomalous mean free path data presented in Figure 7.3(b).

7.4.2 Electrochemical Measurements

Characteristic open circuit potential (OCP) responses, as a function of time, for both the fine- and coarse-grained TiC-316L cermets are shown in Figure 7.4. As it can be seen the OCP is nobler with increase in binder content, which is consistent for both the fine and coarse grained cermets. Table 7.1 shows the mean OCP values achieved after 240 minutes, taken as an average of four OCP repeat tests for each combination of binder volume fraction and grain size.

(a)

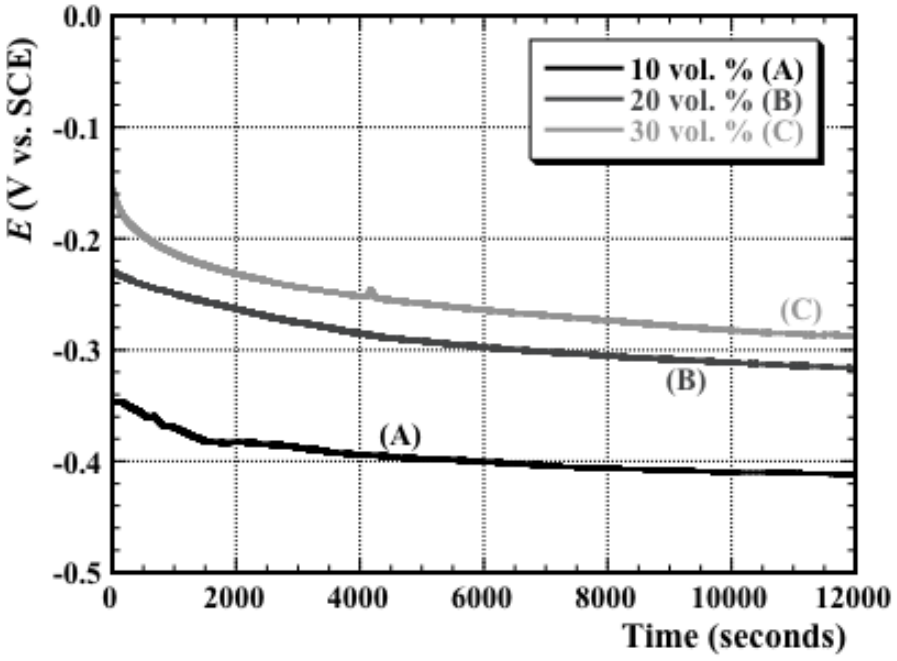

(b)

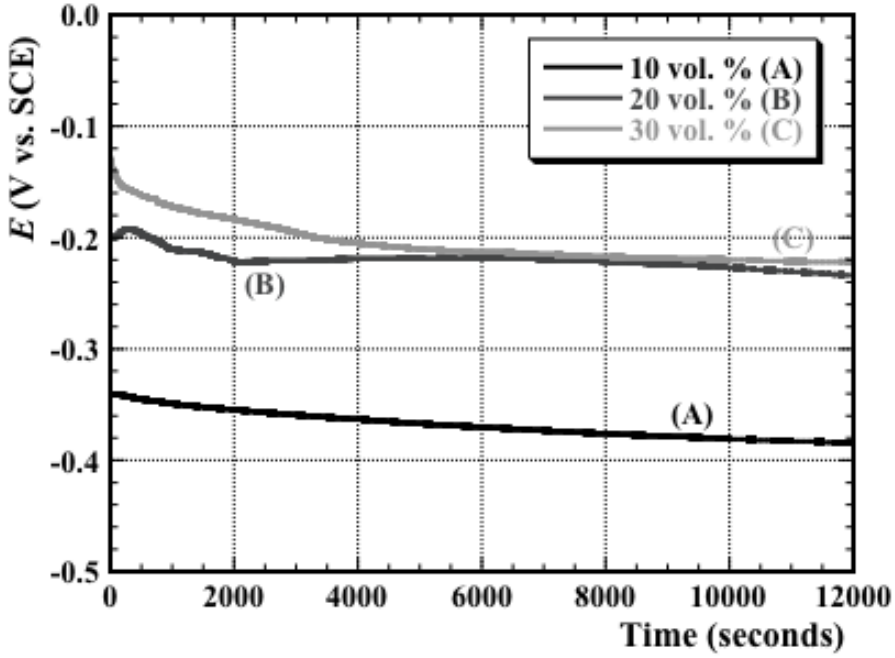

Figure 7.4: The open circuit potential as a function of time for: (a) fine-grained TiC-316L cermets and (b) coarse-grained TiC-316L cermets.

Table 7.1: Open circuit potential values determined for the fine- and coarse-grained TiC-316L cermets; values are an average of 4 repeat tests (standard deviation values are given in parenthesis).

316L content (vol. %)	**Fine**	**Coarse**
10	-0.364 (0.079)	-0.264 (0.089)
20	-0.302 (0.031)	-0.214 (0.070)
30	-0.280 (0.021)	-0.186 (0.053)

In order to calculate the corrosion rates, Tafel polarisation experiments were performed for both the fine- and coarse-grained cermets, with typical representative curves shown in Figure 7.5. The E_{corr} and i_{corr} values determined through the CorrWare analysis of these Tafel plots are presented in Table 7.2. As can be seen from this information, for both the fine- and coarse-grained cermets, the corrosion current densities broadly increase with binder content. However, for the fine-grained cermets with 20 vol. % 316L steel, the i_{corr} value does exhibit a decrease relative to the samples prepared with 10 and 30

vol. % binder, although the general trend still seems to be consistent. It is notable that the corrosion potential, E_{corr} for the coarse-grained TiC based cermets showed an increase with binder content, while for the fine-grained TiC based cermets the opposite behaviour was observed.

(a)

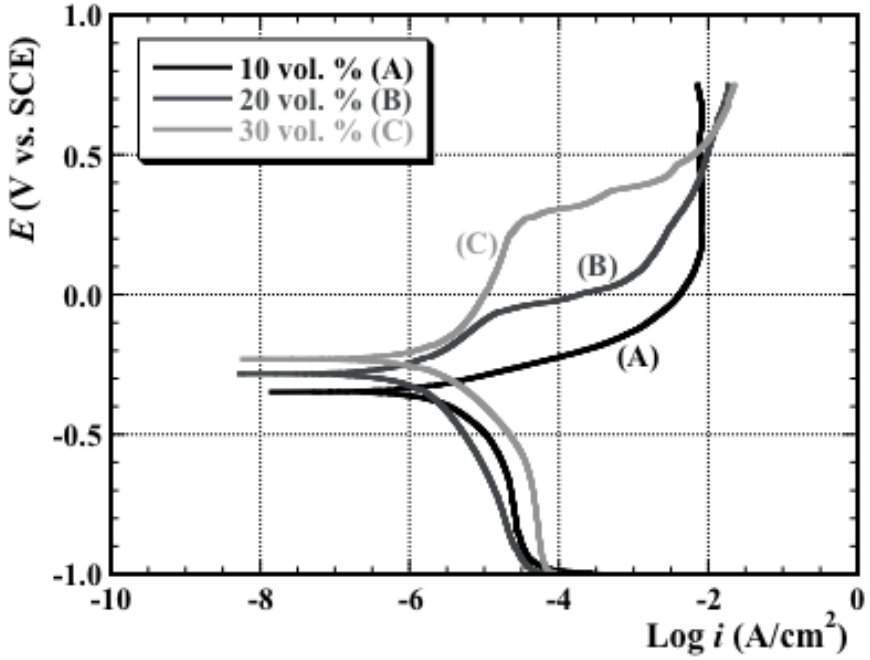

(b)

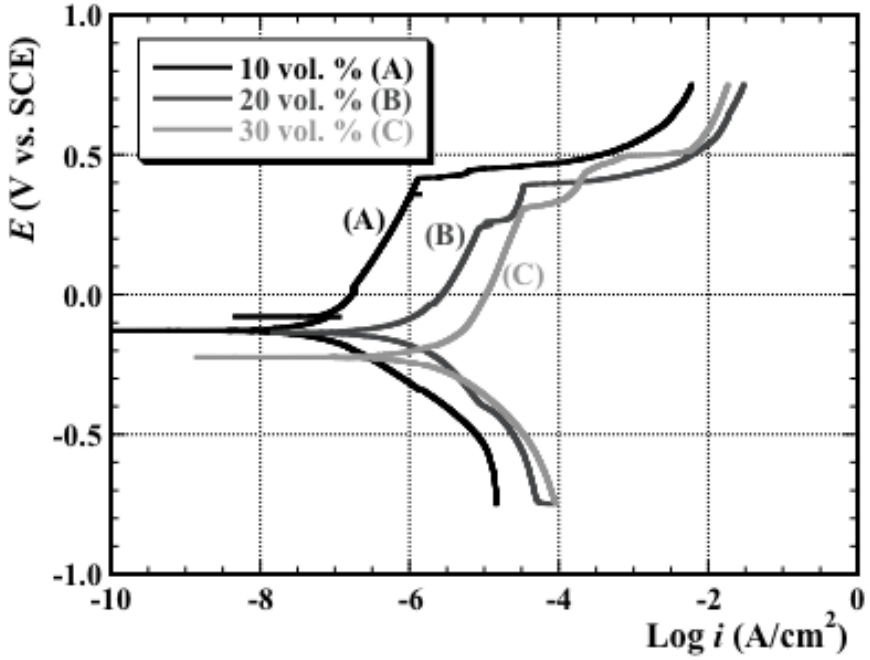

Figure 7.5: Representative examples of the Tafel plots for: (a) the fine-grained TiC-316L cermets and (b) the coarse-grained TiC-316L cermets.

Table 7.2: CorrWare derived results for the Tafel extrapolation procedure, following electrochemical measurements.

316L content (vol. %)	Fine		Coarse	
	E_{corr} (V vs. SCE)	i_{corr} ($\mu A/cm^2$)	E_{corr} (V vs. SCE)	i_{corr} ($\mu A/cm^2$)
10	-0.347	1.628	-0.108	0.085
20	-0.261	0.526	-0.123	0.127
30	-0.246	3.695	-0.223	3.560

As anticipated, the corrosion parameters, E_{corr} and i_{corr}, for the coarse-grained cermets showed an increase with binder content, which mirrors the observations of corrosion behaviour of TiC-304L cermets in our previous studies [196]. However, a somewhat contradictory response was observed for the fine-grained cermets, as shown in both Table 7.2 and Figure 7.5(a). In this instance the E_{corr} values become more noble in character with an increase in the steel binder content. A potential reason for more noble values of E_{corr}, with an increase in steel binder content, may be related to greater constraint due to the surrounding carbide grains expected at cermets with lower binder contents and finer ligament dimensions (i.e. effective the binder mean-free path), which will generate a higher internal stress, but can also be expected to give rise to a higher dislocation density.

Based on results presented in Table 7.2 and Figure 7.5(a), for the fine-grained cermets, with the E_{corr} values more active at lower binder contents, it may be anticipated that the corrosion response would be worse for these materials. However, it is clear that the behaviour is rather more complex. A similarly complex trend in terms of the relative E_{corr} and i_{corr} values has been observed by Ibrahim [204], for shot-peened, powder metallurgically processed Al alloys. It was noted that a more negative E_{corr} for the shot-peened samples compared to those that had not be shot-peened (for the alloy Alumix A321), although the shot peened samples still displayed the best corrosion resistance (i.e. a lower i_{corr}). This response was attributed to the level of stress encountered during shot peening, which affected E_{corr} (i.e. a thermodynamics related response) but had no influence on the i_{corr} (i.e. a kinetics related response). In the present case, for the corrosion response of fine-grained cermets, those with 20 vol. % of the 316L steel binder have the best corrosion resistance with respect to the i_{corr} values. However, the trend is not consistent, and does not reflect the observations made in Figure 7.5(a). The reason for this behaviour is unclear at the present time, but could be related to the more complex microstructural morphology of

fine-grained cermets (i.e. irregularly-shaped grains, rather than the spherical/rounded cube morphology apparent for the coarse-grained cermets), which is affecting their corrosion behaviour; this deviation in microstructure morphology is briefly discussed in the previous section (*Section 7.4.1: Microstructural Analysis*). It is notable that this variation is also apparent in the binder mean free path lengths observed for the fine grained cermets, where there is inconsistent response, and the cermets with 20 vol.% binder content deviate with respect to the 10 and 30 vol. % samples (Figure 7.3(b)), in comparison to both the coarse-grained cermets and those assessed in prior studies [124].

The corrosion rates calculated from the extrapolated Tafel data, for both fine- and coarse-grained cermets, are presented in Figure 7.6. For comparison, the corrosion rates obtained directly from weight loss measurements are shown in Figure 7.7. It is clear that there is a discrepancy between the two techniques, which likely highlights the limitations of the nominally 'instantaneous' Tafel-extrapolation approach. A number of systems (primarily single-phase metals) have been compared using both Tafel and direct measurements, such as weight loss [205-209].

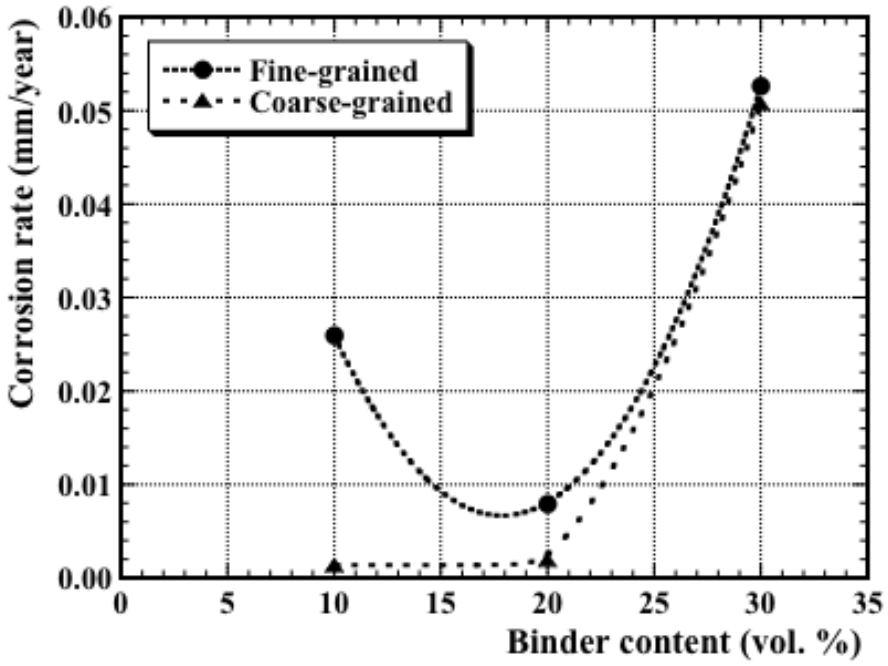

Figure 7.6: The Tafel-derived corrosion rates for both the fine- and coarse-grained TiC-316L cermets.

In some cases the two approaches give similar corrosion rates [205], while in others they exhibit quite significant discrepancies between the Tafel approach and more direct methods [206-209], which is the case in the present study. Clearly, the assessment of TiC-316L stainless steel cermets is complicated by the presence of two phases in the microstructure.

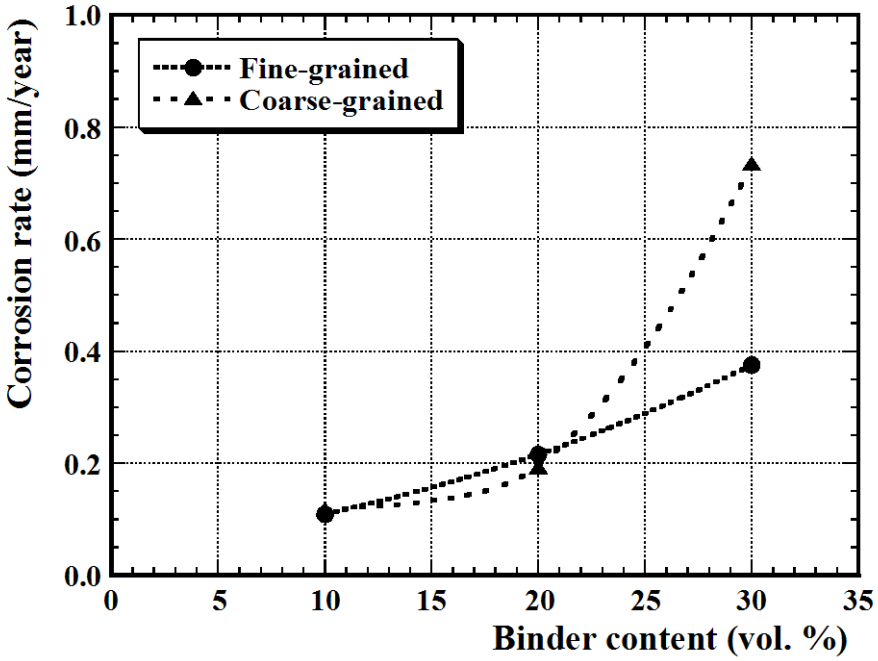

Figure 7.7: The corrosion rates, determined by weight loss measurements, for both the fine- and coarse-grained TiC-316L cermets.

However, for both the Tafel and direct weight loss approach used in the present work it is clear that the corrosion rate essentially increases with steel binder content. It is notable that the Tafel derived corrosion rate for the fine-grained cermet with 10 vol. % binder is higher than for the case of 20 vol. % binder. The reason for this is not clear, however there is a slightly greater level of porosity in the 10 vol. % samples, sintered for just 15 minutes, which may accentuate the corrosion through the presence of a higher surface area (taking into account the porosity). In terms of a direct comparison of the corrosion rates of the present materials with various commercial cermet systems, similar 'Tafel-derived' corrosion rate data are available for a number of common materials, including WC-Co, WC-CoCr and Cr_3C_2-NiCr [198, 199].

Table 7.3 compares the corrosion rates for the present materials with that previously published data. It is important to note that the prior studies relate to coatings, and therefore some differences may be anticipated in terms of the actual corrosion rates. However, through the use of the Tafel derived data in each system, some general observations can be made. The various TiC-stainless steel cermet systems,

including TiC-304L [196], show a significant improvement in corrosion resistance relative to WC-Co and WC-CoCr (by approximately two orders of magnitude).

Table 7.3: A comparison of Tafel derived corrosion rates determined for various high-density, thermal spray cermet materials [198-199], TiC cermets prepared with a 304L binder [196], and the materials developed in the present study*.

Material (compositions in wt. % unless stated otherwise)	**Corrosion rate (mm/year)**
WC-17Co [198]	0.78
WC-10Co4Cr [198]	0.32
Cr_3C_2-25NiCr [198]	0.008-0.014
TiC-304L (10 vol. % (~6 μm TiC grain size)) [196]	0.0084
TiC-316L (10 vol. % coarse (~11 μm))*	0.0013
TiC-316L (20 vol. % fine (~4 μm))*	0.0079
TiC-316L (20 vol. % coarse (~11 μm))*	0.0019

The absolute corrosion rates are also similar to, and often better than, Cr_3C_2-NiCr coatings. While this shows significant promise for the current TiC-stainless steel materials, two further factors need to be taken into account. As noted above, a comparison is being made between bulk materials and coatings, where further coating/substrate galvanic effects may arise if the coating is not fully dense or if there is any cracking in the coating (i.e. allowing transport of the corrosion medium to the coating/substrate interface). Secondly, the coating materials examined in the prior studies have somewhat higher metallic binder contents (in excess of 20 vol. %), which is known to degrade the corrosion resistance, based on both the current study and our prior work on TiC-304L cermets. However, broadly speaking it is clear that the present TiC-stainless steel cermets exhibit corrosion resistance that is comparable to Cr_3C_2-NiCr.

The general trends in terms of the corrosion rates seem to be consistent for both the fine- and coarse-grained cermets. The increase in corrosion rate with binder content is similar to the results of our recent

study on TiC-304L cermets [196], as well as a number of related cermet systems [58, 175, 200]. It can be observed from the previous discussion that coarse-grained TiC based cermets have better corrosion resistance than those with a fine-grained structure. The reason for the relatively poorer corrosion resistance of the fine grained TiC based cermets is likely to be related to the higher interfacial area, which could act as site for galvanic corrosion attack leading to a reduced corrosion resistance. Assuming nominally spherical grains (actually somewhat rounded cubes), with mean diameters of 4 and 11 μm for the fine- and coarse-grained cermets, respectively, the effective interfacial surface area increases by approximately a factor of 2.75 for the fine-grained materials. A further contribution to the coarse-grained cermets having better corrosion resistance may be related to the dislocation density in the steel binder, with a higher dislocation density enhancing corrosion due to increased diffusion rates. It has been proposed that this occurs because the binder is under greater constraint, for finer grains, due to the surrounding carbide matrix and hence attack might begin in these areas leading to deterioration in corrosion resistance [58, 92, 181, 203]. However, it should also be noted that grain boundaries and interfaces are intrinsically regions of higher dislocation density, and a nearly three-fold increase in interface area in the present case would likely result in a comparable increase in the dislocation density.

Typical potentiodynamic polarisation curves are shown in Figure 7.8, for both the fine- and coarse-grained TiC based cermets. As can be seen, the potentiodynamic curves show active, passive and transpassive regions. It is also be noted from these figures that the critical current density increases with steel binder content, for both the fine- and coarse-grained cermets, which provides information about their passivation tendency. It has previously been reported that a low critical anodic current density at the peak of the curve indicates rapid passivation [104], which infers that the reduction in steel binder content is contributing to the corrosion resistance of the cermets.

(a)

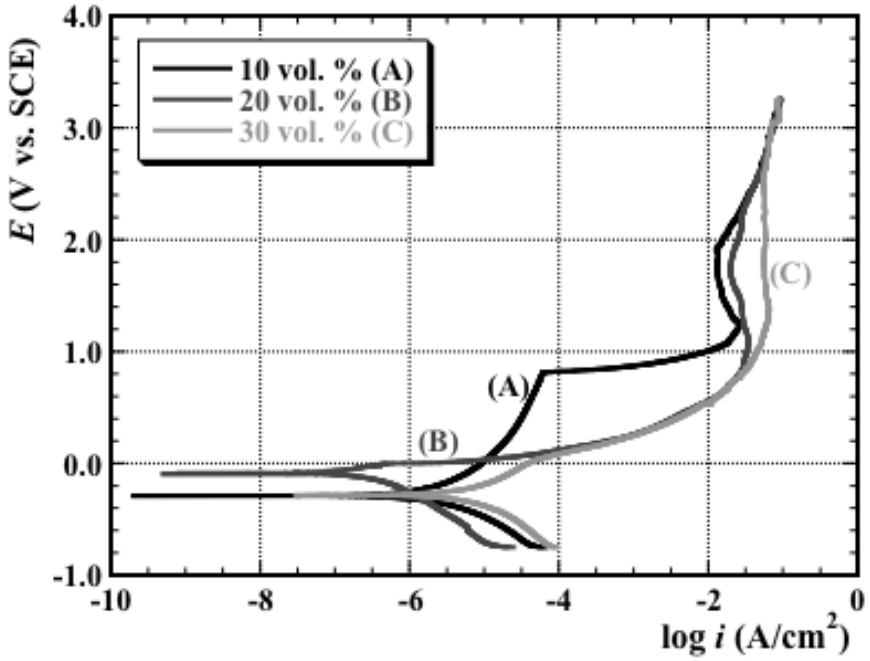

(b)

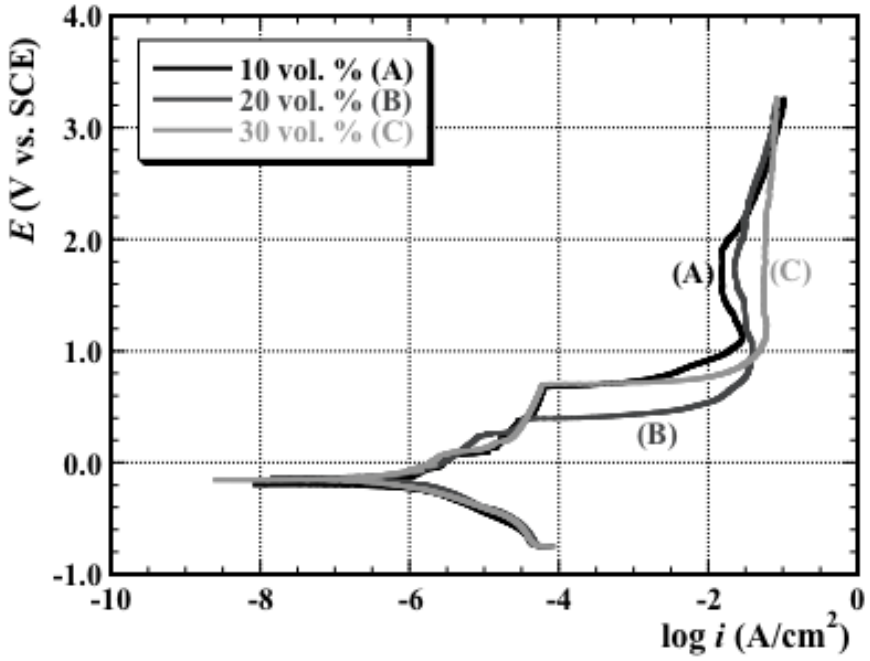

Figure 7.8: Representative potentiodynamic polarisation curves obtained for: (a) fine-grained TiC-316L cermets and (b) coarse-grained TiC-316L cermets.

Similar results have been reported by Sutthiruangwong *et al.* [94], who noted an increase in critical current density with Co binder content in their studies on the corrosion behaviour of WC-Co cermets in aqueous H_2SO_4 solutions. As shown in Table 7.4, the critical current density, i_{crit}, and minimum current density in the pseudopassive region, i_{pp}, are both increasing with the 316L binder content, and the values are also relatively high (~10^{-2} A/cm^2).

Table 7.4: Electrochemical results following potentiodynamic polarisation showing critical current density and minimum current density in the pseudopassive region of fine and coarse-grained TiC based cermets.

316L content (vol. %)	**Fine**		**Coarse**	
	i_{crit} (A/cm^2)	i_{pp} (A/cm^2)	i_{crit} (A/cm^2)	i_{pp} (A/cm^2)
10	0.0259	0.0158	0.0292	0.0156
20	0.0338	0.0201	0.0337	0.0229
30	0.0639	0.0556	0.0584	0.0568

It has been stated that the corrosion behaviour of cermets is dependent upon the electrochemical potential of the system [12]. Under open circuit conditions, or at a low applied potential, there is selective dissolution of the binder phase, whereas as at a higher electrochemical potential, dissolution of the hard phase can occur [8, 94, 170, 172, 174, 181, 182]. A phenomenon known as 'pseudo-passivity' was reported by Human and Exner [8, 172] and more recently by Sutthiruangwong and colleagues [94]. This behaviour is exhibited at high electrochemical potentials, where the passive current density of the cermets is several magnitudes higher than the passive current density of truly passive materials, although the potentiodynamic curves still show apparent active, passive and transpassive regions. It has been reported that the passive current density for a true passive material is around 10 μA cm^{-2} [8, 172, 183], and any that have a passive current that is several orders of magnitude higher than this value are believed to be exhibiting 'pseudo-passive' behaviour.

From Table 7.4 it can be seen that the passive current densities for the fine- and coarse-grained TiC-316L cermets are approximately four orders of magnitude higher than would be expected for a truly passive material. This suggests that the phenomenon of pseudo-passivity is likely to be present for the TiC-316L cermets. The pseudo-passive state is reported to occur in the presence of non-adherent, and consequently semi-protective surface scales (i.e. weak, cracked and/or porous oxides), where the

diffusion-inhibiting corrosion products lead to a limitation of the current density. In contrast to true passive conditions, these current densities remain comparably high [8, 12, 94, 172].

In order to more fully understand the pseudo-passive behaviour of the present cermets, potentiostatic polarisation tests were performed at 1.5 V, which is a potential where the cermets exhibit apparent pseudo-passive behaviour. Application of a potentiostatic potential as high as 1.5 V is justified from the anodic polarisation curves, where the anodic currents are essentially independent of the applied potential, and hence where the cermets are expected to be exhibiting a pseudo-passive behaviour. From the potentiostatic plots for both the fine- and coarse-grained cermets, shown in Figure 7.9, it can be seen that there is an initial current spike. This is expected to be a result of Cl^- ion attack on the intrinsic surface film and, as the film thickness grows during corrosion (or an oxide layer is formed in the absence of an initial film), the current decreases. However it is clear that it still remains high relative to true passive behaviour (i.e. actually exhibiting pseudo-passive behaviour). The decay in current densities and their subsequent stabilisation to steady state values suggest that the cermets develop some passivation characteristics, in line with the observations made from the potentiodynamic polarisation plots shown in Figure 7.8, together with the results presented in Table 7.4.

(a)

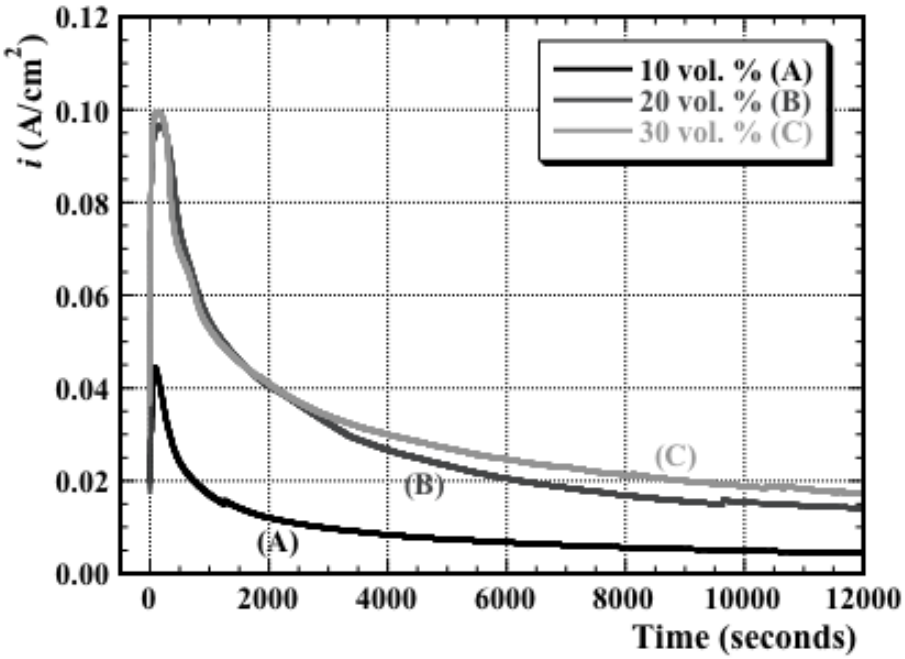

(b)

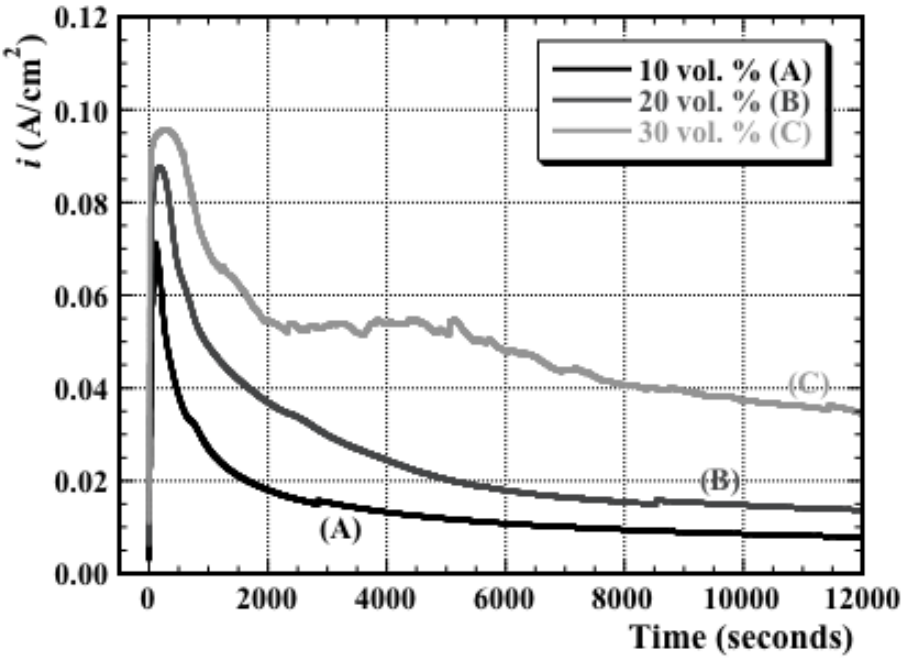

Figure 7.9: Representative potentiostatic polarisation curves for: (a) the fine-grained TiC-316L cermets and (b) the coarse grained TiC-316L cermets.

The high current density observed after polarisation in the pseudo-passive region, as shown in Figure 7.9, is therefore believed to be as a result of the formation of a weak, cracked and/or porous oxide surface layer. As a consequence, the penetration of the electrolyte to the sample surface occurs. Hence, the presence of a low adherence, but diffusion-inhibiting corrosion product, leads to a limitation of the current density [8]. This is also evidenced for the coarse-grained TiC-316L cermets with the highest binder content (i.e. Figure 7.9(b)), which shows oscillations in the potentiostatic curve, suggesting that the oxide layer is not continuous in nature, thereby allowing the presence of aggressive Cl^- ions at the sample surface. It has previously been noted that the presence of heavy oscillations in the potentiostatic curve can highlight the attack of aggressive Cl^- ions on the passive layer [184].

EDS chemical analysis was performed on the cermets following potentiostatic polarisation, as shown in Table 7.5, in order to fully confirm that the presence of an oxide layer led to the progressive decrease in current and phenomenon of pseudo-passivity. It can be seen that there is high amount of Ti, C and O. This observation suggests that the surface layer that is formed consists mainly of a titanium oxide (i.e. TiO_2). This result mirrors the observations of Sutthiruangwong and colleagues [94], who confirmed high amounts of O on the surface of WC cermets.

Table 7.5: EDS analysis of the TiC-316L cermets showing a high amount of TiC and oxygen following potentiostatic polarisation testing.

316L content (vol. %)	**Composition (wt. %)**	
	Fine	**Coarse**
10	Ti: 49.53 C: 7.89 O: 38.78	Ti: 52.50 C: 8.98 O: 32.20
20	Ti: 60.02 C: 15.73 O: 11.73	Ti: 62.16 C: 16.47 O: 9.72
30	Ti: 70.64 C: 18.55 O: 8.01	Ti: 60.17 C: 14.38 O: 13.34

They suggested that the reason for the low dissolution rate of the Co binder in WC-Co cermets, with high WC contents, is related to formation of a semi-protective tungsten oxide (i.e. WO_3) layer on the surface, which inhibits further dissolution. A similar response is clearly observed from Figure 7.9 and Table 7.5 of the present work, where the TiC-316L cermets with the lowest steel binder contents have the lowest measured currents in the pseudo-passive region, combined with the highest surface oxide contents. As a consequence, these cermets also exhibit the best corrosion resistance. In accordance with the behaviour of WC, TiC can be anticipated to form a similarly protective oxide surface layer (i.e. TiO_2) [166, 186], which consequently improves the relative corrosion resistance of cermets with the highest TiC contents, as there can expected to be a concurrently higher presence of TiO_2 on the surface. Ren and colleagues [176] also reported an improvement in the corrosion resistance of TiC coatings, in comparison to 'pure' 304L stainless steel, due to the corrosion resistance gained by the addition of TiC.

7.4.3 Post Corrosion Chemical Analysis

In order to determine the compositions of the dissolved (i.e. metal ions) and fine particulate material in the testing solution, following corrosion experiments, ICP-OES analysis was conducted. The results of the ICP-OES analyses are presented in Figures 7.10 and 7.11, for the fine- and coarse-grained cermets, respectively. In terms of the recovered material following filtration (Figure 7.10), it is apparent that with increasing binder content in the cermets there are increasing quantities of Fe, Ni, Cr and Mo apparent, with concurrently decreasing amounts of Ti.

(a)

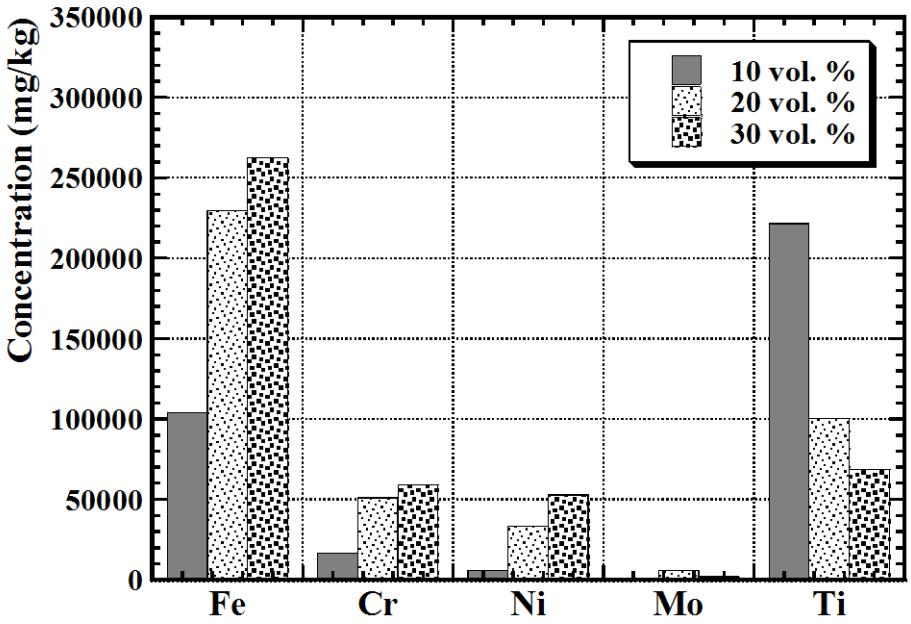

(b)

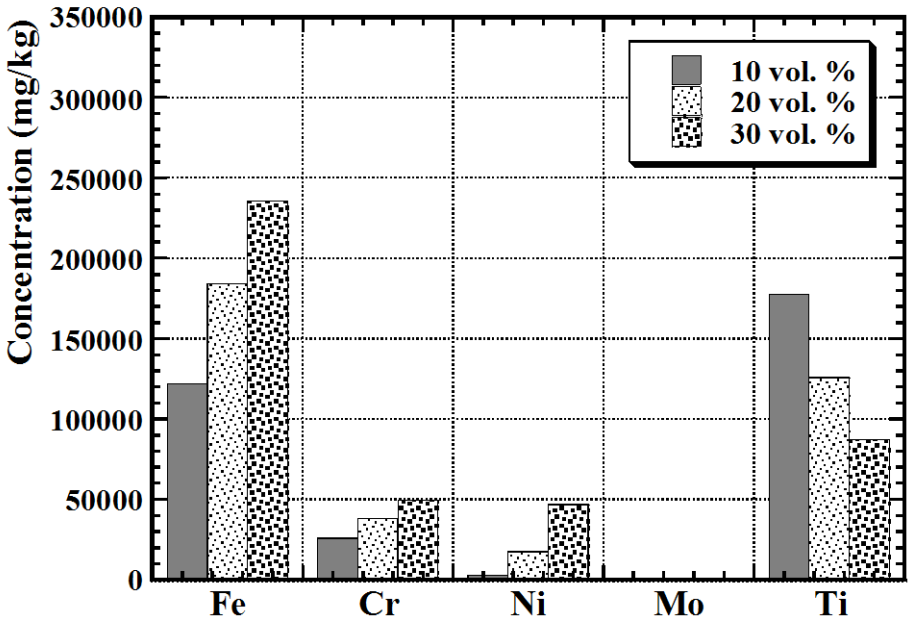

Figure 7.10: ICP-OES analyses of the filtered material removed from the post-test potentiodynamic polarisation solutions for: (a) fine-grained and (b) coarse-grained TiC-316L cermets.

(a)

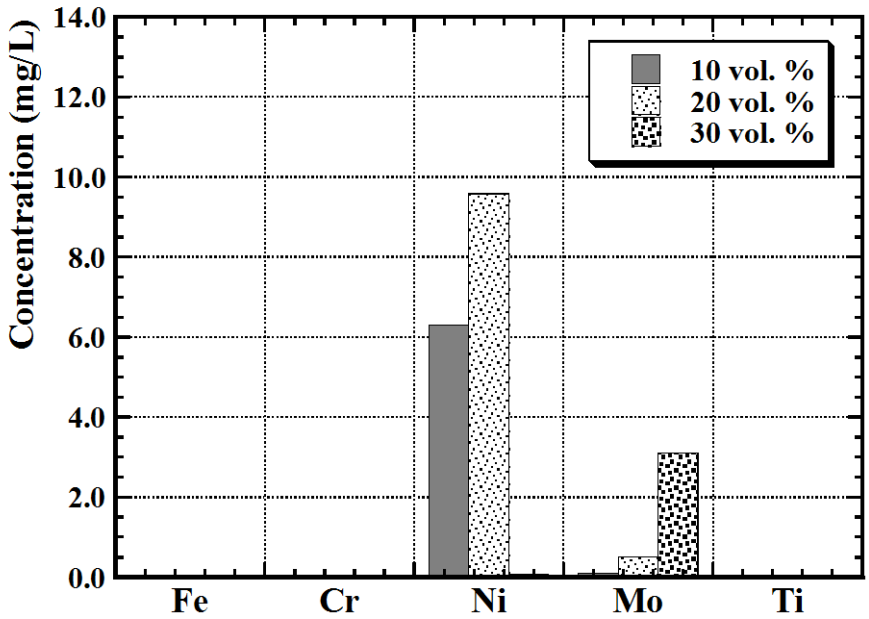

(b)

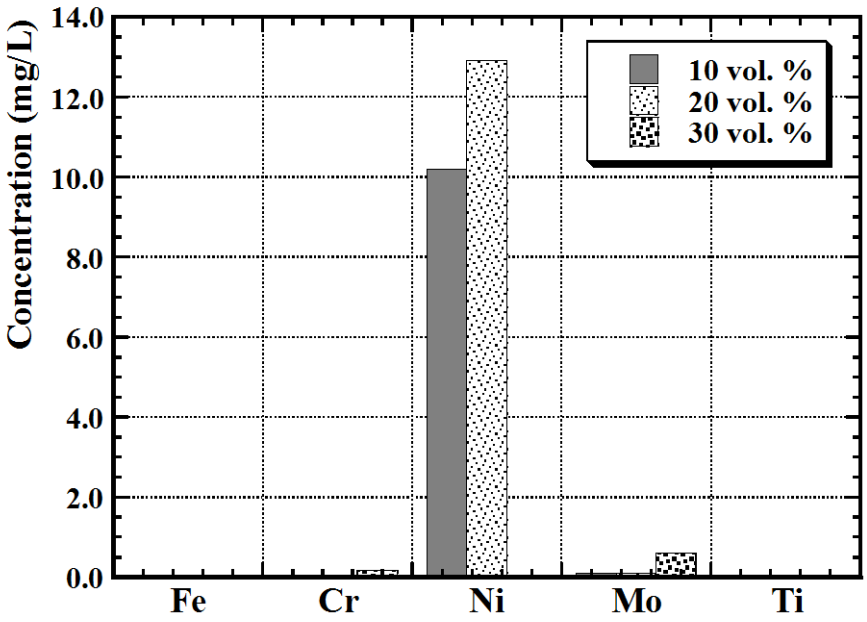

Figure 7.11: ICP-OES analyses of the retained solution (following filtration) following potentiodynamic polarisation testing, for (a) fine-grained and (b) coarse-grained TiC-316L cermets.

The increase in steel constituents suggests that preferential attack of the binder progressed in a nominally linearly manner with increasing binder volume fractions. In addition, comparing the overall extent of dissolution of the fine- and coarse-grained cermets, as shown in Figure 7.10, it is apparent that the degree of metal binder dissolution in the fine-grained cermets is higher than for the coarse-grained equivalent. This observation confirms the electrochemical test results shown in Figures 7.6 and 7.7, together with data presented in Table 7.2, which both indicate improved corrosion resistance for the coarse-grained cermets.

Figure 7.11 demonstrates the concentration of dissolved metal ions found in the remaining post-test solution, following particulate filtration. As it can be seen for both fine- and coarse-grained cermets, there are high amounts of Ni ions in the solutions while other constituents of the metal binder are negligible in comparison. It can also be seen that for the fine-grained cermets (Figure 7.11(a)), there is a loss of Ni and Mo, while the Mo concentration in coarse-grained cermets is minimal. Although the content of Ni ions in the coarse-grained cermets (Figure 7.11(b)) seems to be greater than for the fine-grained cermets, the combined loss of Ni and Mo ions in the latter could explain its overall inferior corrosion resistance compared to the coarse-grained counterpart. The absence of Fe ions from the solution could potentially indicate precipitation of Fe in some form, as the pH of the NaCl solution is in

the range of 5.3-5.8, which is fairly close to the highly acidic corrosive range (i.e. pH 0-4), and justifies the potential for Fe precipitation. This would then lead to a higher Fe content in the filtered solids component of the solution, relative to Ni. It is clear from both Figures 7.10 and 7.11 that there are some subtleties in terms of which metallic components are retained as a fine particulate residue, and which are dissolved in solution, which cannot be readily explained at the present time. However, taking both Figures 7.10 and 7.11 into account, the general observations clearly highlight concurrently increasing binder constituents in the post-corrosion solutions with their increase in the cermets.

In addition to the chemical analysis of the corrosion medium following electrochemical testing, the influence of the tests on the cermet composition were also analysed by comparison of the EDS analyses of the cermets taken both before and after corrosion (Figure 7.12). It is clear that the difference in Ti before and after corrosion is negligible, while for the binder constituents there is significant reduction in the post corrosion concentrations, due to dissolution during the electrochemical tests. It should be noted that the post test surfaces also show high concentrations of O (not shown in Figure 7.12), which likely results in the slight differences in Ti concentration after corrosion.

(a)

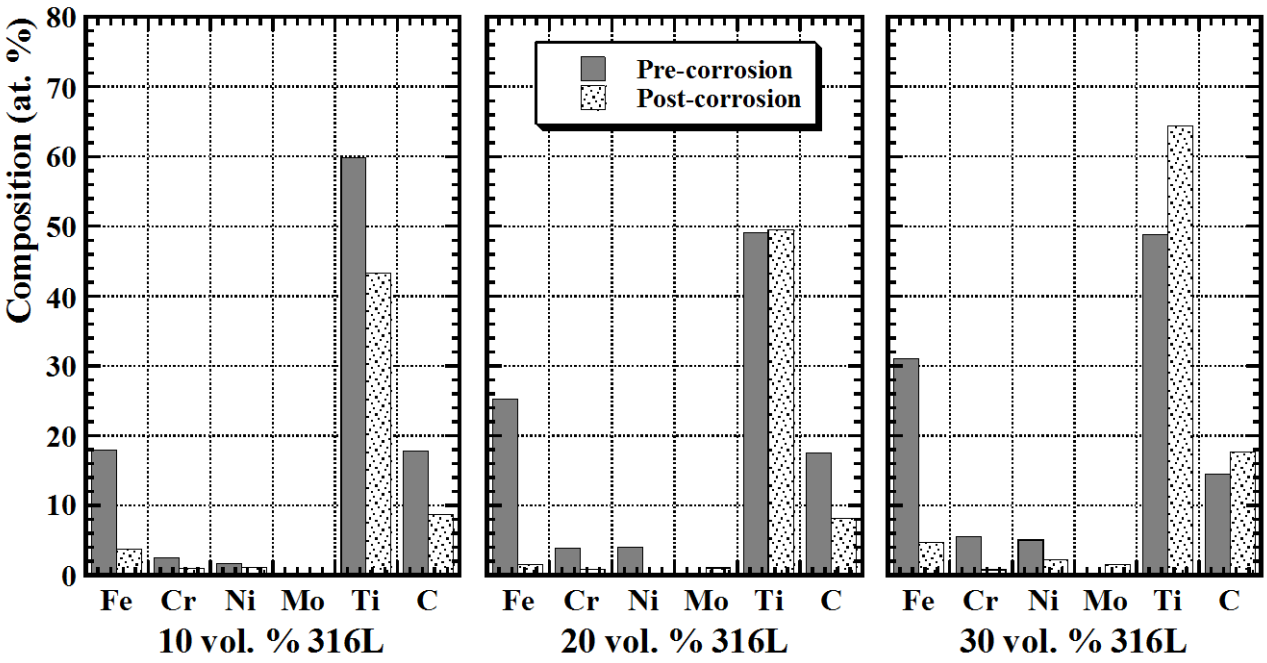

(b)

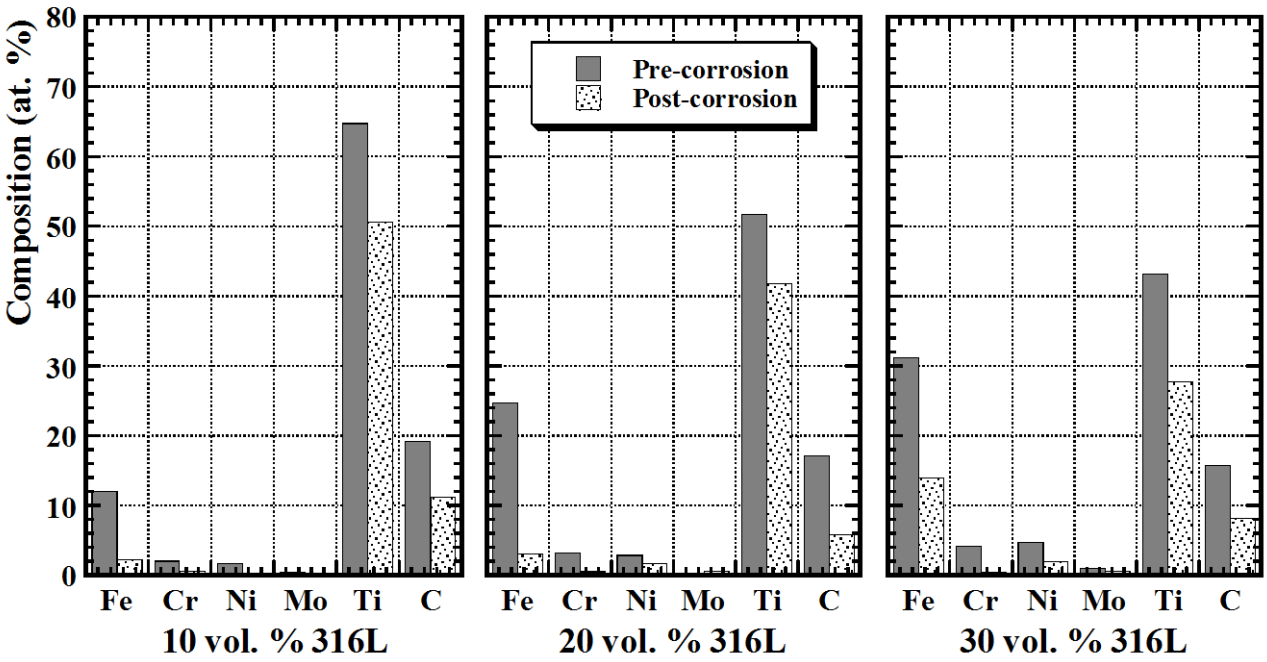

Figure 7.12: EDS analysis of the TiC-316L cermets both before and after corrosion tests: (a) fine-grained and (b) coarse-grained. Note that the compositional balance is comprised of O.

7.4.4 Post-Corrosion Microstructural Characterisation

Typical SEM images following potentiodynamic polarisation are shown in Figures 7.13 and 7.14, for the fine- and coarse-grained cermets, respectively. As it can be seen, it is obvious that there is heavy dissolution of the metal binder, leaving the TiC grains largely unaffected. Comparing the images of the two cermet systems in terms of the metal binder concentration, it is apparent that with an increasing binder content the amount of 'clean' TiC is becoming more pronounced, evidenced by increasingly heavy dissolution of the metal binder, and the retention of 'clean' TiC grain surfaces. The increasing loss of the metal binder with binder content helps to explain the decrease in corrosion resistance, especially for the cermets with the highest steel contents. As noted earlier, this can be attributed to greater protection of the cermet surface that is afforded at higher TiC contents (i.e. the lowest binder contents), through the formation of a TiO_2-based surface protective layer, thereby inhibiting dissolution of the metal binder and leading to an improvement in the corrosion resistance (as shown previously in Figures 7.6 and 7.7, and Table 7.2).

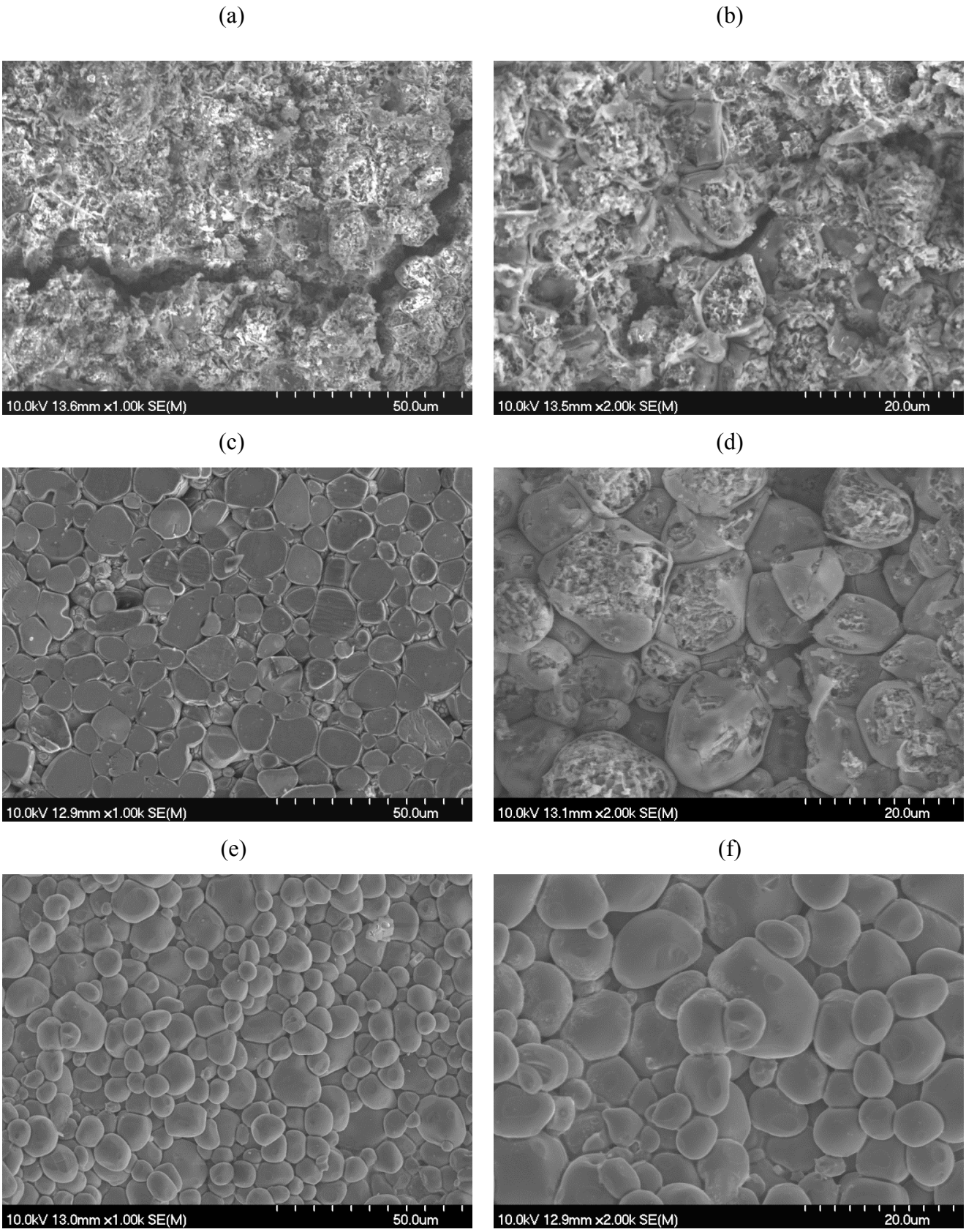

Figure 7.13: SEM images of the fine-grained TiC-316L cermets following potentiodynamic polarisation testing: (a,b) 10 vol. % 316L, (c,d) 20 vol. % 316L, and (e,f) 30 vol. % 316L binder.

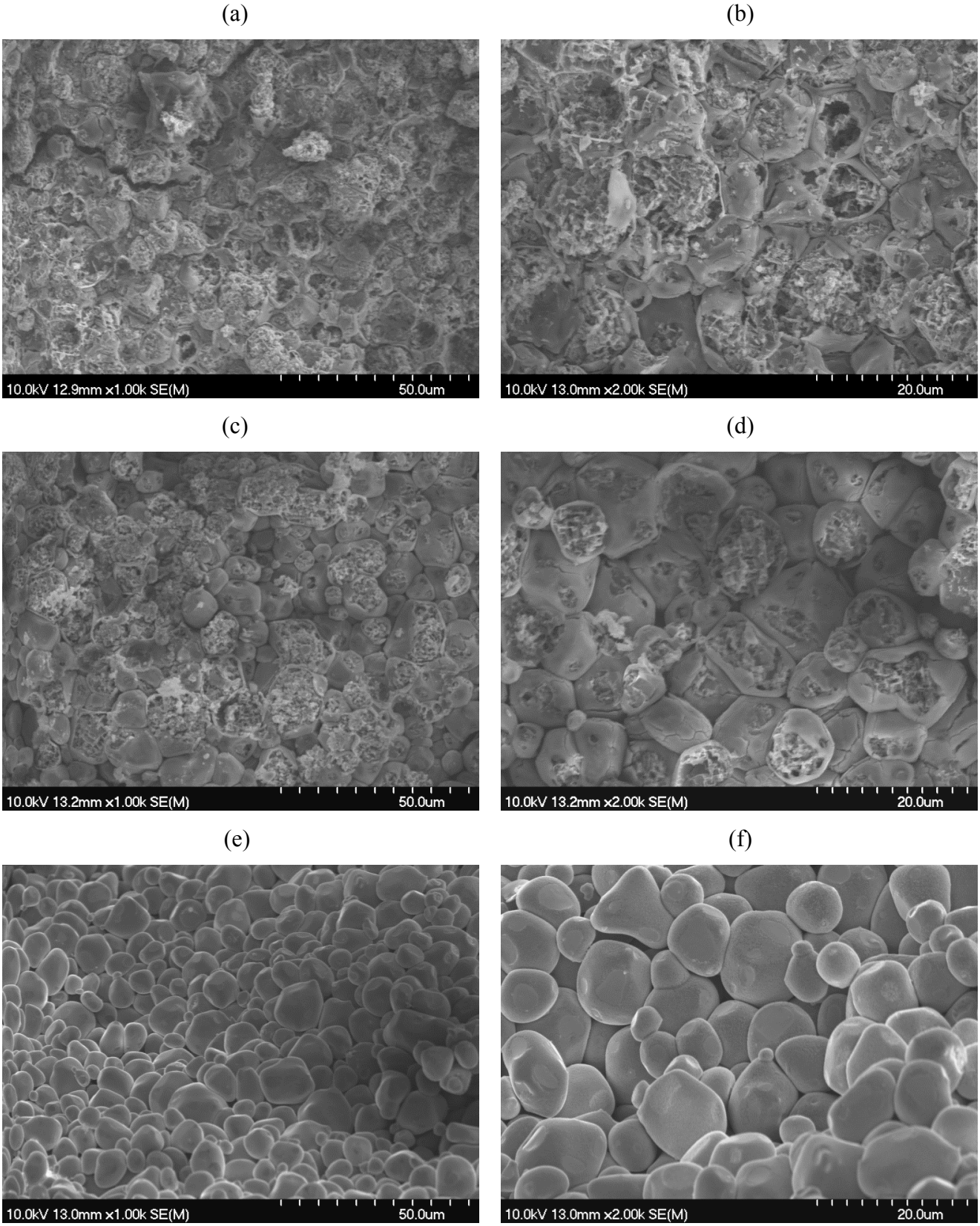

Figure 7.14: SEM images of the coarse-grained TiC-316L cermets following potentiodynamic polarisation testing: (a,b) 10 vol. % 316L, (c,d) 20 vol. % 316L, and (e,f) 30 vol. % 316L binder.

The general microstructural observations of increasing binder dissolution with content, from Figures 7.13 and 7.14, are in agreement with the corrosion rate data presented in Figures 7.6 and 7.7, the potentiostatic response from Figure 7.9, and the ICP-OES/EDS analyses shown in Figures 7.10 to 7.12. Another distinguishable feature, seen occasionally in the SEM images of cermets with the fine-grained structure, is the presence of isolated cracks, as shown in Figure 7.13(a). Such cracks were not observed in the more coarse-structured cermets. By reducing the carbide grain size, the binder mean free path dimension is reduced. Typically, this can be seen to have detrimental impact on the cermet toughness, which is observed in the present materials [Onuoha, Farhat, Kipouros and Plucknett, unpublished research]. It is also postulated that the binder is effectively under a greater degree of constraint, due to the surrounding carbide grains being in closer proximity to one another. Combined with a higher metal:ceramic interfacial area, this leads to an increase in the residual stress at the interface (i.e. an increase in the dislocation density). The presence of cracks on fine grained cermets suggest that these factors all contribute in some way to a greater degree of near surface embrittlement when the steel binder is dissolved. Generally, it can therefore be seen that an increase in the dislocation density can favour increased wear resistance (e.g. through strain hardening) but negatively impacts the corrosion resistance.

Figures 7.15 and 7.16 present typical SEM images of the fine- and coarse-grained cermets, respectively, following potentiostatic polarisation. As it can be seen, there is preferential dissolution and removal of the metal binder, while the TiC grains are again essentially unaffected. It can also be seen that the preferred site for the corrosive attack appears to be at the interface between the TiC grains and the metal binder. The effect of interfacial attack is also more pronounced on cermets with finer grain sizes. This observation demonstrates that galvanic corrosion is likely the driving mechanism for both the fine- and coarse-grained cermets. With finer grain sizes, the interfacial area between the TiC grains and the metal binder is higher (by approximately a factor of three in the present materials) and the extent of galvanic corrosion is increased. Conversely, by increasing the carbide grain size, the degree of galvanic attack can be reduced, leading to improved corrosion resistance with the coarse-grained cermets.

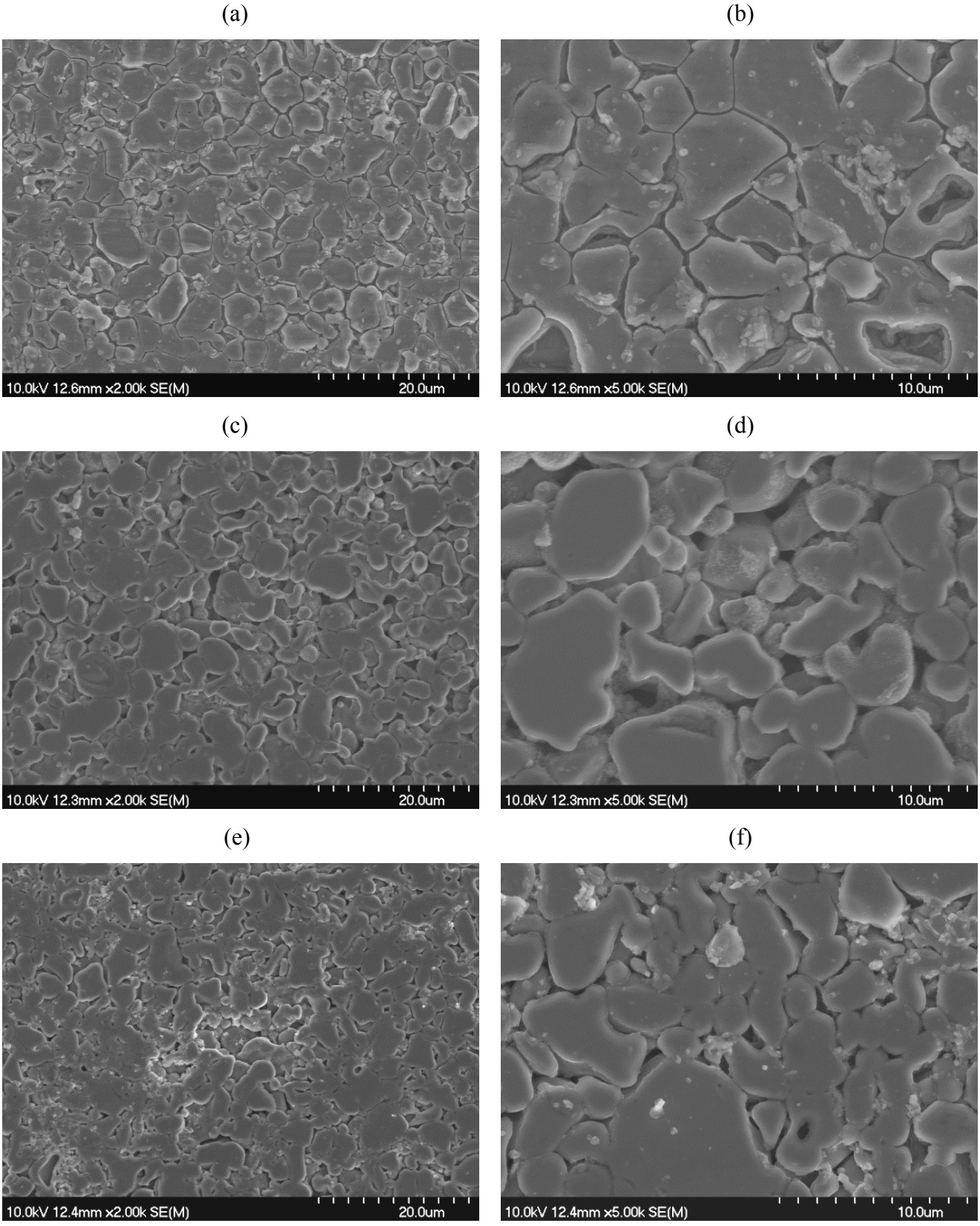

Figure 7.15: SEM images of the fine-grained TiC-316L cermets following potentiostatic polarisation testing: (a,b) 10 vol. % 316L, (c,d) 20 vol. % 316L, and (e,f) 30 vol. % 316L binder.

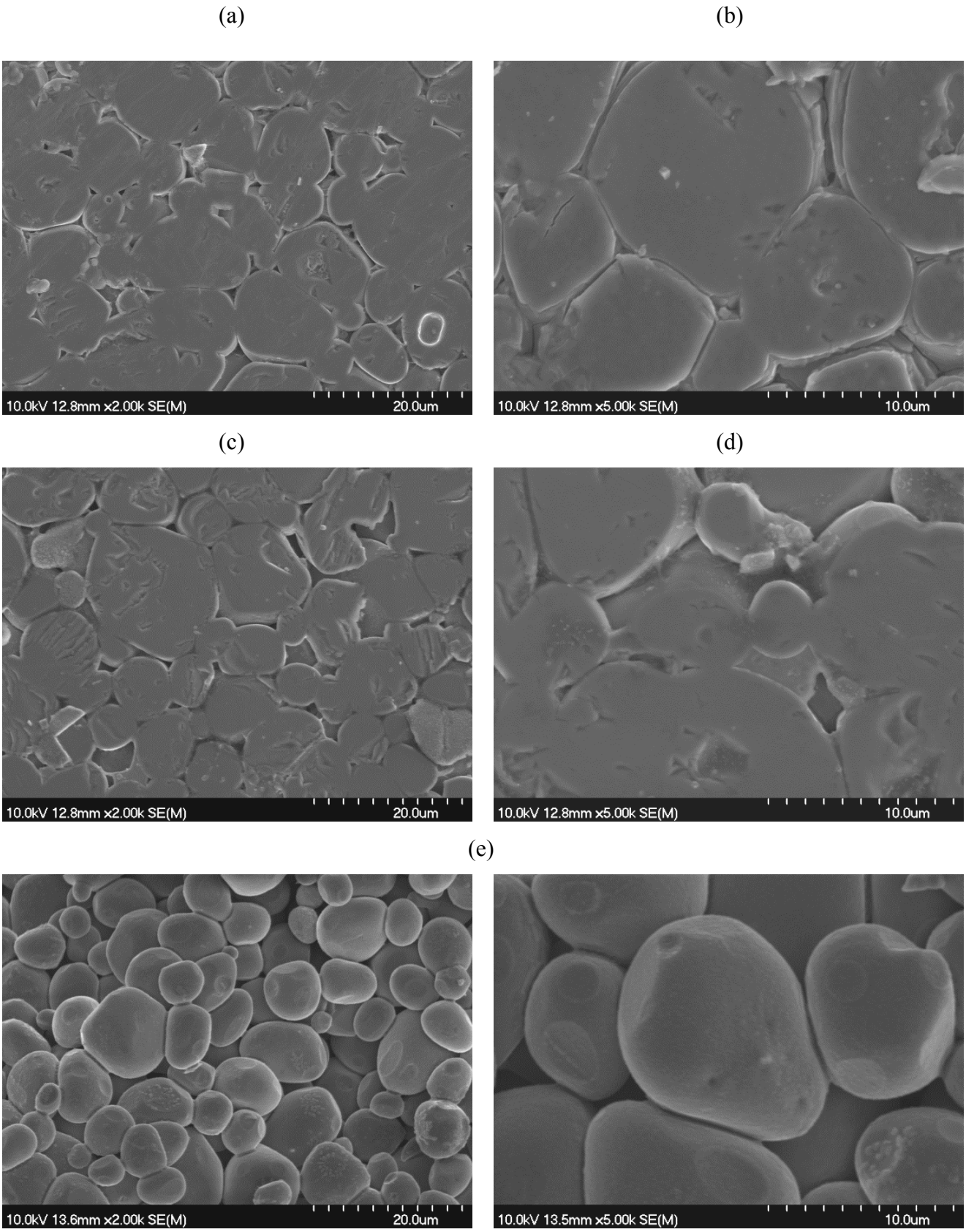

Figure 7.16: SEM images of the coarse-grained TiC-316L cermets following potentiostatic polarisation testing: (a,b) 10 vol. % 316L, (c,d) 20 vol. % 316L, and (e,f) 30 vol. % 316L binder.

Clearly, combining low metallic binder contents, together with relatively coarse carbide microstructures can lead to an enhancement of the corrosion resistance. However, these benefits in terms of corrosion resistance must be weighed against the potential for reduced wear resistance when the carbide structure is coarsened, which is the observation made for the present materials [Onuoha, Farhat, Kipouros and Plucknett, unpublished research].

7.5 Conclusions

The corrosion behaviour of fine- and coarse-grained TiC-316L cermets has been assessed in a simulated seawater solution (containing 3.5 wt. % NaCl), using a variety of electrochemical techniques, including Tafel extrapolation, and both potentiodynamic and potentiostatic polarisation. The electrochemical measurements have been coupled with microstructural and chemical analyses of the cermets, both before and after corrosion. Based on this study, the following conclusions can be drawn:

(1) The corrosion resistance of both fine- and coarse-grained TiC-316L cermets increases with a reduction in the steel binder content (i.e. an increase in the TiC content). This is attributed to an increase in the surface area coverage by a TiO_2 semi-protective layer, with a resultant reduction in the tendency for metallic binder dissolution.

(2) The corrosion resistance of the coarse-grained cermets is slightly superior to that of the fine-grained counterpart. This is believed to be due to reduced (galvanic) interfacial attack, due to a reduction in the metal:ceramic grain boundary area by a factor of approximately three.

(3) The combination of ICP-OES and EDS analyses confirmed an increase in the dissolution of the steel binder with increasing volume fraction, with this effect is slightly more pronounced for the fine-grained cermets.

(4) Microstructural studies also confirmed for both the fine- and coarse-grained cermets that, while there is preferential dissolution of the steel binder, the TiC grains remain largely unaffected.

(5) Based on the various electrochemical measurements performed, it can be concluded that in addition to lowering the binder content of the TiC-316L cermets, increasing the carbide grain size is an additional approach that can be taken to improve the corrosion resistance of these materials.

7.6 Acknowledgements

This study was financially supported by Petroleum Research Atlantic Canada (PRAC) and the Natural Sciences and Engineering Research Council of Canada (NSERC). The Canada Foundation for Innovation, the Atlantic Innovation Fund, and other partners who helped fund the Facilities for Materials Characterisation, managed by the Dalhousie University Institute for Materials Research, are also gratefully acknowledged. The authors would also like to thank Dean Grijm and Patricia Scallion for technical assistance.

8 The Corrosion Behaviour of TiC-Stainless Steel Cermets in a Synthetic Seawater Solution

Chukwuma C. Onuoha, Georges J. Kipouros, Zoheir N. Farhat and Kevin P. Plucknett*

Dalhousie University, 1360 Barrington Street, Materials Engineering Program, Department of Process Engineering and Applied Science, B3H 4R2, Nova Scotia, Canada

Status: Submitted to Canadian Metallurgical Quarterly 2013

8.1 ABSTRACT

A family of TiC-stainless steel ceramic-metal composites (or cermets) was developed in the present study, using steel grades 304L, 316L or 410L as binders. Melt-infiltration was used to prepare the cermets, with binder contents varied between 10 and 30 vol. %. The corrosion behaviour was evaluated using a range of electrochemical techniques in an aqueous, NaCl-containing solution. The test methods included Tafel extrapolation, and potentiodynamic, cyclic and potentiostatic polarisation. The corroded samples were subsequently characterised using SEM and EDS, while the post-corrosion solutions were analysed using ICP-OES to determine the residual ionic and particulate material removed from the cermets. It was demonstrated that the corrosion resistance was enhanced through decreasing the steel binder content, which arises due to the preferential dissolution of the binder phase, while the TiC ceramic remains largely unaffected. For the present materials, TiC prepared with 10 vol. % 304L stainless steel provided the highest corrosion resistance.

Keywords: Ceramic composites; electrochemical characterisation; potentiodynamic polarisation; cyclic polarisation; potentiostatic polarisation; galvanic corrosion; SEM; ICP-OES

*Contact author email: kevin.plucknett@dal.ca

8.2 Introduction

Titanium carbide (TiC) based ceramic-metal composites, or cermets, have become more widely used in wear applications due to their improved capabilities when compared to more traditional 'hardmetals', such as tungsten carbide-cobalt (WC-Co) [1]. TiC based cermets have several properties that typically exceed those of WC, such as increased hardness and toughness, as well as a lower mass (the density of WC is approximately three times that of TiC) [2]. These characteristics, in addition to TiC being of a lower cost than WC, offers the potential for TiC-based cermets to replace WC-Co in a variety of industrial applications.

In terms of the development of cermets for corrosion applications, it is invariably noted that the incorporation of a metallic binder with the ceramic matrix phase degrades the corrosion performance of the material [58, 91, 94, 155, 181, 196]. Available literature on the aqueous electrochemical behaviour of cermets, and in particular WC-Co, shows that the binder metallic phase affects corrosion behaviour due to its selective dissolution, while the ceramic phase remains relatively immune [8, 58, 91, 93, 94, 155, 170-173, 181, 193, 194,196, 197, 210]. Monticelli and colleagues reported a loss in corrosion resistance through the incorporation of Co binder into WC for thermal spray coatings [197]. By comparing the corrosion performance of WC and WC prepared with 5 wt. % Co, the corrosion resistance of WC-Co cermets decreased, and the loss in corrosion resistance was attributed to preferential dissolution of the Co binder in the composite. Dissolution of the Co binder phase in WC-Co cermets has also been reported by other authors [170, 181], and it was confirmed that the loss of the metal binder governs the corrosion behaviour of WC-Co cermets, although it is dependent upon the applied potential. A reduction in the corrosion resistance of WC-Co with increase in Co binder content was also reported by Mori and colleagues [94], who showed an improvement in the corrosion resistance of cermets with a higher dissolved WC content in the Co binder. The corrosion behaviour of TiC-304L and TiC-316L stainless steel based cermets has also recently been reported [155, 196], and it was demonstrated that the corrosion resistance was improved by lowering the steel binder content (i.e. TiC prepared with 10 vol. % steel content). At high binder contents (i.e. TiC with 30 vol. % 304L), microstructural analysis revealed preferential dissolution of the steel, resulting in relatively poor corrosion resistance compared to the materials prepared with 10 vol. % 304L [196]. For TiC-316L cermets, it was shown that the corrosion resistance is degraded when reducing the TiC grain size [155], for a constant steel binder content, which was attributed to galvanic activity at the TiC-steel interface; in this instance cermets with nominal grain sizes of 4 and 11 μm were developed, with the finer grain

sized materials having an approximately three times greater interfacial area than those with the coarse grain size.

In order to reduce the wear and, potentially, corrosion of metallic components, cermets or hard oxide coatings are often used. Generally, cermets coatings consist of WC or chromium carbide (Cr_3C_2) particles embedded in a metal binder, which can be a pure metal or an alloy, for example consisting of a mixture Ni, Cr and/or Co [211]. Hard oxide surface coatings are often based on Cr_2O_3 as the corrosion resistant layer [211]. As many coatings have complex compositions, and multiple components, the possibility of micro-galvanic corrosion activity between the different constituents can arise, which is likely to undermine the surface integrity of the coating [211]. An example includes bulk composites or coatings that undergo tribologically induced compositional changes. For instance, the presence of carbides in a metallic binder typically improves wear resistance, but at the same time may establish a micro-corrosion cell at the carbide-metal interface. This can arise as the carbide is likely to be more cathodic, with respect to the surrounding metallic matrix, leading to the possibility of preferential anodic dissolution of the metallic matrix close to, or at, the matrix-carbide interface. This process can consequently accelerate carbide removal from the surface, and hence reduce the wear-resistant properties [12]. Such behaviour has been reported for the corrosion-wear response of HVOF sprayed WC cermets coatings, with metallic binders of Co, Co-Cr, Cr_3C_2-Ni and Ni, when tested in a strong acidic environments [212]. Considerable micro-galvanic corrosion occurred between the WC particles and the binder, and uniform corrosion occurred in the binder materials of WC-Co, WC-Ni [212]. The occurrence of galvanic corrosion was confirmed in WC-Co cermets by examining the dissolution behaviour of Co, WC and the WC-Co composite itself, and it was demonstrated that there was serious dissolution of Co, while the WC remained essentially unaffected [12]. Perry and colleagues studied the corrosion behaviour of WC-Co and WC-CoCr coatings [213], and reported a general corrosion of the Co binder in the WC-Co coatings, while in the WC-CoCr coatings the corrosion mechanism was of a more localised nature, attacking the interface between the carbide and metal phases.

There is a continuing demand to develop new and improved materials, that can offer superior wear and corrosion resistance, especially in the mining, and oil and gas industries, where corrosion and erosion/wear are major concerns. For instance, the US Navy is currently interested in materials that exhibit superior wear and corrosion resistance [192]. Unfortunately, the microstructural modifications that can enhance wear resistance, may also adversely affect the corrosion resistance. For example, cermets intrinsically consist of a ceramic and metal phase that will likely have differing electrical

characteristics, thereby opening up the possibility of galvanic corrosion at the interface [95]. With that in mind, Wu and colleagues studied the corrosion behaviour of TiC particle-reinforced 2Cr13 stainless steel metal matrix composites (MMCs) in a 5 wt. % HCl aqueous solution (with 0 to 2.5 wt. % TiC) [190], and reported that the addition of TiC resulted in the formation of Cr-rich carbides in the alloy; in this instance the TiC concentration was relatively dilute, and the composite can be viewed as a metal matrix composite, rather than a cermet. The presence of the Cr-rich carbides, together with the more noble TiC particles, led to the formation of galvanic microcells with the adjacent steel matrix. It was also noted that the difference in the thermal expansion coefficient between TiC and the steel matrix resulted in a high dislocation density at the steel matrix/TiC interface, which accelerated the corrosion at higher TiC contents [190-191].

The objective of the present paper is to investigate the corrosion behaviour of TiC-stainless steel cermets in a simulated seawater environment, through the application of selected electrochemical measurements, in combination with microstructural and compositional analysis. Stainless steel grades 304L, 316L and 410 L have been used for the cermet binders, with processing controlled to ensure a nominally constant mean grain size for the TiC in each of the cermets. To further elucidate the behaviour of these cermets, their corrosion response has also been compared to the equivalent 'pure' stainless steel grades (i.e. 304L, 316L and 410L).

8.3 Experimental procedure

8.3.1 Sample Preparation and Characterisation

All of the TiC-based samples were prepared using as-received TiC powder (Grade TiC-2012; Pacific Particulate Materials, Vancouver, BC, Canada), with a mean particle size of ~1.25 μm [96]. TiC preforms were prepared by uniaxial pressing (at ~67 MPa) to produce samples ~31.75 mm in diameter x ~4 mm thick. The preforms were then further compacted by cold isostatic pressing at ~220 MPa. Following compaction, the TiC pellets were weighed and placed onto a layer of bubble alumina within an alumina crucible. An appropriate amount of steel powder was then placed on top of the TiC preforms, with the steel content varied from 10 to 30 vol. % in the final cermet composition. Three stainless steel powders (Alfa Aesar, Ward Hill, MA, USA) were used, each with a nominal particle size of -100 mesh: austenitic grades 304L (Lot # K19M09) and 316L (Lot # A04S008), and the martensitic grade 410L (Lot # 123M43). The nominal composition of each grade of steel used in the present work is provided in Table 8.1[97]. Melt-infiltration was subsequently conducted at 1500°C (for 304L and

316L containing samples) and 1550°C (for the 410L samples), under a dynamic vacuum (better than 20 milliTorr). A graphite resistance furnace (Materials Research Furnaces, Suncook, NH, USA) was used, with heating and cooling rates of 10°C/min and 25°C/min respectively. The sintering temperature was held for a period of 60 minutes in each case. These conditions were selected to provide a nominally equivalent grains size for each of the TiC-stainless steel cermet systems, so that potential interfacial area effects, relating to differing grain sizes, could be minimised [155].

Table 8.1: Nominal compositions for the stainless steel grades used in the present work [97].

Type	**Nominal composition (max. wt. %)**									**Density**
	Cr	**Ni**	**C**	**Mn**	**Si**	**P**	**S**	**N**	**Mo**	**(g/cm^3)**
304-L	18-20	8-12	0.03	2	1	0.045	0.03	0.1	-	8.03
316-L	16-18	10-14	0.03	2	1	0.045	0.03	0.1	2-3	8.03
410-L	11-13.5	0.75	0.03	1	1	0.04	0.03	-	0.75-1.25	7.75

The infiltrated cermet densities were determined using the Archimedes immersion method in water. For microstructural examination and corrosion testing, the densified cermet samples were initially ground flat using a coarse, 149 μm (100 mesh) peripheral diamond wheel (Saint-Gobain Abrasives, Worcester, MA, USA). They were then ground and polished using successively finer grades of diamond, starting with 125 μm diamond pads and finishing at 0.25 μm diamond paste. Microstructural characterisation was subsequently performed using both optical microscopy (Olympus BX-51, Olympus, Tokyo, Japan) and scanning electron microscopy (SEM; Model S-4700 Hitachi High Technologies, Tokyo Japan), the latter with associated energy dispersive X-ray spectroscopy (EDS; Model X-Max/Inca, Oxford Instruments, Concord, MA, USA).

Grain size measurements were made using the linear intercept method on digital SEM images [125]. This allowed determination of the mean grain intercept dimension, which was then multiplied by 1.56 to determine a mean grain size $d_{c,}$ for each material. A minimum of 300 TiC grains were measured for each sample to determine the individual mean grain sizes. In addition, two further microstructural parameters were determined for each of the TiC-stainless steel cermets. The contiguity is a measure of the ratio of carbide-carbide to carbide-binder interfaces that are intercepted per unit line length, and it was determined for each sample following [152]:

$$C = \frac{2N_{c/c}}{2N_{c/c} + 2N_{c/b}} \qquad \text{Equation 5.1}$$

where $N_{c/c}$ and $N_{c/b}$ are the number of carbide-carbide (i.e. TiC-TiC) and carbide-binder (i.e. TiC-steel) interfaces, respectively. The mean free path of the steel binder, d_b, is a measure of the metallic ligament dimensions between individual carbide grains. The mean free path is given by [153]:

$$d_b = \frac{1}{1-C}\left(\frac{V_b}{V_c}\right)d_c \qquad \text{Equation 5.2}$$

where V_b and V_c are the volume fractions of the binder and carbide phases, respectively (for the present case it is assumed that $V_b + V_c = 1$).

8.3.2 Electrochemical Testing

The corrosion response of the TiC-stainless steel cermets was assessed in a simulated seawater environment, containing 3.5 wt% NaCl, at room temperature (nominally 23°C). A standard three-electrode, flat cell configuration was employed, with the cermet sample acting as the working electrode (the exposed surface test area was 1 cm^2). A platinum mesh was employed as the counter electrode, with a saturated calomel electrode (SCE; 0.241 V versus a standard hydrogen electrode) as the reference. All of the potential measurements that are subsequently discussed will consequently be referred to the reference electrode. In order to compare the corrosion behaviour of the cermets, 'pure' 304L, 316L, and 410L stainless steel specimens were used as reference materials; the 'pure' steel grades were sourced commercially from McMaster-Carr (Aurora, OH, USA).

Prior to potentiodynamic polarisation measurement, the samples were immersed for a period of 240 minutes to ensure steady-state conditions. For the actual potentiodynamic polarisation experiments, the potential was scanned from -0.75 to +3.5 V_{SCE}, at a scan rate of 0.1667 mVs^{-1} (EG&G Princeton Applied Research Potentiostat/Galvanostat Model 273, Princeton Applied Research, Oak Ridge, TN, USA). For each test, the corrosion potential (E_{corr}) and the corrosion current density (i_{corr}) were estimated through the use of an instantaneous, Tafel-type fit, derived using CorrWare corrosion analysis software (Scribner Associates, Inc., Southern Pines, NC, USA). The critical current density, i_{crit} (i.e. the current measured at the peak of the active region) and pseudo-passive current density i_{pass} (i.e. the minimum current in the pseudo-passive region) are also used to characterise results obtained

after potentiodynamic polarisation. The Tafel-derived corrosion rate (in mm/year) is then calculated following [107]:

$$\text{Corrosion rate (Tafel)} = \frac{3.27 \times 10^{-3} \times i_{corr} \times W}{D} \qquad \text{Equation 3.1}$$

where W is the equivalent weight of the alloy (i.e. composite), D is the density of alloy (in g/cm^3), and i_{corr} (in μA/cm^2) is the corrosion current density of the specimen extrapolated from the Tafel polarisation plots. In order to have an idea of the actual material lost by corrosion, and for comparison with the electrochemical-derived corrosion rate, the cermets samples were also weighed before and after corrosion, and the weight loss was used to calculate the corrosion rate (in mm/year) following [37]:

$$\text{Corrosion rate (weight loss)} = \frac{87.6 \times M}{T \times A \times D} \qquad \text{Equation 3.2}$$

where M is the weight loss (in g) after exposure time, T (in hours), and A is the area of the exposed specimen (in cm^2). For cyclic potentiodynamic polarisation testing, scans were initiated 240 minutes after the specimen was immersed in the test solution. Each scan was initiated from the open circuit potential (OCP) to the point where a significant current increase was observed in the anodic (positive) direction. As the scan reached a user-programmed threshold current value and/or offset potential, it was reversed and the sample was then scanned in the cathodic (negative) direction. When the reverse and forward scans intersect, the scan was stopped. The scan rate was 0.1667 mVs^{-1} for both the forward and reverse directions. The cyclic potentiodynamic testing allows determination of both the pitting and protection potentials, E_{pit} and E_{prot}, respectively. In this instance the value for E_{pit} was determined from the point where a sudden increase in current was experienced during the forward scan, while the value for E_{prot} was determined from the intersection point of the reverse scan on the forward scan.

Microstructural evaluation of the corroded surfaces was carried out using optical microscopy, SEM/EDS and XRD. In order to determine the concentrations of various elemental species released from the cermets during testing, the solutions remaining after the electrochemical tests were examined using inductively coupled plasma optical emission spectroscopy (ICP-OES; Varian Vista Pro (Radial View), Varian Inc., Mulgrave, Australia). The solutions recovered from the test cell were initially filtered using a Millipore vacuum filtration system (with a 1.0 μm pore size). Filtering allowed the separation of any fine particulate material released from the corroding surfaces, which could then be analysed independently from any dissolved elemental species. The remaining solution following

filtration was directly analysed using ICP-OES. To assess the filtered particulate material, the recovered residue was dried at 105ºC and then weighed. It was then dissolved in a sequence of acids (HF, HNO_3, $HClO_4$), within Teflon beakers, and then dried again. The dried residue was then brought back into solution with HCl, made up to 100 ml in volumetric flasks, and subjected to ICP-OES analysis.

8.4 Results and Discussion

8.4.1 Cermet Characterisation

Following melt-infiltration, all the samples were densified to in excess of 99 % of theoretical (based on a simple rule-of-mixtures related to the starting constituent densities), such that subsequent electrochemical testing can be viewed as being performed on fully planar surfaces (i.e. there are no complicating factors relating to surface connected porosity that would increase the effective surface area). Representative SEM images of the microstructures of the TiC-stainless steel cermets are shown in Figure 8.1, confirming the high degree of densification that was achieved for each compositional variant. In each case there is good homogenisation of the TiC ceramic phase within the steel binder, with little evidence of anomalous grain growth.

(a) (b) (c)

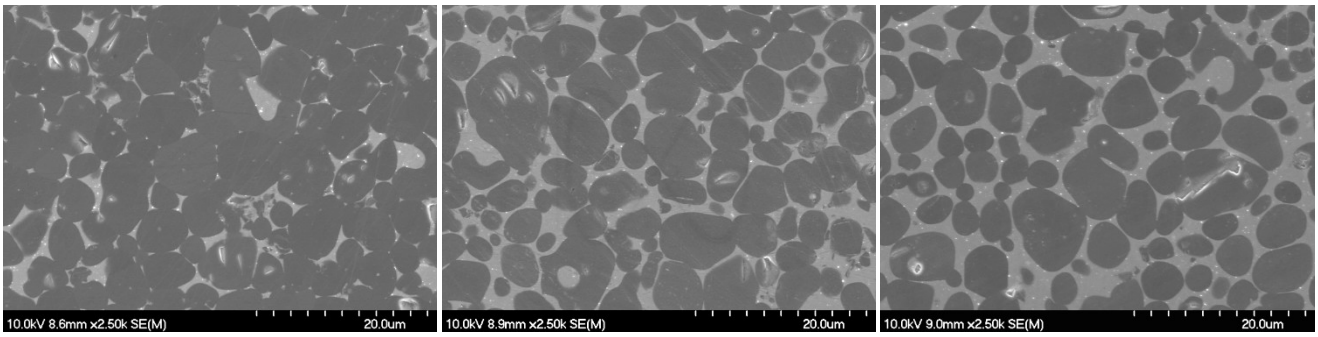

(d) (e) (f)

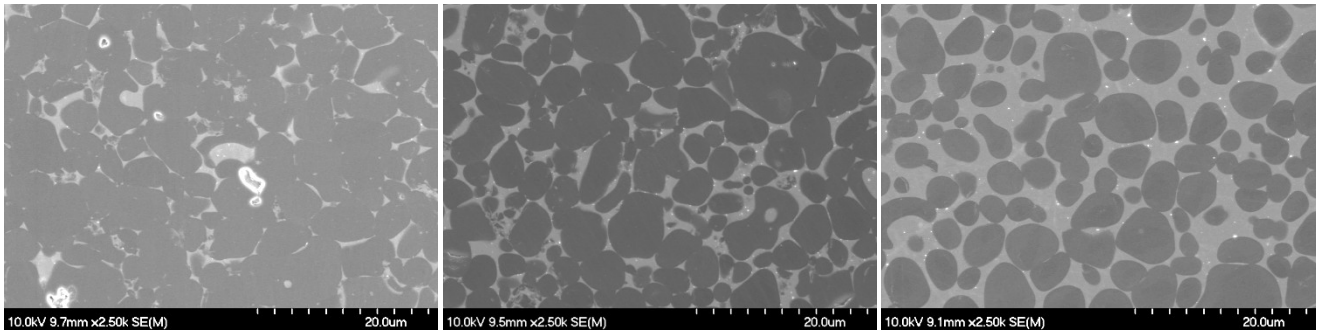

(g) (h) (i)

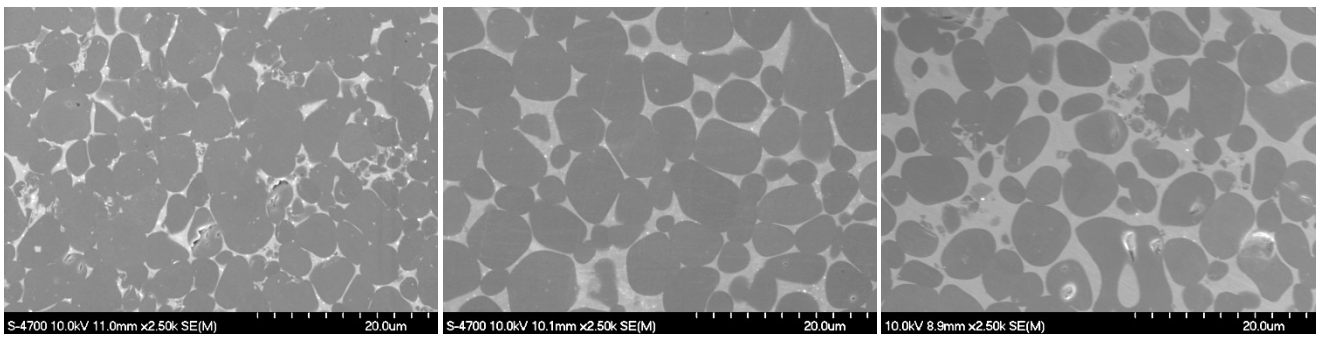

Figure 8.1: Representative SEM images of TiC-stainless steel cermets prepared with: (a) TiC-10 vol. % 304L, (b) TiC-20 vol. % 304L, (c) TiC-30 vol. % 304L, (d) TiC-10 vol. % 316L, (e) TiC-20 vol. % 316L, (f) TiC-30 vol. % 316L, (g) TiC-10 vol. % 410L, (h) TiC-20 vol. % 410L, and (i) TiC-30 vol. % 410L.

The mean grain size, calculated using the linear intercept method, was broadly consistent for each composition at ~6 μm (Figure 8.2(a)). The carbide-carbide contiguity is observed to decrease in a broadly consistent manner with increasing binder content (Figure 8.2(b)), while the binder mean free path increases with the binder content (Figure 8.2(c)). These microstructural observations regarding contiguity and binder mean free path are generally consistent with prior studies of TiC-Ni_3Al cermets [124].

(a)

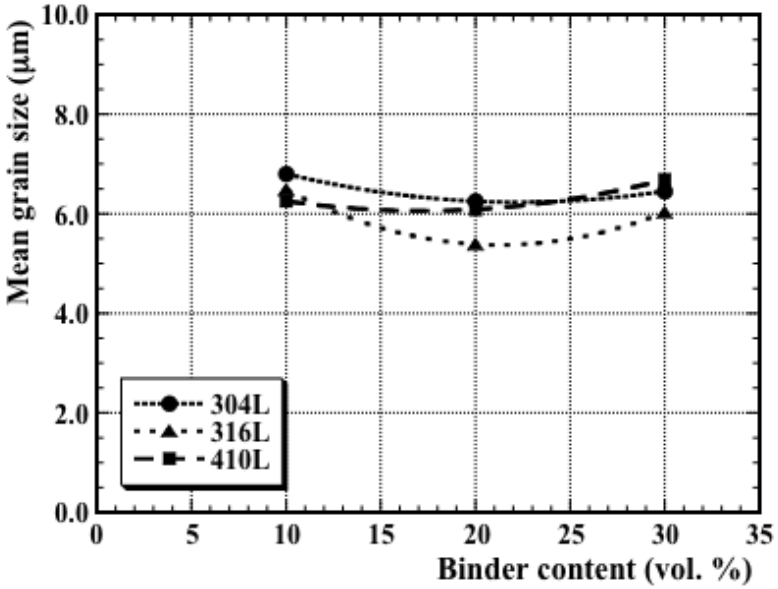
Mean grain size (μm)
10.0
8.0
6.0
4.0
2.0
0.0
0
5
10
15
20
25
30
35
Binder content (vol. %)
304L
316L
410L

(b)

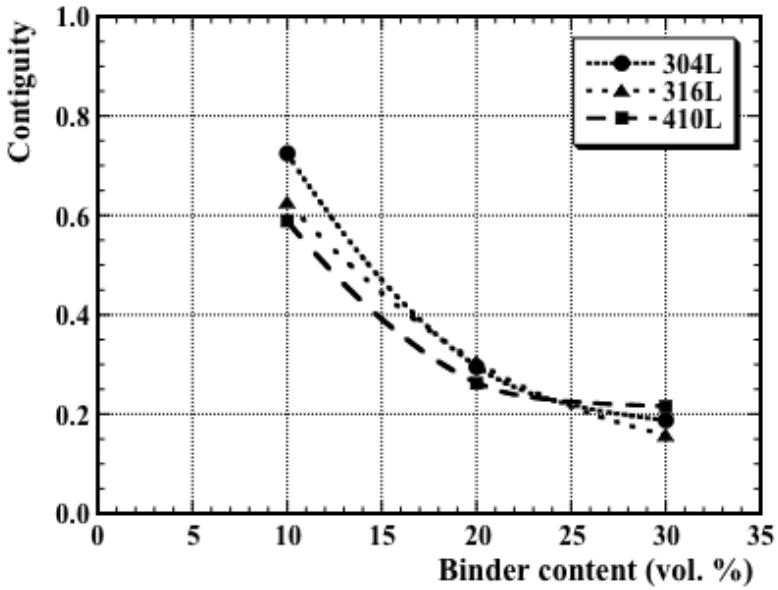
Contiguity
1.0
0.8
0.6
0.4
0.2
0.0
0
5
10
15
20
25
30
35
Binder content (vol. %)
304L
316L
410L

(c)

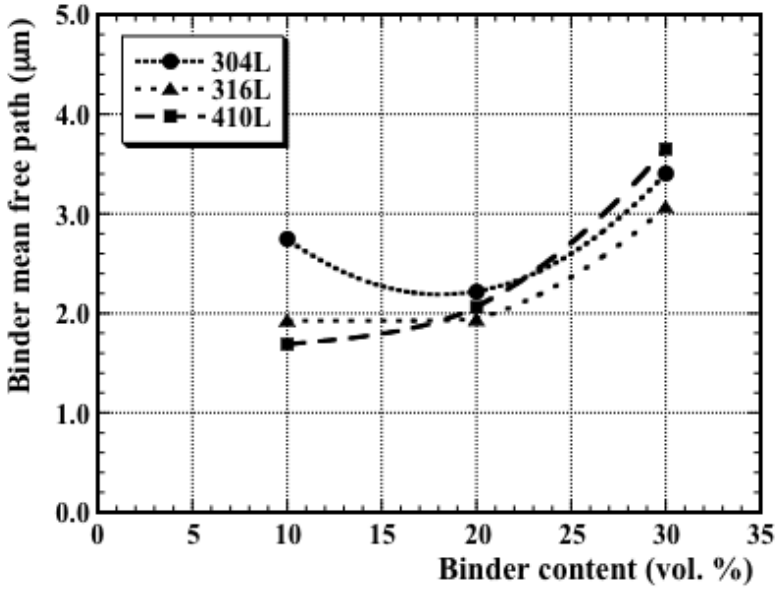

Figure 8.2: The effects of binder composition and content on the various microstructural parameters assessed for the TiC-stainless steel cermets developed in the present work: (a) grain size, (b) contiguity, and (c) the binder mean free path.

8.4.2 Electrochemical Measurements

Typical examples of the plots obtained for the OCP, as a function of time, are shown in Figure 8.3. It is apparent that by increasing the steel binder content, the OCP becomes more negative. The relative parameters determined from the OCP analysis for each of the cermet compositions are presented in Table 8.2.

(a)

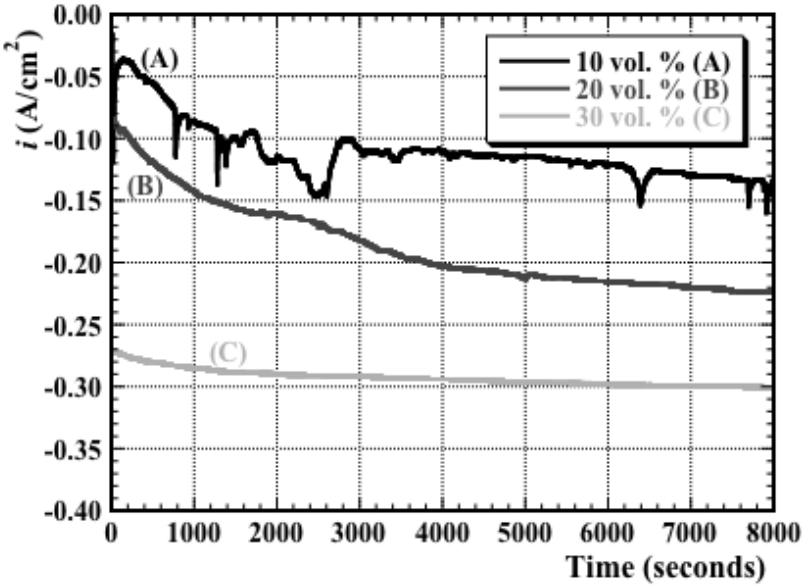
0.00
-0.05
-0.10
-0.15
-0.20
-0.25
-0.30
-0.35
-0.40
i (A/cm²)
(A)
(B)
(C)
10 vol. % (A)
20 vol. % (B)
30 vol. % (C)
0
1000
2000
3000
4000
5000
6000
7000
8000
Time (seconds)

(b)

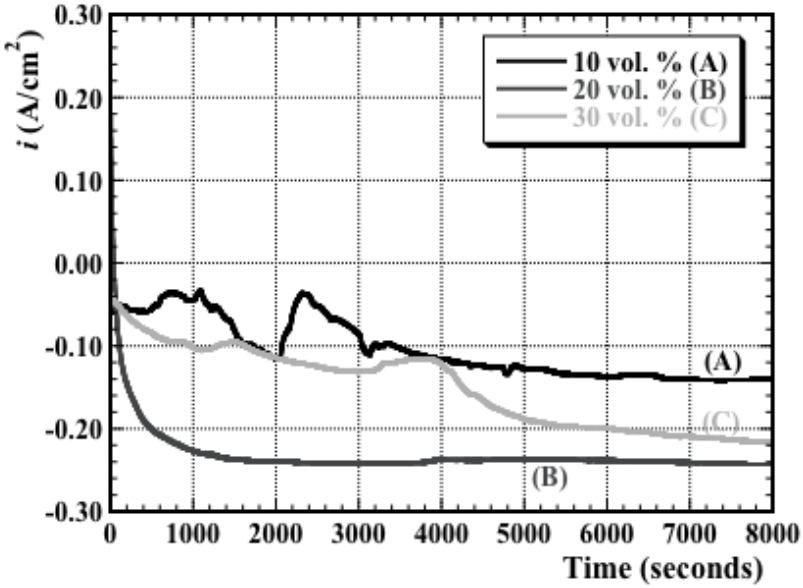
0.30
0.20
0.10
0.00
-0.10
-0.20
-0.30
i (A/cm²)
(A)
(B)
(C)
10 vol. % (A)
20 vol. % (B)
30 vol. % (C)
0
1000
2000
3000
4000
5000
6000
7000
8000
Time (seconds)

(c)

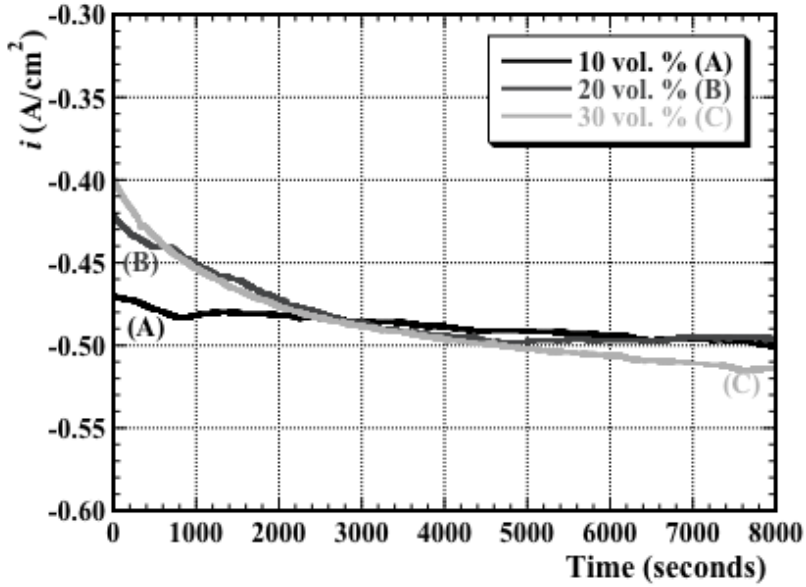

(d)

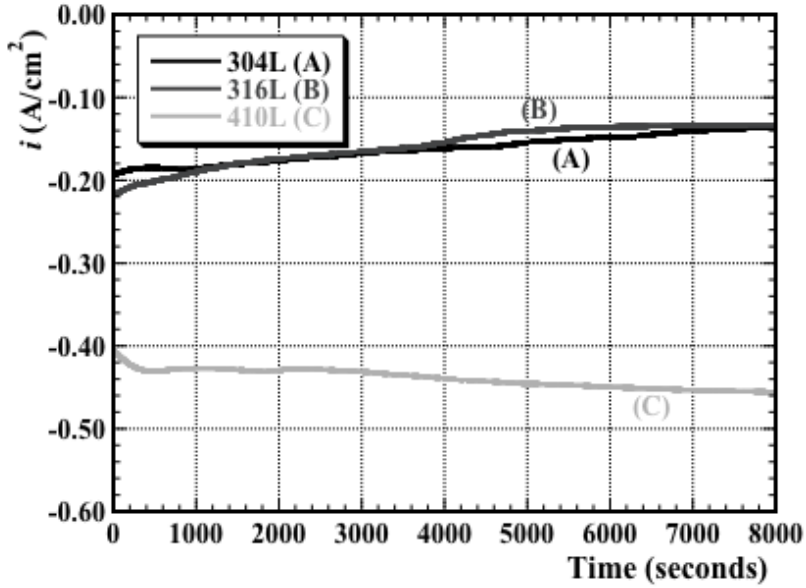

Figure 8.3: Representative OCP curves, demonstrating the effects of binder content for each of the TiC-stainless steel cermets, together with comparison of the 'pure' stainless steels: (a) TiC-304L, (b) TiC-316L, (c) TiC-410L, and (d) the 'pure' grades of stainless steel.

For comparison purposes, values for the OCP obtained with the 'pure' steels are presented in Table 8.3. As can be seen for each of the systems examined, the OCP values for the respective steels are less negative (i.e. more noble) than for the corresponding cermets, which indicates better surface passivation behaviour and, consequently, improved corrosion resistance [214].

Table 8.2: OCP values determined for the cermets as a function of the steel binder content. Each value is the mean of 10 repetitions (standard deviation shown in parentheses).

Binder content (vol.%)	**OCP (V vs. SCE)***		
	TiC-410L	**TiC-316L**	**TiC-304L**
10	-0.470 (0.034)	-0.241(0.058)	-0.224 (0.039)
20	-0.526 (0.018)	-0.264(0.018)	-0.260 (0.027)
30	-0.520 (0.020)	-0.233(0.028)	-0.278 (0.031)

Table 8.3: OCP values determined for the 'pure' steels. Each individual value is the mean of 10 repetitions (standard deviation values are shown in parentheses).

OCP (V vs. SCE)		
304L	**316L**	**410L**
-0.105 (0.021)	-0.123 (0.040)	-0.455 (0.030)
**Values are mean (standard deviation), N = 10		

Slight oscillations in the potential are occasionally observed in the OCP curves (Figure 8.3), which suggests the likelihood of an aggressive action of the Cl^- ions towards the protective surface passivation layer [184]. The OCP values for the cermets broadly increase with steel binder content (i.e. TiC-304L), as shown in Table 8.2, but on occasion show a slight decrease at the highest binder content. This is particularly apparent for TiC-316L, where the OCP value for 30 vol. % binder is actually less negative than for 10 vol. % binder. The more noble OCP values generally observed at the lowest steel binder content for each cermet can be attributed the excellent corrosion resistance offered the protective surface layer, which can be anticipated to be titanium dioxide (TiO_2). TiC behaves in a broadly similar

manner to pure Ti, in that there is formation of a TiO_2 protective oxide layer [37, 215]. The presence of this TiO_2 layer helps in reducing the progression of corrosion [37, 166].

In order to determine the corrosion current density, i_{corr}, and the corrosion potential, E_{corr}, Tafel extrapolations were performed following potentiodynamic polarisation tests, with the results presented in Table 8.4.

Table 8.4: The Tafel-derived values of i_{corr} and E_{corr} determined for the cermets and 'pure'steels. The presented values are the mean for 4 repetitions (standard deviation values are shown in parentheses).

Sample	**E_{corr} (V vs. SCE)**	**i_{corr} (μA/cm^2)**
TiC-10 vol.% 304L	-0.210 (0.047)	0.576 (0.206)
TiC-20 vol.% 304L	-0.288 (0.023)	0.922 (0.033)
TiC-30 vol.% 304L	-0.264 (0.029)	1.440 (0.235)
304L stainless steel	-0.204 (0.023)	0.221 (0.013)
TiC-10 vol.% 316L	-0.211 (0.031)	1.261 (0.808)
TiC-20 vol.% 316L	-0.266 (0.028)	1.522 (0.230)
TiC-30 vol.% 316L	-0.234 (0.023)	3.043 (0.516)
316L stainless steel	-0.221 (0.031)	0.190 (0.022)
TiC-10 vol.% 410L	-0.465 (0.035)	2.298 (0.649)
TiC-20 vol.% 410L	-0.499 (0.001)	4.483 (0.163)
TiC-30 vol.% 410L	-0.506 (0.037)	5.965 (2.426)
410L stainless steel	-0.400 (0.024)	2.004 (0.263)

It is apparent that both i_{corr} and E_{corr} for the cermets increase with steel binder content. In comparison, the values of i_{corr} for each of the 'pure' steels is lower than for the cermets, again indicating better corrosion resistance. From Figure 8.4, based on the Tafel extrapolation data, it can be seen that the corrosion rate increases with binder content for all of the cermets. For the 'pure' steels, it is observed

that the corrosion resistance of 316L is the highest, followed by 304L and then 410L. This response is as expected [42], and relates to the different chemical compositions of the steel grades, as outlined in Table 8.1. It is apparent from the data presented in Figure 8.4 that the best cermet corrosion resistance is achieved for the lowest binder content samples. This response arises from the effectively increasing TiC surface area, at lower binder volume fractions, with the TiC being protected by a TiO_2 surface layer, as outlined earlier [215].

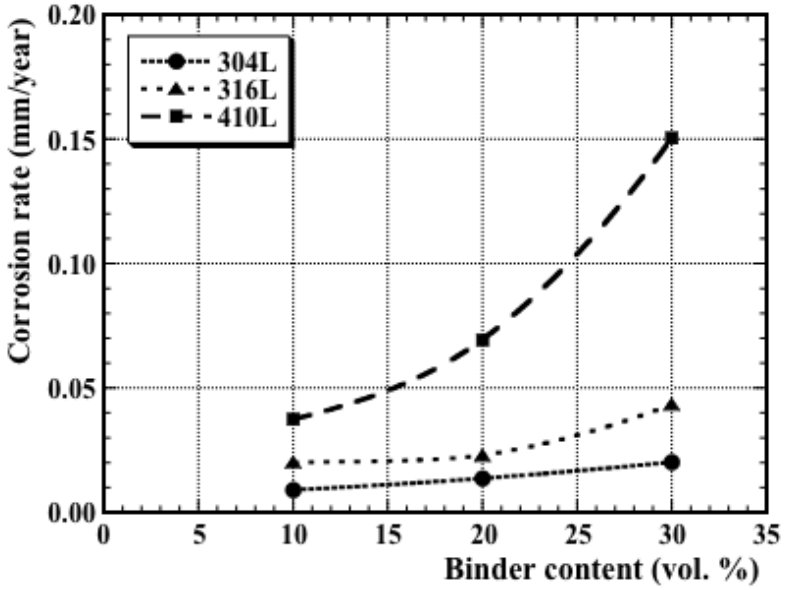

Figure 8.4: The effects of binder composition and content upon the Tafel derived corrosion rates for the TiC-stainless steel cermets.

Another factor that could aid in explaining the improved corrosion resistance, for lower binder content samples, is related to a potential galvanic effect between the TiC and steel binder. Given a nominally constant grain size (Figure 8.2(a)), it is clear that as the binder content is reduced, the carbide-carbide contacts increase (Figure 8.2(b)). The corrosion potential of TiC in 3 wt. % NaCl is +0.28 V [180], which is more noble than the corrosion potentials of the steels used in the present study, within a similar electrolyte. It can consequently be anticipated that the difference in corrosion potentials between the TiC ceramic phase and the steel binder, in a conducting electrolyte, will lead to galvanic activity at the interfaces. As a consequence, cermets with a greater steel binder content are prone to more extensive attack, leading to an increase in the corrosion rate. It can also be seen from Table 8.5 that, of the 'pure' metals, 316L stainless steel has the best corrosion resistance, but when incorporated with TiC into a cermet structure, the TiC-304L cermets have better corrosion resistance than their TiC-316L and TiC-410L counterparts. The reason to this could be related to difference in electrochemical

potentials and galvanic activity between the TiC and 304L, 316L or 410L steel binder. Generally, when two dissimilar materials are incorporated in a conducting electrolyte, and one is more noble (cathodic) while the other is more active (anodic), the difference in potential between the cathode and anode site will indicate the expected degree of galvanic corrosion. Consequently, the smaller the difference in potential, the lower the expected extent of galvanic corrosion [37]. However, changes in electrolyte composition and temperature could also alter the potential positioning in the galvanic series [37].

Table 8.5: The measured corrosion rates for the 'pure' steels used in the present work, based on Tafel extrapolation of potentiodynamic polarization data.

Corrosion rate (mm/year)		
304L	**316L**	**410L**
0.0022	0.0020	0.0219

The OCP of TiC in a similar electrolyte to the current study was determined to be +0.28 V, [180] while those of 304L, 316L and 410L steels are approximately -0.105 V, -0.123 V and -0.455 V, respectively. Comparing the difference in the OCP between TiC (cathodic) and the various steels [37] (anodic), it can be seen that based on this principle, TiC-304L cermets should be expected to have the best corrosion resistance, which is confirmed in Figure 8.4.

Comparing the Tafel-based corrosion rates for the present materials with previously published data, it is apparent that the TiC-stainless steel cermets perform well in comparison with commercially available cermet coating systems. Using a broadly similar approach, Toma and colleagues determined aqueous corrosion rates for WC-Co and WC-CoCr, and demonstrated the former to be ~0.76 mm/year, which is lowered to ~0.32 mm/year through the addition of Cr [198]. The best cermet coating systems for corrosion resistance are presently those based on Cr_3C_2, with a NiCr binder, which have been demonstrated to exhibit aqueous corrosion rates as low as 0.008 mm/year [199]. Some caution should be taken when evaluating these different materials, particularly in comparing bulk cermets and coatings, where coating porosity may play a role in degrading the corrosion properties. However, it is clear that the present materials exhibit generally similar performance, in comparison to the Cr_3C_2-based cermets, when assessing electrochemically derived (i.e. Tafel) corrosion rates.

In addition to estimating the response from the Tafel extrapolation procedure, the corrosion rates of the cermets were also obtained through weight loss measurements (Figure 8.5). It is apparent that the rate

of corrosion determined by weight loss also increases with binder content, confirming the general Tafel observations. It is notable that the TiC-410L cermets exhibited a slightly higher corrosion resistance than the other cermets under selected conditions. However, generally the trend is consistent with the corrosion rates determined from Tafel extrapolation.

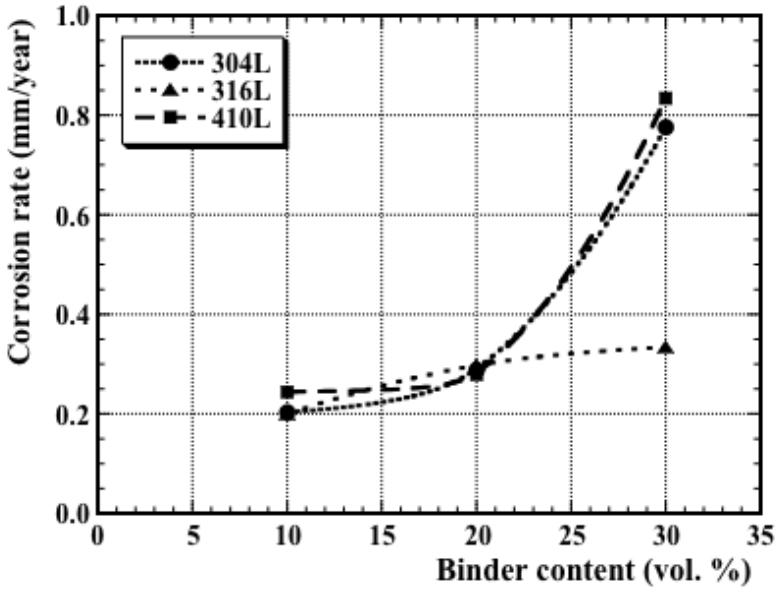

Figure 8.5: The effects of binder composition and content upon the corrosion rates derived from weight loss measurements for the TiC-stainless steel cermets.

It is also apparent that the corrosion rates calculated from the weight loss measurements are approaching one order of magnitude greater than those obtained with the Tafel electrochemical measurement technique. Other authors have also reported significant discrepancies in corrosion rates when comparing electrochemical measurements with weight loss [208, 209], occasionally differing by several orders of magnitude (with weight loss measurements being greater than those obtained electrochemically) [208]. The corrosion rate trends observed from both the Tafel and weight loss approaches are in good agreement with the observations of Sacks [58], who studied the corrosion behaviour of WC-Co composites in tannic acid-based electrolytes, and reported an increase in the corrosion rate with increasing Co binder content. It was demonstrated that there was a preferential dissolution of the Co binder, while the WC grains retained their sharp facets, and are effectively not attacked during the corrosion tests [58].

Representative examples of the potentiodynamic polarisation plots obtained for each of the TiC-stainless steel cermets, as well as the baseline steels, are shown in Figure 8.6. Table 8.6 presents the

accompanying quantitative data obtained after potentiodynamic polarisation experiments. From Figure 8.6 it can be seen that the representative potentiodynamic plots for each of the cermet types show active, passive and transpassive regions. It is also apparent from Table 8.6 that the critical current density, i_{crit}, and pseudo-passive current density, i_{pass}, increase with steel binder content. This response relates to the passivation tendency of the cermets.

(a)

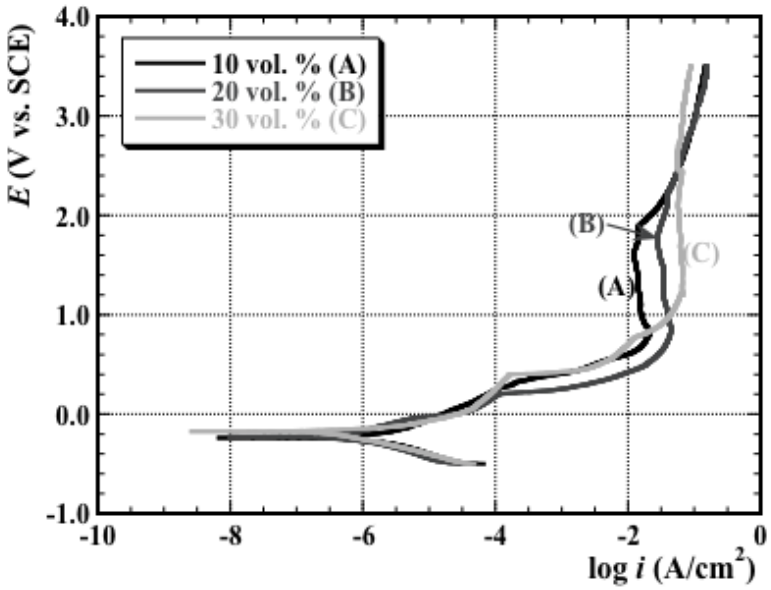

(b)

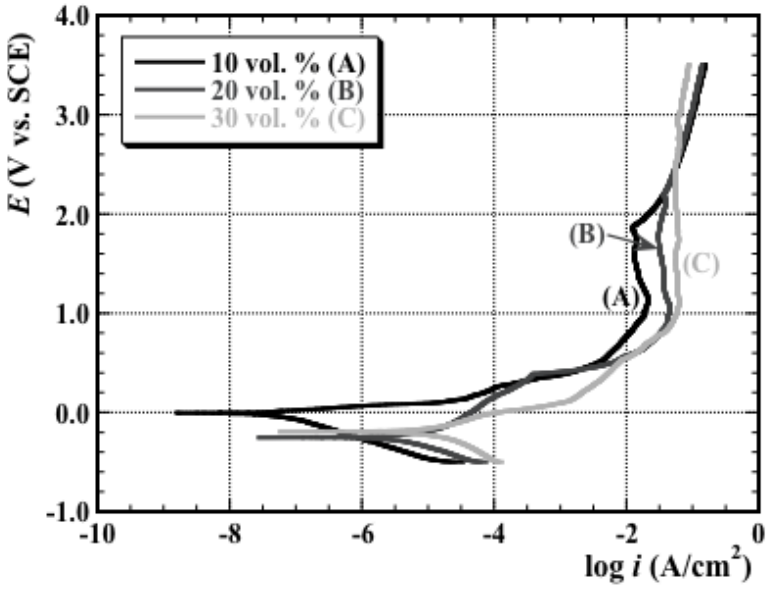

(c)

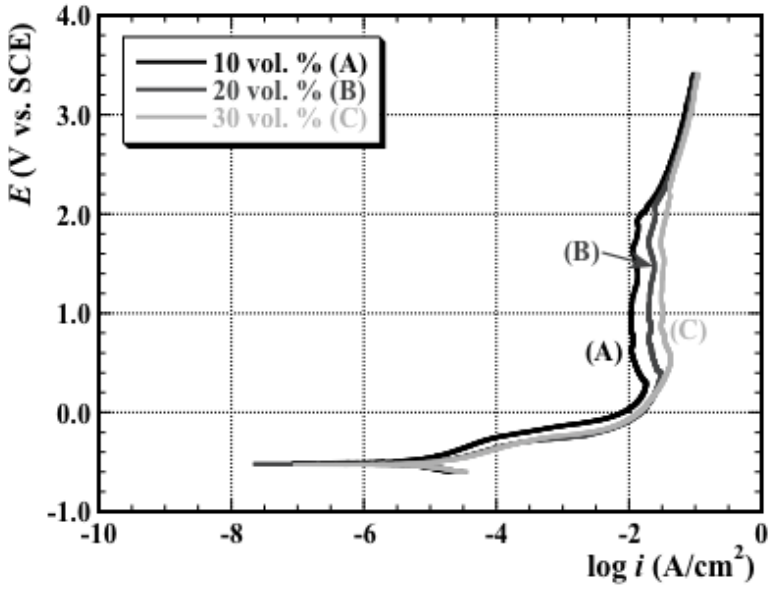

(d)

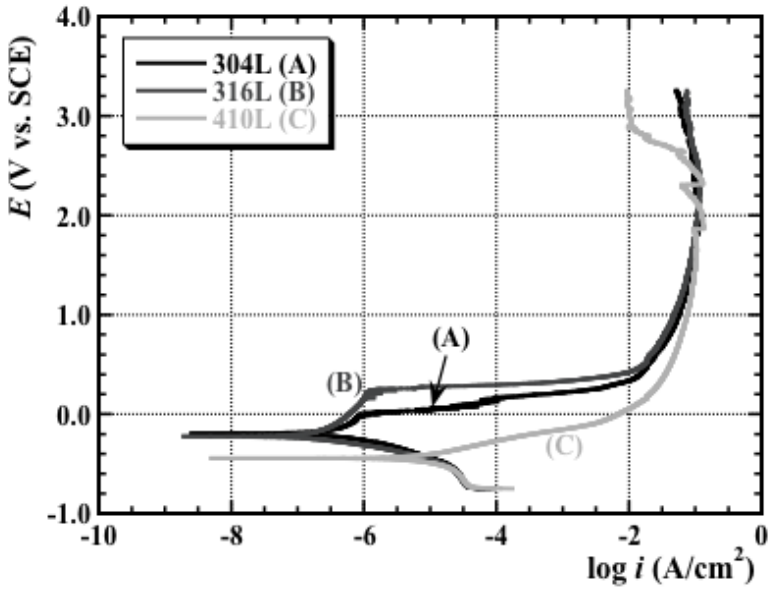

Figure 8.6: Representative potentiodynamic polarisation curves, demonstrating the effects of binder content for each of the TiC-stainless steel cermets, together with comparison of the 'pure' stainless steels: (a) TiC-304L, (b) TiC-316L, (c) TiC-410L, and (d) the 'pure' grades of stainless steel.

Table 8.6: Electrochemical results following potentiodynamic polarisation, showing the critical current density, i_{crit}, and the minimum current density in the pseudopassive region, i_{pass}, for the cermets.

Sample	i_{crit} (A/cm^2)	i_{pass} (A/cm^2)
TiC-10 vol.% 410L	0.018	0.010
TiC-20 vol.% 410L	0.030	0.020
TiC-30 vol.% 410L	0.043	0.031
TiC-10 vol.% 316L	0.024	0.013
TiC-20 vol.% 316L	0.045	0.030
TiC-30 vol.% 316L	0.062	0.056
TiC-10 vol.% 304L	0.021	0.015
TiC-20 vol.% 304L	0.044	0.028
TiC-30 vol.% 304L	0.066	0.057

The low critical anodic current density at the peak of each of the curves indicates that the specimens passivate quickly [104], which indicates that the greater TiC fraction, at the lowest binder contents is contributing to the corrosion resistance of the cermets. Similar results have also been reported by Sacks [58], who noted an increase in i_{crit} with an increase in Co content during corrosion studies of WC-Co cermets. Sutthiruangwong and Mori also reported a decrease in i_{crit}, i_{corr} and i_{pass} with increasing WC content [93], which mirrors the observations presented in Table 8.6.

From both Figure 8.6 and Table 8.6 it can be noted that although the potentiodynamic curves show active, passive and transpassive regions, the current responses in the passive region are relatively high (i.e. of the order of 10^{-2}A/cm^2), which is too high to be viewed as a true passive material [8]. It has previously been stated that Co-based cemented carbides do not passivate, but the potentiodynamic curves show a conventional anodic behaviour, thereby exhibiting a critical potential and breakdown potential [8, 93]. However, the current density obtained for WC-Co cemented carbides, after reaching the critical potential, is several orders of magnitude higher when compared to truly passive materials;

this behaviour is consequently known as pseudo-passivity [8, 93]. Although some precipitation of a semi-protective surface layer occurred in the pseudo-passive region, at the interface between the intact WC-Co cermet and the Co-depleted WC skeleton it is not stable, and it re-dissolves into the corrosive electrolyte [93]. Human and colleagues have indicated that this pseudo-passive behaviour is prominent at very high electrochemical potentials [8, 171, 172]. A material that behaves in a truly passivating manner will have a passivation current not exceeding 10 μA cm^{-2} [8, 183] and any material that exhibits a current several orders of magnitude higher than this value can therefore be regarded as pseudo-passive [8, 93, 172].

Generally, for materials exhibiting pseudo-passivity at high electrochemical potentials, after reaching a critical current density there will be a slight drop in current in the passivation region, as apparent in Figure 8.6. It can be seen that the passive current density measured for each of the cermets, presented previously in Table 8.6, is in the region of four orders of magnitude higher than for a true passive material (i.e. 10μA/cm^{-2}). Consequently, the phenomenon of pseudo-passivity is believed to be happening in the current TiC-steel cermets. The reason for the very high current observed in the pseudo-passive region is related to the formation of a weak, cracked and/or porous oxide, thereby allowing the penetration of the electrolyte to the cermet surface [8]. In other words, the presence of such an oxide scale, which still inhibits diffusion to a certain extent, leads to a limitation of the current density [8]. A further investigation of the phenomenon of pseudo-passivity is presented in a study of the corrosion behaviour of TiC-304L cermets [196].

The cyclic polarisation responses of the cermets and the baseline steels are presented in Figure 8.7. The pitting and repassivation (or protection) potentials (E_{pit} and E_{prot}, respectively) are used to study the susceptibility of materials to localised corrosion. The relative degree of 'self-healing' ability of the surface film is then given by [95]:

$$\Delta E = E_{pit} - E_{prot} \qquad \text{Equation 8.5}$$

The accompanying electrochemical results of the cyclic polarisation experiments are shown in Table 8.7. It is typical that an increase in E_{pit} improves the resistance of the materials to pitting corrosion, while a decrease of ΔE indicates a greater ability towards self-healing of the passively-formed surface film [95]. As can be seen from Figure 8.7, by increasing the steel binder content the pitting resistance of the cermets is improved (i.e. E_{pit} increases with binder content). The lower values of ΔE for TiC cermets prepared with 10 vol. % 304L and 316L highlight their greater self-healing ability for the passive film, compared to the other TiC-steel cermets. It is also notable that these values are even

slightly better than the baseline steels. This indicates that the cermets prepared with 10 vol. % 304L or 316L have the lowest susceptibility to localised corrosion. This behaviour is likely to be related to the protection rendered by the formation of a protective oxide of titanium (i.e. TiO_2) at higher TiC content. However, for both the TiC-410L cermets (and the 410L baseline steel), as well as the TiC-304L cermets with higher binder contents, there is no protection offered, as E_{prot} is below E_{pit}, inferring a high susceptibility to localised corrosion.

(a)

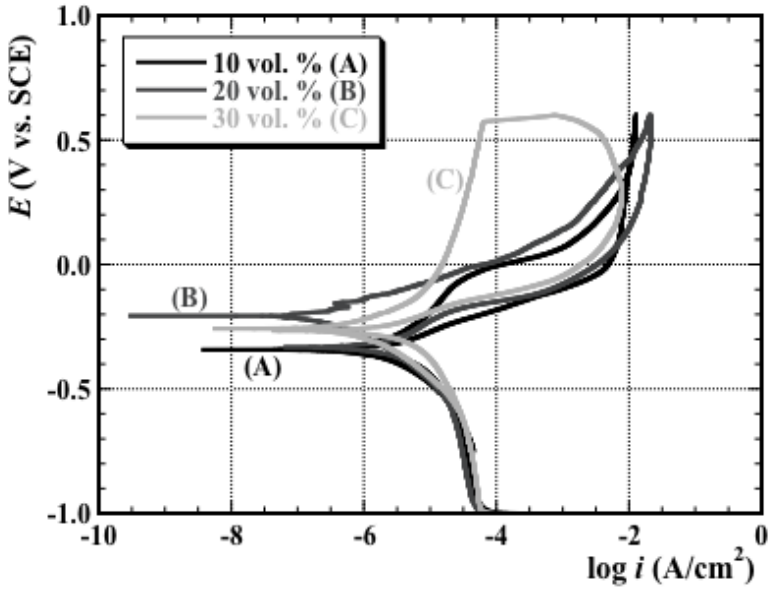

(b)

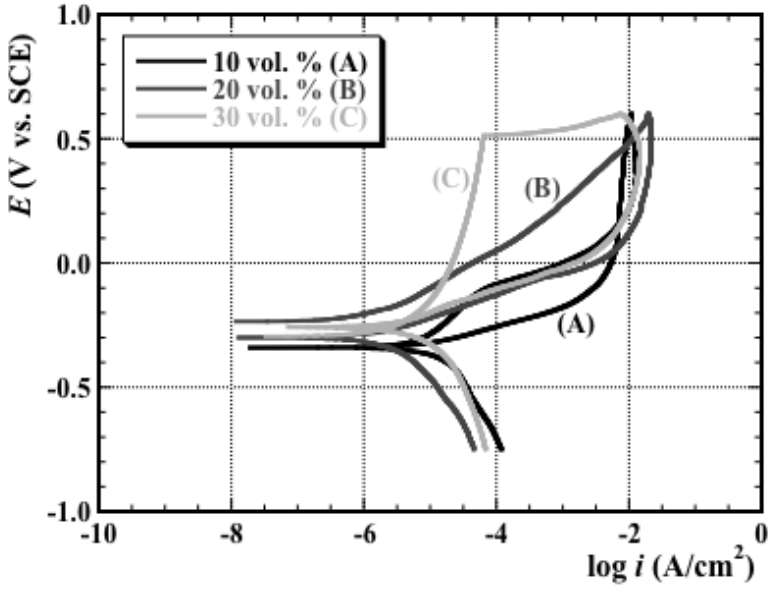

(c)

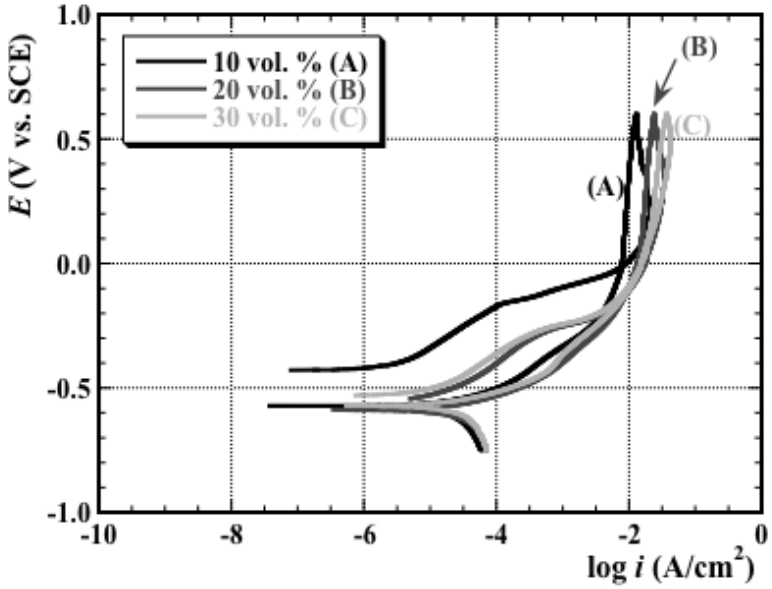

(d)

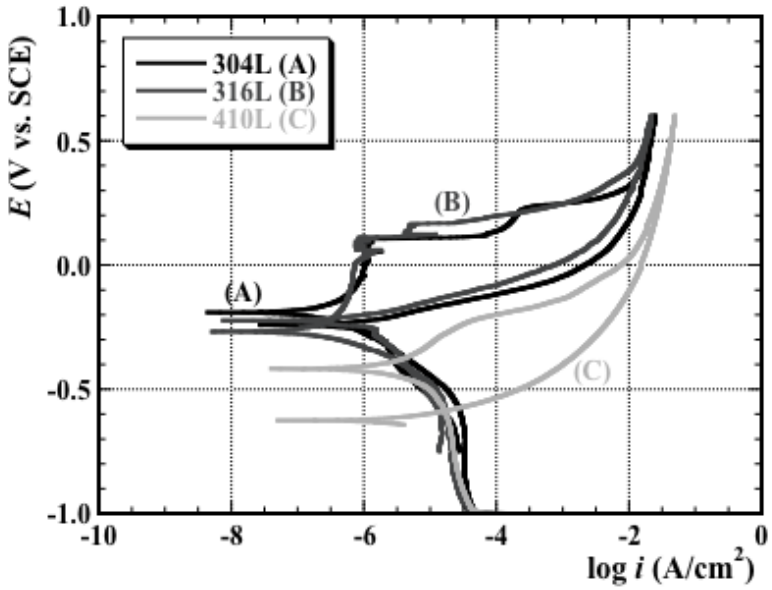

Figure 8.7: Representative cyclic polarisation curves, demonstrating the effects of binder content for each of the TiC-stainless steel cermets, together with comparison of the 'pure' stainless steels: (a) TiC-304L, (b) TiC-316L, (c) TiC-410L, and (d) the 'pure' grades of stainless steel.

Table 8.7: Extrapolation of the pitting and protection potentials from the cyclic polarisation curves.

Sample	E_{pit} (V vs. SCE)	E_{prot} (V vs. SCE)	ΔE (V vs. SCE)
TiC-10 vol.% 304L	-0.068	-0.339	0.271
TiC-20 vol.% 304L	0.150	No protection	NA
TiC-30 vol.% 304L	0.567	No protection	NA
304L stainless steel	0.101	No protection	NA
TiC-10 vol.% 316L	-0.132	-0.335	0.203
TiC-20 vol.% 316L	-0.186	No protection	NA
TiC-30 vol.% 316L	0.513	-0.228	0.741
316L stainless steel	0.014	-0.212	0.226
TiC-10 vol.% 410L	-0.167	No protection	NA
TiC-20 vol.% 410L	-0.276	No protection	NA
TiC-30 vol.% 410L	-0.283	No protection	NA
410L stainless steel	-0.238	No protection	NA

In order to further confirm the observations from cyclic polarisation, and to substantiate the probability of localised corrosion, potentiostatic polarisation tests were conducted for all of the current materials at an applied voltage above E_{pit} (Figure 8.8); the specific polarisation voltages used for each sample are provided in Table 8.8. Generally, the likelihood of localised corrosion is confirmed, depending on the nature of the current response after potentiostatic polarisation tests conducted at voltages above E_{pit}. An *increase* in current above the E_{pit} indicates localised corrosion, while a *decrease* in current with time highlights repassivation, and no tendency towards localised corrosion. As can be seen from Figure 8.8, all of the studied materials showed an *increase* in current with time during the potentiostatic scans above E_{pit}, indicating the probability of localised corrosion. These observations confirm the results of the cyclic polarisation tests, shown previously in Figure 8.7 and Table 8.7.

(a)

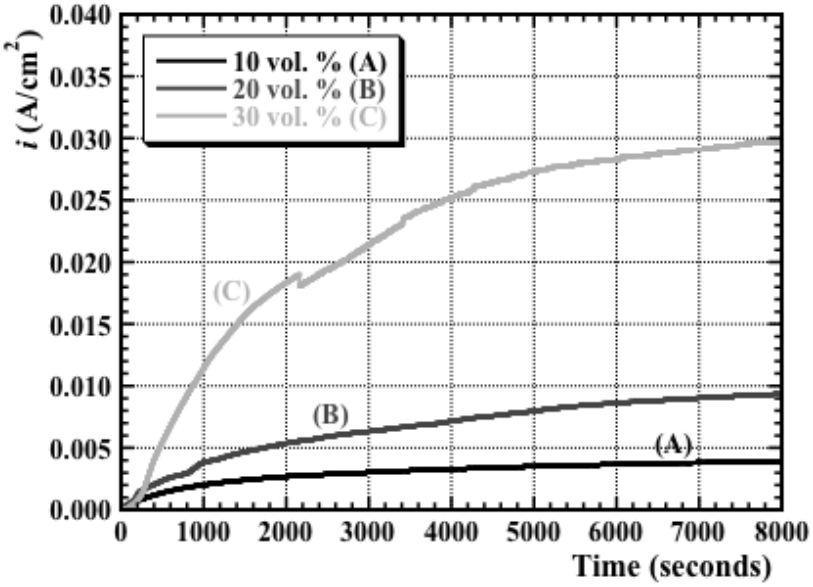
10 vol. % (A)
20 vol. % (B)
30 vol. % (C)
(C)
(B)
(A)
i (A/cm²)
Time (seconds)
0.040
0.035
0.030
0.025
0.020
0.015
0.010
0.005
0.000
0
1000
2000
3000
4000
5000
6000
7000
8000

(b)

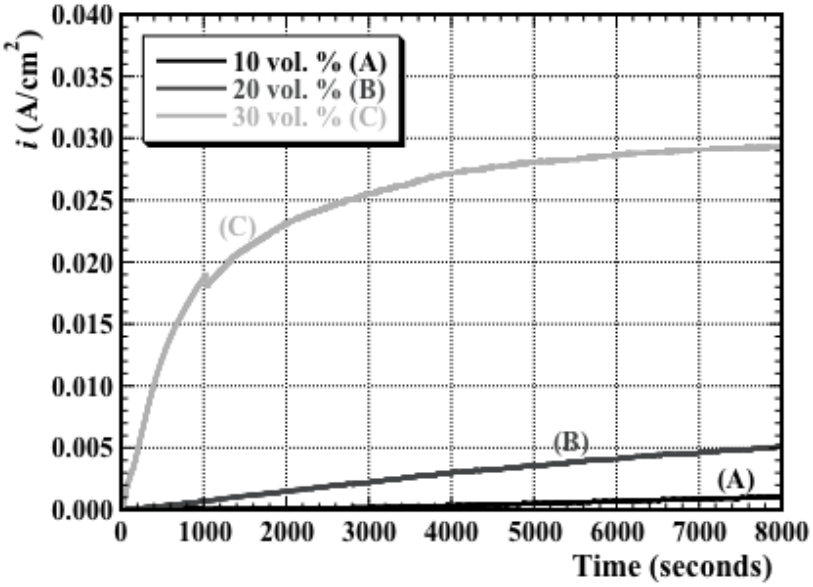
10 vol. % (A)
20 vol. % (B)
30 vol. % (C)
(C)
(B)
(A)
i (A/cm²)
Time (seconds)
0.040
0.035
0.030
0.025
0.020
0.015
0.010
0.005
0.000
0
1000
2000
3000
4000
5000
6000
7000
8000

(c)

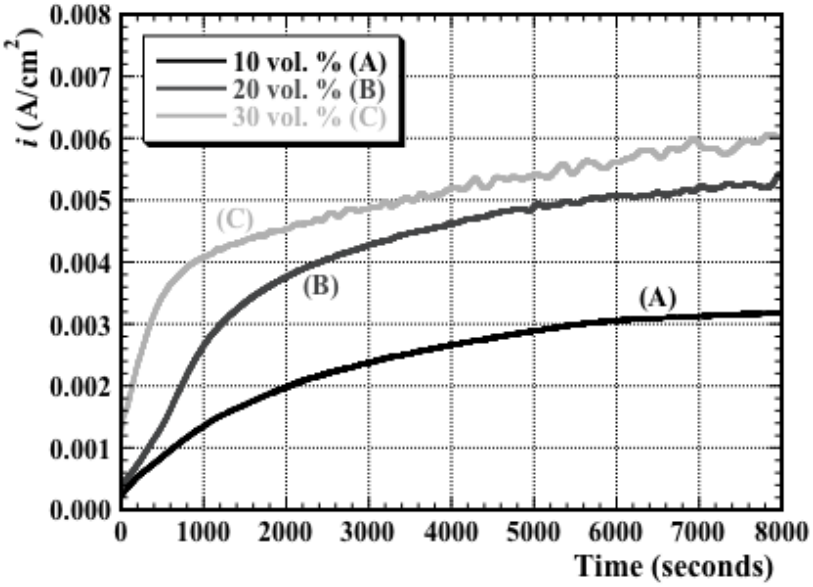

(d)

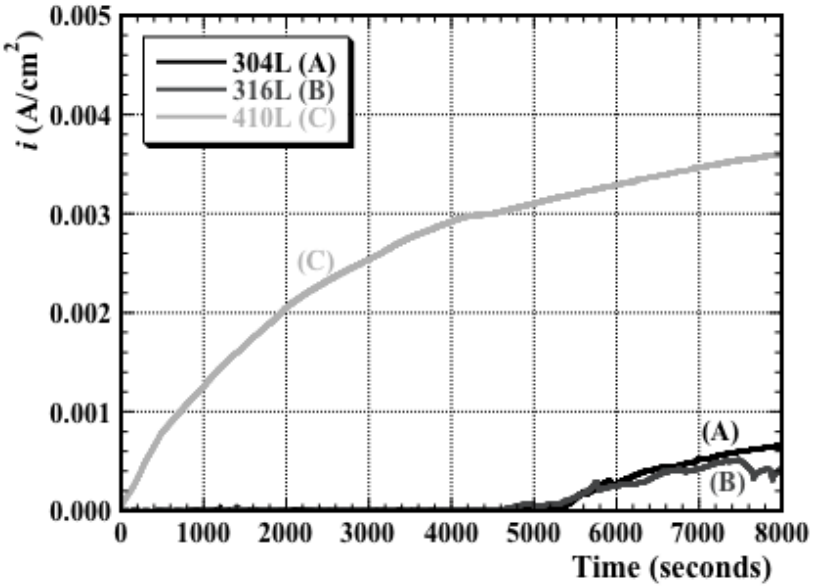

Figure 8.8: Representative potentiostatic polarisation curves, demonstrating the effects of binder content for each of the TiC-stainless steel cermets, together with comparison of the 'pure' stainless steels: (a) TiC-304L, (b) TiC-316L, (c) TiC-410L, and (d) the 'pure' grades of stainless steel.

Table 8.8: The applied voltages used for potentiostatic polarisation testing of the TiC-stainless steel cermets and the 'pure' stainless steel.

Sample	Polarisation voltage (V vs. SCE)		
	304L	**316L**	**410L**
Pure steel	0.10725	0.16475	-0.175
10 vol. % steel	0.02075	-0.0505	-0.127
20 vol. % steel	0.2475	0.01725	-0.2275
30 vol. % steel	0.575	0.52	-0.195

It can also be seen from Figure 8.8 that, while the cermets with 10 vol. % 304L and 316L steel showed an increase in current with time, the effect is relatively small. This again highlights the superior capacity of these low binder compositions towards self-healing of the passive film, when compared to the other cermets studied. The large oscillations observed in the potentiostatic curves for the pure 316L and 304L stainless steels presents evidence of localised corrosion, and an aggressive attack of the passive film by Cl^- ions [184].

8.4.3 Post Corrosion Chemical Analysis

Following the corrosion experiments, the remaining solution from the electrochemical cell was analysed using ICP-OES, in order to determine both the solid (in terms of fine particulate matter) and ionic (dissolved) material present in the solution. Assessment of the primary constituent species is presented in Figures 8.9 and 8.10, for the solid and ionic material, respectively. In terms of the solid constituents, with increasing binder content it is apparent that there are concurrently increasing quantities of the steel components (i.e. Fe, Ni, Cr and Mo) liberated during corrosion testing (Figure 8.9). Conversely, there are relatively decreasing amounts of Ti present. The increase in the assorted steel species indicates that there is a preferential attack of the binder, the extent of which increases in a nominally linear manner with the overall binder content of the cermets. By comparing the dissolution of Fe for the three studied cermet types, it can be clearly seen that TiC-410L cermets have the highest dissolution rate, followed by TiC-316L and lastly, TiC-304L. This observation also confirms the

superior corrosion resistance of TiC-304L cermets over the other developed compositions, as outlined earlier.

(a)

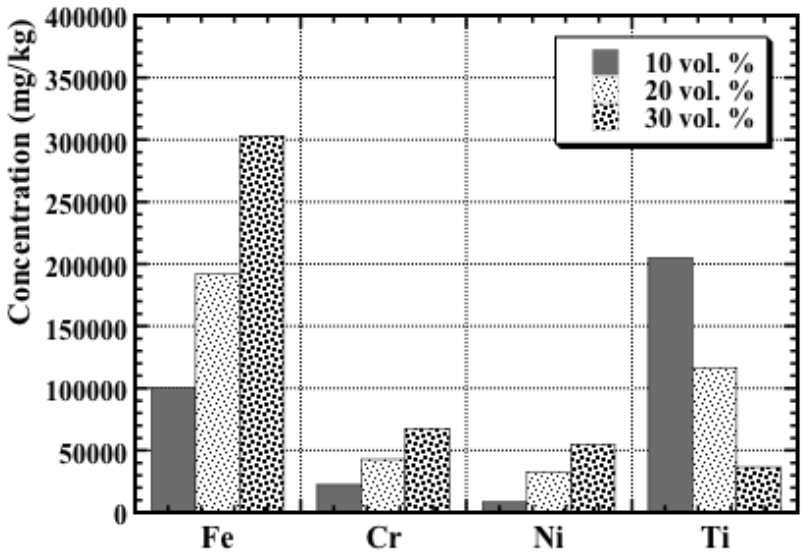

(b)

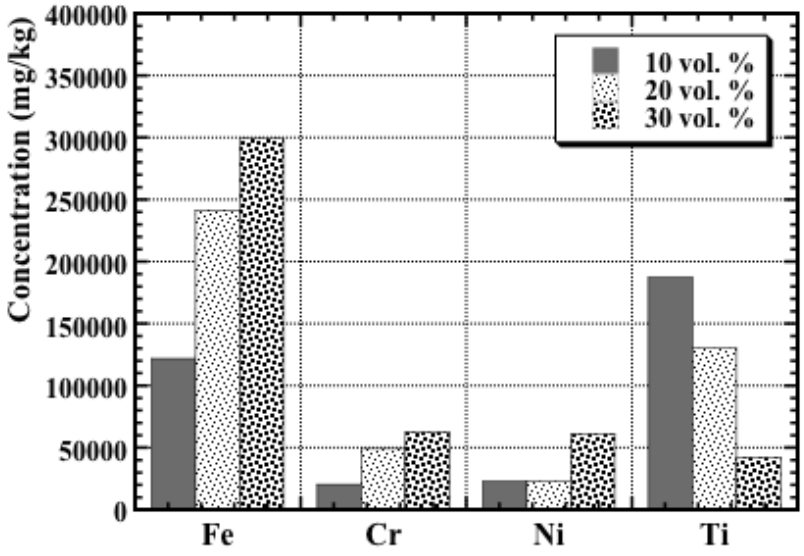

(c)

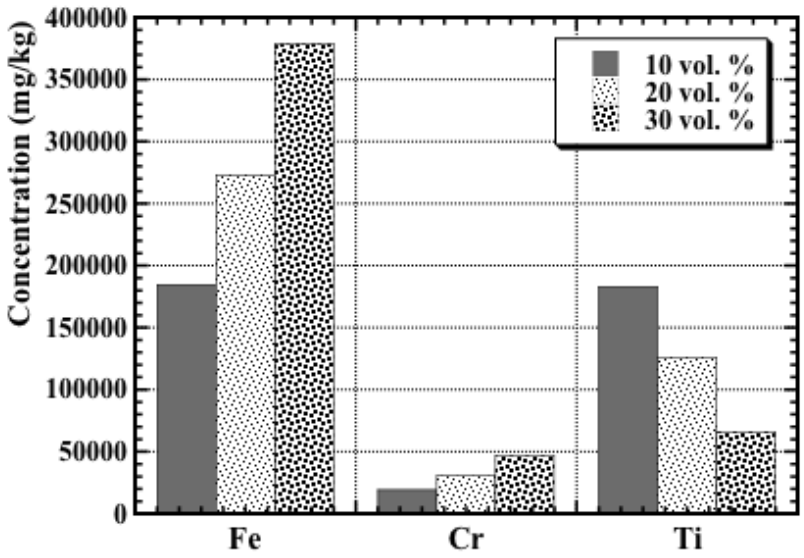

Figure 8.9: ICP-OES chemical analyses of the filtered material removed from the post-test solutions after corrosion testing of the TiC-stainless steel cermets: (a) TiC-304L, (b) TiC-316L, and (c) TiC-410L.

Figure 8.10 shows the ionic content measured in the filtered solutions (i.e. after removal of all particulate material), following the corrosion experiments for each cermet. It can be seen that there is greater amount of Ni and Mo ions in the filtered solutions after testing the TiC-316L compositions (i.e. Figure 8.10(b)) when compared to other cermets. The loss of Ni and Mo ions, which are important components that improve the corrosion resistance of the steel, may indicate why the TiC-316L cermets showed marginally inferior corrosion resistance compared to TiC-304L, where the loss of Ni ions is minimal. The absence of Fe ions from the solution could indicate precipitation of Fe in some form, which would then lead to a higher Fe content in the recovered solids component, relative to Ni. As the pH of the NaCl solution is between 5.3-5.8, which is fairly close to the highly acidic and corrosive pH range [0-4], the possibility of Fe precipitation can be justified [216].

(a)

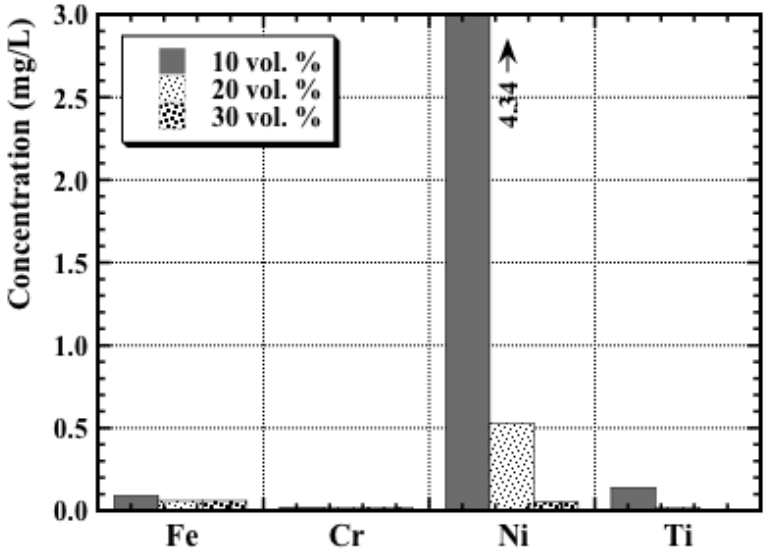
Concentration (mg/L)
3.0
2.5
2.0
1.5
1.0
0.5
0.0
10 vol. %
20 vol. %
30 vol. %
4.34
Fe
Cr
Ni
Ti

(b)

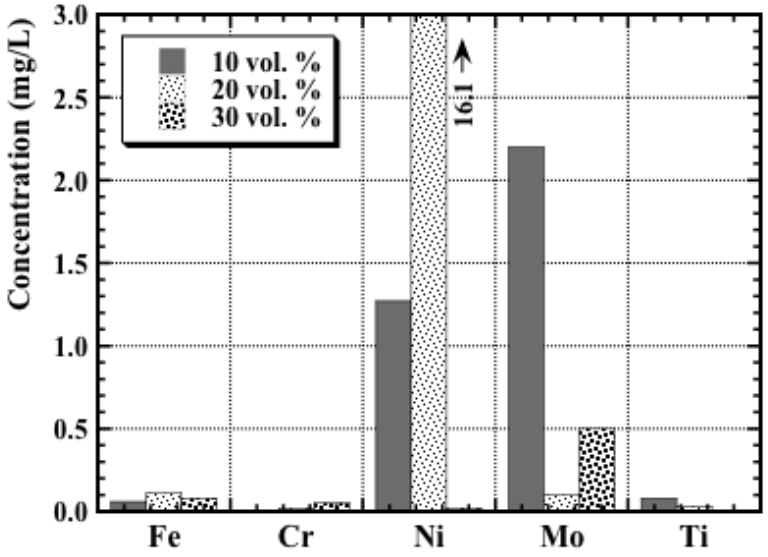
Concentration (mg/L)
3.0
2.5
2.0
1.5
1.0
0.5
0.0
10 vol. %
20 vol. %
30 vol. %
16.1
Fe
Cr
Ni
Mo
Ti

(c)

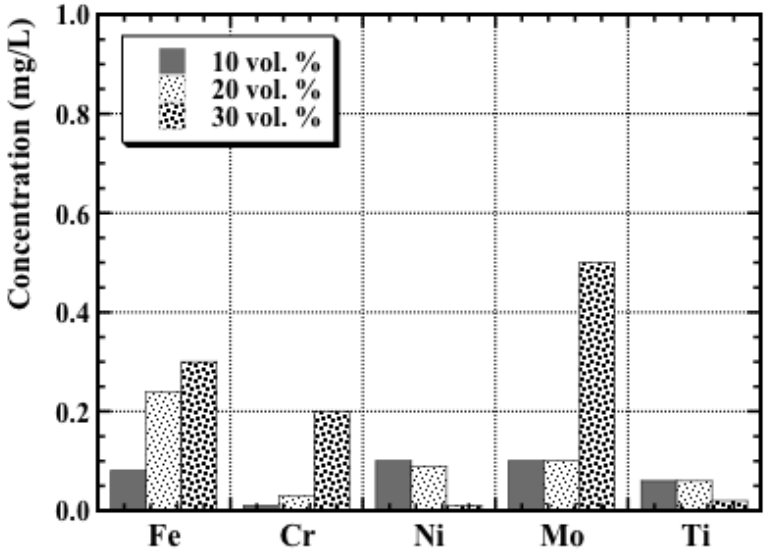

Figure 8.10: ICP-OES chemical analyses of the remaining post-test solution, following filteration to remove particupalte material, after corrosion testing of the TiC-stainless steel cermets: (a) TiC-304L, (b) TiC-316L, and (c) TiC-410L.

In addition to analyses of the various residual corrosion solutions after electrochemical testing, the influence of the tests on the cermet composition was also analysed. Figure 8.11 presents the surface EDS analyses, both before and after corrosion testing, for each of the cermet systems. As can be seen, by comparing the composition of the metal binder both before and after corrosion it is apparent that there is heavy dissolution (and hence removal) of the metal binder components during corrosion, for each of the cermet systems, while the TiC is essentially unaffected. These analyses confirm that there is selective dissolution of the binder, supporting the ICP-OES data presented in Figures 8.9 and 8.10. In the most extreme corrosion cases it can be expected that there will also be a slight loss of Ti (and C), due to the removal of individual TiC grains when the metal binder is degraded (there is no longer sufficient steel binder to keep the surface grains in place); this will not be observed by EDS analysis, as Ti and C will still be the predominant components, but can be observed through SEM imaging as the surface morphology will change from polished (i.e. smooth) to rough (i.e. revealing complete, individual TiC grains).

(a)

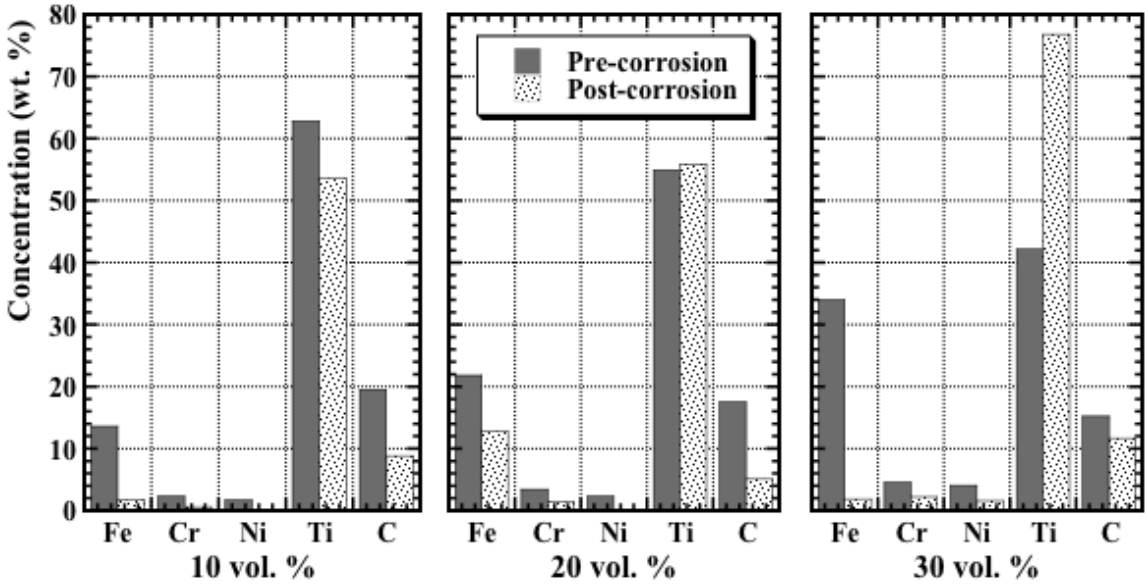
Concentration (wt. %)
Pre-corrosion
Post-corrosion
Fe Cr Ni Ti C
10 vol. %
20 vol. %
30 vol. %

(b)

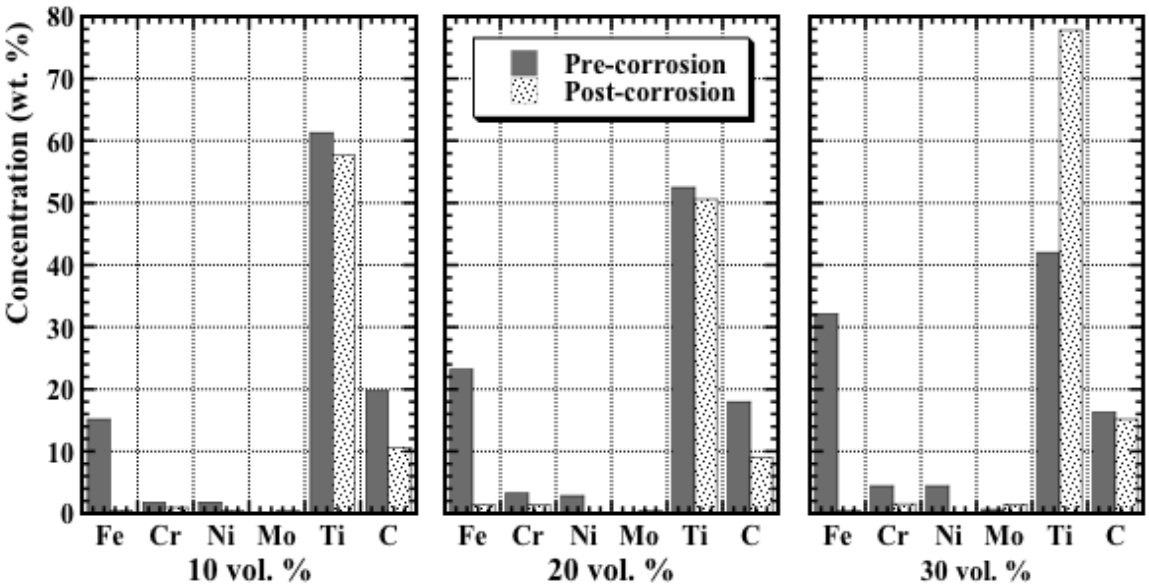
Concentration (wt. %)
Pre-corrosion
Post-corrosion
Fe Cr Ni Mo Ti C
10 vol. %
20 vol. %
30 vol. %

(c)

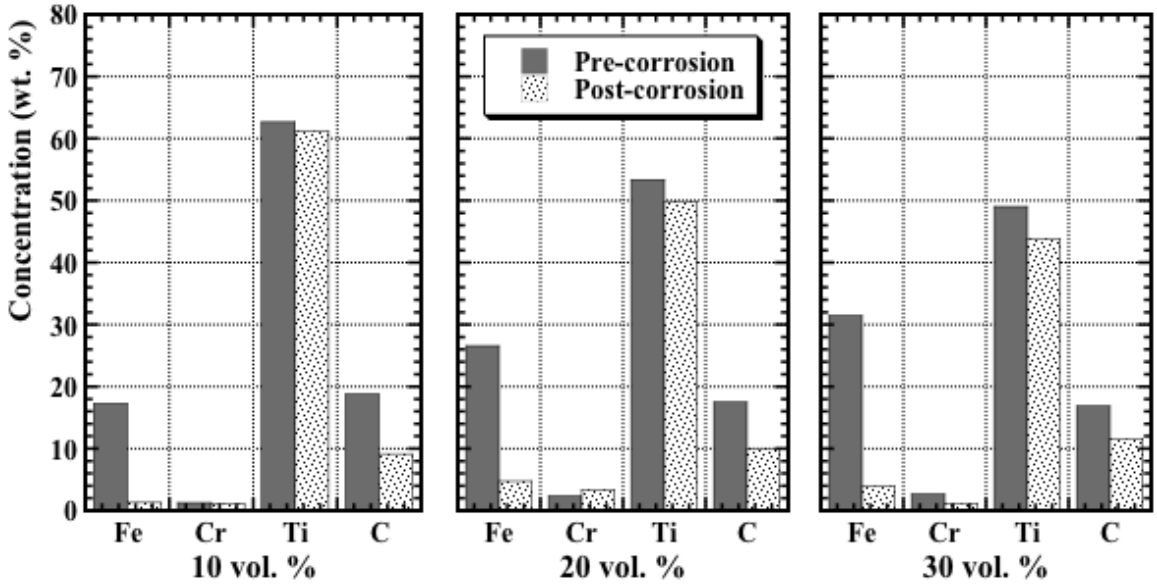

Figure 8.11: Comparative EDS elemental analyses of the surface of TiC-stainless steel samples prepared with 30 vol. % steel binder, both before and after corrosion testing: (a) TiC-304L, (b) TiC-316L, and (c) TiC-410L.

8.4.4 Corroded Sample Characterisation

Typical SEM images of the cermets after potentiodynamic polarisation testing are shown in Figure 8.12. Preferential dissolution of the binder is apparent, while the TiC grains remain largely unaffected following the tests. Even when the steel binder is removed, the TiC particles support each other to a large extent and form a continuous, rigid skeleton. However, some surface TiC grain removal does occur; the presence of remnant, surface grains can be easily observed in the form of a retained, uniform flattened face on each individual grain (e.g. Figure 8.12(f)). It can be clearly seen that at the highest binder contents, essentially all of the interconnecting metal binder content is removed from the near surface region, leaving clean and smooth TiC grains. This observation confirms the lowering of the corrosion resistance with increasing binder contents, as evidenced through the various electrochemical tests previously outlined in *Section 8.3.2: Electrochemical Measurements*. The selective dissolution of the metal binder could be as a result of a galvanic effect, as noted earlier, existing between the TiC ceramic and steel binder, in an aggressive conducting electrolyte.

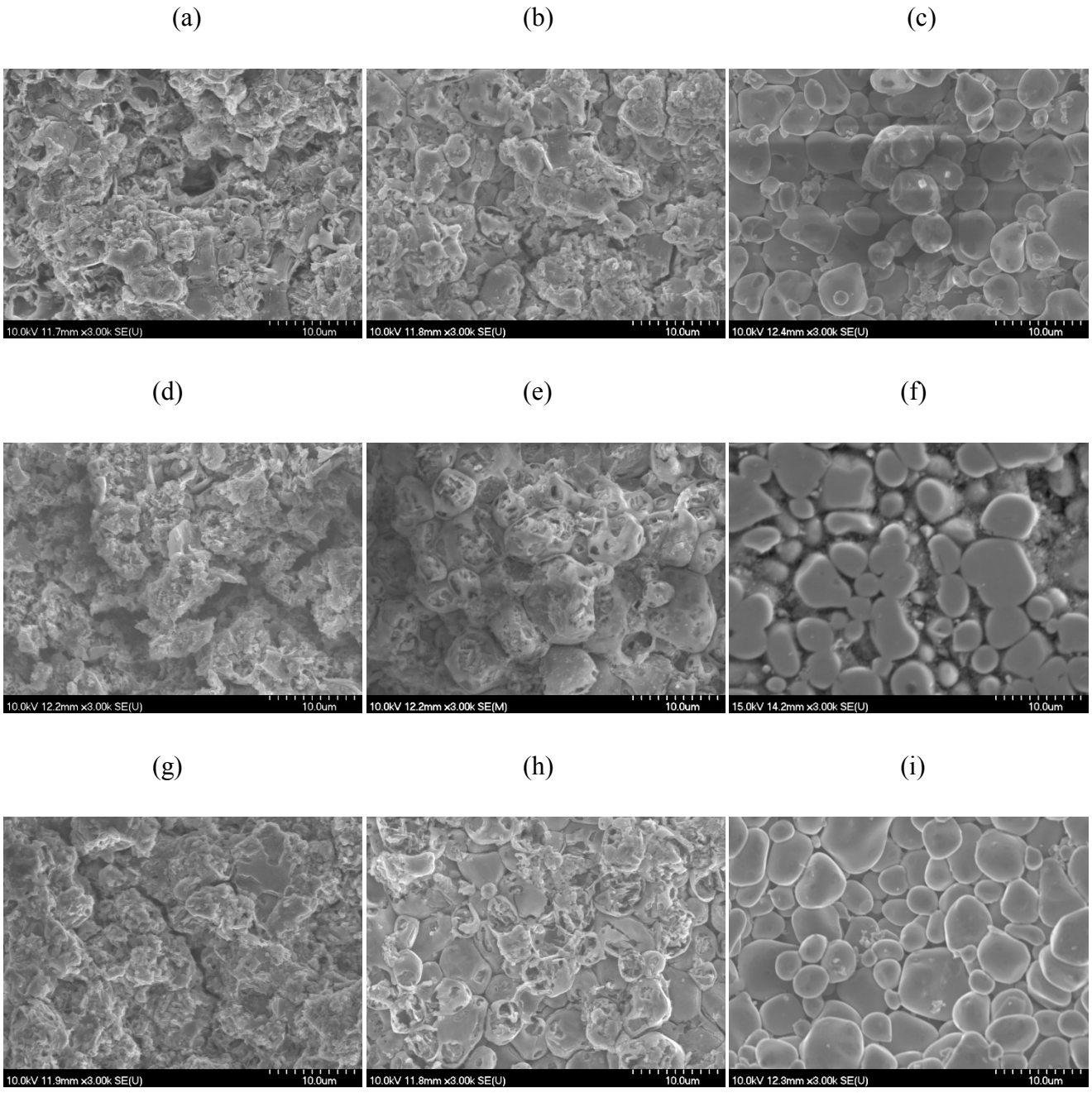

Figure 8.12: Representative SEM images of the corroded surfaces of the TiC-stainless steel cermets following potentiodynamic polarisation testing, for cermets with, respectively: (a-c) 10, 20 and 30 vol. % 304L, (d-f) 10, 20 and 30 vol. % 316L, and (g-i) 10, 20 and 30 vol. % 410L.

TiC particles are reported to have a reasonable electrical conductivity (~2×10^6 $\Omega^{-1}m^{-1}$)[192]. As a consequence, electrochemically, they are more noble than the steel binder. The likelihood therefore exists for creating galvanic activity at the interface, leading to serious dissolution of the steel [95, 190, 192].

The effects of cyclic polarisation on the cermets and the accompanying, baseline steels are shown in Figures 8.13 to 8.15, for the 304L, 316L and 410L based materials, respectively.

(a) (b)

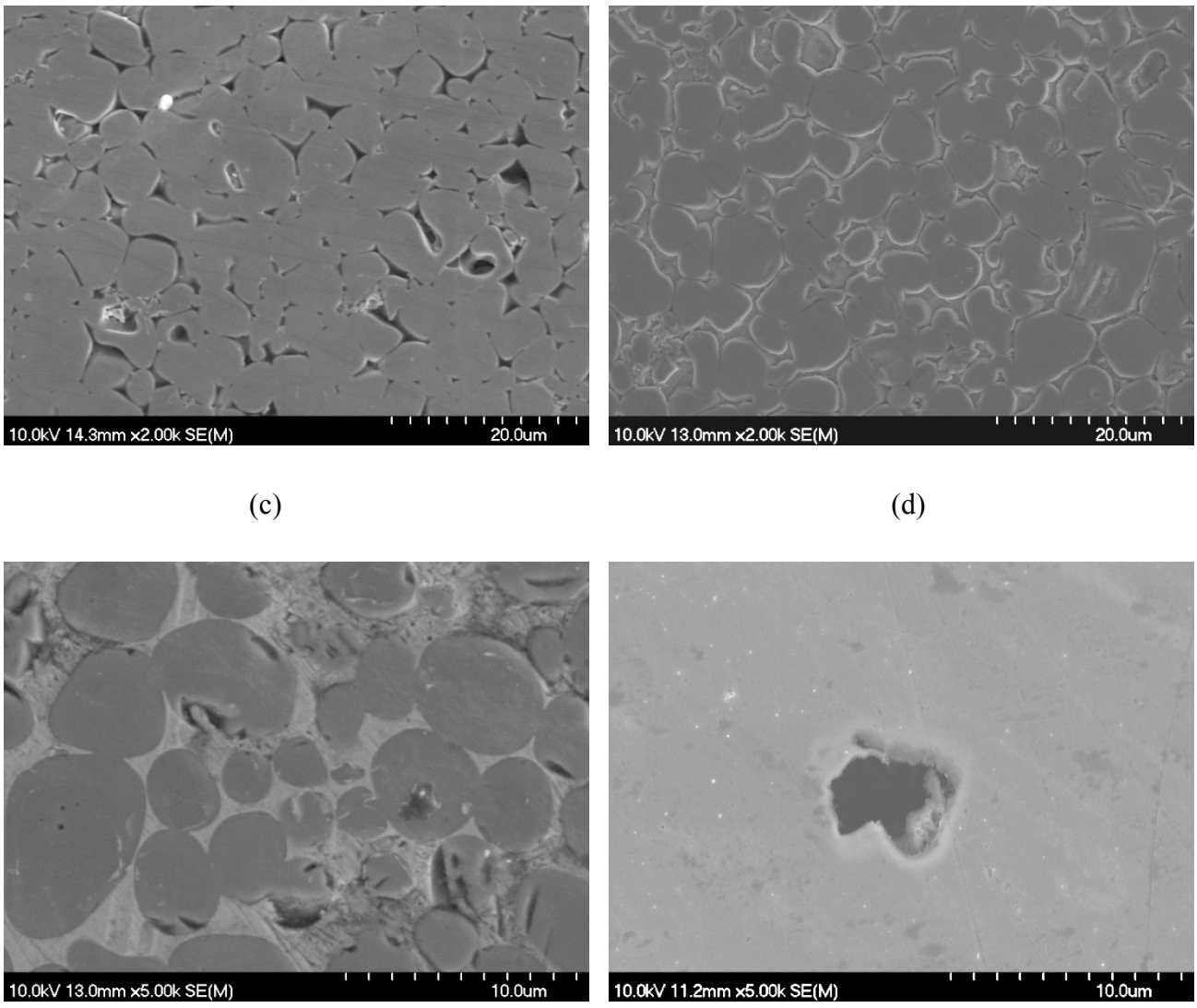

Figure 8.13: Representative SEM images of the corroded surfaces of the TiC-304L cermets and 'pure' 304L steel following cyclic polarisation testing: (a) 10 vol. % 304L, (b) 20 vol. % 304L, (c) 30 vol. % 304L, and (d) 'pure' 304L stainless steel.

(a) (b)

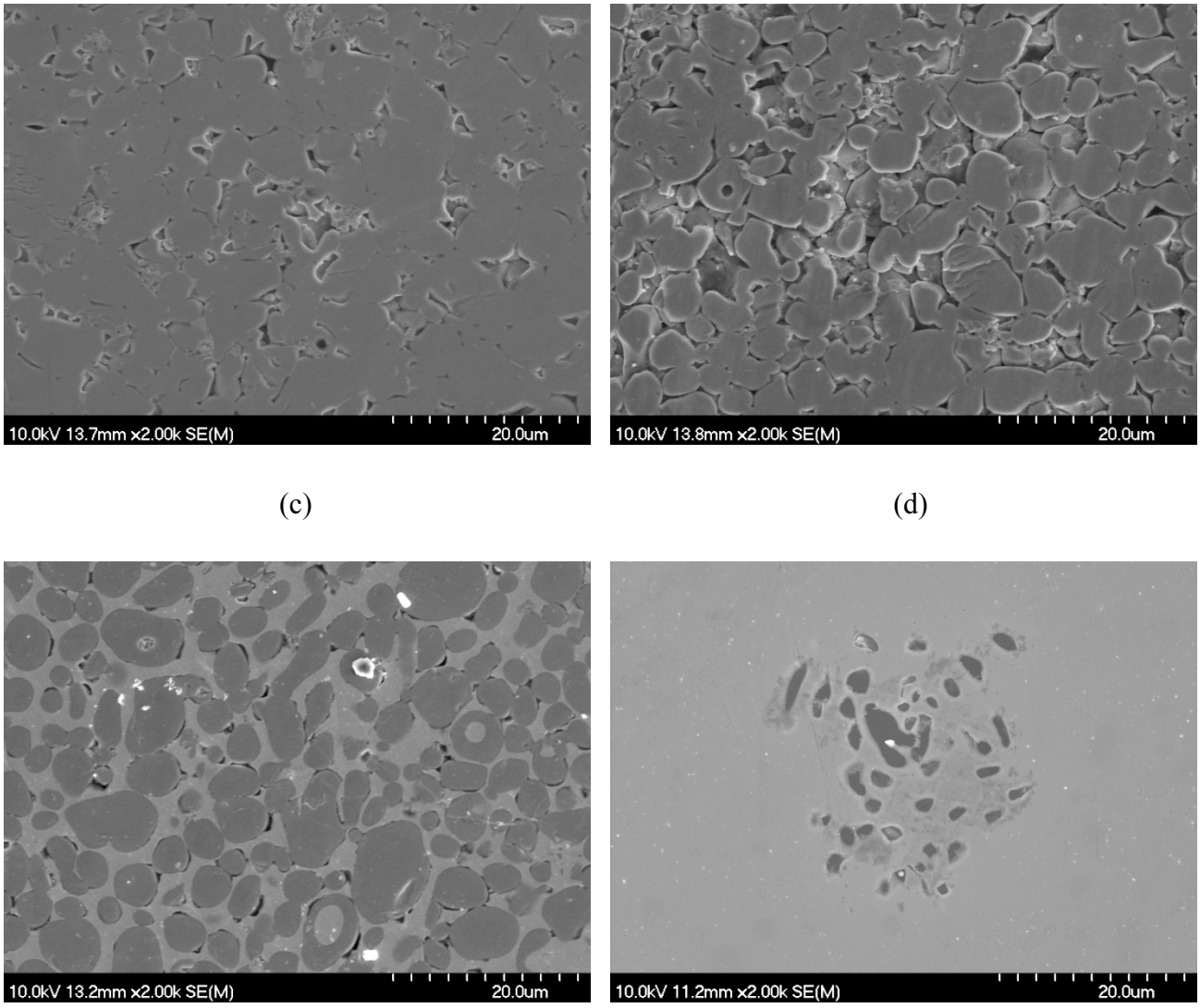

(c) (d)

Figure 8.14: Representative SEM images of the corroded surfaces of the TiC-316L cermets and 'pure' 316L steel following cyclic polarisation testing: (a) 10 vol. % 316L, (b) 20 vol. % 316L, (c) 30 vol. % 316L, and (d) 'pure' 316L stainless steel.

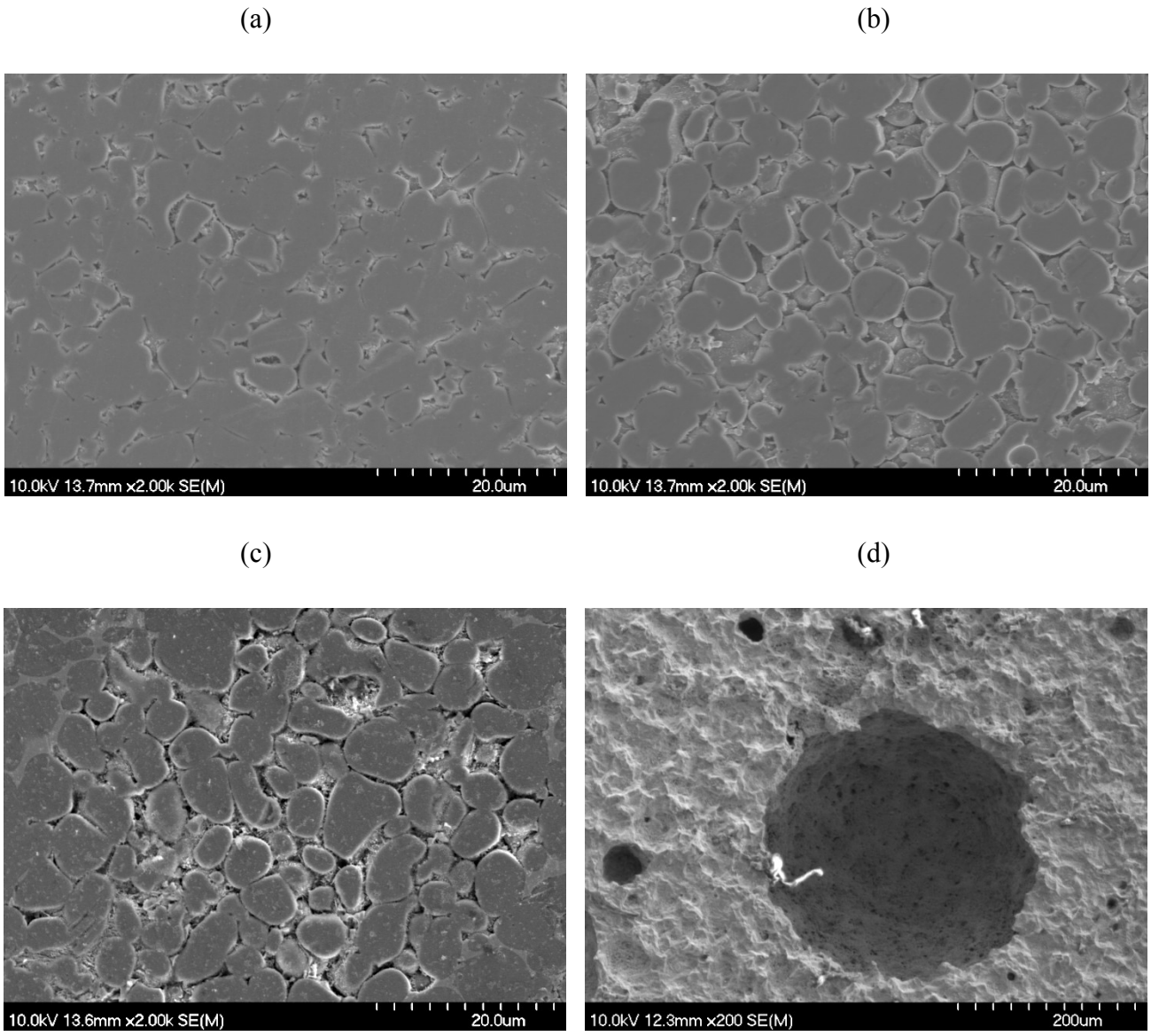

Figure 8.15: Representative SEM images of the corroded surfaces of the TiC-410L cermets and 'pure' 410L steel following cyclic polarisation testing: (a) 10 vol. % 410L, (b) 20 vol. % 410L, (c) 30 vol. % 410L, and (d) 'pure' 410L stainless steel.

It is apparent that there is heavy pitting on each of the baseline steel surfaces, which is in agreement with the experimental results of the cyclic polarisation tests, shown in Figure 8.7. In that instance the values of E_{prot} for the steels (i.e. the protection potential) are more active than E_{pit}, indicating the tendency for localised corrosion. The presence of pits on the three steels also relates to the oscillatory response observed for the steels during the cyclic polarisation experiments (Figure 8.7), which indicates evidence of Cl^- ion attack. However, for the TiC-stainless steel cermets, there is only selective attack occurring locally at the interface between the TiC and steel metal binder (the initial

stages of which are shown in Figure 8.14(c)), resulting in removal of the binder itself. In this instance the TiC ceramic particles are not affected in any obvious way. It is also apparent that the intensity of the corrosive attack increases with binder content, highlighting again that the best corrosion resistance occurs for the lowest binder content (i.e. 10 vol. % steel). The lack of substantial evidence for pitting on the cermets can be attributed to the beneficial protective effect offered by the formation of a surface oxide [186], likely to be TiO_2-based in the present materials. Similar results have also been reported by Wu and colleagues [95], who stated that TiC-containing 304 steel MMCs showed a better resistance to pitting corrosion than the baseline 304 stainless steel, when tested in a 5 wt. % HCl aqueous solution. It was also noted that the addition of an approximately 1μm thick TiC coating (produced by a high-energy micro-arc technique), deposited on a 304 stainless steel substrate, improved the corrosion performance relative to the steel alone, when tested in a 1M H_2SO_4 aqueous solution [176]. This response was attributed to the protection offered by the presence of the continuous TiC coating, which acts as an effective diffusion barrier to the corrosive species. However, from the present work it can be clearly seen that there is a selective interfacial attack on the cermets, resulting in steel binder loss, while the TiC grains are unaffected; in this instance the TiC grains do not form a continuous surface coating. The reason for selective interfacial attack on the cermets could be related to variations in pH at the interface and at the bulk part of the cermets. There is the possibility that a local drop in pH will occur at the interface between steel binder and hard TiC phase, potentially causing an increased instability of the metal and ceramic phases [217]. However, it is likely that the anodic area is the metallic side of interface between the steel binder and hard TiC phase (where metallic dissolution takes place), whereas the adjacent ceramic side of interface is the cathodic region (where oxygen reduction takes place). Within the interface (anodic region), metal dissolution occurs, and increases the migration of chloride ions into at the interface. The formation of metal cations decreases the pH (acidifies the solution) near the interface, due to hydrolysis of metal cations, leading to intensive corrosion in this region. This theory could explain the reason for localised corrosion at the interface of the cermets, but is still subject to further investigation.

Examples of SEM images recorded following potentiostatic polarisation above E_{pit}, for both the cermets and steels, are shown in Figures 8.16 to 8.18, for the materials based on 304L, 316L and 410L, respectively. These microstructural observations can be compared with the electrochemical data resulting from the potentiostatic polarisation tests, shown previously in Figure 8.8. It can be seen that there is general mechanistic agreement between both the electrochemical and compositional observations, and the SEM images.

(a) (b)

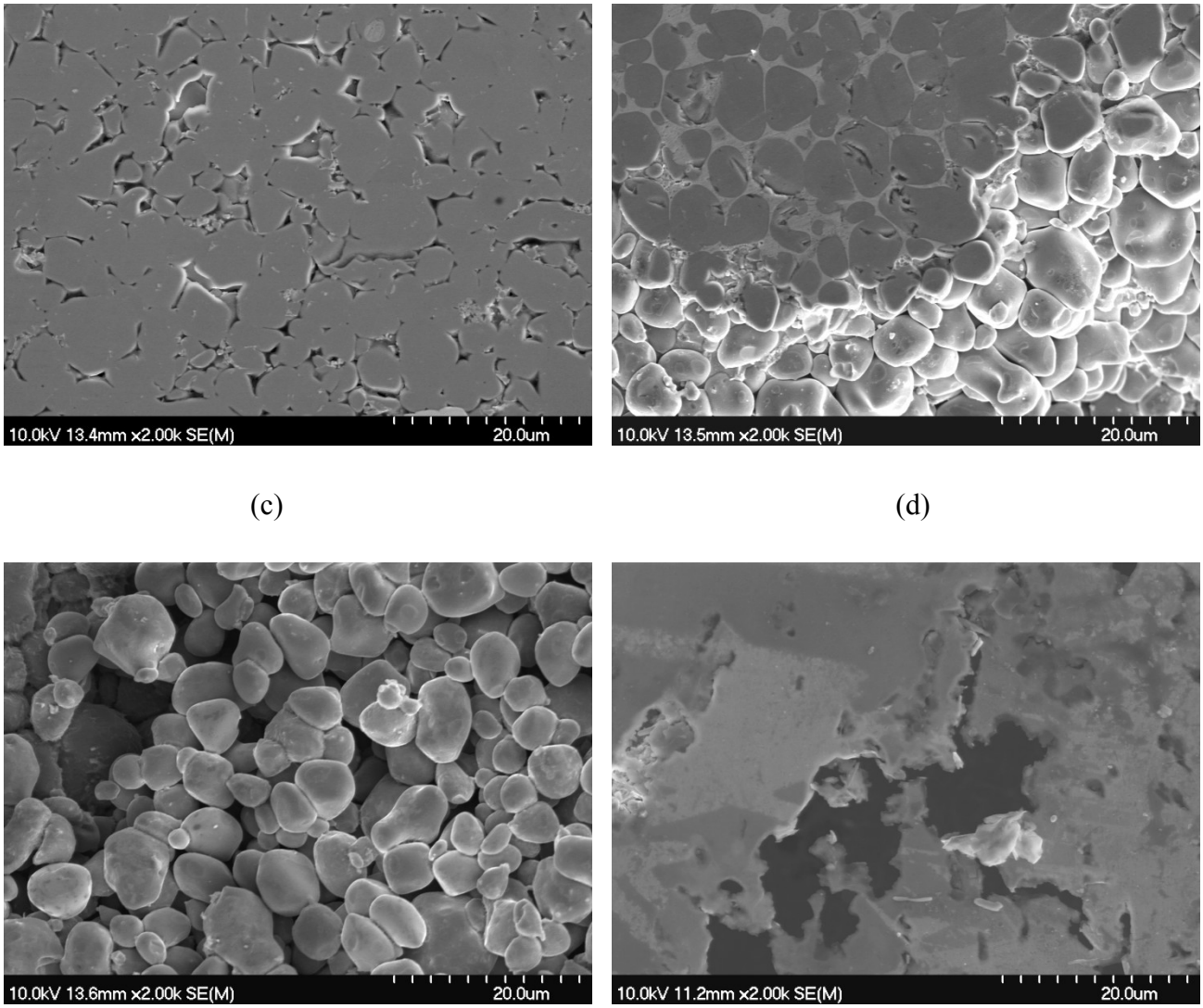

(c) (d)

Figure 8.16: Representative SEM images of the corroded surfaces of the TiC-304L cermets and 'pure' 304L steel following potentiostatic polarisation testing: (a) 10 vol. % 304L, (b) 20 vol. % 304L, (c) 30 vol. % 304L, and (d) 'pure' 304L stainless steel.

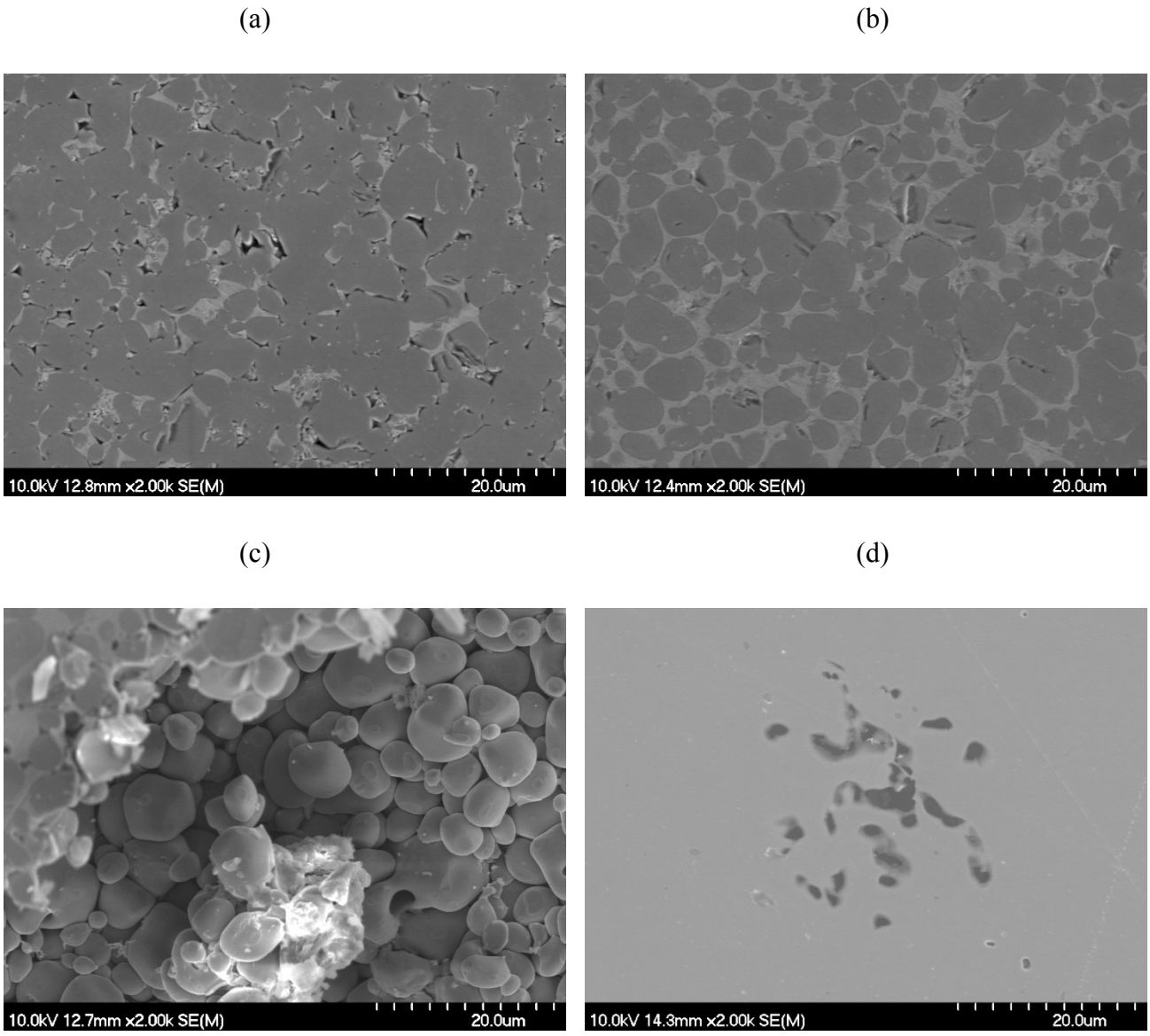

Figure 8.17: Representative SEM images of the corroded surfaces of the TiC-316L cermets and 'pure' 316L steel following potentiostatic polarisation testing: (a) 10 vol. % 316L, (b) 20 vol. % 316L, (c) 30 vol. % 316L, and (d) 'pure' 316L stainless steel.

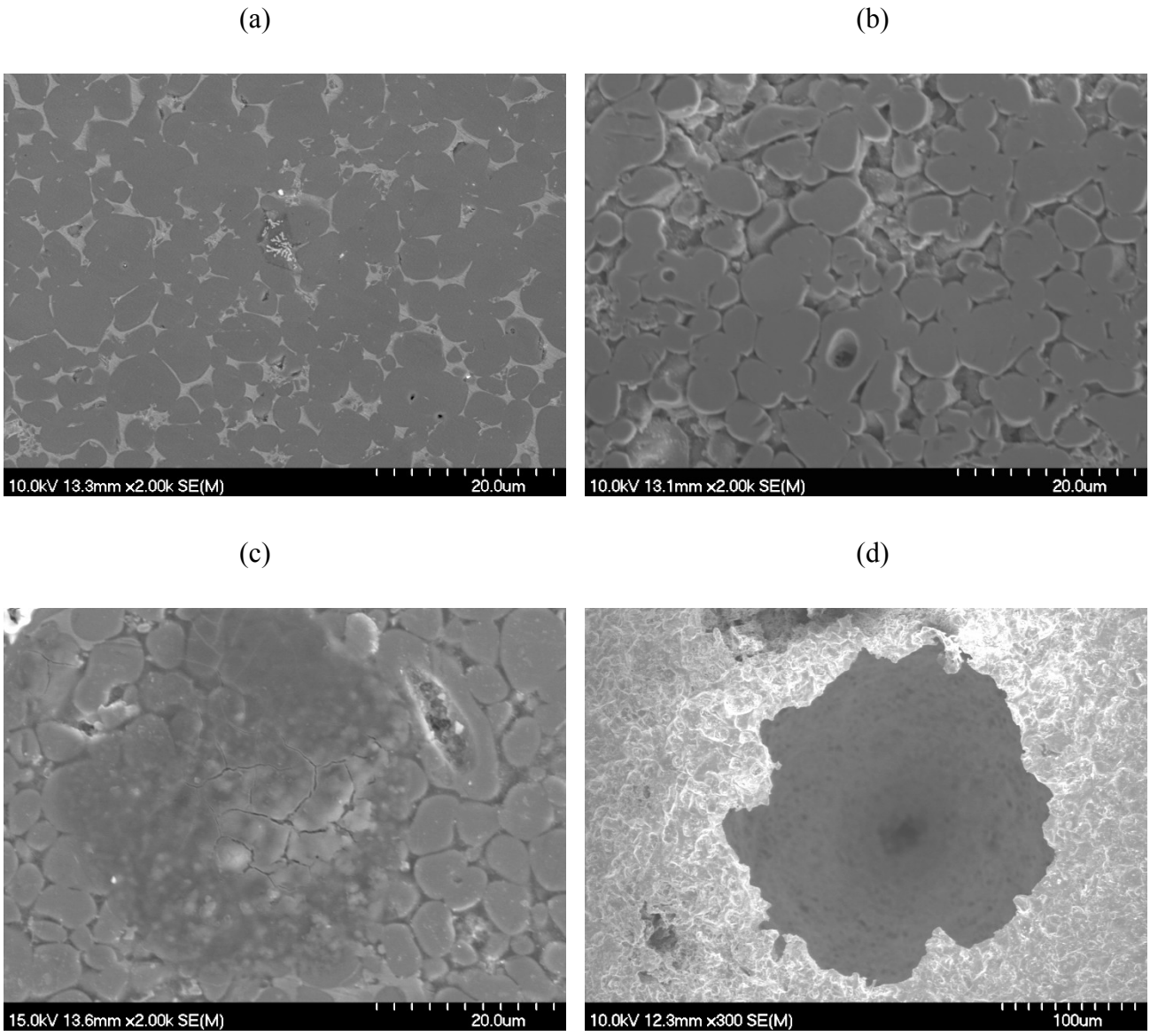

Figure 8.18: Representative SEM images of the corroded surfaces of the TiC-410L cermets and 'pure' 410L steel following potentiostatic polarisation testing: (a) 10 vol. % 410L, (b) 20 vol. % 410L, (c) 30 vol. % 410L, and (d) 'pure' 410L stainless steel.

For the baseline steels there is consistent evidence of localised corrosion on the surface (Figures 8.16 to 8.18), which is confirmed by the increase in current that occurs when holding at a potential above E_{pit} (shown previously in Figure 8.8). For the cermets, a comparable interfacial attack is observed to the cyclic polarisation case, while the intensity of attack increases with the steel binder contact.

It can again be confirmed that cermets with lowest binder contents (i.e. 10 vol. % steel) have the best corrosion resistance, which was also confirmed by the resulting corrosion currents being the lowest following potentiostatic polarisation above E_{pit}.

8.5 Conclusions

The corrosion behaviour of TiC-stainless steel cermets has been assessed in a simulated seawater environment (with 3.5 wt. % NaCl), using a combination of electrochemical and weight loss measurements, together with microstructural and compositional analyses. The cermets have been prepared with 10 to 30 vol. % steel binder, with the stainless steel compositions 304L, 316L and 410L examined. Efforts were also made during cermet processing to ensure an essentially identical grain size, to eliminate any issues arising from changing ceramic-metal interfacial area. Based on this study, the following conclusions can be drawn:

(1) The corrosion resistance of the baseline 316L, 304L and 410L steels is generally better than the TiC-stainless steel cermets, but comparable to the cermets with lowest binder content (i.e. 10 vol. % steel), which would offer significantly superior wear resistance.

(2) For the 'pure' baseline steels, the 316L stainless steel has the best corrosion resistance, followed by 304L and finally 410L. Conversely, for the cermets, the TiC-304L system has the best corrosion resistance, then TiC-316L and lastly TiC-410L.

(3) The corrosion rate of the cermets increases with steel binder content, which is related to selective dissolution of the steel binders. At low binder contents there is also an increased amount of semi-protective TiO_2-based oxide on the sample surface.

(4) Microstructural studies revealed preferential dissolution of the steel binder, while the TiC grains remain largely unaffected.

(5) Chemical analyses, using both ICP-OES and EDS, confirmed an increase in dissolution of the steel binder at higher binder contents.

(6) Based on both the electrochemical measurements and microstructural analyses, it can be concluded that the cermets with the lowest binder content (i.e. 10 vol. %) have the potential to offer a combination of good corrosion resistance and excellent wear resistance, as the dissolution rate of the binder is minimal during aqueous corrosion, while the high TiC would provide enhanced wear resistance.

8.6 Acknowledgements

This study was financially supported by Petroleum Research Atlantic Canada (PRAC) and the Natural Sciences and Engineering Research Council of Canada (NSERC). The Canada Foundation for

Innovation, the Atlantic Innovation Fund, and other partners who helped fund the Facilities for Materials Characterisation, managed by the Dalhousie University Institute for Materials Research, are also gratefully acknowledged. The authors would also like to thank Dean Grijm and Patricia Scallion for technical assistance.

9 Conclusions and Recommendations for Future Work

The present study has assessed the wear and corrosion behaviour of a series of novel TiC-based cermets, prepared with a variety of stainless steel 'binders' (i.e. 304L, 316L and 410L), and with the steel contents varied from 10 to 30 vol. %. All the TiC-steel based cermets were successfully fabricated through melt-infiltration and sintering, with samples typically exhibiting densities in excess of 99 % of theoretical. The high sintered densities of these cermets are confirmed by SEM examination, and there is good homogeneity of the two-phase microstructure, with little evidence of anomalous grain growth. The mean grain size was calculated by using linear intercept method,and was broadly consistent for each composition of the cermets. With increasing binder content, there is also an increase in mean free path of all the studied cermets, as well as a significant decrease in the contiguity.

The reciprocating wear tests were conducted using varying loads (20 to 80 N) and times (15 to 120 minutes), with a ball-on-flat testing geometry. In order to determine the extent of wear, optical profilometry was used to measure the volumetric wear loss and calculate a specific wear rate. It was apparent for all the cermets, that the wear rate increases with both the applied load and the stainless steel binder content. By increasing the binder content, there would be an associated volume reduction of the high hardness/elastic modulus TiC phase. When the TiC content is very high, the composite behaviour is dominated by the ceramic phase and the associated hardness of the composite is high (the contiguity is also high). The TiC particles can resist plastic deformation and offer additional resistance to the effective Hertzian load applied through the WC-Co containing sphere. This beneficial effect is degraded by the addition of the steel metal binder (effectively a soft phase in comparison to the TiC). By increasing the steel binder content, there is a decrease in the contiguity of the TiC particles (with an associated loss of hardness), and an increase in the binder mean free path, which both enhance the toughness of the composite. When the applied load is very low and at higher TiC content, the steel deformation and material removal is effectively minimised due to the contiguity of the TiC grains, which form a rigid, contacting network that resists compression and extrusion of the softer metallic binder. Microstructural analysis confirmed the operating wear mechanisms for these cermets. It is evident that the cermets, wear behaviour is rather complex, but involves a combination of abrasive wear (with a transition from two- to three-body wear), and adhesive/tribo-chemical wear (notably present in the form of a new tribolayer that is present on both the wear track and the counter face WC-Co sphere), which is discussed in more detail in the following paragraphs.

Examination of the wear track revealed that there is essentially no plastic deformation outside of the track. The build-up of deposited material at the ends of the wear track is an indicative of two-body wear. This general behaviour points to an abrasive wear mechanism. In terms of the wear progression, it can initially be expected that the mechanism will be two-body (ploughing wear), with the cermet sliding directly against the WC-6Co counter face sphere. This will eventually result in the formation of debris between the two counter faces, as TiC grains crack and fragment under the Hertzian contact load, and the steel binder is extruded out from between the TiC grains (binder extrusion is more evident at higher steel binder content). As a consequence, there will be a transition from two- to three-body wear, with the debris acting as the third body. Three-body wear ultimately leads to the formation of a tribolayer (the extent of formation of tribolayer increases with load and time), and a further potential transition to an adhesive wear mechanism, which was also confirmed by SEM and analysis of the wear debris. The formation of a tribolayer is promoted by the repeated, cyclic loading, with the third body material rolling back and forward between the two primary counter faces. This leads to a severe and massive refinement in the size of the third body particles. By microstructural analysis of the chemical composition of the of the tribolayer using EDS, it was possible to confirm that a major component within the tribolayer is oxygen, and this is expected to be mostly in the form of oxides associated with components from the steel binder (i.e. Fe, Cr, Ni, and Mo), together with Ti from TiC and a small amount of W from the WC-6Co counter face sphere.

A comparison of the wear behaviour of fine- and coarse-grained TiC-316L cermets followed the same trend as the conventional TiC-steel based cermets, with fine-grained cermets having the superior wear resistance and hardness, while the coarse-grained cermets had the better fracture toughness. Microstructural analysis of the wear debris generated on the coarse-grained cermets showed a coarser morphology than the fine-grained cermets suggesting that fragmentation of TiC observed on coarse grained cermets acted as third-body during the three-body wear scenario leading to the coarser morphology of wear debris. In summary, the smaller the TiC grain size, the better the hardness and wear resistance, while the coarser the TiC grain size, the better the indentation fracture resistance.

Samples for electrochemical assessment were tested within an electrochemical flat cell in a 3.5 wt. % NaCl aqueous solution. OCP tests measure the steady state potential of the cell until equilibrium is established between the sample and the NaCl solution within which it is immersed. Potentiodynamic testing was used to study the overall corrosion behaviour of the cermets, incorporates an applied cathodic potential, and measures the resultant current density of the cermet samples being investigated.

The potentiodynamic test was observed from -0.5 to 3.5 V. Corrosion rates were obtained using both the Tafel extrapolation method and a direct technique, via weight loss measurements. The corrosion rates obtained for the cermets were also compared to that of the equivalent pure steels in order to access the corrosion performance of the cermets. Cyclic polarisation was performed to access the susceptibility of the cermets to localised corrosion, while potentiostatic polarisation was applied at the pitting and/or protection potentials (obtained from cyclic polarisation) to confirm the results obtained from cyclic polarisation. All the tested samples were subsequently analysed to demonstrate any changes in composition or microstructure, using the same analysis tools as previously mentioned, as well as ICP-OES. Based on the electrochemical testing and microstructural/compositional analysis, it was possible to establish a pattern of susceptibility and microstructural response to electrochemical attack.

The corrosion testing results obtained from both weight loss measurements and Tafel extrapolation on the cermets showed broadly similar and consistent results, with an increase in the steel binder contents leading to higher corrosion rates, due to preferential dissolution of the binder. For all the cermets, both the corrosion potential and corrosion current density increase with binder content, indicating better corrosion resistance at lower binder contents. It is proposed that there is potential formation of a protective TiO_2 layer, which improves corrosion resistance at high TiC content. Microstructural observations revealed significant degradation of the samples, with the steel binder preferentially dissolved, while the TiC remained relatively unaffected. Cermets with the lowest binder contents (i.e. 10 vol. %) have the best corrosion resistance. Those based on austenitic steels (i.e. TiC-10% 304L and TiC-10% 316L) showed the highest ability for self-healing of the passive layer, indicating better pitting corrosion resistance. This was also confirmed from cyclic polarisation studies. In terms of the corresponding steels (316L, 304L and 410L), 316L exhibits the best corrosion resistance, followed by 304L and then 410L. Generally speaking the steels have better corrosion resistance than the cermets, but a comparable performance to the corrosion resistance of cermets with the lowest binder contents (i.e. 10 vol. %). However, these cermets would offer an excellent *combination* of wear and corrosion resistance, as dissolution of the binder is significantly reduced, while the higher TiC content considerably enhances the composite wear resistance (approximately 1,000 times better than the steels alone).

The fine- and coarse-grained TiC-316L cermets showed somewhat different corrosion behaviour. The corrosion resistance of both fine- and coarse-grained TiC-316L cermets increases with a reduction in

the steel binder content (i.e. an increase in the TiC content), as with the other TiC-stainless steel systems. This is believed to be as a result of an increase in the surface area coverage by a TiO_2 semi-protective layer, with a resultant reduction in the tendency for metallic binder dissolution. Microstructural studies and analyses also confirmed for both the fine- and coarse-grained cermets that, while there is preferential dissolution of the steel binder, the TiC grains remain largely unaffected. The corrosion resistance of the coarse-grained cermets is slightly superior to that of the fine-grained counterpart. This is believed to be due to reduced (galvanic) interfacial attack, due to a reduction in the ceramic-metal grain boundary area by a factor of approximately three. By using combinations of ICP-OES and EDS analyses, it is confirmed that the dissolution of the steel binder increases with increasing volume fraction, with this effect slightly more pronounced for the fine-grained cermets. It should be emphasised that although the coarse-grained cermets showed better corrosion resistance than the fine-grained variants, these benefits in terms of corrosion resistance must be weighed against the potential for reduced wear resistance when the carbide structure is coarsened.

9.1 Performance Ranking of Cermets

The performance ranking of all the studied cermets in the present study is presented in Table 9.1 As can be seen, the improvement in corrosion and wear resistance at the highest TiC content shows that TiC-steel based cermets have potential for use in highly corrosive and erosive environments. Cermets with the lowest binder content (i.e. 10 vol. % stainless steel content) offer an excellent combination of wear and corrosion resistance, as dissolution of the binder is significantly reduced and pitting corrosion is avoided, while the high TiC content considerably enhances the composite hardness and wear resistance.

9.2 Contributions to Original Thought

The thorough investigations of wear and corrosion studies on TiC-steel based cermets have led to improved understanding of their corrosion and wear behaviour, and resulted in a number of innovations for potential practical applications of these cermets. There is a very high demand in the oil and gas, and mining industries on materials that would offer superior wear and corrosion resistance, while improving on approaches to further understand the behaviour of these materials.

The systematic approach that was originally designed to study the wear and corrosion behaviour of these cermets was based on studying the effects of binder addition and composition behaviour. However, modifying this approach slightly by assessing the effect of coarsening, or making the carbide grain size finer, an improved understanding has been established in terms of how the carbide grain structure affects both the wear and corrosion response of these cermets.

Secondly, a systematic approach that was in place for corrosion studies on these cermets was solely based on using electrochemical testing techniques, but by modifying this approach further through the assessment of non-electrochemical techniques, such as the use of EDS before and after corrosion, and use of ICP-OES to analyse the corroded solution, a significant improvement in the study and behaviour of these cermets has been established.

Lastly, the traditional approach to studying the susceptibility of cermets to localised corrosion is simply by ranking the pitting and protection potentials obtained through cyclic polarisation experiments, but by going one further step and applying potentiostatic polarisation above the pitting potential (obtained through cyclic polarisation experiments), and fully supporting it with microstructural analysis, an improved and comprehensive approach to studying the susceptibility of cermets to localised corrosion has been established.

Table 9.1: Performance ranking of all the studied cermets.

	TiC-304L cermets		
Property investigated	TiC-10 vol.% 304L	TiC-20 vol.% 304L	TiC-30 vol.% 304L
Corrosion resistance	excellent	good	acceptable
Wear resistance	excellent	good	acceptable
Hardness	excellent	good	acceptable
IFR	acceptable	good	excellent
	TiC-316L cermets		
	TiC-10 vol.% 316L	TiC-20 vol.% 316L	TiC-30 vol.% 316L
Corrosion resistance	excellent	good	acceptable
Wear resistance	excellent	good	acceptable
Hardness	excellent	good	acceptable
IFR	acceptable	good	excellent
	TiC-316L cermets (fine)		
	TiC-10 vol.% 316L	TiC-20 vol.% 316L	TiC-30 vol.% 316L
Corrosion resistance	good	excellent	acceptable
Wear resistance	excellent	good	acceptable
Hardness	excellent	good	acceptable
IFR	acceptable	good	excellent
	TiC-316L cermets (Coarse)		
	TiC-10vol.% 316L	TiC-20vol.% 316L	TiC-30vol.% 316L
Corrosion resistance	excellent	good	acceptable
Wear resistance	excellent	good	acceptable
Hardness	excellent	good	acceptable
IFR	acceptable	good	excellent
	TiC-410L cermets		
	TiC-10vol.% 410L	TiC-20vol.% 410L	TiC-30vol.% 410L
Corrosion resistance	excellent	good	acceptable
Wear resistance	excellent	good	acceptable
Hardness	excellent	good	acceptable
IFR	acceptable	good	excellent

9.3 Recommendations for Future Work

Study of the corrosion and wear behaviour of TiC-steel based cermets is still in its infancy, and the current work is a systematic study to further improve understanding of the corrosion and wear behaviour of these materials. The outlined research on the electrochemical response of the TiC-steel based cermets focussed on studying the susceptibility of these materials to corrosion at room temperature. In addition, future studies on the erosion-corrosion behaviour of these cermets is recommended, as this would provide useful information for the use of such materials in the oil and gas and/or mining industries, where these cermets are potentially very relevant materials based on their outstanding wear and corrosion resistance. Studying the susceptibility of these cermets to localised corrosion for the present study was based on applying a potentiostatic polarisation above the pitting potential (obtained after cyclic polarisation experiments), followed by microstructural analysis. A future recommendation would be to apply potentiostatic polarisation below the protection potential and supporting it with microstructural analysis. It is generally believed that the higher diffusion rates and contact stress associated with fine-grained cermets (as a result smaller radius of curvature) is one of the reasons that contributed negatively to their corrosion performance when compared with coarse-grained cermets. It would be worthy of a recommendation to use XRD analyses to assess the stress on both the fine- and coarse -grained cermets before corrosion experiments and relate it to the corrosion response.

With regard to the wear studies, sectioning of the wear tracks using a focused ion beam (FIB) microscope is highly recommended, as the tribolayer and 'ploughed' material at the end of the wear tracks may be further investigated to confirm their thickness and composition throughout the range of the examined layer. By doing this, it would be possible to determine if the tribolayer is truly homogenous or if there is a compositional change throughout the layer. Another benefit that would be derived by using FIB is to confirm the presence of any sub-surface defects that are generated during wear testing, especially the presence of Hertzian cone cracking, as it is an indicative of fatigue failure.

Lastly, the current research focused on the development, testing and evaluation of the wear and corrosion behaviour of TiC-steel based cermets through the application of experimental techniques. It is therefore desirable to develop corrosion (by monitoring the interfacial attack with time) and/or wear models (by using contact mechanics) to further enhance the understanding on the behaviour of these cermets, and to generate a predictive capability for assessing the behaviour of subsequent variations on the present materials.

REFERENCES

[1] H.Y. Liu, J.H. Huang, C.F. Yin, J.G. Zhang and G.B. Lin: 'Microstructure and properties of TiC-Fe cermets coatings by reactive flame spraying using asphalt as carbonaceous precursor, Ceram Int., 33 (2007) 827-835.

[2] P. Ettmayer, H. Kolaska and K. Dreyer, Effect of the sintering atmosphere on the properties of cermets, Powder Metall. Int., 23 (1991) 224-230.

[3] D.J. Miller, J.A. Pask, Liquid-Phase Sintering of TiC-Ni Cermets, J. Am. Cer. Soc. 66 (1983) 236-240.

[4] P. Persson, A.E. Jarfors, S.S Savage, Self-propagating high-temperature synthesis and liquid-phase sintering of TiC/Fe composites, Mat. Proc. Tech. 127 (2002) 131-139.

[5] F. Arenas, C. Rondon, R. Sepulveda, Friction and tribological behaviour of (Ti,V)C-Co cermets, 143 (2003) 822-826.

[6] K. Plucknett and P. F. Becher, Properties of Ni3Al-bonded Titanium Carbide Ceramics, *J.* Eur. Ceram. Soc, 18(1998) 395-400.

[7] R. Subramanian, J.H. Schneibel, FeAl-TiC cermets - melt infiltration processing and mechanical properties, Mater. Sci. Eng., A, 240 (1997) 633.

[8] A.M. Human, H.E. Exner, Electrochemical behavior of tungsten carbide hard metals, Mater. Sci. Eng., A 209 (1996) 180-191.

[9] S.Y. Zhang, Titanium carbonitride-based cermets - Processes and properties, Mater. Sci. Eng., A163 (1993) 141-148.

[10] J.H. Potgieter, N. Thanjekwayo, P. Olubambi, N. Maledi, S.S. Potgieter-Vermaak, Influence of Ru additions on the corrosion behaviour of WC-Co cemented carbide alloys in sulphuric acid, Int. J. Refract. Met. Hard Mater., 29 (2011) 478-487.

[11] A.J. Gant, M.G. Gee, Structure-property relationships in liquid jet erosion of tungsten carbide hardmetals, Int. J. Refract. Met. Hard Mater., 27 (2009) 332-343.

[12] S. Hochstrasser-Kurz, Y. Mueller, C. Latkoczy, S. Virtanen, P.Schmutz, Analytical characterization of the corrosion mechanisms of WC-Co by electrochemical methods and inductively coupled plasma mass spectroscopy, Corros. Sci., 49 (2007) 2002-2020.

[13] N. Durlu, Titanium carbide based composites for high- temperature applications, J. Eur. Ceram. Soc., 19 (1999) 2415-2419.

[14] K. E. Stroms, The Refractory Carbides, Refractory Materials Series, New York: Academic Press, 1967.

[15] L. E. Toth, Transition Metal Carbides and Nitrides, New York: Academic Press, 1971.

[16] O. H. Pierson, Handbook of Refractory Carbides and Nitrides, New Jersey: Noyes Publications, Park Ridge, 1996.

[17] J. J. Gangler, Some Physical Properties of Eight Refractory Oxides and Carbides," J. Eur. Ceram. Soc., 33 (1950) 367.

[18] Y. Shin, X. S. Li, C. Wang, J. R. Coleman and G. R. Exarhos, Synthesis of Hierarchical Titanium Carbide from Titania-Coated Cellulose Paper, Adv Mater, 16 (2004) 1212-1215.

[19] G. Yasuo, F. Kensaku, K. Mikio, O. Yutaka, N. Masanobu and A. Kensuke, Synthesis of Titanium Carbide from a Composite of TiO_2, Nanoparticles/Methyl Cellulose by Carbothermal Reduction, Mater. Res. Bull., 36 (2001) 2263-2275.

[20] P. Huber, D. Manova, S. Mandi and B. Rauschenbach, Formation of TiN, TiC and TiCN by Metal Plasma Immersion Ion Implantation and Deposition, Surf. Coat. Tech., 174-175 (2003)1243-1247.

[21] S. C. Tjong and Z. Y. Ma, "Microstructural and Mechanical Characteristics of in Situ Metal Matrix Composites," Mater.Sci.Eng. R: Reports, 29 (2000) 49-113.

[22] P. Ettmayer, H. Kolaska, W. Lengauer and K. Dreyer, "Ti(C,N)—Metallurgy and Properties, Int. J. Refrac. Metal. Hard Mater., 13 (1995) 334-351.

[23] R. Koc, J. S. Folmer, Carbothermal Synthesis of Titanium Carbide Using Ultrafine Titania Powders, J. Mater. Sci., 32 (1997) 3101-3111.

[24] C. Youjian, Y. Deng, A Novel and Simple Route to Synthesis Nanocrystalline Titanium Carbide via the Reaction of Titanium Dioxide and Different Carbon Source., Mater. Sci. App., 2 (2011) 1622-1626.

[25] D. D. Harbuck, C. F. Davidson and B. Monte, gas phaase production of TiN and TiC powders, J. Metals., 38 (1986) 47.

[26] B. Schultrich, M. L. Berger, J. Henke and A. Oswald, Proceedings of the 2nd Plasma-Technik-Symposium, Lucerne (Plasma-Technik, Wohlen, Switzerland).,2 (1991) 363.

[27] J. B. Holt and Z. Munir, Combustion synthesis of titanium carbide: theory and experiment," J. Mater. Sci. 21 (1986) 251.

[28] R. Schwarzkopf, R. Kieffer, Refractory Hard Metals., New York, USA: Macmillan, 1953.

[29] Schwarzkopf and R. Kieffer, The basic constituents of cemented hard metals and their use as high temperature materials, in Refractory hard metals, borides, carbides, nitrides, and silicides, New York, Macmillan, (1953) 447.

[30] F. Akhtar, and S. F, Guo, Microstructure , mechanical and fretting wear properties of TiC-stainless steel composites, Mater Charact, 59 (2008) 84-90.

[31] S. C. Tjong, K.C. Lau, Sliding wear of stainless steel matrix composite reindorced with TiB_2 particles, Mater. Lett., 41 (1999) 153-158.

[32] C. Wenyi, A. Jian, Preparation and Characterization of stainless steel / TiC Nanocomposite particles by Ball-Mill method, 2008.

[33] H. Reshetnyak, J. Kubarsepp, Mechanical properties of hard metals and their erosive wear resistance, Wear.,177 (1994) 185-193.

[34] I. Hussainova, Some aspects of solid particle erosion cermets, Tribol. Int., 34 (2001) 89-93.

[35] W. Young-Chul, K. Ho-Jae and K. Deug, Formation of TiC particle during carbothermal reduction of TiO_2, J. Eur. Ceram. Soc., 27 (2007) 719-722.

[36] P. Schweitzer, Fundamentals of corrosion, mechanisms, causes, and preventive methods, CRC Press, FL USA, 2010.

[37] J. Denny, Principles and prevention of corrosion, New York: Macmillan Publishing Inc, 1991.

[38] S. Bradford, Corrosion Control, 2nd edition, Alberta Canada: CASTI Publishing Inc, 2001.

[39] M. G. Fontana, Corrosion Engineering, 3rd edition, New York: McGraw-Hill Book, 1986.

[40] J.Sedricks, Corrosion of stainless steels, 2nd ed, New York: John Wiley & Sons, Inc, 1996.

[41] J. Chamberlain, K. R. Tretheway, Corrosion for students of Science and Engineering, Longman Scientific & Technical Ed., Harlow, UK, 1998.

[42] R. W. Revie, H.H. Uhlig, Corrosion and Corrosion Control, 3rd edition, New York, Wiley & Sons, Inc, 1985.

[43] R. N. Mohamed, Ceramic Processing, Florida USA: Taylor & Francis Group, 2007.

[44] D. Bortzmeyer, Die pressing and isostactic pressing in Materials Science and Technology," in Processing of Ceramics, Pt. I, New York, Brook, R,J, Editor, VCH, 1996.

[45] S. J. Glass and K. G. Ewsuk, Ceramic powder compaction, MRS Bull., 22 (1997) 24.

[46] C. William, Introduction to Materials Science and Engineering, 7th edition., New York: John Wiley & Sons, Inc, 2007.

[47] W. D. Kingery, and Editor, Ceramic Fabrication Processes, Cambridge, MA: MIT Press, 1963.

[48] G. M. Randal, Powder Metallurgy Science, 2nd edition., Princeton New Jersey, USA: Metal Powder Industries Federation, 1994.

[49] G. Randall, Coarsening in sintering, grain shep distribution, grain size distribution, grain growth distribution, and grain growth kinetics in solid-pore systems," Crit. Rev. Solid State Mater. Sci., 35 (2010) 263-305.

[50] Y. M. Chiang, B. Dunbar and D. W. Kingery, Physical Ceramics: Principles for ceramic science and engineering, New York: John Wiley and Sons, 1997.

[51] J. Blackford, Sintering and microstructure of ice, J. Phys. D: Appl. Phys., 40 (2007) 355-385.

[52] G. M. Randall, S. Pavan and J. P. Seong, Review on Liquid Phase Sintering., J. Mater. Sci., 44 (2009) 1-39.

[53] R. German, Liquid phase sintering, New York: Plenum Press, 1985.

[54] I. Hussainova, Effect of microstructure on the erosive wear of titanium carbide-based cermets, Wear, 255 (2003) 121-128.

[55] C.C Onuoha, G.J. Kipouros, Z.N. Farhat, K.P. Plucknett., Reciprocating wear behaviour of TiC-Steel based cermets, Wear 303 (2013) 321-333.

[56] B. Bharat, Introduction to Tribology, New York: John Wiley & Sons, 2002 .

[57] G. Zum and K.H, Microstructure and wear of materials, The Netherlands: Elsevier Science Publishers, 1987.

[58] N. Sacks, The wear and corrosive-wear response of tungsten carbide-cobalt hardmetals under woodcutting and three body abrasion conditions' Ph.D Thesis, Nürnberg, Germany: University of Erlangen-Nürnberg, Germany, 2002.

[59] J. D. Lucas, Tribology of 316L Austenitic Stainless Steel Carburized Steel at Low Temperature, MSc Thesis, Cleveland, OH : Case Western University Reserve University, 2010.

[60] A.W. Batchelor, G.W. Stachowiak, Engineering Tribology 3rd edition,. New York: S.L Elsevier Butterworth-Heinemann, 2005.

[61] H. Czichos, Tribology, A Systems Approach to the Science and Technology of Friction, Lubrication, and Wear., New York: Amsterdam; New York: Elsevier Scientific Pub. Co.; New York: distributors for the U.S. and Canada, Elsevier North Holland, 1978.

[62] T. Saada, M. Oike, N. Emori, The effects of abrasive grain size on the transition between abrasive and adhesive wear, Wear, 97 (1984) 291-302.

[63] R.W. Johnson, The use of the scanning electron microscope to study the deterioration of abrasive papers, Wear, 12 (1968) 213-216.

[64] B. Bhushan, R.E. Davies, H.R. Kolar, Metallurgical re-examination of wear modes II: Adhesive and abrasive, Thin Solids. Films. 123 (1985b) 113-126.

[65] N. P. Suh, Tribophysics, Englewood, New Jersey: Prentice-Hall, 1986.

[66] B. Bhushan, Principles and Applications of Tribology, New York: Wiley, 1999.

[67] K. Komac, S. Novak, Mechanical and wear behaviour of TiC cemented carbide, Int. J .Refract.Metal Hard Mater, 4 (1985) 21-26.

[68] J. Pirso, M. Viljus, K. Juhani, S. Letunovits, Two body dry abrasive wear of cermets, Wear 266 (2009) 21-29.

[69] I. Hussainova, Mechanical properties and features of erosion of cermets, Wear, 250 (2001) 818-825.

[70] E. Pagounis, M. Talvitie, V.K. Lindroos, Influence of matrix structure on the abrasion wear resistance and toughness of a hot isostatic pressed white iron matrix composite, Met. Mater. Trans. A, 27 (1996) 4183.

[71] A. Mukhopadhyay, Recent developments on WC-based bulk composites, J. Mater. Sci., 46 (2011) 571-589.

[72] K. Jia, T. M. Fischer, Abrasion resistance of nanostructured and conventional cemented carbides, Wear, 200 (1996) 206.

[73] J. Larsen-Basse, Resistance of cemented carbides to sliding abrasion: role of binder metal, in Science of Hard Materials, Plenum, New York, (1983) 797-811.

[74] L. J. Basse and P. A. Tanouye, Abrasion of WC-Co alloys by loose hard abrasives, proc., Int. Conf on Hard Material Tool Technology, Carnegie-Mellon University, Pittsburgh, PA, (1976) 188-199.

[75] L. J. Basse, Effects of hardness and local fracture toughness on the abrasive wear of WC-Co alloys, in Institute of Mechanical Engineering Conference Publications, (1987), 227-282.

[76] C. Allen, M. Sheen, J. Williams, V.A, Pugsley, The wear of ultrafine WC-Co hard metals. Wear, 250 (2001) 604-610.

[77] Q. Yang, T. Senda, A. Ohmori, Effect of carbide grain size on microstructure and sliding wear behaviour of HVOF-Sprayed WC-12% Co coatings, Wear, 254 (2003) 23-24.

[78] C.S. Kim, Ph.D Thesis-Microstructure, Mechanical Property Relationships in WC-Co Composites, Pittsburgh, PA: Carnegie Mellon University, 2004.

[79] J. Gurland and P. Bardzil, Relation of Strength, Composition, and Grain Size of Sintered WC-Co Alloys, Trans. TMS-AIME, 203 (1995) 311-315.

[80] K. Jia, T.E. Fischer, Sliding wear of conventional and nanostructured cemented carbides, Wear, 203 (1997) 310-318.

[81] R.A Cutlar, V.A. Virkar, The effect of binder thickness and residual stresses on the fracture toughness of cemented carbide, J. Mater Sci, 20 (1985) 3557-3573.

[82] P.R. Robert, Handbook of Corrosion Engineering, New York: McGraw-Hill, 1977.

[83] A. Etor, Electrochemical Measurement of Crevice Corrosion of Type AISI 304 Stainless Steel, MSc Thesis, Saskatoon: University of Saskatoon, Canada, 2009.

[84] Z. Ahmad, Principle of corrosion engineering and corrosion control, Butterworth-Heineman, MA , USA, 2006.

[85] J.W Oldfield, W.H. Sutton, Crevice corrosion of stainless steel: A Mathematical model, Corr. J., 13 (1978) 13-22.

[86] F. Frankel, Pitting Corrosion, corrosion, fundamentals, testing, and protection," in ASTM HANDBOOK, Corrosion, vol. 13A, Ohio, ASM International, 2003, pp. 237-238.

[87] J. Horvath, H. Uhlig, Critical potentials for pitting corrosion of Ni, Cr-Ni, Cr-Fe, and related stainless steels J. Electrochem. Soc., 115 (1968) 791-795.

[88] S. Z. Szklarska, Pitting Corrosion of Metals, NACE, 1986.

[89] A. Sedriks, Effects of alloy composition and microstructure on the localized corrosion of stainless steels,, NACE-Advances in Localized in Localized Corrosion, vol. 9, 1990.

[90] V. Sastri, E. Ghali and E. Mimoun, Corrosion prevention and protection, John Wiley and Sons, Ltd, Sussex, UK, 2007.

[91] B. Kumar and B. Basu, Electrochemical Behaviour of TiCN-Ni-Based Cermets., J. Am .Ceram. Soc, 90 (2007) 205-210.

[92] A. M. Human, The corrosion of tungsten carbide-based cemented carbides. Ph.D. Thesis., Technische Hochschule Darmstadt: Technische Hochschule Darmstadt, 1994.

[93] S. Sutthiruangwong, G. Mori, Corrosion properties of Co-based cemented carbides in acidic solutions, Int J. Refr. Metal. Hard Mater., 21 (2003) 135-145.

[94] G. Sutthiruangwong, G. Mori and R. Kosters, Passivity and pseudopassivity of cemented carbides, Int. J. Refr. Metal. Hard Mater, 23 (2005) 129-136.

[95] Q. Wu, W. Li and N. Zhong, Corrosion behaviour of TiC particle-reinforced 304 stainless steel, Corros. Sci., 53 (2011) 4258-4264.

[96] B. R. Collier and K. P. Plucknett, A comparison of anionic and cationic polyelectrolytes for the aqueous colloidal processing of titanium carbide ceramics, Int. J. Refrac. Metal. Hard Mater, 29 (2011) 298-305.

[97] J.R. Davies, Metals Handbook: Desk Edition', 2nd edn;, Materials Park, OH: ASM International., 1998.

[98] G.R. Anstis, P. Chantikul, B.R. Lawn, D.B. Marshall, A critical evaluation of indentation techniques for measuring toughness: I, Direct crack measurements, J. Am .Ceram. Soc, 64 (1981) 533-538.

[99] K. Niihara, A fracture mechanics analysis of indentation-induced Palmqvist crack in ceramics, J. Mater. Lett., 2 (1983) 221-223.

[100] K. Niihara, R. Morena, D.P.H. Hasselman, Evaluation of KIC of brittle solids by the indentation method with low crack-to-indent ratios, J. Mater. Sci. Lett. 1 (1982) 13-16.

[101] ASTM, ASTM standard C1327; Standard test method for vickers indentation hardness of advanced ceramics, ASTM international, West Conshohocken, PA, 2008.

[102] J. K. Lancaster, The influence of substrate hardness on the formation and endurance of molybdenum disulphide films, Wear, 10 (1967) 103-107.

[103] S. T. Buchholz, Reciprocating Wear Response of Ti(C,N)-Ni_3Al Cermets, MSc Thesis, Dalhousie University, Canada, 2011.

[104] Application Note CORR-4 on Electrochemistry and Corrosion Oak Ridge, TN: Princeton Applied Research.

[105] Application Note CORR-1 on Basics of Corrosion measurements Oak Ridge, TN: Princeton Applied Research.

[106] F. Mansfeld, Electrochemical Methods of Corrosion Testing, Corrosion: Fundamentals, Testing, and Protection,, ASM Handbook, ASM International, vol. 13A, pp. 446-462, 2003.

[107] ASTM. International, G102-89, Standard Practice for Calculation of corrosion rates and Related Information from Electrochemical Measurements, Pennsylvania: ASTM International, 2010.

[108] ASTM G 61 (latest revsion), Corrosion Cyclic Potentiodynamic Polarization measurements for Localized Corrosion Susceptibility of Iron -, Nickel – and Cobalt Based Alloys, Annual Book of ASTM Standards , Volume 3.02, Metal Corrosion, PA USA: ASTM, 1998.

[109] J. A. Beavers, C. L. Durr and N. G. Thompson, Unique Interpretation of Potentiodynamic polarization technique, NACE Corrosion/98, Houston (1998), NACE Corrosion, 1998, p. 300.

[110] J.R. Cahoon, R. Bandyopadhya, L. Tennese, The concept of protection potential applied to the corrosion of metallic orthopedic implants, J. Biomed. Mater. Res., 9 (1975) 259-264.

[111] E. Niki, S. Kohara, M. Tajiri, K. Tatsuzawa, Sintering of nickel-bonded titanium carbides, Trans. Jap. Inst. Met, 5 (1964) 1-8.

[112] S.A. Horton, M.B. Waldron, B.Roebuck, E.A. Almond, Characterization of powders and dislocation structures in processing of WC-Co, (W,Ti)C-Co and TiC-Co hardmetals, Powder Met., 27 (1984) 201-211.

[113] D. Muscat, R.L. Harris, R.A. Drew, The effect of pore-size on the infiltration kinetics of titanium carbide preforms, Acta Metal. Mater., 42 (1994) 4155-4163

[114] J.G. Li, Influence of oxygen partial pressure on the wetting behaviour of titanium carbide by molten copper and other metals, Mater. Lett., 17 (1993) 74-78.

[115] K. Aigner, W. Lengauer, P. Ettimayer, Interactions in iron-based cermet systems, J. Alloy. Compound., 262-263 (1997) 262-263.

[116] J. Beddoes, J.G. Parr, Introduction to stainless steels, 3rd edition,, Materials Park, Ohio: ASM International, 1999.

[117] K.L. Hsu, T.M. Ahn D.A. Rigney, Friction, wear and microstructure of unlubricated austenitic stainless-steels, Wear, 60 (1980) 13-37.

[118] S.C. Tjong, K.C. Lau, Influence of matrix structure on the abrasion wear resistance and toughness of a hot isostatic pressed white iron matrix composite, Met. Mater. Trans. A, 27 (1996) 4183-4191.

[119] C.C. Degan, P.H. Shipway, A comparison of the reciprocating sliding wear behaviour of steel based metal matrix composites processed from self-propagating high temperature synthesised Fe-TiC and Fe-TiB_2 master alloys, Wear., 252 (2002) 832-841

[120] F. Akhtar, S. Guo, On the processing, microstructure, mechanical and wear properties of cermet/stainless steel layer composites, Acta Mater., 55 (2007) 1467–1477.

[121] W.D. Kaplan, D. Rittel, M. Lieberthal, N.M. Frage, Static and dynamic mechanical damage mechanisms in TiC-1080 steel cermets, Scripta Mater., 51 (2004) 37-41.

[122] D. Rittel, N. Frage, M.P. Dariel, Dynamic mechanical and fracture properties of an infiltrated TiC-1080 steel cermet, Int. J. Solid. Struct., 42 (2005) 697-715.

[123] T. Stewart, R.B, Collier, Z.N, Farhat, G.J, Kipouros, K.P, Plucknett, Melt-infiltration processing of titanium carbide-stainless steel cermets," Ceram. Eng. Sci. Proc, 31 (2010) 97-104.

[124] K.P, Plucknett, P.F, Becher, Processing and microstructure development of titanium carbide-nickel aluminide composites prepared by melt-infiltration/sintering (MIS), J. Am. Ceram. Soc., 84 (2001) 55-61.

[125] M.I, Mendelson, Average grain size in polycrystalline ceramics, J. Am. Ceram. Soc. 52 (1969) 443-446.

[126] D.K. Shetty, I.G. Wright, P.N. Mincer, A.H. Clauer, Indentation fracture of WC-Co cermets, J. Mater. Sci. 20 (1985) 1873-1882.

[127] S. Buchholz, Z.N. Farhat, G.J. Kipouros, K.P. Plucknett, The reciprocating wear behaviour of TiC-Ni_3Al cermets, Int. J. Refract. Met. Hard Mater., 33 (2012) 44-52.

[128] S. Buchholz, Z.N. Farhat, G.J. Kipouros, K.P. Plucknett, Reciprocating wear response of Ti(C,N)-Ni_3Al cermets, Can. Metall. Q., 52 (2013) 69-80.

[129] A.L. Yerokhin, A. Leyland, C. Tsotsos, A.D. Wilson, X. Nie, A. Matthews, Duplex surface treatments combining plasma electrolytic nitrocarburising and plasma-immersion ion-assisted deposition, Surf. Coat. Tech. 142-144 (2001) 1129-1136.

[130] C.E. Foerster, F.C. Serbena, S.L.R. de Silva, C.M. Lepienski, C.J. de M. Sequeira, M. Ueda, Mechanical and tribological properties of AISI stainless steel nitrided by glow discharge compared to ion implantation and plasma immersion ion implantation, Nucl. Instrum. Methods Phys. Res. B 257 (2007) 732-736.

[131] F. Delanney, L. Froyen, A. Deruyttere, Review: The wetting of solids by molten metals and its relation to the preparation of metal matrix composites, J. Mater. Sci. 22 (1987) 1-16.

[132] J. Pirso, M. Viljus, S. Letunovits, Friction and dry sliding behavior of cermets, Wear., 260 (2006) 815-824.

[133] J. Pirso, M. Viljus, S. Letunovits, Sliding wear of TiC-NiMo cermets, Tribol. Int. 37 (2004) 817-824.

[134] V.K. Sikka, Compositional effects on processing and properties of nickel aluminides, in: C.T. Liu, A.L. Taub, N.S. Stoloff, C.C. Koch (Eds.), High-Temperature Ordered Intermetallic Alloys, Vol. 133, MRS Symposium Proc., Boston, 1989, pp. 487-492.

[135] S. Qu, C.X. Huang, Y.L. Gao, G. Yang, S.D. Wu, Q.S. Zang, Z.F. Zhang, Tensile and compressive properties of AISI 304L stainless steel subjected to equal channel angular pressing, Mater. Sci. Eng. A 475 (2008) 207-216.

[136] J. Pirso, S. Letunovits, M. Viljus, Friction and wear behaviour of cemented carbides, Wear, 257 (2004) 257-265.

[137] F. Bulbul, H. Altun, V. Ezirmik, O. Kucuk, Investigation of structural, tribological and corrosion properties of electroless Ni-B coating deposited on 316L stainless steel, Proc IMechE Part J: J Eng. Tribol. (2012) 1-11.

[138] J. H. Magee, Wear of stainless steels, 10th edition, ASM International, Materials Park, 1995.

[139] E. Pagounis, V.K. Lindroos, Processing and particulate reinforced steel matrix composites, Mater Sci, Eng., A 246 (1998) 221-234.

[140] E. Pagounis, M.Talvitie, V.K Lindroos, Influence of matrix structure on the abrasion wear resistance and toughness of a hot isostatic pressed white iron matrix composite, Met. Mater. Trans., A 27 (1996) 4183-4191.

[141] O. N. Dogan, J.A. Hawk, J. H. Tylczak, R. D. Wilson, R. D. Govier, Wear of titanium carbide reinforced metal matrix composites, Wear, 225 (1999) 758-769.

[142] J. Gurland, The fracture strength of sintered tungsten carbide-cobalt alloyst in relation to composition and particle spacing, Trans. AIME, 227 (1963) 1146-1150.

[143] H.E. Exner and J. Gurland, A review of parameters influencing some mechanical properties of tungsten carbide-cobalt alloys, Powder Metall. 13 (1970) 13-30.

[144] M.C. Perrott, On the indentation fracture of cemented carbide part II- the nature of surface fracture toughness, Wear, 47 (1978) 81-91.

[145] J. Larsen-Basse, Effect of composition, microstructure and, service conditions on the wear of cemented carbides, J. Metal. 35 (1983) 35-42.

[146] K. Anand, H. Conrad, Microstructure and scaling effects in the damage of WC-Co alloys by single impacts of hard particles, J. Mater. Sci., 23 (1988) 2931-2942.

[147] E.A. Almond, B. Roebuck, Identification of optimum binder phase compositions for improved WC hardmetals, Mater. Sci, Eng A, 105 (1988) 237-248.

[148] J. Chermant, A. Deschanvres, F. Osterstock, Abrasive wear of brittle solids, Powder Met. 20 (1977) 63-69.

[149] J. Kenneth, J. Brooks, Hardmetals and other metals, Int Carbide Data, ASM *International,* USA, (1992).

[150] P. Chivavibul, M.Watanabe, S. Kuroda, K. Shinoda, Effects of carbide size and Co content on the microstructure and mechanical properties of HVOF-sprayed WC–Co coatings, Surf. Coat. Tech., 202 (2007) 509-521.

[151] K. Jia, T.E. Fischer, B. Gallois, Microstructure, hardness, and toughness of nanostructures and conventional WC–Co composites, Nanostruct. Mater., 10 (1998) 875–891.

[152] J. Gurland, The measurement of grain contiguity in two phase alloys, Trans Metall. Soc. AIME, 212 (1958) 452-455.

[153] S. Luyckx, A. Lowe, Empirical quantitative relationships among grain size, mean free path, contiguity and cobalt content in WC-Co hardmetals, Trans. Royal Soc. South Africa, 58 (2003) 145-148.

[154] Y. Zhengui, J.J. Stiglich, T.S. Sudarshan, Nano-grained tungsten carbide-cobalt (WC/Co), (2002).

[155] C.C. Onuoha, G.J. Kipouros, Z.N. Farhat and K.P. Plucknett, The effects of grain size on the corrosion behaviour of TiC-316L stainless steel cermets in a synthetic seawater solution, submitted to Corros. Sci., 2013.

[156] A. K. Mukhopadhyay, Y. W. Mai, Grain size effects and abrasive wear mechanisms in alumina ceramic, Wear (1993) 258-268.

[157] H. Dogan, F. Findik, O, Morgul, Tribology properties of coated ASME 316L SS and comparison with a substrate, Ind. Lubric., Tribol 54 (2004) 5-10.

[158] K. Juhani, J. Pirso, M. Viljus, S. Letunovits, Two-body dry abrasive wear of Cr_3C_2-Ni cermets, Proc. Estonian Acad. Sci. Eng., 12 (2006) 368-376.

[159] C.C. Onuoha, G.J. Kipouros, Z.N. Farhat and K.P. Plucknett, Reciprocating wear behaviour of TiC-Steel based cermets, unpublished research, Dalhousie University Canada.

[160] Y. Guu, J.F. Lin, Analysis of wear behaviour of titanium carbonitride coatings, Wear, 210 (1997) 245-254.

[161] A. J. Gant, M.G. Gee, B. Roebuck, Rotating wheel abrasion of WC/Co hardmetals, Wear, 258 (2005) 178–188.

[162] Z. Guo, J. Xiong, M. Yang, C. Jiang, WC-TiC-Ni cemented carbide with enhanced properties, J. Alloy. Comp., 465 (2008) 157-162.

[163] Y. Chen, Y. Deng, H. Zhang, L. Wang, J. Ma, A novel and simple route to synthesis nanocrystalline titanium carbide via the reaction of titanium dioxide and different carbon source, Mater. Sci. Appl., 2 (2011) 1622-1626.

[164] G. Lee, B. K. Kim, Effect of raw material characteristics on the carbothermal reduction of titanium dioxide, Mater. Trans., 44 (2003) 2145-2150.

[165] J.R. Xie, X.L. Duan, G.Q. Shao, Z.L. Yi, Synthesis of precursor-derived TiC-Ni based nanocomposites by direct reduction and carburization processing, Rev. Adv. Mater. Sci. 5 (2003) 287-291.

[166] R.M. Abou Shabha, W.A. Ghannem, A. El-Sayed El-Shenawy, Corrosion and inhibition of Ti-6Al-4V alloy in NaCl solution, Int. J. Electrochem. Sci. 6 (2011) 5499-5509.

[167] A. Farid, S.J. Guo, F.E. Cui, P.Z. Feng and T. Lin, TiB_2 and TiC stainless steel matrix composites, Mater. Lett., 61 (2007) 189-191.

[168] K.J.A. Brookes, World directory and handbook of hard metals, sixth ed., International Carbide Data, London, 1996.

[169] U. Beste, T. Hasrtzell, H. Engvist, N. Axen, Surface damage on cemented carbide rock-drill buttons, Wear, 249 (2001) 324-329.

[170] W.J. Tomlinson, C.R. Linzell, Anodic polarization and corrosion of cemented carbides with cobalt and nickel binders, J. Mater. Sci., 23 (1988) 914-918.

[171] A.M. Human, I.T. Northrop, S.B. Luyckx, N.M. James, A comparison between cemented carbides containing cobalt- and nickel-based binders, J. Hard Mater., 2 (1991) 245-256.

[172] A.M. Human, H.E. Exner, The relationship between electrochemical behavior and in-service corrosion of WC based cemented carbides, Int. J. Refract. Metal. Hard Mater., 15 (1997) 65-71.

[173] D. Banerjee, G.K. Lal, G.S. Upadhyaya, Effect of binder-phase modification and Cr_3C_2 addition on properties of WC-10Co cemented carbide, J. Mater. Eng., 4 (1999) 563-572.

[174] W.J. Tomlinson, N.J. Ayerst, Anodic polarization and corrosion of WC-Co hard metals containing small amounts of Cr_3C_2 and/or VC, J. Mater. Sci., 24 (1989) 2348-2354.

[175] J. Kubarsepp, V. Kallast, Stainless hardmetals and their electrochemical corrosion resistance' Werkst. Korros., 45 (1994) 452-458.

[176] Y.J. Ren, C.L. Zeng, Corrosion protection of 304 stainless steel bipolar plates using TiC films produced by high-energy micro-arc alloying process, J. Power Source., 171 (2007) 778-782.

[177] C. Yi, H. Fan, J. Xiong, Z. Guo, G. Dong, W. Wan, H. Chen, Effect of WC content on the microstructures and corrosion behavior of Ti(C, N)-based cermets, Ceram. Int., 39 (2013) 503-509.

[178] A. Krell, D. Klaffke, Effects of grain size and humidity on fretting wear in fine-grained alumina, Al_2O_3/TiC, and zirconia, J. Am. Ceram. Soc., 79 (1996) 1139-1146.

[179] R. Stefac, F. Franz, A study of the pitting corrosion of cold-worked stainless steel, Corros. Sci., 18 (1978) 161-168.

[180] V.P Konoval, Corrosion resistance of titanium-chromium diboride and composite material based on it, Refract. Ind. Ceram., 51 (2011) 370-373.

[181] M.H. Ghandehari, Anodic behaviour of cemented WC-6% Co alloy in phosphoric acid solutions, J. Electrochem. Soc., 127 (1980) 2144-2147.

[182] J.C. Lin, J.Y Lin, S. P. Jou, Selective dissolution of the cobalt binder from carbide in acids containing additives, Hydrometallurgy, 43 (1996) 47-61.

[183] H. Kaesche, Metallic Corrosion, second Ed., National Association of Corrosion Engineers, Texas, 1985.

[184] A.V.C. Sobral, W. Ristow Jr, D.S. Azambuja, I. Costa, C.V. Franco, Potentiodynamic tests and electrochemical impedance spectroscopy of injection molded 316L steel in NaCl solution, Corros. Sci., 43 (2001) 1019-1030.

[185] D. Tomashov, The passivation of alloys on titanium bases, Electrochim. Acta, 19 (1974) 159-172.

[186] S. Yu, Corrosion resistance of titanium alloys, corrosion: Fundamentals, testing, and protection, Vol 13A, ASM Handbook, ASM International, (2003) 703-711.

[187] H.O. Pierson, Handbook of refractory carbides and nitrides: Properties, characteristics, processing and applications, first ed., Noyes Publications, New Jersey, 1996.

[188] P. Liu , L. Wei, S. Ye, H. Xu, Y. Chen, Protecting stainless steel by glass coating during slab reheating, Surf. Coat. Tech., 205 (2011) 3582-3587.

[189] F. Goutier, S. Valette, A. Vardelle, P. Lefort, Behaviour of alumina-coated 304L steel in a waste-to-energy plant, Surf. Coat. Tech., 205 (2011) 4425-4432.

[190] Q. Wu, W. Li, Y. Yin, Corrosion behaviour of TiC particle-reinforced 2Cr13 stainless steel, Steel Res. Int., 82 (2011) 719-727.

[191] Q.L. Wu, Y.S. Sun, F. Xue, J. Zhou, Microstructure, mechanical and wear properties of TiC particulate reinforced 2Cr13 steel by in situ reaction and electroslag remelting, Ironmak. Steelmak., 35 (2008) 387-395.

[192] K.P. Cooper, P.L. Slebodnick, K.E. Lucas, E.A. Hogan, Microstructural inhomogeneities and sea water corrosion in laser-deposited Ti-6Al-4V alloy matrix/carbide particulate composite surfaces, J. Mater. Sci., 33 (1998) 3805-3816.

[193] A.M. Human, B. Roebuck, H.E. Exner, Electrochemical polarization and corrosion behaviour of cobalt and Co (W, C) alloys in 1 N sulphuric acid, Mater. Sci. Eng., A 241 (1998) 202-210.

[194] E.J. Wentzel, C. Allen, The erosion-corrosion resistance of tungsten-carbide hard metals, Int. J. Refract. Met. Hard Mater., 15 (1997) 81-87.

[195] M.B. Holmes, A. Ibrahim, G.J. Kipouros, Z.N. Farhat, K.P. Plucknett, The effects of Ni_3Al binder content on the electrochemical response of TiC-Ni_3Al cermets, submitted to Mater. Corros.

[196] C.C. Onuoha, G.J. Kipouros, Z.N. Farhat, K.P. Plucknett, Corrosion behaviour of TiC- 304L cermets in synthetic saline solution, submitted to Corros. Sci., 2013.

[197] C. Monticelli, A. Frignani, F. Zucchi, Investigation on the corrosion process of carbon steel coated by HVOF WC/Co cermets in neutral solution, Corros. Sci., 46 (2004) 1225-1237.

[198] D. Toma W. Brandl, G. Marginean, Wear and corrosion behaviour of thermally sprayed cermet coatings, Surf. Coat. Technol., 138 (2001) 149–158.

[199] M. Rendón-Belmonte, J.T. Pérez-Quiroz, J. Terán-Guillén, J. Porcayo-Calderón, A. Torres-Acosta, G. Orozco-Gamboa, Evaluation of a Cr_3C_2(NiCr) coating deposited on S4400 by means of an HVOF process and used for flow plates of PEM fuel, Int. J. Electrochem. Sci., 7 (2012) 1079-1092.

[200] J.P. Kubarsepp, L.E. Valdma, Corrosion resistance of sintered TiC-steel alloys, Tallin Polytechnic Institute, translated from Poroshkovaya Metallurgiya. 208 (1980) 99-101.

[201] J. Joardar, S.W. Kim, S. Kang, Tribological evaluation of ultrafine Ti(CN) cermets, Mater. Manuf. Processes, 17 (2002) 567-576.

[202] C.-J. Li, Y.-Y. Wang, G.-J. Yang, A. Ohmori, K.A. Khor, Effect of solid carbide particle size of deposition behaviour, microstructure and wear performance of HVOF cermet coatings, Mater. Sci. Tech., 20 (2004) 1087-1096.

[203] F.J. Kellner, H. Hilderbrand, S. Virtanen, Effect of WC grain size on the corrosion behavior of WC–Co based hardmetals in alkaline solutions, Int. J. Refract. Met. Hard Mater., 27 (2009) 806-812.

[204] A.M. Ibrahim, Processing of Alumix 321 PM alloy and its corrosion behaviour in 3.5 wt. % saline solution, PhD Thesis, Dalhousie University, Canada, 2013.

[205] E. McCafferty, Validation of corrosion rates measured by the Tafel extrapolation method, Corrs. Sci., 47 (2005) 3202-3215.

[206] E. Poorqasemi, O. Abootalebi, M. Peikari, F. Haqdar, Investigating the accuracy of the Tafel extrapolation method in HCl solutions, Corrs. Sci. 51 (2009) 1043-1054.

[207] Z. Shi, M. Liu, A. Artrens, Measurement of the corrosion rate of magnesium alloys using Tafel extrapolation, Corros. Sci., 52 (2010) 579-588.

[208] F.V. Adams, A comparison of the corrosion behaviour of 444 ferritic and 316 austenitic stainless steels in acidic chloride media, Masters Dissertation, University of Witwatersrand, Johannesburg, 2009.

[209] G. Rocchini, S.P.A Enel, Corrosion rate monitoring with computerized systems. Werkstoffe und Korrosion., 46 (1995) 582-589.

[210] A. Trueman, D.P. Schweinsberg and G.A. Hope, A study of the effect of cobalt additions on the corrosion of tungsten carbide/carbon steel metal matrix composites', Corros. Sci., 41 (1999) 1377-1389.

[211] R.J.K Wood, Tribo-corrosion of coatings: A review J. Phys. D: Appl. Phys., 40 (2007), 5502-5521.

[212] J.E. Cho, S.Y. Hwang and K.Y Kim, Corrosion behaviour of thermal sprayed WC cermets coatings having various metallic binders in strong acidic environments, Surf. Coat. Technol., 200 (2006) 2653-2662.

[213] J.M. Perry, A. Neville and T. Hodgkiss, A comparison of the corrosion behavior of WC-Co-Cr and WC-Co HVOF thermally sprayed coatings by in situ atomic force microscopy (AFM), J. Thermal Spray Technol., 11 (2002) 536-541.

[214] H.S Isaacs, The localized breakdown and repair of passive surfaces during pitting', Corros. *Sci.*, 29 (1989) 313-323.

[215] R.D. Cowling and H.E. Hintermann, The corrosion of titanium carbide', J. Electrochem. Soc.: Electrochem. Tech., 117 (1970) 1447-1449.

[216] X. Wei, R.C. Viadero Jr. and K.M. Buzby, Recovery of iron and aluminium from acid mine drainage by selective precipitation', Environ. Eng. Sci., 22 (2005) 745-755.

[217] V.A.D Souza and A. Neville, Linking electrochemical corrosion behaviour and corrosion mechanisms of thermal spray cermets coatings (WC-CrNi and WC/CrC-CoCr), Mater. Sci. Eng. *A*, 352 (2003) 202-211.

Appendix A: Materials Characterisation

The following section presents powder and sample characterization results not examined in the previous chapters. Each powder used was analyzed using SEM, XRD and energy-dispersive x-ray spectroscopy (EDS) to ensure accuracy to within the manufacturer's specifications for particle size, crystallographic structure, as well as chemical composition. Figure 10.1 shows the XRD trace for TiC powder and associated peaks from the TiC powder diffraction file, or PDF (#03-065-8416) confirming the same chemical composition provided by the manufacturers. As it can be seen TiC powder showed no unexpected peaks and aligns very well with the PDF in the ICCD database. These results show excellent agreement with the ICCD database confirming that the TiC powder received from Pacific Particulate Materials is of correct crystalline compositions. The density of all the studied cermets is shown in Figure 10.2, as can be seen, the medium-grained cermets (TiC-304L, TiC-316L, TiC-410L cermets) have sintered densities in excess of 99% of theorrtical confirming that mrlt infiltration allows for the formation of high density cermets, even at low steel binder content. However, coarse-grained cermets (Figure 10.2b) have a slightly lower density than fine-grained cermets. The reason for this could probably related to preferential vaporisation and / or pore coarsening associated with sintering at longer times. The XRD of as-sintered TiC-304L cermets is shown in Figure 10.3. As can be seen, all the major peaks are from TiC. In order to calculate the mean grain size of all the studied cermets, linear intercept method is used and presented in a Histogram as shown in Figure 10.4. The mean grain size and sintering conditions of all the studied cermets are presented in Table 10.1 for clarity. In order to gain insight in the changes in the chemical compostion of the steel binder after infiltration, EDS analysis was carried out on the 316L stainless steel starting powder, 316L stainless steel in the infiltrated cermet and TiC in the infiltrated cermet and presented in Table 10.2. As can be seen, there is slight drop in the composition of steel binder (Fe, Cr, Ni and Mo contents) after infiltration. Also it can be seen that carbon content increased after infiltration suggesting that there could be diffusion of carbon from TiC to the steel.

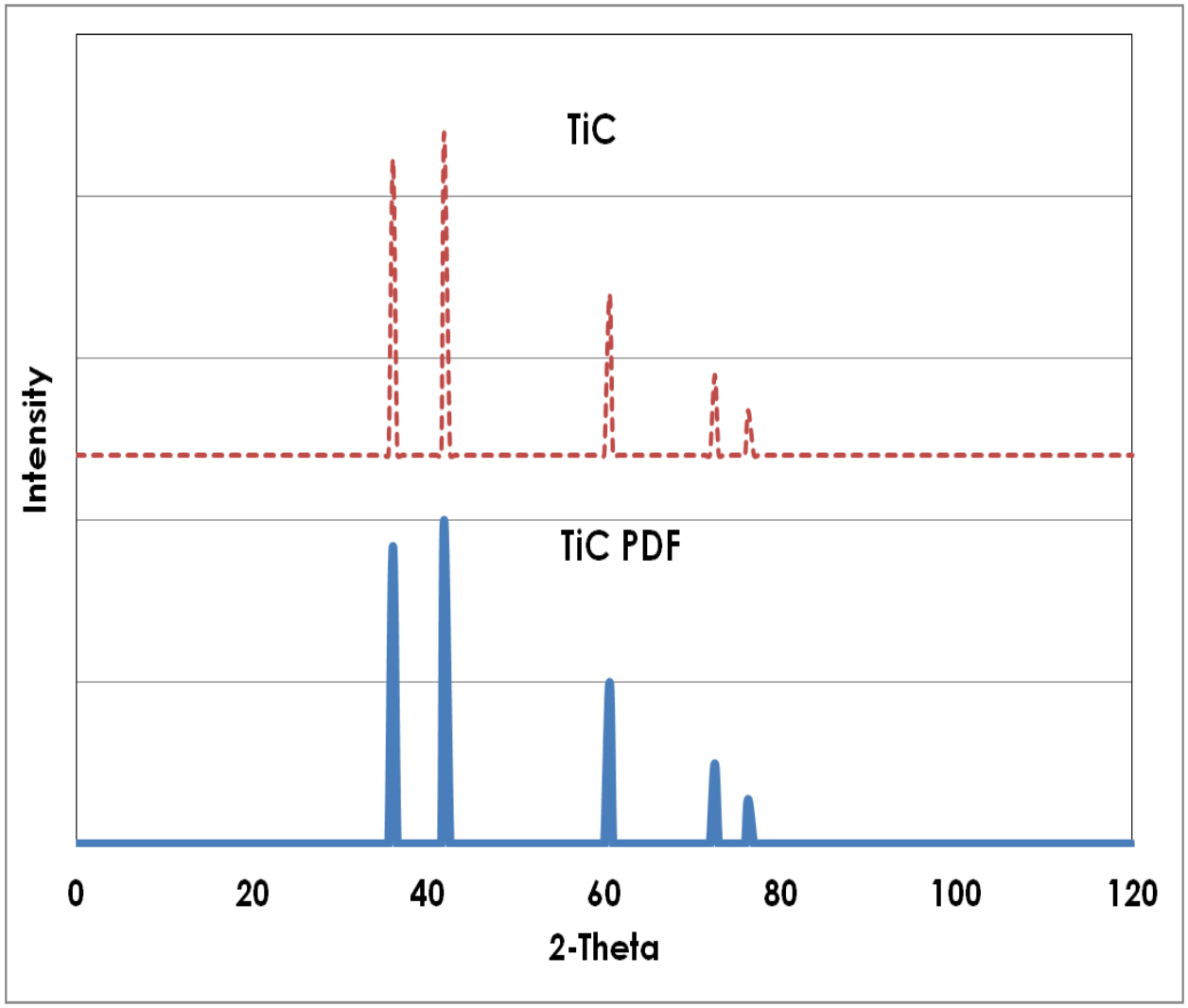

Figure 10.1: XRD trace and PDF Peaks

(a)

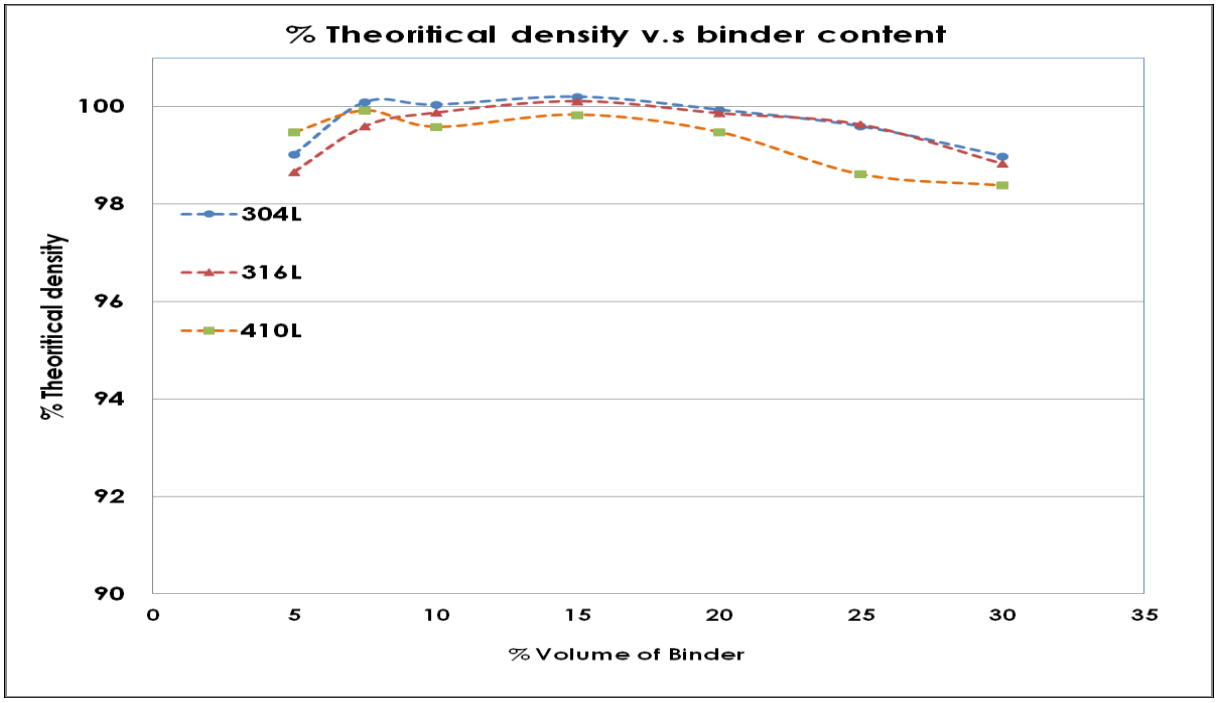

(b)

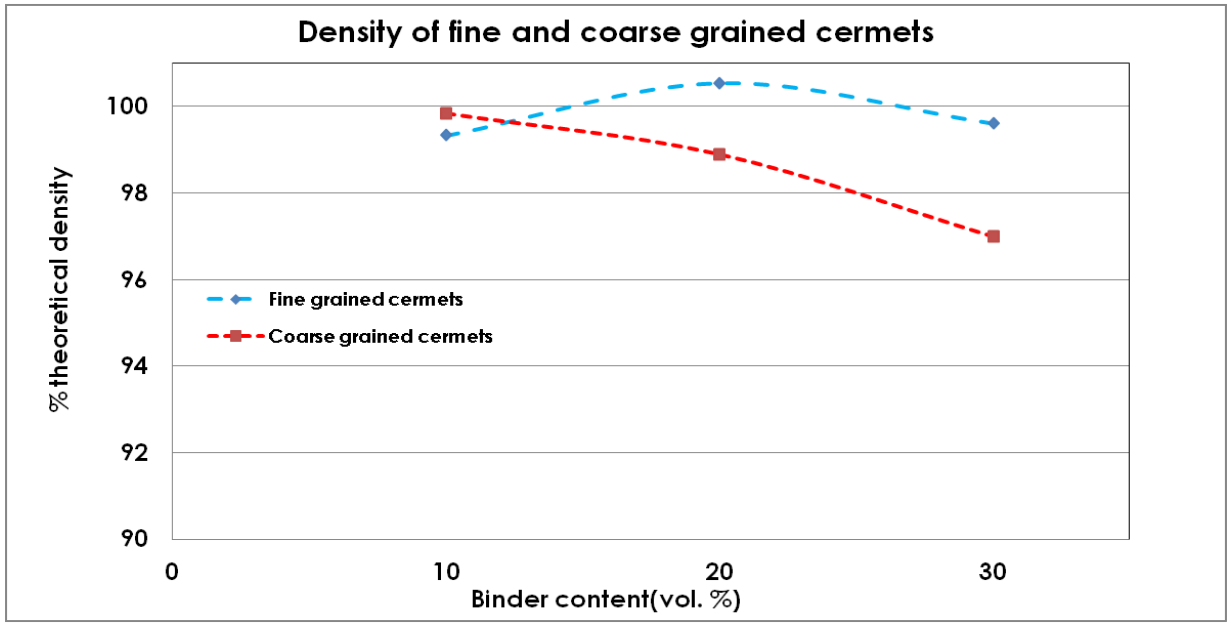

Figure 10.2: Infiltrated density of cermets (% TD) (a) Regular TiC-steel cermets, (b) Fine and coarse grained TiC-316L cermets. All the cermets had sintered densities in excess of 97% of theoretical confirming that melt infiltration allows for the formation of high density cermets, even when low steel contents are used (i.e. 5 vol. %).

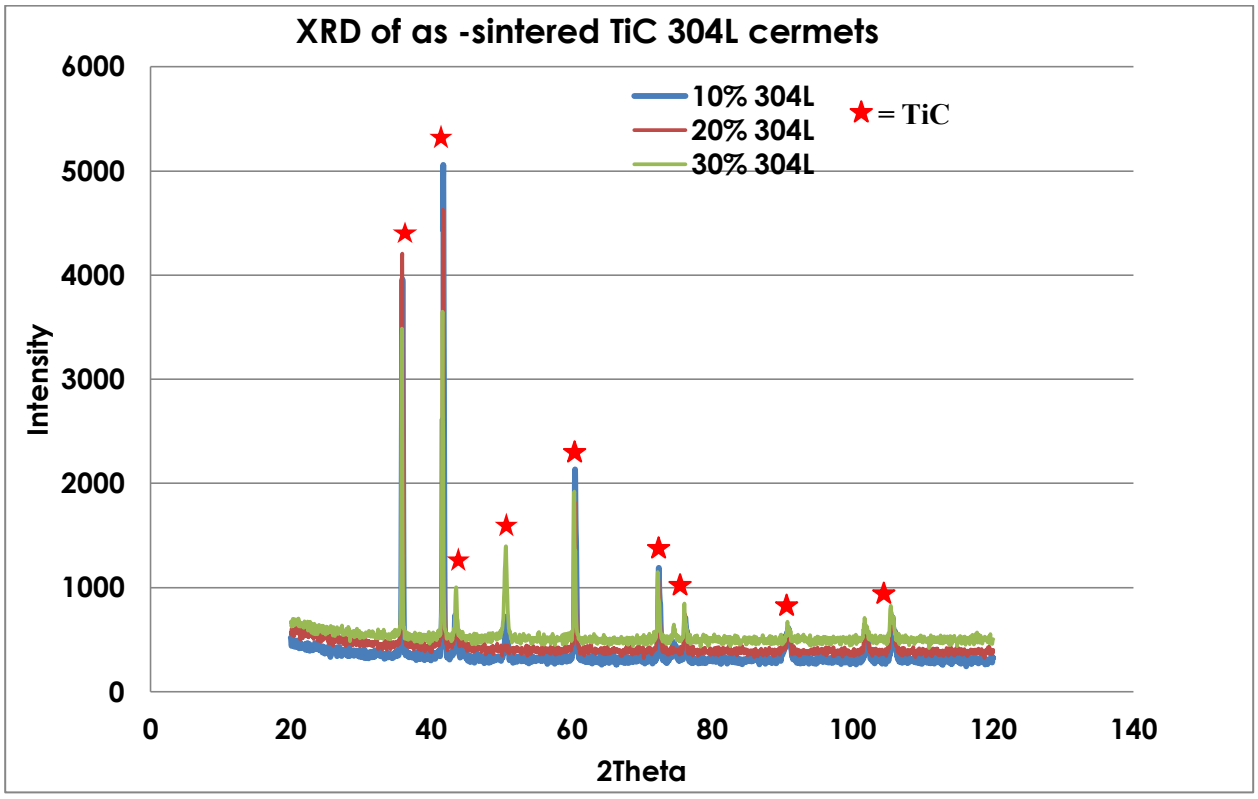

Figure 10.3: XRD of as-sintered TiC-304L cermets. All the major peaks are TiC and the observation is consistent with other cermets.

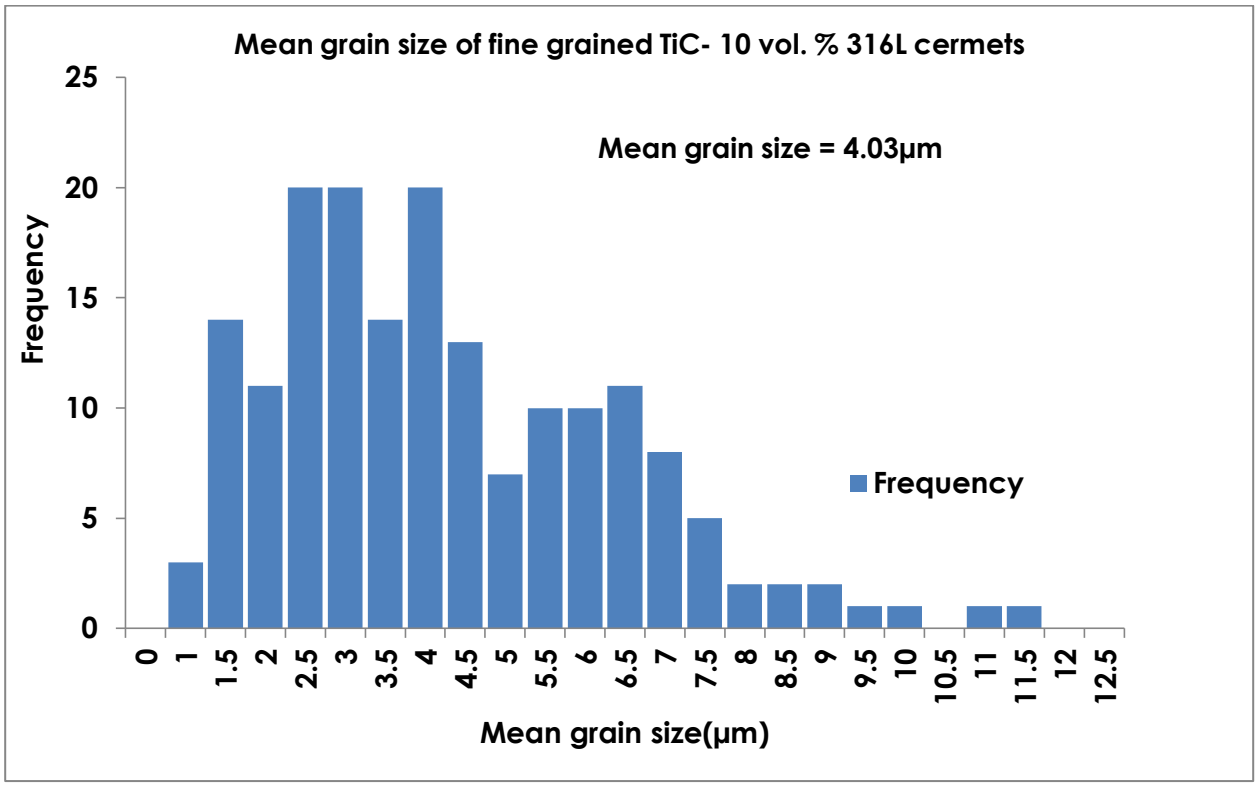

Figure 10.4: A representative histogram of fine grained TiC –10 vol. % 316L cermets used for the determination mean grain sizes of all the studied cermets.

Table 10.1: Mean grain size and sintering conditions of all the studied cermets.

Cermets	Mean grain size(μm)	Sintering conditions
TiC + 10 vol.% 304L	6.80	1500°C/60 minutes
TiC + 20 vol.% 304L	6.25	1500°C/60 minutes
TiC + 30 vol.% 304L	6.45	1500°C/60 minutes
TiC + 10 vol.% 316L	6.48	1500°C/60 minutes
TiC + 20 vol.% 316L	5.38	1500°C/60 minutes
TiC + 30 vol.% 316L	6.03	1500°C/60 minutes
TiC + 10 vol.% 410L	6.25	1550°C/60 minutes
TiC + 20 vol.% 410L	6.09	1550°C/60 minutes
TiC + 30 vol.% 410L	6.68	1550°C/60 minutes
TiC + 10 vol.% 316L(fine)	4.03	1475°C/15 minutes
TiC + 20 vol.% 316L (fine)	3.57	1475°C/15 minutes
TiC + 30 vol.% 316L (fine)	3.63	1475°C/15 minutes
TiC + 10 vol.% 316L (coarse)	10.87	1550°C/240 minutes
TiC + 20 vol.% 316L (coarse)	10.47	1550°C/240 minutes
TiC + 30 vol.% 316L (coarse)	10.40	1550°C/240 minutes

Table 10.2: EDS chemical composition analysis (wt %) of infiltrated TiC-316L cermet with 30 vol. % steel binder content and the 316L starting powder.

Element	316L powder	Steel in infiltrated TiC-30 vol. % 316L	TiC in infiltrated TiC-30 vol. % 316L
C	1.47	2.78	21.88
Cr	14.37	11.95	0.72
Fe	61.25	65.31	1.2
Ni	20.20	16.32	0
Mo	2.04	0.15	0.235
Ti		3.35	75.93

Appendix B: Electrochemical Data

The following section presents results of electrochemical experiments that are not examined in Chapters 6 and 8. In Chapter 7, potentiostatic polarization (held at 1.5V) was performed at the pseudo-passive region of the fine and coarse grained cermets to confirm the tendency of pseudo-passivity on the cermets (TiC-304L cermets) but not examined in other regular cermets (TiC-410L and TiC-316L cermets). The results of the other cermets are presented in this section.

The higher presence of oxygen (shown in Table 10.3) observed for cermets with 10 vol. % 304L steel content shows greater amounts of oxides responsible for the lower current in the passivation range, hence indicating adherence of the film for corrosion protection. The drop in current with time confirmed that the cermets achieved some passivation but the presence of greater oxygen at lower binder content confirms that TiO_2 could be responsible for corrosion protection (EDS analysis shown in Table 10.3). The high current density in the pseudo-passive region confirms that pseudo-passivity could be exhibiting in these cermets. This observation is consistent with other studied cermets that are not presented here (TiC-316L and TiC-410L cermets). By using SEM analysis (Figures 10.6 and 10.7), EDS analysis (Figure 10.8 and Table 10.3), it is clear that TiC-304L cermets with 10 vol percent of binder has better corrosion resistance and higher oxide content with is believed to be TiO_2.

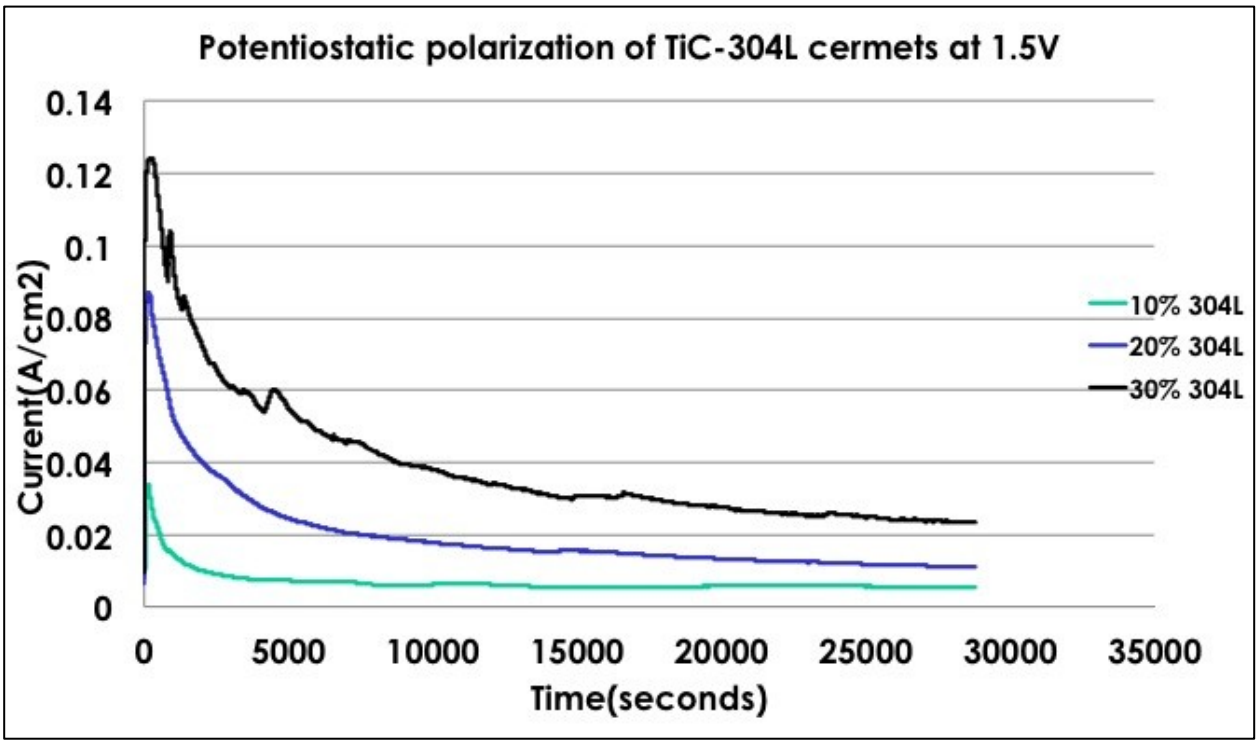

Figure 10.5: Representative potentiodynamic polarisation curves for TiC-304L cermets at 1.5V.

(a)

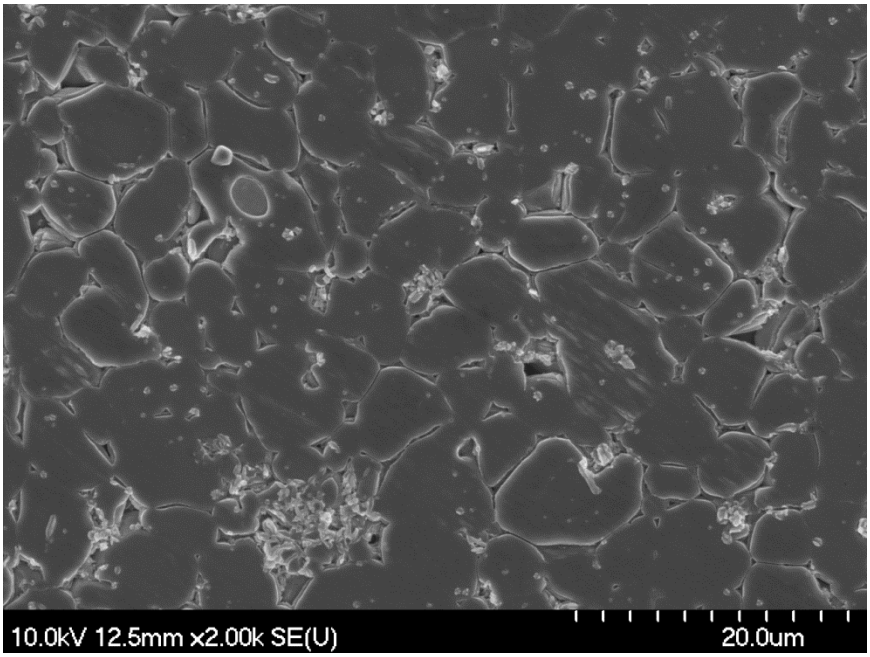

(b)

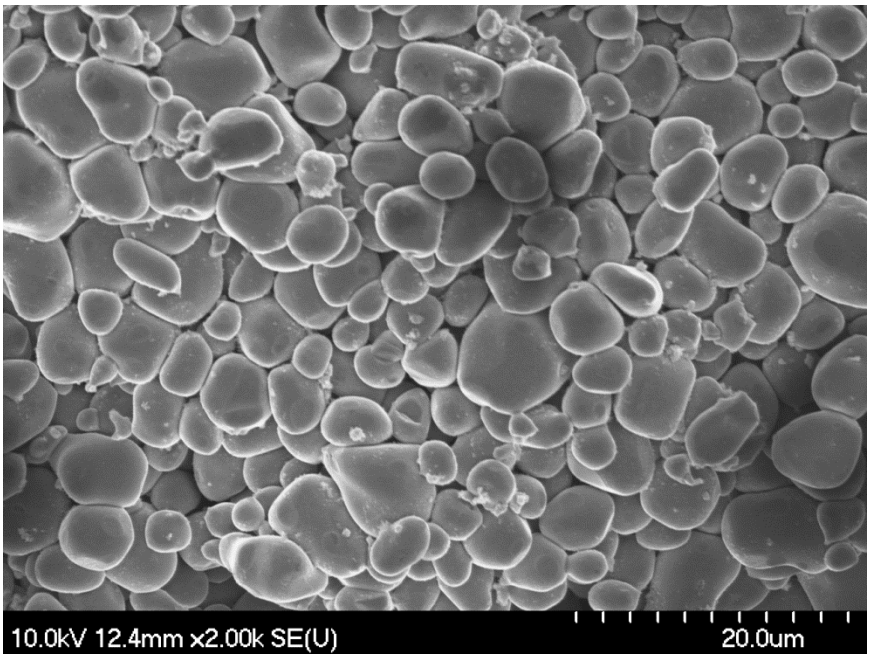

Figure 10.6: SEM of TiC-304L cermets following potentiostatic polarization at 1.5V(a) TiC-10 vol. % 304L (b) TiC-30 vol. % 304L cermets. The less corrosion attack on TiC-10 vol. % 304L cermets is evident and also confirming the lowest current in the passivation region as shown in Figure 10.5.

(a)

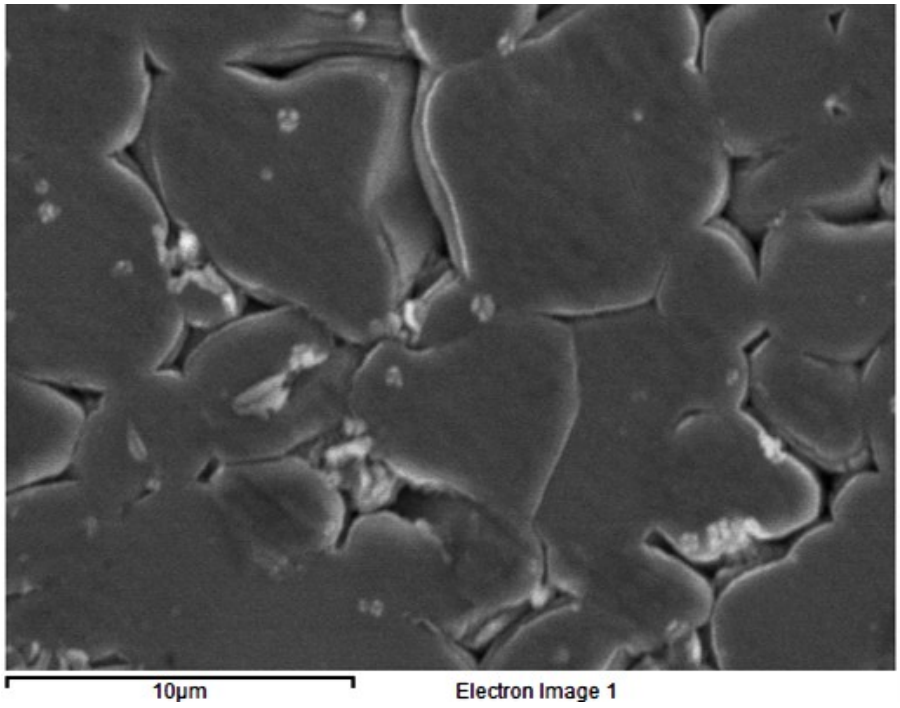

(b)

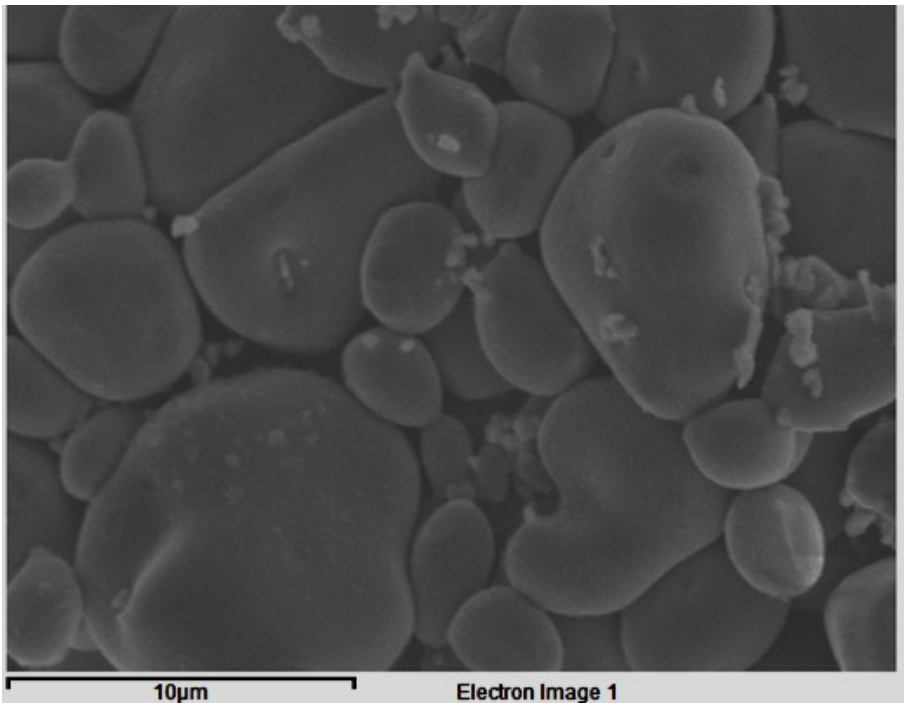

Figure 10.7: SEM image of TiC-304L cermets following potentiostatic polarization at 1.5V. (a) TiC-10 vol. % 304L cermets, (b) TiC-30 vol. % 304L cermets.

(a)

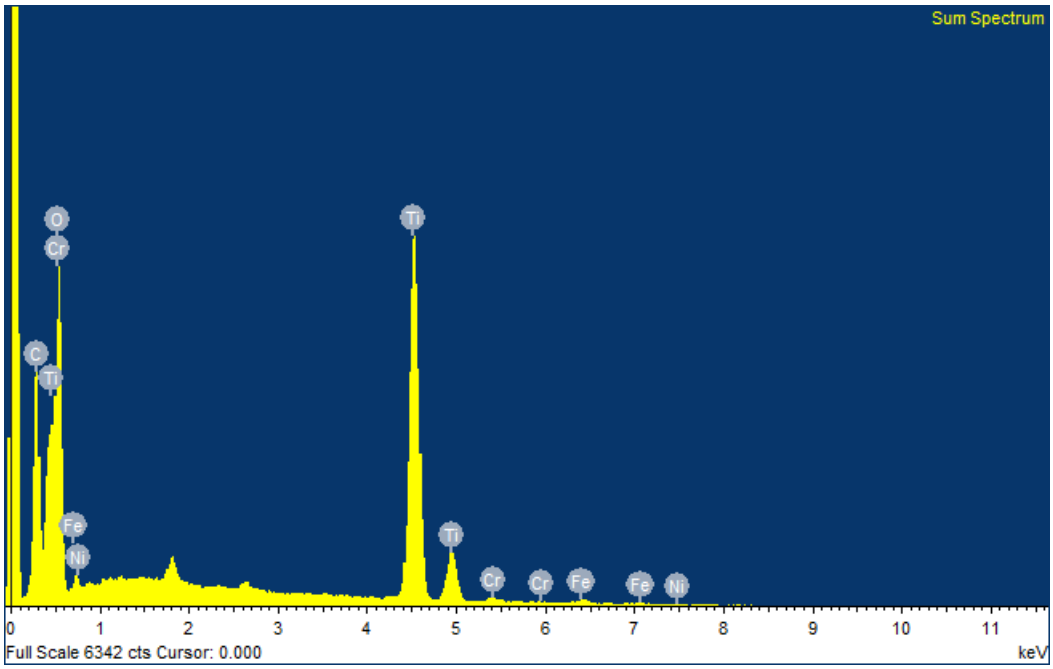

(b)

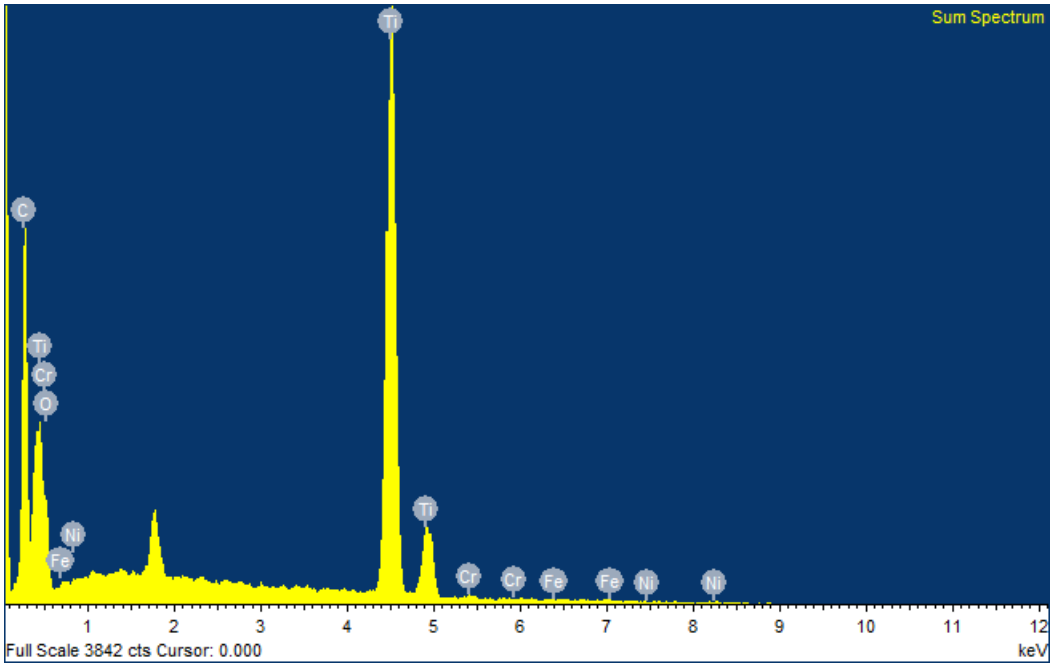

Figure 10.8: EDX spectral analysis of TiC-304L cermets (analysis taken from images of Figure 10.7). (a) TiC-10 vol. % 304L (b) TiC-30 vol. % 304L cermets.

Table 10.3: EDS chemical composition analysis (wt %) of TiC-304L cermets (cermets with 10 and 30 vol. % 304L steel binder) following potentiostatic (analysis taken from images of Figure 10.7). Evidence of higher amount of oxygen at lower binder (TiC- 10 vol. % 304L cermet) content is apparent leading to lowest passivation current density as shown in Figure 10.5.

Element	TiC-10 vol.% 304L	TiC-30 vol.% 304L
C	10.86	15.69
O	28.80	6.07
Ti	56.56	78.55
Cr	1.13	0.68
Fe	2.38	0.33

Appendix C: Reciprocating Wear Data

The following section presents results of hardness, indentation fracture resistance (IFR), and the reciprocating wear of TiC-316L and TiC-410L cermets that are not covered in Chapters 4 and 5. The hardness and IFR (determined using Anstis method as explained in Chapters 4 and 5) of TiC-316L and TiC-410L cermets are shown in Figure 10.9. As can be seen, hardness decreases with increase in steel binder content while IFR increases confirming that the hardness of the cermet is dependent on TiC content while the fracture toughness is dependent on the steel binder content. The COF increases with steel binder content (Figur 10.10) and a slight drop observed at 60N load for both TiC-316L and TiC-410L cermets with 10 steel binder content could depict change in wear mechanism from the initial two-body to three-body wear. The volumetric wear loss (Figure 10.11) increases with load and time as predicted by Lancaster (Details in Chapters 4 and 5) whereas the specific wear rate (Figure 10.12) increases with steel binder content and load. This shows that wear resistance of these cermets is dependent on the TiC content and decreases with load as confirmed by optical profilometry analysis (Figure 10.13). The Microstructural analysis of the wear tracks using SEM and EDS analysis show evidence of ploughing and pushing of materials at the ends of the wear tracks, formation of tribolayer, and mutual transfer of materials from the WC-CO counter face sphere to the cermets (Figures 10.14, 10.15, 10.16 and 10.19 and Table 10.4). All these point to two- to three-body abrasive and adhesive wear mechanism operating in these cermets. The transition from the morphology of the wear debris at lower load (60N as shown in Figure 10.17) and at higher load (80N as shown in Figure 10.18) shows the change of wear mechanism at different loads.

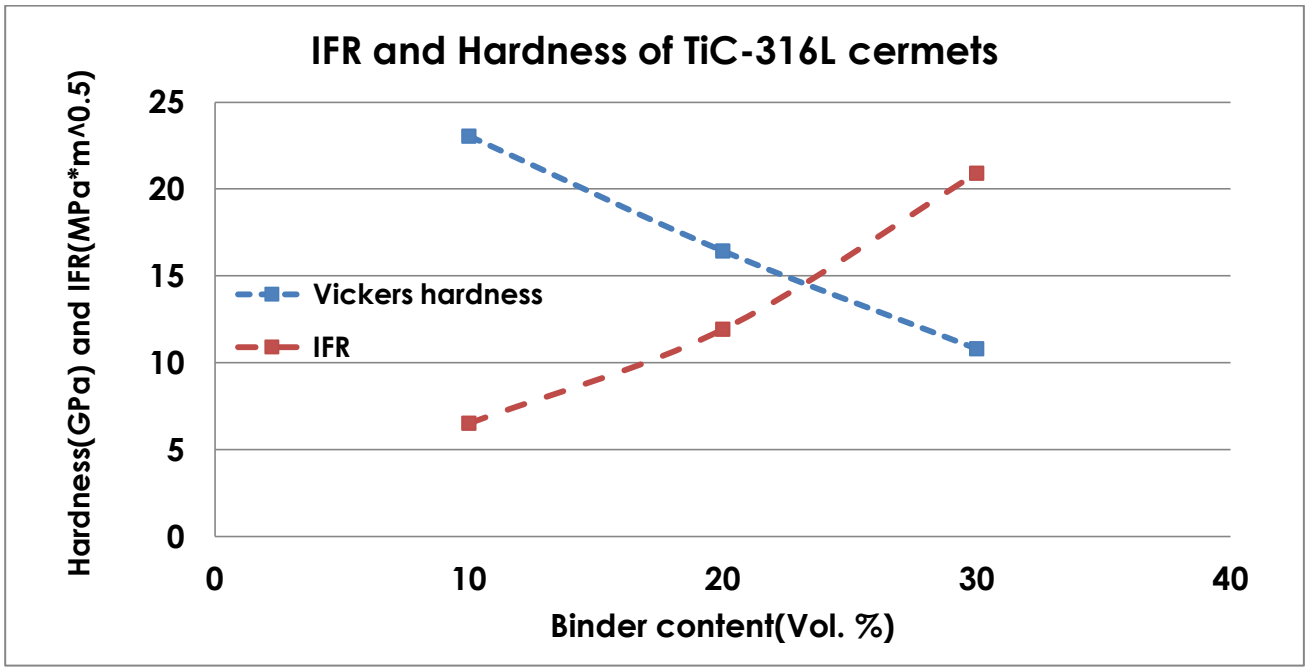

(a) TiC-316L cermets

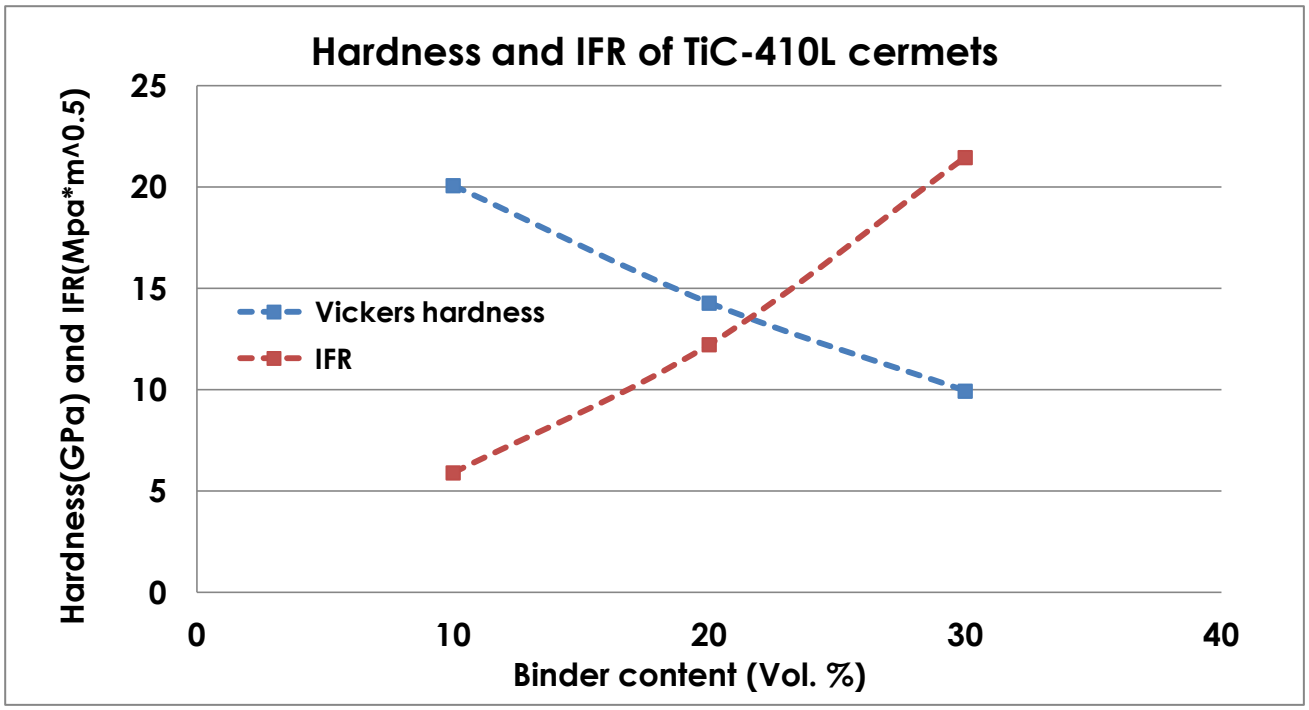

(b) TiC-410L cermets

Figure 10.9: The hardness (measured with a 1 kg load) and indentation fracture resistance (measured with a 50 kg load using Anstis equation) as a function of steel binder content. (a) TiC-316L cermets, (b) TiC-410L cermets. It is apparent that for the two cermets, hardness is dependent on TiC content while indentation fracture resistance is dependent on the steel binder content.

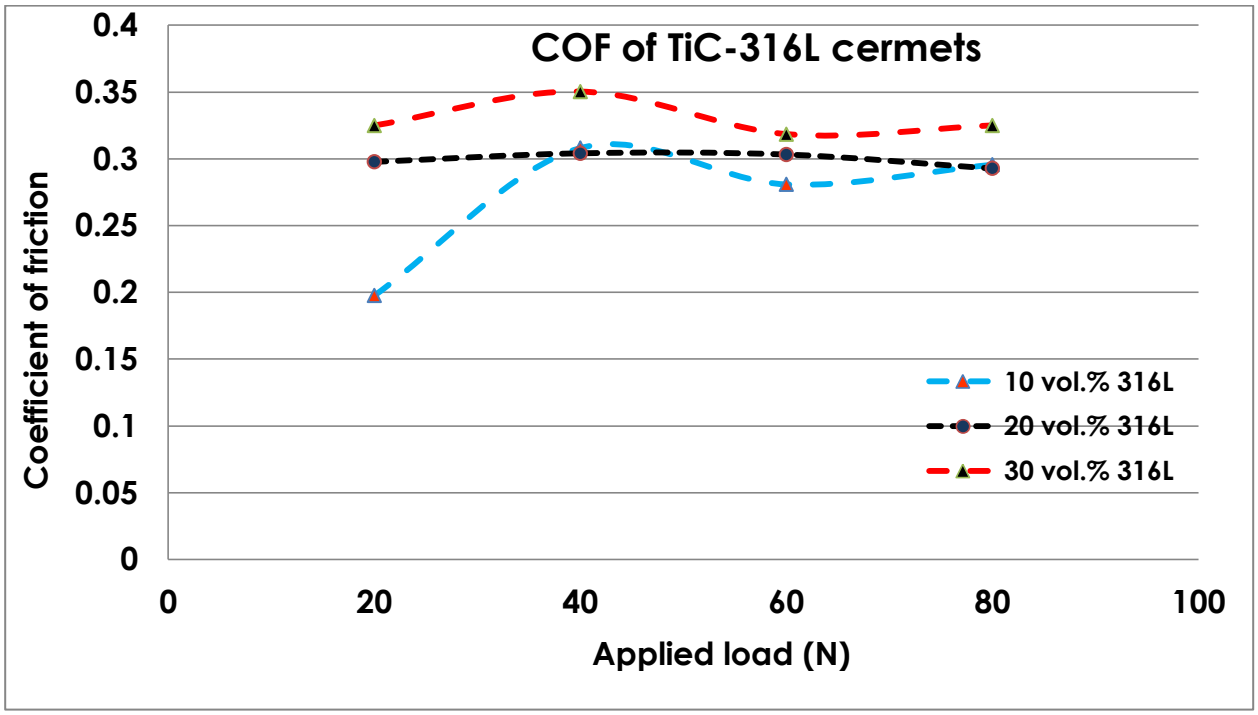

(a) TiC-316L cermets

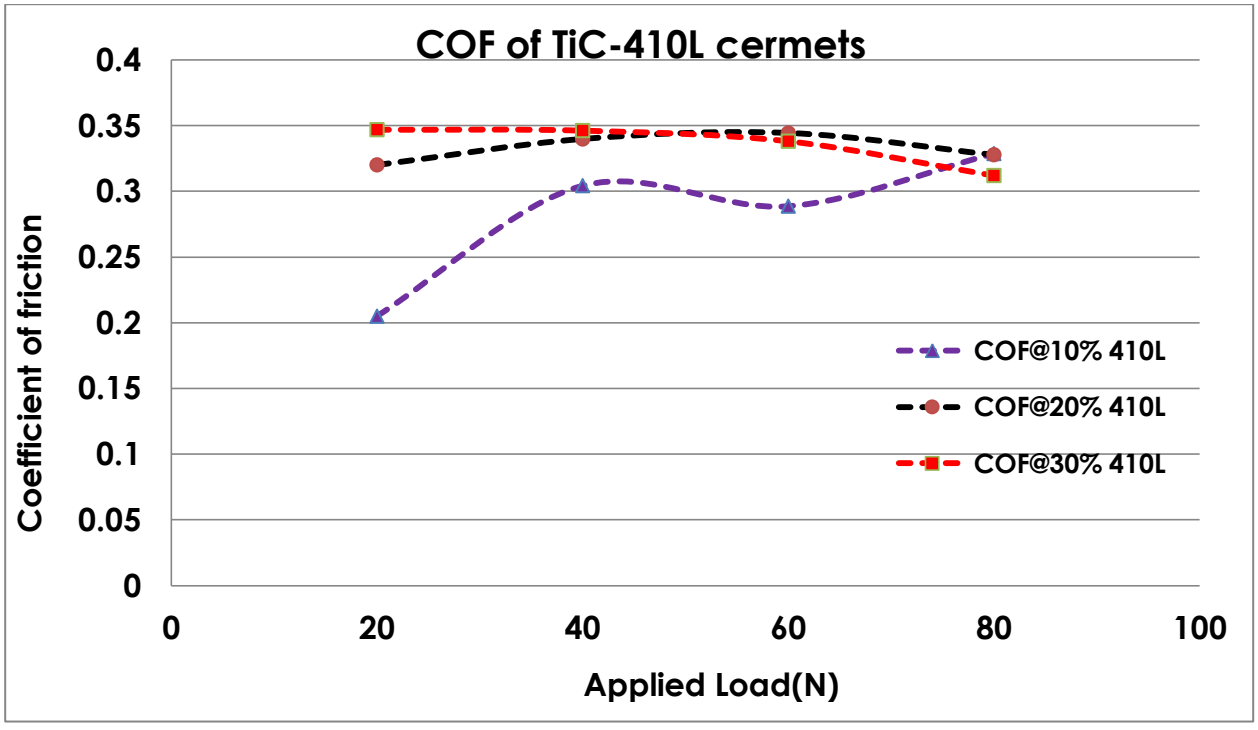

Figure 10.10: The effect of applied load on the COF after 120 minutes of dry sliding, as a function of steel binder content. (a) TiC-316L cermets, (b) TiC-410L cermets. It is apparent that COF increases with binder content.

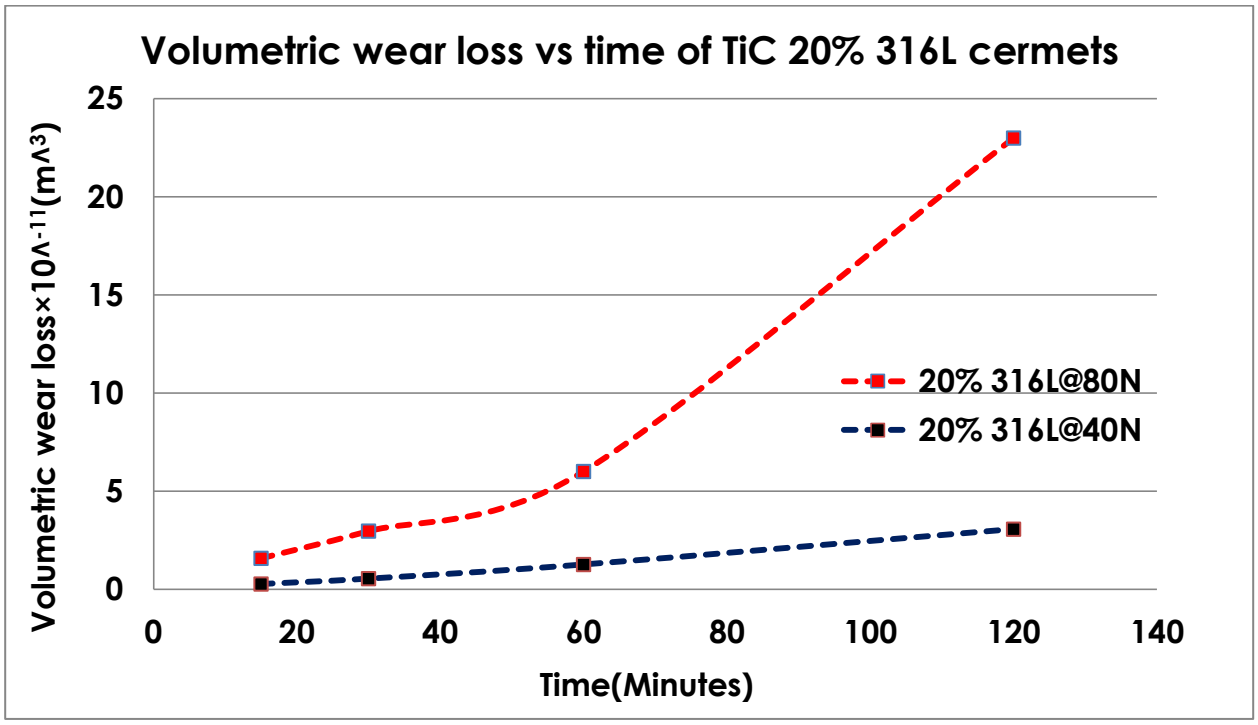

(a) TiC-316L cermets

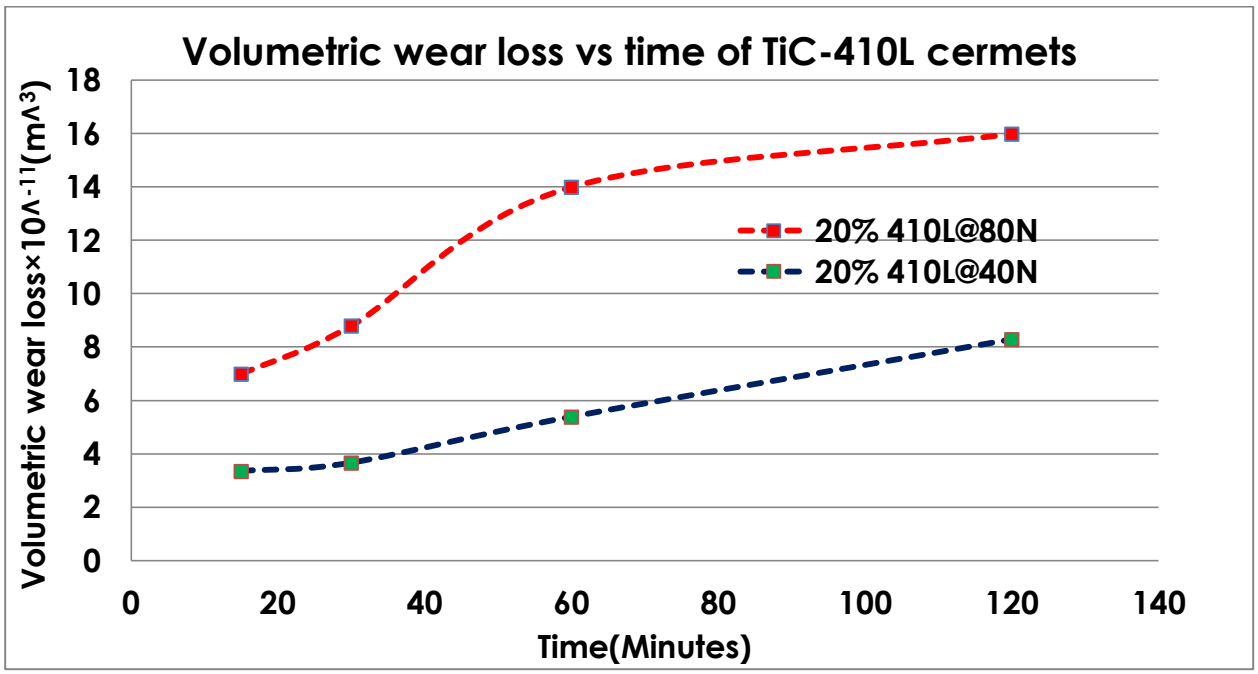

(b) TiC-410L cermets

Figure 10.11: The volumetric wear loss as a function of applied load and dry sliding time. (a) TiC prepared with 20 vol. % 316L binder, (b) TiC prepared with 20 vol. % 410L binder. It can be seen that volumetric wear loss increases with time.

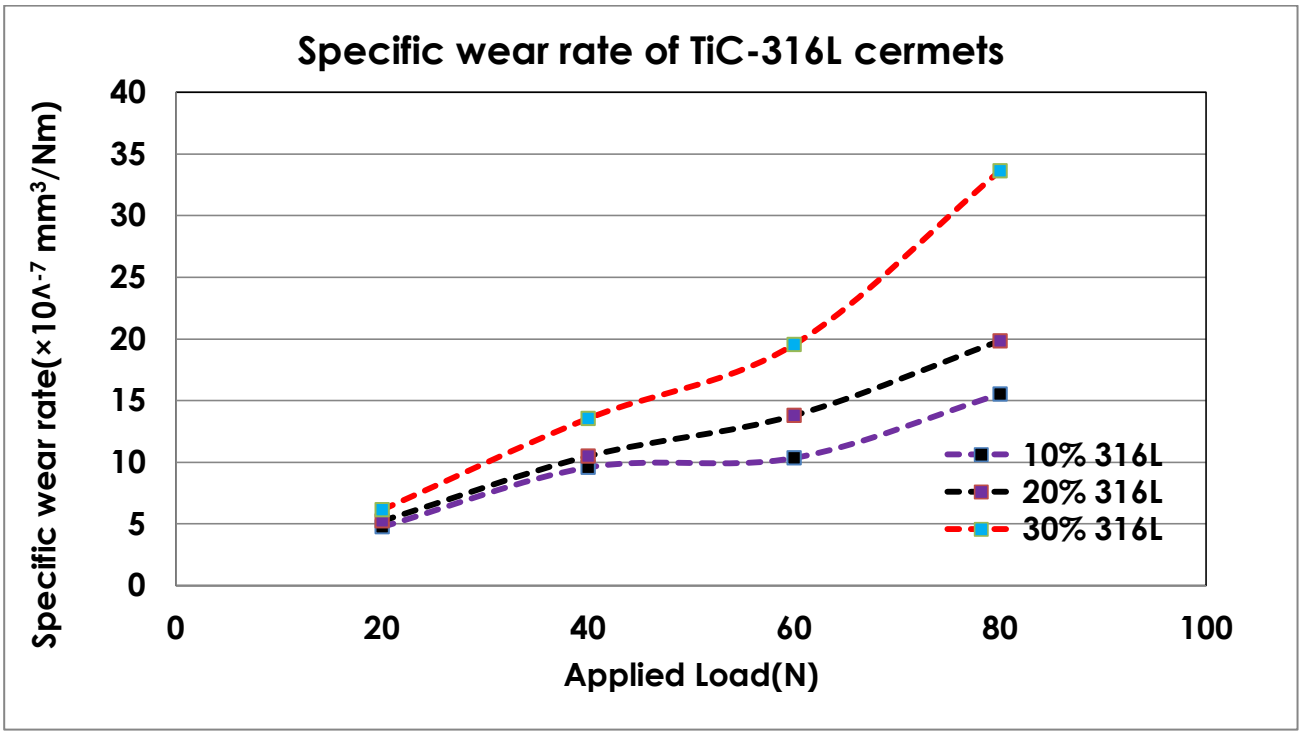

(a) TiC-316L cermets

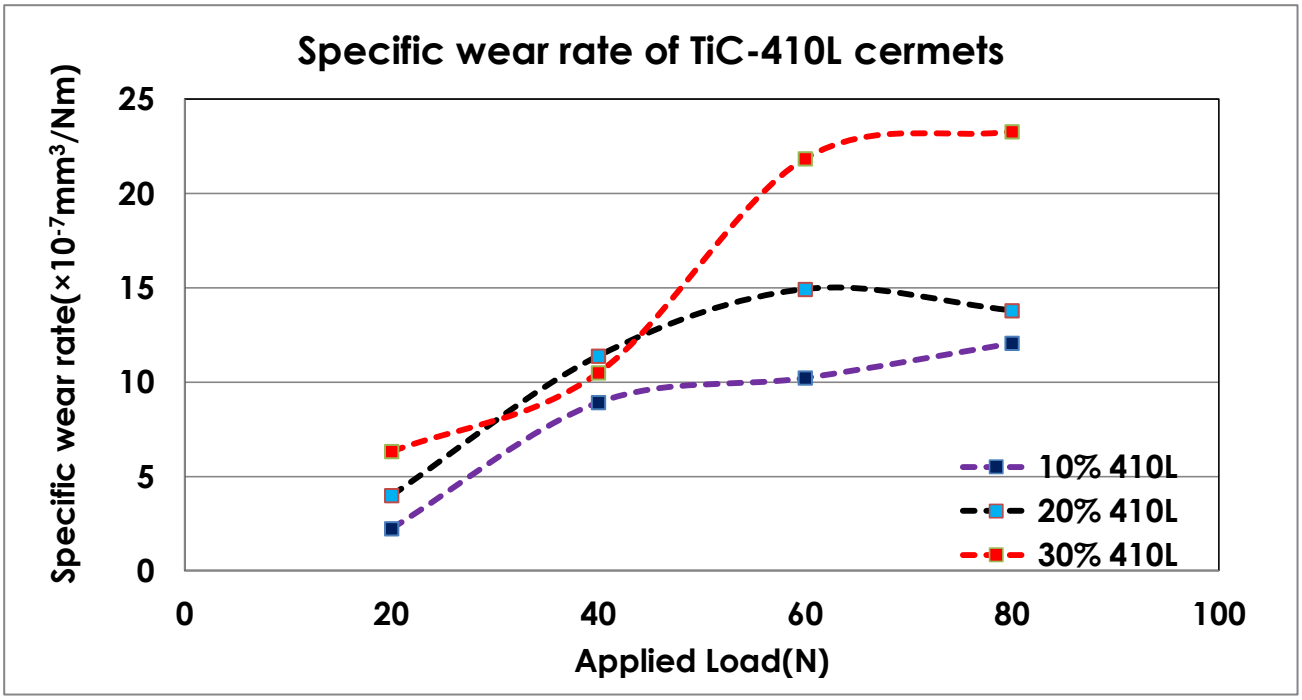

(b) **TiC-410L cermets**

Figure 10.12: The specific wear rate as a function of applied load. (a) TiC-316L cermets, (b) TiC-410L cermets. The specific wear rate increases with load and binder content.

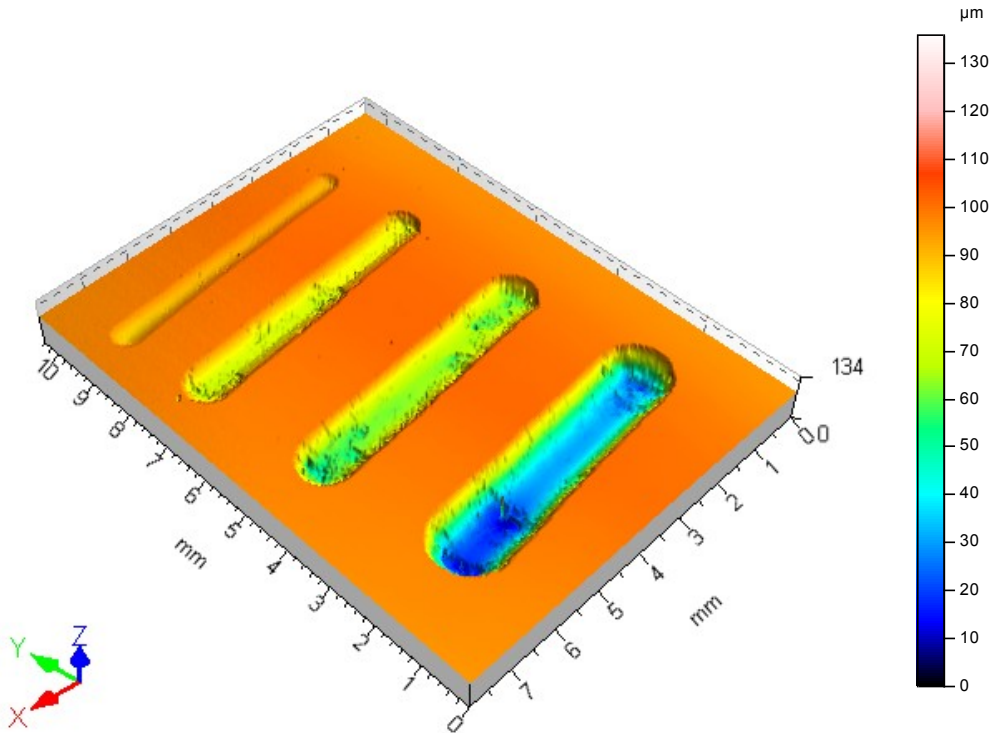

(a)

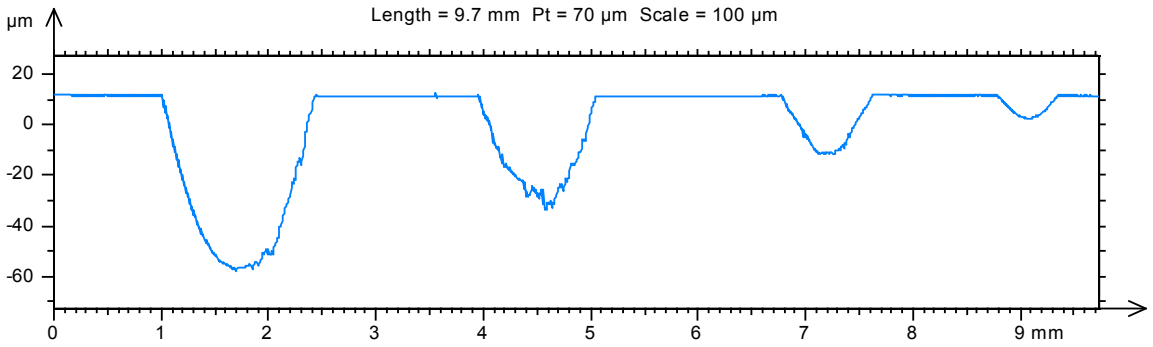

(b)

Figure 10.13: An optical profilometry images showing wear tracks of TiC- 20 vol. % 316L cermets at different loads. (From left to right, 20 to 80N load). (a) Optical profilometer images (b) Wear track profile of (a). It is evident that wear resistance increases with decrease in load judging from the depth of the wear track. This observation is consistent with all the studied cermets.

(a) (b)

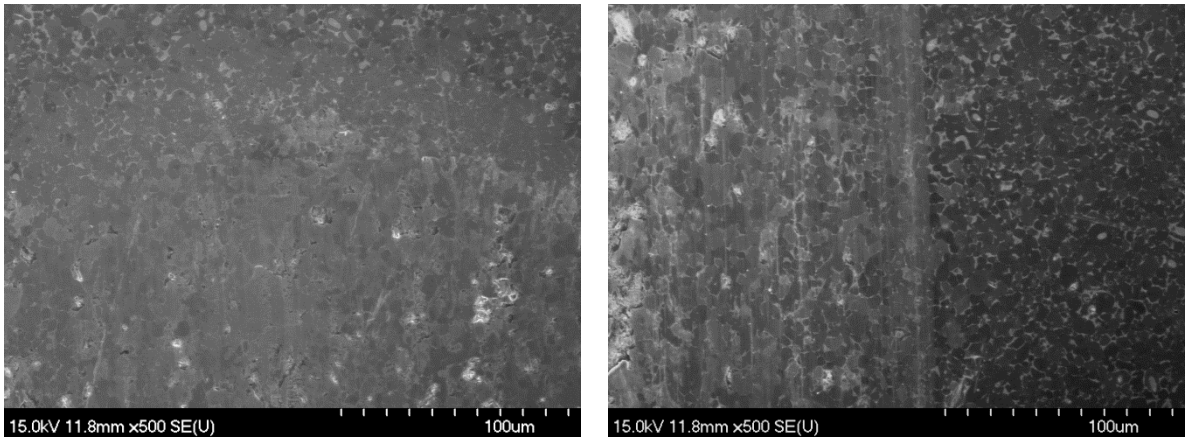

(c) (d)

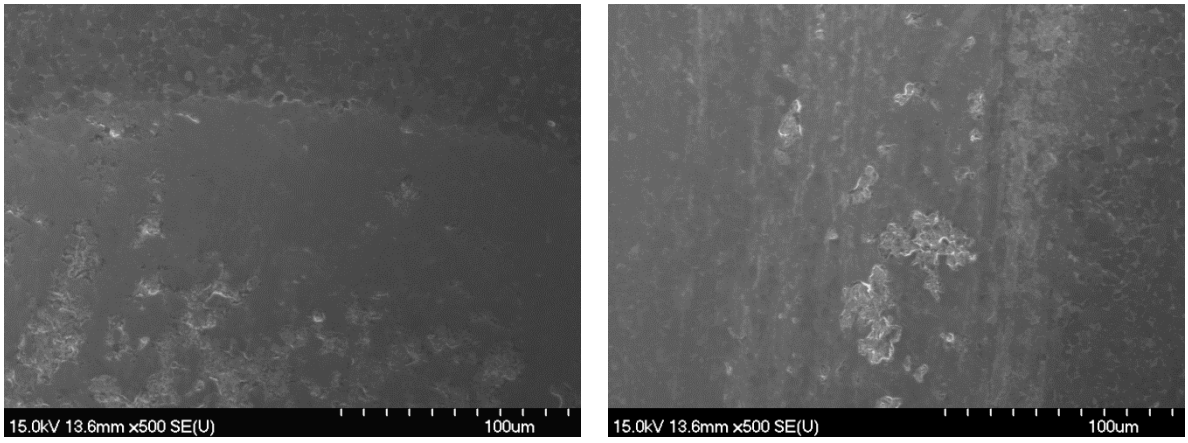

Figure 10.14: SEM images of the wear track formed on TiC- 10 vol. % 316L after testing using 20N and 80 load for 2 hours duration.(total sliding distance ~1.45Km); sliding direction is vertical for all images. (a, b) 10 vol. % 316L of at 20N load showing initial formation of tribolayer and build of material at the end and edge of the wear track, (c, d) 10 vol. % 316L at 80N load depicting increase in build-up of tribolayer and spallation with increase in load.

(a) (b)

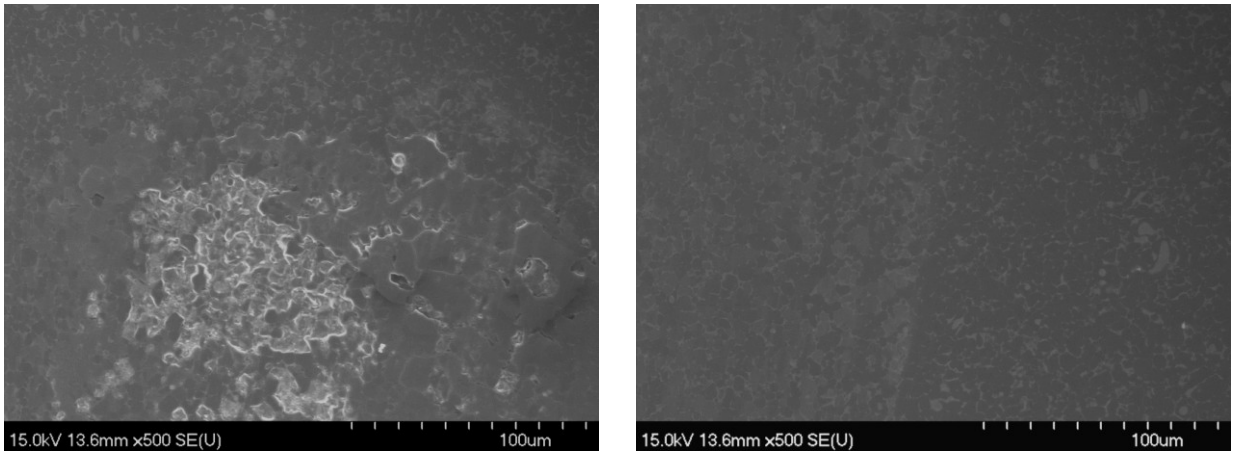

(c) (d)

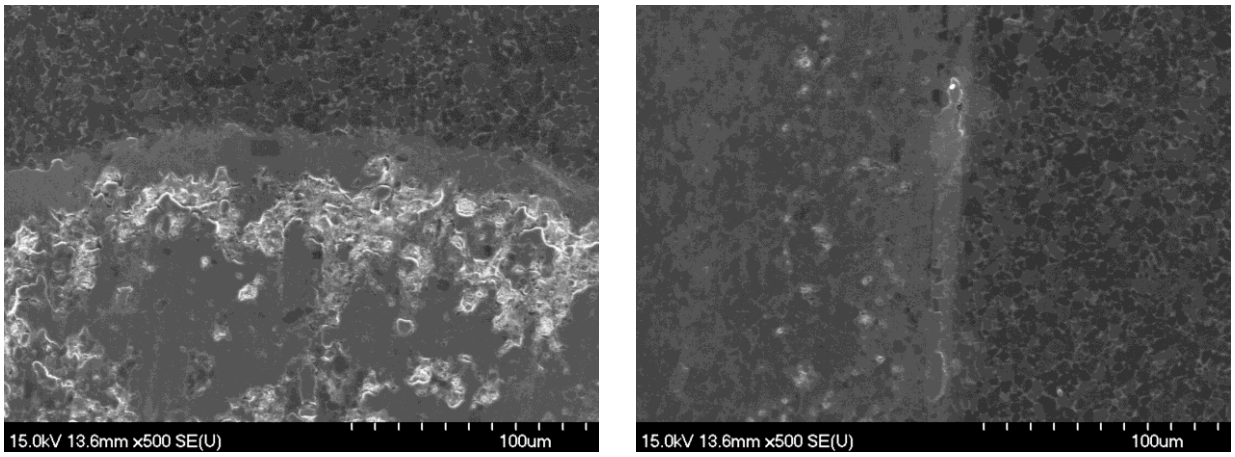

Figure 10.15: SEM images of the wear track formed on TiC- 10 vol. % 410L after testing using 20N and 80 load for 2 hours duration.(total sliding distance ~1.45Km); sliding direction is vertical for all images. (a, b) 10 vol. % 410L of at 20N load showing initial formation of tribolayer and build of material at the end and edge of the wear track, (c, d) 10 vol. % 410L at 80N load depicting increase in build-up of tribolayer and spallation with increase in load.

(a)

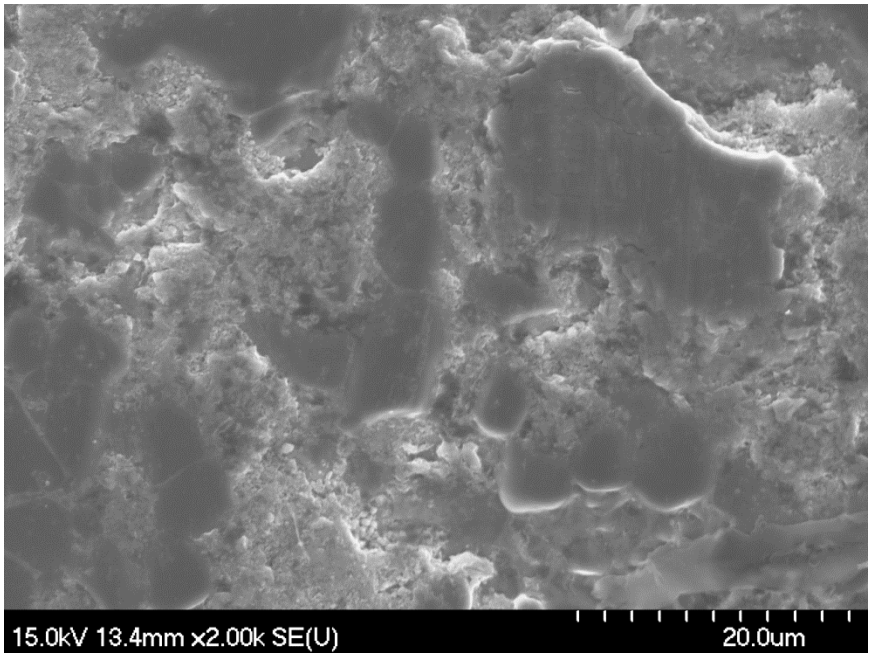

(b)

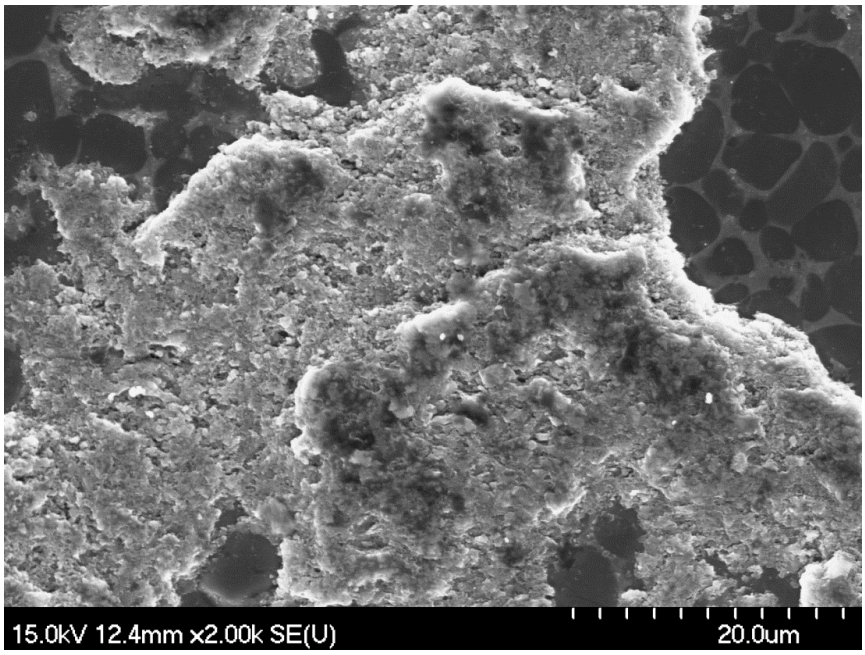

Figure 10.16: SEM images showing a typical tribolayer that is generated at higher load after testing using 80N load for 2 hours duration.(total sliding distance ~1.45Km); sliding direction is vertical for all images. (a) 20 vol. % 316L (b) 20 vol. % 410L.

(a)

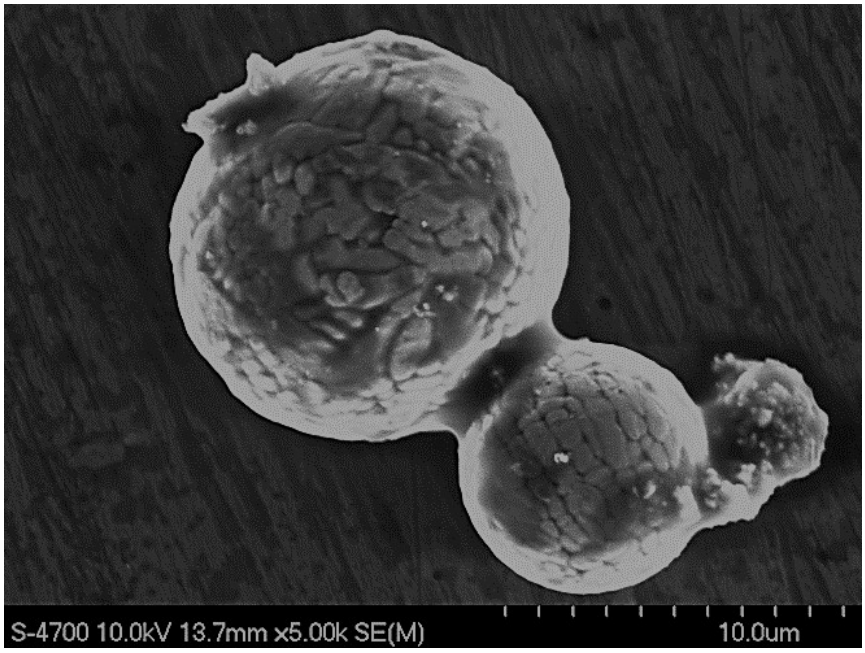

(b)

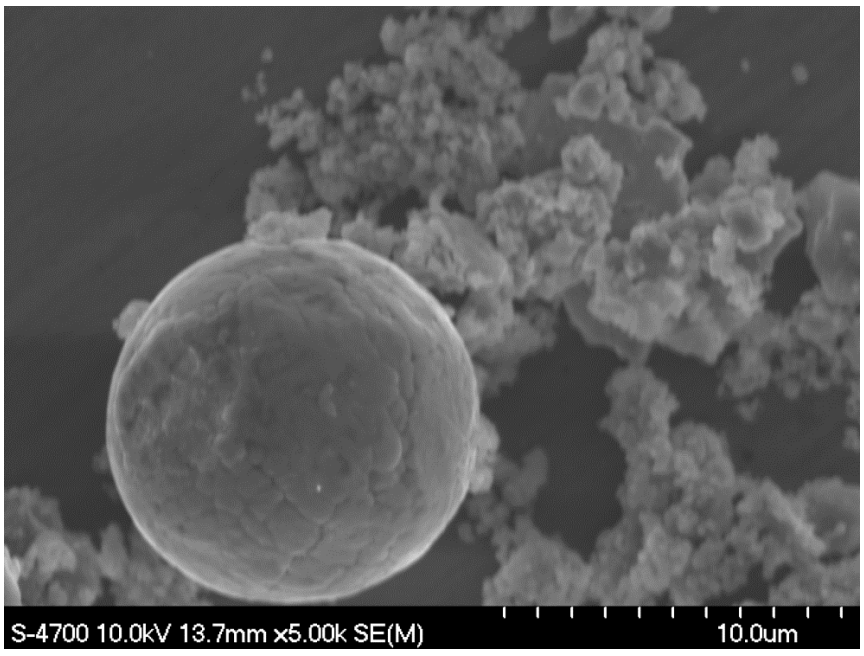

Figure 10.17: SEM Micrographs showing wear debris generated at 60N load, (a) TiC-30 vol. % 316L (b) TiC-30 vol. % 410L cermets. The morphology of the wear debris suggests a combination of 3-body and adhesive wear mechanism.

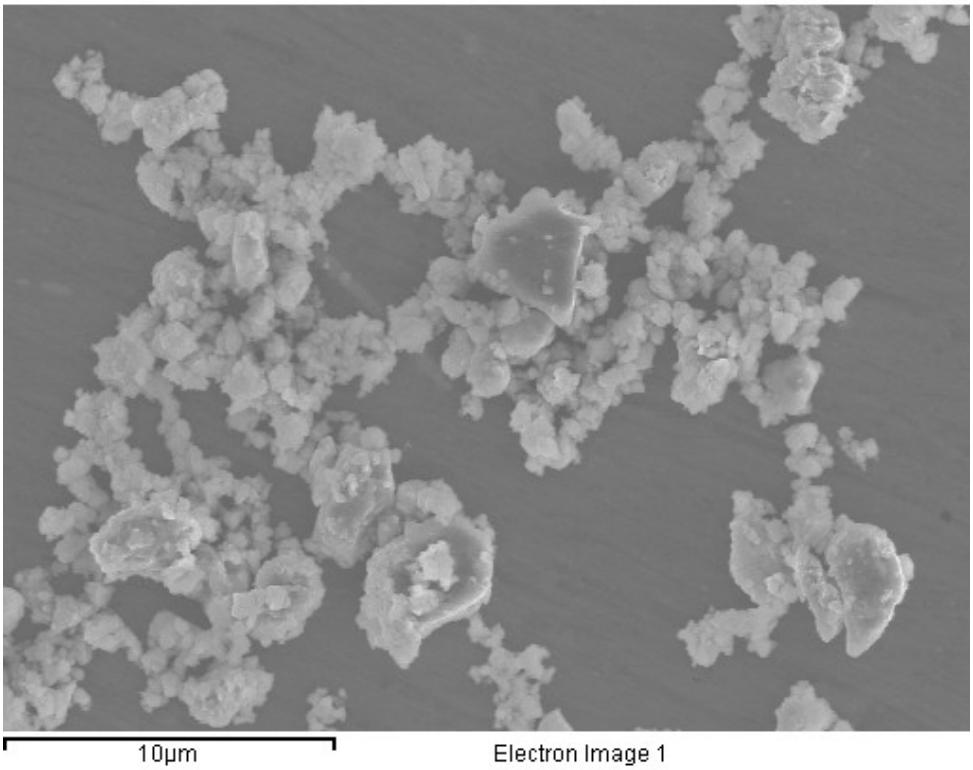

Figure 10.18: A representative EDS image of wear debris generation of TiC-30 vol. % 316L, after dry sliding for 120 minutes under 80N load (analysis shown in Table 10.3). It is apparent that the morphology of the wear debris changed (compared with Figure 10.17a at 60N load) at higher load from spherical to coarser, plate-like and irregular structure inferring the change of wear mechanisms at different loads.

Table 10.4: An example of the wear debris generation determined using EDS (analysis of Figure 10.18), for TiC- 30 vol. % 316L, after dry sliding for 120 minutes under 80N load. The wear debris contains cermets elements as well as WC from counter face sphere.

Element(Line)	Weight %	Atomic %
C (K)	11.26	25.02
O (K)	27.97	46.68
Ti (K)	22.67	12.64
Cr (K)	3.36	1.72
Fe (L)	22.38	10.70
Ni (L)	3.35	1.52
Mo (L)	0.58	0.16
W(M)	7.40	1.08

(a)

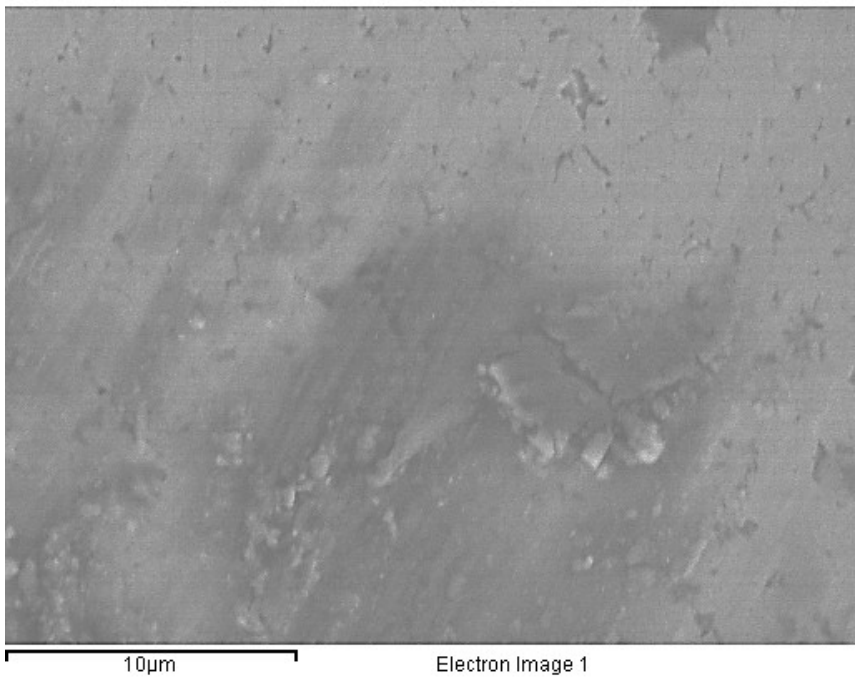

(b)

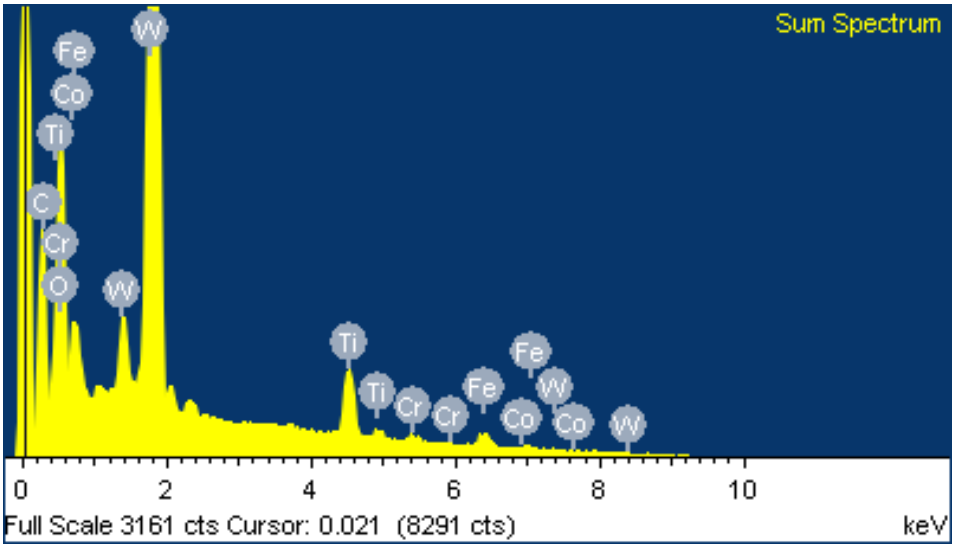

Figure 10.19: EDS analysis on wear scar of WC-6Co counter face sphere used on TiC-30 vol. % 410L, after dry sliding for 120 minutes under 80N load. (a) EDS image of the WC-6Co counter face sphere (b) Spectral analysis of the counter face sphere(shown in a). It is apparent that there is mutual transfer of material from cermet material to the WC-6Co counter face sphere (and vice-versa).